

transactions of the ASME

Published Quarterly by
The American Society of
Mechanical Engineers
Volume 94 • Series C • Number 2
MAY 1972

Journal of heat transfer

EDITORIAL STAFF

Editor, **J. J. JAKLITSCH, JR.**
Production Editor, **JIM MOBLEY**

HEAT TRANSFER DIVISION

Chairman, **W. H. COOK**
Secretary, **R. W. GRAHAM**
Senior Technical Editor, **W. H. GIEDT**
Technical Editor, **L. H. BACK**
Technical Editor, **J. C. CHEN**
Technical Editor, **A. E. BERGLES**

POLICY BOARD, COMMUNICATIONS

Chairman and Vice-President
JAMES O. STEPHENS

Members-at-Large
P. G. HODGE, JR.
J. De S. COUTINHO
M. ALTMAN
W. G. CORNELL

Policy Board Representatives

Basic, **J. W. HOLL**
General Engineering, **W. R. LARSON**
Industry, **G. P. ESCHENBRENNER**
Power, **G. P. COOPER**
Research, **E. L. DAMAN**
Codes and Stds., **W. H. BYRNE**
Nom. Com. Rep., **H. A. NAYLOR, JR.**

Business Staff
345 E. 47th St.
New York, N. Y. 10017
212/752-6800

Dir., Com., **C. O. SANDERSON**
Production Manager,
GERTRUDE KELLER

OFFICERS OF THE ASME

President, **KENNETH A. ROE**
Exec. Dir. & Sec'y, **ROGERS B. FINCH**
Treasurer, **HENRY N. MULLER, JR.**

CONSULTANT

O. B. SCHIER, II

EDITED and PUBLISHED quarterly at the offices of The American Society of Mechanical Engineers, United Engineering Center, 345 E. 47th St., New York, N. Y. 10017. Cable address, "Mechanear," New York. Second-class postage paid at New York, N. Y., and at additional mailing offices.

CHANGES OF ADDRESS must be received at Society headquarters seven weeks before they are to be effective. Please send old label and new address.

PRICES: To members, \$15.00, annually; to nonmembers, \$30.00. Single copies, \$10.00 each. Add \$1.50 for postage to countries outside the United States and Canada.

STATEMENT from By-Laws. The Society shall not be responsible for statements or opinions advanced in papers or . . . printed in its publications (B13, Par. 4).

COPYRIGHT 1972 by The American Society of Mechanical Engineers. Reprints from this publication may be made on condition that full credit be given the TRANSACTIONS OF THE ASME, SERIES C—JOURNAL OF HEAT TRANSFER, and the author and date of publication stated.

INDEXED by the Engineering Index, Inc.

- 129 **Cryo-Immunology: Surgical Approach and Thermal Regimen for Freezing the Elements of the Male Rabbit Reproductive System (70-WA/HT-17)**
E. Zappi and S. Shulman
- 132 **Abstract of: Preservation of Blood Components at Cryogenic Temperatures (70-WA/HT-20)**
Arthur W. Rowe
- 133 **A Probe Technique for Determining the Thermal Conductivity of Tissue (70-WA/HT-18)**
T. E. Cooper and G. J. Trezek
- 141 **Cryo-Immunology: The Antigenic Properties of the Male Rabbit Reproductive System as Studied by Selective Freezing of Its Components (70-WA/HT-19)**
S. Shulman and E. Zappi
- 144 **The Influence of Electric Fields on Convective Heat and Mass Transfer from a Horizontal Surface under Forced Convection**
S. E. Sadek, R. G. Fax, and M. Hurwitz
- 149 **Mathematical and Experimental Modeling of the Circulation Patterns in Glass Melts (70-WA/HT-11)**
J. J. Noble, L. A. Clomburg, A. F. Sarofim, and H. C. Hottel
- 155 **Heat and Mass Transfer in the Vicinity of the Vapor-Gas Front in a Gas-Loaded Heat Pipe (71-WA/HT-29)**
D. K. Edwards and B. D. Marcus
- 163 **Thermal Effects of Power Plants on Lakes**
F. K. Moore and Y. Jaluria
- 169 **The Effect of Lateral Rod Displacement on Laminar-Flow Transfer**
Chia-Jung Hsu
- 174 **Experimental Investigation of Heat Transfer from Partially Ionized Argon with an Applied Transverse Magnetic Field (based on 70-HT/SPT-43)**
E. J. Roschke
- 181 **Volume Interchange Factors for Nonhomogeneous Gases (based on 71-HT-19)**
D. K. Edwards and A. Balakrishnan
- 189 **Fundamental and Higher-Mode Density-Wave Oscillations in Two-Phase Flow (based on 71-HT-13)**
G. Yadigaroglu and A. E. Bergles
- 196 **Optimization of a Heat Pipe with a Wick and Annulus Liquid Flow (71-HT-V)**
H. Hwang-Bo and W. E. Hilding
- 203 **Improved Point-Matching Techniques Applied to Multi-Region Heat Transfer Problems (71-HT-T)**
D. M. France and T. Ginsberg
- 211 **Developing Flow with Combined Forced-Free Convection in an Isothermal Vertical Tube (71-HT-6)**
B. Zeldin and F. W. Schmidt
- 224 **An Experimental and Analytical Study of Radiative and Conductive Heat Transfer in Molten Glass (based on 70-WA/HT-10)**
N. D. Eryou and L. R. Glicksman
- TECHNICAL BRIEFS**
- 231 **Impingement Heat-Transfer Rates from Torch Flames**
E. H. Schulte
- 233 **Thermal and Combined Entry Problems for Laminar Flow between Parallel Porous Plates**
John R. Doughty and Henry C. Perkins, Jr.
- 234 **Some Remarks on Thermoconvective Instability in Completely Confined Regions**
P. A. Jennings and R. L. Sani
- 236 **Explosive Vapor Formation**
P. Groenvelt
- 238 **Evaporation from a Semi-infinite Region with a Nonvolatile Solute**
K. R. Chun

(Contents continued on page 140)

CONTENTS

(CONTINUED)

- 240 **Forced Heat Transfer over Thin Needles**
Jai Prakash Narain and Mahinder S. Uberoi
- 242 **Turbulent-Boundary-Layer Measurements along a Supersonic Nozzle with and without Wall Cooling**
Lloyd H. Back and Robert F. Cuffel
- 244 **Response of Finite-Thickness Gardon Heat-Flux Sensors**
Robert H. Kirchhoff
- 245 **Radiation and Convection Heat Transfer from an Internally Heated Slab, Cylinder, or Sphere**
F. C. Wessling, Jr.
- 246 **Interfacial Shear Stress in Annular-Mist Condensing Flow**
M. R. Berry, Jr. and W. P. Goss
- 248 **The Vapor Shear Boundary Condition for Laminar Film Condensation**
V. South III and V. E. Denny
- 249 **Thermal Conductivity of Two-Phase Systems**
Pradeep B. Deshpande and James R. Couper
- 251 **On the Freezing of Tissue**
T. E. Cooper and G. J. Trezek
- 254 **Discussion of previously published papers**

E. ZAPPI

Research Associate Professor.

S. SHULMAN

Professor.

Department of Microbiology,
New York Medical College,
New York, N. Y.

Cryo-Immunology: Surgical Approach and Thermal Regimen for Freezing the Elements of the Male Rabbit Reproductive System

The destructive freezing of living tissue often stimulates the host animal to produce antibodies against its own tissue. This phenomenon, the expression of an autoimmune process, is currently employed in this laboratory for exploring the antigenic properties of the male rabbit reproductive system. In this paper, the anatomic features of this reproductive system are briefly described. Details are offered of the surgical techniques used to approach these organs, and of the thermal regimes used in the destructive freezing of the target tissues.

Introduction

THE DESTRUCTION of some tissue in a living animal may elicit an immune response. This phenomenon is primarily related to the presence of antigenic substances in these tissues. When the destructive process occurs, these antigens are liberated from their natural, cellular location, and after entering the lymphatic or the blood circulation they meet some elements of the immune system of the host animal. A reaction is thus started whose result is the immune response, in the form either of circulating antibodies or of histologic changes, or of a combination of both features. Since in this particular case the antigens which elicit the immune response are components of the host animal, they are called "autoantigens," and the immune response is correspondingly called an "autoimmune" response.

The study of autoantigenic stimulation and autoimmune response presents a matter of great theoretical and even practical interest. The male rabbit reproductive system offers several important advantages as an experimental model for these studies:

1 This system is known to possess autoantigenic properties [1, 2],¹ and the damage of some of its components often stimulates the host animal toward the production of such an immune response [3-5].

2 The anatomic components of this system are quite isolated, and some of them can be individually stimulated, provided that precise enough techniques are available.

¹ Numbers in brackets designate References at end of paper.

Contributed by the Heat Transfer Division and presented at the Winter Annual Meeting, New York, N. Y., November 29-December 3, 1970, of THE AMERICAN SOCIETY OF MECHANICAL ENGINEERS. Manuscript received by the Heat Transfer Division August 17, 1970; revised manuscript received April 5, 1971. Paper No. 70-WA/HT-17.

3 The reproductive system is not a vital one, so that damage of its components will not endanger the life of the host animal so much as damage of the nervous system or of the kidney, for instance, would do.

For the experimental production of tissue lesions, freezing techniques can be used with great advantages; the ice formation leads to intensive damage with cell disruption and necrosis but with very mild, if any, denaturation [6, 7].

In this paper, the surgical approaches used in the analysis of the antigenic properties of the male rabbit reproductive system will be briefly described. Details are offered of some of the freezing schedules used for the cryostimulation of these organs.

Materials and Methods

Anatomic Considerations. In these studies, male adult New Zealand White rabbits were used. The reproductive system of this animal is composed, besides some minor elements, of four major intra-abdominal organs (seminal vesicle, coagulating gland, prostate gland, and bulbo-urethral gland) and two extra-abdominal paired organs located in the scrotum (testis and epididymis) (Fig. 1).

According to the situation of these organs, two principal surgical approaches can be used to reach them: the abdominal and the inguinal. The abdominal approach is primarily used for the seminal vesicle and the coagulating gland (Fig. 2), although the testes and the epididymis can also be reached through it. The inguinal approach (Fig. 3) is specifically used in unilateral operations on the latter two organs. A third, perineal, approach for reaching the lowest of the abdominal organs, i.e., the bulbo-urethral gland, is still under study.

Cryosurgical Considerations. The goal of the cryosurgical process is the destruction of target tissue through physical changes induced by the formation of ice crystals. Two mechanisms should

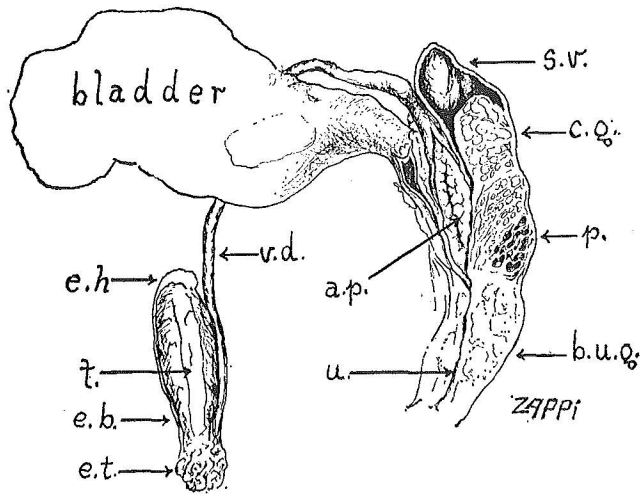


Fig. 1 Anatomic elements of the reproductive system of the male domestic rabbit; a.p. = ampullar portion of the vas deferens; b.u.g. = bulbourethral gland; c.g. = coagulating gland; e.b. = body of the epididymis; e.h. = head of the epididymis; e.t. = tail of the epididymis; p. = prostate gland; s.v. = seminal vesicle; t. = testis; v.d. = vas deferens; u. = urethra; reprinted with permission of *Cryogenics in Surgery*

be mentioned in regard to the destructive effect of freezing. According to some of their thermal characteristics, these are called the "rapid cooling-slow rewarming" and the "slow cooling" mechanisms [8].

The sequence of events known as rapid cooling-slow rewarming occurs when an initial thermal descent of more than 100 deg C is produced in the target tissue in the first minute of the cooling phase. In this condition, in addition to the extracellular ice formation, which is the general feature observed in every tissue freezing, intracellular ice formation also occurs. The intracellular, very small-sized crystals grow, if the rewarming of the tissues proceeds at low enough rates, to much larger size, in a process called "granular" or "migratory" recrystallization. These new crystals damage the intracellular structures mechanically, before melting, and thus produce cellular death [9].

When the thermal descent in the target tissue occurs at rates lower than 100 deg C in the first minute, only extracellular ice crystals are produced. This is followed by a shift of water from the intracellular compartment to the interstitial space. The solution remaining in the interior of the cell becomes more and more concentrated, and acquires a pH value widely different from the normal one, and this induces irreversible damage to the vital cell structures.

Since thermal descents of more than 100 deg C in the first minute can be induced only in the tissue zone very close to the thermal sink (even when operating with liquid-nitrogen-fed devices), it is assumed that the tissue damage produced during cryosurgery is related to the slow cooling mechanism.

It has been observed that the most effective damaging temperatures lie between -5 and -50 deg C. The -5 deg C level corresponds to the point at which ice formation, and therefore the first damaging event, occurs in the tissues. The -50 deg C limit for the freezing damage should be related to the physical changes which occur below the eutectic temperature.

Freezing Techniques and Control of the Thermal Changes. In the freezing experiments performed in this laboratory, a CE-2 Linde cryosurgical unit and cryoprobes of various types connected to it were used. The cryounit was operated with liquid nitrogen and permitted one to set temperatures in a range of 37 to -196 deg C for the desired time intervals [10]. The cryoprobe used most often was the straight round-tipped one, called the PR-2 probe, whose shaft has a diameter of 4.72 mm. The tip of the probe was firmly applied to the tissue by a support rack; its tip constituted the heat sink in the thermal experiment.

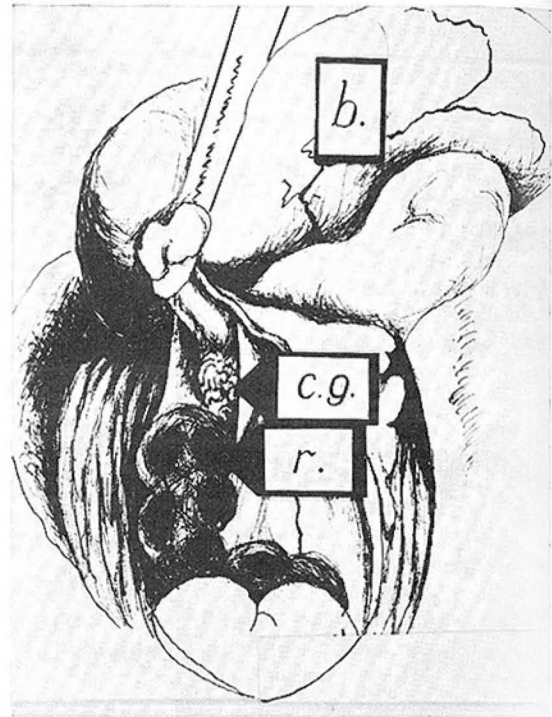


Fig. 2 Abdominal approach to some of the male rabbit accessory reproductive organs; the bladder (b.) is displaced from the abdominal cavity; the seminal vesicle is grasped with a forceps; immediately below, the coagulating gland (c.g.) is seen; r. = rectum

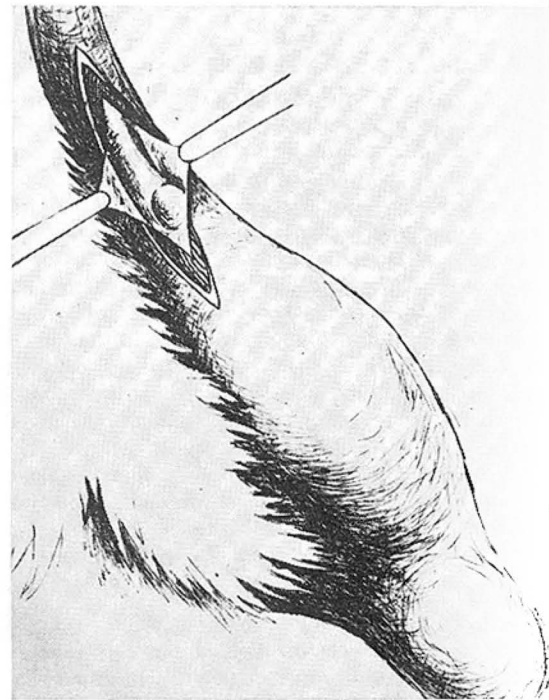


Fig. 3 Inguinal approach to the rabbit testis and epididymis; the left inguinal canal is open and its walls are grasped with forceps; the spermatic cord and the superior pole of the testis are visible in the cavity

In former cryo-immunologic trials performed in this laboratory, the freezing technique consisted of rapid cooling of the tissues to the lowest desired temperature and allowing a gradual rewarming by setting the cryounit at progressively higher levels until the body temperature was regained. Freezing schedules based on this technique produced rather diffuse changes with ill-defined

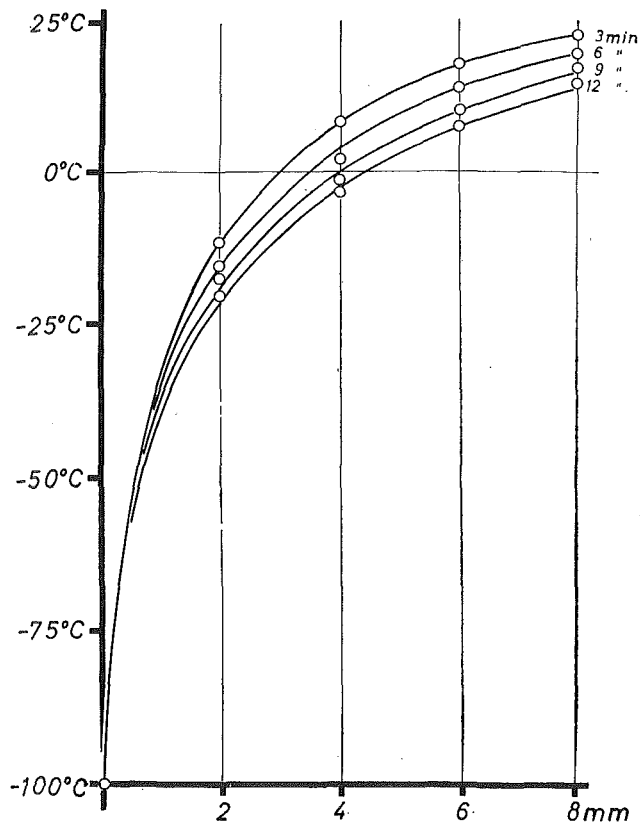


Fig. 4 Temperature gradients from 0 to 8 mm from the wall of the probe (corresponding to the coordinate axis), at 3, 6, 9, and 12 min when cooling living rabbit muscle with the PR-2 cryoprobe at -180 deg C

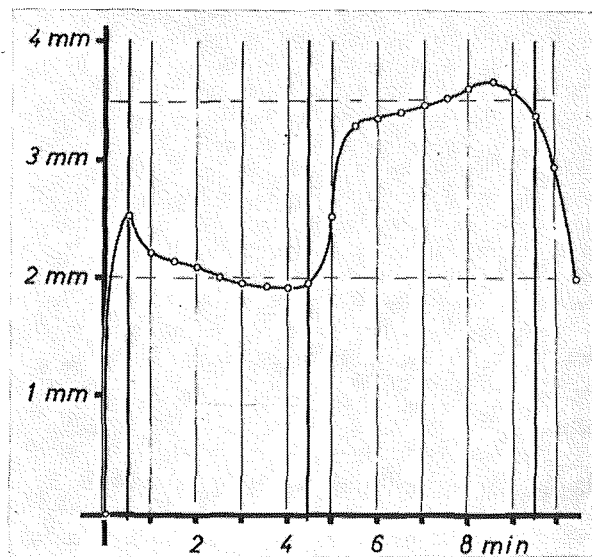


Fig. 5 Displacement of the freezing boundary (-5 deg C isotherm) from the wall of the cryoprobe (represented by the coordinate axis) when cooling living rabbit muscle with the $(-160/0.5) + (-40/4.0) + (-80/4.0)$ schedule, using the PR-2 cryoprobe; reprinted with permission of Cryobiology

limits in the target tissue and histologic damage of changing intensity. Despite the continuous monitoring of the temperature during freezing by thermocouples placed around the target area, damage in the neighboring organs was produced and death of the animals often occurred.

After the experimental studies of the temperature changes induced in the tissues by different cooling regimes, this technique was replaced by another one of much simpler features. This one,

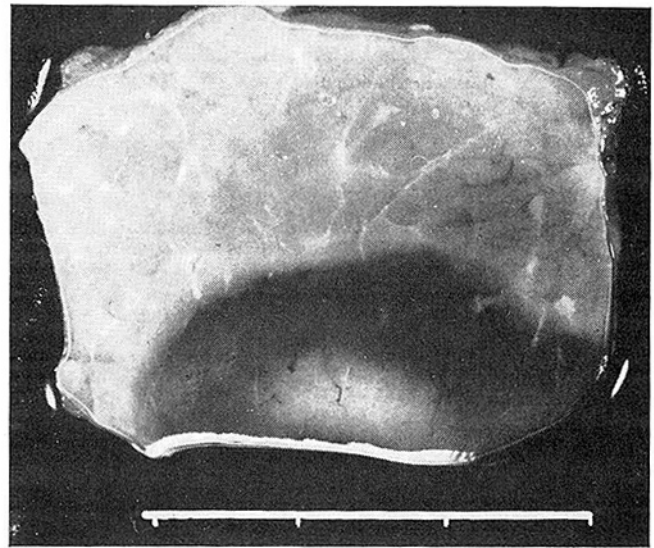


Fig. 6 Median section of the cryolesion produced on living rabbit muscle under the condition mentioned in Fig. 5; the animal was injected with a 2 percent Evans blue solution intravenously, in order to facilitate the visualization of the lesion; in the core of the lesion, a massive zone of necrosis is seen (pale zone); this zone is delimited by a ring of deeply stained but not necrotic tissue; one division on the scale = 10 mm

on which the freezing schedules presently used in this laboratory are based, consists of setting particular temperatures in the cryo-unit which are empirically known to expand and stabilize the freezing front at specific distances around the heat sink. When the period of time necessary to injure the target tissue has elapsed, the cryogenic unit is turned off, or it may be set at a lower temperature in order to expand the freezing injury to another point. The rewarming phase is considered a noncritical one in the production of the cryoinjury, and therefore is allowed to proceed spontaneously from the heat flow of the surrounding tissues, once the cryogenic unit is turned off.

The freezing schedule based on this technique that is used most often is a combination of two 4-min freezing periods, the first one at -40 and the second one at -80 deg C. When the PR-2 probe is used, the freezing boundary is successively moved to 2.0 and 3.5 mm from the wall of the probe. Intensive and sharply delimited damage is produced in the treated area which reaches a final diameter of 11.7 mm including that of the probe. This schedule, called schedule No. 2, is initiated by a brief period of intensive cooling ($1/2$ min at -160 deg C) with the purpose of obtaining a firm mechanical attachment of the tip of the probe to the target area. For practical purposes it is abbreviated as: $(-160/0.5) + (-40/4.0) + (-80/4.0)$. Since the expansion of the frozen zone is predetermined, no monitoring of the thermal changes is necessary.

Results

Fig. 4 shows temperature gradients in the target tissue at several moments during a cooling procedure. The thermal data (means of three similar experiments) used for drawing the curves were obtained from thermocouples placed at 2, 4, 6, and 8 mm from the wall of the probe.

Fig. 5 shows the displacement of the freezing boundary in the target tissue, when freezing living rabbit muscle with PR-2 and schedule $(-160/0.5) + (-40/4.0) + (-80/4.0)$.

Fig. 6 shows the actual cryolesion produced in living rabbit muscle which was frozen as explained above. The diameter of the necrotic zone corresponds actually to that one of 11.7 mm mentioned in the section on Freezing Techniques and Control of the Thermal Changes and gives a total volume of killed tissue of about 0.5 cm³.

Acknowledgments

The authors wish to thank Miss Barbara Flouton and Mr. Thomas Byro for excellent technical assistance. This study was supported by a research grant from the John A. Hartford Foundation, Inc.

References

- 1 Shulman, S., Yantorno, C., Barnes, G., Gonder, M. J., Soanes, W. A., and Witebsky, E., "Studies on Autosensitization to Prostatic Tissue and Related Tissues," *Annals of the New York Academy of Sciences*, Vol. 124, 1965, pp. 279-291.
- 2 Shulman, S., *Tissue Specificity*, Springer-Verlag, Berlin, 1971, in press.
- 3 Yantorno, C., Gonder, M. J., Soanes, W. A., and Shulman, S., "The Freezing of Tissues during Surgery and the Production of Antibodies," *Federation Proceedings*, Vol. 25, 1966, p. 731.
- 4 Yantorno, C., Soanes, W. A., Gonder, M. J., and Shulman, S., "Studies in Cryo-Immunology. I. The Production of Antibodies to Urogenital Tissues in Consequence of Freezing Treatment," *Immunology*, Vol. 12, 1967, pp. 395-410.
- 5 Shulman, S., Yantorno, C., and Bronson, P., "Cryo-Immunology: A Method of Autoimmunization to Autologous Tissue," *Proceedings of the Society for Experimental Biology and Medicine*, Vol. 124, 1967, pp. 658-661.
- 6 Lovelock, J. E., "Denaturation of Lipid-Protein Complexes as Cause of Damage by Freezing," *Proceedings of the Royal Society, Section B*, Vol. 147, 1957, pp. 427-433.
- 7 Pennell, R. B., "Low-Temperature Preservation of Proteins," *Federation Proceedings*, Vol. 24, Supp. 15, pp. S269-272.
- 8 Leibo, S. P., Farrant, J., Mazur, P., Hanna, M. G., Jr., and Smith, L. H., "Effects of Freezing on Marrow Stem Cells Suspensions: Warming Rates in the Presence of PVP, Sucrose or Glycerol," *Cryobiology*, Vol. 6, 1970, pp. 315-332.
- 9 Zappi, E., and Shulman, S., "Cryo-Immunization. The Cold Propagation in the Target Tissue and the Resulting Volume of the Lesion," *Cryobiology*, Vol. 8, 1971, pp. 235-243.
- 10 Garamy, G., "Engineering Aspects of Cryosurgery," in: *Cryosurgery*, Rand, R. W., Rinfret, A. P., and von Leden, H., eds., Thomas Publ., Springfield, Ill., 1968, pp. 92-123.

Preservation of Blood Components at Cryogenic Temperatures¹

Dr. Arthur W. Rowe

New York Blood Center, New York, N. Y.

Abstract

The application of cryogenic technology to medical problems has resulted in the development of methods for freeze-preserving two of the cellular components of blood. Cryopreservation of different cell types, e.g., nucleated leukocytes and non-nucleated erythrocytes, cannot be achieved successfully unless techniques designed to prevent cellular damage induced by freezing are used. Unprotected cells can, depending upon the rate of freezing, be damaged in a variety of ways, principally through dehydration, solute effects, and ice-crystal formation. When cryoprotective compounds, such as glycerol, DMSO, etc. are used and the cooling rate is controlled, cell damage can be circumvented, however. A slow cooling rate with an intracellular additive has been found better for preserving nucleated white blood cells, whereas very rapid freezing techniques have in general proven more successful for preserving non-nucleated red blood cells for transfusion. Ultra-rapid freezing of blood in the form of droplets is a useful means of preserving red cells for blood-group studies. Storage and prolonged preservation of biological specimens have been more successful at cryogenic temperatures (e.g., -196 deg C) than at higher storage temperatures (e.g., -85 deg C).

¹ This work was supported by research grants from the National Heart and Lung Institute, NIH, HE-09011, and Union Carbide Corp.

Contributed by the Heat Transfer Division and presented at the Winter Annual Meeting, New York, N. Y., November 29–December 3, 1970, of THE AMERICAN SOCIETY OF MECHANICAL ENGINEERS. Manuscript received by the Heat Transfer Division August 17, 1970; revised manuscript received April 5, 1971. Paper No. 70-WA/HT-20. A partial reproduction of the complete paper 70-WA/HT-20, the abstract of which appears here, may be found in *Mechanical Engineering*, Vol. 93, No. 5, May 1971, pp. 37–42.

T. E. COOPER

Assistant Professor,
Department of Mechanical Engineering,
Naval Postgraduate School,
Monterey, Calif.
Assoc. Mem. ASME

G. J. TREZEK

Associate Professor,
Department of Mechanical Engineering,
Thermal Systems Division,
University of California,
Berkeley, Calif.
Mem. ASME

A Probe Technique for Determining the Thermal Conductivity of Tissue

A small needle-like probe has been developed for the determination of the thermal conductivity of either in-vitro or in-vivo tissue. This probe consists of a copper cylinder having a diameter of 1.5 mm and a length of 22.5 mm. Constantan and copper leads are attached to the center and top of the cylinder, respectively, and as a consequence the probe acts as a thermocouple. The distinguishing characteristic of this probe is that when it is suddenly embedded into a medium at a different temperature, the duration of its temperature-time response is such that it can be related to the thermal properties of the medium. This is accomplished by a match with an analytically determined response curve which accounts for metabolic heat generation, blood flow, and conductive effects. By nondimensionalizing the governing equations for the probe-tissue system, three nondimensional groups for time, temperature, and blood flow emerge. The results of a parametric study of these effects are presented in tabular form. Initially, the probe technique was used to determine the thermal conductivity of a 1 percent agar-water mixture and the results were within 5 percent of water. Subsequently, experimental thermal-conductivity data were obtained on the following in-vitro human organs: liver, kidney, heart, spleen, whole brain, brain gray matter, and brain white matter. In addition, density, specific-heat, and water-content measurements were also obtained on these organs. In-vivo conductivity data have recently been obtained for canine liver with and without blood flow. These data indicate that the in-vivo value without blood flow is approximately the same as the in-vitro value after the organ had been removed and refrigerated for 24 hr. Blood flow, if not considered, resulted in apparent conductivities which were 15 to 25 percent higher than that of the tissue.

Introduction

IN GENERAL, a biological medium, *in-vivo* tissue, contains metabolic heat generation and heat addition or removal by the blood supply due to tissue vascularity. Consequently, the prediction of steady-state and transient temperature fields and heat flows requires not only a knowledge of these parameters but also a knowledge of the thermal properties of the medium itself, namely, the thermal conductivity (k) or the thermal diffusivity ($\kappa = k/\rho c$), where ρ is the density and c the heat capacity. Due to both the *in-vivo* condition and the nature of biological matter, even in its *in-vitro* state, thermal-property determinations of tissue are generally not made using the classical techniques which are satisfactory for common materials. However, a thermal-conductivity cell apparatus which resembled the hot-plate approach was used by Ponder [1]¹ and Poppendiek [2] in their thermal-property measurements.

¹ Numbers in brackets designate References at end of paper.

Contributed by the Heat Transfer Division and presented at the Winter Annual Meeting, New York, N. Y., November 29-December 3, 1970, of THE AMERICAN SOCIETY OF MECHANICAL ENGINEERS. Manuscript received by the Heat Transfer Division August 17, 1970; revised manuscript received April 5, 1971. Paper No. 70-WA/HT-18.

Various types of probing techniques have been developed for obtaining thermal properties of biological materials. One technique involves measuring the temperature field induced in the media by the probe and then deducing the properties of the medium by matching the field data with the appropriate governing equation [3]. Other techniques require either measuring both the probe surface temperature and the temperature at a point in the field, or controlling the probe heat flux and using these measurements to ultimately deduce the properties [4, 5]. The thermal-inertia method, which yields the group $k\rho c$, has been used [6] for determining the properties of *in-vivo* intact human skin.

Previous experiences [3, 7] with the field-matching technique have shown it to be somewhat error-prone in that the relative positioning of the field thermocouples becomes critical. This is due to the fact that biological tissue has a relatively low thermal diffusivity (as that of water), and the size of the tissue specimen is on the order of several millimeters; thus the thermocouples must be positioned close to the probe if a transient field is to be obtained in a reasonable length of time. In addition, the data analysis and analytical field computations, which must be carried out parametrically for a range of property values and then matched to the data, are time-consuming and costly.

Consequently, a probe which can be easily inserted or implanted

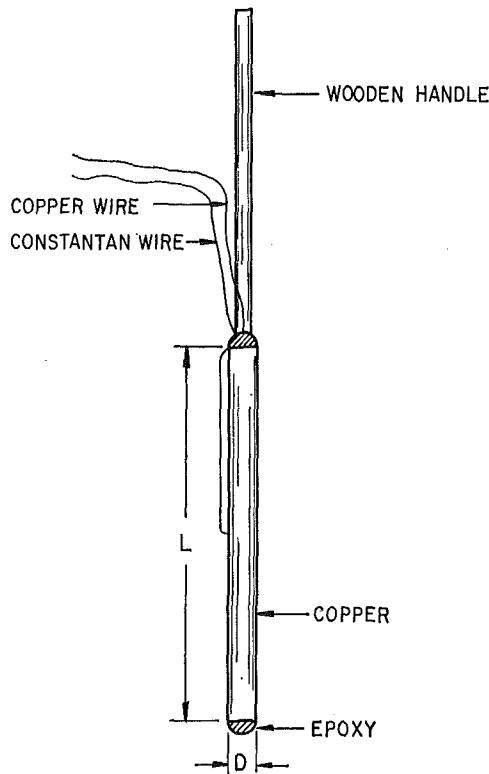


Fig. 1 Needle-probe assembly

in a biological medium and not require additional thermocouples in the medium would be ideally suited for thermal-property measurements. A spherical probing technique, in which a temperature difference is maintained between the probe surface and a thermocouple in the field, was developed and used by Grayson [4]. This technique was sophisticated by Chato [5] and applied in an *in-vitro* situation. Both probes require initial calibration with materials of known properties. Additional circuitry is required for heating and accurately controlling the probe surface temperature.

The so-called "needle probe" was developed for the determination of both *in-vivo* and *in-vitro* tissue thermal properties (Fig. 1). In essence, this probe is a needle-like copper cylinder which acts as a thermocouple when a junction with a constantan wire is created at its center. The probe, which has an initial temperature different than the tissue's, can be easily and rapidly inserted into the tissue. The thermal properties of the medium can be deduced by studying the resulting probe temperature-time response. The distinguishing characteristic of the needle probe is that it has a response time which is quite large compared to the response time of a typical thermocouple. It is this lengthy response time which forms the basis of the thermal-property

determination. A discussion of the theory and application of this probing technique follows.

Theoretical Model

In-vivo tissue, unlike other media, has blood continuously flowing through it as well as internal heat generation due to metabolism. Perl [8-10] has suggested that the energy equation take the form

$$\nabla \cdot (k \nabla T) + \dot{m}_b c_b (T_b - T) + S_m = \rho c \frac{\partial T}{\partial t} \quad (1)$$

when applied to biological systems.

The effect of blood flow is accounted for by the term $\dot{m}_b c_b (T_b - T)$ in equation (1). T_b is the temperature of the blood as it enters a small region of tissue and T is the temperature as it leaves the region. Equating the exiting blood temperature to the temperature of the tissue in the region is equivalent to assuming that heat is exchanged between the tissue and the blood with 100 percent efficiency. This assumption seems reasonable when one considers the micron distances involved in the capillaries and the small blood flow velocities on this level. T_b will, in general, have a value that is between the systemic arterial blood temperature and the local tissue temperature. As such, it may be a function of both position and time. To obtain analytical solutions, however, T_b is generally treated as a constant. Similarly, \dot{m}_b may also be a function of temperature, time, and position. It, too, is generally treated as a constant, which may be taken to be the average blood flow rate over a certain temperature range. The assumptions of constant T_b and \dot{m}_b cause the blood flow term to behave as a volumetric heat source (or sink) which is directly proportional to temperature.

The effect of metabolism on energy transport through tissue appears as a term S_m in equation (1). It, also, may be a function of temperature, time, and position. Again, however, to facilitate analysis it is treated as a constant.

Equation (1) is the general equation that is used to describe the temperature change induced in a biological tissue as a result of suddenly embedding the needle probe in the tissue. In order to obtain an analytical solution to the problem, the following assumptions are made: The probe is at a uniform temperature T_{p0} different than the initial tissue temperature T_0 . The probe is infinite in extent in the axial direction. The tissue is homogeneous and infinite in extent. There is no contact resistance between the probe and the tissue. The probe is a perfect conductor of heat since it has a small diameter and is made from high-thermal-conductivity material. All properties are constant. T_b is equal to the systemic arterial blood temperature. S_m is constant.

When cylindrical coordinates are introduced and the above assumptions invoked, equation (1) takes the form

$$\frac{k}{r} \frac{\partial (r \frac{\partial T}{\partial r})}{\partial r} + \dot{m}_b c_b (T_b - T) + S_m = \rho c \frac{\partial T}{\partial t} \quad (2)$$

Nomenclature

A = probe surface area, cm^2
 c = specific heat of tissue, cal/gm-deg C
 c' = specific heat of probe, cal/gm-deg C
 c_b = specific heat of blood, cal/gm-deg C
 k = thermal conductivity, cal/cm-deg C-sec
 κ = thermal diffusivity, cm^2/sec
 \dot{m}_b = blood mass flow rate, gm/cc-sec
 r = radial position in field, cm

r_0 = probe radius, cm
 R = nondimensional radius (r/r_0)
 S_m = metabolic heat-generation rate, cal/cc-sec
 t = time, sec
 T = temperature of tissue, deg C
 T_b = temperature of blood, deg C
 T_0 = temperature of tissue far from probe, deg C
 T_p = temperature of probe, deg C
 T_{p0} = initial probe temperature, deg C
 u = dummy variable of integration
 V = probe volume, cm^3

ρ = density of tissue, gm/cc
 ρ' = probe density, gm/cc
 α = ratio of volume heat capacities ($2\rho c/\rho' c'$), nondimensional
 β = blood flow parameter ($\dot{m}_b c_b r_0^2/k$), nondimensional
 τ = Fourier number ($\kappa t/r_0^2$), nondimensional
 θ = nondimensional tissue temperature $(T - T_0)/(T_{p0} - T_0)$
 θ_p = nondimensional probe temperature $(T_p - T_0)/(T_{p0} - T_0)$

Table 1 Probe temperature (θ_p) versus time (τ) and blood flow (β) for volumetric heat capacity (α) equal to 2.0

τ	β	0.00	0.05	0.10	0.15	0.20	0.25	0.50	1.00
0.0	1.0000	1.0000	1.0000	1.0000	1.0000	1.0000	1.0000	1.0000	1.0000
0.1	0.5137	0.5131	0.5125	0.5119	0.5112	0.5105	0.5010	0.4098	
0.2	0.4010	0.3998	0.3987	0.3974	0.3962	0.3949	0.3829	0.2945	
0.3	0.3352	0.3335	0.3318	0.3301	0.3283	0.3264	0.3123	0.2270	
0.4	0.2902	0.2881	0.2859	0.2837	0.2814	0.2792	0.2632	0.1811	
0.5	0.2569	0.2544	0.2517	0.2491	0.2465	0.2438	0.2264	0.1475	
0.6	0.2311	0.2281	0.2251	0.2214	0.2191	0.2162	0.1975	0.1220	
0.7	0.2103	0.2069	0.2036	0.2003	0.1970	0.1937	0.1741	0.1020	
0.8	0.1931	0.1894	0.1858	0.1822	0.1787	0.1751	0.1547	0.0859	
0.9	0.1786	0.1747	0.1708	0.1669	0.1632	0.1594	0.1383	0.0729	
1.0	0.1662	0.1620	0.1579	0.1538	0.1498	0.1459	0.1243	0.0622	
1.1	0.1556	0.1511	0.1467	0.1425	0.1383	0.1342	0.1123	0.0533	
1.2	0.1462	0.1415	0.1369	0.1325	0.1282	0.1239	0.1018	0.0458	
1.3	0.1379	0.1330	0.1283	0.1237	0.1192	0.1148	0.0925	0.0395	
1.4	0.1306	0.1255	0.1205	0.1158	0.1112	0.1067	0.0844	0.0342	
1.5	0.1240	0.1187	0.1136	0.1087	0.1040	0.0995	0.0771	0.0297	
1.6	0.1181	0.1126	0.1073	0.1024	0.0976	0.0930	0.0706	0.0258	
1.7	0.1127	0.1070	0.1017	0.0966	0.0917	0.0870	0.0648	0.0225	
1.8	0.1078	0.1019	0.0965	0.0913	0.0864	0.0817	0.0596	0.0196	
1.9	0.1033	0.0973	0.0917	0.0865	0.0815	0.0767	0.0549	0.0171	
2.0	0.0991	0.0931	0.0874	0.0820	0.0770	0.0722	0.0506	0.0150	
3.0	0.0709	0.0639	0.0576	0.0519	0.0467	0.0421	0.0239	0.0042	
4.0	0.0552	0.0476	0.0411	0.0355	0.0305	0.0264	0.0120	0.0013	
5.0	0.0452	0.0373	0.0308	0.0256	0.0210	0.0174	0.0063	0.0004	
6.0	0.0383	0.0302	0.0238	0.0188	0.0149	0.0117	0.0034	0.0001	
7.0	0.0332	0.0250	0.0189	0.0142	0.0107	0.0081	0.0019	0.00004	
8.0	0.0293	0.0211	0.0152	0.0109	0.0079	0.0057	0.0010	0.00001	
9.0	0.0263	0.0180	0.0124	0.0085	0.0058	0.0040	0.0006	0.000004	

Table 2 Probe temperature (θ_p) versus time (τ) and blood flow (β) for volumetric heat capacity (α) equal to 2.1

τ	β	0.00	0.05	0.10	0.15	0.20	0.25	0.50	1.00
0.0	1.0000	1.0000	1.0000	1.0000	1.0000	1.0000	1.0000	1.0000	1.0000
0.1	0.5000	0.4994	0.4988	0.4982	0.4975	0.4968	0.4889	0.4099	
0.2	0.3875	0.3863	0.3851	0.3839	0.3827	0.3814	0.3710	0.2937	
0.3	0.3225	0.3208	0.3191	0.3174	0.3157	0.3139	0.3012	0.2260	
0.4	0.2784	0.2763	0.2741	0.2719	0.2697	0.2675	0.2531	0.1801	
0.5	0.2459	0.2434	0.2408	0.2382	0.2357	0.2331	0.2171	0.1467	
0.6	0.2208	0.2178	0.2149	0.2120	0.2091	0.2062	0.1890	0.1213	
0.7	0.2006	0.1973	0.1941	0.1909	0.1877	0.1845	0.1663	0.1013	
0.8	0.1840	0.1804	0.1769	0.1734	0.1699	0.1665	0.1475	0.0854	
0.9	0.1701	0.1662	0.1624	0.1586	0.1550	0.1513	0.1318	0.0725	
1.0	0.1582	0.1541	0.1500	0.1461	0.1422	0.1384	0.1183	0.0618	
1.1	0.1480	0.1436	0.1393	0.1352	0.1311	0.1272	0.1067	0.0530	
1.2	0.1390	0.1344	0.1299	0.1256	0.1214	0.1173	0.0966	0.0456	
1.3	0.1311	0.1263	0.1216	0.1172	0.1128	0.1086	0.0878	0.0394	
1.4	0.1240	0.1190	0.1142	0.1096	0.1052	0.1009	0.0800	0.0341	
1.5	0.1177	0.1126	0.1076	0.1029	0.0984	0.0940	0.0731	0.0296	
1.6	0.1120	0.1067	0.1016	0.0968	0.0922	0.0878	0.0669	0.0257	
1.7	0.1069	0.1014	0.0962	0.0913	0.0866	0.0821	0.0614	0.0224	
1.8	0.1022	0.0966	0.0913	0.0862	0.0815	0.0770	0.0564	0.0196	
1.9	0.0979	0.0922	0.0868	0.0817	0.0769	0.0723	0.0519	0.0171	
2.0	0.0940	0.0881	0.0826	0.0775	0.0726	0.0681	0.0478	0.0149	
3.0	0.0672	0.0604	0.0543	0.0489	0.0440	0.0395	0.0225	0.0042	
4.0	0.0523	0.0450	0.0388	0.0334	0.0288	0.0248	0.0113	0.0013	
5.0	0.0429	0.0353	0.0291	0.0239	0.0197	0.0162	0.0059	0.0004	
6.0	0.0363	0.0286	0.0225	0.0177	0.0139	0.0110	0.0032	0.0001	
7.0	0.0315	0.0236	0.0178	0.0134	0.0100	0.0076	0.0017	0.00004	
8.0	0.0278	0.0199	0.0143	0.0103	0.0074	0.0053	0.0009	0.00001	
9.0	0.0249	0.0170	0.0116	0.0080	0.0055	0.0037	0.0005	0.000004	

with boundary conditions

$$T_p = T \quad \text{at} \quad r = r_0$$

$$\rho'c'V \frac{dT}{dt} = kA \frac{\partial T}{\partial r} \quad \text{at} \quad r = r_0$$

$$T \rightarrow T_0 \quad \text{as} \quad r \rightarrow \infty$$

and initial conditions

$$T_p = T_{p0} \quad \text{at} \quad t = 0$$

$$T = T_0 \quad \text{at} \quad t = 0$$

Equation (2) and its boundary and initial conditions may be cast in nondimensional form by introducing the following set of quantities:

$$\theta_p = \frac{T_p - T_0}{T_{p0} - T_0}, \quad \theta = \frac{T - T_0}{T_{p0} - T_0}, \quad T_0 = T_b + \frac{S_m}{\dot{m}_b c_b}, \quad R = \frac{r}{r_0},$$

$$\beta = \frac{\dot{m}_b c_b r_0^2}{k}, \quad \alpha = \frac{2\rho c}{\rho'c'}, \quad \tau = \frac{\kappa t}{r_0^2}, \quad \kappa = \frac{k}{\rho c}$$

When these quantities are substituted in equation (2), it takes the form

$$\frac{1}{R} \frac{\partial(R \partial\theta/\partial R)}{\partial R} - \beta\theta = \frac{\partial\theta}{\partial\tau} \quad (3)$$

with boundary conditions

$$\theta = \theta_p \quad \text{at} \quad R = 1$$

$$\frac{d\theta_p}{d\tau} = \alpha \frac{\partial\theta}{\partial R} \quad \text{at} \quad R = 1$$

$$\theta \rightarrow 0 \quad \text{as} \quad R \rightarrow \infty$$

and initial conditions

$$\theta_p = 1 \quad \text{at} \quad \tau = 0$$

$$\theta = 0 \quad \text{at} \quad \tau = 0$$

With the differential equation cast in the form of equation (3), it is seen that blood flow enters into the equation as a nondimen-

sional blood flow parameter β . It is interesting to note that β has a geometry factor contained in it, r_0^2 , and as such is strongly dependent on the size of the probe. This suggests that the blood flow term will influence the response rate of a large probe to a much greater extent than a small probe. This has important design implications depending on whether one wishes to experience a large blood flow effect or to make this effect negligible. Physically β may be interpreted as a ratio of convective effects due to blood flow, $\dot{m}_b c_b r_0$, and conductive effects, k/r_0 .

It should also be noted that S_m does not appear explicitly in equation (3) but has been accounted for by adjusting the reference temperature from T_b to T_0 through the relationship $T_0 = T_b + S_m/\dot{m}_b c_b$.

The solution to equation (3), with the appropriate boundary and initial conditions, is obtained using the standard Laplace transformation technique. The details of the solution may be found in reference [11]. It is found that the nondimensional probe temperature is given by

$$\theta_p = \frac{4\alpha e^{-\beta\tau}}{\pi^2} \int_0^\infty \frac{e^{-ru^2} du}{u\Delta(u)} \quad (4)$$

where

$$\Delta(u) = \{(u + \beta/u)J_0(u) - \alpha J_1(u)\}^2 + \{(u + \beta/u)Y_0(u) - \alpha Y_1(u)\}^2$$

and J_0, J_1, Y_0, Y_1 are Bessel functions and u is a dummy variable of integration.

Equation (4) gives the probe temperature, in nondimensional form, as a function of the nondimensional physical parameters of the system (α, β, τ). It is not possible to integrate the expression under the integral exactly, so a numerical integration was performed using Simpson's rule. The results of these integrations are presented in tabular form in Tables 1-6. The values of α that were examined are those in the range of biological interest. In particular, since the volumetric heat capacity of the probe is that of copper ($\rho'c' = 0.818$ cal/cm³-deg C), and since biological tissues have a volumetric heat capacity that is approximately that of water, α 's in the range of 2.0 to 2.5 were examined in increments of 0.1. For each value of α the probe response rate was examined for eight values of β : 0.00, 0.05, 0.10, 0.15, 0.20, 0.25, 0.50, and 1.00.

Table 3 Probe temperature (θ_p) versus time (τ) and blood flow (β) for volumetric heat capacity (α) equal to 2.2

τ	β	0.00	0.05	0.10	0.15	0.20	0.25	0.50	1.00
0.0	1.0000	1.0000	1.0000	1.0000	1.0000	1.0000	1.0000	1.0000	1.0000
0.1	0.4868	0.4862	0.4856	0.4850	0.4844	0.4837	0.4770	0.4087	
0.2	0.3747	0.3735	0.3724	0.3712	0.3699	0.3687	0.3594	0.2919	
0.3	0.3106	0.3089	0.3073	0.3055	0.3038	0.3021	0.2906	0.2242	
0.4	0.2674	0.2653	0.2631	0.2610	0.2588	0.2566	0.2433	0.1786	
0.5	0.2357	0.2332	0.2307	0.2281	0.2256	0.2231	0.2082	0.1454	
0.6	0.2113	0.2084	0.2055	0.2026	0.1998	0.1969	0.1809	0.1202	
0.7	0.1918	0.1885	0.1853	0.1822	0.1790	0.1759	0.1589	0.1004	
0.8	0.1757	0.1722	0.1687	0.1653	0.1619	0.1586	0.1408	0.0846	
0.9	0.1623	0.1585	0.1548	0.1511	0.1475	0.1440	0.1256	0.0718	
1.0	0.1509	0.1468	0.1429	0.1390	0.1352	0.1315	0.1126	0.0613	
1.1	0.1410	0.1367	0.1326	0.1285	0.1246	0.1207	0.1015	0.0525	
1.2	0.1324	0.1279	0.1235	0.1194	0.1153	0.1113	0.0918	0.0452	
1.3	0.1248	0.1201	0.1156	0.1113	0.1071	0.1030	0.0834	0.0390	
1.4	0.1180	0.1132	0.1085	0.1041	0.0998	0.0956	0.0760	0.0338	
1.5	0.1120	0.1070	0.1022	0.0976	0.0932	0.0890	0.0693	0.0293	
1.6	0.1066	0.1014	0.0965	0.0918	0.0874	0.0831	0.0634	0.0255	
1.7	0.1017	0.0963	0.0913	0.0866	0.0820	0.0777	0.0581	0.0222	
1.8	0.0972	0.0917	0.0866	0.0818	0.0772	0.0728	0.0534	0.0194	
1.9	0.0931	0.0875	0.0823	0.0774	0.0728	0.0684	0.0491	0.0169	
2.0	0.0893	0.0837	0.0784	0.0734	0.0687	0.0643	0.0452	0.0149	
3.0	0.0638	0.0573	0.0514	0.0462	0.0415	0.0373	0.0212	0.0042	
4.0	0.0497	0.0427	0.0367	0.0315	0.0271	0.0233	0.0106	0.0013	
5.0	0.0407	0.0334	0.0275	0.0226	0.0186	0.0153	0.0055	0.0004	
6.0	0.0345	0.0271	0.0212	0.0167	0.0131	0.0103	0.0030	0.0001	
7.0	0.0299	0.0224	0.0168	0.0126	0.0094	0.0071	0.0016	0.00004	
8.0	0.0264	0.0189	0.0135	0.0097	0.0069	0.0049	0.0009	0.00001	
9.0	0.0237	0.0161	0.0110	0.0075	0.0051	0.0035	0.0005	0.000004	

Table 5 Probe temperature (θ_p) versus time (τ) and blood flow (β) for volumetric heat capacity (α) equal to 2.4

τ	β	0.00	0.05	0.10	0.15	0.20	0.25	0.50	1.00
0.0	1.0000	1.0000	1.0000	1.0000	1.0000	1.0000	1.0000	1.0000	1.0000
0.1	0.4623	0.4617	0.4611	0.4604	0.4598	0.4592	0.4539	0.4031	
0.2	0.3513	0.3501	0.3490	0.3478	0.3466	0.3454	0.3374	0.2858	
0.3	0.2890	0.2874	0.2857	0.2840	0.2824	0.2807	0.2706	0.2188	
0.4	0.2476	0.2444	0.2434	0.2413	0.2392	0.2371	0.2253	0.1739	
0.5	0.2175	0.2150	0.2125	0.2101	0.2076	0.2052	0.1919	0.1414	
0.6	0.1944	0.1915	0.1888	0.1860	0.1832	0.1805	0.1661	0.1168	
0.7	0.1760	0.1729	0.1698	0.1668	0.1638	0.1608	0.1455	0.0976	
0.8	0.1610	0.1576	0.1543	0.1510	0.1478	0.1446	0.1286	0.0822	
0.9	0.1485	0.1449	0.1413	0.1378	0.1344	0.1311	0.1144	0.0698	
1.0	0.1380	0.1340	0.1302	0.1266	0.1230	0.1195	0.1024	0.0596	
1.1	0.1287	0.1247	0.1207	0.1169	0.1132	0.1096	0.0921	0.0511	
1.2	0.1208	0.1165	0.1124	0.1084	0.1046	0.1009	0.0832	0.0440	
1.3	0.1138	0.1093	0.1051	0.1010	0.0970	0.0932	0.0754	0.0380	
1.4	0.1076	0.1030	0.0986	0.0944	0.0903	0.0864	0.0686	0.0329	
1.5	0.1020	0.0973	0.0927	0.0884	0.0843	0.0804	0.0625	0.0286	
1.6	0.0970	0.0922	0.0875	0.0831	0.0789	0.0750	0.0571	0.0249	
1.7	0.0925	0.0875	0.0828	0.0783	0.0741	0.0701	0.0523	0.0217	
1.8	0.0884	0.0833	0.0785	0.0739	0.0697	0.0656	0.0480	0.0189	
1.9	0.0847	0.0795	0.0745	0.0699	0.0656	0.0616	0.0441	0.0166	
2.0	0.0813	0.0759	0.0709	0.0663	0.0619	0.0579	0.0406	0.0145	
3.0	0.0580	0.0519	0.0465	0.0416	0.0373	0.0334	0.0189	0.0041	
4.0	0.0451	0.0386	0.0331	0.0283	0.0243	0.0208	0.0094	0.0012	
5.0	0.0370	0.0303	0.0248	0.0203	0.0166	0.0136	0.0049	0.0004	
6.0	0.0314	0.0245	0.0191	0.0149	0.0117	0.0091	0.0026	0.0001	
7.0	0.0272	0.0203	0.0151	0.0113	0.0084	0.0063	0.0014	0.00004	
8.0	0.0240	0.0171	0.0122	0.0086	0.0061	0.0044	0.0008	0.00001	
9.0	0.0215	0.0146	0.0099	0.0067	0.0046	0.0031	0.0004	0.000004	

Jaeger [12] has solved a similar problem for a probe embedded in an infinite medium with no heat sources or sinks and also presents a table of θ_p vs. τ over a broad range of α . Jaeger's table of θ_p vs. τ is in exact agreement with the values presented here for the case of $\beta = 0$ and $\alpha = 2.0$ (the only values that could be compared with Jaeger).

Experimental Probing Technique

Several probes were constructed and tested on a 1 percent agar-water mixture before tests were conducted on tissue. In addition to developing the actual physical probing technique, tests were run on the mixture to ascertain the minimum length-to-diameter ratio, L/D , necessary to produce results that would be compatible with the theoretical assumption that the probe is in-

Table 4 Probe temperature (θ_p) versus time (τ) and blood flow (β) for volumetric heat capacity (α) equal to 2.3

τ	β	0.00	0.05	0.10	0.15	0.20	0.25	0.50	1.00
0.0	1.0000	1.0000	1.0000	1.0000	1.0000	1.0000	1.0000	1.0000	1.0000
0.1	0.4743	0.4737	0.4731	0.4725	0.4719	0.4712	0.4653	0.4064	
0.2	0.3627	0.3615	0.3604	0.3592	0.3580	0.3567	0.3482	0.2892	
0.3	0.2995	0.2978	0.2961	0.2944	0.2928	0.2910	0.2803	0.2218	
0.4	0.2571	0.2550	0.2529	0.2508	0.2487	0.2465	0.2341	0.1765	
0.5	0.2263	0.2237	0.2212	0.2188	0.2163	0.2138	0.1998	0.1436	
0.6	0.2025	0.1996	0.1968	0.1940	0.1912	0.1884	0.1733	0.1186	
0.7	0.1836	0.1804	0.1773	0.1742	0.1711	0.1681	0.1519	0.0991	
0.8	0.1681	0.1646	0.1612	0.1579	0.1546	0.1513	0.1345	0.0835	
0.9	0.1551	0.1514	0.1478	0.1442	0.1407	0.1373	0.1198	0.0709	
1.0	0.1441	0.1401	0.1363	0.1325	0.1289	0.1253	0.1074	0.0605	
1.1	0.1346	0.1304	0.1264	0.1225	0.1186	0.1149	0.0967	0.0519	
1.2	0.1263	0.1220	0.1177	0.1136	0.1097	0.1059	0.0874	0.0446	
1.3	0.1190	0.1145	0.1101	0.1059	0.1018	0.0979	0.0793	0.0386	
1.4	0.1126	0.1079	0.1033	0.0990	0.0948	0.0908	0.0721	0.0334	
1.5	0.1068	0.1019	0.0973	0.0928	0.0886	0.0845	0.0658	0.0290	
1.6	0.1016	0.0966	0.0918	0.0873	0.0830	0.0788	0.0601	0.0252	
1.7	0.0969	0.0917	0.0869	0.0822	0.0779	0.0737	0.0551	0.0220	
1.8	0.0926	0.0873	0.0824	0.0777	0.0732	0.0691	0.0506	0.0192	
1.9	0.0887	0.0833	0.0782	0.0735	0.0690	0.0648	0.0465	0.0168	
2.0	0.0851	0.0796	0.0745	0.0697	0.0652	0.0609	0.0428	0.0147	
3.0	0.0607	0.0544	0.0488	0.0438	0.0393	0.0352	0.0199	0.0042	
4.0	0.0473	0.0406	0.0348	0.0299	0.0256	0.0220	0.0100	0.0012	
5.0	0.0388	0.0318	0.0260	0.0214	0.0175	0.0144	0.0052	0.0004	
6.0	0.0328	0.0257	0.0201	0.0158	0.0124	0.0097	0.0028	0.0001	
7.0	0.0285	0.0213	0.0159	0.0119	0.0089	0.0067	0.0015	0.00004	
8.0	0.0252	0.0179	0.0128	0.0090	0.0065	0.0046	0.0008	0.00001	
9.0	0.0226	0.0153	0.0104	0.0070	0.0048	0.0033	0.0005	0.000004	

Table 6 Probe temperature (θ_p) versus time (τ) and blood flow (β) for volumetric heat capacity (α) equal to 2.5

τ	β	0.00	0.05	0.10	0.15	0.20	0.25	0.50	1.00
0.0	1.0000	1.0000	1.0000	1.0000	1.0000	1.0000	1.0000	1.0000	1.0000
0.1	0.4507	0.4501	0.4496	0.4489	0.4483	0.4477	0.4429	0.3990	
0.2	0.3405	0.3393	0.3382	0.3370	0.3358	0.3346	0.3272	0.2819	
0.3	0.2792	0.2755	0.2759	0.2743	0.2726	0.2709	0.2613	0.2154	
0.4	0.2386	0.2365	0.2345	0.2324	0.2303	0.2283	0.2170	0.1710	
0.5	0.2092	0.2068	0.2044	0.2019	0.1996	0.1972	0.1845	0.1390	
0.6	0.1868	0.1840	0.1823	0.1786	0.1759	0.1732	0.1594	0.1147	
0.7	0.1690	0.1659	0.1629	0.1599	0.1570	0.1541	0.1394	0.0958	
0.8	0.1545	0.1511	0.1479	0.1447	0.1416	0.1385	0.1230	0.0807	
0.9	0.1424	0.1388	0.1353	0.1319	0.1286	0.1254	0.1094	0.0685	
1.0	0.1322	0.1284	0.1247	0.1211	0.1176	0.1142	0.0978	0.0585	
1.1	0.1233	0.1194	0.1155	0.1118	0.1081	0.1046	0.0879	0.0501	
1.2	0.1157	0.1115	0.1075	0.1036	0.0999	0.0963	0.0794	0.0432	
1.3	0.1089	0.1046	0.1005	0.0965	0.0926	0.0889	0.0719	0.0373	
1.4	0.1030	0.0985	0.0942	0.0901	0.0862	0.0824	0.0653	0.0323	
1.5	0.0976	0.0930	0.0886	0.0844	0.0804	0.0766	0.0595	0.0281	
1.6	0.0929	0.0881	0.0836	0.0793	0.0753	0.0714	0.0544	0.0244	
1.7	0.0885	0.0837	0.0791	0.0747	0.0706	0.0667	0.0498	0.0213	
1.8	0.0846	0.0796	0.0749	0.0705	0.0664	0.0625	0.0457	0.0186	
1.9	0.0810	0.0759	0.0712	0.0667	0.0625	0.0586	0.0419	0.0163	
2.0	0.0777	0.0725	0.0677	0.0632	0.0590	0.0551	0.0386	0.0143	

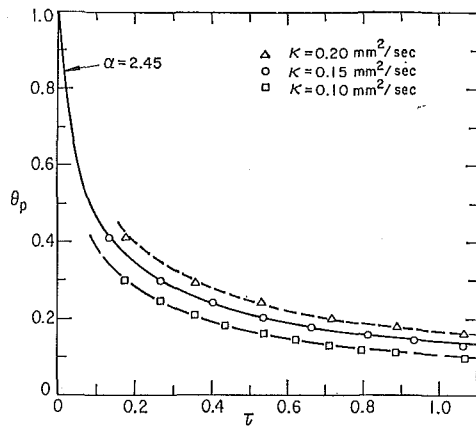


Fig. 2 Probe temperature response versus nondimensional times for a 1.5-mm-dia probe in a 1 percent agar-water mixture

generated by a copper-constantan thermocouple experiencing a temperature change of 20 deg C is about 0.79 mv. The probe was quickly plunged into the center of a 1000-cc beaker containing the 1 percent agar-water mixture. Extreme care was taken to embed the probe up to the plane where the wood-dowel handle joined the copper, but not past this plane. Total insertion time was estimated to be on the order of 0.1 sec. Immediately after the probe had been inserted, the handle was released and the probe was allowed to cool to the temperature of the mixture. The total response time of the 2.56-mm-dia probe was on the order of 3 min with over 90 percent of the temperature change occurring in the first 25 sec.

The experimentally generated response curves of the 2.56-mm-dia probes with varying L/D ratios were matched to the analytically generated curve, equation (4), to produce the thermal diffusivity of the agar-water mixture. The following results were obtained:

Run number	$L/D = 25$ $\kappa \left(\frac{\text{mm}^2}{\text{sec}} \right)$	$L/D = 20$ $\kappa \left(\frac{\text{mm}^2}{\text{sec}} \right)$	$L/D = 15$ $\kappa \left(\frac{\text{mm}^2}{\text{sec}} \right)$
1	0.144	0.151	0.153
2	0.144	0.152	0.154
3	0.145	0.150	0.155

These results show that the probe with the length-to-diameter ratio of 25 yields results which are within 2.5 percent of the diffusivity of the mixture (0.141 mm²/sec). The probes with the L/D ratios of 20 and 15 give diffusivity values which differ by 7 and 9 percent, respectively.

Unfortunately, in experimental animals, such as cats and dogs, many of the major organs have characteristic lengths which are smaller than 38.4 mm, i.e., the length of the 2.56-mm-dia probe with an L/D ratio of 15. For instance, a cat brain has a characteristic length in the vertical direction of about 25 mm [13]. If

the brain characteristic length is used as a constraint on the total length of the probe, it is obvious that a smaller-diameter probe must be used. An additional constraint on the probe size is that the probe diameter must be large enough to produce a response time which can be accurately recorded. With these two constraints in mind, a probe was constructed with a diameter of 1.5 mm and a length of 22.5 mm and was tested on a 1 percent agar-water mixture.

The diffusivity results obtained with the 1.5-mm-dia probe were in a range of 0.143 to 0.148 mm²/sec which is in better agreement with the mixture diffusivity than those obtained with the 2.56-mm-dia probe with a similar L/D ratio.

The sensitivity of the probing technique to changes in diffusivity can be shown by plotting experimental data versus nondimensional time τ for different values of the thermal diffusivity. This has been done in Fig. 2 for experimental data obtained with the 1.5-mm-dia probe. Three separate sets of nondimensional time were generated using actual time and assumed values of diffusivity equal to 0.10, 0.15, and 0.20 mm²/sec. It should be noted that while the curve generated for a diffusivity equal to 0.15 mm²/sec (the value obtained using the standard data-reduction method) fits the analytical curve almost exactly, curves corresponding to diffusivity values of 0.10 and 0.20 mm²/sec are displaced from the actual curve by amounts varying from 15 to 20 percent, depending on which portion of the transient is examined. This indicates that the technique is quite sensitive to changes in diffusivity.

Results

Experimental Results on *In-Vitro* Human Organs. Experiments were conducted on *in-vitro* human heart, kidney, liver, spleen, whole brain, brain gray matter, and brain white matter to determine the density, specific heat, water content, and thermal diffusivity of these organs. This portion of the experimental study was conducted at the Kaiser Hospital, Oakland, Calif., in the Department of Pathology. The following cases were tested:

Case number	Sex	Age	Cause of death	Race	Hours dead
1	male	66	coronary	Caucasian	15
2	female	66	cancer of pancreas	Caucasian	14
3	male	66	leukemia	Caucasian	14
4	male	83	postoperative bowel obstruction	Caucasian	16
5	male	83	coronary	Caucasian	19
6	male	59	cancer of esophagus	Caucasian	21
7	female	84	coronary	Caucasian	18
8	male	59	coronary	Caucasian	16

Density was measured using a simple water-displacement technique. The organ was cut into 5-gram sections and placed in a 100-cc graduated cylinder. A Mettler precision scale, with an accuracy of 0.1 gm, was used to weigh the tissue and cylinder without water and then the tissue and cylinder filled with water

Table 7 Thermal properties of *in-vitro* human organs

Organ	Number of Runs	Density (gm/cm ³)	Heat Capacity (cal/gm °C)	% Water	Thermal Diffusivity (cm ² /sec x 10 ⁵)	Thermal Conductivity (cal/cm sec °C x 10 ⁵)
Kidney	8	1.05	0.93	84	132 (11.7)*	130
Heart	5	1.06	0.89	81	148 (9.9)	140
Spleen	6	1.05	0.89	80	138 (15.1)	130
Liver	10	1.05	0.86	77	150 (10.0)	135
Brain, White	21	1.04	0.86	71	134 (10.1)	120
Brain, Gray	10	1.05	0.88	83	143 (9.1)	135
Brain, Whole	22	1.05	0.88	78	138 (10.7)	126

*Standard deviation of the runs.

to the 100-cc level. The volume of the tissue was obtained by subtracting the water volume, which is equivalent to the mass of the conglomerate minus the mass of the tissue, from 100 cc. The tissue density was then determined by dividing the mass of the tissue by its volume. The results of the density measurements are presented in Table 7.

Specific-heat measurements on the various organs were made with a Perkin-Elmer differential scanning calorimeter (DSC). The calorimeter measures the quantity of heat necessary to raise, or lower, the temperature of a known mass of material at a predetermined rate. The method is of a differential nature in that the quantity of heat which is actually measured is the difference between the heat required to raise the temperature of a sample and the aluminum container in which it is placed and a separate empty aluminum container. A 0.1307-gm sapphire, of known specific heat, is used as a standard. The material which is to be tested is run in the calorimeter and its heating curve is compared to a similar curve for the sapphire. The specific heat of the material is then obtained by comparing the two curves.

For the organ specific-heat determinations, a typical tissue sample was on the order of 0.0200 gm. This is in contrast to the 30 or 40 gm that were used in the density determinations. A Mettler high-precision scale, which was accurate to within 0.0001 gm, was used to measure the tissue mass. To prevent evaporation from occurring during the transient portion of the test, the DSC was run in a cooling mode, starting at 25 deg C and scanning to 0 deg C at a rate of 10 deg C/min. The samples were weighed before and after the test and in all cases there was less than 1 percent loss of mass. Since the calorimeter was scanning toward an ever lower temperature, it is believed that none of the loss occurred during the cooling transient. To give an indication of the accuracy of the technique, the specific heat of a small aluminum sample was measured and found to have a value of 0.21 cal/gm-deg C which is in agreement with the referenced value of 0.208 cal/gm-deg C [14]. Tissue specific-heat results are presented in Table 7.

Water-content measurements were also made on the various organs. The percent of water in each organ was determined by comparing the mass of a "wet" tissue sample with the mass of the dehydrated tissue sample. These results are also presented in Table 7.

The 1.5-mm-dia probe, with an L/D ratio of 15, was used to determine the thermal-diffusivity values of the organs. The organs were removed from the cadaver, sectioned into 100-gm samples, and placed in individual plastic containers which were then refrigerated for 12 hr to a uniform temperature of approximately 5 deg C. After the organ sections had cooled, they were probed in exactly the same manner as the agar-water mixture.

The tissue accepted the probe with ease and closed tightly around it. In fact, when the probe was removed from the tissue, it was very difficult to ascertain where it had been placed as the hole created by the probe quickly closed. The total response time of the 1.5-mm-dia probe, when used on human organs, was always less than 90 sec.

Three different sets of property values were obtained for brain tissue, namely those for white matter, gray matter, and whole brain. If the cerebrum of the brain is sectioned, it is possible to isolate large regions of white matter. This was done and probings were made on these regions. Isolating a large section of gray matter proved more difficult. However, it was found that if the cerebellum was sectioned properly, a region of gray matter which was sufficiently large to completely accept the probe could be exposed. The gray-matter data were obtained from this region. Data on whole brain were obtained by inserting the probe into regions where there appeared to be an intermixing of gray and white matter.

In order to reduce the experimental data and obtain thermal-diffusivity values for an organ, it is necessary to specify a value of the volumetric specific-heat parameter α of the organ. This was accomplished by using the density, ρ , and specific-heat, c , values obtained on each of the organs. The thermal-diffusivity results are summarized in Table 7.

Experimental Results on In-Vivo Canine Liver. A series of four experiments was performed on dogs under heavy anesthesia to determine the thermal diffusivity of *in-vivo* tissue and also to study the effect of blood flow on the probe response. In a typical experiment the animal was given 20 mg of Acepromazine tranquilizer, an anesthetic tranquilizer, $1/2$ hr prior to beginning the experiment, and 10 min before the initial incision enough sodium pentobarbital was injected intravenously to render the animal unconscious. The animal was then positioned on its back on the operating table. In these experiments it was decided to concentrate solely on the liver so a single incision was made through the soft tissue of the stomach below the rib cage. Working through this incision, the veterinarian was able to expose the liver enough to allow the 1.5-mm-dia probe to be inserted.

Eight to 10 probings were made during each experiment. A typical experiment lasted for $1\frac{1}{2}$ hr, during which time the animal's body temperature dropped from 37 deg C to approximately 34 deg C. The liver was probed in a variety of locations and was never probed in the same location twice. For some of the probings, the veterinarian forcefully brought the liver partially outside of the animal's body. After each probing, however, the liver was returned to the body cavity and the incision was held closed so as to allow the liver to return to body temperature. Approximately 5 min were allowed between probings. This was con-

Table 8 Apparent thermal properties of *in-vivo* canine liver

Animal	Density (gm/cm ³)	Heat Capacity (cal/gm °C)	% Water	Thermal Diffusivity (Apparent) (cm ² /sec. x 10 ⁻⁵)			Thermal Conductivity (Apparent) (cal/cm.sec °C x 10 ⁻⁵)		
1 male German Shepherd	1.07	0.85	75	166	200	182	149	180	164
				177	239	179	159	215	161
2 female German Shepherd	1.07	0.84	74	183	197	180	165	178	162
				178	169	180	160	152	162
				170	160	150*	153	144	135*
3 male German Shepherd	1.08	0.83	72	180	129	165	162	116	148
				192	152	173	170	137	156
				194	165	193	173	146	173
				183			164		
4 male German Shorthair	1.09	0.83	73	153***	184	157*	138	166	141*
				155***	205	154**	140	184	139**
				172***	189	150**	155	170	135**
				199	178	153**	179	160	138**
				211			190		

*Immediately after expiration.
 **24 hours after expiration.
 ***Liver constricted.

sidered sufficient time as the liver was being perfused with blood from within and was also bathed in body fluids. After several of the probings, profuse bleeding was observed after the probe was removed from the liver, indicating that a large blood vessel was probably punctured.

After completion of the *in-vivo* experiments with blood flow, an overdose of sodium pentobarbital was administered to terminate the animal. Immediately after the cessation of heart activity, the animal's liver was again probed. The results of these probings were still *in-vivo* results as the animal's tissue remains viable for several minutes after the last heartbeat. In some instances, more than one run was made after death. However, after death the animal's ability to maintain a constant body temperature is gone, and the body temperature begins to approach the temperature of its surroundings. As such, large temperature gradients probably develop throughout the body. This is highly undesirable in the probing technique.

The final step in the *in-vivo* experimental procedure was to remove the liver so that postmortem density, specific-heat, and water-content measurements could be made. In the case of experimental animal No. 4, three *in-vitro* thermal-diffusivity measurements were made on liver tissue that had been refrigerated for 24 hr.

The results of the *in-vivo* experiments are presented in Table 8.

Discussion of Results

With the needle-probe technique, it is theoretically possible to determine both the thermal diffusivity and conductivity from a single-probe temperature-time response curve. This is due to the fact that the analytically computed response curves (θ_p vs. τ) all pass through unity (Fig. 2), are parametric with the volumetric heat capacity (ρc), and as a result there is a unique analytical response curve which corresponds to a particular probe response. Thus, since theoretically both diffusivity and volume heat capacity can be obtained uniquely, the conductivity can then be deduced. Unfortunately, for the range of the present experimental data ($0.1 < \theta_p < 0.5$ and $0.1 < \tau < 1$), the analytical response curves appear as being translated within the narrow range of the volumetric-heat-capacity parameter which is of pertinent interest. Consequently, an independent measurement of ρc is necessary.

Values of diffusivity (κ) can be obtained in a straightforward manner by plotting the experimental-probe temperature-time response data on the family of analytical response curves for the particular value of volume heat capacity (ρc) and by selecting the value of κ which yields the best agreement. The entire procedure of probing and plotting the data is quite expedient relative to other thermal-property-determination techniques. The efficiency of reducing the experimental data was increased by employing the following computerized data-reduction scheme. Using the analytical response results given in Tables 1-6, a fifth-order polynomial of the form

$$\tau = a_0 + a_1\theta_p(t) + a_2\theta_p(t)^2 + \dots + a_5\theta_p(t)^5$$

was fitted to the tabular values for 10 separate values of α . The quantity $\theta_p(t)$ is formed from the experimental-probe temperature-time response data by putting in values of $T_p(t)$ vs. t into the program. The proper τ curve is selected by specifying the appropriate volumetric heat capacity, that is, the curve having coefficients corresponding to the value of α consistent with the medium in which the response curve was obtained. Values of τ , and subsequently diffusivity ($\kappa = \tau r_0^2/t$), are then computed for various times in the experimental run. This type of comparison was made for 10 points over the range of τ from 0.1 to 1.0 and the resulting mean value of κ (total dispersion of values generally being less than 5 percent) was taken as being that of the particular medium.

The probing technique and the subsequent analytical temperature-time response determination have been successfully applied

to the measurement of *in-vivo* thermal diffusivity. As previously mentioned in the analytical development, the effect of blood flow, i.e., tissue vascularity, is taken into account through the β parameter ($\beta = \dot{m}_b c_b r_0^2/k$) which includes the blood flow rate \dot{m}_b . Thus, both α and β parameters must be incorporated in the data-matching procedure. If blood flow is not accounted for in equation (4), i.e., if β is taken as zero, the blood flow effect will be contained in an "apparent" diffusivity which is greater than the actual medium diffusivity. Introducing the correct value of β into equation (4) has the effect of separating blood flow effects from conductive effects and as such the true medium diffusivity can be deduced. When the analysis was applied to the *in-vivo* liver measurements, setting the β parameter equal to zero (no blood flow) yielded an average apparent value of thermal diffusivity of 0.173×10^{-2} cm²/sec and average thermal-conductivity values of 0.165×10^{-2} cal/cm-sec-deg C. Using a perfusion rate of 0.02 gm/cm²-sec for liver [15] gives a value of β equal to 0.08 which subsequently yields a value of κ equal to 0.161×10^{-2} cm²/sec and a value of k equal to 0.151×10^{-2} cal/cm-sec-deg C. This perfusion rate is about a factor of two to three too low since allowing β to equal 0.25 yields values of κ and k of 0.151×10^{-2} cm²/sec and 0.144×10^{-2} cal/cm-sec-deg C, respectively, which are consistent with the values of κ and k which were measured in the tissue immediately after the cessation of blood flow.

Since the perfusion rate is a measure of the total amount of blood entering the organ, local variations within the tissue can be expected due to the nonuniform nature of the vascularity within the tissue. The range of values (Table 8) obtained for κ would indicate that the probings were not always performed in a region of uniform or similar blood flow.

During a set of *in-vivo* measurements, which were performed on dog No. 4, the liver was manually constricted so that perfusion was impaired. The apparent conductivities which were obtained ranged between 0.138 to 0.145×10^{-2} cal/cm-sec-deg C which is in good agreement with the immediate after-death (cessation of blood flow) value of 0.141×10^{-2} cal/cm-sec-deg C. In some experiments bleeding was observed to be occurring around the probe. This would increase the temperature-time response of the probe and have the net effect of increasing the apparent thermal diffusivity value.

It is important to note that the apparent *in-vivo* diffusivity and conductivity values are not general, but apply only to the technique used to obtain them. By accounting for blood flow, *in-vivo* property values of the medium may be determined and are of greater utility in that they can be used for general heat-transfer analysis; this is not the case for apparent quantities.

The results obtained on animal No. 4 (Table 8) suggest that *in-vivo* and *in-vitro* thermal-conductivity values of tissue are essentially the same, that is, an *in-vivo* value of 0.141×10^{-2} cal/cm-sec-deg C was obtained compared to values of 0.135×10^{-2} , 0.138×10^{-2} , and 0.139×10^{-2} cal/cm-sec-deg C for refrigerated *in-vitro* tissue. The slight variation between the *in-vivo* and *in-vitro* values can be partially accounted for by the fact that the *in-vivo* value was obtained in a temperature range of 20-37 deg C and the *in-vitro* values in the range 5-20 deg C. If a temperature variation the same as pure water is assumed for tissue thermal conductivity, the *in-vitro* values will have an average value of 0.142×10^{-2} cal/cm-sec-deg C in the range 20-37 deg C. Thus far these results indicate that well-preserved *in-vitro* tissue will exhibit the same thermal properties as its *in-vivo* counterpart. This would imply that tissue thermal-property data obtained on refrigerated *in-vitro* samples of tissue apply to *in-vivo* tissue as well.

The *in-vitro* property values obtained for the canine liver are approximately the same as those of human liver and the water content of both tissues is also similar. These results are in agreement with the theory suggested by Poppendiek [2], namely, that there is a correlation between the water content and thermal properties of tissue.

Acknowledgment

The authors wish to thank Mr. Webster Johnson and Mr. Steve Slaton who assisted in various phases of the data collection and reduction, the staff of the Department of Pathology, Kaiser Hospital, Oakland, Calif., for assistance in collecting the human-property data, and Miss Suz Moore who patiently prepared several revisions of the manuscript.

This work was supported in part by NINDS grant NS-08236-02-NEUA.

References

- 1 Ponder, E., "The Coefficient of Thermal Conductivity of Blood and of Various Tissues," *J. Gen. Physiol.*, Vol. 45, 1962, pp. 545-551.
- 2 Poppendiek, H. F., et al., "Thermal Conductivity Measurements and Predictions for Biological Fluids and Tissues," *Cryobiology*, Vol. 3, No. 4, 1966, pp. 318-327.
- 3 Trezek, G. J., and Cooper, T. E., "Analytical Determination of Cylindrical Source Temperature Fields and Their Relation to Thermal Diffusivity of Brain Tissue," *Thermal Problems in Biotechnology*, ASME, New York, N. Y., 1968, pp. 1-15.
- 4 Grayson, J., "Internal Calorimetry in the Determination of Thermal Conductivity and Blood Flow," *J. Physiol.*, Vol. 118, No. 1, 1952, pp. 52-72.
- 5 Chato, J. C., "A Method for the Measurement of the Thermal Properties of Biological Materials," *Thermal Problems in Biotechnology*, ASME, New York, N. Y., 1968, pp. 16-25.
- 6 Lipkin, M., and Hardy, J. D., "Measurement of Some Thermal Properties of Human Tissues," *J. Appl. Physiol.*, Vol. 7, 1954, p. 212.
- 7 Trezek, G. J., Jewett, D. L., and Cooper, T. E., "Measurements of *In-Vivo* Thermal Diffusivity of Cat Brain," *Proceedings of NBS Seventh Conference on Thermal Conductivity*, Gaithersburg, Md., 1967.
- 8 Perl, W., "Heat and Matter Distribution in Body Tissues and Determination of Tissue Blood Flow by Local Clearance Methods," *Journal of Theoretical Biology*, Vol. 2, 1962, pp. 201-235.
- 9 Perl, W., "An Extension of the Diffusion Equation to Include Clearance by Capillary Blood Flow," *Annals of the New York Academy of Sciences*, Vol. 108, 1963, p. 92.
- 10 Perl, W., and Hirsh, R. L., "Local Blood Flow in Kidney by Heat Clearance Measurement," *Journal of Theoretical Biology*, Vol. 10, 1966, pp. 251-280.
- 11 Cooper, T. E., "Bio-Heat Transfer Studies," PhD thesis, University of California, Berkeley, Calif., March 1970.
- 12 Jaeger, J. C., "Conduction of Heat in an Infinite Region Bounded Internally by a Circular Cylinder of a Perfect Conductor," *Aust. J. Phys.*, Vol. 9, 1956, pp. 167-179.
- 13 Jasper, H. H., and Ajmone-Marson, *A Stereotaxic Atlas of the Diencephalon of the Cat*, The National Research Council of Canada, Ottawa, Canada.
- 14 Weast, R. C., ed., *Handbook of Chemistry and Physics*, 48th ed., The Chemical Rubber Co., Cleveland, Ohio, 1962.
- 15 Spector, W. S., ed., *Handbook of Biological Data*, W. B. Saunders Co., Philadelphia, Pa., 1956.

S. SHULMAN

Professor.

E. ZAPPI

Research Associate Professor.

Department of Microbiology,
New York Medical College,
New York, N. Y.

Cryo-Immunology: The Antigenic Properties of the Male Rabbit Reproductive System as Studied by Selective Freezing of Its Components

Immunologic analysis of antisera and comparative studies of their properties provide important data about the number and the localization of antigens in the various organs of the reproductive system of the rabbit. The advantages of cryostimulation for eliciting immune responses in the reproductive system of the male rabbit are discussed in this paper, and examples are given of the study of such antisera through different immunologic techniques.

Introduction

A FREEZING injury is often an effective stimulus for inducing the treated animal to produce antibodies [1].¹ The injury disrupts histologic structures of the target tissue and liberates cellular components which are then recognized as antigens by the host animal. It can be considered that the stimulus has broken the natural tolerance barrier of the host animal to these particular components of itself. If the effectiveness of the cryostimulus in eliciting an immune response resides only in the liberation of the cellular components, or whether the freezing also acts by modifying the chemical structure of the liberated substances, is still not known. At any rate, cryostimulation is a very useful tool for studying the antigenic properties of an organ or a group of organs. The present paper provides an example of this, in the study of the antigenicity of the male rabbit reproductive system, as performed by freezings of its components.

Some basic definitions should be given here.

Antigen: a substance (a) able to elicit an immune response and (b) also able to react with the antibody produced by this response.

Antibody: a protein belonging to the class of the immunoglobulins, that may be formed as a result of an immune procedure.

Antiserum: a serum containing antibodies, usually produced as a result of an immunization procedure.

Materials and Methods

The sera of the treated animals were examined using both qualitative and quantitative serologic methods, i.e., gel precipitation and passive hemagglutination.

Gel Precipitation. This method is based on the immunologic phenomenon of precipitation, which sometimes occurs when an antigen reacts with its corresponding antibody. In this study, Ouchterlony's technique of gel precipitation was used. This technique consists of placing the antigen and the antiserum in small wells cut in a layer of agar. The antigens in the well diffuse radially and meet the serum proteins, which diffuse from the opposite well. If the reacting antibodies have precipitating activity, lines of insoluble complexes will be formed between the wells. More than one precipitation line indicates, in fact, that several antibodies were present, which migrated in the gel at different rates and met their corresponding antigens closer or farther from the well where the serum was placed.

Passive Hemagglutination. The passive hemagglutination test is based on another immunologic phenomenon, i.e., agglutination. In this case, red blood cells treated with a weak solution of tannic acid (in order to make their surfaces more adherent) are mixed with an antigen; the red cells become coated with it. Equal volumes of coated cell suspension are dropped into a series of small tubes with constant volumes of increasing dilutions of the serum which is being tested. If this antibody displays agglutinating properties, the red blood cells will form aggregates which sediment in the bottom of the tube giving a characteristic pattern, quite different from the negative ones. The result of the test is quantitated as a function of the highest dilution of a serum giving a positive pattern. The alternative use of red blood cells coated with different antigens in successive tests performed with a particular serum gives a better understanding of the immunologic

¹ Numbers in brackets designate References at end of paper.

Contributed by the Heat Transfer Division and presented at the Winter Annual Meeting, New York, N. Y., November 29–December 3, 1970, of THE AMERICAN SOCIETY OF MECHANICAL ENGINEERS. Manuscript received by the Heat Transfer Division August 17, 1970; revised manuscript received April 5, 1971. Paper No. 70-WA/HT-19.

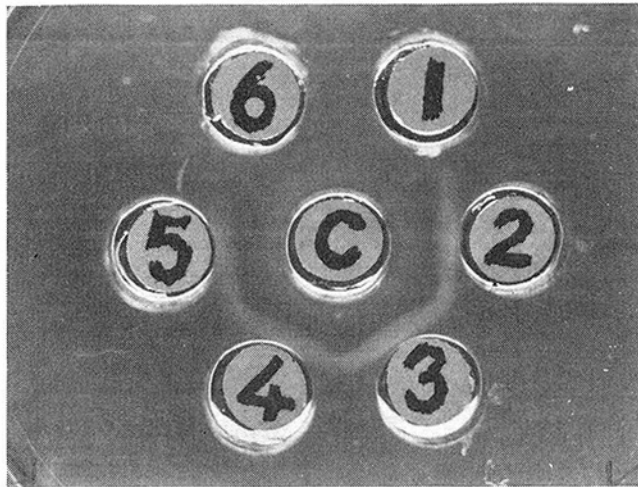


Fig. 1 Gel diffusion experiment in Ouchterlony's technique. The wells, about 3 mm deep and with a diameter of 5 mm, are separated by a minimal edge-to-edge distance of 3 mm

properties of this serum. In some cases, the test of inhibition of passive hemagglutination may also be tried.

Inhibition of Passive Hemagglutination. The test of inhibition of passive hemagglutination is used to explore the possible reactivity of several antigens against the same antiserum. A serum—which is known to react positively to an antigen A—is mixed and incubated for 30 min with an antigen X. After incubation, its reactivity against antigen A is checked in a regular hemagglutination test; if this reactivity remains unchanged, this means that the antiserum did not react with the antigen X during the incubation period. If the serum has lost its reactivity against the antigen A, it means, on the contrary, that it did react with the antigen X or, in other words, that the antigens A and X have common properties with respect to this antiserum. The simultaneous performance of the test with increasing dilutions of the antigen X and a constant concentration of the antiserum, permits one to quantitate the inhibitory activity of the antigen X.

The use of the analytical serologic procedures will be exemplified.

Results

Antisera of cryo-immunized rabbits have often not enough activity to give precipitation lines in gel diffusion experiments. Some of the samples obtained from rabbit 78 (R 78) constitute a useful exception. This animal was submitted to three cryostimulations involving the simultaneous freezing of some of the so-called accessory reproductive organs (1): seminal vesicle, coagulating gland, prostate gland, and vas deferens. After the last cryostimulation, the antibodies in the blood reached an unusually high level; the antiserum sample in the central well in Fig. 1 was obtained from R 78, just after the third cryostimulation. The distribution of the wells adopted in the experiment shown in Fig. 1 permits an interesting comparison of the reactivity of this antiserum against extracts of several of the accessory reproductive organs of the male rabbit; a precipitation line is formed between the central well and well 2, and this line continues with the line formed between the central well and wells 3, 4, and 5. This means that one and the same reacting antigen is present in the extracts placed in wells 2 to 5, which are, respectively: extracts of accessory reproductive organs, seminal vesicle, coagulating gland, and prostate gland. The extracts in wells 6 and 1 (bulbo-urethral gland and epididymis) are unreactive with respect to the R 78 serum.

Using the Ouchterlony technique, the antibody present in the serum of R 78 can also be compared with those in the serum of R 471, immunized against male rabbit accessory reproductive

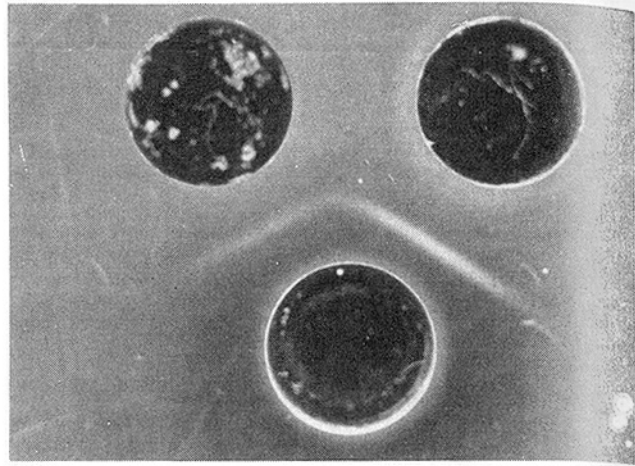


Fig. 2 Experiment similar to that in Fig. 1. The wells, about 3 mm deep and with a diameter of 5 mm, are separated by a minimal edge-to-edge distance of 3 mm

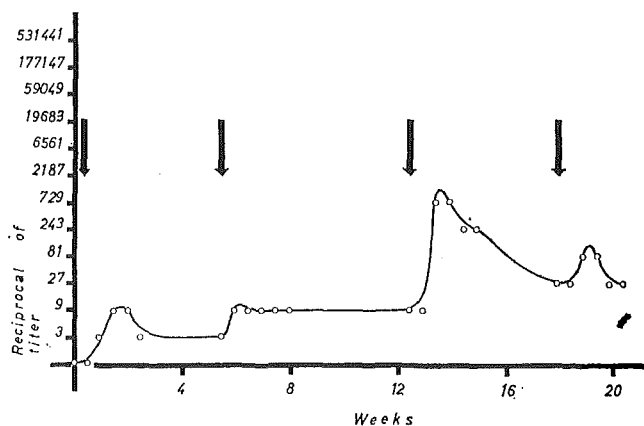


Fig. 3 Antibody responses of R 139 after three cryostimulations; the first stimulation corresponds to the ordinate axis, the other two are indicated by arrows

organs in a completely different way, which included several injections of extracts of these organs. The serum from this animal was placed in the right upper well, whereas that of R 78 was placed in the left upper one. In the lower well, extract of the accessory reproductive organs was dropped (Fig. 2). The interaction of the extract with the two antisera produced a continuous line. This proves the identity of the antibody present in both sera. Since the precipitation line on the right is stronger than that on the left, it can be inferred that the antibody concentration in R 471 serum is higher than in R 78.

If similar gel diffusion experiments are tried with the sera of R 139 and R 176, *selectively* cryo-immunized against the coagulating gland and the seminal vesicle, respectively, no precipitation reaction occurs, suggesting either that no antibody against these extracts exists, or that the antibody titers are too weak to give visible precipitation lines. The exploration of these sera through the passive hemagglutination test, which is a more sensitive one than gel diffusion, discloses, in fact, peaks of antibody activity, closely related to the cryostimulations (Fig. 3). The first freezing does not produce a visible immune response, but seems to sensitize the animal to further freezings.

Table 1 presents the results of a passive hemagglutination test, performed on sera from R 78, R 139, and R 176, using whole accessory reproductive organ extracts as coating antigen. In this particular case, sera of the pre-immunization bleeding (pre), and of a bleeding of these animals obtained during the immunization procedure (imm), were selected. The pre-immunization sera give negative results, as expected. From the immunization sera,

Table 1 Passive hemagglutination titers of sera from R 78, R 139, and R 176

Reciprocal of titer	R 78		R 139		R 176	
	pre imm	imm	pre imm	imm	pre imm	imm
3	-	+	-	+	-	+
9	-	+	-	+	-	+
27	-	+	-	+	-	+
81	-	+	-	+	-	+
243	-	+	-	+	-	+
729	-	+	-	+	-	+
2187	-	+	-	+	-	+
6561	-	+	-	+	-	+
19683	-	+	-	+	-	+
59049	-	+	-	+	-	+
177147	-	+	-	+	-	+
531441	-	+	-	+	-	+
1594323	-	+	-	+	-	+

that of R 78 shows the highest titer. This is understandable, since this animal underwent more extensive freezings than the two others, since they were selectively frozen on the coagulating gland and the seminal vesicle, respectively. The comparative use of several coating antigens reveals further properties of the three same antisera (Table 2); R 78 imm is the strongest reacting one against the three chosen extracts. The weaker reacting R 139 imm and R 176 imm sera show their highest titers against coagulating gland and seminal vesicle extract, respectively. All these features are again to be explained in terms of the immunization procedure to which the animals have been submitted.

The fact that R 139 reacts weakly to seminal vesicle extract, and that R 176 imm do not react at all with an extract of coagulating gland, could indicate that each of these two organs possesses its own antigens, not present in the other one. This question is partially answered by the results of the test of inhibition of passive hemagglutination shown in Table 3. Since the seminal vesicle extract does inhibit the activity of R 139, this indicates that this organ should share some antigenic properties with the coagulating gland. In an analogous way, it can be said that the bulbo-urethral gland does not share antigenic properties with the coagulating gland.

Discussion

Cryo-immunization is being actively used in this laboratory for exploring the antigenic properties of the male rabbit reproductive system. The rabbits R 78, R 139, and R 176 were selected from three different groups of animals in order to provide an example of a comparative study of the reactivity of three different types of antisera against extracts of several accessory reproductive organs of this animal.

The results presented here, reinforced by others obtained in other studies in the same groups of animals, and by reports of other cryo-immunology studies [2, 3], indicate the probable presence of a common antigen in most of the accessory reproductive organs. The existence of specific antigens in some of the explored organs, namely the seminal vesicle and the coagulating gland, cannot be excluded. On the other hand, the antigenic properties of the accessory reproductive organs of the male rabbit—as studied by cryostimulation—seem to be not related to those present in the testis and epididymis of this animal [4, 5]. The individual reactivity of the seminal vesicle and the coagulating gland to cryostimulations has also been established in another report [6].

Acknowledgments

The authors wish to thank Miss Barbara Flouton and Mr. Thomas Byro for excellent technical assistance. This study was

Table 2 Variations in the passive hemagglutination titers of R 78, R 139, and R 176 when changing the coating antigen

Reciprocal of titer	Coating antigen								
	1			2			3		
	R 78	R 139	R 176	R 78	R 139	R 176	R 78	R 139	R 176
3	+	+	+	+	+	-	+	+	+
9	+	+	+	+	+	-	+	+	+
27	+	+	+	+	+	-	+	+	+
81	+	+	-	+	+	-	+	-	+
243	+	+	-	+	+	-	+	-	+
729	+	-	-	+	+	-	+	-	+
2187	+	-	-	+	+	-	+	-	-
6561	+	-	-	+	-	-	+	-	-
19683	+	-	-	+	-	-	+	-	-
59049	+	-	-	+	-	-	-	-	-
177147	+	-	-	+	-	-	-	-	-
531441	+	-	-	+	-	-	-	-	-
1594323	-	-	-	-	-	-	-	-	-

- 1= whole male rabbit accessory glands extract
- 2= coagulating gland extract
- 3= seminal vesicle extract

Table 3 Inhibition of the agglutination activity of R 139 serum by various organ extracts

Reciprocal of antigen dilution	Inhibiting antigen			
	1	2	3	4
3	-	-	-	+
9	-	-	-	+
27	-	-	-	+
81	-	-	+	+
243	+	-	+	+
729	+	-	+	+
2187	+	-	+	+
6561	+	+	+	+
19683	+	+	+	+
59059	+	+	+	+

- 1= whole male rabbit accessory glands extract.
- 2= coagulating gland.
- 3= seminal vesicle extract.
- 4= bulbourethral gland.

supported by a research grant from the John A. Hartford Foundation, Inc.

References

- 1 Zappi, E., and Shulman, S., "Cryo-Immunology: Surgical Approach and Thermal Regimen for Freezing the Elements of the Male Rabbit Reproductive System," *JOURNAL OF HEAT TRANSFER, TRANS. ASME, Series C, Vol. 94, No. 2, May 1972, pp. 129-132.*
- 2 Shulman, S., Brandt, E. J., and Yantorno, C., "Studies in Cryo-Immunology. II. Tissue and Species Specificity of the Auto-antibody Response and Comparison with Iso-Immunization," *Immunology, Vol. 14, 1968, pp. 149-158.*
- 3 Shulman, S., and Zappi, E., "Cryo-Immunology," in: *Cryogenics in Surgery* (von Leden, H., and Cahan, W., eds.), Medical Examination Publ. Co., Flushing, N. Y. (in press).
- 4 Zappi, E., and Shulman, S., "Cellular and Humoral Responses after Freezing Damage of the Rabbit Testis and Epididymis," *Federation Proceedings, Vol. 30, 1971, p. 416.*
- 5 Zappi, E., and Shulman, S., "Cryo-Immunology. Antibody Response to Epididymis Freezing in the Rabbit," (to be published).
- 6 Zappi, E., Orsini, F., and Shulman, S., "Cryo-Immunization. Antibody Response after Selective and Repeated Cryo-Stimulations of the Coagulating Gland and the Seminal Vesicle of the Male Rabbit," (to be published).

S. E. SADEK

R. G. FAX

Dynatech R/D Co.,
Cambridge, Mass.

M. HURWITZ

Consultant,
Auburndale, Mass.
Mem. ASME

The Influence of Electric Fields on Convective Heat and Mass Transfer from a Horizontal Surface under Forced Convection

This paper presents the results of an investigation of the electrohydrodynamic augmentation of drying under forced convection. Heat and mass transfer coefficients were calculated from the drying rates of sponges, using the analogy between heat and mass transfer. The test setup used was a flat plate with tangential air flow. Electrical forces, used to disturb the boundary layer, were applied by placing a high-voltage electrode above the sponge which was maintained at ground potential. Augmented heat and mass transfer coefficients were correlated to nondimensional terms developed from similarity and modeling principles.

Introduction

ELECTROCONVECTIVE augmentation of heat transfer in gases has been under investigation since 1931 when Senftleben [1]¹ first published data indicating that in the presence of electric fields heat transfer rates may be increased substantially beyond natural convection rates. Since then, extensive data have been gathered [2-7] and a number of correlations have been proposed to describe the results. The earlier correlations argue that the electroconvective augmentation is a consequence of the electrostrictive forces resulting from the variation of the electrical properties of the gas due to its nonuniform temperature [2-4]. The net effect of the field was said to be analogous to the effect of gravity on a fluid having adverse density gradients in destabilizing the boundary layer.

In early analyses, ion-drag forces were totally neglected. These forces have been observed as early as 1899 in the form of a "corona wind" [8, 9]: The transfer of momentum between the ions propelled by the electric field at high velocities and the surrounding air creates the corona wind and significant air velocities have been detected. It is only recently that ion-drag forces have been recognized as the major contributors toward the electroconvective augmentation of heat transfer where ionization of the gas occurs [5-7]. Tests with natural convection showed that augmentation of heat transfer correlated well with power dissipated by the corona [5]; other tests confirmed rela-

tionships derived for estimating the augmentation of natural convection with ion-emitting electrodes [6, 7].

The investigation of the effect of ion-drag forces in heat transfer and mass transfer in gaseous systems where momentum forces are significant has largely been neglected, and limited data exist on the effect of electroconvective forces—or using more correct terminology in this case, electrohydrodynamic forces—on heat transfer under forced convection [10, 11]. This paper presents an attempt at correlating electrohydrodynamic-augmentation data in a forced-convection system wherein the increases in both heat and mass transfer coefficients were due solely to the electric forces produced by ion-emitting electrodes. The heat and mass rate data were gathered during drying tests conducted with a material whose drying rate was totally controlled by the gas-phase transfer mechanisms. Tests were conducted within the laminar boundary-layer flow regime.

Theory

The electrical force density acting on a dielectric medium is, in general, the sum of coulomb and polarization forces [12]. Coulomb forces result from an interaction of free charges with an imposed electric field wherein the charges transmit individually their force to the neutral medium. Polarization forces are created when pairs of charges (dipoles) transmit the electrical force to the medium. Polarization forces are generally classified according to whether they arise from inhomogeneities in the polarizability of the medium (Korteweg-Helmholtz forces) or from the concentration of polarizabilities caused by volumetric charges (electrostrictive forces).

When a potential V is applied to an electrode consisting of an array of wires or points, the gas in the vicinity of the electrode ionizes. These ions are then propelled by the coulomb forces and

¹ Numbers in brackets designate References at end of paper.

Contributed by the Heat Transfer Division and based on a paper presented at the Winter Annual Meeting, New York, N. Y., November 29-December 3, 1970, of THE AMERICAN SOCIETY OF MECHANICAL ENGINEERS. Manuscript received by the Heat Transfer Division February 16, 1971; revised manuscript received July 26, 1971.

travel at high velocities toward the opposite electrode. As they travel, the ions collide with un-ionized gas molecules with which they exchange momentum: The result is ion-drag flow or corona wind. The ion-drag force acting normal to a grounded area parallel to the emitter electrode is [9]

$$F_c \cong \alpha \epsilon A \left(\frac{V - V_0}{s} \right)^2 \quad \text{for } V > V_0$$

$$= 0 \quad \text{for } V \leq V_0$$
(1)

Here α is a numerical factor which depends on the system geometry ($8/9$ for parallel electrodes) and s is the spacing between the ion emitter and the grounded area. V_0 is the threshold voltage below which ionic currents are insignificant. For any particular system, V_0 may be determined by plotting the square root of the measured corona current against the applied voltage. The threshold value is then determined by extrapolating the data to the zero-current level.

By comparison, in a parallel-electrode system where a region of nonuniform electrical properties exists (i.e., within the gas boundary layer adjacent to the ground plane in the experiments to be described), the Korteweg-Helmholtz polarization force [12, 13] is

$$F_p = - \left(\frac{1}{2} \right) \left(\frac{V^2}{s^2} \frac{\epsilon_i - \epsilon_\infty}{\delta} \right) (A\delta)$$
(2)

Since the permittivity of most gases varies only slightly with temperature or composition, the polarization force due to property gradients in typical boundary layers is very small. Consequently, at voltages only slightly above the threshold corona voltage, the ion-drag force F_c is much larger than the polarization force F_p [14]. Accordingly, the polarization force F_p is neglected in the discussion which follows. It should also be noted that the electrostrictive force density

$$-1/2(\epsilon E \cdot E)(\rho/\epsilon)(d\epsilon/d\rho)$$

simply contributes to the total pressure in an electrohydrodynamic system; this force, therefore, cannot have any effect on incompressible dynamics [12].

In systems dealing with forced convection of heat or mass, the electrical force competes with the momentum forces. The dimensionless parameter which defines the ratio between the dominant electrical force (the ion-drag force in the presence of ionization currents) and the momentum force can be expressed as

$$\chi^2 \cong \frac{\epsilon}{\rho} \left(\frac{V - V_0}{su} \right)^2 \quad \text{for } V > V_0$$

$$= 0 \quad \text{for } V \leq V_0$$
(3)

Where ion drag is the dominant electrical force, the parameter χ^2 must be included in heat and mass transfer relationships to account for the electroconvective augmentation under forced convection. When the sole mode of heat or mass transfer is convective, any such relationship must reduce to the classical ones in the absence of an electrical field. If it is assumed that the electrical forces act additively to the momentum forces, the transfer relationships can be stated in general form

$$Nu = Nu^0 [1 + f(\chi^2)]$$
(4a)

and

$$Sh = Sh^0 [1 + f(\chi^2)]$$
(4b)

The terms Nu and Sh denote the Nusselt and Sherwood numbers. These are the ratios of the characteristic system dimension l to the heat and mass transfer boundary-layer thicknesses δ_h and δ_m , respectively. The superscript 0 denotes the Nusselt and Sherwood numbers in the absence of the electrical field.

In the systems where convective transfer dominates, the same function f will describe both the heat and mass transfer relationships owing to the analogy between heat and mass transfer mechanisms.

Finally, one may suspect that the exponent n on the force ratio χ^2 in a relationship of the type

$$f(\chi^2) = \beta(\chi^2)^n$$
(5)

will be the same as that on the momentum force in the classical forced-convection transfer relationships, i.e., the same as the exponent on the Reynolds number in the classical equations (15). In the laminar boundary-layer flow regime, $n = 0.5$ and the augmentation equations may be expected to be linear with χ and of the form

$$Nu = Nu^0 [1 + \beta\chi]$$
(6a)

and

$$Sh = Sh^0 [1 + \beta\chi]$$
(6b)

Apparatus and Procedure

Drying rates were measured using a flat cellulose sponge 6.5 in. wide and 3.8 in. long, placed in an 8-in. by 8-in. tunnel 6 ft long. The velocity of the air entering the tunnel was varied from approximately 0.7 to 5.2 fps; the temperature was varied up to 250 deg F. Fig. 1 illustrates schematically the experimental setup. Heated air flowed longitudinally over the wet test sponge which was mounted on top of another similar wet sponge. The lower sponge acted as a temperature shield. Aluminum foil placed between the two sponges acted as a moisture barrier. A thin sheet of tissue paper was laid flat on the surface of the

Nomenclature

A = area	s = spacing between electrode and surface	μ = viscosity
C = specific heat	Sc = Schmidt number = $\mu/\rho D$	ρ = gas density
D = diffusion coefficient	Sh = Sherwood number = $kl/D = l/\delta_m$	χ = square root of force ratio
E = electrical field	t = time	Subscripts
f = function	u = air velocity	c = corona or ion drag
F = force	V = electrode voltage	h = heat transfer
h = heat transfer coefficient	W = mass of water in sponge	i = interface
k = mass transfer coefficient	α = geometric factor in equation (1)	m = mass transfer
l = characteristic length	β = constant in equation (5)	0 = corona threshold value
L = latent heat of vaporization	Δ = difference between augmented and unaugmented value	p = polarization
n = exponent on χ^2 in equation (5)	δ = boundary-layer thickness	∞ = bulk air
Nu = Nusselt number = $hl/\lambda = l/\delta_h$	ϵ = permittivity of gas	Superscripts
p = water-vapor partial pressure	λ = thermal conductivity	0 = unaugmented value
P = atmospheric pressure		$-$ = averaged over length
Pr = Prandtl number = $C\mu/\lambda$		$'$ = molar quantity
Re = Reynolds number = $\rho ul/\mu$		

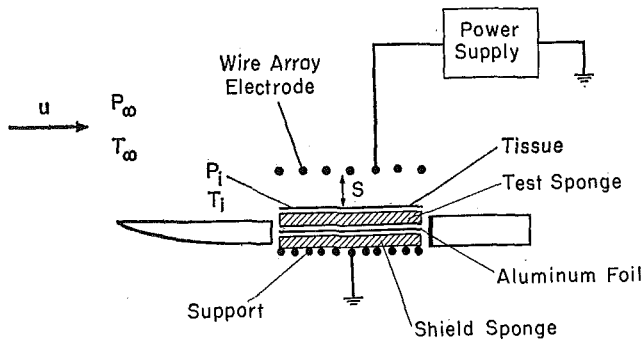


Fig. 1 Schematic diagram of test section

upper sponge, and a sharp leading edge led the air flow over the test sponge.

A high voltage could be applied to an electrode suspended above the drying sponge. The voltage was supplied by a negative, filtered d-c supply. Two electrode spacings could be selected: 1 in. and 1.85 in.; these represent the distance between the emitting surface and the drying surface. Most of the tests were performed with an electrode consisting of an array of 0.030-in.-dia wires pitched 1 in. apart and strung across the tunnel over the sponge. Another electrode was made of common pins set in a fine-mesh screen and pitched 1/2 in. apart in a square array. One test was performed with a smooth flat-plate electrode to confirm the prediction that polarization forces are negligible for this system.

The air temperature was measured by means of a thermocouple inserted in the gas about 4 in. upstream of the leading edge of the sponge. Air velocity was determined by measuring the volumetric flow entering the tunnel via an orifice meter. The partial pressure of moisture in the air was determined from the ambient wet- and dry-bulb temperatures. The drying rate was measured by weighing the wet sponge (containing about 85 percent moisture on a wet basis) just before it was placed in the tunnel and then reweighing it after a measured period of time.

Data Reduction Scheme

Heat and mass transfer coefficients were calculated from the drying rates determined experimentally. The rate of drying of a wet cellulose sponge is governed by simultaneous heat and mass transfer in the heating gas; when the sponge contains a large excess of free water, diffusional resistance within the sponge may be neglected. Under these conditions, drying occurs within the constant-rate drying regime and the drying rates can be directly related to the gas-phase transfer coefficients [16]. It was verified that the measurements were made in the constant-rate drying regime by weighing the sponge after different drying periods under the same test conditions [14]. Accordingly, the drying rate may be expressed in terms of the heat and mass transfer relationships. Neglecting sensible heat effects in the heat transfer equation, the drying rate is given by

$$-(dW'/dt) = \bar{h}A(T_\infty - T_i)/L' \quad (7)$$

$$= \bar{h}A\rho'[(p_i - p_\infty)/P] \quad (8)$$

where dW'/dt is the molar flux of water from the sponge, L' is the molar latent heat of vaporization, and ρ' is the molar density of bulk gas. The temperature T_i and the partial pressure of the moisture p_i at the drying surface are constant over the surface and are interrelated; since there is a large excess of free water at the drying surface, this relation is defined by the vapor-pressure relationship of pure water. That is,

$$p_i = p(T_i) \quad (9)$$

Finally, equations (4a) and (4b) allow the definition of the ratio (\bar{h}/\bar{k}) under conditions of convective transfer

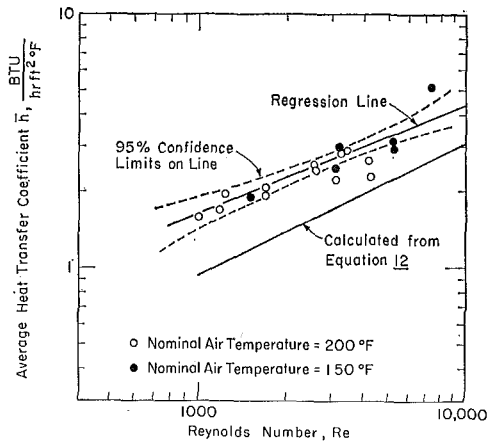


Fig. 2 Average heat transfer coefficients—base-line data

$$(\bar{h}/\bar{k}) = (\bar{Nu}^\circ/\bar{Sh}^\circ)(\lambda/D) \quad (10)$$

Under forced convection, the Nusselt and Sherwood numbers are proportional to the Prandtl and Schmidt numbers raised to the 1/3 power [15]. Therefore,

$$(\bar{h}/\bar{k}) = (Pr/Sc)^{1/3}(\lambda/D) \quad (11)$$

Equations (7), (8), (9), and (11) can now be solved simultaneously to determine the values of T_i , p_i , \bar{h} , and \bar{k} from experimental data when the drying rate at a specified bulk air temperature and humidity is known.

Results and Discussion

Base-line data were first determined in the absence of electric fields. The results of these tests are shown in Fig. 2, where the experimental average heat transfer coefficients are plotted against the air velocity. The Reynolds numbers investigated (based on the length of the sponge) ranged between 900 and 7300, well below the normal critical Reynolds number above which the boundary layer becomes turbulent. Under laminar boundary-layer flow conditions, analysis of the heat and mass transfer rates yields a relationship for the transfer coefficients. If it is assumed that the hydrodynamic leading edge is the same as the drying edge, then the average Nusselt number is [15]

$$\bar{Nu} = 0.664Re^{1/2}Pr^{1/3} \quad (12a)$$

(where the Nusselt and Reynolds numbers are based on the drying length and the driving force is the bulk air temperature T_∞ minus the interface temperature T_i).

Similarly, the average Sherwood number is expressed by

$$\bar{Sh} = 0.664Re^{1/2}Sc^{1/3} \quad (12b)$$

The relationship expressed in equation (12a) is shown plotted in Fig. 2 together with the base-line data. The regression line through the experimental data falls above the theoretical relationship because:

- 1 Flow separation at the leading edge of the sponge produced turbulence which probably increased the drying rate.
- 2 The hydrodynamic leading edge was, in fact, not the same as the drying edge.
- 3 Some stratification of the flow at the lower air flow rates resulted in the actual flow rate over the sponge being greater than the average.
- 4 Imperfect thermal shielding caused heat leaks into the sponge.

Results of electroconvective tests with the wire electrode placed 1 in. away from the surface of the sponge are shown in Fig. 3. Since the ratio $(Pr/Sc)^{1/3}$ is approximately unity, the

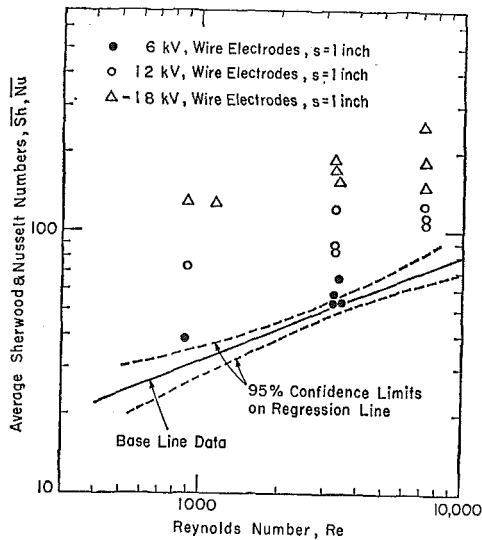


Fig. 3. Average Nusselt and Sherwood numbers—augmented data

Nusselt and Sherwood numbers are essentially equal; both the Nusselt and Sherwood numbers are plotted against the Reynolds numbers for the different runs. The regression line through the base-line data and the 95 percent confidence limits on the line are also shown in Fig. 3. Data gathered with hydrodynamic augmentation at the higher voltages show a clear increase in Nusselt and Sherwood numbers over the base-line data; at all Reynolds numbers investigated the extent of augmentation improves as the magnitude of the applied voltage is increased; at a voltage of -6 kv a negligible effect on the heat transfer coefficients is observed, but the effect becomes dramatic at -18 kv.

A single test with a flat-plate electrode maintained at -18 kv and spaced 1 in. above the sponge showed no increase in drying rate above the corresponding base-line point. Since corona was nonexistent with the flat plate (the current reading was essentially zero) but the field strength at the surface of the sponge was approximately the same as that with the wire electrode at the same potential, the results of this test support the theory that augmentation of drying depends on the corona and ion-emission properties of the electrode, and not on the electric field strength near the drying surface.

In order to correlate all the data gathered by means of a relationship of the form expressed in equations (4a) and (4b), the threshold corona voltage must be determined. This is done by plotting the square root of the measured corona current against the applied voltage [9]. The results of some of these tests are shown in Fig. 4. The threshold voltage for the wire-array electrode spaced 1 in. away from the sponge is -9.2 kv. It is found to be insensitive to temperature within the range investigated (150 – 210 deg F). At a spacing of 1.85 in. the threshold voltage of that same electrode was -15 kv. The threshold voltage for the pin electrode at a spacing of 1 in. was -6 kv, reflecting the fact that it is a more efficient ion emitter than the wire electrode.

In equations (6a) and (6b) it was concluded that the augmented Nusselt and Sherwood numbers will increase linearly with χ . To examine this hypothesis, a plot of $(\Delta Nu/Nu^0)$ and $(\Delta Sh/Sh^0)$ against χ was made. Heat and mass transfer data with wire electrodes at spacings of 1 in. and 1.85 in. and with pin electrodes at a spacing of 1 in. are plotted in Fig. 5. On this logarithmic plot the data from all three systems scatter around the regression line having a slope of unity. The equation of that regression line is

$$\Delta \overline{Nu}/\overline{Nu}^0 = 1.85\chi \quad (13a)$$

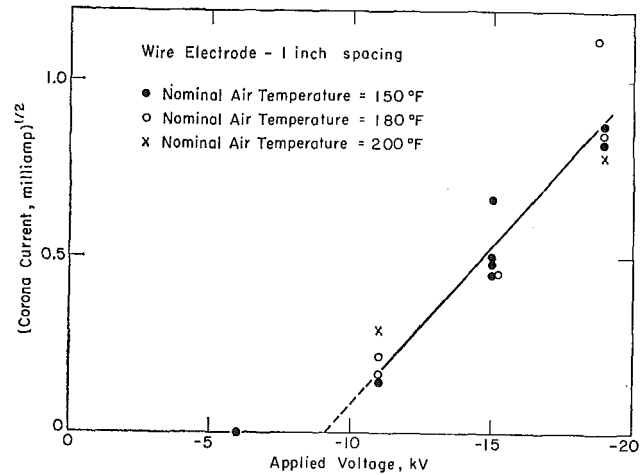


Fig. 4. Determination of threshold corona voltage for wire electrode at 1-in. spacing

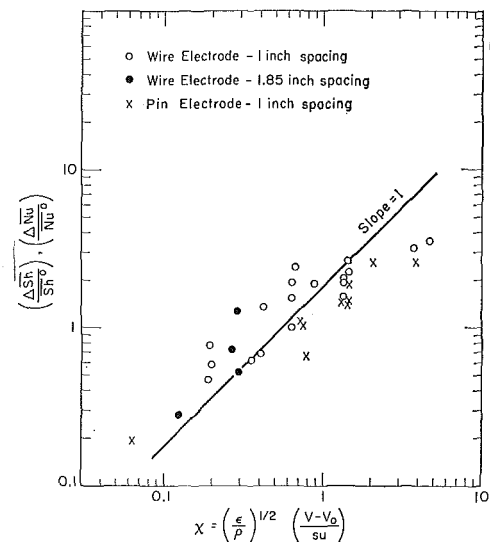


Fig. 5 Correlation between increase in Nusselt and Sherwood numbers and the force ratio χ^2

or

$$\Delta \overline{Sh}/\overline{Sh}^0 = 1.85\chi \quad (13b)$$

The scatter in the data at low values of χ is due to the fact that the ratios $(\overline{Nu}/\overline{Nu}^0)$ and $(\overline{Sh}/\overline{Sh}^0)$ are only slightly greater than unity and small errors in determining the heat and mass transfer coefficients are greatly magnified in this range. At high values of χ , the scatter may be attributed to the thermal stratification of the air flow at the low air velocities used.

Conclusions

The results of these tests support the hypothesis that the electrohydrodynamic augmentation of heat and mass transfer rates with small-diameter or sharp-pointed electrodes is due to ion-drag forces. Augmentation of heat and mass transfer (with such electrodes) under forced convection may be correlated by means of the ratio of ion-drag and momentum forces $\chi^2 = \epsilon/\rho(V - V_0/s)^2$. A generalized correlation based on this approach leads to the expression of the increase of heat and mass transfer coefficients in terms of the force ratio χ^2

$$\Delta \overline{Nu}/\overline{Nu}^0 = f(\chi^2)^n \quad (14a)$$

and

$$\Delta \overline{Sh} / \overline{Sh}^{\circ} = f(\chi^2)^n \quad (14b)$$

When it is assumed that the ion-drag force acts additively with the momentum force, then n is equal to the exponent on the Reynolds number in the generalized heat and mass transfer correlations. This assumption appears to be confirmed for the laminar boundary-layer regime where experimental data indicate that $n = 0.5$.

References

- 1 Senftleben, "Die Einwirkung elektrischer und magnetischer Felder auf das Wärmeleitvermögen von Gasen," *Phys. ZS.*, Vol. 32, No. 14, 1931, p. 550.
- 2 Kronig, R., and Schwarz, N., "On the Theory of Heat Transfer from a Wire in an Electric Field," *Appl. Sci. Res.*, A1, 1947, p. 35.
- 3 Aarås, S., and Legvold, S., "Electroconvective Heat Transfer in Gases," *J. Chem. Phys.*, Vol. 29, 1958, p. 531.
- 4 Lykondis, P. S., and Yu, C. P., "The Influence of Electrostrictive Forces in Natural Thermal Convection," *International Journal of Heat and Mass Transfer*, Vol. 6, 1963, p. 853.
- 5 Franke, M. E., "Effect of Vortices Induced by Corona Discharge on Free-Convection Heat Transfer From a Vertical Plate," *JOURNAL OF HEAT TRANSFER*, TRANS. ASME, Vol. 91, Series C, No. 3, Aug. 1969, pp. 427-433.
- 6 Velkoff, H. R., "Electrofluidmechanics: Investigation of the Effects of Electrostatic Fields on Heat Transfer and Boundary Layers," ASD-TDR-62-650, AF Aero-Propulsion Laboratory, Wright-Patterson AFB, Ohio, 1962.
- 7 Marco, S. M., and Velkoff, H. R., "Effect of Electrostatic Fields on Free Convection Heat Transfer from Flat Plates," ASME Paper No. 63-HT-9.
- 8 Chattock, A. P., "On the Velocity and Mass of Ions in the Electric Wind in Air," *Philosophy Magazine*, Vol. 48, 1899, p. 401.
- 9 Stuetzer, O. M., "Ion Drag Pressure Generation," *Journal of Applied Physics*, Vol. 30, 1959, p. 984.
- 10 Velkoff, H. R., "An Exploratory Investigation of the Effects of Ionization on the Flow and Heat Transfer with a Dense Gas," ASD-TDR-63-842, AF Aero-Propulsion Laboratory, Wright-Patterson AFB, Ohio, 1963.
- 11 Moss, R. A., and Grey, J., "Heat Transfer Augmentation by Steady and Alternating Electric Fields," *19th Proceedings, Heat Transfer and Fluid Mechanics Institute*, June 1966, pp. 210-235.
- 12 Melcher, J. R., *Field Coupled Surface Waves*, M.I.T. Press, Cambridge, Mass., 1963, pp. 22-23.
- 13 Stratton, J. A., *Electromagnetic Theory*, McGraw-Hill, New York, N. Y., 1941, p. 145.
- 14 Sadek, S. E., Fax, R. G., and Hurwitz, M., "Electrohydrodynamic Augmentation of Heat and Mass Transfer in Air under Forced Convection," *Augmentation of Convective Heat and Mass Transfer*, Bergles, A. E., and Webb, R. L., eds., ASME, New York, N. Y., 1970, pp. 118-123.
- 15 Eckert, E. R. G., and Drake, R. M., *Heat and Mass Transfer*, 2nd ed., McGraw-Hill, New York, N. Y., 1959, chap. 7.
- 16 Treybal, R. E., *Mass Transfer Operations*, 2nd ed., McGraw-Hill, New York, N. Y., 1968, chap. 12.

J. J. NOBLE
L. A. GLOMBURG
A. F. SAROFIM
H. C. HOTTEL

Department of Chemical Engineering,
Massachusetts Institute of Technology,
Cambridge, Mass.

Mathematical and Experimental Modeling of the Circulation Patterns in Glass Melts

Natural convection currents in a rectangular two-dimensional enclosure representative of the longitudinal section of an industrial glass-melting furnace have been established by both model experiments and numerical calculation. For the latter a finite-difference method has been employed to solve the time-dependent coupled flow and energy equations. The highly generalized mathematical model makes allowance for buoyancy, temperature-dependent viscosity, and diffusive radiation. Generalized boundary conditions are employed to permit specification of any combination of temperature, flux, or mixed thermal boundary conditions. Representative temperature and flow contour maps obtained from the calculations are shown to agree well with experimental results obtained with a $1/20$ scale model in which glycerine was employed as the modeling fluid.

Introduction

GLASS IS normally produced in open-hearth furnaces in which the glass ingredients are flame-heated from above to form a melt. The raw materials (batch) are fed at one end of the furnace and float on the surface to form the so-called batch heap or cover. The charge reacts, is mixed by natural convection and by diffusion, and the product glass is withdrawn at the opposite end of the furnace.

A full understanding of the various transport processes and chemical reactions occurring in a glass tank is an enormous task. The overall problem involves characterization of the radiant heat transfer from the flame-fired refractory-lined gas volume above the surface of the melt. These transfer rates are intimately coupled with convective rates within the melt, the magnitudes of which are determined by the interaction of radiant transfer, conductive transfer, and, in the area of the feed port, by melting, chemical reaction, and gas generation and disengagement. It is not, therefore, surprising that the design of these furnaces has developed as an art. It has been recognized [5, 6, 7],¹ however, that the natural circulation currents within the melt homogenize the glass and that the modification of these currents can exert a profound influence on product quality.

Previous efforts to improve our understanding of circulation patterns within the melt have taken several directions. Since experimental measurements with the prototype prove both difficult and costly, a need for model studies, mathematical or experimental or both, is evident. Prior laboratory models [2],

however, have been based on qualitative scaling of the hydrodynamic effects and due attention has not been paid to the coupled energy transfer rates. Similarly, mathematical modeling of the prototype via finite-difference techniques has been characteristically beset with difficulties associated with numerical instability and excessive computation times. Results [7] published to date have thus been limited. A more thorough review of prior modeling studies has been published by Steinke [6].

The work reported here describes part of a continuing research effort directed toward a more fundamental understanding of glass-furnace operation through the use of both laboratory and computational modeling. Experimental modeling provides the advantage of permitting the matching of geometrical complexity in the prototype but is restricted by the modeling fluid to satisfying at best only several of the relevant dimensionless groups. Mathematical modeling, on the other hand, is restricted by computational difficulties to the solution of two-dimensional problems. Complementary experimental and theoretical analyses can be used to extend the range of utility of each, by using experiments to determine the importance of three-dimensionality and by use of computations to test the importance of groups that cannot be modeled exactly in experiments. The major aim in this paper is to compare the results of experimental and computational models in the range of applicability of both while retaining the more salient features of the prototype. The problem therefore has been restricted to two dimensions and—in order to provide unambiguously defined thermal boundary conditions in the experiments—to the case of no-slip velocity boundary condition at all surfaces.

Mathematical Modeling

Statement of the Problem. The present approach is to treat circulations as those of a purely viscous fluid in a rectangular enclosure, neglecting the effect of bubbles and chemical reaction.

¹ Numbers in brackets designate References at end of paper. Contributed by the Heat Transfer Division and presented at the Winter Annual Meeting, New York, N. Y., November 29–December 3, 1970, of THE AMERICAN SOCIETY OF MECHANICAL ENGINEERS. Manuscript received by the Heat Transfer Division August 13, 1970; revised manuscript received June 20, 1971. Paper No. 70-WA/HT-11.

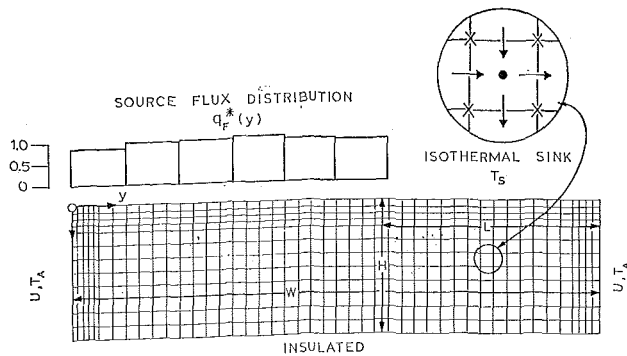


Fig. 1 Refined grid system and computational boundary conditions

A second major simplification results from the fact that radiant heat transfer in molten glass may be adequately represented by the Rosseland diffusion equation [1]. Thus the radiant transfer is described with an "effective" thermal conductivity rather than integral expressions (optical depths of over 200 are typical for the dominant wavelengths).

The specific problem considered here is shown in Fig. 1. A viscous fluid is confined in a rectangular two-dimensional enclosure of height H and width W . Fluid motion, generated by density gradients, is taken to satisfy the no-slip hydrodynamic boundary conditions on all four walls of the enclosure. In addition to temperature-dependence of density, allowance is also made for thermal variation of viscosity and of thermal conductivity. The fluid, in particular, is taken to be an optically thick absorber-emitter of thermal radiation.

In the mathematical model, the flame-side and melt-side energy transfer are decoupled. With relation to the prototype, the batch cover is idealized as a plane of extent L which is maintained at some appropriate sink temperature T_s , representative of the bottom-surface temperature of the batch.

Similarly, heat transfer into the melt by the flame radiation is idealized by some assumed energy-flux distribution $q_F(y)$. This

function may be estimated for the prototype from firing rates and heats of combustion using the conventional zone method of calculation [3]. Clearly this procedure could be refined by an iterative process in which the assumed surface-temperature distribution used in calculating the flux distribution is compared with the glass-surface temperatures as calculated with the present procedure. This process would be terminated when the surface temperature assumes that value at which the energy rates to and from the glass surface become equal.

Lastly, it is assumed that the endwalls of the furnace lose heat to the ambient at temperature T_A and that these walls have an overall heat transfer coefficient U . The bottom of the furnace is taken as insulated. For simplicity in the design of the companion experiment, no fluid throughput is permitted, i.e., the momentum rates associated with feed addition and product withdrawal are assumed to be negligible, although allowance is made for the thermal effects. (Computations not reported here, made with and without material flow through the furnace, have shown that the temperature and flow fields are insensitive to the net material flow, provided that proper allowance is made for the energy requirements of the material flow.)

Differential Problem Statement. For unsteady two-dimensional motion, the governing dimensionless differential equations for natural convection in Cartesian coordinates (Fig. 1) are given by the usual Boussinesq approximation [4, 8] as

Energy Equation

$$\frac{DT^*}{Dt^*} = \frac{\partial}{\partial x^*} k_e^* \frac{\partial T^*}{\partial x^*} + \frac{\partial}{\partial y^*} k_e^* \frac{\partial T^*}{\partial y^*} \quad (1)$$

Vorticity Transport Equation

$$\frac{1}{N_{Pr}} \frac{D\omega^*}{Dt^*} = N_{Ra} \frac{\partial T^*}{\partial y^*} + \frac{\partial}{\partial x^*} \mu^* \frac{\partial \omega^*}{\partial x^*} + \frac{\partial}{\partial y^*} \mu^* \frac{\partial \omega^*}{\partial y^*} \quad (2)$$

Velocity Definitions

$$u^* = \frac{\partial \psi^*}{\partial y^*} \quad v^* = -\frac{\partial \psi^*}{\partial x^*} \quad (3a, b)$$

Nomenclature

$A = W/H$, aspect ratio of enclosure, dimensionless	Q = total heat flux	$\theta = \frac{T - T_s}{T_R}$, dimensionless temperature
$C = L/W$, fractional batch coverage, dimensionless	Q_{sink} = integral heat loss	μ = fluid viscosity
c_p = isobaric heat capacity	$q_F(y)$ = flux density to top surface	ν = fluid kinematic viscosity
E = constant in variable-viscosity law	t = time	ρ = fluid density
g = acceleration due to gravity	T = temperature	σ = Stefan-Boltzmann constant
H = height of enclosure	T_A = ambient temperature	ψ = stream function
k = true thermal conductivity	$T_{A,L}$ = ambient temperature—left	ω = vorticity
$k_e = k + \frac{16 \sigma n^2 T^3}{3 K}$, effective thermal conductivity	$T_{A,R}$ = ambient temperature—right	$\nabla^2 = \frac{\partial^2}{\partial x^{*2}} + \frac{\partial^2}{\partial y^{*2}}$, two-dimensional Laplacian operator in Cartesian coordinates
K = Rosseland mean absorption coefficient	T_0 = temperature at which properties are evaluated	$\frac{D}{Dt^*} = \frac{\partial}{\partial t^*} + \frac{\partial(u^*)}{\partial x^*} + \frac{\partial(v^*)}{\partial y^*}$, substantial derivative in two-dimensional Cartesian coordinates, dimensionless
L = length of batch cover	$T_R = \frac{q_{F, \text{ave}} H}{k_{e0}}$, reference temperature	
n = index of refraction, dimensionless	T_s = top-sink temperature	
$N_{Pr} = \frac{\mu_0 c_p}{k_{e0}}$, Prandtl number based on effective thermal conductivity	U = overall heat transfer coefficient for endwalls	
$N_{Ra} = \frac{\beta g q_{F, \text{ave}} H^4}{\alpha_{e0} \nu_0 k_{e0}}$, Rayleigh number based on average heat flux	u, v = two-dimensional Cartesian velocity components in the x and y dimensions, respectively	
$N_{RC} = \frac{16 \sigma n^2 T_0^3}{3 k K}$, radiation-conduction number	W = width of enclosure	
$N_{vis} = \frac{E}{T_R}$, viscosity number	x, y = Cartesian position coordinates defined in Fig. 1	
	Z = depth of enclosure into plane of motion	
	α_e = effective thermal diffusivity, based on radiative thermal conductivity	
	β = volumetric coefficient of thermal expansion	

Subscripts

R = indicates reference quantity
 0 = denotes physical property evaluated at temperature T_0
 s = denotes physical property evaluated at temperature T_s

Superscripts

$*$ = denotes dimensionless quantity
 $'$ = denotes modified dimensionless quantity defined by equation (8)

Poisson Equation

$$\frac{\partial^2 \psi^*}{\partial x^{*2}} + \frac{\partial^2 \psi^*}{\partial y^{*2}} = -\omega^* \quad (4)$$

where

$$N_{Ra} \equiv \frac{\beta g T_R H^3}{\alpha_{e0} \nu_0} \quad N_{Pr} \equiv \frac{\nu_0}{\alpha_{e0}}$$

and

$$\mu^* \equiv \exp \frac{E}{T_R} \left[\frac{1}{T^*} - \frac{1}{T_0^*} \right] \quad (5a)$$

$$k_e^* \equiv \frac{1 + N_{RC} T^{*3} / T_0^{*3}}{1 + N_{RC}} \quad (5b)$$

with

$$N_{RC} \equiv \frac{16 \sigma n^2 T_0^3}{3 kK}$$

Specification of the initial and boundary conditions completes the problem statement. These are taken as

Initial Conditions

$$T(x^*, y^*, 0) = f(x^*, y^*) \quad 0 < x^* < 1 \quad (6a)$$

$$\psi(x^*, y^*, 0) = g(x^*, y^*) \quad 0 < y^* < A \quad (6b)$$

Boundary Conditions. For $t > 0$ and

$$-k_e^* \frac{\partial T^*}{\partial x^*} = q_F^*(y^*) \quad x^* = 0, 0 < y^* < A(1 - C) \quad (7a)$$

$$T^* = T_s^* \quad x^* = 0, A(1 - C) < y^* < A \quad (7b)$$

$$\frac{\partial T^*}{\partial x^*} = 0 \quad x^* = 1, 0 < y^* < A \quad (7c)$$

$$k_e^* \frac{\partial T^*}{\partial y^*} = N_{Nu}(T^* - T_A^*) \quad y^* = 0, 0 < x^* < 1 \quad (7d)$$

$$-k_e^* \frac{\partial T^*}{\partial y^*} = N_{Nu}(T^* - T_A^*) \quad y^* = A, 0 < x^* < 1 \quad (7e)$$

where

$$q_F^*(y^*) = \frac{q_F(y)}{q_{F,ave}}$$

and

$$N_{Nu} \equiv \frac{UH}{k_{e0}}$$

$$x^* = \frac{x}{H}, \quad y^* = \frac{y}{H}, \quad t^* = \frac{t}{t_R}, \quad \text{and}$$

$$T^* = \frac{T}{T_R}, \quad \psi^* = \frac{\psi}{\psi_R}, \quad u^* = \frac{u}{u_R}, \quad \omega^* = \frac{\omega}{\omega_R}$$

with the scale or reference quantities taken as

$$\psi_R = \alpha_{e0}, \quad u_R = \frac{\alpha_{e0}}{H}, \quad \omega_R = \frac{1}{t_R} = \frac{\alpha_{e0}}{H^2}, \quad T_R = \frac{q_{F,ave} H}{k_{e0}}$$

An examination of the dimensionless equations and boundary conditions reveals that the problem statement is a function of some ten dimensionless groups:

$$N_{Pr}, N_{Ra} \text{—from equations,}$$

$A, C, N_{Nu}, T_A^*, T_s^*$ —from boundary conditions,

and $N_{vis} \equiv \frac{E}{T_R}, N_{RC}, T_0^*$ —from property laws,

in addition to the dimensionless flux-density distribution $q_F^*(y^*)$.

The form of the temperature scaling is dictated by the nonlinear property laws. In the special case where

$$\frac{T - T_0}{T_0} \ll 1$$

additional simplifications may be effected. For this case the dimensionless groups may be redefined as

$$\theta \equiv \frac{T - T_s}{T_R} \quad (8a)$$

$$N_{Ra}' \equiv \frac{\beta g H^3 T_R}{\alpha_{e0} \nu_s} \quad (8b)$$

$$N_{vis}' \equiv \frac{E T_R}{T_0^2} \quad (8c)$$

$$N_{Pr}' \equiv \frac{\nu_s}{\alpha_{es}} \quad (8d)$$

$$N_{RC}' \equiv \frac{3 N_{RC} \frac{T_R}{T_0}}{1 + N_{RC} \left(1 + 3 \frac{T_s - T_0}{T_0} \right)} \quad (8e)$$

The equations then become

$$\frac{D^* T^*}{D t^*} = \nabla^* (1 + N_{RC}' T^*) \nabla T^*$$

$$\frac{1}{N_{Pr}'} \frac{D^* \omega^*}{D t^*} = N_{Ra}' \frac{\partial T^*}{\partial y^*} + \nabla^* [\exp(-N_{vis}' T^*)] \nabla^* \omega^*$$

and the boundary condition at $x^* = 0, A(1 - C) \leq y^* \leq A$ becomes $T^* = 0$. These redefinitions result in a reduction from 10 to 8 in the number of dimensionless groups.

Two important conclusions result from the scaling procedure. First equation (2) implies that for $N_{Pr} \gg 1$ inertial forces are negligible with the result that the problem is not a function of N_{Pr} . Similarly, since scaling was performed with the effective and not the true thermal conductivity the N_{RC} group may also be unimportant so long as the percentage changes in absolute temperature are small. This may be seen from examination of equation (5b).

Method of Solution

Finite-Difference Approach. Equations (1)–(5) were solved on a digital computer via finite-difference methods. The problem addressed here differs from prior numerical studies [4, 8] involving enclosed natural convection primarily through generalization of boundary conditions and allowance for temperature-dependence of fluid properties. The basic method of solution involves casting the problem as a transient initial-value problem and extending the solution to steady state. For this purpose both motionless isothermal initial conditions and the results of a previous run were used to start the calculations.

The theoretical aspect of this work included extensive numerical experimentation directed toward improved methods of solution of the flow equations. Implicit methods and 10×40 uniform grid were used. In the case of the vorticity transport equation the general computational algorithm follows that outlined by Wilkes [8] and Noble [4]. A detail of the grid arrangement used for the calculations is shown in Fig. 1. The primary grid

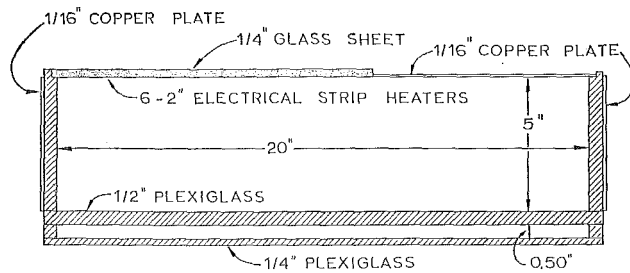


Fig. 2 Front view of experimental apparatus

points (the black dots) on which T^* and ω^* were defined are noted to be located at the centers of each zone. The stream function ψ^* , however, was defined at the corners of each cell (the crosses in Fig. 1). Finally, Fig. 1 also indicates that the velocity components (the arrows) were interlaced, being defined at the mid-points of the sides of each cell. This velocity arrangement guaranteed, in particular, mass conservation within each cell [4].

The results reported in this paper at the higher Rayleigh numbers were obtained by an iterative solution of the biharmonic equation using a "refined" grid [9], shown to exact scale in Fig. 1. Here a total of 540 zones was employed with smaller (non-square) cells located under the top surface and along the endwalls of the enclosure. The refined grid was constructed by replacing the top two and right-hand two grids of the uniform grid arrangement by four of half the width and by replacing the two left-hand grids by five equally separated grids.

Experimental Modeling

Design of the Experiment. A companion experimental program was carried out to verify the numerical model and calculations. Glycerine was employed as the modeling fluid and the experiment was designed to approximate a 1:20 scale model of a small fiberglass furnace for which data were available.

Table 1 summarizes the design of the experimental model expressed in terms of the pertinent dimensionless input parameters. Corresponding estimates for the prototype are also included for reference. One major difference between the experimental model and the prototype was that the model was operated with a no-slip boundary condition on the top surface rather than a free surface so that the experimental thermal boundary conditions would be known more exactly.

Experimental Apparatus. Fig. 2 depicts a front view of the apparatus. The enclosure was 5-in. in height, 20 in. wide, and 24 in. deep to minimize three-dimensional effects. Construction was primarily of Plexiglas. Heat was supplied to the fluid via six 2-in. electrical strip heaters cemented to a glass backing plate mounted on the top left portion of the enclosure. The thermal effects of batch cover and material input were simulated with an 8-in.-wide water-cooled copper plate.

Endwall losses were controlled by backing the 1/2-in. Plexiglas walls with water-cooled copper plates. Contact resistance between the Plexiglas and copper was minimized through the use of a grease film. The endwall boundary conditions were thus taken as the mixed type in which the ambient temperature T_A was assumed to be that of the copper plate, and the overall heat transfer coefficient U was assumed to be simply the conductance of the Plexiglas.

Both the front and bottom of the enclosure were of double-wall Plexiglas construction to minimize heat losses and to provide transparent surfaces. The top and back were insulated with a fiberglass mat and 4 in. of styrofoam. Similarly, the bottom was insulated with 2 in. of styrofoam except for a 1-in. gap running the width of the enclosure to allow for vertical-sheet illumination.

Fifty 0.003-in. copper-constantan thermocouples were used to obtain temperature measurements. These were mounted on a tree constructed of 2-mm glass rod which was placed 6 in. from the rear wall of the model.

Streak photographs were made for comparison with the calculations. For this purpose fine tracer particles of crystalline azobenzene were used. The latter were essentially insoluble in the glycerine and were neutrally buoyant (specific gravity 1.20). Illumination was provided by vertical-sheet illumination through the bottom of the enclosure. Two 300-w spotlights and a convergent-divergent lens system were used to generate this plane of parallel light. Because of the small heating rates, a water I.R. filter was used to minimize perturbations by the energy from the lamp.

Both time-lapse and multiple-exposure photographs were made through the frontal viewing surface with a Polaroid camera. The former (ASA 400/f5.6/3 to 8-min exposure time) proved the better technique for qualitative understanding of the flow. (Flow velocities were of the order of an inch per minute.) Quantitative velocity measurements, however, were best made from the multiple exposures (ASA 3000/f5.6/1-sec exposure time/30-sec intervals).

Results and Discussion

A series of computer runs was performed in an attempt to simulate the experimental results as precisely as possible. Uncertainties in the experimental endwall boundary conditions and the fluid viscosity (strongly dependent on moisture content) suggested that a sensitivity test be performed with the calculations. The computed results are presented first, and then the computer "base case" is compared with the experimental results.

Computed Results. Input data for the base-case run are summarized in Table 1. Table 2 summarizes the differences between the base case (run 94) and four additional computer runs in which the Rayleigh number, the endwall Nusselt number, and the ambient temperatures were varied. In these runs the grid system was also varied. Typical computed isotherm and streamline maps are shown in Figs. 3 and 4. The plotting convention employed with the streamline maps was to draw nine ψ^* contours between the maximum and minimum values parametrized with the (constant) increment $\Delta\psi^*$ as noted. Crowding of the stream-

Table 1 Dimensionless design parameters

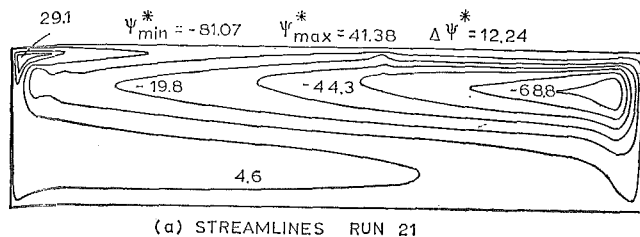
Parameter	Prototype	Experimental model and computer model (base case) run 94
N_{Pr}	400	4560
N_{Ra}	2.53×10^7	5.54×10^7
A	12	4.0
C	0.3-0.6	0.4
N_{Nu}	0.23	8.60
T_A^*	0.15	1.109
T_s^*	0.625	1.123
N_{vis}	10.65	24.5
N_{RC}	~ 20	0.0
T_0^*	0.717	1.23
N_{Pr}'	4080	4560
N_{Ra}'	6.1×10^6	5.54×10^7
θ_A	-0.475	-0.0143
N_{vis}'	20.7	19.4
N_{RC}'	6.27	0.0

Table 2 Summary of computer runs

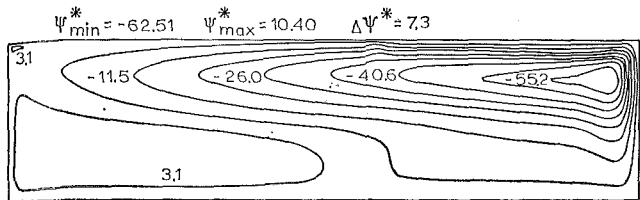
Run	Grid	$\theta_{A,L}$	$\theta_{A,R}$	N_{Nu}	N_{Ra}'
21	uniform (10 × 40)	+0.002	0.000	7.28	2.0×10^7
27	refined 1 ^a	+0.002	0.000	7.28	2.0×10^7
30	refined 1	+0.021	+0.021	8.01	1.5×10^7
37	refined 1	+0.021	+0.021	8.01	7.5×10^7
94	refined 2 ^b	-0.015	-0.014	8.60	5.5×10^7

^a Refined 1 = 12 × 45; basic zone size 0.10 × 0.10 as shown in Fig. 1.

^b Refined 2 = 15 × 34; basic zone size 0.10 × 0.20, refined near top, bottom, left, and right boundaries and in the region below the end of the batch cover.



(a) STREAMLINES RUN 21



(b) STREAMLINES RUN 27

Fig. 3 Effect of grid choice on computed streamlines

lines thus denotes regions of high velocity. The extrema ψ_{\min}^* , ψ_{\max}^* are by their usual definition measures of volumetric flow rate. It should also be noted that the boundary of the enclosure is itself a streamline having the value $\psi^* = 0$ and that this curve is not one of the nine equally spaced contours. The isotherm plots are drawn with a similar convention.

Fig. 4(a) shows that, in large measure, the melt is thermally stratified in the bulk fluid. Regions of large temperature gradient exist under the top surface and along the endwalls. Additionally, the basic fluid motion, Figs. 3(a), 3(b), and 4(b), consists of two large circulation cells of opposite rotational sense, the primary and secondary cells. The only difference between Figs. 3(a) and 3(b) is the choice of space grid. As the mesh is refined the small-scale cell in the upper left corner of Fig. 3(a) is suppressed. It is quite evident then that imprudent choice of the zone arrangement can give rise to spurious effects. The secondary cell does not disappear in Fig. 3(b); its strength merely becomes too small for the plotting routine to resolve.

A detailed examination of Fig. 4 and the associated velocity-output data yields some interesting conclusions. First, the largest horizontal velocity components occur in the vicinity of the terminus of the batch cover. Indeed, as indicated from the isotherms in Fig. 4(a), this region is the prime mover for flow in the

Table 3 Computer output parameters

Run	(a) Extrema of the stream function			
	ψ_{\max}^*	$(x, y)_{\max}^*$	ψ_{\min}^*	$(x, y)_{\min}^*$
21	13.63	(0.65, 0.35)	-81.07	(0.25, 3.85)
27	10.40	(0.75, 0.65)	-62.51	(0.25, 3.825)
30	6.24	(0.75, 0.65)	-61.69	(0.25, 3.825)
37	12.06	(0.75, 0.45)	-101.86	(0.25, 3.825)
94	9.42	(0.75, 0.50)	-56.54	(0.175, 3.825)

Run	Temperatures		Heat fluxes ($Q_{\text{source}}^* = 2.400$)			
	θ_{\max}	θ_{\min}	Sink	(% of Q_{source}^*) Left	Right	Error
21	0.1590	0.0254	80.18	10.79	8.98	0.05
27	0.1578	0.0172	89.17	9.51	6.39	4.95
30	0.1650	0.0260	90.50	6.73	2.13	0.64
37	0.1334	0.0268	95.44	5.03	2.13	2.60
94	0.1496	-0.0006	80.08	12.02	8.16	0.21

melt and acts in the nature of a "thermal pump." The primary cell serves largely to convect energy from source to sinks. Fluid under the top surface is rapidly accelerated under the action of this thermal pump and then again as it is cooled along the right endwall. The secondary cell is relatively weak and is driven by the primary-cell and left-endwall heat losses.

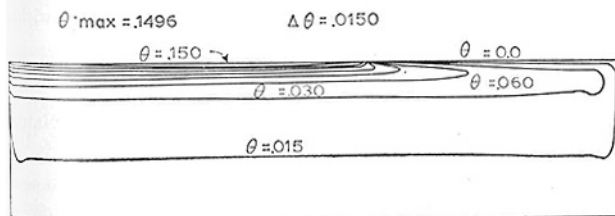
The flow pattern of Fig. 4(b) is perhaps made clearer with reference to the corresponding velocity profiles in Fig. 5. Here vertical traverses of v^* at the two stations $y^* = 1.18$ and 2.66 clearly show the nature of the fluid acceleration under the top surface and indicate more directly the relative strengths of the primary and secondary cells.

Table 3 summarizes computed output data for the five runs defined in Table 2. Here again ψ_{\min}^* and ψ_{\max}^* denote the dimensionless volumetric flow rates of the primary and secondary cells, respectively. To be especially noted here is the large effect of grid size on the stream function (run 21 vs. run 27). Our experience with calculations of this sort suggests that the refined grid does indeed provide a reasonable description of the flow.

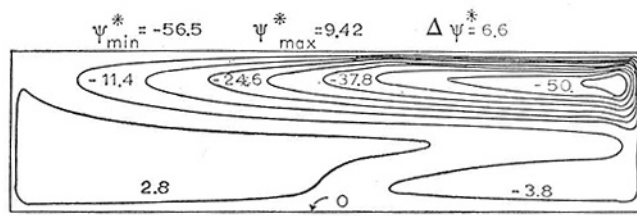
Also indicated, Table 3(b), are the maximum and minimum temperatures and the computed heat balances for the entire enclosure. It is clear from these data that the largest energy transfer occurs between the top-surface source-sink pair.

Comparison of Computed and Experimental Results. Both the experimental temperature and velocity data compare well with the computed results. Fig. 5, for example, shows good agreement for

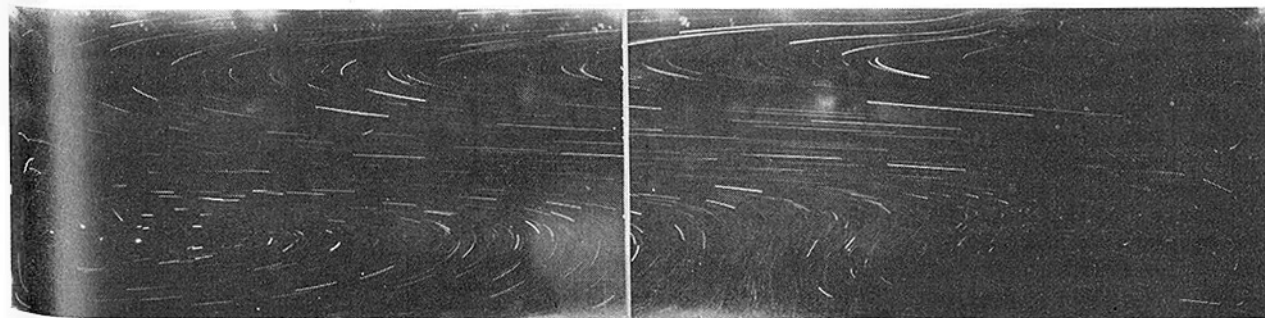
Fig. 4 Comparison of experimental and computed (run 94) results



(a) TEMPERATURE FIELD



(b) STREAMLINES



(c) Experimental streak photograph

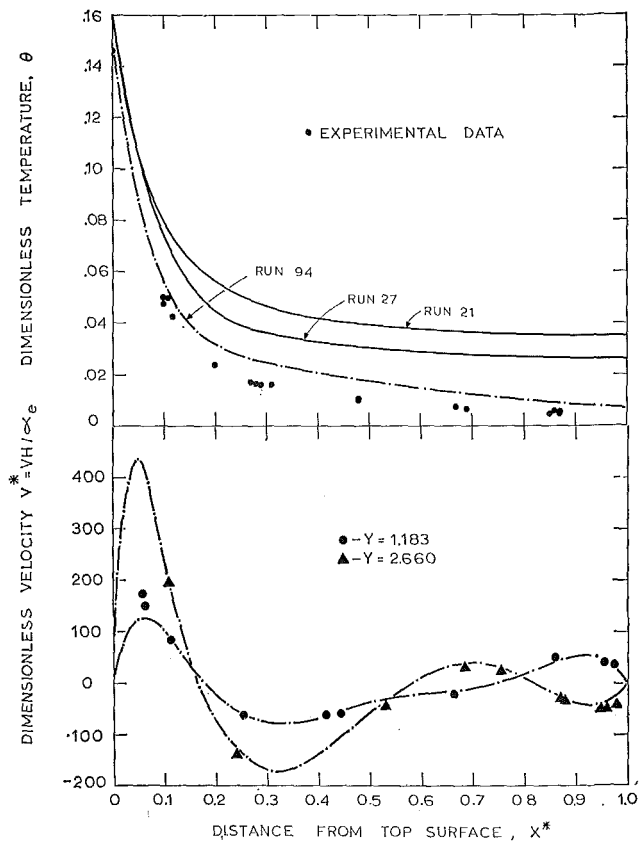


Fig. 5 Temperature and velocity traverses, computed and experimental

a vertical temperature traverse taken near the midpoint of the source. The experimental measurements used to construct this plot were not a strong function of lateral position, and thus they substantiate the dominance of thermal stratification and the boundary-layer nature of the temperature field under the top surface. Included in Fig. 5 are the temperature traverses of runs 21 and 27 which show the effect of grid size on temperature profile. These suggest that the discrepancy between run 94 and the experimental data is due to the coarseness of the grid near the center of enclosure. In any case, it should be recognized that Fig. 5 represents a severe comparison of the data, since the computer was supplied with a flux rather than with a characteristic maximum temperature. Finally, as a check on both the numerical and experimental data, measured and computed heat balances are compared in Table 4. The experimental data were obtained by monitoring cooling-water flow rates and inlet and outlet differential temperatures. The agreement certainly lends confidence to both the predicted and measured results.

Fig. 5 shows a comparison of numerical and experimental velocity traverses at the dimensionless distances $y^* = 1.18$ and $y^* = 2.66$. In general the experimental velocities fall quite close to those predicted. Minor errors in the velocities can be attributed to difficulties in locating the position of tracer particles in the photographs. Overall, the experimental data shown in Fig. 5 serve to quantitatively support the numerical results.

The most satisfying comparison is embodied in the experimental streak photographs of Fig. 4(c). Note in particular that the upflow or "fountain" near the bottom of the enclosure was predicted by the computer. This feature of the flow pattern has also been observed in the prototype.

It should be noted that the major emphasis here was on a comparison of computation and experiment in the range of conditions of glass-furnace operation and not on an exact match of prototype conditions. The no-slip velocity boundary condition, the neglect

of the momentum flux in the entering and leaving glass streams, and the differences in radiation-conduction number were approximations introduced to simplify the construction of the experimental model. All three parameters have minor effects on the flow and temperature fields and can be modeled exactly by the computational program.

Conclusions

A computer code has been developed which produces stable and convergent results at sufficiently large Rayleigh numbers to simulate industrial glass-furnace operation. Calculations in rough correspondence with a small fiberglass prototype have been experimentally verified with a $1/20$ scale glycerine laboratory model. Streak photographs and temperature and velocity measurements obtained from the experiment are shown to be in excellent accord with the predictions of the code. The computations reported here demonstrate the necessity of prudent selection of grid arrangement. Indeed, unless precautions are taken to resolve small-scale wall effects, extraneous motions may well be predicted.

The computer code thus provides a means to explore the effect, in a two-dimensional cross section, of variables which cannot be modeled experimentally and thus greatly increases the confidence with which models may be used to predict the complex mixing processes in glass melts.

Acknowledgment

This work was sponsored, in part, through grants from the Owens-Illinois Corp. and P.P.G. Industries. The cooperation of the sponsors in generously providing prototype data is gratefully acknowledged. The computations were performed in part at the M.I.T. Information Processing Center.

References

- 1 Genzel, L., "Zur Berechnung der Strahlungsleitfähigkeit der Glaser," *Glastechn. Ber.*, Vol. 26, 1953, pp. 69-71.
- 2 Hamilton, J. C., Rough, R. R., and Silverman, W. B., "Improved Techniques for Studying the Design and Operation of Glass Melting Furnaces by Means of Models," *Advances in Glass Technology*, Part 1, Plenum Press, New York, N. Y., 1962, pp. 190-195.
- 3 Hottel, H. C., and Sarofim, A. F., *Radiative Transfer*, McGraw-Hill, New York, N. Y., 1967.
- 4 Noble, J. J., "The Effect of Radiative Transfer on Natural Convection in Enclosures: A Numerical Investigation," PhD thesis, Massachusetts Institute of Technology, Department of Chemical Engineering, Cambridge, Mass., Apr. 1968.
- 5 Peyches, I., "Convection Currents in a Glass Tank," *The Glass Industry*, Vol. 29, 1948, p. 19.
- 6 Steinke, G., "Die Wannenströmung—ein Gleichgewichtsproblem," *Sprechsaal*, Vol. 99, 1966, p. 329.
- 7 Trier, W., "Zusammenhang zwischen Temperaturfeld und Strömungsfeld bei freier Konvektion in Glasschmelzen," *Glastechn. Ber.*, Vol. 38, 1965, pp. 282-292.
- 8 Wilkes, J. O., "The Finite-difference Computation of Natural Convection in an Enclosed Rectangular Cavity," PhD thesis, University of Michigan, Ann Arbor, Mich., 1963.
- 9 Clomburg, L. A., Jr., "Mathematical and Experimental Modeling of the Circulation Patterns in Glass Melts," ScD thesis, Department of Chemical Engineering, Massachusetts Institute of Technology, Cambridge, Mass., Aug. 1971.

Table 4 Comparison of experimental and predicted heat fluxes

Location	Dimensionless energy rate			
	Experimental*	%	Predicted (run 94)	%
Top right	-1.910	79.6	-1.922	80.1
Left side	-0.300	12.5	-0.285	12.0
Right side	-0.190	7.9	-0.192	8.1
Input	+2.310	96.3	+2.400	100.0
Error = sum	-0.090	-3.7	+0.001	0.2

* Based upon sum of energy removed = 2.400.

D. K. EDWARDS
Professor,
School of Engineering,
University of California
at Los Angeles,
Los Angeles, Calif.

B. D. MARCUS
Manager,
Heat Pipe Projects,
Materials Science Staff,
TRW Systems Group,
Redondo Beach, Calif.

Heat and Mass Transfer in the Vicinity of the Vapor-Gas Front in a Gas-Loaded Heat Pipe

An analysis is presented of axially conducting gas-controlled heat pipes leading to a predictive capability for the heat and mass transfer along the heat pipe. In addition, experimental results are presented which verify the analysis, and computational results are presented which show the relative influence of various parameters which affect the system behavior. In particular it was found that axial heat conduction is of much greater importance than axial mass diffusion in establishing the wall temperature profiles and condenser heat-transfer characteristics of gas-loaded heat pipes. However, mass diffusion and, consequently, the choice of working fluid and control gas are of considerable importance in establishing the "diffusion freezeout rate" if the potential exists for freezing of vapor which penetrates the gas-blocked portion of the condenser. It is believed that the analysis and associated computer program are useful tools for designing gas-loaded heat pipes.

Introduction

THE HEAT PIPE is rapidly becoming a key design element in the solution of a multitude of thermal-control and heat-transfer problems. In most cases such applications involve conventional heat pipes consisting of a sealed, internally wicked vessel which contains an appropriate quantity of a single working fluid. Such heat pipes are nearly uniform in temperature over their entire surface under most steady-state and transient conditions.

There are several situations, however, where one purposefully introduces a second, *noncondensable* fluid into the heat pipe so that it will not operate at a uniform temperature. One such situation involves the use of noncondensable gas to effect heat-pipe temperature control [1, 2].¹ Another uses noncondensable gas to aid startup from a frozen state [3-5].

Whenever a heat pipe contains a noncondensable gas in addition to its primary working fluid, its ability to transfer heat is altered significantly from that of a conventional heat pipe. During operation of such a heat pipe, vapor flows from the evaporator to the condenser region. As a consequence, any noncondensable gas present in the vapor is swept along and, since it does not condense, accumulates at the condenser end, forming a gas plug, Fig. 1. This gas plug represents a diffusion

barrier to the flowing vapor and very nearly "shuts off" that portion of the condenser which it fills. Consequently, by varying the length of this gas plug, one varies the active condenser area and, hence, the heat transfer from the system.

In applying this principle to the design of heat pipes, it has generally been assumed in analytical models that axial conduction can be neglected and that there exists a sharp interface between the vapor and noncondensable gas [1, 2]. This "flat-front" assumption is, however, inconsistent with experimental observations which show that the decrease in vapor concentration and the corresponding increase in gas concentration occur smoothly over an appreciable length of the heat pipe. As a consequence, the flat-front theory does not predict performance very well [2] and is incapable of predicting the rate at which frozen working fluid accumulates when the condenser sink temperature falls below the freezing point.

This paper presents an analysis of axially conducting, gas-controlled heat pipes leading to a predictive capability for the heat and mass transfer along the heat pipe. In addition, experimental results are presented which verify the analysis and computational results are presented which show the relative influence of various parameters which affect the system behavior. In particular it is shown that axial conductance is of principal importance for practical design situations.

Formulation

The condensing section of the pipe is assumed to reject heat by radiation and convection from a fin of perimeter P with an effectiveness η as shown in Fig. 2. The net heat loss from a length of condenser dz is thus taken to be

¹ Numbers in brackets designate References at end of paper. Contributed by the Heat Transfer Division and presented at the Winter Annual Meeting, Washington, D. C., November 28-December 2, 1971, of THE AMERICAN SOCIETY OF MECHANICAL ENGINEERS. Manuscript received by the Heat Transfer Division April 26, 1971; revised manuscript received November 8, 1971. Paper No. 71-WA/HT-29.

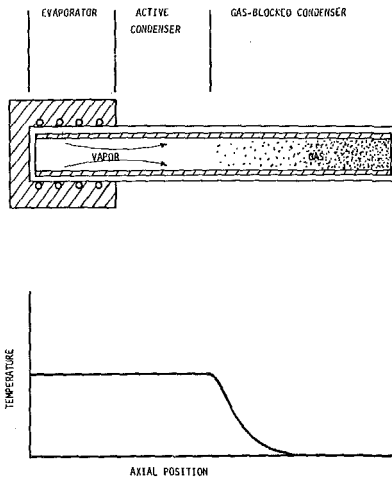


Fig. 1 Schematic diagram and temperature distribution of a gas-loaded heat pipe

$$d\dot{Q} = [\epsilon\sigma T_w^4 + h(T_w - T_f) - q_{abs}] \eta P dz \quad (1)$$

where ϵ is total hemispherical emittance, σ the Stefan-Boltzmann constant, T_w the wall temperature, h the convective heat-transfer coefficient, if any, T_f the external fluid temperature, and q_{abs} the power absorbed per unit area from the surrounds, αH in the case of irradiation H onto the condenser surface of absorptance α . For simplicity all parameters are taken to be constants, but a step change is allowed between sections of condenser.

In the usual heat-pipe application the difference between the wick-vapor-interface temperature T_i and the condenser wall temperature T_w is small compared to the absolute temperature level. For this reason equation (1) is written in a linearized form

$$d\dot{Q} = S dz (T_w - T_c) \quad (2)$$

where

$$S(z) = [4\epsilon\sigma T_i^3 + h] \eta P \quad (3)$$

and

$$T_c(z) = \frac{3\epsilon\sigma T_i^4(z) + q_{abs} + hT_f}{4\epsilon\sigma T_i^3 + h} \quad (4)$$

We adopt the unusual sign convention that the power \dot{Q} is measured in the *negative* z direction. Then Fourier's law is written without the usual negative sign. Heat flows into an element of pipe dz long at $z + dz$ and out at z by axial conduction. Heat also flows across the wick by conduction at the rate

$$\frac{2\pi k_e dz}{D_i + 2\delta} (T_i - T_w) = K dz (T_i - T_w) \quad (5)$$

where k_e is the equivalent conductivity of the liquid-filled wick, D_i the inside diameter of the wick, and δ the wick thickness. Equation (5) defines K . The heat balance on an element of condenser is then

$$C \frac{d^2 T_w}{dz^2} + K(T_i - T_w) - S(T_w - T_c) = 0 \quad (6)$$

where C is the axial-conductivity-area product for the condenser cross section

$$C = \sum_{n=1}^N k_n A_{c,n} \quad (7)$$

In equation (7) k_n is the effective axial conductivity, allowing for slots or other anisotropies, and $A_{c,n}$ the cross-sectional area of the n th element in the pipe. These elements may include the pipe wall, the wick and any arteries, and the fin wall, as shown in Fig. 2. Even if the wick artery is not in intimate thermal contact with the condenser wall, its axial conductance is included in equation (7) because the temperature gradient in it tends to follow dT_i/dz which in turn tends to follow dT_w/dz when K is large compared to S .

The wick interface temperature T_i is the saturation temperature for the partial pressure of the vapor above the interface, since the net condensation rate is far from the absolute rate of condensation (kinetic limit). Other simplifying assumptions introduced, which are reasonable for most applications, are

Nomenclature

A_c = cross-sectional area
 C = axial-conductivity-area product
 D = diameter
 \mathfrak{D} = diffusion coefficient for non-condensable in condensable
 E = empirical constant for temperature dependence of \mathfrak{D}
 F^* = nondimensional quantity defined in Appendix
 H = irradiation onto condenser surface
 K = radial wick conductance
 L = length of condenser
 M = molecular weight of condensable
 \mathfrak{M} = molar inventory of non-condensable
 P = heat-transfer perimeter of fin
 P_i = partial pressure of non-condensable at temperature T_i
 \dot{Q} = heat-transfer rate
 Q_s^* = nondimensional quantity defined in Appendix

R = gas constant for condensable
 R_u = universal gas constant
 S = radial conductance from condenser
 T = temperature
 T_0 = characteristic temperature of fluid defined by equation (8b)
 V = mole average velocity
 c = molar concentration
 h = coefficient of heat transfer
 h_{fg} = latent heat of vaporization
 k = thermal conductivity
 \dot{m} = mass flow rate
 q = heat flux
 x = mole fraction
 z = axial position
 α = absorptance of condenser surface
 δ = wick thickness
 ϵ = total hemispherical emittance of condenser surface
 ϕ = dimensional variable defined by equation (10)
 $\Phi_1, \Phi_2, \Phi_3, \Phi_4$ = dimensionless groupings defined in Appendix

η = effectiveness of condenser fin
 σ = Stefan-Boltzmann constant

Subscripts

abs = absorbed from surrounds
 b = bulk-average (area-velocity-weighted) value
 c = effective sink conditions
 e = equivalent value
 ev = evaporator conditions
 f = external fluid conditions
 i = wick surface conditions
 min = minimum
 $nominal$ = initialized value for numerical solution
 n = cross-sectional element of pipe
 s = spatial (area-weighted) average
 w = condenser wall conditions

Superscript

* = denotes nondimensional variable

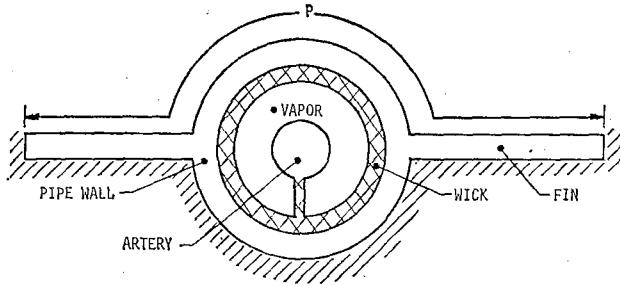


Fig. 2 Cross section of condenser

negligible vapor-side pressure loss and a simple vapor-pressure law derived from the Clausius-Clapeyron relation. The mole fraction of the *noncondensable* at the interface x_i and the interface temperature T_i are then related in the following way:

$$x_i = 1 - \exp[-(h_{fg}/RT_{ev})(T_{ev}/T_i - 1)] \quad (8a)$$

$$T_i = \frac{T_{ev}}{1 + \frac{RT_{ev}}{h_{fg}} \ln \frac{1}{1-x_i}} = \frac{T_{ev}}{1 + \frac{T_{ev}}{T_0} \ln \frac{1}{1-x_i}} \quad (8b)$$

Conservation of noncondensable gas requires that the diffusion plus convection in the tube sum to zero,

$$-c\mathcal{D} \frac{dx_s}{dz} - cVx_b = 0 \quad (9)$$

where c is the molar concentration, \mathcal{D} the diffusion coefficient for the noncondensable diffusing in the vapor, x_s the spatial or area-weighted average mole fraction, V the mole average velocity (in the negative z direction), and x_b the bulk (area-velocity-weighted) average. At least in the region of the condenser which is gas-controlled, the radial velocity rates will be sufficiently low so that the bulk, spatial, and wall values of mole fraction of noncondensable will be nearly the same. This assumption is made for the entire condenser so that the subscripts i , s , and b on x will be dropped in what follows.

To obtain an equation having the grouping $\dot{m} = cVA_cM$, the condensable flow rate, equation (9), is multiplied by A_cM , where M is the molecular weight of the condensable working fluid. In addition, the dependent variable is transformed from mole fraction x to ϕ by introducing

$$\phi = \ln \frac{1}{x}, \quad x = e^{-\phi} \quad (10)$$

Equation (9) then becomes

$$A_cM\mathcal{D} \frac{d\phi}{dz} + \dot{m} = 0 \quad (11)$$

Conservation of mass shows that increase in mass flow rate with distance from the end of the condenser is equal to the condensation rate which in turn is equal to the product of wick conductance and temperature difference across the wick divided by the latent heat of vaporization or sublimation.

$$\frac{d\dot{m}}{dz} = K(T_i - T_w)/h_{fg} \quad (12)$$

Equations (6), (11), and (12) form a set of three simultaneous differential equations in three unknowns: T_w , ϕ , and \dot{m} . The temperature T_i is related to ϕ through the highly nonlinear relations equations (10) and (8). The coefficient S defined by equation (3) is also nonlinear. An explicit energy equation for the liquid or vapor is not written because subcooling of liquid in the wick and superheating of the vapor in the pipe are not considered to be key physical phenomena, and are neglected in the present treatment. Equations (12) and (6) will give an

entirely correct energy balance when x_i , x_s , and x_b are identical, the wick resistance small, and no freezing occurs.

A boundary condition on (6), (11), and (12) is taken to be

$$\dot{m} = 0 \quad \text{at } z = 0 \quad (13)$$

In addition, either one of two conditions may be prescribed: a total heat rate rejected

$$\dot{Q} = \int_0^L S(T_w - T_c) dz \quad (14a)$$

or a total number of moles of noncondensable present

$$\mathfrak{N} = A_c \int_0^L [P_i(T_i(z))/R_u T_i] dz \quad (14b)$$

In computing \mathfrak{N} a more accurate vapor-pressure law than equation (8) must be used. An exponential of a polynomial in the reciprocal of T_i is thought best.

Strictly speaking, since equation (6) is second-order, two more conditions must be specified, such as a zero CdT_w/dz at $z = 0$ and $z = L$. However, an approximation is made that the first and second derivatives of T_w with respect to z are equal to those of T_i . As is shown in the Appendix this approximation reduces the set of equations to two first-order ones so that equations (13) and (14) are sufficient. The condition on CdT_w/dz is met at $z = 0$, and at $z = L$ it is met in practical effect when the evaporator is purged of gas. The approximation regarding the derivatives of T_w and T_i is, of course, exact when the wick resistance is zero.

A review of the features of the analysis and assumptions made are as follows:

1 Radiation and convection from a finned pipe is considered. Absorbed radiation from the surrounds is included. Provision for a step change in condenser properties and ambient conditions is made.

2 The condenser wall temperature T_w is assumed close to the wick interface temperature T_i . The first and second derivatives of T_w and T_i with respect to z are assumed equal, respectively. In essence high wick conductance is assumed.

3 Axial conduction of heat in the pipe wall, wick, and fin and one-dimensional axial diffusion of the condensable species, which carries latent heat, is accounted for.

4 Vapor-pressure drop in the pipe is neglected. In calculating the shape of the wall-temperature and wick-temperature distributions, an approximate vapor-pressure law derived from Clausius-Clapeyron is used. But in calculating the pressure in the pipe and the amount of noncondensable present a more accurate expression is used.

5 The condition of zero wall temperature gradient is met at $z = 0$. Either the total number of moles of noncondensable present in the pipe or the total heat rejected by the pipe is specified.

Numerical Solution

The Appendix shows how equations (6), (11), and (12) are reduced by virtue of assumption 2 above to a set of two simultaneous first-order differential equations in ϕ and V^* , a dimensionless velocity, or \dot{m} . An initial value T_i at $z = 0$ is used to fix $\phi(0)$, and a fourth-order Runge-Kutta routine is used to solve for $\phi(z)$ and $V^*(z)$. Either the amount of gas in the pipe or the value of \dot{Q} obtained at length L is then compared to the required value, and $\phi(0)$ is adjusted. This procedure is repeated until the calculated value of \mathfrak{N} or \dot{Q} agrees within $1/10$ of 1 percent with the specified value.

The following input information is required for the numerical solution:

Fluid Characteristics. Vapor-pressure-law constants, molecular weight of condensable, binary mass diffusivity of noncondensable

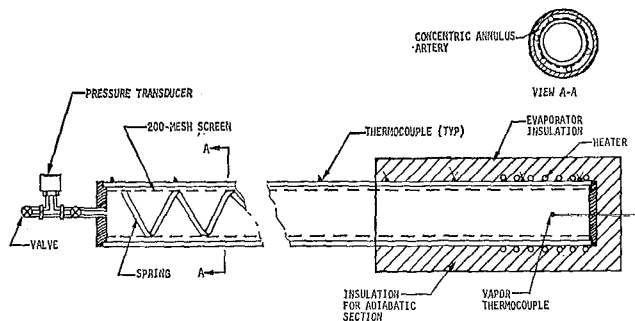


Fig. 3 Schematic diagram of experimental heat pipe

into condensable, temperature exponent of diffusivity, and latent heat of vaporization.

Vapor Flow, Pipe and Wick Characteristics. Outside diameter, wall thickness, and thermal conductivity of pipe; thickness and effective thermal conductivity of wick; diameter of internal artery, reservoir, or reservoir feed tube, if any.

Condenser Characteristics for Each of Two Condenser Sections. Perimeter, length, effectiveness, heat-transfer coefficients, emissivity, thickness, and effective axial conductivity of the fin; ambient fluid temperature and power per unit area absorbed on the heat-transfer surface.

Operating Conditions. (a) Evaporator temperature and total heat dissipated, or (b) evaporator temperature and moles of gas present in the pipe (in this case a nominal estimate of \dot{Q} (\dot{Q}_{nominal}) must be input because it is used for convenience in making dimensionless the equations shown in the Appendix).

The program output consists of profiles of x_i , T_i , T_w , $\mathfrak{M}(Z)$, \dot{m} , and $\dot{Q}(z)$ versus z . In addition, the missing value of $\mathfrak{M}(L)$ for case (a) above or a correct value of $\dot{Q}(L)$ for case (b) is obtained.

Comparison with Experiment

A series of measurements was made with a laboratory gas-loaded heat pipe to provide a basis for testing the predictive capability of the gas-front computer program. The design details of the heat pipe are presented in Fig. 3 and Table 1.

The heat pipe was instrumented with 24 chromel-alumel thermocouples, 23 on the outside wall and one within the vapor core in the evaporator. In addition, a strain-gage pressure transducer was attached to the fill tube. Heat input to the 12-in. evaporator was supplied with glass-insulated nichrome heating wire close-wound around the pipe wall. The evaporator and adiabatic sections were insulated with 2 in. of polyurethane foam. Heat transfer from the condenser was by radiation and natural convection to ambient.

Additional instrumentation included an ammeter and voltmeter for power measurements, a multipoint recorder and a hand-balanced potentiometer for temperature measurements, a digital voltmeter and transducer power supply for pressure measurements, and a precision thermometer and barometer for measuring ambient conditions.

The experimental procedure involved simply setting a fixed power input to the heater, allowing the system to equilibrate (using the multipoint recorder as an indicator), and then recording the appropriate data (using the potentiometer for accurate temperature measurements). Five runs were made in total, such that the vapor-gas interface traversed the entire condenser.

The noncondensable gas inventory was determined using the pressure transducer attached to the fill tube. The procedure was to turn off the power to the heaters and allow at least 12 hr for the pipe to equilibrate. This rather lengthy equilibration period was required for the vapor and gas to thoroughly diffuse, yielding a uniform mixture. The internal total pressure was then measured. The partial pressure of gas was determined by subtracting the vapor pressure of water at measured ambient

Table 1 Heat-pipe design details

Working fluid: water

Inert gas: air ($2.67 \times 10^{-6} \pm 5\%$ lb-mole)

Pipe: material: stainless steel
 outside diameter: 0.565 in.
 wall thickness: 0.036 in.
 overall length: 54.75 in.
 condenser length: 30.25 in.
 evaporator heat-input length: 12.5 in.
 adiabatic-section length: 12.0 in.

Wick structure: material: 200-mesh stainless-steel screen
 description: concentric annulus artery (0.015-in. gap width) with two wraps of screen held in place by a spring

temperature from the total pressure as measured by the transducer. The molar inventory of gas was then calculated from the perfect-gas law since the total void volume of the pipe and the gas temperature were also known. Such measurements were made at the beginning of the test program, midway through it, and at the end. All measurements yielded the same gas inventory indicating that no leakage or gas generation occurred during the test program.

The gas-front computer program was then utilized to obtain performance predictions for each of the test runs. All but two of the required inputs are either known bulk properties of the materials or directly measured quantities. The exceptions are the emissivity ϵ of the test pipe and the convective heat-transfer coefficient h_c . The former could not be measured *in situ* because of the high curvature of the surface, the instrumentation available being capable of accommodating flat specimens only. The latter was somewhat in doubt because of the lack of completely still conditions in the test room. Since the predicted heat dissipation for a given temperature distribution is quite sensitive to the assumed values, it was necessary to measure an effective value of h to represent convection and radiation, where the value was determined from Newton's cooling law as

$$h = \frac{\dot{Q}}{P \int_0^L (T_w - T_c) dz}$$

where \dot{Q} is the measured power, $T_w(z)$ the measured temperature distribution, and T_c the measured room temperature. The values of h so obtained are of correct magnitude as indicated below:

Measured values		Calculated values ($T_w = T_{ev}$)			
T_{ev}	T_c	\bar{h}	h_c	h_r	\bar{h}
$^{\circ}\text{R}$	$^{\circ}\text{R}$	Btu/hr-ft 2 - $^{\circ}\text{F}$	Btu/hr-ft 2 - $^{\circ}\text{F}$	Btu/hr-ft 2 - $^{\circ}\text{F}$	Btu/hr-ft 2 - $^{\circ}\text{F}$
740	536.7	3.66	2.08	1.35	3.43
682.5	536.7	3.23	1.95	1.05	3.00
667.1	535.8	3.21	1.89	1.01	2.90
637.6	534.9	2.92	1.74	0.94	2.68

The calculated values are based upon $\text{Nu} = 0.52 \text{ Ra}^{1/4}$ and $\epsilon = 0.66$, which are respectively a standard relation for free convection on a horizontal cylinder ($10^4 < \text{Ra} < 10^8$) and a nominal value for emissivity of black oxide on 321 stainless steel. Only a slightly higher value of h_c or ϵ would eliminate the small discrepancies indicated in the table above. The calculations are based on $T_w = T_{ev}$, which limits the comparison between measured and calculated values to those runs for which the condenser heat rejection associated with the vapor-gas front is a small fraction of the total.

The effect of using a constant value of h in the program is to obtain predictions of gas-vapor fronts somewhat steeper than would be predicted if h_c were allowed to vary with $(T_w - T_c)^{1/4}$ and h_r with $(T_w + T_c)(T_w^2 + T_c^2)$. Diffusion freezeout rates

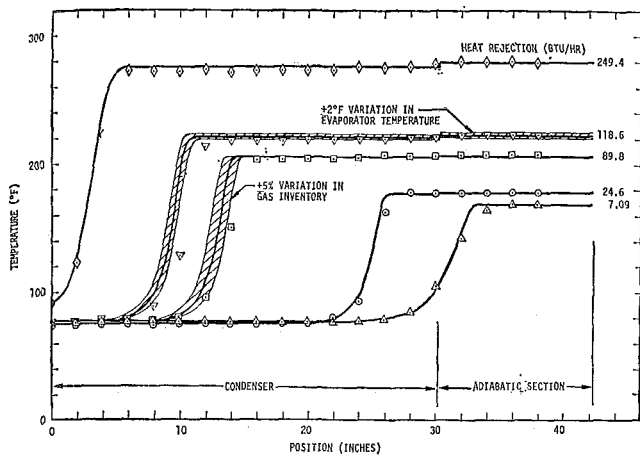


Fig. 4 Comparison of measured and predicted temperature profiles for a gas-loaded heat pipe with 12-in. adiabatic section

would consequently be overpredicted and thus be conservative. Since the profiles are iterated by the computer until the gas inventory is correct, the shape but not the location of the front would change slightly.

Fig. 4 presents both the measured and predicted temperature profiles. As is apparent, the gas-front program predicts the position of the gas front quite well. This is particularly true in view of the sensitivity of the system to gas inventory and evaporator temperature. The shaded band around one curve in Fig. 4 represents the predicted front positions for a ± 5 percent variation in gas inventory. This is about the limit of accuracy estimated for this measurement. The effect of a ± 2 deg F measurement error in evaporator temperature is shown as a shaded band on a second curve. Again, this represents the limit of accuracy estimated for absolute temperature measurements with the system used.

The program does a credible job in predicting the shape of the temperature profile despite the fact that a constant value of h was employed and despite the fact that the radial wick resistance was treated approximately. The latter factor causes a prediction of a somewhat higher condensation rate at the high-temperature end of the front than actually occurs and thus combines with the former to steepen the predicted temperature profile. The temperature predictions are indeed somewhat steeper than the data, but not greatly so.

Also of interest is the ability of the analysis and computer program to predict the heat-rejection vs. evaporator-temperature characteristic of the heat pipe. This characteristic describes the steady-state performance of gas-loaded heat pipes from a system-design point of view. Fig. 5 shows the comparison between measured data and the computer predictions. Very good agreement is evidenced between measured and predicted results.

Parametric Study of Gas-Front Behavior

With the analysis and computer program experimentally verified, a series of computations was performed to examine the influence of pertinent variables on the nature of the vapor-gas front. Several of the most important results, showing the influence of working fluid, axial wall conductivity, and operating (evaporator) temperature, are presented here.

A single geometry was used for all calculations so as to isolate the effect of the variable under study. This consisted of a 5-ft tubular condenser section which was assumed to radiate from its surface to an arbitrary heat sink.

The parameters defining the cases studied are presented in Table 2. All are self-explanatory except for the "nominal gas length." An input option in the computer program allows one to specify the gas inventory either as the number of moles present or the length of condenser which the gas would occupy based on

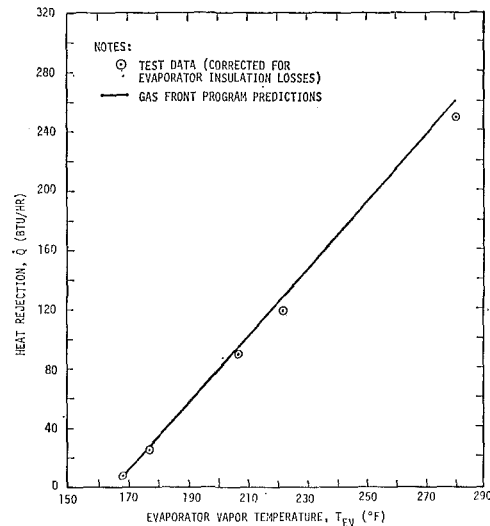


Fig. 5 Comparison of predicted and observed heat-transfer rates as a function of heat-pipe evaporator temperature

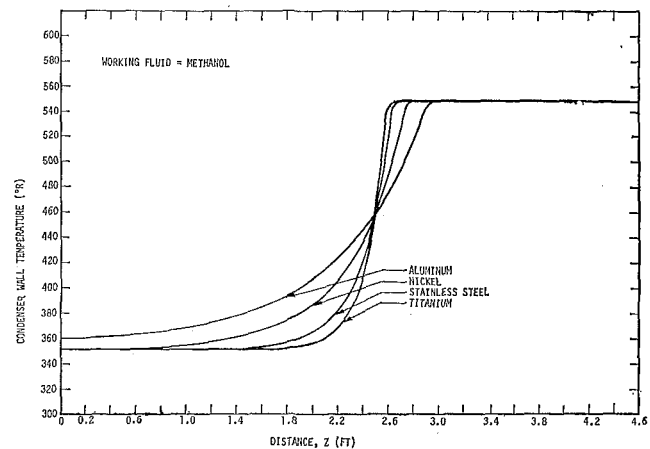


Fig. 6 Effect of axial wall conductance

flat-front theory. Using the latter option it was possible to position the fronts approximately midway up the condenser for all cases without tedious calculation of appropriate molar inventories. This permitted a clear comparison of the profiles when comparing different fluids or operating temperatures (and pressures).

Effect of Wall Conductivity. It was expected that axial conduction in the pipe wall and radiator fins (if any) would play a substantial role in defining the vapor-gas interface. To examine the magnitude of this effect, calculations were performed for titanium, stainless-steel, nickel, and aluminum heat pipes with methanol and ammonia as the working fluids.²

The calculated temperature profiles along the condenser for methanol are shown in Fig. 6. One clearly sees that wall conductance tends to spread the front over the condenser, and that this can be a very large effect with high-conductivity materials like aluminum. Diffuse vapor-gas fronts are undesirable in gas-controlled heat pipes. They tend to decrease control sensitivity [2].

The calculations also yielded the heat transfer from that portion of the condenser which is downstream of the point at which T_i has risen 99 percent of the way from the sink temperature to the evaporator temperature. This transfer represents the minimum power required to keep the gas-blocked zone from

² The known chemical incompatibility of aluminum and methanol was not of concern in this study.

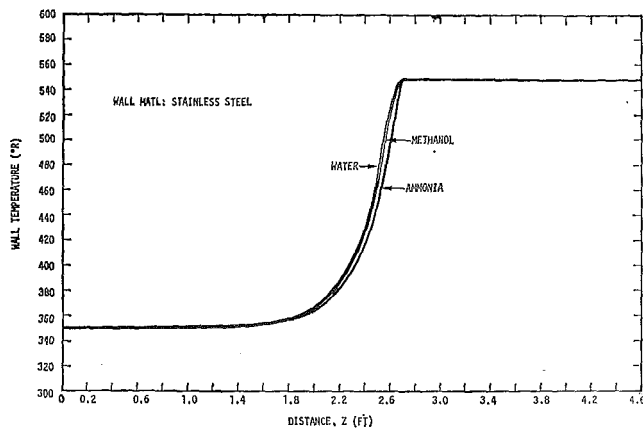


Fig. 7 Effect of working fluid

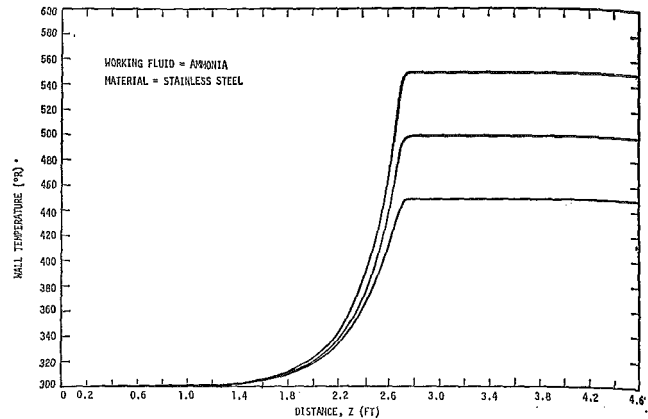


Fig. 8 Effect of operating temperature

entering the evaporator (or adiabatic section if there is one) to any appreciable extent. The results, which are presented in Table 3, clearly show that this value is also sensitive to wall conductance, increasing with increasing k . A large Q_{min} is also undesirable in gas-controlled heat pipes in that it decreases the variable conductance ratio.

The computer program also yields the axial mass transport at any position along the condenser. This quantity at the position where the wick reaches the freezing point of the fluid yields the rate at which diffusing vapor freezes and is lost to the system. This "diffusion freezeout rate" is also tabulated in Table 3. There are no results shown for the runs corresponding to Fig. 6 because the sink temperature (350 deg R) was above the freezing point of methanol (322.7 deg R). However, the ammonia results with a sink temperature below the freezing point show that the freezeout rate increases with decreasing conductivity. This behavior is not surprising in that one expects the diffusion rate to vary with the temperature gradient. Sharp fronts represent high temperature gradients and thus high diffusion rates. Thus one must examine the magnitude of the diffusion freezeout rate in a given application and, if of consequence, trade this off against the advantages of sharp fronts (lower Q_{min} , better temperature control) in establishing the axial conductance.

Effect of Working Fluid. The effect of working fluid is shown in Fig. 7 for water, methanol, and ammonia in a stainless-steel

heat pipe. The results are quite significant. One sees that the profiles are very similar, indicating a relative lack of fluid influence. Such behavior suggests that heat transport by mass diffusion is minimal and axial conduction dominates. This observation is substantiated by the minimum power predictions, which are also nearly equal for the three fluids (Table 3).

Although axial mass diffusion does not appear to significantly affect the wall temperature profile, it is both finite and important, for it is the mechanism behind the diffusion freezeout phenomenon. In this regard, Table 3 indicates substantially different values of predicted diffusion freezeout rates for the three fluids. This variance is due to a combination of factors including differences in vapor-gas diffusivity, total pipe pressure, and freezing point. Thus in situations where diffusion freezeout is of potential concern, the choice of working fluid can be of principal importance.

Effect of Operating Temperature. The primary influence of operating temperature (evaporator temperature) is to alter the pressure in the system. Thus, in view of the previous discussion, one would expect similar temperature profiles as T_{ev} is varied. This is clearly seen in Fig. 8 for ammonia. Varying the operating temperature from 450 to 550 deg R has little effect on the shape of the profile. In each case the curves exhibit the characteristic conduction-dominated shape.

Although the effect of pressure on axial diffusion is not re-

Table 2 Summary of cases studied

Common variables:

condenser length: 5 ft
 outside diameter: 0.5 in.
 wall thickness: 0.022 in.
 wick thickness: 0.020 in.
 surface emissivity: 0.8
 noncondensable gas: nitrogen
 nominal gas length: 2.5 ft

Variable matrix:

Run	Fluid	Material	Evaporator temp. (°R)	Effective sink temp (°R)
1	methanol	titanium	550	350
2	methanol	stainless steel	550	350
3	methanol	nickel	550	350
4	methanol	aluminum	550	350
5	ammonia	titanium	550	300
6	ammonia	stainless steel	550	300
7	ammonia	nickel	550	300
8	ammonia	aluminum	550	300
9	ammonia	stainless steel	550	350
10	water	stainless steel	550	350
11	ammonia	stainless steel	500	300
12	ammonia	stainless steel	450	300
13	methanol	stainless steel	550	300
14	methanol	stainless steel	500	300
15	methanol	stainless steel	450	300

Table 3 Results of calculations: diffusion freezeout rate, minimum power and total power

Run	Freezeout rate (cc/hr)	Minimum power (Btu/hr)	Total power (Btu/hr)
Effect of wall material: methanol			
1 (titanium)	...	1.9	34.1
2 (stainless)	...	2.5	34.2
3 (nickel)	...	4.2	34.5
4 (aluminum)	...	7.1	35.0
Effect of wall material: ammonia			
5 (titanium)	10.0×10^{-4}	2.1	36.7
6 (stainless)	6.7×10^{-4}	2.7	36.5
7 (nickel)	3.6×10^{-4}	4.7	35.9
8 (aluminum)	2.0×10^{-4}	7.9	35.2
Effect of fluid:			
2 (methanol)	...	2.5	34.2
9 (ammonia)	3.0×10^{-5}	2.5	34.1
10 (water)	6.4×10^{-2}	2.8	34.6
Effect of operating temperature: ammonia			
6 (550°R)	6.7×10^{-4}	2.7	36.5
11 (500°R)	1.6×10^{-3}	2.1	24.2
12 (450°R)	5.0×10^{-3}	1.6	14.9
Effect of operating temperature: methanol			
13 (550°R)	9.0×10^{-7}	2.7	36.5
14 (500°R)	4.1×10^{-6}	2.0	24.3
15 (450°R)	2.8×10^{-5}	1.4	15.0

ected in the conduction-dominated temperature profiles, it is obvious when one examines the predicted diffusion freezeout rates. Table 3 shows that for both methanol and ammonia the diffusion freezeout rate increases as the operating temperature and, hence, total pressure is lowered.

Summary and Conclusions

A study was performed on the heat- and mass-transfer characteristics of heat pipes containing noncondensable gases. An analysis was formulated based on a one-dimensional model which included (1) simultaneous radiation and convection from a finned condenser; (2) axial conduction in the walls, fins, and wicks; (3) binary mass diffusion between the vapor and gas; and (4) an approximate treatment of wick resistance which is accurate for high-conductance wicks. The governing equations were programmed for numerical solution on a digital computer such that the program can be used for heat-pipe design or performance-prediction calculations.

Parametric calculations showed an important influence of axial conductance upon the behavior of gas-loaded heat pipes. In fact, over the range of variables considered, axial diffusion had negligible impact on the shape of the wall temperature profiles compared with the conduction effect. Thus, the choice of working fluid had little effect on the temperature profiles. Axial diffusion is, however, important in establishing the diffusion freezeout rate for conditions under which this occurs. The freezeout rate varies widely with working fluid and, for a given fluid, increases with decreasing operating temperature (total pressure).

Experimental measurements made with a laboratory heat pipe were in excellent agreement with calculated performance. In particular, the temperature profiles along the pipe wall and the operating characteristic for the pipe (heat rejection vs. evaporator temperature) were correctly predicted.

The experimental verification of the analysis and associated computer program suggests that these may be useful tools for designing gas-loaded heat pipes.

Acknowledgments

The authors wish to express their appreciation to Mr. George Fleischman of TRW for his efforts in both the experimental and computational phases of this work.

This paper is based on work performed under NASA Ames Research Center contract NAS 2-5503 and has been assigned NASA report no. CR 114300. Mr. J. P. Kirkpatrick serves as NASA project manager for this contract.

References

- 1 Bienert, W., "Heat Pipes for Temperature Control," *Proceedings of the Fourth Intersociety Energy Conversion Engineering Conference*, Washington, D. C., Sept. 1969.
- 2 Marcus, B. D., and Fleischman, G. L., "Steady-State and Transient Performance of Hot Reservoir Gas-Controlled Heat Pipes," ASME Paper No. 70-HT/SpT-11.
- 3 Hinderman, J. D., Madsen, J., and Waters, E. D., "An ATS-E Solar Cell Space Radiator Utilizing Heat Pipes," AIAA Paper No. 69-630, AIAA 4th Thermophysics Conference, San Francisco, Calif., June 1969.
- 4 Deverall, J. E., "Mercury as a Heat Pipe Fluid," ASME Paper No. 70-HT/SpT-8.
- 5 Clausen, O. W., Marcus, B. D., Piske, W. E., and Turner, R. C., "Circumferential Heat Pipe Systems for Large Structures," Final Report, NASA contract no. NAS 9-10299, Dec. 1970.

APPENDIX

Dimensionless Governing Equations

The mass flow rate, mass diffusivity, temperatures, and other parameters were made dimensionless so that orders of magnitudes could be assessed and for convenient numerical solution. The dimensionless quantities are

$$\begin{aligned} z^* &= z/D_e \\ V^* &= \dot{m}h_{fg}/\dot{Q}_{\text{nominal}} \\ \mathfrak{D}^* &= M(c_{\text{ev}}\mathfrak{D}_{\text{ev}}/D_e)A_c h_{fg}/\dot{Q}_{\text{nominal}} \\ T_i^* &= T_i/T_{\text{ev}} \\ T_w^* &= T_w/T_{\text{ev}} \\ T_0^* &= T_0/T_{\text{ev}} \\ T_c^* &= T_c/T_{\text{ev}} \\ Q_o^* &= \frac{d\dot{Q}^*}{dz^*} = S^*(T_w^* - T_c^*) \\ S^* &= F^*(4\epsilon T_i^{*3} + H^*) \\ F^* &= \eta P D_e \sigma T_{\text{ev}}^4 / \dot{Q}_{\text{nominal}} \\ H^* &= h/\sigma T_{\text{ev}}^3 \\ C^* &= C T_{\text{ev}} / D_e \dot{Q}_{\text{nominal}} \\ K^* &= K D_e T_{\text{ev}} / \dot{Q}_{\text{nominal}} \end{aligned}$$

where T_{ev} is the evaporator temperature which sets the total pressure in the system and D_e is an equivalent diameter allowing for the presence of arteries within the pipe,

$$D_e = (4A_c/\pi)^{1/2}$$

where A_c is the cross-sectional area available for vapor flow. An exponent E is an empirical factor to account for the temperature variation of the mass diffusivity defined by

$$c\mathfrak{D} = c_{\text{ev}}\mathfrak{D}_{\text{ev}}(T_i/T_{\text{ev}})^E$$

Equations (6), (11), (12), and (8) written in dimensionless form become

$$C^* \frac{d^2 T_w^*}{dz^{*2}} + K^*(T_i^* - T_w^*) - S^*(T_w^* - T_c^*) = 0 \quad (15)$$

$$\frac{d\phi}{dz^*} = \frac{V^*}{\mathfrak{D}^* T_i^{*E}} \quad (16)$$

$$\frac{dV^*}{dz^*} = K^*(T_i^* - T_w^*) \quad (17)$$

$$1 - e^{-\phi} = e^{-T_0^*(1/T_i^* - 1)} \quad (18)$$

Under approximation 2 in the list in the text, equation (15) is approximated as

$$C^* \frac{d^2 T_i^*}{dz^{*2}} + K^*(T_i^* - T_w^*) - S^*(T_w^* - T_c^*) = 0 \quad (15a)$$

The simplifying feature of this approximation is that the second derivative in equation (15a) can now be eliminated. Equation (18) is differentiated with respect to z^* , and equation (16) is used to eliminate $d\phi/dz^*$. The result multiplied by C^* is

$$C^* \frac{dT_i^*}{dz^*} = C^* \frac{e^{-\phi} T_i^{*2-E}}{(1 - e^{-\phi})\mathfrak{D}^* T_0^*} V^* \quad (19)$$

Equation (19) is differentiated again with respect to z^* , equation (16) is used again to eliminate $d\phi/dz^*$, and equation (19) itself is used to eliminate dT_i^*/dz^* .

$$C^* \frac{d^2 T_i^*}{dz^{*2}} = \Phi_1 \frac{dV^*}{dz^*} - \Phi_1 \Phi_2 \Phi_3 \quad (20)$$

where the functions Φ_1 , Φ_2 , Φ_3 are

$$\Phi_1(\phi) = C^* \frac{e^{-\phi} T_i^{*2-E}}{(1 - e^{-\phi})\mathfrak{D}^* T_0^*} \quad (21)$$

$$\Phi_2(\phi) = 1 - (2 - E)(T_i^*/T_0^*)e^{-\phi} \quad (22)$$

$$\Phi_3(\phi, V^*) = V^{*2}/(1 - e^{-\phi})\mathfrak{D}^*T_i^{*E} \quad (23)$$

Equation (15a) together with equations (17) and (20) now can be written

$$\frac{dV^*}{dz^*} = Q_e^* - \Phi_1\Phi_4 \quad (24)$$

where

$$\Phi_4(\phi, V^*) = \frac{Q_e^*(\phi) - \Phi_2(\phi)\Phi_3(\phi, V^*)}{1 + \Phi_1(\phi)} \quad (25)$$

Equations (16) and (24) together with (18) and the definitions of Φ_j in equations (21), (22), (23), and (25) form a set of two simultaneous nonlinear first-order ordinary differential equations which can be numerically solved by, say, a fourth-order Runge-Kutta routine. The initial conditions are $V^* = 0$ and $\phi = \phi_0$

at $z = 0$. Values of \mathfrak{M} and \dot{Q} for a length of pipe L can be obtained versus ϕ_0 for a given set of parameters and an evaporator temperature T_{ev} . An iterative routine can be used to find ϕ_0 for a prescribed value of either \mathfrak{M} or \dot{Q} .

When a discontinuity in pipe axial conductance occurs, the assumption of small wick resistance admits very high condensation rates which then lead to a discontinuity in mass flow. Heat flow, temperature, and composition are continuous, of course. At the discontinuity between condenser sections the new value of V^* required from continuity of heat flow is

$$V_2^* = V_1^* \frac{1 + \frac{C_1^*}{V_1^*} \left(\frac{dT_i^*}{dz^*} \right)_1}{1 + \frac{C_2^*}{V_2^*} \left(\frac{dT_i^*}{dz^*} \right)_2} \quad (26)$$

where the temperature-gradient terms are obtained from equation (19).

F. K. MOORE

Y. JALURIA

Department of Thermal Engineering,
Cornell University,
Ithaca, N. Y.

Thermal Effects of Power Plants on Lakes

The natural thermal cycle of a stratified water body used for power-plant cooling will be disturbed both by heat addition and the mixing effect of withdrawal and return. A perturbation analysis for these effects is made with a model based on the assumption that a Richardson number is constant at the base of any stratified layer. On a further assumption about the profiles of wind-driven return currents, constant heat flux from that layer is inferred. This heat flux, and the diffusion coefficient at the thermocline, are the critical parameters of the simple one-dimensional line-segment model, and are chosen to give good imitation of the known natural cycle of Cayuga Lake. The model is then perturbed in terms of both heat flux and diffusion to give power-plant impact for that lake. Both transient and final cycle changes of summer and winter temperatures and stratification and overturn are calculated. It is shown that the heat and diffusion effects are comparable, and that the latter may be dominant if the discharge is diluted to meet a thermal standard. Certain implications as to strategy of water use are developed.

Introduction

THE CONDENSERS of a large nuclear power plant can be conveniently and economically cooled by cold water available at depth in stratified lakes such as Cayuga. Studies at Cornell [1, 2]¹ and C.A.L. [3, 4] indicate that the yearly average surface temperature of Cayuga Lake, which is 66 sq mi in area, would increase by about 1 deg F in response to a heat input of 6.4×10^9 Btu/hr. This heat addition would correspond to a 940-MW plant operated at 33 percent thermal efficiency.

This result follows from the surface heat-exchange equation [1, 5]

$$q_s = K(T_e - T_s) \quad (1)$$

where T_e is an "equilibrium temperature" depending on the thermal environment of the water surface. In this paper K will be taken to be 70 Btu/ft²-day-deg F in the winter and 104 in the summer [1, 2]. The yearly natural average of q_s must nearly vanish. Thus if q_s has a negative yearly increment to balance heat received from the plant, then the yearly average level of T_s must increase. Alternatively, the effect of pure heat addition may be represented as a nearly level increase of T_e given by the rate of heat rejection divided by surface area and a suitably averaged value of K . The present New York State regulatory standard, following FWPCA guidelines [6], limits surface-temperature changes on lakes such as Cayuga to 3 deg F. On a yearly average basis, this rule would tend to permit establishment of three lake-cooled plants.

For assessment of the biological impact of this use of lake

water, one needs to know the effect of heat addition throughout the lake depth and throughout the yearly cycle, although one might be satisfied with surface-averaged results, in view of the vigor of transverse mixing processes.

To achieve this level of detail, in depth and time, one must evaluate the mixing effect of pumping cooling water from deep levels and discharging near the surface. For the postulated 940-MW plant, a flow of about 1200 cfs is required, assuming a temperature change through the condensers of 24 deg F. In the winter, when the lake is fully mixed, this extra mixing action is negligible. In the summer, the thermally stratified lake is characterized by a very small minimum diffusion coefficient D_m at the thermocline, taken in this paper to be constant at 12 ft²/day [1]. Thus, natural diffusional exchange is greatly inhibited in the summer (supporting stratification, of course). Obviously, the pumped exchange of 1200 cfs tends to "short-circuit" this barrier, and artificially enhances the exchange of cold and warm water. This effect will alter temperature profiles by redistributing thermal energy, and will also affect the distribution of nutrients and dissolved oxygen in the lake.

The foregoing summer mixing enhancement has been estimated [1] to be equivalent to a 10 percent increase of D_m . This estimate will be increased to 20 percent in a later section of this paper. If more than one plant uses the water, or if more water is pumped to cool the discharge by dilution, then the effective change of D_m is increased proportionately, in the latter case to 60 percent for a single plant diluting its discharge to give an 8 deg F rise.

In this paper we develop a simple theoretical model for the thermal structure of a stratified lake. The model is made to fit the observed cycle of Cayuga Lake [7] by careful choice of model parameters. Then the model is perturbed by various changes in T_e and D_m to represent heat addition and mixing effects of power plants on the thermal cycle of the lake.

¹ Numbers in brackets designate References at end of paper.

Contributed by the Heat Transfer Division and presented at the Winter Annual Meeting, Washington, D. C., November 28–December 2, 1971, of THE AMERICAN SOCIETY OF MECHANICAL ENGINEERS. Manuscript received by the Heat Transfer Division July 20, 1971.

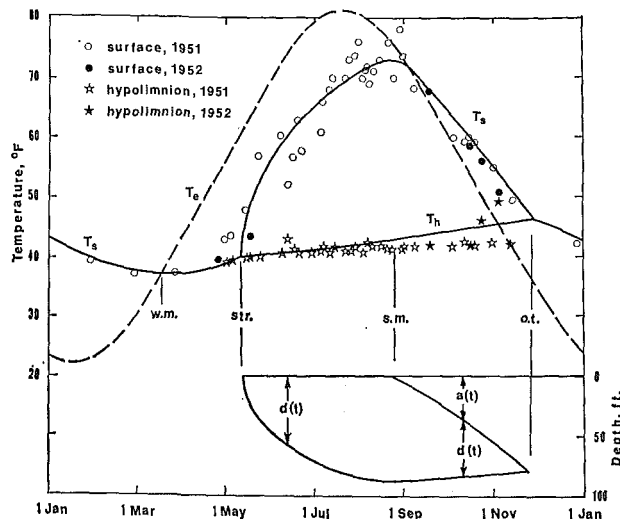


Fig. 1 Calculated cycle of thermal stratification, with equilibrium temperature T_e from [1] and measured temperatures from [7] superposed; below, calculated cycle of epilimnion depth

Other calculations of power-plant thermal impact have been reported in references [2, 3]. The present analysis depends on information developed in reference [2], and retains the simplicity of that analysis, but takes better account of the progressive deepening and subsequent erosion of the stratified layer.

Natural Thermal Cycle

Before developing the theoretical model, a brief description of certain features of the thermal cycle of Cayuga Lake should be provided, based on reference [7], recently supplemented by C.A.L. studies [4].

The lake is a kind of thermal oscillator driven by heat exchange with sun and atmosphere, expressed in terms of T_e . Very accurately, T_e may be represented as a harmonic wave obeying the formula [1]

$$T_e = 51.2 - 29.3 \cos \frac{2\pi}{365} (t - 19) \quad (2)$$

where time is measured from 1 January. This function is dis-

played in Fig. 1. In the winter the lake loses heat and is fully mixed by the wind, and hence is isothermal. Typically, a winter minimum of 37 deg F occurs on 22 March. (These figures, and those to follow, are typical rather than exact.) Then, by 11 May, the difference between T_e and T_s is so great that the heat flux described by equation (1) suffices to establish a thermal stratification at $T_s = 40.1$ deg F, in opposition to wind mixing. Figs. 2(a) and 2(b) show typical temperature profiles of the deepening epilimnion in spring and early summer. The vagaries of wind and weather, surface flows, and internal seiches make it difficult to draw conclusions from profiles measured in one place, as these are.

In late summer T_e falls, and Fig. 1 shows that the surface begins to lose heat. The summer maximum value of T_s is 73 deg F on 25 August. Following that time, Fig. 2(c) shows how the temperature profile changes shape to accommodate a deepening, unstable, isothermal upper portion of the epilimnion. A corresponding sharpening of the thermocline occurs. Finally, the erosion of the epilimnion is completed on 24 November, at $T_s = 46$ deg F, and the lake reverts to an isothermal state. This reversion or "fall overturn" is, of course, a gradual process to which, for definiteness, we assign a particular date and temperature.

Stability Criterion

To form a model to imitate the yearly process just described, we must adopt a stability principle for stratification. In laminar-shear flow, stability is assured [8] if the Richardson number

$$Ri \equiv \frac{g \partial \rho / \partial z}{\rho (\partial u / \partial z)^2} \quad (3)$$

exceeds $1/4$. Here we suggest that stable stratification in our turbulent wind-driven flow may similarly be associated with a sufficiently large specific value of Ri . Further, we note that $\partial \rho / \partial z = -\beta \rho \partial T / \partial z$ and that $q = -\rho C_p D \partial T / \partial z$. Hence, on a flux basis,

$$Ri = \frac{g \beta}{\rho C_p (\partial u / \partial z)^2} \frac{q}{D} \quad (4)$$

The velocity gradient $\partial u / \partial z$ should next be related to turbulent shear stress. It is not clear how this may plausibly be done with the inadequate knowledge we have of wind-driven currents,

Nomenclature

a = thickness of isothermal zone in fall, Fig. 2(c)
 C_p = specific heat of water
 c = coefficient, equations (5) and (6)
 D, D_m = coefficient of turbulent vertical diffusion of heat; D_m is minimum value presumed to occur at base of epilimnion
 d = depth of variable-temperature part of epilimnion, Fig. 2
 g = acceleration due to gravity
 K = coefficient of heat exchange at water surface, equation (1), taken as 70 Btu/ft²-deg F-day in unstratified period, 104 when stratified
 l = model depth of lake, Fig. 2
 N = coefficient of stratification delay, equation (6)

q, q_s = downward heat flux; q_s flux downward into water surface
 q_e = downward heat flux for stability, equation (5)
 Ri = Richardson number, equation (3)
 T, T_s, T_h = water temperature, temperature at surface, and in hypolimnion
 T_e = "equilibrium temperature," a measure of heat input from sun and atmosphere, equation (1)
 t = time measured in days from 1 January
 u = transverse velocity of wind-driven currents
 v = vertical diffusion velocity, equation (22)
 z = vertical coordinate measured downward from surface
 α = dimensionless version of a

β = coefficient of thermal expansion of water, $-\frac{1}{\rho} \frac{\partial \rho}{\partial T}$
 γ = "concentration" of cold water, equation (21)
 δ = dimensionless d , equation (10)
 λ = dimensionless l , equation (10)
 ρ = density of water
 τ = dimensionless time, equation (10)

Superscripts

* = dimensionless quantity, equations (10) and (16)
 = signifies d/dr

Subscripts

ot = at "fall overturn"
 sm = at summer maximum of T_s
 str = at onset of stratification
 wm = at winter minimum of T_s

especially at the base of the epilimnion where we wish to apply equation (4). We do know, however, that D may vary by 2 orders of magnitude through the epilimnion [1, 4], decreasing with depth. Thus it may not be unreasonable to associate stability with a particular minimum critical value of heat flux

$$q_c = cD_m; \quad c \equiv \frac{Ri\rho C_p(\partial u/\partial z)_c^2}{g\beta} \quad (5)$$

where we assume that $(\partial u/\partial z)_c^2$ may be assigned an average value and therefore that c can be assumed constant.

Accordingly, we define the base of the epilimnion as the place where the downward heat flux just equals q_c , and in the summer we expect $q_s > q_c$.

The spring onset of stratification presents a special problem. It would seem reasonable to suppose that to begin stratification of a fully mixed lake having large turbulent eddies would require a heat flux larger than that needed to maintain an established stratification. Accordingly, we will assume that stratification begins when

$$q_s = q_{str} \equiv N(\beta) + c(\beta)D_m \quad (6)$$

We note that the typical $T_{str} = 40.1$ deg F is not greatly in excess of 39.2 deg F, which is the temperature of maximum density ($\beta = 0$); later, we will need to recall from equation (5) that stability is proportional to β .

At this stage we regard the quantities q_c , D_m , and N to be parameters whose values remain to be chosen empirically.

Thermal Model

Next, for model purposes, we adopt the straight-line-segment temperature profile shown in Fig. 2. The quantities T_s , T_h , and d are functions of time, to be determined. We represent the late-summer shape change by permitting development of an upper isothermal layer of thickness a . Thus, d vanishes both at stratification and overturn.

Cayuga Lake has a maximum depth of 430 ft and an average depth of 179 ft. Our model is one-dimensional and hence surface-averaged. However, one may argue that shallow shore regions should be excluded, and we think it prudent to regard our model depth l to be a fourth parameter requiring empirical determination.

At depth d , stability requires that $q = q_c$, or

$$\rho C_p D_m \frac{T_s - T_h}{d} = q_c \quad (7)$$

It should be noted that the assumed straight-line profile does not imply a constant heat flux in the epilimnion; in most of that region, $D > D_m$, and q at $z = d$ would be a minimum for that region.

A heat balance for the entire lake, based on the summer profile shown in Fig. 2(b), gives, when equation (1) is used,

$$K(T_e - T_s) = \rho C_p \frac{d}{dt} \left[l T_h + \frac{1}{2} d(T_s - T_h) \right] \quad (8)$$

For the hypolimnion only,

$$(l - d)\rho C_p \frac{dT_h}{dt} = q_c \quad (9)$$

Next, we may introduce new variables

$$T^* \equiv \frac{K}{q_c} T; \quad \delta, \lambda \equiv \frac{K}{\rho C_p D_m} (d, l); \quad \tau \equiv \left(\frac{K}{\rho C_p} \right)^2 \frac{t}{D_m} \quad (10)$$

and rearrange the foregoing equations to yield for the summer

$$T_s^* - T_h^* = \delta \quad (11)$$

$$\delta \dot{\delta} + \delta = T_e^* - T_h^* - \lambda \dot{T}_h^* \quad (12)$$

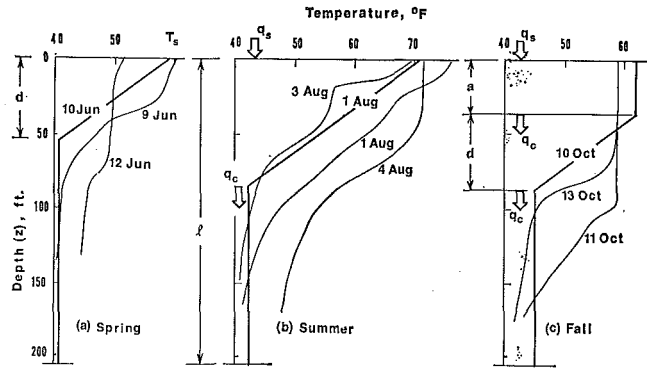


Fig. 2 Comparison of idealized calculated temperature profiles (straight, darker lines) and certain measured profiles for 1951 [7]; region $0 < z < a + d$ is the model epilimnion and region $a + d < z < l$ is the model hypolimnion

$$(\lambda - \delta)\dot{T}_h^* = 1 \quad (13)$$

In the winter, when $\delta = 0$, equation (12) gives

$$\lambda \dot{T}_s^* = T_e^* - T_s^* \quad (14)$$

At stratification, setting $\delta = 0$ in equations (12) and (13) would yield $T_e^* - T_s^* = 1$, or $q_s = q_c$. Thus, to apply equation (6) we must permit δ to be infinite:

$$[\delta \dot{\delta} - (T_e^* - T_s^* - 1)]_{str} = 0 \quad (15)$$

$$(T_e^* - T_s^* - 1)_{str} = N^* \equiv \frac{N}{q_c} \quad (16)$$

Hence, δ must commence parabolically

$$\delta \approx (2N^*\tau)^{1/2} \quad (17)$$

as illustrated in Fig. 1.

At summer maximum, when $(\dot{T}_s)_{sm} = 0$, equations (11), (12), and (13) yield $(T_e^* - T_s^*)_{sm} = 1$, or $q_s = q_c$. That is, q_s has fallen to the point where it can just supply the necessary q_c to the hypolimnion. Following summer maximum, the epilimnion must obviously lose heat, and an isothermal upper layer must appear because $q < q_c$. As illustrated in Fig. 2(c), we assume that $q = q_c$ at both breaks in the profile.

The applicable energy balances for the three regions of Fig. 2(c) may be manipulated to show that $\alpha + \delta + T_h^*$ is constant (α is a , nondimensionalized) and that the following equations apply after summer maximum:

$$T_s^* - T_h^* = \delta \quad (11)$$

$$\alpha + \delta + T_h^* = (T_e^*)_{sm} - 1 \quad (18)$$

$$\alpha \dot{\alpha} + \alpha = (T_e^*)_{sm} - T_e^* \quad (19)$$

$$(\lambda - \delta - \alpha)\dot{T}_h^* = 1 \quad (20)$$

Equation (18) tells us that in this model, if T_h^* is increasing, the lower margin of the stratified region must rise, as part of the general process of heat loss in the fall.

Application to Cayuga Lake

The foregoing first-order nonlinear equations have been solved by high-speed computer, assuming equation (2) for T_e and $K = 70$ (winter), 104 (summer), for various values of N , D_m , l , and q_c in ranges known to be reasonable. In each case, a starting value of T_s was chosen on 1 January and the calculation proceeded through several yearly cycles (usually 6 cycles sufficed) until annual repetition within 0.01 deg F was achieved. Step size was 1 day, except near stratification and overturn, when 0.01-day steps were employed.

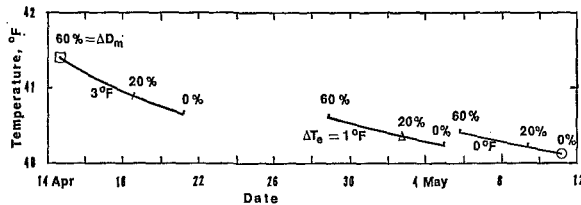


Fig. 3 Lake temperature at onset of stratification; circle represents natural lake; triangle, one 940-MW plant pumping 1200 cfs; square, three such plants

Parameter choices were made to fit the measured data presented in Fig. 1. Our choices of "target" values for stratification date and temperature, summer maximum temperature, etc., represent our impressions of the requirements of these data, but are certainly not definitive. For example, most of the data refer only to 1951. The filled points refer to 1952. Clearly, stratification in 1952 was later, and overturn was earlier and much more abrupt than in 1951.

Especially in view of the uncertainties of the data, we include in Table 1 an indication of the sensitivity of target values to parameter choices in the ranges indicated, when the parameters were changed one at a time.

Fig. 1, then, shows the yearly cycle we propose as a representation of the natural lake, including the development of and erosion of an epilimnion which reaches a depth of about 90 ft. Fig. 2 shows the model profiles calculated for three particular dates. We believe that this model is a reasonable basis for estimating power-plant perturbation.

However, before proceeding we might note how Table 1 could be used to conform the model to different judgments as to target values. Suppose one wished to see a deeper epilimnion. One might decrease q_c , but then D_m should be decreased to keep $(T_s)_{sm}$ high enough. It is probably necessary to keep $(T_s)_{wm}$ at the 37 deg level, so either l or N^* must be increased. Since N^* would tend to make the depth shallower again, one would have to accept the cooler and later overturn due to increased l . A certain increase of N^* would nevertheless be needed to keep $(T_s)_{str}$ at the 40 deg level. Thus, we see that no combination of parameter changes in the present model will very efficiently deepen the epilimnion.

Perturbations by Power Plants

In the Introduction, we outlined the scheme we will now follow. We represent pure heat addition from a 940-MW plant of 33 percent thermal efficiency by raising the level of T_e by 1 deg F (changing the first term of equation (2) from 51.2 to 52.2). We consider also the possibility of three such plants, raising T_e by 3 deg F.

In combination with the changes of T_e , we also change D_m to represent the mixing effect of withdrawal and return of water. To derive this correspondence we follow reference [1], representing the epilimnion as a region of diffusional exchange between a reservoir of hot water "particles" at T_s and one of cold water at T_h . We define a "concentration" of cold water

$$\gamma \equiv \frac{T_s - T(z)}{T_s - T_h} \quad (21)$$

and a "diffusion velocity" of cold water in the classical form

$$v \equiv -D \frac{\partial \ln \gamma}{\partial z} \quad (22)$$

From our model, we would then derive that

$$v = D_m \frac{dT/dz}{T_s - T_h} = \frac{D_m}{d} \quad (23)$$

Table 1 Cycle quantities and model parameters

Parameter	N^*	D_m (ft ² /day)	l (ft)	q_c (Btu/ft ² - day)
Chosen value	5	12	205	250
Parameter variation	4 to 6	11 to 13	179 to 250	250 to 300
Cycle quantity	Target value	Target-value variation due to parameter variation		
$(T_s)_{wm}$	37.1°F	+0.8	+0.4	+0.9
$(T_s)_{str}$	40.1	+2.1	+0.4	-0.3
(date) _{str}	11 May	+14 days
$(T_s)_{sm}$	72.9	...	-0.7	...
$(T_s)_{ot}$	46.3	+2.6	+0.6	-2.8
(date) _{ot}	24 Nov.	-5	...	+8
$(d)_{sm}$	89 ft	-4	+10	...
				-16

The cold-water velocity due to our power plant, assuming a 24 deg F temperature drop through the condensers, is the volume flow rate of 1200 cfs distributed over 66 sq mi, or 0.056 ft/day. Thus, the total cold-water velocity would be

$$\frac{D_m}{d} + 0.056 = \frac{D_m}{d} \left(1 + \frac{0.056}{D_m} d \right) \quad (24)$$

The effects of this change can apparently be represented as being due to an increase of D_m by the fraction $(0.056)d/D_m$.

Although d is time-dependent, the approximate nature of this analysis suggests that a summer average be used. From Fig. 1, one may estimate the average of d to be 56 ft. Recalling that $D_m = 12$ ft²/day, we find the average fractional increase of D_m to be about 26 percent.

This estimate may be supported by application of equation (23) to the measured profiles of Fig. 2. Taking the profiles of 9 June, 1 August, and 13 October as typical, and using the maximum value of dT/dz in each case, the quantity $(dT/dz)/(T_s - T_h)$ assumes the values 0.033, 0.011, and 0.18 ft⁻¹, and, with $D_m = 12$ ft²/day, the diffusion velocities are 0.40, 0.13, and 2.2 ft/day, of which the pumping velocity (0.056 ft/day) is 14, 43, and 2.5 percent. Making allowance for the extreme fluctuations of the measured profiles, these last results are consistent with a summer-average mixing enhancement of 26 percent.

Turning again to the present model, one may form this mixing estimate in another way. We have argued that downward heat flux from the epilimnion is $q_c = 250$ Btu/ft²-day. Quite apart from the rejection of heat, the pumping of hypolimnetic water to the surface in effect also causes a downward heat flux, in the amount of $\rho C_p (0.056)(T_s - T_h) = 3.5(T_s - T_h)$ Btu/ft²-day. For the three dates in Fig. 2, this artificial heat flux would be, in comparison to 250 Btu/ft²-day, 26, 40, and 24 percent. These three percentages may be compared with those previously calculated on the basis of diffusion velocity. The yearly average of $T_s - T_h$ is about 19 deg F, which yields an average artificial heat flux during the stratified period of 66 Btu/ft²-day, or 26 percent of the natural value. Now, referring to equation (5), we recall that q_c is proportional to D_m . Thus again our postulated power plant may apparently be considered to enhance the effective average summer value of D_m by about 26 percent. To be conservative, we will tentatively take a 20 percent increase to correspond to a single plant with a pumping rate of 1200 cfs.

In view of the foregoing estimates, we have independently perturbed our model value of D_m by 20 and 60 percent for the natural lake and for the 1 deg F and 3 deg F perturbations of T_e . In each case a new cycle was calculated. Roughly, we may imagine the 1 deg F, 20 percent combination to represent one plant, while the 3 deg F, 60 percent case would represent three plants. The 1 deg F, 60 percent combination would represent one plant, with dilution to give a discharge temperature of 8 deg F rather than 24 deg F, while the 1 deg F, 0 percent combination would refer to one plant with a surface or shallow intake and discharge arrangement designed not to short-circuit the thermocline.

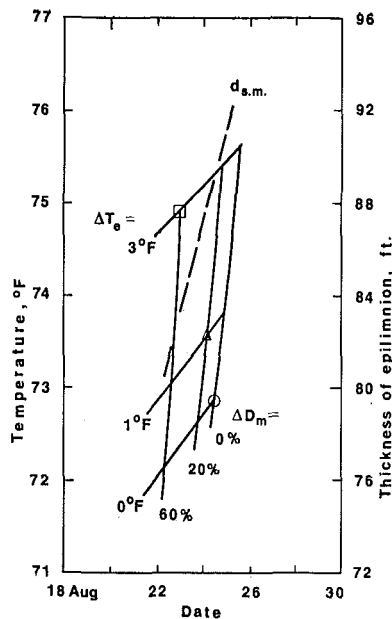


Fig. 4 Summer-maximum surface temperature and thickness of epilimnion (single dashed line which essentially covers all heat and diffusion cases calculated)

Before describing the results of these calculations, we should explain how the stratification criterion, equation (6), was modified. A change in D_m has only a slight direct effect on q_{str} because N is much larger than q_c . However, any change in T_{str} which results from either ΔT_e or ΔD_m affects buoyancy by changing β . Both N and c must vary inversely with β , and, because only about 1 deg F separates T_{str} and 39.2 deg F, we may assume β proportional to $T_s - 39.2$. Thus our perturbed stratification criterion may be written as

$$q_{str} = (N + c_0 D_m) \frac{(T_{str} - 39.2)_0}{T_{str} - 39.2} \quad (25)$$

where subscript 0 refers to the natural-lake model. We might note that apart from the small effect of changes in D_m , incorporation of equation (1) and information from Table 1 into equation (25) gives

$$[(T_e - T_s)(T_s - 39.2)]_{str} = 20 \quad (26)$$

Equation (26) is almost exactly the criterion adopted in reference [2] on the basis of a physical argument matched to observational details near stratification.

We turn now to the results of the power-plant perturbations. Rather than display results in the manner of Fig. 1 for each of the heat-diffusion combinations, we present in Figs. 3-7 the matrix points through which such curves would pass at the critical times of stratification, summer maximum, overturn, and winter minimum. From these points, each complete perturbed temperature history can easily be imagined or sketched by reference to Fig. 1.

Stratification Onset. On the right of Fig. 3 the circled point represents the natural-lake model, which stratifies on 11 May. A single plant (triangle) would advance stratification by 8 days. All the various estimates [1, 2, 3] seem in essential agreement on this point. Three plants (square) would advance stratification by 26 days and raise the temperature of stratification by more than 1 deg F. Clearly stratification is advanced by heat addition because buoyancy is increased.

Diffusion enhancement by pumping also advances stratification, essentially because more heat is transferred to the hypolimnion in the summer and the lake is therefore warmer during the winter and readier to stratify in the spring; notice in Fig. 3 that ΔD_m markedly increases T_{str} . A single power plant with three-

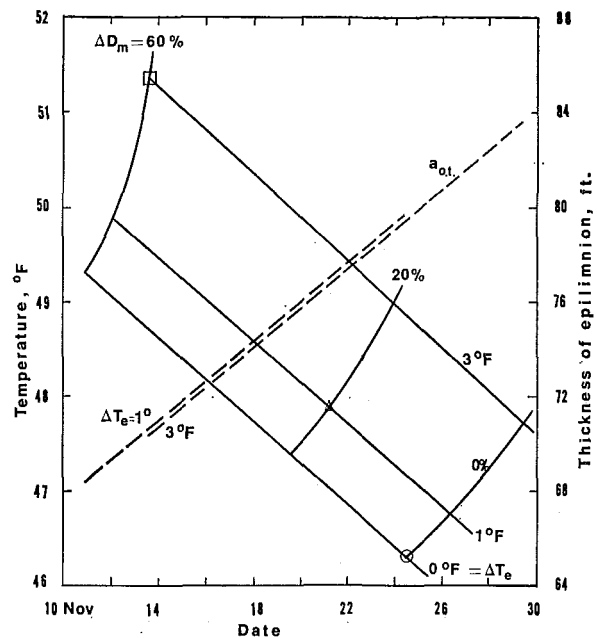


Fig. 5 Temperature and epilimnion thickness (dashed lines) at fall overturn

fold dilution would advance stratification 12 days, whereas if a surface intake were used the advance would still be 6 days. Apparently heat addition has a dominant effect on onset of stratification.

Summer Maximum. Fig. 4 shows that heat and diffusion enhancement are opposite in their effects on summer-maximum surface temperature because they represent mechanisms of heat increase and heat loss for the epilimnion, respectively. Again, heat addition seems dominant, though a single plant with threefold dilution would produce no change at all in summer-maximum surface temperature. Three plants would typically increase the summer maximum by 2 deg F. The time of occurrence of summer maximum is not significantly changed by these perturbations.

The maximum depth of the epilimnion is affected both by heat and diffusion perturbations, but the curves are so close together that we show them as a single line. For example, our single plant or three plants would make the epilimnion shallower by 1 ft or 7 ft, respectively, owing chiefly to the more rapid heat loss associated with an increase of q_c .

Overturn. Fig. 5 indicates that fall overturn is delayed by heat and advanced by diffusion, as one would infer from the heat gain and loss of the epilimnion by these causes. Diffusion is dominant in this case; our typical single plant advances overturn by 3 days, while three plants cause an advance of 11 days. A surface intake would apparently cause overturn to be delayed. It might be interesting to note that, although the overall period of stratification would be lengthened by $8 - 3 = 5$ days by a single plant with deep intake and no dilution, threefold dilution would actually shorten the duration of stratification by 3 days.

Again the final epilimnion depth is nearly a function of time alone. For a single plant, the depth is less by 2 ft, and for three plants, less by 9 ft.

Temperature at overturn is raised both by heat and by diffusion enhancement, especially the latter. A single plant with surface intake would raise the overturn temperature by only 0.5 deg F, whereas a plant with deep intake would raise the temperature by almost 2 deg F. With threefold dilution, the increase would be almost 4 deg F, and three plants would produce a rise of more than 5 deg F. These temperature effects are very important because they mean a significant temperature increase of the hypolimnion. The average increase of hypolimnion temperature in the summer would be nearly the average of the increases displayed in Figs. 3 and 5. We show in Fig. 6 the predicted average hypolimnion

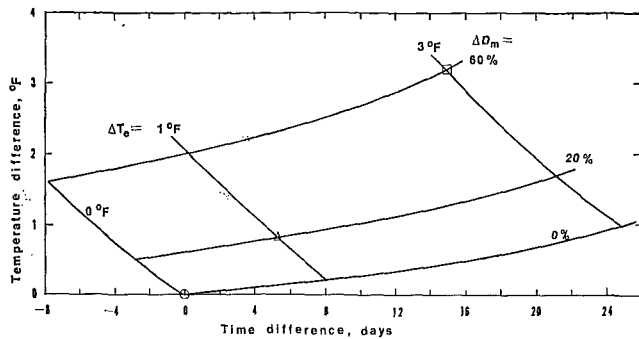


Fig. 6 Increase of average hypolimnion temperature vs. increase of duration of stratification

temperature increase as a function of the increase of length of the stratification period.

Winter Minimum. Fig. 7 shows that heat and mixing both increase the winter minimum temperature with the date of occurrence being essentially unchanged. It is perhaps important that for 5 weeks (see Fig. 1) the natural, fully mixed lake is at a temperature less than that for which water has its maximum density (39.2 deg F). Following winter minimum, the heat being added to the lake therefore produces a negative buoyancy, obviously promoting mixing and isothermy. This situation prevails until only a week before the onset of stratification. In our model we have taken this effect into account by making an empirical choice of N^* and by relating N^* to β . However, if there are three plants, or even one plant with slightly more than threefold dilution, there is no negative buoyancy at all, according to Fig. 7. In such circumstances our stratification criterion N^* may be irrelevant and stratification might occur as early as a week after winter minimum, that is, about 24 March or 7 weeks earlier than at present.

Concluding Remarks

The theoretical model presented in this paper has been made as simple as possible, not in order to save computer time but in the belief that a simple model exposes uncertainties more clearly and, if the uncertainties are as numerous as they are in this problem, is just as reliable as a more elaborate model. Also, of course, a simple model is more readily extended to deal with situations of greater complexity, such as sounds or estuaries.

Clearly our most difficult problem is to properly relate the "mixing strength" of a power plant to that of the natural lake. It is felt that the most crucial environmental-impact questions hinge on this particular point, and therefore more research is needed to achieve an understanding firm enough to justify public decisions of far-reaching importance to water-resource management and power-plant economics.

To emphasize this point, we return to our prediction of hypolimnion temperature increase, Fig. 6. The biological importance of this effect relates to dissolved-oxygen concentration, which would be lowered both by increased temperature and extended time of stratification. With this and other concerns in view, the FWPCA guidelines [6] suggest that no heat be added to the hypolimnion of cold lakes. New York State, and perhaps others, presently prohibits thermal discharges into the hypolimnion. These requirements are consistent only if one imagines that the thermocline is a sort of impermeable membrane; in that case the power plant would draw down the thermocline, but not change the hypolimnion temperature. The present study emphasizes that the natural mass exchange across the thermocline, though weak, is still larger than the pumped exchange. Thus the power-plant pumping must be considered only to modify the natural diffusional process, and the increase of hypolimnion temperature,

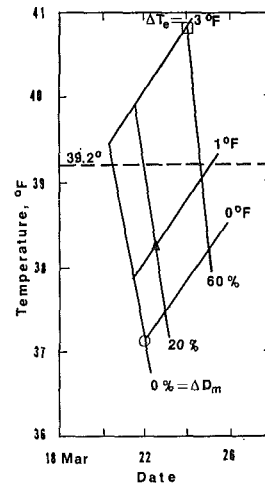


Fig. 7 Winter-minimum temperature; dashed line is temperature at which water has maximum density ($\beta = 0$)

though caused indirectly and amounting to only about half that of the average surface temperature, cannot be neglected.

Finally, the results of the present study suggest that surface (or shallow) intakes or closed-circuit condenser cooling which eliminate the diffusion enhancement due to pumping would diminish what are perhaps the most serious environmental thermal-impact effects. Changes of hypolimnion temperature and summer-maximum surface temperature would be minimized (as well as nutrient pumping, a matter beyond the scope of this paper), though the period of summer stratification would be extended, perhaps catastrophically, in the case of three plants.

The opposite strategy, to pump additional water to dilute the thermal discharge to the regulated temperature level (3 deg F increase) would seem to be out of the question. Our model, which is based on the natural lake, could not cope with changes of the magnitude that would follow from an eightfold dilution. Even a threefold dilution for a single plant would probably transform the character of the lake beyond the range of our empirical parameter selections.

References

- Moore, F. K., Brutsaert, W. R., Cady, K. B., Revelle, C. S., Seebass, A. R., and Shepherd, D. G., "Engineering Aspects of Thermal Discharges to a Stratified Lake," College of Engineering, Cornell University, Ithaca, N. Y., Feb. 1969.
- Moore, F. K., and Mackenzie, J. F., "A Prediction of Changes in the Thermal Cycle of a Stratified Lake used to Cool a 1000 MW Power Plant," Cornell University Water Resources and Marine Sciences Center, Ithaca, N. Y., Publication No. 32, Jan. 1971; see also Mackenzie, J. F., MS thesis, Cornell University, Ithaca, N. Y., June 1970.
- Sundaram, T. R., and Rehm, R. G., "The Effects of Thermal Discharges on the Stratification Cycle of Lakes," AIAA 9th Aerospace Sciences Meeting, New York, N. Y., Jan. 1971, Paper No. 71-16.
- Sundaram, T. R., Easterbrook, C. C., Piech, K. R., and Rüdinger, G., "An Investigation of the Physical Effects of Thermal Discharges into Cayuga Lake," CAL Nos. VT-2616-0-1 and VT-2616-0-2, Cornell Aeronautical Laboratory, Buffalo, N. Y., Nov. 1969.
- Edinger, J. E., and Geyer, J. C., "Heat Exchange in the Environment," Edison Electric Institute Publication No. 65-902, Johns Hopkins University, 1965; see also Edinger, J. E., Duttweiler, D. W., and Geyer, J. S., "The Response of Water Temperatures to Meteorological Conditions," *Water Resources Research*, Vol. 4, No. 5, 1968, pp. 1137-1143.
- "Water Quality Criteria," Report of the National Technical Advisory Committee to the Secretary of the Interior, Federal Water Pollution Control Administration, Washington, D. C., Apr. 1969.
- Henson, E. B., Bradshaw, A. S., and Chandler, D. C., "The Physical Limnology of Cayuga Lake, N. Y.," Memoir 378, Agricultural Experiment Station, Cornell University, Ithaca, N. Y., Aug. 1961.
- Miles, J. W., "On the Stability of Heterogeneous Shear Flows," *Journal of Fluid Mechanics*, Vol. 10, 1961, pp. 496-508.

CHIA-JUNG HSU

Brookhaven National Laboratory,
Upton, N. Y.

The Effect of Lateral Rod Displacement on Laminar-Flow Transfer¹

Heat transfer in longitudinal laminar flow through tightly packed rod bundles is analyzed for a rod displaced from its symmetrical position. The influences of the P/D ratio, the magnitude of σ , and the type of thermal boundary condition, etc. on the variation of the coolant temperature field and the rod-average Nusselt number are investigated. Average Nusselt numbers for the displaced rod are calculated for rod bundles with $1.00 \leq P/D \leq 2.0$ and $0 \leq \sigma \leq 0.8$. The results for the special case of $\sigma = 0$ (i.e., for symmetrical rod bundle) show excellent agreement with those reported by Dwyer and Berry [1],² who analyzed numerically the corresponding problem for symmetrical rod bundles.

Introduction

THE effect of lateral rod displacement on the heat transfer behavior of the displaced rod was recently studied by the present author [2] based on the assumption of slug flow. The purpose of this paper is to present some of the results obtained for the corresponding problem in laminar flow. As before [2], two representative types of rod displacement [$p_0 \rightarrow q$ and $p_0 \rightarrow s$ as shown in Figs. 1(a) and 2(a), respectively] are considered for the thermal boundary conditions of (B.C. 1) uniform wall temperature in the circumferential direction and uniform wall heat flux in the axial direction, and (B.C. 2) uniform wall heat flux in both the circumferential and axial directions. For brevity, discussion will be restricted only to the case where the central rod is displaced along the path $p_0 \rightarrow q$.

Analysis

Boundary Condition 1. Under the conventional assumptions, the fully developed temperature field in the elemental coolant flow area is governed by the energy equation

$$\frac{Q}{2kM} \left[\frac{r_0^2}{4A} (\xi^2 - 1) - \left(\frac{1}{2\pi} + \frac{r_0^2}{2A} \right) \ln \xi + \sum_{n=1}^{\infty} \delta_n (\xi^{-n} - \xi^n) \cos n\theta \right] = \frac{\partial^2 T}{\partial \xi^2} + \frac{1}{\xi} \frac{\partial T}{\partial \xi} + \frac{1}{\xi^2} \frac{\partial^2 T}{\partial \theta^2} \quad (1)$$

where $T = t - t_w$ and $\xi = r/r_0$. In equation (1) the series coefficients δ_n and the numerical values for M , which denotes the double integral

$$\frac{Q_f}{2Ar_0^2} \left(\frac{1}{\mu} \frac{\partial p}{\partial z} \right) = \sum_{i=1}^4 \int_{\Delta_{i-1}}^{\Delta_i} \int_1^{\xi_i(\theta)} \left[\frac{r_0^2 \xi}{4A} (\xi^2 - 1) - \left(\frac{1}{2\pi} + \frac{r_0^2}{2A} \right) \xi \ln \xi + \sum_{n=1}^{\infty} \delta_n (\xi^{1-n} - \xi^{n+1}) \cos n\theta \right] d\xi d\theta = M$$

can be obtained, by analogy between the momentum and heat transfer, from the previous slug-flow analysis [2]. The appropriate boundary conditions to equation (1) are

$$T = 0 \quad \text{at} \quad \xi = 1 \quad (2)$$

$$\frac{\partial T}{\partial \theta} = 0 \quad \text{at} \quad \theta = 0 \quad \text{and} \quad \theta = \pi \quad (3)$$

$$\mathbf{n}_i \cdot \text{grad } T = 0 \quad \text{at} \quad \xi = \xi_i(\theta)$$

$$\text{and for } \Delta_{i-1} \leq \theta \leq \Delta_i \quad (i = 1 \sim 4) \quad (4)$$

$$Q = -2 \int_0^\pi k \left(\frac{\partial T}{\partial \xi} \right)_{\xi=1} d\theta \quad (5)$$

where $\Delta_0 = 0$, $\Delta_i = \sum_{j=1}^i \theta_j$ ($i = 1, 2, 3$), $\Delta_4 = \pi$, and the functions $\xi_i(\theta)$ ($i = 1 \sim 4$) are defined in the Nomenclature.

In terms of the dimensionless temperature $\Theta = T/(Q/2kM)$, the temperature solution can be written as

$$\Theta = T/(Q/2kM) = \alpha_0 + \alpha_1 \xi^2 + \alpha_2 \xi^4 - \alpha_3 \xi^2 \ln \xi + \alpha_4 \ln \xi + \sum_{n=1}^{\infty} H_n (\xi^{-n} - \xi^n) \cos n\theta + \sum_{n=1}^{\infty} \delta_n \left\{ \frac{\xi^{2-n}}{4(1-n)} - \frac{\xi^{2+n}}{4(1+n)} - \frac{n \xi^n}{2(1-n^2)} \right\} \cos n\theta \quad (6)$$

¹ This work was performed under the auspices of the U. S. Atomic Energy Commission.

² Numbers in brackets designate References at end of paper.

Based on a paper contributed by the Heat Transfer Division and presented at the Winter Annual Meeting, New York, N. Y., November 29-December 3, 1970, of THE AMERICAN SOCIETY OF MECHANICAL ENGINEERS. Manuscript received by the Heat Transfer Division September, 1970; revised manuscript received June 24, 1971.

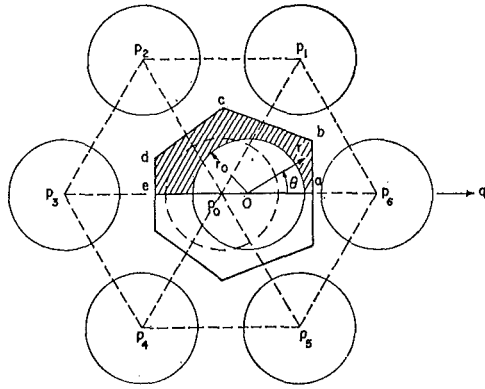


Fig. 1(a)

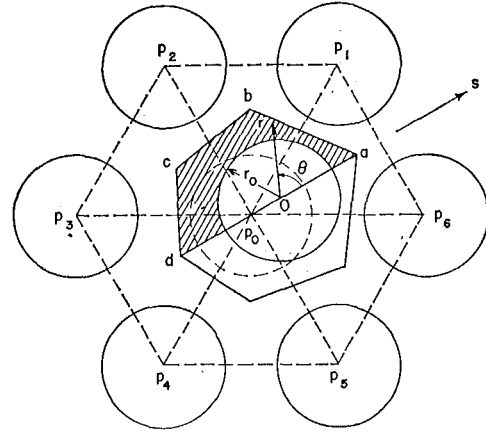


Fig. 2(a)

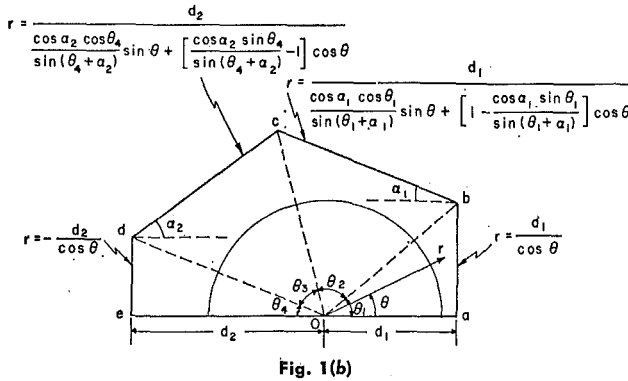


Fig. 1(b)

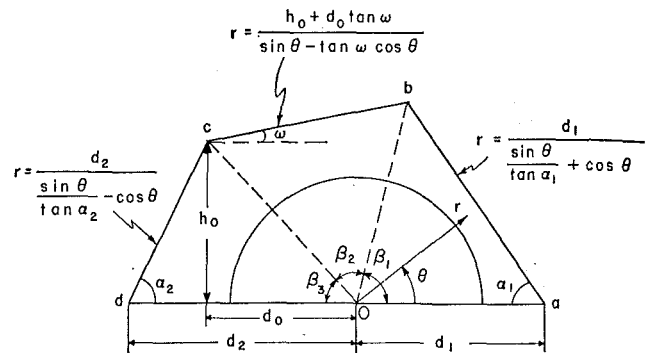


Fig. 2(b)

Fig. 1 Cross section of asymmetrical rod bundle for the case where the central rod is displaced toward an adjacent rod ($p_0 \rightarrow q$ displacement)

Fig. 2 Cross section of asymmetrical rod bundle for the case where the central rod is displaced toward the midpoint of the line connecting the centers of two neighboring rods ($p_0 \rightarrow s$ displacement)

where

$$H_n = 2kMD_n/Q, \quad \kappa_0 = -\left(\frac{5r_0^2}{64A} + \frac{1}{8\pi}\right),$$

$$\kappa_1 = \frac{1}{8\pi} + \frac{r_0^2}{16A}, \quad \kappa_2 = \frac{r_0^2}{64A}, \quad \kappa_3 = \frac{1}{8\pi} + \frac{r_0^2}{8A},$$

$$\text{and } \kappa_4 = -\left(\frac{1}{8\pi} + \frac{r_0^2}{16A} + \frac{M}{\pi}\right)$$

The only unknowns in equation (6) are the series expansion coefficients H_n , which will be determined so that equation (4) is satisfied. By taking the dot product of n_i ($i = 1 \sim 4$) and the gradient of T , these conditions can be seen to be tantamount to (at $\xi = \xi_i(\theta)$ and for $\Delta_{i-1} \leq \theta \leq \Delta_i$):

Nomenclature

$A = 2 \times$ [cross-hatched area in Fig. 1(a)]

$C_p =$ specific heat

$D =$ diameter of rods

$D_n =$ constants

$P =$ pitch, or the distance between rod centers

$Q =$ heat transfer rate per unit length

$Q_f = A\bar{u}$, volumetric flow rate

$k =$ thermal conductivity of coolant

$k_1 = \cos \alpha_1 \cos \theta_1 / \sin(\theta_1 + \alpha_1)$

$k_2 = 1 - [\cos \alpha_1 \sin \theta_1 / \sin(\theta_1 + \alpha_1)]$

$m_1 = \cos \alpha_2 \cos \theta_4 / \sin(\theta_4 + \alpha_2)$

$m_2 = [\cos \alpha_2 \sin \theta_4 / \sin(\theta_4 + \alpha_2)] - 1$

n_i ($i = 1 \sim 4$) = unit vectors normal to the outer boundary lines ab , bc , cd , and

de in Fig. 1(b)

$p =$ fluid pressure

$q_w =$ local wall heat flux

$r =$ radial coordinate distance

$r_0 =$ radius of rods

$t =$ temperature

$t_b =$ bulk fluid temperature

$t_w =$ wall temperature

$t_0 =$ uniform inlet fluid temperature

$\bar{u} =$ average fluid velocity

$w_1 = d_1/r_0$

$w_2 = d_2/r_0$

$z =$ axial coordinate distance

$\alpha_1, \alpha_2 =$ angles shown in Fig. 1(b) or 2(b)

$\Gamma_1 = \sin \theta / w_1$

$\Gamma_2 = \frac{1}{\xi_2}$

$\times \left[\frac{\tan \alpha_1 \sin \theta - \cos \theta}{\tan \alpha_1 \cos \theta + \sin \theta} \right]$

$\Gamma_3 = \frac{1}{\xi_3}$

$\times \left[\frac{\cos \theta + \tan \alpha_2 \sin \theta}{\tan \alpha_2 \cos \theta - \sin \theta} \right]$

$\Gamma_4 = -\sin \theta / w_2$

$\theta =$ azimuthal angle defined in Fig. 1(a)

θ_i ($i = 1 \sim 4$) = angles shown in Fig. 1(b)

$\mu =$ viscosity of fluid

$\xi_1 = w_1 / \cos \theta$

$\xi_2 = w_1 / (k_1 \sin \theta + k_2 \cos \theta)$

$\xi_3 = w_2 / (m_1 \sin \theta + m_2 \cos \theta)$

$\xi_4 = -w_2 / \cos \theta$

$\rho =$ density of fluid

$\sigma =$ actual displacement distance/ d_{\max} where d_{\max} is the maximum distance possible for the displacement

$$\frac{\partial T}{\partial \xi} = \Gamma_i(\theta) \frac{\partial T}{\partial \theta} \quad (i = 1 \sim 4) \quad (7)$$

where Γ_i ($i = 1 \sim 4$) are shown in the Nomenclature.

Evaluating $\frac{\partial T}{\partial \xi}$ and $\frac{\partial T}{\partial \theta}$ from equation (6) and substituting them into equation (7), the following equation is obtained for the determination of the H_n coefficients:

$$\sum_{n=1}^{\infty} n H_n \{ (\xi_i^{-n-1} + \xi_i^{n-1}) \cos n\theta - \Gamma_i(\theta) (\xi_i^{-n} - \xi_i^n) \sin n\theta \} = \frac{\xi_i}{8\pi} + \frac{1}{16} \frac{r_0^2}{A} \xi_i^3 - \left(\frac{1}{4\pi} + \frac{r_0^2}{4A} \right) \xi_i \ln \xi_i$$

$$- \left(\frac{1}{8\pi} + \frac{r_0^2}{16A} + \frac{M}{\pi} \right) \frac{1}{\xi_i} + \sum_{k=1}^{\infty} \delta_k \left\{ \frac{(2+k-k^2)\xi_i^{1-k} - (2-k-k^2)\xi_i^{1+k} - 2k^2\xi_i^{k-1}}{4(1-k^2)} \right\} \cos k\theta$$

$$+ \Gamma_i(\theta) \sum_{k=1}^{\infty} \delta_k \left\{ \frac{k(1+k)\xi_i^{2-k} - k(1-k)\xi_i^{k+2} - 2k^2\xi_i^k}{4(1-k^2)} \right\} \sin k\theta \quad (8)$$

The technique which involves construction of a set of orthonormal vectors, followed by solving a set of simultaneous equations, was employed to determine those coefficients. The details of this technique were described in the previous paper [2]. For reference, some of the H_n coefficients thus calculated are tabulated in Table 1 for $P/D = 1.10$ and for $\sigma = 0.0$ and 0.5 . Having determined the H_n coefficients, the rod-average Nusselt number, for example, can be derived as follows:

$$\overline{Nu}_t = \frac{- \left[\frac{2AM^2}{\pi^2 r_0^2} \right]}{\sum_{i=1}^4 \int_{\Delta_{i-1}}^{\Delta_i} \int_0^{\xi_i} \xi G(\xi, \theta) \Theta d\xi d\theta} \quad (9)$$

where

$$G(\xi, \theta) = \frac{r_0^2}{4A} (\xi^2 - 1) - \left(\frac{1}{2\pi} + \frac{r_0^2}{2A} \right) \ln \xi$$

$$+ \sum_{n=1}^{\infty} \delta_n (\xi^{-n} - \xi^n) \cos n\theta$$

Boundary Condition 2. Redefining the dimensionless temperature as $T = (t - t_0)/(\pi r_0 q_w / kM)$ and letting $\eta = 4Mz/(\pi r_0 Pe)$ where $Pe = 2A \bar{u} \rho C_p / \pi r_0 k$ denotes the Peclet number, the governing energy equation, in this case, takes the form

$$\left[\frac{r_0^2}{4A} (\xi^2 - 1) - \left(\frac{1}{2\pi} + \frac{r_0^2}{2A} \right) \ln \xi \right.$$

$$\left. + \sum_{n=1}^{\infty} \delta_n (\xi^{-n} - \xi^n) \cos n\theta \right] \frac{\partial T}{\partial \eta}$$

$$= \frac{\partial^2 T}{\partial \xi^2} + \frac{1}{\xi} \frac{\partial T}{\partial \xi} + \frac{1}{\xi^2} \frac{\partial^2 T}{\partial \theta^2} \quad (10)$$

The appropriate thermal boundary conditions are those given by equations (3), (4), and

$$\partial T / \partial \xi = -M/\pi \quad \text{at} \quad \xi = 1$$

The temperature solution to this problem can ultimately be written as

$$T = \eta + \left(\frac{1}{8\pi} + \frac{r_0^2}{16A} \right) \xi^2 + \frac{r_0^2}{64A} \xi^4 - \left(\frac{1}{8\pi} + \frac{r_0^2}{8A} \right) \xi^2 \ln \xi$$

$$+ A_1 - \left\{ \frac{M}{\pi} + \frac{1}{8\pi} + \frac{r_0^2}{16A} \right\} \ln \xi + \sum_{n=1}^{\infty} D_n' (\xi^n + \xi^{-n}) \cos n\theta$$

$$+ \sum_{n=1}^{\infty} \delta_n \left\{ \frac{\xi^{2-n}}{4(1-n)} - \frac{\xi^{n+2}}{4(1+n)} - \frac{\xi^n}{2(1-n^2)} \right\} \cos n\theta \quad (11)$$

Table 1 Calculated series coefficients for the $p_0 \rightarrow q$ displacement with $P/D = 1.1$

n	$\sigma=0.0$			$\sigma=0.5$		
	δ_n	H_n	D_n'	δ_n	H_n	D_n'
1	-1.1129(8)*	-1.5301(9)*	3.4447(7)*	-2.438(2)*	-2.4183(3)*	-8.0748(3)*
2	-4.9054(7)	-3.0627(8)	-1.5181(7)	3.5233(4)	-2.0531(5)	-1.9117(4)
3	1.4131(8)	9.6145(10)	-1.1729(8)	-2.5703(5)	6.5676(7)	1.5573(5)
4	-2.2078(7)	-6.4986(9)	-2.1572(8)	-3.3793(4)	-2.0061(5)	1.0029(4)
5	-1.0667(8)	-5.0589(10)	-9.4729(9)	-1.9641(3)	-6.6555(5)	1.1685(5)
6	-4.5067(3)	-4.5699(5)	-3.3942(4)	-4.2714(3)	-4.6557(7)	-3.9841(4)
7	7.5164(9)	2.9629(10)	6.4045(9)	4.3993(4)	-1.6419(5)	-7.7652(5)
8	7.7998(9)	-9.3784(10)	-1.6315(9)	3.2042(6)	2.7564(6)	-1.1592(5)
9	-2.8009(9)	-5.4028(11)	-6.9481(10)	1.3026(5)	9.3269(8)	1.0752(6)
10	5.8344(9)	-3.7396(10)	-7.8002(10)	4.9420(5)	-5.3511(7)	3.0779(6)
11	1.7136(10)	-2.1738(11)	2.0398(10)	9.9733(5)	-2.4986(6)	-9.4432(7)
12	8.5523(5)	-4.0645(6)	1.0503(7)	9.3555(5)	-3.1536(6)	-3.8002(6)
13	1.0681(9)	4.6827(11)	-1.0879(10)	7.1461(6)	7.5364(7)	-3.9820(6)
14	-2.0149(9)	-6.7392(11)	2.6075(10)	-5.9610(7)	9.8489(8)	-1.1192(6)
15	6.3072(9)	1.7283(10)	-4.9207(10)	2.1168(6)	3.1573(8)	4.5898(7)
16	9.0043(9)	2.1559(10)	-6.2983(10)	5.0561(6)	3.7198(8)	5.6559(7)
17	-4.0762(9)	-1.0772(10)	2.7793(10)	6.4202(6)	1.0608(8)	-1.5087(7)
18	4.0616(6)	-5.2324(8)	-1.2467(7)	3.0507(6)	2.3086(8)	-1.0549(6)
19	2.7605(9)	7.0827(11)	-1.9469(10)	-3.5988(7)	3.8415(8)	-4.6253(7)
20	-3.9731(9)	-9.7977(11)	3.1198(10)	-3.9604(8)	-1.1655(9)	2.6122(8)

* X(a) means X x 10^{-a}

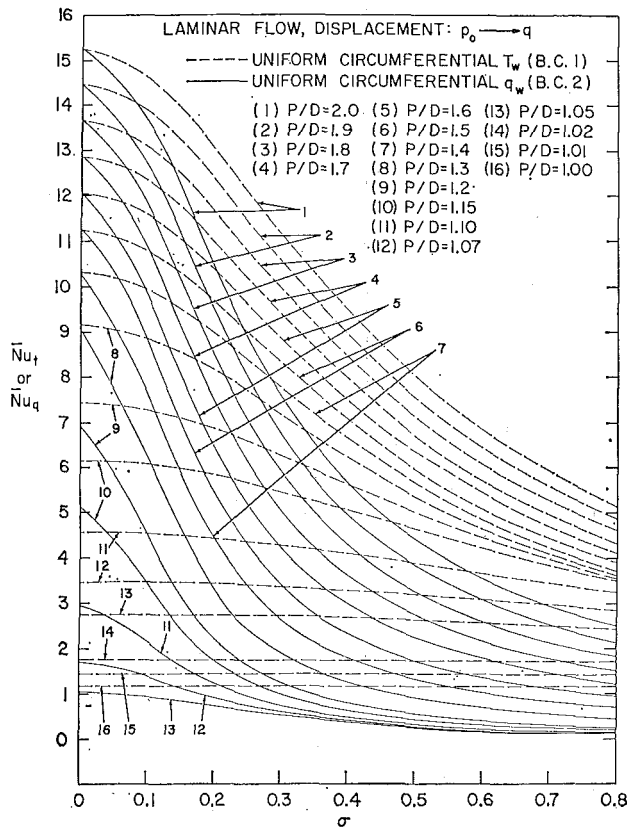


Fig. 3 Calculated rod-average Nusselt numbers for the $p_0 \rightarrow q$ displacement under boundary conditions 1 and 2

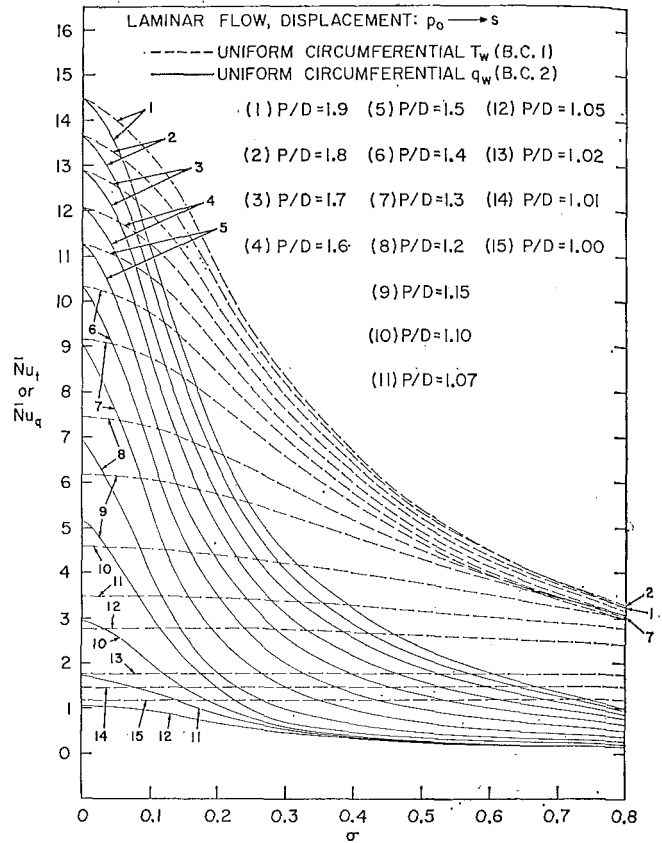


Fig. 4 Calculated rod-average Nusselt numbers for the $p_0 \rightarrow s$ displacement under boundary conditions 1 and 2

where A_1 can be calculated by using the following equation:

$$A_1 = \frac{-1}{M} \sum_{i=1}^4 \int_{\Delta_{i-1}}^{\Delta_i} \int_1^{\xi_i} \xi \left[\frac{r_0^2}{4A} (\xi^2 - 1) - \left(\frac{1}{2\pi} + \frac{r_0^2}{2A} \right) \ln \xi \right. \\ \left. + \sum_{n=1}^{\infty} \delta_n (\xi^{-n} - \xi^n) \cos n\theta \right] \left[\kappa_1 \xi^2 + \kappa_2 \xi^4 - \kappa_3 \xi^2 \ln \xi \right. \\ \left. + \kappa_4 \ln \xi + \sum_{n=1}^{\infty} D_n' (\xi^n + \xi^{-n}) \cos n\theta \right. \\ \left. + \sum_{n=1}^{\infty} \delta_n \left\{ \frac{\xi^{2-n}}{4(1-n)} - \frac{\xi^{n+2}}{4(1+n)} - \frac{\xi^n}{2(1-n^2)} \right\} \cos n\theta \right] d\xi d\theta$$

Some of the calculated D_n' coefficients are also tabulated in Table 1. The expression for the average Nusselt number, based on the average temperature difference, $(t_w - t_b)_{av} = \frac{1}{\pi} \int_0^\pi (t_w - t_b) d\theta$ in this case, can be derived as

$$\bar{Nu}_q = \frac{(2AM/\pi^2 r_0^2)}{\kappa_1 + \kappa_2 + A_1} \quad (12)$$

Discussion of the Computational Results

To verify the correctness of the temperature solutions obtained, the H_n coefficients determined by constructing the orthonormal set of functions and by solving the system of simultaneous equations were employed to calculate the function given by the left-hand side of equation (8) for the integral angles ranging from 0 to 180 deg. The numerical values of this function were then compared with the right side of the equation and excellent agreement was obtained. This verifies that the temperature solutions obtained in this study indeed satisfy the required boundary conditions.

The calculated average Nusselt numbers \bar{Nu}_t and \bar{Nu}_q are

shown in Figs. 3 and 4 for the $p_0 \rightarrow q$ and $p_0 \rightarrow s$ displacements respectively. The Nusselt numbers corresponding to $\sigma = 0$ represent those for the case of symmetrical rod bundles (i.e., rod bundles with zero displacement). They were found to agree very well with those reported by Dwyer and Berry [1], who analyzed the corresponding problem for symmetrical rod bundles by using the finite-difference numerical approach.

Figs. 3 and 4 clearly show that displacing a rod from its symmetrical position can cause considerable reduction in the average Nusselt number of the displaced rod. To what extent the displacement affects the heat transfer depends not only on the magnitude of σ and the P/D ratio of rod bundles, but also on the type of boundary condition imposed. In general, the effect is much larger if the heat transfer occurs under boundary condition 2. For example, for a rod bundle with P/D of 1.1, a displacement corresponding to $\sigma = 0.5$ in the $p_0 \rightarrow q$ direction causes roughly 14 percent reduction in \bar{Nu}_t , while \bar{Nu}_q is reduced by as much as 88 percent. If the results shown in Figs. 3 and 4 are compared with those for slug flow reported in the previous paper [2], it can be concluded that the effect of rod displacement is, in general, larger for laminar flow than for slug flow. This is to be expected because nonuniformity in velocity field tends to cause a larger circumferential variation of coolant fluid temperature. For the aforementioned example, the corresponding percentage reductions in \bar{Nu}_t and \bar{Nu}_q for slug flow are 9 and 83 percent, respectively.

To illustrate more clearly how the effect of rod displacement depends on the P/D ratio of rod bundle, the fractional displacement distance σ , and the type of thermal boundary condition imposed, the normalized Nusselt numbers, $\bar{Nu}_q/[\bar{Nu}_q]_0$ or $\bar{Nu}_t/[\bar{Nu}_t]_0$, are plotted in Figs. 5 and 6 as a function of both σ and D/P . The normalized Nusselt number is defined to be the ratio of the average Nusselt number to the Nusselt number corresponding to $\sigma = 0$ (i.e., zero displacement). It can be observed that, for a fixed P/D ratio, the normalized Nusselt number is more sensitive to the

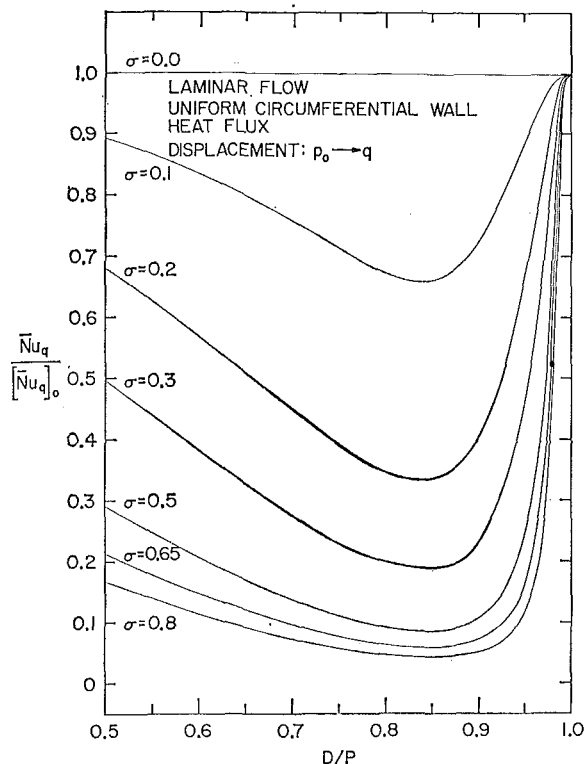


Fig. 5 Normalized average Nusselt numbers for the $p_0 \rightarrow q$ displacement under boundary condition 2

variation of σ if the heat transfer occurs under boundary condition 2. It is of particular interest to note from Fig. 5 that for all the σ values considered, the curves for $\bar{Nu}_q/[\bar{Nu}_q]_0$ go through a minimum at D/P of ≈ 0.83 (or equivalently at P/D of ≈ 1.205). In other words, for heat transfer in laminar flow subject to boundary condition 2, the effect of rod displacement is most severe if the P/D ratio of the rod bundle is in the vicinity of 1.205. In the previous study it was found that, for slug flow, such a curve goes through a minimum at $P/D \approx 1.11$. It is pertinent to remark that, for a symmetrical rod bundle, if the average heat transfer coefficient (instead of average Nusselt number) is plotted versus the P/D ratio, it will be observed that such a curve goes through a maximum at P/D of ≈ 1.205 for laminar flow and at $P/D \approx 1.115$ for slug flow. Such curves have been prepared by Dwyer and Berry and are shown in reference [1]. For heat transfer subject to uniform wall heat flux in all directions, the P/D ratio of rod bundle for which the effect of rod displacement is most severe is thus seen to coincide with that of a symmetrical rod bundle for which the average heat transfer coefficient is a

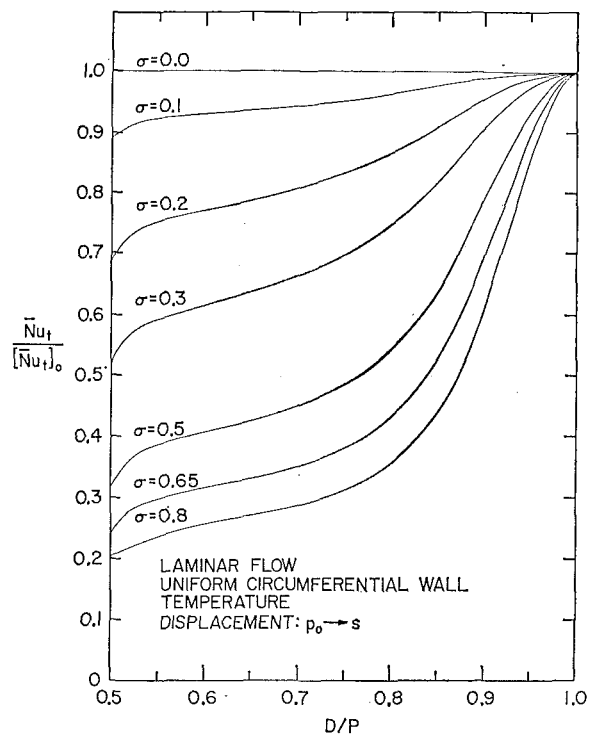


Fig. 6 Normalized average Nusselt numbers for the $p_0 \rightarrow s$ displacement under boundary condition 1

maximum. This observation also tends to attest to the consistency of the present analysis. For heat transfer under boundary condition 1, however, the behavior of the normalized Nusselt number is quite different, as can be seen from Fig. 6. In this case, the effect of rod displacement is largest if the P/D ratio of the rod bundle is 2.0; it diminishes continuously as the P/D ratio approaches unity. It is to be noted that the largest P/D ratio considered in this study is 2.0 and that for a fixed set of P/D and σ the actual distance the rod is displaced is larger for the $p_0 \rightarrow s$ displacement than for the $p_0 \rightarrow q$ displacement.

References

- 1 Dwyer, O. E., and Berry, H. C., "Laminar-Flow Heat Transfer for In-Line Flow through Unbaffled Rod Bundles," *Nucl. Sci. Eng.*, Vol. 42, 1970, p. 81.
- 2 Hsu, Chia-Jung, "Effect of Rod Displacement on Heat Transfer in Slug Flow Through Unbaffled Rod Bundles," *Liquid-Metal Heat Transfer and Fluid Dynamics*, ASME, New York, N. Y., 1970, p. 58.

E. J. ROSCHKE
Member, Technical Staff,
Jet Propulsion Laboratory,
California Institute of Technology,
Pasadena, Calif.

Experimental Investigation of Heat Transfer from Partially Ionized Argon with an Applied Transverse Magnetic Field¹

Wall heat transfer measurements were obtained for laminar flow of partially ionized argon flowing within the conducting walls of a square channel, with and without an applied transverse magnetic field. Tests were conducted for subsonic flows and for flows which were supersonic before a magnetic field was applied. Increases in Stanton number by a factor of as much as six were observed at field strengths approaching 10 kG as compared to values at zero magnetic field. These large increases in heat transfer are believed to have been due to (1) a small amount of joule heating augmented or accompanied by (2) magnetically induced ionization. Heat transfer and flow data were used to estimate effective values of the joule heating parameter, Hall coefficient, and current density. The experimental data have been compared to theoretical predictions for several limiting cases.

Introduction

FEW EXPERIMENTAL results for convective heat transfer in internal flows of partially ionized gases with applied fields are available. This investigation was undertaken to obtain experimental heat transfer distributions for an ionized gas flowing in a channel under the influence of an applied transverse magnetic field. There were no applied electric fields in these experiments. Argon was pre-ionized by means of a conventional electric-arc heater and then flowed into a square constant-area channel. The four walls of the channel were cooled individually and formed a continuous hollow metallic conductor. Heat transfer measurements were made in a region 4.5 to 6.5 channel heights downstream of the anode exit of the arc heater in a test section situated between the pole pieces of a d-c electromagnet. Flows were laminar and subsonic in most cases, but in some tests the flow entering the test section was supersonic before the magnetic field was applied.

Heat transfer changes brought about by a magnetic field arise primarily through changes in temperature distribution in the gas provided that ionization effects, heating of the walls by electron

bombardment, and thermal radiation are negligible. Many theoretical heat transfer analyses are available for laminar incompressible flow with applied electric and magnetic fields [1-5]²; these results do not account for ionization, thermal radiation, wall conductance, or Hall effects. Finite wall conductance has been considered by Yen [6] and Snyder [7]; Hwang et al. [8] have considered compressibility. Eraslan and Eraslan [9] included Hall effects in their analyses and obtained results for strong Hall effects, but their treatment is unrealistic physically for thermally ionized gases. None of the analyses cited can be applied rigorously to the present experiment.

From a simplified theory such as was presented by Back [5], large increases in convective heat transfer are predicted for laminar flow with large joule heating. An applied magnetic field alone should produce an increase in wall heat transfer compared to a zero-field condition because the electric field induced in the moving fluid alters the temperature distribution within the fluid such that larger gradients occur at the wall. It is interesting that experiments with liquid metals and electrolytes [10-12] show the opposite effect, that is, application of a magnetic field produced a reduction in convective heat transfer. However, those results were performed for flow in the turbulent regime under conditions when joule heating was small or negligible. In general, the decrease in heat transfer found experimentally for turbulent flow of liquids in a transverse magnetic field has been ascribed to the suppression of turbulence by the magnetic field.

Two sources of heat transfer data for partially ionized argon with an applied magnetic field are available. Dukowicz [13] performed experiments in a square shock tube that had conduct-

¹ This work presents the results of one phase of research carried out in the Propulsion Research and Advanced Concepts Section of the Jet Propulsion Laboratory, California Institute of Technology, under contract NAS7-100, sponsored by the National Aeronautics and Space Administration.

Based on a paper contributed by the Heat Transfer Division and presented at the Space Technology and Heat Transfer Conference, Los Angeles, Calif., June 21-24, 1970, of THE AMERICAN SOCIETY OF MECHANICAL ENGINEERS as Paper No. 70-HT/SpT-43. Manuscript received by the Heat Transfer Division April 3, 1970; revised manuscript received November 26, 1970.

² Numbers in brackets designate References at end of paper.

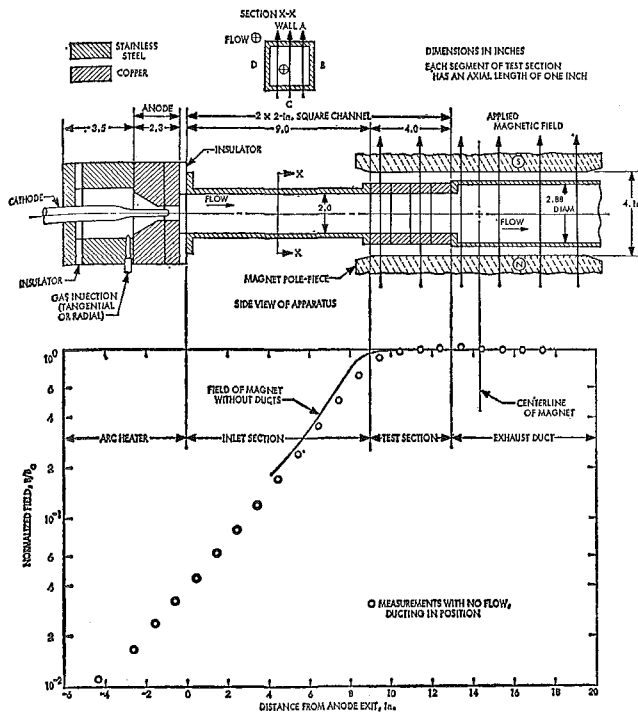


Fig. 1 Heat transfer apparatus and distribution of magnetic field along channel centerline

ing walls. Carlson [14] used a linear accelerator of nearly square cross section operating at open-circuit conditions. Carlson's results were obtained for steady supersonic flow. Both investigators [13, 14] found large increases in heat transfer due to an applied magnetic field, but their results are difficult to compare with the present results because of differences in test conditions and differences in presenting data.

Test Apparatus and Instrumentation

The heat transfer apparatus shown schematically in the upper portion of Fig. 1 consisted of an arc heater, inlet section, test section, and exhaust duct. The inlet section and the test section together formed a 2-in. square channel having a constant cross-sectional area, whereas the arc heater and exhaust duct were axisymmetric. The anode throat was 0.75 in. in diameter and formed an exit orifice for the arc heater. Argon was injected at subat-

mospheric pressures upstream of the electric arc, either tangentially or radially. Gas temperatures at the exit of the arc heater were typically of the order of 18,000 deg R, but were usually much less at the entrance to the test section. Individual walls in the square channel were designated A, B, C, D (Fig. 1). The square channel was isolated electrically from the rest of the apparatus and acquired its own floating potential with respect to the plasma. The apparatus was connected to a vacuum system so that mass rate of flow and pressure in the test section could be varied independently. All parts were cooled with distilled water. Each wall of the inlet section was cooled in a single axial pass so that longitudinal distribution of heat transfer in the inlet section was not determined. Pressure taps were distributed axially along each of the four walls of the inlet section but only along side walls B and D in the test section. Each wall of each of the four copper segments of the test section was cooled individually; water flow was transverse to the direction of gas flow.

Rectangular cavities were located in upper wall A and lower wall C of the second and fourth segments of the test section. These cavities did not affect the heat transfer results for zero-field conditions seriously, so that the zero-field results are presented for the second and third segments of the test section. However, at high magnetic fields the cavities caused significant disturbances to the local heat flux [15] so that results with an applied magnetic field are presented only for the first segment of the test section.

Magnetic field distribution with respect to the apparatus is shown in Fig. 1 for zero-flow conditions. This distribution was essentially independent of the strength of the field B_z at the center of the pole pieces. Maximum field strengths available at the center of the magnet pole pieces were nearly 10 kG. The direction of field indicated in Fig. 1 is designated as "forward" field; with reverse polarity on the magnet the field was opposite in sense to that shown and this is designated "reverse" field. There were no applied electric fields.

Argon mass rate of flow and inlet total temperature were measured by means of calibrated rotometers and a total-temperature thermocouple. Power input to the arc was determined from separate measurements of arc current and voltage; overall energy balances on the system accounted for the electric power input to within 3 or 4 percent. Static pressures along the walls of the channel were measured by means of oil manometers. Coolant-water flow rates were measured for each coolant passage using calibrated rotometers and were recorded simultaneously with direct-printout thermocouple readings for water temperature rise in each passage. Gas-side wall temperature in the copper seg-

Nomenclature

a = channel half-height, $2a = 2$ in.
 B = applied magnetic field strength
 E = electric field strength
 Ec = Eckert number, $Ec = \bar{u}^2/c_p(T_i - T_w)$
 H = enthalpy per unit mass
 Ha = Hartmann number, $Ha = Ba \times (\sigma_0/\mu)^{1/2}$
 h' = local heat transfer coefficient, $h' = q_w/(H_b - H_w)$
 j = electric current density, current per unit area, induced
 K = electric field factor or load factor, $K = E/\bar{u}B$
 k = thermal conductivity
 l = length of channel in direction of flow
 \dot{m} = mass rate of flow
 n = particle number density, per unit volume
 Pr = Prandtl number, $Pr = \mu c_p/k$

p = static pressure at wall
 Q^* = nondimensional local wall heat flux, $Q^* = 2ac_p q_w/k_i(H_{t,i} - H_w)$
 \bar{Q} = nondimensional heat transfer group, $\bar{Q} = q_w(2a/\bar{u}^2\mu)$
 q = local heat flux
 Re = Reynolds number, $Re = \dot{m}/(2a)\mu$
 Re_m = magnetic Reynolds number, $Re_m = \mu_0\sigma_0\bar{u}(2a)$ where μ_0 = magnetic permeability
 S = joule heating parameter, $S = Ha^2Ec(1 - K)^2Pr$
 St = Stanton number, $St = h'/\bar{p}\bar{u}$
 T = absolute temperature
 \bar{u} = bulk gas velocity in axial direction
 x = axial coordinate, positive in direction of flow
 \bar{x} = nondimensional axial coordinate, $\bar{x} = (x/2a)/Re Pr$

z = transverse coordinate perpendicular to x and direction of B
 α = ionization fraction, $\alpha = n_e/(n_e + n_a)$
 β_e = Hall coefficient, $\beta_e = \omega_e\tau_e$
 μ = viscosity
 ρ = density
 σ_0 = scalar electrical conductivity, zero magnetic field
 τ = shear stress in fluid

Subscripts

a, e = refer to atom, electron respectively
 b = bulk value
 eff = effective
 i = inlet condition
 0 = condition at zero applied magnetic field
 t = total or stagnation condition
 w = wall

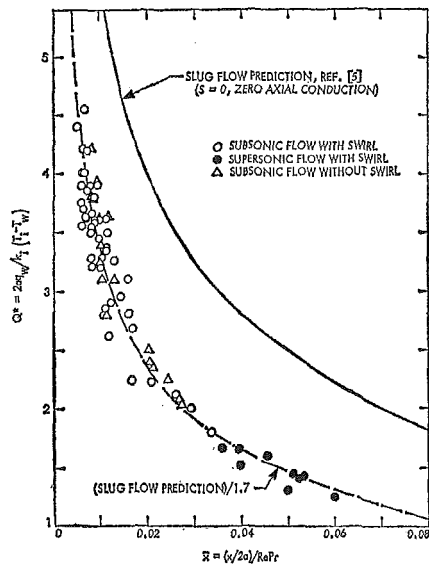


Fig. 2 Laminar heat transfer in a square channel, zero magnetic field

ments of the test section varied from 300 to 700 deg F. Heat flux distributions to the walls of the channel were determined calorimetrically. This method yielded a measure of the total heat transfer to the walls due to all contributory mechanisms. No internal or spectroscopic measurements were made.

Experimental Procedure and Data Analysis

The desired steady-state flow condition was established without an applied magnetic field by selecting mass rate of flow, pressure in the test section, and arc current; a magnetic field was applied in selected increments of field strength according to several procedures [15]. An entire set of data was recorded at steady-state conditions for each value of applied magnetic field without altering any pre-set flow conditions or arc conditions. Such a set of data comprised a "test series." Most of the tests were conducted using tangential injection (flow with swirl) because a considerably higher input energy was imparted to the gas for the same test-section pressure and arc current than for radial injection (flow without swirl).

Average or bulk values of the total enthalpy along the duct were established by an energy balance. Total enthalpy obtained this way was independent of the presence or absence of nonequilibrium. The unknown factors were static temperature and density, bulk velocity, and ionization fraction. Assuming equilibrium conditions, bulk values for the unknown factors were computed by iteration of the conservation equations [15]. Transport properties were taken from DeVoto [16]. Stagnation conditions were computed from entropy relations assuming an isentropic process between the static state and the total or stagnation state. Semi-local bulk values of the flow parameters were obtained along the channel by this procedure; calculations were performed by electronic computer. The ranges of flow parameters covered in these experiments have been given previously [15].

Results for Zero Applied Magnetic Field

Heat transfer results at zero magnetic field are presented in terms of the nondimensional heat flux Q^* and the axial variable \bar{x} (Fig. 2) for convenient comparison with the constant-property slug-flow model of Back [5] for zero joule heating. In this representation it was necessary to determine inlet conditions which, in this case, were taken to correspond to the point of flow attachment within the inlet section, Fig. 1. The procedure for accomplishing this has been outlined previously [15]. Results shown in Fig. 2 include data for the second and third segments of

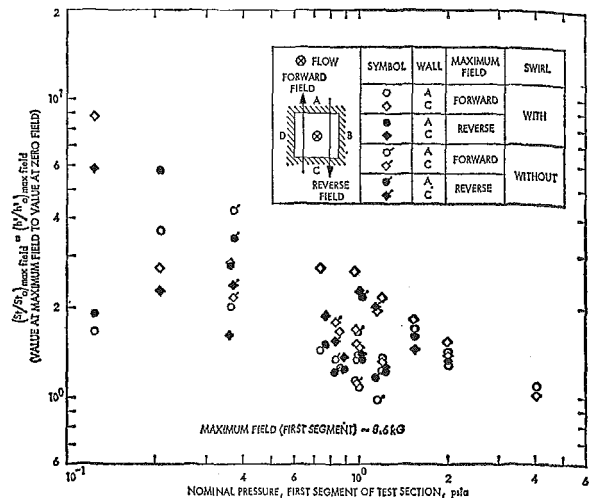


Fig. 3 General heat transfer results for first segment of test section at maximum applied magnetic field

the test section; equilibrium was assumed. The latter assumption would lead to estimates of static bulk temperature that would be too large if nonequilibrium conditions existed.

Fig. 2 indicates that the experimental results are about 70 percent below the slug-flow prediction. This is in general agreement with the work of Back and Witte [17] who have shown that the actual heat flux for low-speed constant-property flow over a flat plate is 70 percent less than a slug-flow prediction for $Pr = 1.0$. Within the scatter of the data, no consistent or significant effects of swirl, free-stream ionization, or nonequilibrium were apparent. Several other comparisons have been made with theories available, but these have not been included in Fig. 2. The experimental data are approximately 17 percent below a variable-property prediction of Back [18] for highly cooled flat plates with $Pr = 0.667$ in the range $0.005 < \bar{x} < 0.05$. The present data exceed the constant-property prediction of Montgomery and Wilbulsas [19] for a square duct with $Pr = 0.72$. However, the agreement was relatively good, in the latter case, such that the prediction was within 5 percent of the data in the range $0.005 < \bar{x} < 0.03$.

Direct comparison with published experimental results for an argon plasma is difficult because few data are available within an equivalent range of flow parameters, and results are usually presented in terms of other heat transfer groups. Schmidt and Leppert [20] have published data for argon in a 0.5-in-dia tube; absolute gas temperatures in their experiments exceeded those obtained here by a factor of two or more so that thermal radiation may have contributed significantly to their results. On a Nusselt number basis, the present data slightly overlap the data of Schmidt and Leppert at lower \bar{x} but fall below their data at higher \bar{x} by factors varying from two to three [15].

General Results at Maximum Magnetic Field

The data obtained with a magnetic field will be presented in terms of the local Stanton number St and the local heat transfer coefficient h' because these groups involved no transport properties and were not dependent on an assumption of thermal equilibrium.

$$h' = q_w / (H_{t,b} - H_w) \quad (1)$$

and

$$St = h' / (\rho \bar{u}) \quad (2)$$

A zero subscript attached to these parameters is used to designate values for zero magnetic field. Since the mass flux $\rho \bar{u}$ was not influenced by the magnetic field in these experiments,

Table 1 Values of parameters at center of first segment of test section for selected tests with swirl (arc input current of 2000 amp)*

Item	Test Series 18H		Test Series 25H		Test Series 26H	
	Zero Field	Maximum Forward Field	Zero Field	Maximum Forward Field	Zero Field	Maximum Forward Field
\dot{m}	0.007		0.005		0.007	
p (Avg) psia	0.856	0.901	0.363	0.424	0.211	0.320
$H_{t,b}$ Btu/lb	2,795	2,431	3,906	2,997	2,921	2,213
T_b °R	16,670	15,980	17,340	16,500	15,310	14,520
\bar{w} ft/sec	1,365	1,235	2,505	1,965	5,030	3,100
Re	270	260	230	200	260	260
Re F^2	81	87	57	59	93	104
Ec	0.028	0.027	0.066	0.054	0.36	0.18
α	0.037	0.023	0.088	0.047	0.028	0.012
n_e per cm ³	1.65 × 10 ¹⁵	1.10 × 10 ¹⁵	1.50 × 10 ¹⁵	1.05 × 10 ¹⁵	0.34 × 10 ¹⁵	0.23 × 10 ¹⁵
**Re m	—	0.05	—	0.09	—	0.095
**Ha	—	64	—	71	—	56
** j_z amp/in ²	—	435	—	780	—	825
**S (for K = 0)	—	37	—	80	—	230

*Computed from energy balance, assuming equilibrium.

**Based on scalar electrical conductivity [16].

$$\frac{St}{St_0} = \frac{h'}{h_0'} \quad (3)$$

A summary of the general effect that maximum magnetic field had on convective heat transfer is given (Fig. 3) in terms of the static pressure in the test section. These results refer to the first segment of the test section and are given only for upper wall A and lower wall C, both of which were perpendicular to the direction of the applied magnetic field. Side walls will be discussed later. The ratio St/St_0 represents the relative increase in Stanton number caused by the magnetic field over the value obtained at zero field. Although there is considerable scatter in the data, the trend with pressure is unmistakable. Examination of Fig. 3 reveals no obvious or consistent differences arising from the orientation of the applied field or from the presence of swirl in the flow. Swirl velocities were probably small compared to axial velocities since the tangential injection velocity upstream of the arc heater never exceeded 15 percent of the axial velocity in the test section.

Results for Selected Tests with Applied Magnetic Field

Flow deceleration caused by the magnetic field was accompanied by an increased static pressure, and pressure peaks occurred in the inlet section. In addition, the magnetic field caused a decrease in both enthalpy and static temperature, due to the increased heat transfer, and more pronounced axial temperature gradients. Increases in static pressure due to the magnetic field were larger on walls perpendicular to the magnetic field than for walls parallel to the magnetic field [15]. Table 1 presents a list of parameters computed for the first segment of the test section when the arc current was 2000 amp.

Again, Stanton number was used as the dependent variable and the local heat transfer coefficient was based on bulk total-enthalpy difference. The applied magnetic field was used directly as the independent variable because it was the only parameter varied deliberately within a test series. The joule heating parameter S , which is a nondimensional form of the term j^2/σ appearing in the energy equation [5], was discarded for use because of the uncertainty associated with establishing the gas electrical conductivity in the present experiments. In the absence of Hall or ion-slip effects, the joule heating term is written

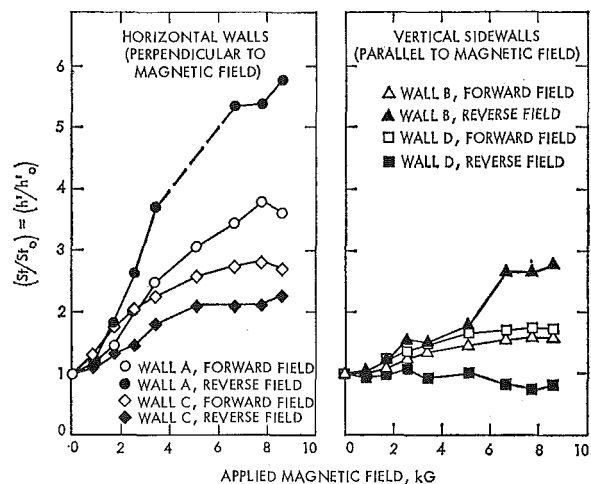


Fig. 4 Effect of magnetic field on heat transfer in first segment of test section, test series 26H (flow with swirl)

$$(j^2/\sigma_0) = (j_z^2/\sigma_0) = \sigma_0 \bar{u}^2 B^2 (1 - K)^2 \quad (4)$$

which is nondimensionalized as

$$S = (j^2/\sigma_0)[a^2/k_i(T_i - T_w)] = Ha^2 Ec(1 - K)^2 Pr \quad (5)$$

In the absence of an applied electric field, $K = 0$, so that the joule heating parameter reduces to $S = Ha^2 Ec Pr$. The term joule heating is misleading when no applied electric field is present because a magnetic field does not alter the total energy content of the gas. Although it is theoretically possible for a magnetic field to cause a positive axial bulk-temperature gradient for laminar incompressible flow [5], this was never observed in the present experiments.

Heat transfer results for test series 26H are given in Fig. 4; horizontal walls A and C were perpendicular to the direction of the applied magnetic field whereas side walls B and D were parallel to the direction of the applied field. Heat transfer to horizontal walls A and C generally increased as the strength of the applied magnetic field increased, regardless of the direction of the applied field. Results for other test series are given in [15]. With the possible exception of test series 26H there was no evidence that any effect of swirl existed because the trends of the curves did not show any consistent dependence on the direction of the magnetic field. Results obtained without swirl were the same qualitatively and exhibited the same trends as cases of flow with swirl.

Results for side walls B and D differed from results for walls A and C and varied from test series to test series. In test series 18H one of the side walls experienced only small increases in heat transfer, whereas the opposite wall experienced a sharp decrease in heat transfer. The effect on the walls became reversed when the magnetic field was reversed; this result was confirmed by visual observation of lateral (side-to-side) deflection of the exhaust plume. The same behavior occurred in test series 25H except that increases in heat transfer were evident as well as decreases. However, in test series 26H (Fig. 4), forward magnetic field produced moderate increases in heat transfer on both side walls and a different result when the magnetic field was reversed.

The large relative increases in Stanton number produced at walls A and C as a result of the magnetic field (Figs. 3 and 4) are clearly significant. In order to show that these increases often offset any decreases in heat transfer to the side walls, the average Stanton numbers for the four walls are displayed in Fig. 5 for three test series. The fact that the curves are reasonably symmetric with respect to the zero-field condition indicates that the direction of the applied magnetic field was not very important. The increases in average relative heat transfer were significant for test series 25H and 26H but not for test series 18H.

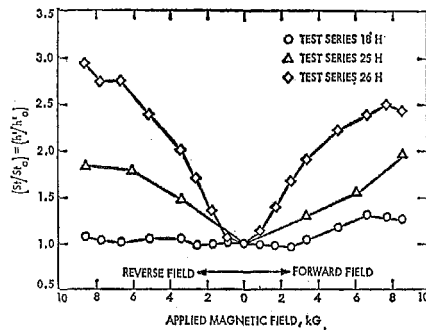


Fig. 5 Heat transfer in first segment of test section averaged over four walls of channel

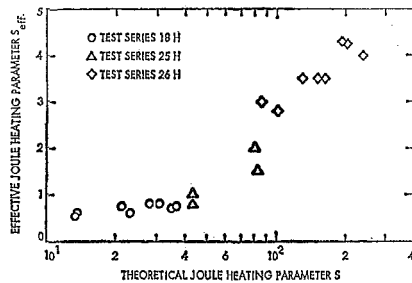


Fig. 6 Comparison of effective joule heating parameter with theoretical values; S_{eff} obtained from forced correlation between experiment and modified slug-flow theory [5]; theoretical S calculated for $K = 0$

Factors Affecting Flow and Heat Transfer

A detailed discussion of the many factors that could have influenced the convective heat transfer in these experiments is beyond the scope of this paper. The importance of several factors has been estimated [15]; the effects of axial heat conduction, thermal radiation, ionization, free convection, and swirl in the flow were not considered significant.

For zero magnetic field the combined cumulative effects due to experimental scatter and other factors could have been of the order of 20 to 30 percent. However, the effects of the magnetic field on total transfer to the wall were, in many cases, much larger than that. Departures from thermal equilibrium are believed to have been small with zero magnetic field; with strong magnetic field the likelihood of nonequilibrium and enhanced ionization fraction may have been large [21, 22]. Even if internal measurements of electron and heavy-particle temperature had been made in the present experiments, the effect of nonequilibrium on heat transfer would not have been clearly established because of uncertainty associated with gas transport properties.

The effect of the magnetic field on heat transfer was probably controlled to a large extent by the magnitude and direction of the induced current flow within the gas. Because the walls were relatively cold in these experiments, the adjacent boundary layers were of low electrical conductivity. It is believed that current flow did not penetrate the boundary layers and was confined to the gas despite the presence of conducting walls; heating of the walls by electron impingement or by internal electrical power dissipation were not considered significant [15].

If ionization, thermal radiation, and electron heating effects are excluded, local heat transfer to a wall could increase due to (1) an increased temperature gradient at the wall, (2) an increased thermal conductivity of the gas at or near the wall, or (3) a combination of (1) and (2). In the present experiments, the applied magnetic field produced large increases in heat transfer to the walls at a given axial location, despite reductions in the local bulk temperature and enthalpy of the gas. At walls perpendicular to the direction of the applied field, it is expected that the thickness of both the velocity and thermal boundary layers would be de-

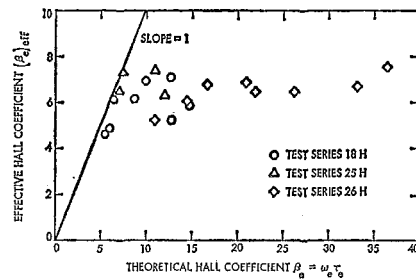


Fig. 7 Comparison of effective Hall coefficient with theoretical values; $(\beta_e)_{eff}$ obtained from results of Fig. 6

creased by the action of the magnetic field. This would cause higher velocity and temperature gradients at the wall compared to zero-field conditions. However, the thermal conductivity of the gas would not have been greatly altered at those walls, and could have been enhanced in the presence of nonequilibrium ionization. Thus, the temperature profile across the channel must have been altered in such a way as to yield increased gradients at the wall consistent with an overall reduction in gas energy, as would be obtained from an integral or average value across the channel.

Estimates of Joule Heating, Hall Effect, and Flow of Electric Current

Large values of the joule heating parameter S were calculated for these experiments. In Table 1, for example, $S = 230$ at maximum magnetic field for test series 26H. Such a large value of S is not consistent with the experimental measurements because the measured Q^*/Q_0^* for that case was much smaller than the theoretical value [15]. Several qualitative and quantitative observations suggested that Hall effects were prominent in this investigation: (1) behavior of the heat transfer to side walls, i.e., walls parallel to the magnetic field, (2) static pressure measurements at the side walls, and (3) visual observations of lateral deflections of the exhaust plume. Hall and ion-slip coefficients and their contribution to a first-order correction to the joule heating parameter S have been examined [15], but ion-slip coefficients were two orders of magnitude less than Hall coefficients for argon at pressures of interest here. Corrected values of S due to the Hall effect were calculated from

$$S' = S / (1 + \beta_e^2) \quad (6)$$

where $\beta_e = \omega_e \tau_e$ is the Hall coefficient. In these experiments, theoretical values of β_e were so large that the corrected values S' were negligible, even for the case of $K = 0$. The theoretical value of Hall coefficient for test series 26H was $\beta_e \sim 300$, for which $S' \sim 0$ from equation (6). Thus, neither the theoretical values of S nor β_e were consistent with experimental observations.

The experimental results for zero field were less than the slug-flow prediction by approximately 70 percent (Fig. 2). However, the slug-flow approximation should be valid at high values of magnetic field [5]. A data-fitting procedure was adopted [15] to determine effective values of S using theoretical values of S calculated for $K = 0$. Essentially, values of S_{eff} were read from a chart by plotting experimental values of Q^*/Q_0^* on a set of theoretical curves of Q^*/Q_0^* versus \bar{x} with S as parameter; theoretical values of both Q^* and Q_0^* were adapted from Back [5], but Q_0^* was reduced by a factor of 1.7 in view of Fig. 2. Experimental values of heat transfer only for $B > 5000$ G were utilized in the fitting process; heat transfer results for walls A and C were averaged. Using the values of S_{eff} so obtained, values of $(\beta_e)_{eff}$ were computed from a relation similar to equation (6). Results are shown in Figs. 6 and 7. Values of $(\beta_e)_{eff}$ appear to be reasonable. The flat trend with increasing magnetic field was also obtained by Louis [23]; however, his values of $(\beta_e)_{eff}$ were approximately half the values obtained here.

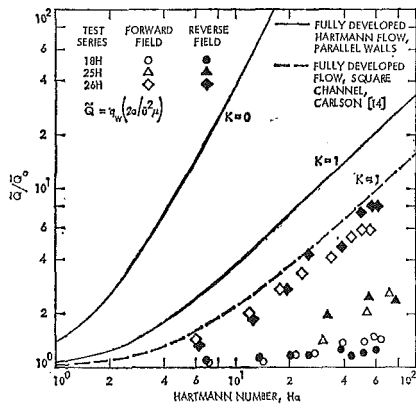


Fig. 8 Comparison of experimental heat transfer results with several theoretical predictions; Hartmann number based on scalar electrical conductivity; experimental results are for walls perpendicular to the direction of the applied magnetic field (average heat flux of walls A and C)

Direct measurements of internal current flow were not available. An attempt was made to determine the transverse component of current $(j_x)_{\text{eff}}$ from an axial momentum balance [15].

$$-\frac{dp}{dx} - (\rho u) \frac{d\bar{u}}{dx} = j_x B + \tau_w \left(\frac{2}{a} \right) \quad (7)$$

This is a tedious procedure that requires a trial-and-error iteration of $(\beta_e)_{\text{eff}}$. The final results were calculated from

$$(j_x)_{\text{eff}} = (\beta_e)_{\text{eff}} \sigma \bar{u} B / [1 + (\beta_e)_{\text{eff}}^2] \quad (8)$$

$$(j_z)_{\text{eff}} = \sigma \bar{u} B / [1 + (\beta_e)_{\text{eff}}^2] \quad (9)$$

$$(j)_{\text{eff}}^2 = (j_x)_{\text{eff}}^2 + (j_z)_{\text{eff}}^2 \quad (10)$$

The iteration was not accurate for low values of B ; effective values of the total current density obtained by this method were approximately one-eighth of the theoretical transverse current density for test series 18H. Values of $(\beta_e)_{\text{eff}}$ from the momentum balance compared well with those obtained from the heat transfer correlation in Fig. 7 [15], but were not accurate for $\beta_e < 5$.

Comparison with Theory

It is difficult to compare the present experimental results with theoretical predictions because of uncertainty in the gas transport properties. Because measurements of the current flow within the gas or within the walls were not made, it is difficult to define the physical nature of the flow or to specify a distinct value for the load factor K . Although the four walls of the channel formed a continuous hollow conductor, it was concluded that current flow was confined to the gas because of the highly cooled walls and low conductivity of the boundary layers. For this case, the flow could not have been externally short-circuited because that condition requires good electrical contact between the fluid and the walls. However, absence of an external applied electric field formally means that $K = 0$, which corresponds to a short-circuit condition, as the term is usually defined.

The present experiment probably corresponded more nearly to an open-circuit case ($K = 1$), with nonconducting walls and circulating currents within the gas, such as was considered by Carlson [14]. However, for the purposes of comparing theory and experiment for walls perpendicular to the direction of the applied magnetic field, it is not entirely inconsistent to utilize Back's results for the short-circuit condition, as was done to obtain the results of Fig. 6. Back [5] examined the heat transfer to parallel nonconducting walls (insulators) that were perpendicular to the direction of the applied magnetic field; his solution is not valid for K near unity. For the open-circuit case, the transverse current vanishes in Back's treatment but not in Carlson's treatment; neither author considered Hall effects or nonequilibrium.

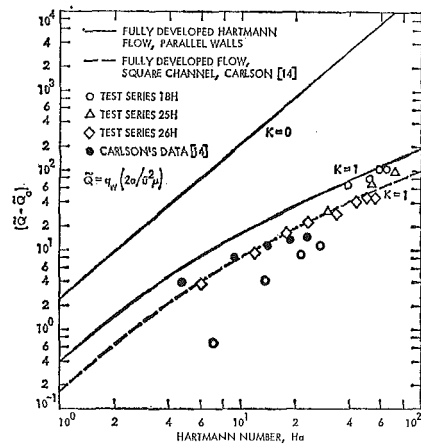


Fig. 9 Comparison of experimental heat transfer results with several theoretical predictions; Hartmann number based on scalar electrical conductivity; experimental results are for total heat transfer to all four walls of the confining channel

Carlson's analysis takes into account circulating currents within the gas in a square duct with nonconducting walls (open-circuit condition with $K = 1$). Experimental results will be compared to theoretical predictions for the two cases $K = 0$ and $K = 1$.

The heat transfer solution for the fully developed thermal region, valid for any K , is given by Back in his equation (22). This solution for fully developed one-dimensional Hartmann flow may be written as

$$\bar{Q} = \frac{q_w}{\bar{u}^2 \mu} = 2Ha^2 \left[(K - 1)^2 + \frac{\tanh(Ha)}{Ha - \tanh(Ha)} \right] \quad (11)$$

The limiting value of \bar{Q} as Ha approaches zero is $\bar{Q}_0 = 6.0$. Equation (11) applies for flow between parallel plates; it is plotted in Fig. 8 as a function of Hartmann number for values of $K = 0$ and $K = 1$, and has been normalized with respect to its value at zero magnetic field \bar{Q}_0 .

The lowest curve in Fig. 8 represents Carlson's solution [14] for fully developed flow in a square channel and was obtained by solving his equations (6) and (11) on a computer. His heat transfer group, herein designated by Q_C^* , is defined as

$$Q_C^* = Q / 4\bar{u}^2 \mu l \quad (12)$$

where Q is the total heat generation rate within the fluid by combined viscous and ohmic action. The limiting value of Q_C^* as Ha approaches zero is $(Q_C^*)_0 = 7.113$. Equation (12) can be written in terms of the wall heat flux assuming $Q = 8alq_w$ for a square channel. Thus, the heat transfer group Q_C^* for the four walls of a square channel is equivalent in magnitude to \bar{Q} for Hartmann flow between parallel plates. This distinction is not important unless the side-wall heat transfer is significant compared to that for walls perpendicular to the applied magnetic field.

The present experimental data for the three test series are indicated in Fig. 8 for comparison with theory. Data from the upper wall A and the lower wall C were averaged in this figure; side walls were not included. Clearly, the data were not consistent with a short-circuit condition (uncorrected for Hall effect). However, except for test series 26H, the data do not agree well with Carlson's theory for open-circuit conditions in this representation.

Carlson [14] obtained data for unseeded argon in an accelerator operating at open-circuit conditions; his experimental conditions correspond most nearly to those present in test series 26H. Carlson's data and the present data may be compared most readily by using his representation of heat transfer, i.e., $(\bar{Q} - \bar{Q}_0)$ rather than \bar{Q}/\bar{Q}_0 . Results are presented in Fig. 9; all experimental data are

for total heat transfer to all four walls of the confining channel. Again, theoretical curves for fully developed Hartmann flow for $K = 0$ and $K = 1$ are plotted, as well as Carlson's theoretical prediction.

Experimental results for test series 26H agree reasonably well with Carlson's data; they are lower than Carlson's data at low Hartmann number, whereas the opposite situation exists at higher Hartmann numbers. Except for test series 18H for $Ha < 40$, all experimental data agree quantitatively and, further, agree with Carlson's open-circuit theory in trend. It is interesting that better agreement between experiment and theory is evident for the representation of data given in Fig. 9 than for Fig. 8.

Acknowledgments

The author gratefully acknowledges many helpful discussions with P. F. Massier and L. H. Back, the assistance of M. B. Noel in conducting experiments, and the computational assistance of S. J. Kikkert.

References

- 1 Michiyoshi, I., and Matsumoto, R., "Heat Transfer by Hartmann's Flow in Thermal Entrance Region," *International Journal of Heat and Mass Transfer*, 1964, Vol. 7, pp. 101-112.
- 2 Erickson, L. E., Wang, C. S., Hwang, C. L., and Fan, L. T., "Heat Transfer to Magnetohydrodynamic Flow in a Flat Duct," *Z. Angew. Math. Phys.*, 1964, Vol. 15, pp. 408-418.
- 3 Dhanak, A. M., "Heat Transfer in Magnetohydrodynamic Flow in an Entrance Section," *JOURNAL OF HEAT TRANSFER, TRANS. ASME, Series C*, Vol. 87, No. 2, May 1965, pp. 231-236.
- 4 Hwang, C. L., Knieper, P. J., and Fan, L. T., "Heat Transfer to MHD Flow in the Thermal Entrance Region of a Flat Duct," *International Journal of Heat and Mass Transfer*, 1966, Vol. 9, pp. 773-789.
- 5 Back, L. H., "Laminar Heat Transfer in Electrically Conducting Fluids Flowing in Parallel-Plate Channels," *International Journal of Heat and Mass Transfer*, 1968, Vol. 11, pp. 1621-1636.
- 6 Yen, J. T., "Effect of Wall Electrical Conductance on Magnetohydrodynamic Heat Transfer in a Channel," *JOURNAL OF HEAT TRANSFER, TRANS. ASME, Series C*, Vol. 85, No. 4, Nov. 1963, pp. 371-377.
- 7 Snyder, W. T., "The Influence of Wall Conductance on Magnetohydrodynamic Channel-Flow Heat Transfer," *JOURNAL OF HEAT TRANSFER, TRANS. ASME, Series C*, Vol. 86, No. 4, Nov. 1964, pp. 552-558.
- 8 Hwang, U. P., Fan, L. T., and Hwang, C. L., "Compressible Laminar MHD Flow Inside a Flat Duct with Heat Transfer," *AIAA Journal*, 1967, Vol. 5, pp. 2113-2121.
- 9 Eraslan, A. H., and Eraslan, N. F., "Heat Transfer in Magnetohydrodynamic Channel Flow," *Phys. Fluids*, 1969, Vol. 12, pp. 120-128.
- 10 Lykoudis, P. S., "Experimental Studies for the Determination of Transport Properties in the Presence of a Magnetic Field for a Conducting Medium Flowing Turbulently," *International Symposium on Properties and Applications of Low-Temperature Plasma*, Moscow, USSR, July 1965.
- 11 Blum, E. Y., "Effect of a Magnetic Field on Heat Transfer in the Turbulent Flow of Conducting Liquid," *High Temperature* (translated from Russian), Jan.-Feb. 1967, Vol. 5, pp. 68-74.
- 12 Kovner, D. S., Krasilnikov, E. Y., Nikolaenko, V. S., and Panevin, I. G., "Experimental Study of the Effect of a Transverse Magnetic Field in the Turbulent Flow of an Electrically Conducting Fluid in a Channel," (in Russian), *Akad. Nauk SSSR, Izvestiia, Mekhanika Zhid. Gaza*, Mar.-Apr. 1968, pp. 91-94.
- 13 Dukowicz, J. K., "A Magnetohydrodynamic Flow in the Shock Tube Boundary Layer with Transverse Magnetic Field," *UTIAS Rept. No. 115*, Institute for Aerospace Studies, University of Toronto, Canada, July 1966.
- 14 Carlson, G. A., "Circulating Currents in Linear, Cross-Field Generators and Accelerators," *NASA Technical Note D-5244*, May 1969.
- 15 Roschke, E. J., "Experimental Investigation of Heat Transfer from Partially Ionized Argon Flowing in a Conducting Channel with an Applied, Transverse Magnetic Field," *Technical Report No. 32-1510*, Jet Propulsion Laboratory, Pasadena, Calif., Dec. 1970.
- 16 DeVoto, R. S., "Argon Plasma Transport Properties," *SUDAER Report No. 217*, Department of Aeronautics and Astronautics, Stanford University, Stanford, Calif., Feb. 1965; also *Phys. Fluids*, Feb. 1967, Vol. 10, pp. 354-364.
- 17 Back, L. H., and Witte, A. B., "Prediction of Heat Transfer From Laminar Boundary Layers, With Emphasis on Large Free-Stream Velocity Gradients and Highly Cooled Walls," *JOURNAL OF HEAT TRANSFER, TRANS. ASME, Series C*, Vol. 88, No. 3, Aug. 1966, pp. 249-256.
- 18 Back, L. H., "Effects of Surface Cooling and Heating on Structure of Low-Speed, Laminar Boundary-Layer Gas Flows, with Constant Free-Stream Velocity," *Technical Report 32-1301*, Jet Propulsion Laboratory, Pasadena, Calif., 1968.
- 19 Montgomery, S. R., and Wibulswas, P., "Laminar Flow Heat Transfer for Simultaneously Developing Velocity and Temperature Profiles in Ducts of Rectangular Cross Section," *Appl. Sci. Res.*, 1967, Vol. 18, No. 4, pp. 247-259.
- 20 Schmidt, P. S., and Leppert, G., "Heat Transfer From Plasma in Tube Flow," *JOURNAL OF HEAT TRANSFER, TRANS. ASME, Series C*, Vol. 92, No. 3, Aug. 1970, pp. 483-489.
- 21 Rosa, R. K., *Magnetohydrodynamic Energy Conversion*, chap. 5, "Nonequilibrium Ionization," McGraw-Hill, New York, N. Y., 1968.
- 22 Zauderer, B., "Experimental Study of Nonequilibrium Ionization in a Linear MHD Generator," *AIAA Journal*, 1968, Vol. 6, pp. 701-707.
- 23 Louis, J. F., "Effective Ohm's Law in a Partially Ionized Plasma with Electron Density Fluctuations," *Phys. Fluids*, 1967, Vol. 10, pp. 2062-2064.

D. K. EDWARDS

Professor.
Mem. ASME

A. BALAKRISHNAN

Postgraduate Research Engineer.

School of Engineering
and Applied Science,
University of California,
Los Angeles, Calif.

Volume Interchange Factors for Nonhomogeneous Gases

Interchange factors describing the radiation heat transfer between two gas-volume elements or between one such element and a wall element are shown to be convenient for treating a variety of engineering problems, such as those involving combustion chambers, furnaces, and plumes. When the gas is not homogeneous in temperature, composition, or pressure, gas-volume interchange factors are found to be complex functions of the geometrical arrangement and the temperature, composition, and pressure fields which affect the radiant properties in the gas within and between the elements. A simplified expression is derived for the rapid calculation of such factors, and comparisons are made with exact numerical computations. Both take into account nongray spectral variations in gas properties. The case of adjoining elements is shown to require special treatment, and results are presented. Volume interchange factors and the machine time necessary to compute them are reported to demonstrate the relative ease with which such factors can be obtained using the approximations developed in this paper.

Introduction

THE NEED for accurate predictions of the temperature distributions and heat fluxes in combustion chambers and furnaces has come closer to fulfillment with the development of high-speed large-memory computers. The need exists, for example, in predicting the rates of formation of nitric oxide in burner flames and combustion chambers and the effects of recirculation and steam injection. Spalding and co-workers (Gosman et al. [1]¹) have recently published a program for the calculation of temperature and concentration profiles in recirculating flows based upon a finite-difference representation of the steady Navier-Stokes equations with an eddy diffusivity based upon the Kolmogorov-Prandtl model and the energy and species equations. Radiation transfer is not included in this treatment of the energy equation. It of course should enter as a heat loss per unit volume equal to the divergence of the radiative heat flux. The present work is concerned with evaluating radiation interchange factors so that radiation can be treated in such a program.

DeSoto [2] computed the divergence of the radiative heat flux by computing the radiative flux itself at several locations in a circular pipe containing pure CO₂ and obtained the divergence by numerical differencing. In order to do so the entire temperature field was specified as that of a previous iteration. Each iteration consequently required a recalculation of the radiant fluxes. In

order to keep computation time on the order of 10 min, deSoto used very coarse subdivisions, 6 in radius and 12 in length. At the surfaces of each subdivision the net radiant flux was computed by summing contributions from 72 lines of sight for each of 13 spectral wavenumbers. For each wavenumber a numerical quadrature involving up to 30 steps was made along each line of sight. Gas properties were allowed to vary with temperature, and spectral absorption lines were assumed to be overlapped.

Hottel and Cohen [3] and Einstein [4] subdivided a gas volume with uniform composition into a number of elements, and, in contrast to the approach taken by deSoto, computed a volume interchange factor ($g_i g_j$) between volume elements i and j for a gas homogeneous in composition and with temperature-independent radiant properties. The divergence of the radiative flux for a gas with overlapped spectral lines for volume i is then given by

$$(\text{div } q_r)_i = \frac{1}{V_i} \sum_{j=1}^N \sum_{m=1}^M (g_i g_j) v_m (\pi I_{p,i,m} - \pi I_{p,j,m}) \Delta v_m$$

where $I_{p,i,m}$ is the Planck intensity for volume i and wavenumber v_m ,

$$I_{p,i,m} = \frac{2hc^2 v_m^3}{e^{hc v_m / kT_i} - 1}$$

N is the number of volume elements, and M is the total number of wavenumbers used (deSoto used $N = 72$, $M = 13$). If the approach taken by Hottel and Cohen had been used by deSoto, it would have been possible to iterate the temperature field several times before recomputing the set of ($g_i g_j$) factors. Whether considerable economy could have been achieved depends upon whether the 72 j values of ($g_i g_j$) could have been found with no

¹ Numbers in brackets designate References at end of paper.

Based on a paper contributed by the Heat Transfer Division and presented at the ASME-AIChE Heat Transfer Conference, Tulsa, Okla., August 15-18, 1971, as Paper No. 71-HT-19. Manuscript received by the Heat Transfer Division April 20, 1971; revised manuscript received September 14, 1971.

more computation time than the 72 line-of-sight values calculated by deSoto.

It is the purpose of this paper to present a simple scheme for calculating volume interchange factors in a gas, nonhomogeneous in temperature and composition and with temperature-dependent radiant properties, using, in most cases, only a single line of sight per pair of volume elements. Furthermore, both overlapped and nonoverlapped spectral lines are considered. The approximations derived are compared with detailed numerical calculations and are found to be useful.

Analysis

Volume Interchange between Infinitesimal Elements. Consider a gas volume in which the temperature, composition, and/or pressure vary. Let k be the spectral absorption coefficient per unit mass, a quantity which then varies with position within the gas and with wavenumber or wavelength throughout the infrared spectrum of interest. A gas composed of combustion products and soot, but few or no metal-oxide particles, will not scatter radiation appreciably. Furthermore, such a gas will be nearly in a state of thermodynamic equilibrium described by the local state variables $T(r)$, $P(r)$, and a set of $x_i(r)$ or $m_i(r)$, where T is temperature, P is total pressure, x_i is the mole fraction of species i , and m_i is the mass fraction. The quantity r is a length measured along some ray. For such a gas the basic equation of transfer is

$$\frac{dI}{dr} = \rho k(I_p - I) \quad (1)$$

where I is the spectral radiant intensity (power per unit normal area, unit solid angle, and unit spectral bandwidth), ρ is density, and I_p is the Planck spectral intensity for black-body thermodynamic equilibrium radiation.

The quantity $\rho k dr$ appearing when equation (1) is written in differential form is thus both the absorptivity and the emissivity of a differential volume of gas for a beam piercing it such that a distance dr along the beam lies within the volume. For a finite path within the gas, the absorptivity and transmissivity may be found from the homogeneous solution for equation (1)

$$\alpha = 1 - e^{-\int_0^r \rho k dr} \quad (2)$$

$$\tau = e^{-\int_0^r \rho k dr} \quad (3)$$

For an optically thin volume of gas dV_1 , the power emitted is isotropic (unless there is some peculiar situation such as elongated particles lined up by an electric or magnetic field). This fact may be seen, for example, by treating a spherical volume using an

emissivity of $\rho k(D \cos \theta)$, where θ is the angle of a ray from a normal to the surface of the sphere, and realizing that any differential volume can be approximated as accurately as desired by a close packing of spheres of various radii, absorption of radiation from one sphere by the others being negligible because of the optical thinness of the small volume. This requirement of optical thinness is simply that $\rho_1 k_1 r_{\max,1} \ll 1$ be met where r_{\max} is the longest ray through the volume. The radiation is isotropic in the 4π steradians of solid angle surrounding dV_1 provided the receiver is at a distance $R \gg r_{\max,1}$. The power per unit solid angle ω is then

$$\frac{d\dot{Q}_{e,1}}{d\omega} = (\rho_1 k_1 dV_1) I_{p,1} \quad (4)$$

Let a second optically thin volume element dV_2 be located a distance R away, $R \gg r_{\max,1}$ and $r_{\max,2}$. For the sake of simplicity we can take the element to be a portion of a spherical shell with volume $dV_2 = R^2 d\omega \Delta r$ where Δr is the thickness. Then the one-way transfer of radiation emitted by element 1 and absorbed by element 2 follows from equations (4) and (3) by eliminating $d\omega$.

$$d\dot{Q}_{e,1,2} = [I_{p,1} \rho_1 k_1 dV_1] [dV_2 / R^2 \Delta r] \left[e^{-\int_0^R \rho k dr} \right] [\rho_2 k_2 \Delta r] \quad (5)$$

$$d\dot{Q}_{e,1,2} = \pi I_{p,1} \frac{\rho_1 k_1 dV_1 \rho_2 k_2 dV_2}{\pi R^2} e^{-\int_0^R \rho k dr}$$

The volume interchange factor F_{1-2} from the first infinitesimal element to the second is then

$$4\rho_1 k_1 dV_1 F_{1-2} = \frac{d\dot{Q}_{e,1,2}}{\pi I_{p,1}} = \frac{\rho_1 k_1 dV_1 \rho_2 k_2 dV_2}{\pi R^2} e^{-\int_0^R \rho k dr} \quad (6)$$

Note that

$$4\rho_1 k_1 dV_1 F_{1-2} = 4\rho_2 k_2 dV_2 F_{2-1} \quad (7)$$

Practical Calculation of Volume Interchange between Finite Elements.

As a mathematical formality equation (6) can be integrated for finite volumes, for example, such as those arranged as shown in Fig. 1.

$$4\rho_1 k_1 V_1 F_{1-2} = \int_{V_2} \int_{V_1} e^{-\int_0^R \rho k dr} \frac{\rho_1 k_1 dV_1 \rho_2 k_2 dV_2}{\pi R^2} \quad (8)$$

However, in order to compute F_{1-2} precisely from this definition, one would have to subdivide V_1 and V_2 so that the required conditions on equation (6) were met, that is, so that $\rho_1 k_1 r_{\max,1}$ and $\rho_2 k_2 r_{\max,2}$ were much less than unity and so that R was much greater than $r_{\max,1}$ or $r_{\max,2}$. But in spectral regions of intense absorption, in the 4.3 micron CO_2 band, for example, making

Nomenclature

a = constant
 A = area
 b = constant
 B = length of side
 c = constant
 c = speed of light
 C = band absorption correlation constant
 d = line spacing
 D = diameter
 F = dimensionless exchange factor
 g = exchange factor
 h = parameter
 h = Planck's constant
 I = intensity
 k = mass absorption coefficient
 k = Boltzmann constant
 l = geometric-mean beam length
 m = mass fraction

M = number of wavenumbers
 n = exponent
 N = number of volumes
 P = total pressure
 q = heat flux
 \dot{Q} = heat flow
 r = distance along ray
 R = distance between centroids
 S = line intensity, transmissivity integral
 T = temperature
 V = volume
 x = mole fraction, coordinate
 y = coordinate
 z = coordinate
 α = absorptivity
 β = line-width parameter
 γ = line width
 ζ = line-effect integral

θ = angle between ray and normal
 ν = wavenumber
 ξ = line-intensity integral
 π = 3.1415927...
 ρ = density
 σ = Stefan-Boltzmann constant
 τ = transmissivity
 ω = solid angle

Subscripts

c = corner
 e = emitted (one-way)
 f = face
 i = i th volume, "in"
 j = j th volume
 m = m th wavenumber
 o = "out"
 p = Planck
 s = surface

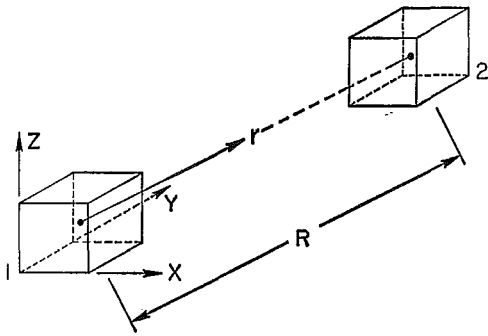


Fig. 1 Geometry of volume interchange

$\rho_1 k_1 r_{\max,1}$ less than unity would necessitate using $r_{\max,1}$ on the order of a few hundredths of an inch. In an industrial furnace one would like to deal with volume elements on the order of a foot or so on a side. To have to subdivide a hundred or more such elements each into 10^6 or even 10^8 subelements would raise the requisite calculation time to an absurd value.

The spectral nature of the radiation process creates difficulties as well. To calculate a total value one must integrate over wave-number

$$\langle 4\rho_1 k_1 V_1 F_{1-2} \rangle = \frac{1}{\sigma T_1^4 - \sigma T_2^4} \int_0^\infty [4\rho_1 k_1 V_1 F_{1-2}] \times [\pi I_p(T_1, \nu) - \pi I_p(T_2, \nu)] d\nu \quad (9)$$

Usually such integration requires calculating 10 to 100 spectral values and summing numerically. However, when line effects are important at atmospheric and subatmospheric pressures, a straightforward calculation would require on the order of 10 times as many calculations.

For these reasons approximations are made as indicated below. These approximations have the goal of achieving engineering accuracy, say ± 10 percent, without requiring more than a single line-of-sight calculation for a volume-element pair and without requiring more than a few spectral calculations per absorption band.

An Approximation for Remote Volumes, Overlapped Lines. In the case of remote volumes an approximate relation can be derived for finite spheres whose centers are a distance R apart and whose radii R_1 and R_2 are small fractions of R . If the volume elements are very roughly spherical, such as cubes, one might suppose that the result for spheres, suitably expressed, would give an engineering approximation, particularly since shape is not of consequence for remote, optically thin elements. For two remote spheres the approximation is made that the transmittance of all paths between the surfaces of the spheres is nearly [3]

$$\tau_{1,2} \doteq e^{-\int_{l_1}^{R-l_2} \rho k dr} \quad (10)$$

where r is measured from the centroid of volume 1 to the centroid of volume 2, and l_1 and l_2 are the geometric-mean beam lengths [5, 6]

$$l_1 = \frac{4V_1}{A_1} \quad l_2 = \frac{4V_2}{A_2} \quad (11)$$

The areas A_1 and A_2 are those of the total surfaces of the volumes, $4\pi R_1^2$ and $4\pi R_2^2$ respectively for spheres. The parameter h allows for the fact that the path from surface to surface will be less than the centroid-to-centroid distance R . For cubes facing each other, h would be $\frac{3}{4}$.

For finite spheres, to the mean beam length approximation [5, 6], the emissivity of sphere 1 and the absorptivity of sphere 2 are

$$(1 - e^{-\rho_1 k_1 l_1}) \quad \text{and} \quad (1 - e^{-\rho_2 k_2 l_2})$$

respectively. The shape factor from the surface of sphere 1 to that of sphere 2 is nearly $\pi R_2^2/4\pi R^2$ or $A_2/16\pi R^2$ when the spheres are remote. The one-way transfer from 1 to 2 is then

$$\dot{Q}_{e,1,2} = \pi I_{p,1} (1 - e^{-\rho_1 k_1 l_1}) A_1 (A_2/16\pi R^2) \tau_{1,2} (1 - e^{-\rho_2 k_2 l_2})$$

When this expression is divided by $\pi I_{p,1}$ and the result is compared to the left-hand equality in equation (6), there is found

$$4\rho_1 k_1 V_1 F_{1-2} \doteq \frac{A_1 A_2}{16\pi R^2} (1 - e^{-\rho_1 k_1 l_1}) (1 - e^{-\rho_2 k_2 l_2}) \tau_{1,2} \quad (12)$$

This result will be tested for practical calculations by comparing with exact calculations carried out by time-consuming numerical quadratures based on equation (6).

An Approximation for Remote Volumes, Nonoverlapped Lines. For nonoverlapped lines the effective transmissivity $\bar{\tau}$ is not given by equation (3) but is given to good accuracy by the Curtis-Godson approximation [7]

$$\bar{\tau}(r, r') = \exp \left[\frac{-\xi}{(1 + \xi^2/\zeta)^{1/2}} \right] \quad (13)$$

where

$$\xi = \int_{r'}^r \bar{k}(r'') \rho(r'') dr'' \quad (14)$$

$$\zeta = \int_{r'}^r \bar{k}(r'') \beta(r'') \rho(r'') dr'' \quad (15)$$

The local values of $\bar{k}(r'') = S/d$, the mean-line-intensity-to-spacing ratio, and $\beta(r'') = \pi\gamma/d$ (or $4\gamma/d$ depending on the narrow-band model), the mean-line-width-to-spacing parameter, are obtained using band model calculations substantiated by experimental data, e.g., [8].

Equation (5) of reference [7] gives the radiant intensity coming back upon a target at the origin of a line of sight of length L . For the present case, to apply this equation we must measure backward from the point at which the beam is presumed to have entered gas volume 2 ($r_{i,2}$) to obtain the intensity entering volume 2. When the coordinates are transformed to the forward r direction, there results

$$I'_{e,1,2} = \int_{r_{i,1}}^{r_{o,1}} I_{p,1} \frac{d}{dr} \bar{\tau}(r_{i,2}, r) dr = I_{p,1} [\bar{\tau}(r_{i,2}, r_{o,1}) - \bar{\tau}(r_{i,2}, r_{i,1})]$$

The integration with respect to dr acts only from $r_{i,1}$ to $r_{o,1}$, because when computing F_{1-2} the source intensity I_p is turned on only within volume 1. By the same reasoning the intensity emitted by the portion of the beam within volume 1 and leaving volume 2 is

$$I_{e,1,2} = \int_{r_{i,1}}^{r_{o,1}} I_{p,1} \frac{d}{dr} \bar{\tau}(r_{o,2}, r) dr = I_{p,1} [\bar{\tau}(r_{o,2}, r_{o,1}) - \bar{\tau}(r_{o,2}, r_{i,1})]$$

The one-way transfer from the length of beam in volume 1 between $r_{i,1}$ and $r_{o,1}$ to volume 2 between $r_{i,2}$ and $r_{o,2}$ is consequently

$$d\dot{Q}_{e,1,2} = (\cos \theta_1 dA_1 d\omega) (I'_{e,1,2} - I_{e,1,2})$$

Making the approximations involved in equation (12) then yields

$$4\rho_1 k_1 V_1 F_{1-2} \doteq \frac{A_1 A_2}{16\pi R^2} [\bar{\tau}(r_{i,2}, r_{o,1}) + \bar{\tau}(r_{o,2}, r_{i,1}) - \bar{\tau}(r_{i,2}, r_{i,1}) - \bar{\tau}(r_{o,2}, r_{o,1})] \quad (16)$$

Reciprocity, equation (7), holds, of course. To obtain $4\rho_2 k_2 V_2 F_{2-1}$ from equation (16), not only are the subscripts 1 and 2 interchanged but the i (in) subscript must be replaced with the o (out) subscript and vice versa, and the order of the arguments in $\bar{\tau}(r_{i,2}, r_{o,1})$ is reversed. The resulting expression remains identical to the right side of equation (16).

Table 1 Comparison of approximate with exact results for a case of remote volumes (2,2,0)* in a gaseous medium with overlapped lines

OPTICAL DEPTH $\rho k B$	APPROXIMATION	EXACT	HOTTEL AND COHEN
0.2	0.00093	0.00094	0.00093
0.4	0.00216	0.00219	0.00215
0.6	0.00286	0.00289	0.00285
0.8	0.00302	0.00305	0.0030
1.0	0.00279	0.00283	0.00281
1.2	0.00238	0.00244	
1.4	0.00193	0.0020	

* (2,2,0) is the difference in the x, y, z coordinates of two equal cubes aligned with the coordinate axes.

The limits $r_{i,1}$, $r_{o,1}$, $r_{i,2}$, $r_{o,2}$ are found in the same manner as for equation (10)

$$\begin{aligned} r_{o,1} &= h l_1 & r_{i,1} &= h l_1 - l_1 \\ r_{i,2} &= R - h l_2 & r_{o,2} &= R - h l_2 + l_2 \end{aligned} \quad (17)$$

Adjacent Volumes. The approximations leading to equations (12) and (16) which are expected to be very good for remote volumes are not expected to be good for adjacent volumes, for we do not meet the criterion of $R \gg l_1$ or l_2 . As a result of this expectation, three cases of adjacent configurations are distinguished and treated in the Appendix. The three types of configurations are (1) face-contacting, (2) edge-contacting, and (3) corner-contacting. For cubes arranged parallel to the coordinate axes whose centroids are displaced (Δx , Δy , Δz) in a rectangular coordinate system, a face-contacting case is (1, 0, 0), an edge-contacting case (1, 1, 0), and a corner-contacting case (1, 1, 1).

It is proposed that most engineering situations can be treated with one of two temperature-profile idealizations, one with temperature jump and one giving linear source-intensity variation. Combining these two additional possibilities with the previous three adjacent-configuration possibilities gives six different adjacent-volume situations. Temperature jump at the boundary should be a useful idealization for a volume with a thin boundary layer at a wall or two volumes separated by a thin mixing layer. In other situations the temperature and composition vary slowly and continuously from one volume to the next. In this case a reasonable idealization is to assume linear variations.

A doubling of the number of possible cases occurs when one distinguishes the case of overlapped from that of nonoverlapped lines. Thus 12 situations can be discerned. For nonoverlapped lines only the face-contacting configuration was considered. It is believed a line-effect multiplying factor can be used to account for line effects in the other cases.

For face-contacting cubes of side B with temperature jump and overlapped lines a two-path approximation was employed

$$4\rho_1 k_1 V_1 F_{1-2} \doteq B^2 \left\{ \frac{1}{2} (1 - e^{-3/2\rho_1 k_1 l_1})(1 - e^{-1/2\rho_2 k_2 l_2}) + \frac{1}{2} (1 - e^{-1/2\rho_1 k_1 l_1})(1 - e^{-3/2\rho_2 k_2 l_2}) \right\} \quad (18)$$

For the other cases the following approximation was employed:

$$4\rho_1 k_1 V_1 F_{1-2} \doteq B^2 \frac{a}{(1 + b\rho_m k_m B)^n} (1 - e^{-c\rho_1 k_1 l_1})(1 - e^{-c\rho_2 k_2 l_2}) \quad (19)$$

The following values were assigned:

Edge-contacting cubes with temperature jump, overlapped lines

$$a = 0.44, \quad b = 1.0, \quad c = 1.0, \quad n = 1$$

Corner-contacting cubes with temperature jump, overlapped lines

$$a = 0.135, \quad b = 0.5, \quad c = 1.5, \quad n = 2$$

Table 2 Volume interchange factors for remote cubes, overlapped lines

OPTICAL DEPTH $\rho k B$	2,0,0		2,1,0	
	APPROXIMATION	HOTTEL & COHEN	APPROXIMATION	HOTTEL & COHEN
0.2	0.0022	0.00235	0.00168	0.00171
0.4	0.00607	0.0063	0.00442	0.00446
0.6	0.00947	0.0095	0.00658	0.00668
0.8	0.0117	0.0123	0.00776	0.0079
1.0	0.0128	0.0138	0.00807	0.0083
1.2	0.0129	0.0139	0.00775	0.00805
1.4	0.0123	0.0135	0.00706	0.00738
	2,1,1		2,2,1 or 3,0,0	
0.2	0.00134	0.00137	0.00080	0.00079
0.4	0.00338	0.00341	0.00181	0.00179
0.6	0.00482	0.00482	0.00231	0.0023
0.8	0.00545	0.00541	0.00234	0.00236
1.0	0.00543	0.00536	0.00209	
1.2	0.0050	0.00494	0.00172	
1.4	0.00437		0.00135	

Face-contacting cubes with linear source intensity, overlapped lines

$$a = 0.63, \quad b = 0.5, \quad c = 1.0, \quad n = 1$$

Edge-contacting cubes with linear source intensity, overlapped lines

$$a = 0.34, \quad b = 0.5, \quad c = 1.0, \quad n = 2$$

Corner-contacting cubes with linear source intensity, overlapped lines

$$a = 0.24, \quad b = 0.5, \quad c = 1.0, \quad n = 3$$

For the case of nonoverlapped lines a single-path calculation based upon the Curtis-Godson technique was proposed:

Face-contacting cubes with temperature jump, nonoverlapped lines

$$4\rho_1 k_1 V_1 F_{1-2} = B^2 \left\{ \frac{1}{2} [1 + \bar{\tau}(r_{o,2}, r_{i,1}) - \bar{\tau}(r_{o,1}, r_{i,1}) - \bar{\tau}(r_{o,2}, r_{i,2})] + \frac{1}{2} [1 + \bar{\tau}(r_{o,2}', r_{i,1}') - \bar{\tau}(r_{o,1}', r_{i,1}') - \bar{\tau}(r_{o,2}', r_{i,2}')] \right\} \quad (20)$$

where r is measured along the line between centroids from the point at which this line penetrates the shared face, and

$$\begin{aligned} r_{i,1} &= -\frac{3}{2}l_1 & r_{i,1}' &= -\frac{1}{2}l_1 \\ r_{o,1} &= r_{i,2} = r_{o,1}' = r_{i,2}' = 0 \\ r_{o,2} &= +\frac{1}{2}l_2 & r_{o,2}' &= +\frac{3}{2}l_2 \end{aligned}$$

Face-sharing cubes with linear source intensity, nonoverlapped lines

$$4\rho_1 k_1 V_1 F_{1-2} = cB^2 \{ (S_{1,i} - S_{1,o}) + (S_{2,i} - S_{2,o}) - (r_{o,1} - r_{i,1})[\bar{\tau}(r_{i,2}, r_{i,1}) - \bar{\tau}(r_{o,2}, r_{i,1})] - (r_{o,2} - r_{i,2})[\bar{\tau}(r_{o,2}, r_{o,1}) - \bar{\tau}(r_{o,2}, r_{i,1})] \} \quad (21)$$

where, in this case,

$$\begin{aligned} c &\doteq 0.7 \\ r_{i,1} &= -l_1 & r_{o,1} &= r_{i,2} = 0 & r_{o,2} &= +l_2 \\ S_{1,i} &= \int_{r_{i,1}}^{r_{o,1}} \bar{\tau}(r_{i,2}, r) dr & S_{1,o} &= \int_{r_{i,1}}^{r_{o,1}} \bar{\tau}(r_{o,2}, r) dr \\ S_{2,i} &= \int_{r_{i,2}}^{r_{o,2}} \bar{\tau}(r, r_{o,1}) dr & S_{2,o} &= \int_{r_{i,2}}^{r_{o,2}} \bar{\tau}(r, r_{i,1}) dr \end{aligned}$$

Table 3 Volume interchange factors for face-contacting cubes (1, 0, 0), overlapped lines

OPTICAL DEPTH $\rho k B$	LINEAR SOURCE INTENSITY PROFILE APPROXIMATION EQ. (19)		TEMPERATURE JUMP AT BOUNDARY APPROXIMATION EQ. (18)	
	APPROXIMATION	EXACT	APPROXIMATION	EXACT
1/16	0.00102	0.000923	0.00125	0.00139
1/8	0.00379	0.00347	0.00480	0.00528
1/4	0.0132	0.0122	0.0177	0.0192
1/2	0.0402	0.0383	0.0604	0.0641
1	0.0994	0.0969	0.179	0.183
2	0.171	0.171	0.421	0.41
4	0.182	0.189	0.723	0.68
8	0.125	0.142	0.930	0.87

Table 4 Volume interchange factors for edge- and corner-contacting cubes in a medium with overlapped lines

OPTICAL DEPTH $\rho k B$	EDGE-CONTACTING CUBES (1,1,0)			
	LINEAR SOURCE INTENSITY PROFILE APPROXIMATION EQ. (19)	EXACT	TEMPERATURE JUMP AT BOUNDARY APPROXIMATION EQ. (19)	EXACT
1/16	0.00053	0.00052	0.00069	0.00064
1/8	0.00193	0.00190	0.00250	0.00238
1/4	0.00634	0.00640	0.00830	0.00817
1/2	0.0175	0.0184	0.0236	0.0244
1	0.0358	0.0388	0.0521	0.0560
2	0.0461	0.0489	0.0795	0.0847
4	0.0327	0.0307	0.0762	0.0742
CORNER-CONTACTING CUBES (1,1,1)				
1/16	0.00038	0.00035	0.00047	0.00040
1/8	0.00133	0.00126	0.00165	0.00146
1/4	0.00414	0.00410	0.00522	0.00480
1/2	0.0103	0.0109	0.0134	0.0131
1	0.0175	0.0197	0.0239	0.0256
2	0.0169	0.0185	0.0252	0.0276
4	0.0080	0.0068	0.0145	0.0137

Results

Remote Volumes, Overlapped Lines. Table 1 shows results of approximate calculations based upon equation (12), more detailed calculations based upon equation (8), and previously reported values from Hottel and Cohen [3] for cubes of side B within a homogeneous gas. Agreement is excellent, within 4 percent in each case. Each approximate calculation required 0.015 sec of IBM 360/75 computer time using Fortran IV-G.

Table 2 shows further comparisons with the work of Hottel and Cohen [3]. Relative location of the cubes is designated by three numbers indicating, in sides of length B , the displacement measured along each axis of cubes arranged parallel to a rectangular coordinate system as shown in Fig. 1.

Adjacent Volumes, Overlapped Lines. Table 3 gives values for face-contacting cubes of side B . Two cases are distinguished, that of linear source-intensity profile and that of temperature jump across the boundaries. The results are distinctly different. For the former case, the interchange factor $4\rho_1 k_1 V_1 F_{1-2}$ rises at first like $(\rho k B)^2$ as $\rho k B$ is increased, reaches a maximum, and then decreases to zero inversely with increasing $\rho k B$. The agreement between the approximate relation, equation (19), and more accurate integration based upon an exact formulation is surprisingly good. For the latter case no maximum is reached at intermediate values of $\rho k B$, and the agreement between the two-path approximation, equation (18), and the exact formulation is quite adequate for engineering purposes.

Table 4 shows exact values and comparisons with approximate calculations based upon equation (12) for cubes which share one edge (1, 1, 0) or one corner (1, 1, 1). Again the agreement is not as good as for the case of remote volumes but is adequate for most engineering purposes.

Table 5 Line effects on volume interchange in a nonhomogeneous gas

TOTAL PRESSURE ATM	VOLUME INTERCHANGE FACTOR F_{1-2}^2
0.25	0.000145
0.50	0.000163
1.0	0.000188
2.0	0.000219
4.0	0.000250
8.0	0.000273
16.0	0.000287
64.0	0.000293
∞	0.000293

The total values of the volume interchange factor are those integrated over the 6.3μ H₂O band. The cubical volumes are one foot on a side and arranged in the (3,0,0) configuration. The partial pressure of H₂O is 0.18 atmospheres, and the temperature varies linearly, having a value of 1000°R at the centroid of volume 1 and 2000°R at the centroid of volume 2.

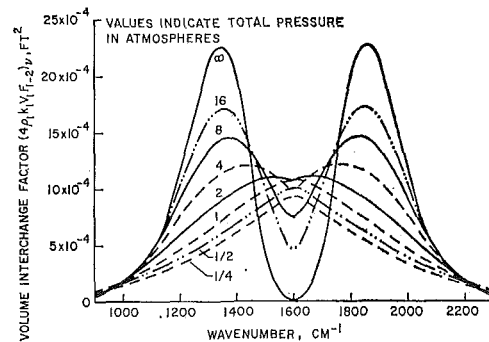


Fig. 2 Line effects on volume interchange between remote cubes (see Table 5 for a description of the conditions existing in the gas and for integrated values)

Line Effects. Approximate calculations were carried out using equation (16). Cubes of 1 ft separated by $\Delta x = 3$ ft, $\Delta y = 0$, and $\Delta z = 0$ were selected. The $6.3\text{-}\mu$ H₂O band was selected for the example. A partial pressure of H₂O equal to 0.18 atm was taken. This partial pressure results from the combustion of a 1-atm stoichiometric mixture of air and methane. To evaluate the effects of line overlapping, however, the total pressure was varied from 0.25 to 16 atm. In the band model used [8, 9] total pressure affects only the degree of line overlapping. New values of line-overlapping parameter $\beta = C_2^2 P / (4 C_1 C_3)$ were computed according to [8]. A linear temperature profile having a value of 1000 deg R at the centroid of cube 1 and 2000 deg R at the centroid of cube 2 was taken. Spectral integration was made using a large number, 36, of spectral wavenumbers. No attempt was made to reduce this number to the 3 or 4 values per band used by deSoto. A calculation time of 0.017 sec per wavenumber was found necessary.

Results are presented in Fig. 2. As total pressure is increased, the lines become overlapped so that transfer between lines in the intense central portions of the band is reduced. In the wings of the band the redistribution of emissivity from the line centers to the regions between lines increases the volume-to-volume transfer.

Table 5 shows integrated results corresponding to the cases plotted in Fig. 2. The interesting feature is that while the figure shows large spectral changes occurring with pressure even after the pressure is as high as 16 atm, the integrated values are relatively insensitive to pressure after a value of 4 atm is reached.

Results for face-contacting cubes (1, 0, 0) are shown in Fig. 3. Calculations were made using equation (21) for linear source-intensity variation in 1-ft cubes, one having a temperature of 1000 deg R and the other 2000 deg R as in the previous situation. Again the partial pressure of H₂O was 0.18 atm. In this case

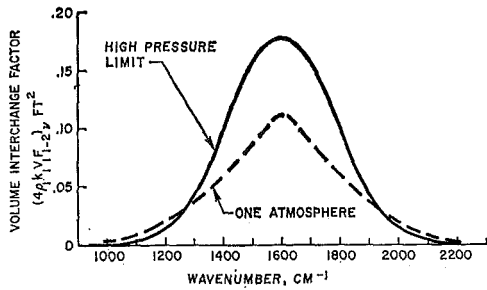


Fig. 3 Line effects on volume interchange between face-contacting cubes (properties are based upon the exponential-band model for the $6.3\text{-}\mu$ H_2O gas band and an assumed linear temperature profile having a value of 1000 deg R at the centroid of volume 1 and 2000 deg R at the centroid of volume 2; a partial pressure of 0.18 atm of H_2O and a total pressure of 1 atm exist within the two 1-ft cubes)

there is no intervening gas between the volumes to attenuate radiative transfer in the central regions of the band, and these regions are not sufficiently intense to reduce the transfer below the maximum indicated in Table 3 at $\rho k B \approx 4$. The dip in transfer in the center of the band seen in Fig. 2 is thus not seen in Fig. 3.

Discussion

Two theoretically sound approximations, equations (12) and (16), have been developed for rapid calculation of volume-to-volume interchange. Comparisons with more exact calculations and the previous work of Hottel and Cohen have shown agreement within 4 percent. By using equation (16) it is possible to account for line effects, which in the example of Table 5 caused a 36 percent reduction below the overlapped-line prediction. The restrictions in equations (12) and (16) are that the volumes must be roughly spherical or cubical in shape (or optically thin) and must be remote. "Remote" was shown by the comparisons to be only as far away as three mean beam lengths, centroid to centroid. Thus the case of cubes as close as (2, 0, 0) can be accommodated.

Further approximations were developed for adjacent volumes. Agreement on a spectral basis with more exact calculations was within approximately 10 percent. When integration is carried out over a complete band some cancellation of errors occurs; when an exponential band model was employed to obtain $\rho k B$ for overlapped lines as a function of wavenumber, and integrations were carried out using the results in Tables 3 and 4, the integrated results differed at most 7 percent and more often less than 5 percent.

It would be expected that these latter approximations could be applied to gas-volume-to-wall transfer as well as volume-to-volume transfer, since a black wall is in reality a thin volume with a large absorption coefficient. For remote-volume-to-wall transfer, equations (12) and (16) could be employed by regarding the wall to be volume 2 with a very large absorption coefficient, but, to account for the wall volume not being spherical in shape, replacing $A_2/4$ by $A_{s,2} \cos \theta$, the area of the side of the wall element facing the gas multiplied by the cosine of the angle between the surface normal and the ray from the centroid of the area to the centroid of the volume. In this case the centroid-to-centroid distance R must be much greater than the size of the area or volume so that the solid angle subtended by the wall area as viewed from the volume will be nearly $A_{s,2} \cos \theta / R^2$.

The approximations then make it possible to calculate volume-to-volume or volume-to-wall transfer approximately accounting for nonhomogeneous radiation properties in the gas.

In the examples presented, the exponential-band model was employed. However, any wide-band model can be used which embodies a narrow-band-model transmissivity which is a function of the mean-line-intensity-to-spacing ratio and the mean-line-width-to-spacing ratio. The suitability of the exponential-band model for approximate engineering calculations has been estab-

lished by comparison with experimental data for the case of transfer from the gas, isothermal or not, to a nonselective wall [9]. But there exists for volume-to-volume transfer only indirect evidence such as the experiments of Schimmel, Novotny, and Olsofka [10], who show good agreement with the exponential model and relatively poor agreement with the box and gray-gas models. That the box model and exponential model yield substantially different results is corroborated by Pearce and Emery [11].

In some cases, the radiating bands of the combustion products, fuel, and oxidizer do not overlap significantly. In these cases expressions for interchange factors may be formulated on a wide-band basis instead of the narrow-band basis employed here. When single-line-of-sight calculations are suitable, recent work by Chan and Tien [12], Cess and Wang [13], and Edwards and Morizumi [14] is applicable. However, preliminary work by the present authors indicates that wide-band scaling laws used to obtain approximate values of radiant flux may not give good results for volume-to-volume interchange. These questions are being explored, but at present it is felt that the narrow-band approach taken here will prove to be more useful for hydrocarbon-air combustion where band overlapping is a significant factor.

One method recommended [15] for making engineering calculations is to represent real-gas behavior with a number of gray and transparent bands. When the number of bands chosen to represent real-gas behavior is large, the method quite accurately describes total emissivity versus path length, but the fitting of the multi-band parameters to the emissivity is difficult. However, a single gray band plus transparent band can yield good results for the total emissivity over a limited range of path lengths, as is shown in Fig. 6-26 of [15].

While the representation of a real gas by a one-gray-band-plus-one-transparent-band model is convenient to use and yields good results for total emissivity and total transfer between an isothermal gas and a wall, it is not clear that it can do so for gas-element-to-gas-element transfer. As has been shown, the transfer between remote volumes tends to occur in the wings of strong bands, when the lines are well overlapped, or between strong lines, when the lines are nonoverlapped.

For a comparison of the one-gray-band-plus-one-transparent-band model with the exponential-band model, the portion of the total emissivity contributed by the $6.3\text{-}\mu$ band was computed for $L = 1\text{ ft}$ and $L = 3\text{ ft}$ with the conditions of total and partial pressure indicated in Table 5. A mean temperature of 1500 deg R was used. The result was

$$\epsilon_p = 0.159(1 - e^{-0.736L}) \quad L \text{ in ft}$$

The volume-to-volume transfer was then found from Table 2 for the (3, 0, 0) configuration to be

$$4\rho_1 k_1 V_1 F_{1-2} = 0.159(0.00233) = 0.00037 \text{ ft}^2$$

(one-gray-band-plus-one-clear-band)

For comparison, spectral integration yielded the results shown in Table 5

$$4\rho_1 k_1 V_1 F_{1-2} = 0.000188 \text{ ft}^2$$

(exponential-band model)

The result from the gray-band-plus-clear-band representation is nearly a factor of two greater than the results obtained according to the methods presented in this paper.

The feasibility of incorporating radiative transfer into a program such as that of Gosman et al. [1] using approximations developed here is demonstrated by the short computation times achieved. It will not be efficient, however, to treat each node point as discrete from a radiation point of view. To keep the number of requisite calculations to a low figure will require considering small-nodal-volume elements only at close range and lumping quite remote nodal volumes into large-volume elements. We expect to report examples showing the practical utility of such calculations in the near future.

Summary and Conclusions

A method has been presented for computing rapidly volume-to-volume interchange factors between volumes within a *nonhomogeneous* nongray gas with discrete or overlapped vibration-rotation line spectra. Computational speeds of 0.015 sec per spectral calculation were achieved. Comparisons with much slower but more accurate calculations showed agreement within a few percent when the spectral values were integrated over an entire band. The methods show promise for use in accounting for radiant transfer in combustion chambers and the effluents from such chambers.

Acknowledgment

Computations were carried out at the UCLA Campus Computing Network. Mr. Balakrishnan gratefully acknowledges support received from State of California Air Pollution Grant No. 4-402567.

References

- Gosman, A. D., Pun, W. M., Runchal, A. K., Spalding, D. B., and Wolfshtein, W., *Heat and Mass Transfer in Recirculating Flows*, Academic Press, London, 1969.
- deSoto, S., "Coupled Radiation, Conduction and Convection in Entrance Region Flow," *International Journal of Heat and Mass Transfer*, Vol. 11, 1968, pp. 39-53.
- Hottel, H. C., and Cohen, E. S., "Radiant Heat Exchange in a Gas Filled Enclosure: Allowance for Nonuniformity of Gas Temperature," *AIChE Journal*, Vol. 4, 1958, pp. 3-14.
- Einstein, T. H., "Radiant Heat Transfer to Absorbing Gases Enclosed in a Circular Pipe with Conduction Gas Flow, and Internal Heat Generation," Technical Report R-156, National Aeronautics and Space Administration, 1963.
- Dunkle, R. V., "Geometric Mean Beam Lengths for Radiant Heat-Transfer Calculations," *JOURNAL OF HEAT TRANSFER, TRANS. ASME, Series C*, Vol. 86, No. 1, Feb. 1964, pp. 75-80.
- Tien, C. L., and Wang, L. S., "Band Absorption Laws, Gas Body Geometries, and the Mean Beam Length," *Proceedings of the 1965 Heat Transfer and Fluid Mechanics Institute*, Charwat, A. F., ed., Stanford University Press, Stanford, Calif., 1965, pp. 345-357.
- Edwards, D. K., and Weiner, M. M., "Comment on Radiative Transfer in Non-isothermal Gases," *Combustion and Flame*, Vol. 10, 1966, pp. 202-203.
- Weiner, M. M., and Edwards, D. K., "Theoretical Expression of Water Vapor Spectral Emissivity with Allowance for Line Structure," *International Journal of Heat and Mass Transfer*, Vol. 11, 1968, pp. 55-65.
- Edwards, D. K., Glassen, L. K., Hauser, W. C., and Tuchscher, J. S., "Radiation Heat Transfer in Nonisothermal Nongray Gases," *JOURNAL OF HEAT TRANSFER, TRANS. ASME, Series C*, Vol. 89, No. 3, Aug. 1967, pp. 219-229.
- Schimmel, W. P., Novotny, J. L., and Olsofka, F. A., "Interferometric Study of Radiation-Conduction Interaction," *Heat Transfer, 1970*, preprints of papers presented at the Fourth International Heat Transfer Conference, Elsevier Publishing Co., Amsterdam, 1970, Vol. III, paper R2.1.
- Pearce, B. E., and Emery, A. F., "Heat Transfer by Thermal Radiation and Laminar Forced Convection to an Absorbing Fluid in the Entry Region of a Pipe," *JOURNAL OF HEAT TRANSFER, TRANS. ASME, Series C*, Vol. 92, No. 2, May 1970, pp. 221-230.
- Chan, S. H., and Tien, C. L., "Total Band Absorptance of Nonisothermal Infrared Radiating Gases," *Journal of Quantitative Spectroscopy and Radiative Transfer*, Vol. 9, 1969, pp. 1261-1271.
- Cess, R. D., and Wang, L. S., "A Band Absorptance Formulation for Nonisothermal Gaseous Radiation," *International Journal of Heat and Mass Transfer*, Vol. 13, 1970, pp. 547-556.
- Edwards, D. K., and Morizumi, S. J., "Scaling of Vibration-Rotation Band Parameters for Nonhomogeneous Gas Radiation," *Journal of Quantitative Spectroscopy and Radiative Transfer*, Vol. 10, 1970, pp. 175-188.
- Hottel, H. C., and Sarofim, A. F., *Radiative Transfer*, Section 6.11, McGraw-Hill, New York, N. Y., 1967.
- Abu-Romia, M. M., and Tien, C. L., "Appropriate Mean Absorption Coefficients for Infrared Radiation of Gases," *JOURNAL OF HEAT TRANSFER, TRANS. ASME, Series C*, Vol. 89, No. 4, Nov. 1967, pp. 321-327.

APPENDIX

Adjacent Volumes with Temperature Jump, Overlapped Lines. In the case of contacting volumes a physically reasonable approach to finding the transfer is to simply multiply the contact area by a mean emissivity-absorptivity product. It is clear that the mean requires quadrature over the contact area and over solid angle or direction. The variation of emissivity and absorptivity with orientation of a ray is quite different in the central and edge areas. In the center of the contact area a ray normal to the area has a high emissivity and a high absorptivity while one at grazing incidence has both somewhat lower. But near an edge a ray at grazing incidence has a low emissivity and a high absorptivity or vice versa. The fraction of the contacting area for which this situation is the case is large. It is thus suggested that a crude model is one based on two rays in this edge region, one having a longer length, say $^{3/2}l_1$, in volume 1 and a shorter one, say $^{1/2}l_2$, in the other volume and vice versa.

$$4\rho_1k_1V_1F_{1-2} \doteq A_{1,2} \frac{1}{2} \left\{ (1 - e^{-^{3/2}\rho_1k_1l_1})(1 - e^{-^{1/2}\rho_2k_2l_2}) + (1 - e^{-^{1/2}\rho_1k_1l_1})(1 - e^{-^{3/2}\rho_2k_2l_2}) \right\}$$

This crude model is the basis for equation (18).

For corner-contacting volumes the "contact area" must be broadly interpreted. In the optically thick limit only rays passing through an area on the order of $[1/(\rho_c k_c)]^2$ can transfer power. On the other hand, in the optically thin limit, equation (8) shows the transfer must be proportional to $(\rho_1k_1B)(\rho_2k_2B)$. For this reason equation (19) was contrived; it behaves correctly in both limits when $n = 2$. A similar argument can be employed for the edge-contacting case with $n = 1$.

Adjacent Volumes with Linear Source Intensity, Overlapped Lines.

For face-contacting volumes in the optically thick limit the transfer is simply the contact area multiplied by the radiation conductivity and the temperature gradient. In the optically thin limit equation (8) modified to take into account the gradient in source intensity again indicates that the transfer should behave as $(\rho_1k_1B)(\rho_2k_2B)$. Again equation (19) may be employed with $n = 1$ for face-contacting volumes, $n = 2$ for edge-contacting ones, and $n = 3$ for corner-contacting ones. The correct asymptotic behaviors are then assured.

Adjacent Volumes with Nonoverlapped Lines. In the case of temperature jump across the face of contacting volumes, the Curtis-Godson approximation may be employed in the same two-path model used for face-contacting volumes with overlapped lines. We found equation (16) replaced equation (12). Equation (18) consists of two terms identical in form to those in equation (12). We replace these terms with the appropriate ones indicated by equation (16). The result is equation (20).

In the case of face-contacting volumes with linear profile in the source intensity we wish to write

$$\dot{Q}_{\text{net},1,2} = -4\rho_1k_1V_1F_{1-2}\pi R \frac{dI_p}{dr} \quad (22)$$

We approximate the transfer by multiplying the net exchange of energy along a single line by an appropriate area-solid-angle product, $c\pi A_{1,2}$. For this reason we write

$$\dot{Q}_{\text{net}} \doteq c\pi A_{1,2} \left\{ [I_{e,1,2}(r_{i,2}) - I_{e,1,2}(r_{o,2})] - [I_{e,2,1}(r_{o,1}) - I_{e,2,1}(r_{i,1})] \right\} \quad (23)$$

where, from the Curtis-Godson approximation

$$I_{e,1,2}(r_{i,2}) = \int_{r_{i,1}}^{r_{o,1}} \frac{d}{dr} \tau(r_{i,2}, r) \left[I_f + \left| \frac{dI_p}{dr} \right| (r_{o,1} - r) \right] dr \quad (24a)$$

$$I_{e,1,2}(r_{o,2}) = \int_{r_{i,1}}^{r_{o,1}} \frac{d}{dr} \tau(r_{o,2}, r) \left[I_f + \left| \frac{dI_p}{dr} \right| (r_{o,1} - r) \right] dr \quad (24b)$$

$$I_{e,2,1}(r_{o,1}) = \int_{r_{i,2}}^{r_{o,2}} - \frac{d}{dr} \tau(r, r_{o,1}) \left[I_f - \left| \frac{dI_p}{dr} \right| (r - r_{i,2}) \right] dr \quad (24c)$$

$$I_{e,2,1}(r_{i,1}) = \int_{r_{i,2}}^{r_{o,2}} - \frac{d}{dr} \tau(r, r_{i,1}) \left[I_f - \left| \frac{dI_p}{dr} \right| (r - r_{i,2}) \right] dr \quad (24d)$$

The I_f terms cancel when equations (24a-d) are substituted into equation (23). Integration by parts results in equation (21) shown in the text, and the r 's are measured as explained in the text below equation (21).

As an alternative to the single-line-of-sight concept used to derive equation (23), one can merely modify equation (19) to account for line structure. In the optically thick limit for non-overlapped lines, Abu-Romia and Tien [16] have shown that the Rosseland conductivity goes like the reciprocal of $\rho \bar{k} \tanh(2\beta)$ instead of $\rho \bar{k}$. In the optically thin limit for two face-contacting volumes, the exchange factor must vary as $(\rho_1 k_1 l_1)(\rho_2 k_2 l_2)$. Equation (19) with $n = 1$ may be rewritten for nonoverlapped lines in the form

$$4\rho_1 k_1 V_1 F_{1-2} = B^2 \frac{a}{[1 + b\rho \bar{k} B \tanh(2\beta)]} \times [1 - \tau(r_{o,1}, r_{i,1})][1 - \tau(r_{i,2}, r_{o,2})] \quad (25)$$

This form satisfies both asymptotic limits.

G. YADIGAROGLU

Assistant Professor,
Department of Nuclear Engineering,
University of California,
Berkeley, Calif.

A. E. BERGLES

Professor,
Department of Mechanical Engineering,
Georgia Institute of Technology,
Atlanta, Ga.
Mem. ASME

Fundamental and Higher-Mode Density-Wave Oscillations in Two-Phase Flow

This paper treats the oscillatory two-phase flow instabilities commonly referred to as density-wave oscillations. A dynamic analysis of the single-phase region of a boiling channel, accounting for wall heat capacity and the effect of pressure variations on the movements of the boiling boundary, is summarized. Experiments conducted with a Freon-113 channel at atmospheric pressure revealed the existence of "higher-mode" oscillations. These appeared at high subcoolings and low power levels and were characterized by unexpectedly short periods that were fractions of the transit time. The presence of the higher modes and other observations are explained in terms of the dynamic behavior of the boiling boundary.

Introduction

THE PARTICULAR subject of this paper, the so-called density-wave oscillations, will first be situated within the larger framework of thermohydrodynamic stability of two-phase flows.

Two-Phase Flow Instabilities. Macroscopic channel instabilities which, in contrast to local or microscopic instabilities, involve the entire two-phase flow system are characteristically associated with time constants of the order of a few seconds and can essentially be categorized as either instabilities of flow distribution among several parallel channels or flow instabilities in a single channel. The major distinction between single and parallel channels stems from the formulation of the boundary conditions. Whenever the conditions at the channel boundaries are sufficiently specified at all times, the problem reduces to a single-channel instability.

There has been considerable confusion in the past, as many experiments were designed without making an effort to clearly define the limits of the unstable part of the system. In particular, system-induced instabilities have often interfered with basic oscillation mechanisms of the heated channel. Furthermore, the term "parallel channels" has been used frequently to recall a constant-pressure-drop boundary condition, while it might have been used more properly to denote flow distribution phenomena.

The thermohydrodynamic instabilities of a single boiling channel should be identified according to the physical mechanisms involved. The literature is generally quite difficult to follow since the blanket term "two-phase flow instabilities" has been used for dissimilar mechanisms. Recent publications [1-3]¹

¹ Numbers in brackets designate References at end of paper.

Based on a paper contributed by the Heat Transfer Division and presented at the ASME-AIChE Heat Transfer Conference, Tulsa, Okla., August 15-18, 1971, as Paper No. 71-HT-13. Manuscript received by the Heat Transfer Division April 19, 1971; revised manuscript received January 26, 1972.

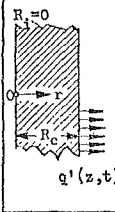
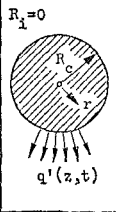
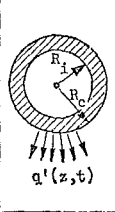
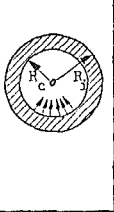
have finally brought some order, clarity, and classification. Major classifications are static and dynamic instabilities. Density-wave oscillations are perhaps the most frequently observed and analyzed dynamic instabilities.

Density-Wave Oscillations—The Physical Mechanism. The density-wave oscillations are due to the multiple regenerative feedbacks between the flow rate, the vapor generation rate, and the pressure drop ("flow-void feedback instabilities" [1]). Inlet flow fluctuations create enthalpy perturbations in the single-phase region. When these reach the boiling region, they are transformed into void-fraction perturbations that travel with the flow along the channel, creating a dynamic pressure-drop oscillation in the two-phase region. Since the total pressure drop is imposed upon the channel externally, this two-phase pressure perturbation produces a perturbation of the opposite sign in the single-phase region, which in turn creates further inlet flow variations. With correct timing, the perturbations can acquire appropriate phases and become self-sustained. Therefore, transportation delays in the channel are of paramount importance for the stability of the system ("time-delay oscillations"), although inertia effects are also responsible for the generation of phase shifts.

A number of auxiliary phenomena, such as transient heat storage in the channel walls, variation of the saturation enthalpy with pressure, compressibility of the gas phase, thermal non-equilibrium, variable heat transfer, and changes in the relative velocity between the phases, contribute to the fundamental feedback mechanism described above by altering the phase of the various perturbations.

The density-wave oscillations considered here will be further specialized by the boundary condition that the pressure drop across the boiling channel be maintained constant. This boundary condition is applicable to the most unstable channel of a large array of parallel channels. A natural-circulation loop can be described in this fashion if the cold leg is included as part of the channel [1].

Table 1 Heater geometries and corresponding functions $M(x)$**

Flat Plate*	Solid Cylinder	Externally Cooled Pipe	Internally Cooled Pipe
			
$M(x)$			
$\cosh(x)$	$I_0(x)$	$I_0(x) + \frac{I_1(R_i \sqrt{\frac{\beta}{\alpha}})}{K_1(R_i \sqrt{\frac{\beta}{\alpha}})} K_0(x)$	

** I_0 , K_0 and I_1 , K_1 are the modified Bessel functions of zero and first order, respectively.

* In the case of a flat plate r is the cartesian coordinate.

Analytical Approach. The fundamental mass-, momentum-, and energy-conservation equations need not be repeated here. These equations must be used together with appropriate boundary conditions and a stability criterion to predict the performance of the boiling channel.

Although the notion of the (bulk) boiling boundary (BB), i.e., the point of the channel where the mixed-mean enthalpy reaches saturation, is rather artificial, it will be used extensively throughout this work. Subcooled boiling upstream of the BB has a relatively minor effect on the pressure drop, as the resulting changes in the gravitational and frictional components of the pressure drop tend to cancel.² Ignoring the presence of subcooled boiling, it is advisable to treat the single-phase and the two-phase regions separately in order to incorporate in each formulation all the essential features; the boiling boundary provides a mathematically convenient separation. Moreover, as shown later, and elsewhere [4, 6], a number of experimental observations can be explained by considering the dynamics of the boiling boundary alone.

The stability of the channel at some given state can be investigated analytically by oscillating sinusoidally the inlet flow and calculating the total pressure-drop perturbation, which is the sum of the perturbations in the single-phase region, $\delta\Delta p_1$, and in the two-phase region, $\delta\Delta p_2$. The channel will be at the threshold of the instability if there is a frequency ω for which

$$\delta\Delta p(\omega) = \delta\Delta p_1(\omega) + \delta\Delta p_2(\omega) \rightarrow 0 \quad (1)$$

² Subcooled boiling is further discussed in the section on the flow-to-enthalpy transfer function.

satisfying the boundary condition $\Delta p = \text{constant}$.

The approach is equivalent to an examination of the inlet-flow-to-pressure-drop transfer function, frequently called hydraulic impedance [1, 5]. Other investigators have used power-to-pressure-drop, power-to-flow, or power-to-void transfer functions. The flow-to-pressure-drop transfer function, however, seems to provide the most representative and valuable analytic description of a boiling channel, although experimentally it might be easier to oscillate the heat input rather than the flow. Indeed, the variations of the heat input have a secondary importance for density-wave oscillations, and are completely eliminated in the case of a steady heat source with negligible heat capacity. It has also been shown [5, 6] that the flow-to-pressure-drop transfer function can be computed with relative facility and accuracy, and used for the stability analysis.

The complete stability analysis of a boiling channel is beyond the scope of this paper. Only the results of a recent formulation of the dynamics of the single-phase region [6] will be summarized here in order to explain some new experimental findings, namely the occurrence of "higher-mode" oscillations. Additional effects that can be explained in terms of the dynamics of the BB alone, such as the effect of nonuniform heat-flux distributions and the variation of the period of the oscillations, have been discussed elsewhere [4, 6].

Dynamics of the Single-Phase Region

The single-phase region is defined as the portion of the channel extending from the upstream constant-pressure point (inlet of the channel) to the *instantaneous* position of the BB. The length of this region will vary in time as the flow oscillates.

The dynamics of the heat source will be examined first. Subsequently the energy equation of the coolant will be solved to produce the enthalpy perturbations along the channel and the corresponding flow-to-enthalpy transfer function. Finally, the enthalpy perturbation at the BB will be considered, together with the pressure perturbations, to yield the movements of the BB and the flow-to-position-of-the-BB transfer function.

Dynamics of the Heat Source. A number of investigators, e.g., [7, 8], have considered heat-source dynamics. The incentive was to predict the time-dependent temperature distribution in the heater with variable heat-generation rate. In the present problem, it is the flow that is externally controlled. A derivation of the temperature distribution in the wall, similar to the one given by Smets [7], but simpler, can be found in [6]. The solutions for the various plane and cylindrical heater geometries of Table 1 are presented here.

The following assumptions were made in the derivation:

- (a) The heat generation rate is steady.
- (b) Average, constant values of the thermophysical properties are used.

Nomenclature

A = flow area
 a = coefficient defined by equation (2)
 b = coefficient defined by equation (8)
 c = specific heat of wall
 c_f = specific heat of liquid
 h = enthalpy
 h_c = forced-convection heat-transfer coefficient
 j = imaginary unit
 k = thermal conductivity of wall
 P = heated perimeter of channel
 p = pressure
 q = total heat input rate
 q' = heat input rate per unit length of heated channel

r = radial coordinate
 s = Laplace variable or complex frequency (to be evaluated as $j\omega$)
 T = temperature
 t = time
 V = velocity
 w = mass flow rate
 x = quality
 z = axial coordinate, measured from inlet of heated section
 z_{in}^0 = equivalent inertia length
 α = thermal diffusivity of wall
 λ = wavelength
 ρ = density of wall
 ρ_f = density of liquid
 τ = period of oscillation

ω = angular frequency, $2\pi/\tau$

Subscripts

b = bulk (mixed-mean)
 bb = boiling boundary
 f = liquid phase
 fg = transition from liquid to vapor
 g = gas phase
 1 = single-phase region
 2 = two-phase region

Additional symbols are defined in text. Steady-state and transient parts of variables are distinguished by subscript 0 or superscript 0 and prefix δ , e.g., $X(t) = X^0 + \delta X(t)$.

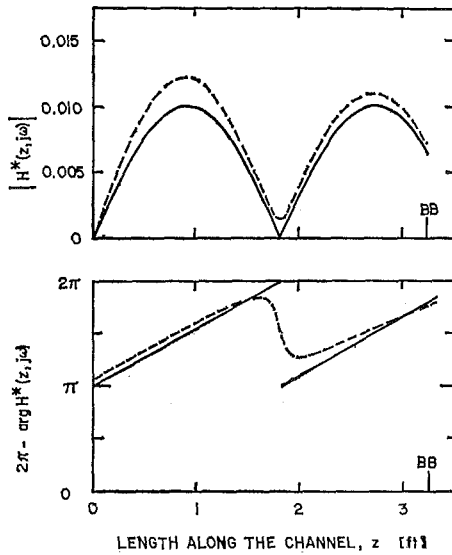


Fig. 1 Flow-to-enthalpy transfer function along the channel. Uniform heat flux distribution, $\lambda = 1.83$ ft, $\tau = 4.46$ sec, Freon-113 at 81 deg F. The solid line is the high-frequency approximation (Table 2) of the solution, equation (7), shown in dotted line. (Circular channel simulated by a flat plate.)

(c) The surface of the heater at $r = R_i$ (see Table 1) is insulated or conducting a steady heat flux (external heating or heat loss).

(d) Heat transfer to the coolant at $r = R_c$ is governed by a heat-transfer coefficient which depends on the instantaneous value of the average flow. Lacking a better description of the transient convective boundary condition and ignoring thermal entrance effects, it was simply assumed that for small and slow variations, quasi-steady-state conditions hold. If the steady-state heat-transfer coefficient h_c^0 varies like the a th power of the flow (for turbulent flow generally $a = 0.8$),

$$\frac{\delta h_c(t)}{h_c^0} = a \frac{\delta w(t)}{w_0} \quad (2)$$

(e) The heat input profile $q_0'(z)$ varies smoothly along the channel, and axial heat conduction can be neglected.

As no source term appears in the time-dependent part of the conduction equation, the transient solution will be independent of the radial heat-source distribution. Furthermore, the boundary condition at $r = R_i$ allows inclusion in this treatment of the case of a wall without internal heat generation. Physically this means that the transient heat flux to the coolant springs entirely from the heat stored in the heater.

The Laplace transform³ of the transient part of the temperature distribution in the wall is

$$\delta T(z, r, s) = \frac{C \delta T_b(z, s) - \frac{R_c}{P} E(z) \delta w(s)}{\pm \sqrt{\tau_k s} M'(\sqrt{\tau_k s}) + CM(\sqrt{\tau_k s})} M\left(r \sqrt{\frac{s}{\alpha}}\right) \quad (3)$$

(the minus sign in the denominator applies to the case of the internally cooled pipe only), with

$$C \equiv \frac{h_c^0}{k/R_c} \quad (4)$$

$$E(z) \equiv \frac{a q_0'(z)}{k w_0}$$

where $\tau_k = R_c^2/\alpha$ is the conduction time constant. The function M is given in Table 1 for each particular geometry considered.

³ The same symbols are used for the transformed functions with the argument t replaced by the complex frequency s .

M' is the derivative of M . For $r = R_c$, equation (3) yields the temperature of the cooled wall.

Flow-to-Enthalpy Transfer Function. The following necessary and customary simplifications are made:

(a) The radial temperature and velocity distributions are considered not to be affected by the oscillations of the flow (quasi-steady profiles).

(b) Subcooled boiling is ignored.

(c) The flow is assumed incompressible; average values of the fluid properties are used.

(d) The kinetic- and potential-energy terms in the energy equation are neglected.

The first two assumptions require some discussion. The concept of perfect or instantaneous mixing implied by (a) is questionable. Indeed there is a delay involved in the diffusion of heat from the wall toward the center of the channel [9], which results in a temporal distortion of the temperature profile. Furthermore, the propagation of the enthalpy perturbations might be significantly altered by the changes of the radial velocity profile in the coolant [10].

The axial void distribution in the subcooled region is essentially determined by the position of the point of net vapor generation. The analyses of Levy [11], Staub [12], and other authors indicate that fluctuations of the velocity and the temperature profiles will alter the position of this point. Therefore, two-dimensional treatments of transient or oscillating flow will be of little use unless the details of subcooled vapor generation are also considered. The simple notion of the boiling boundary should then be replaced by simultaneous consideration of the effects of the time-varying velocity and temperature profiles at the point of net vapor generation.

Unfortunately, at the present time there is no analysis that will permit incorporation of the radial effects in the dynamics of the single-phase region; it is then consistent to ignore both the radial effects and subcooled boiling. The model presented here might be inaccurate under some conditions, but nevertheless it correctly predicts the experimental trends and offers a foundation on which future corrections can be added.

The energy equation of the coolant was linearized and Laplace-transformed with the initial and boundary conditions $\delta T_b(z, 0) = 0$ and $\delta T_b(0, t) = 0$. The resulting linear differential equation was integrated along the channel to yield the flow-to-enthalpy transfer function

$$H(z, s) \equiv \frac{\delta h(z, s)}{\delta w(s)} = -L(s) e^{-K(s)z} \int_0^z \frac{q_0'(z')}{\bar{q}_0'} e^{K(s)z'} dz' \quad (5)$$

where

$$K(s) \equiv \frac{1}{V_0} \left[s + \frac{1}{\tau_c} \frac{F(s)}{F(s) + C} \right] \quad (6)$$

$$L(s) \equiv \frac{\bar{q}_0'}{w_0^2} \left[(1 - a) + a \frac{C}{F(s) + C} \right]$$

$$F(s) = \pm \sqrt{\tau_k s} \frac{M'(\sqrt{\tau_k s})}{M(\sqrt{\tau_k s})}$$

the minus sign applying again to the internally cooled pipe, and

$$\tau_c \equiv \frac{\rho_f c_f A}{Ph_c^0}$$

\bar{q}_0' is some reference linear heat-input rate and V_0 is the reference coolant velocity, $w_0/A\rho_f$. In a nondimensional form,

$$H^*(z, s) \equiv \frac{\delta h(z, s)/h_{fs}}{\delta w(s)/w_0} = \frac{w_0}{h_{fs}} H(z, s)$$

Once the linear heat-rate distribution $q_0'(z)$ is specified, the

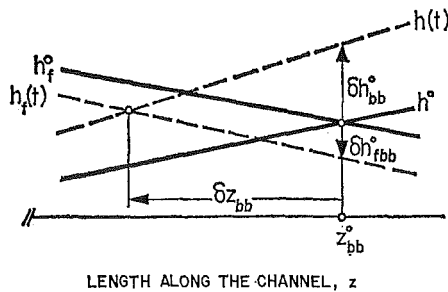


Fig. 2 Effect of the coolant- and saturation-enthalpy variations on the movements of the boiling boundary

integral in equation (5) can be evaluated to yield explicitly $H(z, s)$. For example, in the case of a uniform heat-flux distribution

$$H(z, s) = -\frac{L(s)}{K(s)} [1 - e^{-K(s)z}] \quad (7)$$

The solutions for other cases of interest can be found in [6]. The availability of fast computers, programmable to execute complex algebra, and special-function subroutine packages eliminates the incentive for approximation of these expressions by simpler formulas. The variation of the transfer function at a given frequency along the channel is shown in Fig. 1 for a set of conditions representative of the experiments reported in [6].

Characteristic Constants—Time-Dependence and Space-Dependence. The time-dependence of the enthalpy perturbations can be characterized by three constants, namely:

the wall-conduction time constant,

$$\tau_k = \frac{R_c \rho c}{k/R_c} = \frac{R_c^2}{\alpha}$$

the film-conductance time constant,

$$\tau_h = \frac{R_c \rho c}{h_c^0} = \frac{R_c k}{\alpha h_c^0}$$

and the coolant-heat-capacity time constant,

$$\tau_c = \frac{\rho_f c_f A}{h_c^0 P}$$

Excluding geometry factors, these time constants are formed as the ratios of wall heat capacity $R_c \rho c$, heater conductance k/R_c , film conductance h_c^0 , and coolant heat capacity $\rho_f c_f A/P$. Notice that C , equation (4), is equal to τ_k/τ_h .

The limiting forms of $H^*(z, j\omega)$ at high and low frequencies and for the intermediate case of negligible temperature gradient in the wall are given in Table 2. Heat storage in the wall plays an important role when the period is shorter than either $2\pi\tau_k$ or $2\pi\tau_c$.

Stenning and Veziroglu [2], in a similar derivation, did not consider the wall dynamics but did account for flow-dependent heat flux by writing $\delta q'/q_0' = a\delta w/w_0$ in the energy equation. This results in the high-frequency approximation of Table 2. This approximation was a rather poor one in the range of interest in the present work (2- to 10-sec periods). The low-frequency approximation amounts to completely neglecting the heat storage in the walls and was equally unacceptable.

The "wavelength," $\lambda = V_0\tau$, appearing in the first term, s/V_0 , of the exponent $K(s)$, equation (6), determines the space-dependence of the solutions. The periodic character of the solutions in space is justified as follows.

The axial position z of a fluid particle that spent a time Δt in the heater will depend on Δt and on the time at which the particle entered the heated section (Lagrangian description). For a

Table 2 Limiting cases of the flow-to-enthalpy transfer functions; uniform heat-flux distribution

	$F(j\omega) \rightarrow$	$K(j\omega) \rightarrow$	$\frac{V_0^2}{g_0'} \frac{1}{\tau_c} \rightarrow$	$\left[\frac{10^6 h_c^0}{g_0'} \right] \frac{1}{\tau_c} \rightarrow$
High-Frequency Approximation $\tau \ll 2\pi\tau_k$ and $\tau \ll 2\pi\tau_c$	$\sqrt{\frac{\tau_k \omega^2}{2}} (1+j) \rightarrow \infty$	$\frac{j\omega}{V_0} \left[\frac{1}{1+j} + \frac{1}{j\omega\tau_c} \right] + \frac{j\omega}{V_0}$	$(1-a)$	$\frac{-j\omega \tau_c}{(1-a)} \rightarrow 0$
Negligible Temp. Gradient in Heater $\tau \gg 2\pi\tau_k$ or $k \rightarrow \infty$ with $R_c \rho c \neq 0$	0	$\frac{j\omega}{V_0} \left[\frac{1}{1+j} + \frac{1/\tau_c}{j\omega + 1/\tau_h} \right]$	$(1-a) + \frac{a/\tau_h}{j\omega + 1/\tau_h}$	$\left[\frac{j\omega(1-a) + \frac{1}{\tau_h}}{\left(\frac{1}{1+j} + \frac{1}{\tau_h} \right) + j\omega} \right] \frac{-K(j\omega)z}{j\omega} \rightarrow 0$
Low-Frequency Approximation $\tau \gg 2\pi\tau_k$ and $\tau \gg 2\pi\tau_h$ or $(R_c \rho c) \rightarrow 0$	0	$\frac{j\omega}{V_0}$	1	$\frac{-j\omega \tau_c}{j\omega} \rightarrow 0$

uniform and steady heat input to the fluid, the enthalpy gained by a fluid particle is directly proportional to its residence time Δt . Assuming a sinusoidal variation of the flow, if Δt is chosen equal to the period of the oscillation τ , all particles will reach the same point of the channel at Δt , regardless of their entrance time during the cycle, and therefore gain the same amount of enthalpy on the way. Therefore, the enthalpy variation will resemble a standing wave with nodes equally spaced by a wavelength $\lambda = V_0\tau$, as is clearly shown in Fig. 1. Any unsteadiness or non-uniformity of the heat input to the fluid will tend to blunt the sharp nodes. Heat storage in the walls produces such an effect.

Position of the Boiling Boundary. The time-varying position of the boiling boundary $z_{bb}(t)$ is determined by the enthalpy variations of the coolant. In a low-pressure system, however, the movements of the BB are also affected by pressure variations. The perturbations at the instantaneous position of the BB will be approximated by their values at the reference position of the BB, z_{bb}^0 .

Fig. 2 shows the profiles around the BB of the coolant enthalpy h and the saturation enthalpy h_s at steady state and at some time during the oscillation. The static pressure variations along the channel are responsible for the slope of the saturation-enthalpy profile. The dynamic pressure oscillations are due to changes in flow that produce a change in the frictional component and add an inertial component. These will cause the vertical displacement of $h_f(z)$.

Assuming that the total steady-state frictional pressure drop in the single-phase region can be expressed as $\Delta p_{1fr}^0 = \text{constant} \cdot w_0^b$ (where b is generally equal to 1.8 for turbulent flow), and that the friction factor obtained from steady-state experiments is applicable to a dynamic situation, the frictional component becomes

$$\left(\frac{\partial p_1^0}{\partial w} \right)_{z_{bb}^0} \delta w = b \Delta p_{1fr}^0 \frac{\delta w}{w_0} \quad (8)$$

The inertia term is given by

$$-\frac{d\delta w}{dt} \int_{z_{inlet}}^{z_{bb}^0} \frac{dz}{A(z)} = -\frac{z_{in}^0}{A} \frac{d\delta w}{dt}$$

where z_{in}^0 is the equivalent inertia length for the single-phase region. The two dynamic terms will displace the saturation-enthalpy profile by δh_{fbb}^0 , and all the combined static and dynamic effects will cause a net movement of the BB (Fig. 2) equal to

$$\delta z_{bb} = \frac{-\delta h_{bb}^0 + \delta h_{fbb}^0}{\left(\frac{dh^0}{dz} \right)_{bb} - \left(\frac{dh_f^0}{dz} \right)_{bb}} \quad (9)$$

Cast as a transfer function, equation (9) becomes

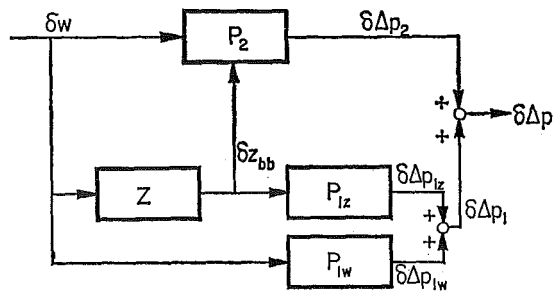


Fig. 3 Simplified block diagram of the boiling channel

$$Z(s) \equiv \frac{\delta z_{bb}(s)}{\delta w(s)} = \frac{-H(z_{bb}^0, s) + \left(\frac{dh_f}{dp}\right)_{p_{bb}^0} \cdot P_{1w}(s)}{q_0'(z_{bb}^0) - \left(\frac{dh_f}{dp}\right)_{p_{bb}^0} \cdot P_{1z}} \quad (10)$$

where $(dh_f/dp)_{p_{bb}^0}$ is the derivative of the liquid saturation enthalpy evaluated at p_{bb}^0 ,

$$P_{1z} = \left(\frac{\partial p_1^0}{\partial z}\right)_{z_{bb}^0} \quad (11)$$

is the pressure gradient at z_{bb}^0 , and

$$P_{1w}(s) = b \frac{\Delta p_{1f}^0}{w_0} - \frac{z_{in}^0}{A} s \quad (12)$$

is the flow-to-pressure-drop-in-the-single-phase-region transfer function.

The dynamic corrections δh_{fb}^0 are generally small or even negligible, except when the non-boiling length becomes very large and the period is short. The dynamic terms may increase or decrease the delay of δz_{bb} , depending on the relative magnitudes of the frictional and inertial contributions. The static pressure term $(dh_f/dz)_{bb}$ has only an attenuating effect on δz_{bb} . Therefore, the phase of the oscillation of the BB depends in most cases uniquely on the phase of the enthalpy perturbation at the steady-state location of the BB. For this reason, the two transfer functions $H(s)$ and $Z(s)$ can be used almost interchangeably in investigating the stability of the channel.

Block Diagram of the Channel. Fig. 3 shows the block diagram of a boiling channel. The single-phase region is represented by three transfer functions, namely, Z , P_{1z} , and P_{1w} , given by equations (10), (11), and (12), respectively. The two-phase region is described by a transfer or describing function, P_2 . Conventional methods for the calculation of the pressure-drop perturbations in the boiling region do exist [1, 2, 5]. A new and numerically efficient method based on a Lagrangian approach is described in [6]. The total pressure-drop perturbation and the stability criterion are given by equation (1). The block diagram of Fig. 3 can be easily transformed into a closed-loop diagram to permit application of conventional control-theory methods [6].

Experimental Detection of Higher-Mode Oscillations

The experimental work that led to the detection of the higher-mode oscillations has been presented elsewhere [4, 6]. A long, heated, Freon-113 channel, subject to a constant pressure drop from inlet to exit, was used in the experiments. Tests were conducted slightly above atmospheric pressure. Details of the apparatus and procedure and the data can be found in [6]. During an experimental run the channel power, the exit pressure, and the inlet temperature were maintained constant, while the inlet pressure and the flow were decreased continuously so that the channel was led through a continuum of stable states and eventually reached the threshold of stability.

Fig. 4 is a typical stability map in the dimensionless enthalpy-subcooling plane. The subcooling, Δh_1 , is defined as $h(z_{bb}^0) -$

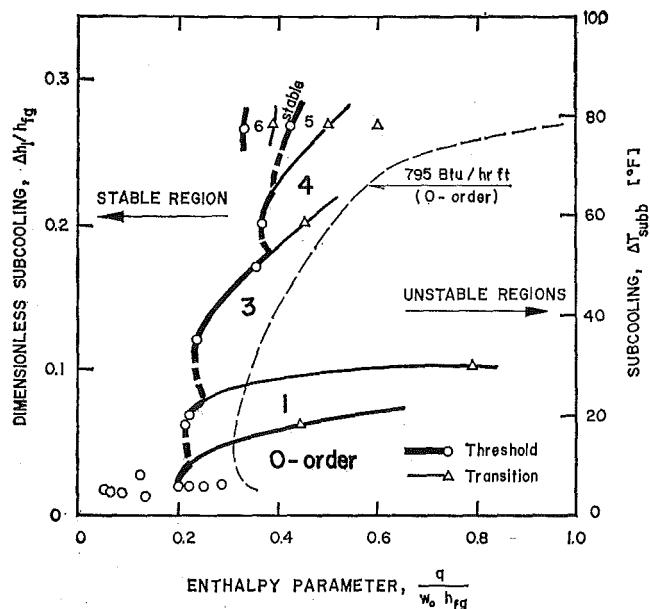


Fig. 4 Experimental stability map at 265 Btu/hr-ft. Uniform heat-flux distribution. (Smoothed threshold line for zero-order oscillations at 795 Btu/hr-ft also shown in dotted line.)

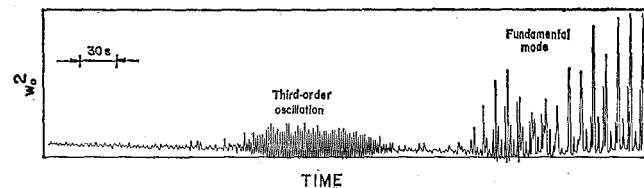


Fig. 5 Inlet flow trace showing two different oscillation modes; $q_0' = 795$ Btu/hr-ft, $\Delta T_{subb} = 65.4$ deg F. Uniform heat-flux distribution.

$h(0)$. As shown in this figure, the flow was stable at low values of the enthalpy parameter. Experimental threshold points are shown in circles. The scatter of the threshold points at very low subcooling is believed to be partly due to the coolant containing dissolved air that precipitated boiling and the occurrence of oscillations.

With Freon-113 as the test fluid, the experiments could be pursued beyond the threshold (i.e., within the unstable region) without encountering excessive wall temperatures. Thus the discovery of sudden changes in the oscillation pattern, referred to here as *transitions*, was made possible. Transition points and approximate transition boundaries are also shown in Fig. 4. These transitions are related to phenomena that will be referred to as higher-mode (or order) oscillations for reasons that will soon become apparent. The following observations led to their detection:

(a) In the enthalpy-subcooling plane at high subcoolings, the threshold lines should rapidly curve toward the right [13, 14]. Such a behavior was not observed; the stability boundaries remained vertical or even curved to the left.

(b) It has been well established [2, 15, 16] that the period of the oscillation is approximately equal to twice the "transit time" in the channel, and is a continuous function of subcooling [13]. In the higher-mode region the measured periods were equal to a small, approximately constant fraction of the expected period.

(c) Finally, during the experiments, as the average flow was slowly reduced, there were these sudden changes in the oscillation pattern and period, named "transitions." Often the oscillations seemed to decay, only to diverge again with a different frequency. Fig. 5 shows the flow trace for such a transition point. At other times the transitions occurred, without decay of the oscillation, by a mixture of the two modes over a few cycles.

The dynamic analysis of the single-phase region has revealed the existence of enthalpy nodes separated by a wavelength λ . The oscillations were assigned an order according to the relative position of the BB. If the BB is in the first wavelength ($z_{bb}^0/\lambda < 1$), the oscillation will be called "fundamental" or of "zero order." In general,

$$\text{order of oscillation} = \text{integer part of } z_{bb}^0/\lambda$$

When the unstable region was further subdivided according to the order of the oscillations, a consistent stability map emerged. The transition points became "threshold" points for some adjacent region, exhibiting a different, generally lower, order of instability. All the boundaries curved, as expected, to the right (Fig. 4).

The theory shows that the portion of the channel from the inlet to the last node before the BB should not be taken into account for the calculation of the transit time.⁴ This correction makes the "unexpectedly" short periods legitimate. The periods of the oscillations, plotted separately for each mode, varied smoothly with subcooling.

Although no reports on experimental observations of higher-mode oscillations were found in the literature,⁵ their existence has been predicted by stability analyses showing that more than one line of neutral stability exists [6, 16, 18]. Apparently there seems to be a dynamically acceptable range of periods (approximately 2 to 10 sec in the present case). As the period of the oscillation is related to the transit time, each point in the stability map can be assigned, a priori, a potential fundamental oscillation period [6, 19]. At low subcoolings and high power levels, as the fundamental period becomes short, the occurrence of higher modes with even shorter periods is unlikely. On the other end, when the transit time becomes excessively long the fundamental period is broken into smaller fractions.

When the inlet flow is gradually decreased, as in the present experiments, the locations of both the enthalpy nodes and of the BB change, and their relative positions must be considered. For example, as the BB reaches an enthalpy node, or as the channel crosses a neutral stability line, the oscillation might no longer be sustained and another mode might emerge. These considerations are unfortunately complicated by the existence of strong nonlinearities within the unstable region. Regions where extensive mixing of modes occurs are probably indifferent to the order of the oscillation. In one instance, at very low inlet velocity, it has been possible to observe visually a change of mode. There seemed to be a sudden shift of the average position of the oscillating BB to a location a few inches upstream, suggesting that delays in nucleation might be occasionally present before the transitions. It is evident, however, that the higher oscillation modes are not caused by nucleation instabilities.

The amplitude of the oscillations decreased with increasing order; however, even the higher-order oscillations would be of sufficient amplitude to cause control problems in a real system.

Experiments to Confirm the Mechanism of Higher-Order Oscillations.

In the case of higher-mode oscillations, with uniform heat distribution, the portion of the channel up to the last enthalpy node before the BB does not contribute much to the enthalpy perturbation at the BB. It should then be possible to remove the heat input from this portion of the channel and provide the corresponding enthalpy rise by an equivalent increase of the inlet temperature without affecting the stability.

A reference transition point having a wavelength approximately equal to the test length⁶ was chosen, in order to be able to cut off the power from portions of the channel that were multi-

⁴ This is equivalent to subtraction of multiples of 2π from the argument of the enthalpy perturbation.

⁵ Fabrega [17] has observed in rare instances a "second oscillation boundary" which might have been a transition boundary.

⁶ The heated channel was divided into seven individually heated test lengths.

ples of the wavelength. Unfortunately, such a procedure assures exact similitude of the enthalpy perturbations at the reference state of the channel only. Nevertheless, four experimental runs were made with the power cut off from the first $n = 0, 1, 2,$ and 3 wavelengths, respectively. In the vicinity of the reference point, a remarkably similar pattern of oscillations and transitions from mode to mode was observed. The experimental threshold and transition points, plotted with the corrected coordinates

$$q^* = q + n\Delta q \quad \text{and} \quad \Delta h_1^* = \Delta h_1 + \frac{n\Delta q}{w_0}$$

where Δq is the heat input to a test length, fitted well in the enthalpy-subcooling map, confirming the explanation given above [6].

Conclusions

The stability of a boiling channel to density-wave oscillations can be investigated by oscillating the inlet flow.

The movements of the boiling boundary were predicted taking into account both the static and the dynamic pressure-drop perturbations. The importance of the dynamic terms is predicted to increase in proportion to the length of the single-phase region, and with the frequency of the oscillation. However, in most cases the movements of the boiling boundary are uniquely determined by the enthalpy perturbations at the steady-state location of the boiling boundary. Therefore, the delay of the enthalpy perturbation at the average position of the boiling boundary is of primary importance for the stability of the channel. Under certain conditions heat storage in the channel walls can play an important role.

The space-dependence of the enthalpy perturbations along the channel was shown to be periodic. This periodicity led to the concept of ordering the oscillations according to the number of complete wavelengths present in the single-phase region. At high subcoolings and low heat inputs, the channel exhibited higher modes of oscillation with frequencies that were multiples of the fundamental frequency. Sudden changes in the period of the oscillations were also recorded in this region. These phenomena were explained in terms of the dynamic behavior of the boiling boundary.

Acknowledgment

This study was supported in part by the Office of Naval Research under Contract Nonr 3963 (15) which was carried out in the M.I.T. Department of Mechanical Engineering.

References

- 1 Neal, L. G., Zivi, S. M., and Wright, R. W., "The Mechanisms of Hydrodynamic Instabilities in Boiling Systems," *Proceedings of the Symposium on Two-Phase Flow Dynamics*, EURATOM—The Technological University of Eindhoven, The Netherlands, 1967.
- 2 Stenning, A. H., and Veziroglu, T. N., "Density-Wave Oscillations in Boiling Freon-11," ASME Paper No. 66-WA/HT-49; also "Flow Oscillations in Forced Convection Boiling," Vol. II, NASA CR-72122, Feb. 1967.
- 3 Bouré, J. A., Bergles, A. E., and Tong, L. S., "Review of Two-Phase Flow Instability," ASME Paper No. 71-HT-42.
- 4 Yadigaroglu, G., and Bergles, A. E., "Fundamental and Higher-Mode Density-Wave Oscillations in Two-Phase Flow: The Importance of the Single-Phase Region," ASME Paper No. 71-HT-13.
- 5 Anderson, T. T., "Hydraulic Impedance: A Tool for Predicting Boiling Loop Stability," *Nuclear Applications and Technology*, Vol. 9, 1970, pp. 422-433.
- 6 Yadigaroglu, G., and Bergles, A. E., "An Experimental and Theoretical Study of Density-Wave Oscillations in Two-Phase Flow," M.I.T. Eng. Proj. Lab. Report DSR-74629-3, Massachusetts Institute of Technology, Cambridge, Mass., Dec. 1969.
- 7 Smets, H. B., "Nuclear Power Plant Transfer Functions," S.M. thesis, Chemical Engineering Department, Massachusetts Institute of Technology, Cambridge, Mass., Sept. 1957.
- 8 Storrer, F., "Temperature Response to Power, Inlet Coolant

Temperature and Flow Transients in Solid Fuel Reactors," APDA 132, 1959.

9 Shotkin, L. M., "Flow of Boiling Water in Heated Pipes," *Nuclear Science and Engineering*, Vol. 26, 1966, pp. 293-304.

10 Akcasu, A. Z., "Theoretical Feedback Analysis in Boiling Water Reactors," ANL-6221, Oct. 1960.

11 Levy, S., "Forced Convection Subcooled Boiling—Prediction of the Vapor Volumetric Fraction," *International Journal of Heat and Mass Transfer*, Vol. 10, 1967, pp. 951-965.

12 Staub, F. W., "The Void Fraction in Subcooled Boiling—Prediction of the Initial Point of Net Vapor Generation," *JOURNAL OF HEAT TRANSFER*, TRANS. ASME, Series C, Vol. 90, No. 1, Feb. 1968, pp. 151-157.

13 Crowley, J. D., Deane, C., and Gouse, S. W., Jr., "Two-Phase Flow Oscillations in Vertical, Parallel, Heated Channels," *Proceedings of the Symposium on Two-Phase Flow Dynamics*, EURATOM—The Technological University of Eindhoven, The Netherlands, 1967.

14 Gouse, S. W., Jr., and Andrysiak, C. D., "Flow Oscillations in a Closed Loop with Transparent, Parallel, Vertical, Heated Chan-

nels," M.I.T. Eng. Proj. Lab. Report DSR-8973-2, Massachusetts Institute of Technology, Cambridge, Mass., June 1963.

15 Masini, G., Possa, G., and Tacconi, F. A., "Flow Instability Thresholds in Parallel Heated Channels," *Energia Nucleare*, Vol. 15, 1968, p. 777.

16 Ishii, M., and Zuber, N., "Thermally Induced Flow Instabilities in Two-Phase Mixtures," *Heat Transfer 1970, Fourth International Heat Transfer Conference*, Vol. 5, paper B5.11, Paris, France, 1970.

17 Fabrega, S., "Instabilités hydrodynamiques limitant la puissance des réacteurs à eau bouillante," EURATOM Report EUR-1509 f, 1965.

18 Davies, A. L., and Potter, R., "Hydraulic Stability: An Analysis of the Causes of Unstable Flow in Parallel Channels," *Proceedings of the Symposium on Two-Phase Flow Dynamics*, EURATOM—The Technological University of Eindhoven, The Netherlands, 1967.

19 Dijkman, F. J. M., "Some Hydrodynamic Aspects of a Boiling Water Channel," D. Eng. Sc. thesis, Report WW-R144, Technological University of Eindhoven, The Netherlands, 1969.

H. HWANG-BO

Mechanical Engineer,
Fairchild Space and Electronics Div.,
Fairchild Industries,
Germantown, Md.
Mem. ASME

W. E. HILDING

Professor of Mechanical Engineering,
University of Connecticut, Storrs, Conn.
Mem. ASME

Optimization of a Heat Pipe with a Wick and Annulus Liquid Flow

An analytical model has been formulated for the parametric study of liquid flow characteristics in the heat pipe, which consists of a porous tube, a closed outer container tube, and an annulus between them. The analytical model includes the effect of the rate of change of momentum, surface tension forces, the frictional forces in the body of wicking material and at the wall, as well as the axial variation of static pressure supporting the capillary meniscus at the liquid-vapor-wick interface in the vapor passage. The length of the condenser of the heat pipe was optimized as a function of the radial heat flux rate and the ratio of the liquid flow rate in the annulus to that within the wick, W_a/W_w . The effect of pressure loss and recovery in the vapor passage of the heat pipe on the optimum length of condenser was investigated.

Introduction

THE MAIN role of the wick material in the heat pipe is to provide a liquid-vapor surface with a capillary meniscus. In the evaporator the liquid-vapor meniscus has a more concave surface due to evaporation of the working fluid. In the condenser it becomes nearly flat. Thus a pressure gradient is set up, driving the fluid back to the evaporator, see Fig. 1. It is, therefore, beneficial to provide a liquid annulus between the wick and the solid wall for the additional return of the condensate to the evaporator. However, the liquid layer may give an additional resistance to radial heat flow, so that the overall heat conductance becomes smaller. If the thermal conductivity of the liquid is large as with liquid metals, the liquid annulus would be advantageous for avoiding the "dry-out" limit of the wick.

For the parametric study of liquid flow characteristics in the heat pipe Kunz et al. [1]¹ have formulated an analytical model which includes the effect of rate of change of momentum, surface tension forces, and the frictional forces in the body of the wicking material. In their analysis it is assumed that the static vapor pressure is constant in the vapor passage, but it is not true for the heat pipe operating at low vapor pressure. As the local static pressure in the liquid passage is determined by the vapor pressure supporting the capillary meniscus (wick-liquid-vapor interface) in the vapor passage, the effect of the axial variation of static vapor pressure is included in the present analysis.

¹ Numbers in brackets designate References at end of paper.

Contributed by the Heat Transfer Division for publication (without presentation) in the JOURNAL OF HEAT TRANSFER. Manuscript received by the Heat Transfer Division February 3, 1970. Paper No. 71-HT-V.

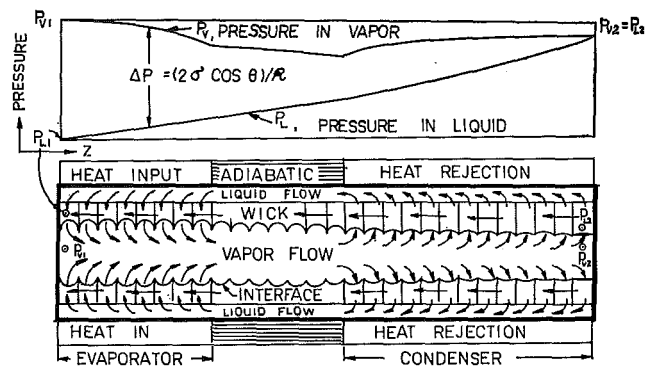


Fig. 1 Schematic of a heat pipe: distribution of pressure in the heat pipe operating at low vapor pressure

Liquid Flow Analysis

An analytical model has been formulated for the parametric study of liquid flow characteristics in the heat pipe, which consists of a porous tube, a closed outer container tube, and an annulus between them. The annulus permits increased liquid return from the condenser to the evaporator. The analytical model includes the effect of the rate of change of momentum, surface tension forces, the frictional forces in the body of wicking material and at the wall, as well as the axial variation of static pressure supporting the capillary meniscus at the liquid-vapor-wick interface in the vapor passage.

The following assumptions are made concerning the liquid flow model shown in Fig. 2.

- 1 The wicking material is isotropic, is of constant thickness,

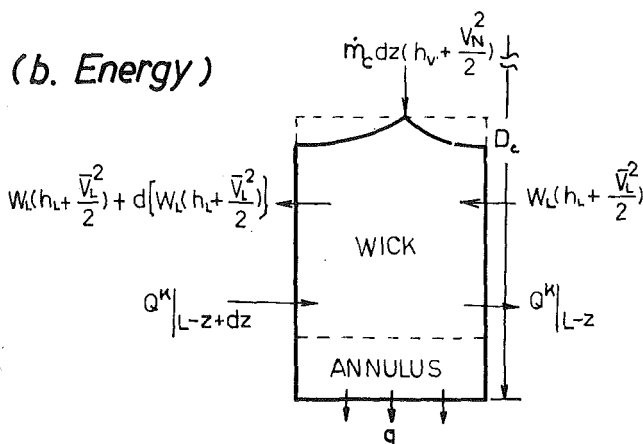
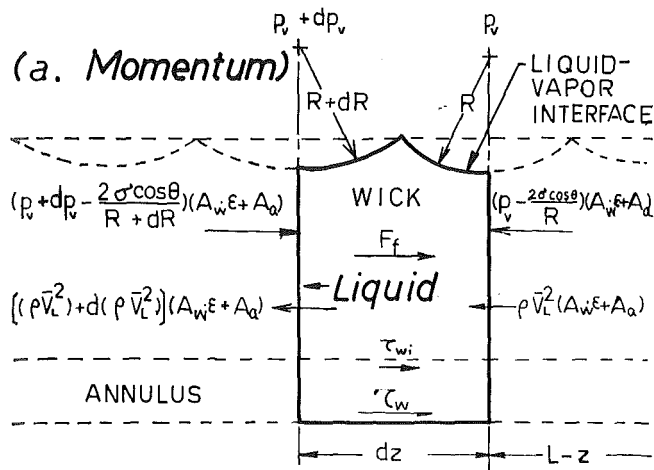


Fig. 2 Liquid control volume in the condenser section

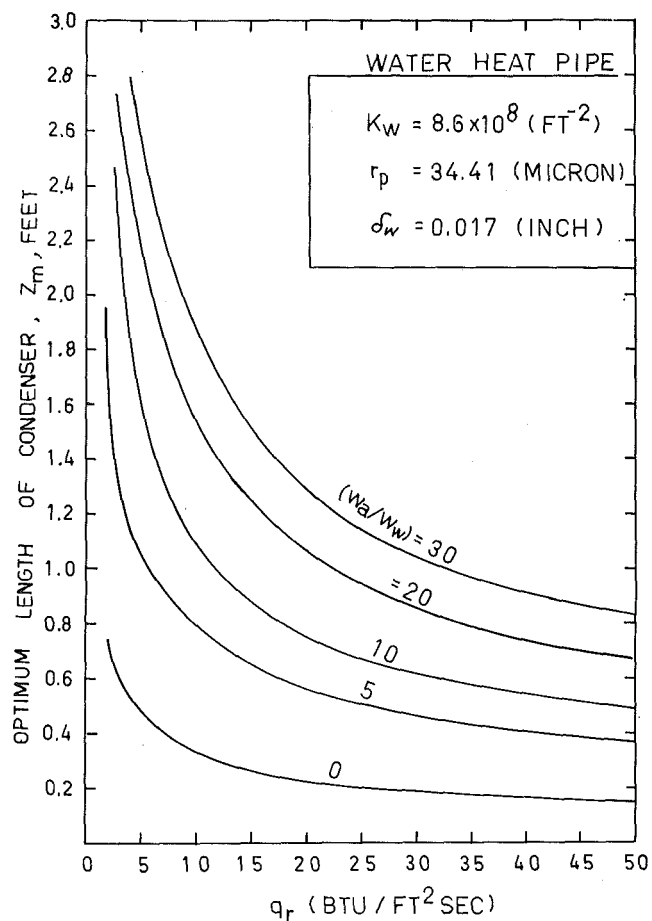


Fig. 3 Optimum condenser length vs. heat flux of rejection

Nomenclature

A_1, A_2 = form coefficients
 A_a = cross-sectional area of liquid annulus
 A_w = cross-sectional area of porous tube (wick)
 B_1, B_2 = form coefficients
 B' = coefficient of proportionality
 C_s = dimensionless correction factor for annulus flow past the screen cylinder
 D_a = mean diameter of liquid annulus
 D_c = outside diameter of liquid annulus
 D_w = inside diameter of liquid annulus (wick-annulus interface)
 F_u = viscous drag force
 F_p = external pressure force
 h_{fg} = enthalpy of evaporation
 h_L = enthalpy of saturated liquid
 h_v = enthalpy of saturated vapor
 K_a = annulus friction factor

K_w = wick friction factor
 $m = \sqrt{\epsilon K_w}$
 \dot{m}_c = mass rejection rate per unit length of condenser (condensing rate)
 $N = (\rho_L h_{fg} \sigma / \mu_L)$
 P = absolute static pressure in the annulus
 \bar{P} = absolute static pressure in the wick
 P_{vL} = absolute stream pressure at downstream end of condenser (vapor side)
 P_{vm} = absolute stream pressure at axial distance $z = z_m$ (vapor side)
 q = radial heat flux rate
 \dot{q} = volumetric flow rate
 R_0 = inside radius of porous tube
 R_i = inside radius of liquid annulus
 R_2 = outside radius of liquid annulus
 r = radial direction coordinate
 R = radius of curvature
 u_w = axial velocity of liquid in wick

u_a = axial velocity of liquid in annulus
 u_i = slip velocity at wick-liquid interface
 V_L = average liquid velocity
 W_L = total mass rate of flow of liquid
 W_a = mass rate of flow of liquid in annulus
 W_w = mass rate of flow of liquid in wick
 z = positive axial direction coordinate
 z' = negative axial direction coordinate
 z_m = optimum condenser length
 δ_a = thickness of annular liquid layer
 δ_w = average wick thickness
 ϵ = porosity of wick
 θ = contact angle
 μ = dynamic viscosity
 ρ_L = mass density of liquid
 σ = surface tension of liquid

and is saturated with a wetting liquid along the entire length of heat pipe.

2 The liquid is at the same temperature along the entire liquid passage.

3 At any given point of the same axial distance, the liquid-vapor interface meniscus can be characterized by one radius of curvature.

4 The velocity of the liquid in the wick and annulus V_L is the average velocity in the wick and annulus, and has a z component only.

5 Any terms containing differentials raised to the second or higher powers are neglected.

The summation of forces acting in the axial direction on the element of a porous tube saturated with liquid and with an annular liquid layer of length dz gives the differential equation of z -direction momentum, see Fig. 2(a).

Positive forces	Negative forces
1 $\left(P_v - \frac{2\sigma}{R}\right)(\epsilon A_w + A_a)$	1 $\left(P_v + dP_v - \frac{2\sigma}{R + dR}\right)(\epsilon A_w + A_a)$
2 $V_L W_L$	2 $(V_L + dV_L)(W_L + dW_L)$
3 $\left(\frac{dP_L}{dz}\right)(\epsilon A_w + A_a)dz$	3 $\left(\frac{dP_L}{dz}\right)(\epsilon A_w + A_a)dz$

(1)

Summing up the positive and negative forces, eliminating differentials of higher order, and dividing throughout by $(\epsilon A_w + A_a)dz$ results in the following expression

$$\left(\frac{dP_v}{dz}\right) + \frac{1}{(\epsilon A_w + A_a)} \frac{d(W_L V_L)}{dz} + \frac{2\sigma}{R^2} \left(\frac{dR}{dz}\right) + \left(\frac{dP_L}{dz}\right) = 0 \quad (2)$$

Neglecting the changes in kinetic energy and axial conduction of heat, the energy equation can be expressed for the liquid element in Fig. 2(b) as follows

$$(\dot{m}_c dz) h_v = \frac{d(W_L h_L)}{dz} dz + q\pi D_c dz \quad (3)$$

where \dot{m}_c is mass rejection rate per unit length of condenser, D_c is the inside diameter of container tube, and q is time rate of heat transfer per unit area (the heat flux rate).

But from the equation of mass conservation we have

$$\dot{m}_c dz = \rho_L \left(\frac{dV_L}{dz}\right) (\epsilon A_w + A_a) dz \quad (4)$$

Substituting equation (4) into equation (3) yields the combined energy-continuity differential equation

$$V_L \rho_L \left(\frac{dh_L}{dz}\right) - (h_v - h_L) \rho_L \frac{dV_L}{dz} + \frac{q\pi D_c}{(\epsilon A_w + A_a)} = 0 \quad (5)$$

Assuming that the axial gradient of the liquid enthalpy is negligible and integrating equation (5) one can show that the average liquid velocity varies linearly with z in the condenser, thus

$$V_L = \frac{q\pi D_c z}{h_{fg}(\epsilon A_w + A_a)\rho_L} \quad (6)$$

The total liquid flow rate then becomes

$$W_L = \frac{q\pi D_c}{h_{fg}} z \quad (7)$$

Because of the low flow rates and velocities encountered with capillary flow in a wick, Darcy's law can be applied to the liquid flow through porous media. The annulus flow produced by the

net capillary forces can be assumed to be both laminar and relatively free from inertial effects. Applying Darcy's law for the flow in porous medium and Stokes' equation for the slow, viscous flow past a circular screen annulus, the radial velocity profile in the liquid passage was derived in Appendix A and the axial pressure drop in the liquid passage was derived in Appendix B as

$$\frac{dP_L}{dz} = K_w \left(\frac{\mu_L}{\rho_L}\right) \frac{W_L}{\pi D_w \delta_w (1 + W_a/W_w)} \quad (8)$$

where W_w is liquid flow rate in the wick, W_a is liquid flow rate in the annulus, K_w is the wick friction factor, and D_w is mean diameter of the wick tube.

Substituting equations (6), (7), and (8) into equation (2), and integrating we then obtain an integral-continuity-momentum-energy equation as follows

$$\int dP_v + \int \frac{d(W_L V_L)}{(A_w \epsilon + A_a)} + \int \frac{2\sigma}{R^2} dR + \int dP_L = 0 \quad (9)$$

or

$$\int_L^{L-z_m} \frac{2q^2 z dz}{h_{fg}^2 \rho_L (\epsilon \delta_w + \delta_a)^2} + \int_L^{L-z_m} K_w \left(\frac{\mu_L}{\rho_L}\right) \frac{qz dz}{h_{fg} \delta_w \left(1 + \frac{W_a}{W_w}\right)} = \int_{P_v L}^{P_v m} -dP_v - \int_{\infty}^{R_{\min}} 2\sigma \frac{dR}{R^2} \quad (10)$$

where $(\epsilon A_w + A_a) \simeq \pi D_c (\epsilon \delta_w + \delta_a)$ and $D_{wi} \simeq D_c$ were introduced.

The maximum output of the capillary pump can be obtained when the following conditions are satisfied in the heat pipe

$$\begin{aligned} \text{at } z = L, & \quad R \rightarrow \text{infinite} \\ \text{at } z = L - z_m, & \quad R \rightarrow R_{\min} \end{aligned} \quad (11)$$

where R_{\min} is the minimum radius of curvature that the wicking material can support, and z_m is the optimum (maximum) condenser length. Using the limits of equation (11), equation (10) can be integrated and solved for z_m to obtain

$$z_m = \left\{ N \left[\frac{2}{R_{\min}} + \frac{(P_{vL} - P_{vm})}{\sigma} \right] \right\}^{1/2} \left[\frac{K_w q}{2} \left[\frac{1}{\delta_w (1 + W_a/W_w)} + \frac{2q}{\mu_L h_{fg} (\epsilon \delta_w + \delta_a)^2 K_w} \right] \right] \quad (12)$$

where

$$N = (\rho_L h_{fg} \sigma / \mu_L)$$

The maximum heat transfer capability of the heat pipe can be obtained by equation (13), if the radial heat rejection flux rate q is specified, thus

$$Q_{\max} = q\pi D_c z_m \quad (13)$$

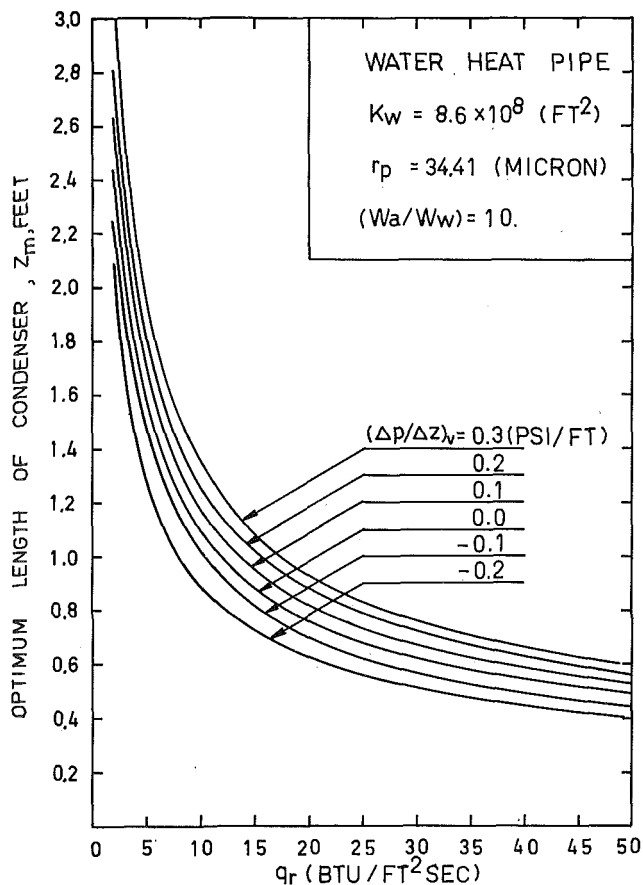


Fig. 4 Effect of pressure recovery and loss on optimum condenser length

Results and Conclusions

The optimum condenser length of a water heat pipe was calculated by equation (12) and presented in Fig. 3 as a function of the radial heat rejection rate q_r , and the ratio of the liquid flow rate in the annulus to that in the wick, W_a/W_w . The effect of pressure loss and recovery in the vapor passage of the heat pipe on the optimum length of condenser is shown in Fig. 4.

The pressure recovery of the vapor in the condenser section of the heat pipe contributes to a more favorable pressure gradient for the liquid flow to the evaporator.

The "dry-out" limit of the wick can be increased by the presence of a liquid annulus between the wick and the solid wall, but the liquid layer can be an additional resistance to radial heat transfer if the thermal conductivity of the liquid is small. A radial temperature profile in the condenser section of the heat pipe is shown in Fig. 5 [2].

The increase of the liquid flow in the annulus with respect to the liquid flow rate in the wick increases the heat transfer capability of the heat pipe, if the thermal conductivity of the liquid is large.

Acknowledgment

The authors wish to acknowledge the financial support of the University of Connecticut Research Foundation and Yeong-Nam University.

References

- 1 Kunz, H. R., Langston, L. S., Hilton, B. H., Wyde, S. S., and Nashick, G. H., "Vapor-Chamber Fin Studies—Transport Properties and Boiling Characteristics of Wicks," NASA CR-812, June 1967.
- 2 Hwang-Bo, H., "An Analytical and Experimental Study of the Heat Pipe Operating at Low Vapor Pressures," PhD thesis, University of Connecticut, Storrs, Conn., June, 1970.
- 3 Shen, C. C., "Stokes Flow Past a Thin Screen, Part I, and Viscous Flows Past Porous Bodies of Finite Size, Part II," PhD thesis, California Institute of Technology, Pasadena, Calif., May 1968.

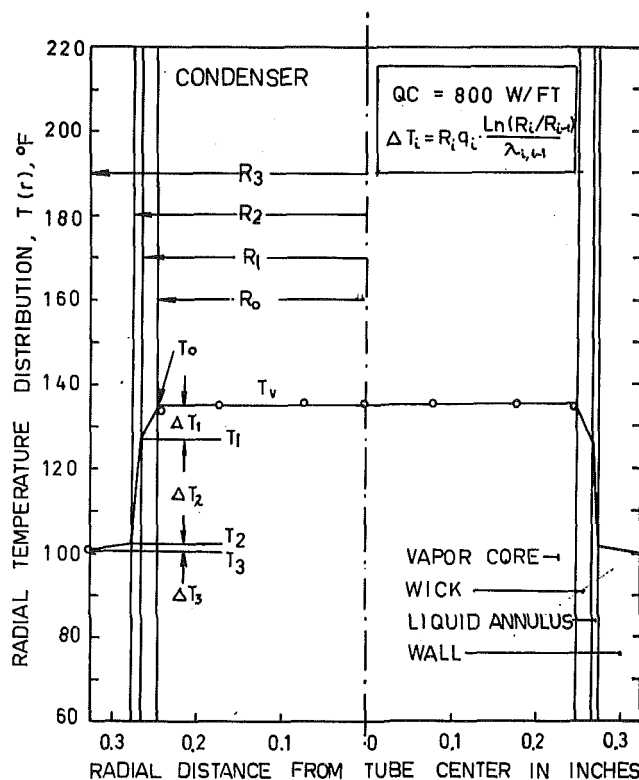


Fig. 5 Temperature profile in condenser

4 Scheidegger, A. E., *The Physics of Flow Through Porous Media*, Macmillan, New York, N. Y., 1960, pp. 68–90.

5 Kemme, J. E., "Ultimate Heat Pipe Performance," Thermionic Conversion Specialist Conference, Framingham, Mass., Oct. 1968.

APPENDIX A

Velocity Profiles of Liquid Flow in the Wick and Annulus

Because of the complexity of the flow in the pores we can regard the porous region as a homogeneous regime in which the original microscopic flow is represented by an apparent mean flow, and we may consider the liquid flow in the wick and annulus as two distinct homogeneous regions. These two regions are separated by a geometrical interface located at the physical boundary of the porous body. A schematic representation of a shear flow within and above a porous circular cylinder (annulus) is shown in Fig. 6.

The slow, viscous flow through a circular screen annulus can be analyzed based on Stokes' equations and the flow in the porous medium by Darcy's equation. In the immediate vicinity of the interface the velocity can vary rapidly under the direct influence of the external shear. Darcy's law ceases to apply here, and the field macroscopic equation must be used.

The general macroscopic equations of motion for liquid flow through porous media, when only the Reynolds number is small, have been derived in Shen [3].

$$\nabla \cdot \mathbf{u}_w = 0 \quad (1A)$$

$$-\nabla \bar{P} + \frac{\mu_L}{\epsilon} \nabla^2 \mathbf{u}_w = K_w \mu_L \mathbf{u}_w \quad (2A)$$

where \mathbf{u}_w is the velocity vector in the wick, μ_L is the coefficient of viscosity, ϵ is the porosity of the wick, and K_w is the wick friction factor.

For incompressible, viscous flows in which the inertial effect is negligible, Stokes' equations are:

$$\nabla \cdot \mathbf{u}_a = 0 \quad (3A)$$

$$-\nabla P + \mu_L \nabla^2 \mathbf{u}_a = 0 \quad (4A)$$

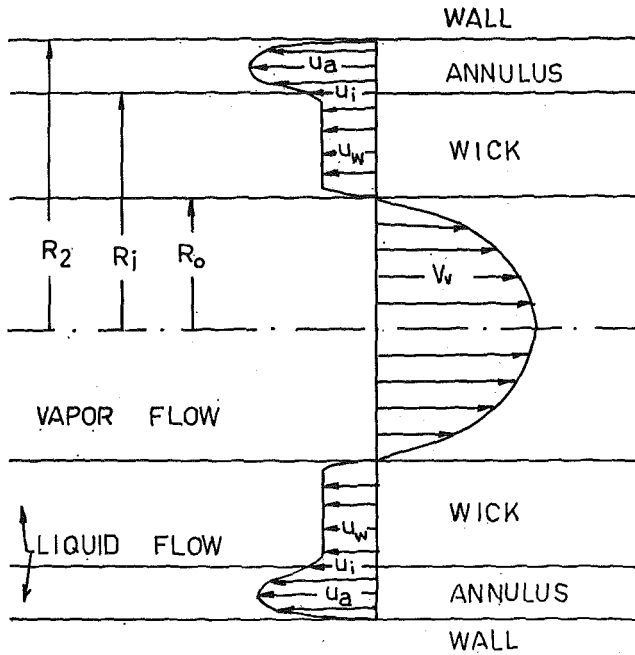


Fig. 6 Schematic representation of velocity profiles in the heat pipe

where u_a is the velocity vector in the liquid annulus.

For the flow in the porous cylinder equations (1A) and (2A) in plane polar coordinates reduce to

$$\frac{d^2 u_w}{dr^2} + \frac{1}{r} \frac{du_w}{dr} - K_w \epsilon u_w = -\frac{\epsilon}{\mu_L} \left(\frac{d\bar{P}}{dz'} \right) \quad (5A)$$

$$\frac{d\bar{P}}{dr} = 0, \quad \text{and} \quad \frac{d\bar{P}}{dz} = \text{const.} \quad (6A)$$

where $dz = -dz'$ is used.

For the axisymmetrical viscous flow between a solid and porous cylinder equations (3A) and (4A) in plane polar coordinates reduce to

$$\frac{d^2 u_a}{dr^2} + \frac{1}{r} \frac{du_a}{dr} = -\frac{1}{\mu_L} \left(\frac{dP}{dz'} \right) \quad (7A)$$

$$\frac{dP}{dz'} = \text{const.}, \quad \frac{dP}{dr} \ll \frac{dP}{dz'}, \quad \text{and} \quad \frac{du_a}{dz} = \text{const.} \quad (8A)$$

These equations (6A) and (8A) together with the non-slip boundary condition on the wall and the following interface boundary conditions between a viscous flow region and a porous medium are sufficient to determine the solution of the flow within the porous medium (5A) and in the annulus past a porous cylinder (7A).

Interface boundary conditions

$$u_w = u_a = u_i, \quad \text{at} \quad r = R_i \quad (9A)$$

$$P = \bar{P} \quad (10A)$$

Non-slip boundary conditions at the solid wall

$$u_a = 0, \quad \text{at} \quad r = R_2 \quad (11A)$$

and

$$u_w = 0, \quad \text{at} \quad r = R_0 \quad (12A)$$

The general solution of equation (7A) is

$$u_a = A_1 \ln r + B_1 - \frac{r^2}{4\mu_L} \left(\frac{dP}{dz'} \right) \quad (13A)$$

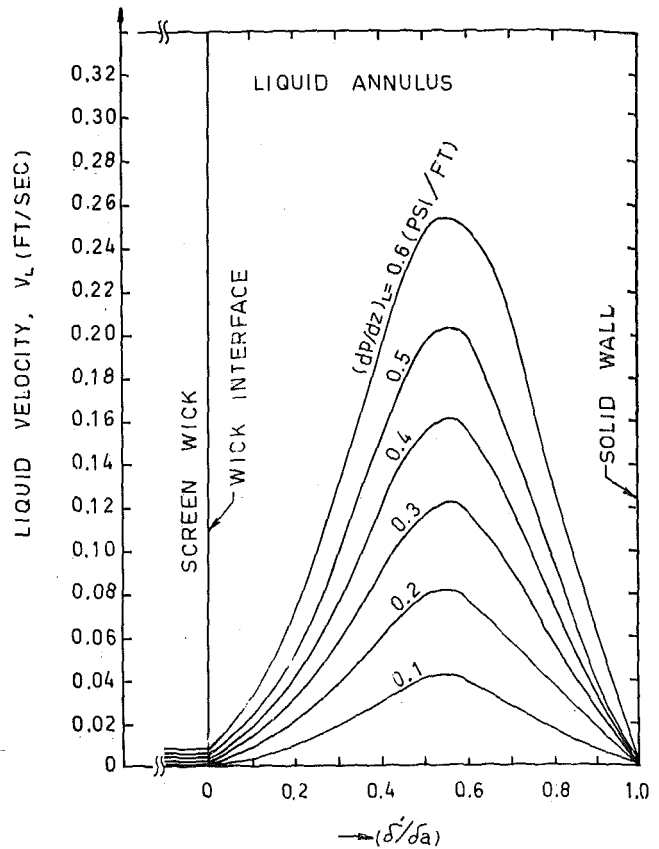


Fig. 7 Radial velocity profiles of an annular liquid flow past the porous tube

and the general solution of equation (5A) is

$$u_w = A_2 \mathcal{J}_0(i\sqrt{\epsilon K_w} r) + B_2 \mathcal{Y}_0(i\sqrt{\epsilon K_w} r) - \frac{\epsilon r^2}{4\mu_L} \left(\frac{d\bar{P}}{dz'} \right) \quad (14A)$$

The form coefficients A_1 , B_1 , A_2 , and B_2 can be readily determined by a simple application of the boundary conditions (9A), (10A), (11A), and (12A).

$$A_1 = \frac{X(R_2) - X(R_i) - u_i}{\ln(R_2/R_i)} \quad (15A)$$

$$B_1 = \frac{-[X(R_2) - X(R_i) - u_i] \ln R_2 + X(R_2) \ln(R_2/R_i)}{\ln(R_2/R_i)} \quad (16A)$$

where $X(r) = (r^2/4\mu_L)(dP/dz')$

$$A_2 = \frac{[u_i + \epsilon X(R_i)] \mathcal{Y}_0(imR_0) - \epsilon X(R_0) \mathcal{Y}_0(imR_i)}{[\mathcal{J}_0(imR_i) \mathcal{Y}_0(imR_0) - \mathcal{J}_0(imR_0) \mathcal{Y}_0(imR_i)]} \quad (17A)$$

$$B_2 = \frac{[u_i + \epsilon X(R_i)] \mathcal{J}_0(imR_0) - \epsilon X(R_0) \mathcal{J}_0(imR_i)}{[\mathcal{Y}_0(imR_i) \mathcal{J}_0(imR_0) - \mathcal{Y}_0(imR_0) \mathcal{J}_0(imR_i)]} \quad (18A)$$

where

$$m = \sqrt{\epsilon K_w}$$

In order to satisfy the interface boundary condition ($\bar{P} = P$) it is required that the pressure gradients for the both flow regions be equal.

$$\frac{d\bar{P}}{dz'} = \frac{dP}{dz} = -K_w \mu u_w \quad (19A)$$

The slip velocity at the interface u_i is unknown, but it could be

determined by applying another approximate interface boundary condition [3]

$$\epsilon \left(\frac{\partial \mathbf{u}_a}{\partial r} \right) = \left(\frac{\partial \mathbf{u}_w}{\partial r} \right), \quad \text{at } r = R_i \quad (20A)$$

For the present investigation it was assumed that the slip velocity is equal to the average velocity in the wick.

$$\mathbf{u}_i = \bar{\mathbf{u}}_w \quad (21A)$$

Substituting equations (19A) and (21A) into equations (13A) and (14A) we can obtain the velocity profiles in the wick and the annulus. Fig. 7 shows the velocity profile of the liquid flow in the annulus between wick and wall as a function of axial pressure gradient.

APPENDIX B

Wick and Annulus Friction Factor

The equations governing the flow through the porous medium were established empirically by Darcy. It was assumed that the velocity within the porous medium, \mathbf{u}_w , and hence $d\mathbf{u}_w/dz$ is proportional to \dot{q}/A_w , where \dot{q} is the volumetric flow rate, and the total surface involved is proportional to the bulk volume, $A_w L$, of porous material. The viscous drag on the fluid can be expressed as (4)

$$F_w = \mu_L \left(\frac{d\mathbf{u}_w}{dz} \right) A_w = B' \mu_L \left(\frac{\dot{q}}{A_w} \right) (A_w L) = B' \mu_L \dot{q} L \quad (1B)$$

where B' is a proportional coefficient, and L is the length of the wick. The external force acting on the fluid contained within the porous material is

$$F_p = (P_L - P_0) \epsilon A_w \quad (2B)$$

Neglecting body force due to gravity and assuming that the viscous drag force is equal to the external force we obtain Darcy's equation

$$B' \mu_L \dot{q} L = (P_L - P_0) \epsilon A_w \quad (3B)$$

or

$$\left(\frac{d\bar{P}}{dz} \right) = \frac{(P_L - P_0)}{L} = \left(\frac{B'}{\epsilon} \right) \frac{\mu_L}{A_w} \dot{q} = K_w \frac{\mu_L}{A_w} \left(\frac{W_w}{\rho_L} \right) \quad (4B)$$

where $K_w = (B'/\epsilon)$ is a constant of proportionality called the friction factor of the wick and W_w , ρ_L , μ_L , and A_w are mass flow rate, density, viscosity, and cross-sectional area of the wick perpendicular to the flow, respectively.

The annulus flow produced by the capillary force can be assumed also to be both laminar and relatively free from inertia effect. The pressure drop of liquid flow in the annular channel with solid walls has been expressed by Kemme [5] as

$$\frac{dP}{dz} = \frac{12}{\pi D_a \delta_a^3} \frac{\mu_L}{\rho_L} W_a \quad (5B-1)$$

where

- δ_a = average width of annulus
- W_a = mass flow rate in the annulus
- D_a = mean diameter of the annulus
- μ_L = viscosity of liquid
- ρ_L = density of liquid

Since the annulus flow past a screen cylinder usually behaves very much like an annulus flow with solid walls [3], a dimensionless correction factor C_s was introduced in equation (5B-1) for the annular flow past a cylindrical porous tube to take into account the wick surface effect.

$$\frac{dP}{dz} = \frac{12 C_s}{\pi D_a \delta_a^3} \frac{\mu_L}{\rho_L} W_a \quad (5B-2)$$

If we define an annulus friction factor as

$$K_a = \frac{12 C_s}{\delta_a^2} \quad (6B)$$

we can write equation (5B-2) as

$$\frac{dP}{dz} = K_a \frac{\mu_L}{\rho_L} \left(\frac{W_a}{\pi D_a \delta_a} \right) \quad (7B)$$

If both pressure drops in the two liquid flow regions of the heat pipe are assumed to be the same, the ratio of mass flow rate in the annulus to that of the wick can be obtained from equations (4B) and (7B). With

$$\frac{d\bar{P}}{dz} = \frac{dP}{dz} \quad (8B)$$

$$\frac{W_a}{W_w} = \left(\frac{K_w}{K_a} \right) \left(\frac{D_a}{D_w} \right) \left(\frac{\delta_a}{\delta_w} \right) \quad (9B)$$

Using the relation $W_L = W_a + W_w$, equation (9B) can be written as

$$W_w = \frac{W_L}{1 + \left(\frac{K_w}{K_a} \right) \left(\frac{D_a}{D_w} \right) \left(\frac{\delta_a}{\delta_w} \right)} \quad (10B)$$

Substituting equation (10B) into equation (4B), the pressure drop in the wick and annulus can be expressed as

$$\frac{dP}{dz} = K_w \frac{\mu_L}{\rho_L \pi D_w \delta_w} \left[\frac{W_L}{1 + (W_a/W_w)} \right] \quad (11B)$$

determined by applying another approximate interface boundary condition [3]

$$\epsilon \left(\frac{\partial \mathbf{u}_a}{\partial r} \right) = \left(\frac{\partial \mathbf{u}_w}{\partial r} \right), \quad \text{at } r = R_i \quad (20A)$$

For the present investigation it was assumed that the slip velocity is equal to the average velocity in the wick.

$$\mathbf{u}_i = \bar{\mathbf{u}}_w \quad (21A)$$

Substituting equations (19A) and (21A) into equations (13A) and (14A) we can obtain the velocity profiles in the wick and the annulus. Fig. 7 shows the velocity profile of the liquid flow in the annulus between wick and wall as a function of axial pressure gradient.

APPENDIX B

Wick and Annulus Friction Factor

The equations governing the flow through the porous medium were established empirically by Darcy. It was assumed that the velocity within the porous medium, \mathbf{u}_w , and hence $d\mathbf{u}_w/dz$ is proportional to \dot{q}/A_w , where \dot{q} is the volumetric flow rate, and the total surface involved is proportional to the bulk volume, $A_w L$, of porous material. The viscous drag on the fluid can be expressed as (4)

$$F_w = \mu_L \left(\frac{d\mathbf{u}_w}{dz} \right) A_w = B' \mu_L \left(\frac{\dot{q}}{A_w} \right) (A_w L) = B' \mu_L \dot{q} L \quad (1B)$$

where B' is a proportional coefficient, and L is the length of the wick. The external force acting on the fluid contained within the porous material is

$$F_p = (P_L - P_0) \epsilon A_w \quad (2B)$$

Neglecting body force due to gravity and assuming that the viscous drag force is equal to the external force we obtain Darcy's equation

$$B' \mu_L \dot{q} L = (P_L - P_0) \epsilon A_w \quad (3B)$$

or

$$\left(\frac{dP}{dz} \right) = \frac{(P_L - P_0)}{L} = \left(\frac{B'}{\epsilon} \right) \frac{\mu_L}{A_w} \dot{q} = K_w \frac{\mu_L}{A_w} \left(\frac{W_w}{\rho_L} \right) \quad (4B)$$

where $K_w = (B'/\epsilon)$ is a constant of proportionality called the friction factor of the wick and W_w , ρ_L , μ_L , and A_w are mass flow rate, density, viscosity, and cross-sectional area of the wick perpendicular to the flow, respectively.

The annulus flow produced by the capillary force can be assumed also to be both laminar and relatively free from inertia effect. The pressure drop of liquid flow in the annular channel with solid walls has been expressed by Kemme [5] as

$$\frac{dP}{dz} = \frac{12}{\pi D_a \delta_a^3} \frac{\mu_L}{\rho_L} W_a \quad (5B-1)$$

where

- δ_a = average width of annulus
- W_a = mass flow rate in the annulus
- D_a = mean diameter of the annulus
- μ_L = viscosity of liquid
- ρ_L = density of liquid

Since the annulus flow past a screen cylinder usually behaves very much like an annulus flow with solid walls [3], a dimensionless correction factor C_s was introduced in equation (5B-1) for the annular flow past a cylindrical porous tube to take into account the wick surface effect.

$$\frac{dP}{dz} = \frac{12 C_s}{\pi D_a \delta_a^3} \frac{\mu_L}{\rho_L} W_a \quad (5B-2)$$

If we define an annulus friction factor as

$$K_a = \frac{12 C_s}{\delta_a^2} \quad (6B)$$

we can write equation (5B-2) as

$$\frac{dP}{dz} = K_a \frac{\mu_L}{\rho_L} \left(\frac{W_a}{\pi D_a \delta_a} \right) \quad (7B)$$

If both pressure drops in the two liquid flow regions of the heat pipe are assumed to be the same, the ratio of mass flow rate in the annulus to that of the wick can be obtained from equations (4B) and (7B). With

$$\frac{dP}{dz} = \frac{dP}{dz} \quad (8B)$$

$$\frac{W_a}{W_w} = \left(\frac{K_w}{K_a} \right) \left(\frac{D_a}{D_w} \right) \left(\frac{\delta_a}{\delta_w} \right) \quad (9B)$$

Using the relation $W_L = W_a + W_w$, equation (9B) can be written as

$$W_w = \frac{W_L}{1 + \left(\frac{K_w}{K_a} \right) \left(\frac{D_a}{D_w} \right) \left(\frac{\delta_a}{\delta_w} \right)} \quad (10B)$$

Substituting equation (10B) into equation (4B), the pressure drop in the wick and annulus can be expressed as

$$\frac{dP}{dz} = K_w \frac{\mu_L}{\rho_L \pi D_w \delta_w} \left[\frac{W_L}{1 + (W_a/W_w)} \right] \quad (11B)$$

DISCUSSION

V. E. Schrock² and K. C. Sockalingam³

The authors have presented an analysis of the capillary pumping limit of performance for a heat pipe with an annular flow path between the wick and pipe wall for return of the liquid from the condenser to the evaporator. The discussers are also investigating this design which promises increased performance for those cases limited by capillary pumping (flow resistance of the wick). The annulus serves to reduce flow resistance in the axial direction, thereby raising the pumping limit, but it simultaneously increases the radial thermal resistance and therefore lowers the heat load limit attributed to nucleate boiling. Our first experiment [6] resulted in nucleate boiling limit rather than the expected pumping limit in our annular-wick water heat pipe.

Several aspects of the present paper deserve comment. The authors' premise that the vapor pressure in the core determines the adjacent liquid pressure is doubtful. It is more reasonable to assume that, so long as the wick can sustain the liquid-vapor interface at the wick surface, both the liquid and vapor pressure distributions are "internally" determined. The local meniscus shape is then determined by the local pressure differential across the meniscus as determined by the liquid and vapor pressure profiles.

Equations (1) and (2) are misleading. The term dP_L/dz is not a pressure gradient but rather the net frictional force (due to Darcy flow in the wick and laminar flow in the annulus) gradient per unit cross-sectional area. The liquid pressure term is the first term listed in equation (1), i.e.,

² Professor of Nuclear Engineering, University of California, Berkeley, Calif. Mem. ASME.

³ Research Assistant, University of California, Berkeley, Calif.

$$P_L = P_v - \frac{2\sigma}{R}$$

The *frictional* term is subsequently derived as equation (8) and then used to eliminate the authors' dP_L/dz from equation (2).

Equations (6), (7), and (10) are inconsistent with the coordinate description in Fig. 1. The variable z should be replaced by $L - z$ where L is the pipe length (not defined in the paper). Equation (12) will obtain only from a corrected equation (10).

Choice of the conditions, equation (11), assumes that the maximum capillary pumping head is available to drive the liquid flow through the condenser alone. If this were true, what would cause the liquid to flow through the adiabatic section of the pipe and into the evaporator? We may also note that the authors' premise is not consistent with the meniscus shapes shown in Fig. 1. Thus we cannot agree that equation (12) will correctly predict a length of condenser corresponding to Q_{\max} . It should seriously overestimate Q_{\max} .

Fig. 3 must be plotted for a specific value of the parameter $(P_{vL} - P_{vm})/\sigma$. What is this constant? What determines whether the vapor pressure rises or drops in the condenser? How would one use Fig. 4?

Appendix A develops the radial profiles of the axial component of velocity in the annulus and in the wick. Both these solutions neglect change in flow rate (which is considered in the analysis in the body of the paper) in the axial direction due to condensation. This neglect will produce large potential errors, particularly near the end of the pipe. Subject to the assumptions inherent in equation (7A) the authors' solution for the flow in the annulus is correct; however, the same is not true for their solution of equation (5A) for the flow in the wick. Specifically the general solution, equation (14A), should be⁴

$$u_w = A_2 I_0(\sqrt{\epsilon} \kappa_w r) + B_2 K_0(\sqrt{\epsilon} \kappa_w r) + \frac{1}{\mu_L \kappa_w} \left(\frac{dP}{dz} \right)$$

(The values given for the constants A_2 and B_2 are, of course, also incorrect as a result of the error in the particular solution.) Since the solutions contain the common interface velocity u_i , the final solutions can be obtained only after determining its value. The authors propose to set u_i equal to a constant \bar{u}_w as given by equation (19A). This equation is inconsistent with the level of detail described in equation (2A), and it does not provide the correct u_i . Continuity of the shear stress at the interface does, as the authors alternatively propose, provide the necessary information to obtain u_i . No final solution is presented, however, from this latter condition. Fig. 7 shows no radial variation in the wick and the geometric factor R_2/R_3 , which must be a parameter, is not given.

More important, in connection with Appendix A, is the fact that the authors have not used their analysis to obtain the necessary frictional term for the one-dimensional analysis in the body of the paper. Lacking this, Appendix A does not appear pertinent to the objective of the paper. Instead the authors develop, in Appendix B, an equation for the net frictional term

⁴ For the authors' assumptions there is no need for the vector notation on u . Another minor change in our corrected equation is to use the common notation for the modified Bessel functions (Bessel functions of imaginary arguments).

using plane Poiseuille flow for the annulus and the one-dimensional Darcy equation for the wick. These choices are not unreasonable, however inconsistent with Appendix A, if the model of constant axial flow is valid. The latter assumption is not true in the condenser or evaporator of the heat pipe. This fact is more important than the errors and irrelevance of Appendix A.

Additional Reference

6 Sockalingam, K. C., and Schrock, V. E., "Performance Characteristics of Water Heat Pipes of Annular Wick Configuration," *Transactions of the American Nuclear Society*, Vol. 14, No. 2, 1971, pp. 436-437.

Authors' Closure

The discussion submitted by Professor V. E. Schrock and K. C. Sockalingam is welcomed as an interesting supplement to the paper.

There appears to be a misconception in their discussion on the momentum balance. The dP_L/dz of equation (1) is the pressure gradient in the liquid passage due to frictional forces. Hence the frictional force on the fluid element shown in Fig. 2a was given by

$$F_f = \left(\frac{dP_L}{dz} \right) (\epsilon A_w + A_a) dz$$

Due to Darcy flow in the wick and laminar flow in the annulus, dP_L/dz of equation (8) was derived in Appendix B and substituted in equation (2).

It should be noted that the liquid flows in the $-z$ direction, while the vapor flows in the $+z$ direction. That is the reason why equation (10) was integrated from $z = L$ to $z = L - z_m$. One may replace z in equations (6) and (7) by $L - z$, then he will get the optimum condenser length, $L - z_m$, as equation (12).

The present analysis was made only in the condenser section of the heat pipe. Therefore, R_{\min} used in this analysis should represent the minimum radius of capillary meniscus in the condenser section only. Similar analysis can be extended for the evaporator section.

The pressure recovery or drop in the vapor passage of the condenser section is an important design factor, especially when the heat pipe is operating at low vapor pressure. $P_{vL} - P_{vm}$ occurs mainly due to the momentum change of the decelerating vapor flow and the frictional force at the liquid-vapor-wick interface. This term can be predicted by the compressible vapor flow analysis in the vapor passage. The pressure-recovery term was coupled with σ to be consistent with the adding term $2/R_{\min}$. Notice that the pressure difference across the capillary meniscus $\Delta P = P_v - P_L = 2\sigma/R$ or $2/R = \Delta P/\sigma$. Therefore, $\sigma \left(\frac{2}{R_{\min}} + \frac{P_{vL} - P_{vm}}{\sigma} \right)$ will give the actual pressure drop in the vapor passage of the condenser and across the capillary interface.

Appendix A was derived to show the liquid flow profiles in the annulus and the wick. Fig. 7 shows the liquid velocity profile in the annulus from equation (13A). The result of equation (14A), which happened to be erroneous, was not used in the analysis.

We wish to thank the discussers for this correction.

D. M. FRANCE

Assistant Mechanical Engineer.

T. GINSBERG

Assistant Mechanical Engineer.

Engineering and Technology Div.,
Argonne National Laboratory,
Argonne, Ill.

Improved Point-Matching Techniques Applied to Multi-Region Heat Transfer Problems

An analytical method is presented which extends the series solution of the Laplace and Poisson equations with irregular boundary conditions to multi-cell problems. The method employs a least-squares technique of satisfying the boundary conditions on the irregular boundaries and eliminates the use of a finite number of boundary points to satisfy these conditions. The technique is applied to the calculation of the fully developed temperature distribution of a constant-velocity fluid flowing parallel to a semi-infinite square array of circular nuclear fuel rods. The bounding wall of the array is located such that the flow area of the cell associated with the rod adjacent to the wall is different from the (equal) areas of all the other cells. The series solution is compared to a finite-difference solution for a sample case of two cells. The results for the semi-infinite array indicate that while the array temperature distribution is markedly affected by the difference in flow areas, the Nusselt numbers of the rods are relatively unaffected. Typical results are presented for a pitch-to-diameter of 1.2; the flow area of the first cell is 3.67 percent greater than the area of the other cells.

Introduction

CONSIDERABLE attention has been given to the problem of obtaining analytical solutions to the Laplace and Poisson equations for arbitrary boundary conditions in domains with irregular boundaries. One method that has been used with various degrees of success in obtaining solutions of this type of problem requires the assumption of a series solution with unknown coefficients which are determined by satisfying the boundary conditions. The characteristic feature of this problem, however, is that at least one of the boundaries is irregular with respect to the coordinate system used.

The various reported techniques of solving this type of problem with an assumed series solution differ in the manner in which the boundary conditions on the irregular boundaries are satisfied. In most of the earlier works, the boundary conditions were applied at a finite number of points on the boundary, equal to the number of unknown coefficients. This technique of satisfying the boundary conditions will be called "point matching." Using this approach, Sparrow [1]¹ obtained a solution for the temperature field in a solid embedded with a triangular infinite array of cylinders with constant wall temperatures. Problems of this

general type will be referred to as "infinite-array" or "single-cell" problems. Geometric symmetry considerations enable one to isolate a symmetry sector out of the infinite array, to identify all boundary conditions, and to solve the entire problem using this representative sector.

Inaccuracies in the point-matching technique of determining the unknown coefficients are indicated in [2, 3]. Alternate methods are discussed in [2-4] and are applied to infinite-array problems. Of these approaches, only the method of [2] completely eliminates the number of boundary points as a parameter in the solution. It is considered to be a more direct approach than the orthonormalization technique of [4] which requires the availability of special computer codes.

Nijsing and Eifler [5] used the point-matching technique to obtain a solution for the temperature field in an infinite triangular array of nuclear reactor fuel pins, cooled by liquid sodium flowing parallel to the fuel pins. This multi-region analysis considers the effects of the fuel, bond, clad, and coolant regions of a 30-deg symmetry sector. Point matching was used to satisfy the boundary condition on the irregular coolant boundary. Temperatures and heat flows were matched at the boundaries of the adjacent regions. Therefore, neither the temperature nor the heat flux need be specified at the fuel-pin-coolant interface.

The point-matching technique was used by Schmid [6] in the solution of what will be termed a "multi-cell" problem. Schmid obtained a solution for the laminar velocity distribution of a fluid flowing parallel to a semi-infinite square array of cylinders. The domain considered is bounded on one side by a solid wall.

¹ Numbers in brackets designate References at end of paper.

Contributed by the Heat Transfer Division for publication (without presentation) in the JOURNAL OF HEAT TRANSFER. Manuscript received November 16, 1970; revised manuscript received June 17, 1971. Paper No. 71-HT-T.

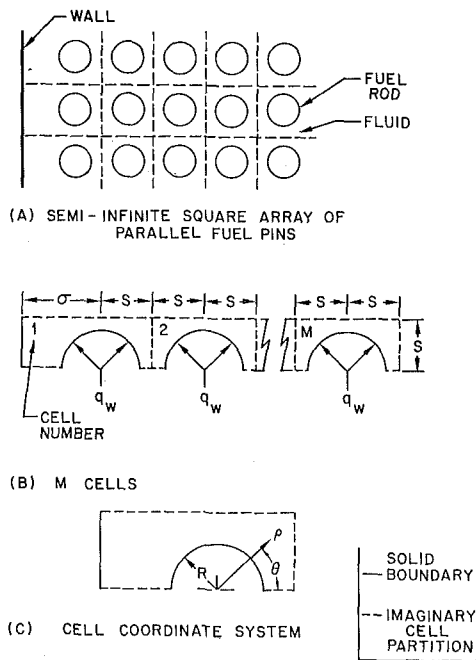


Fig. 1 Geometric configuration for multi-cell problem

The characteristic feature of this type of problem is that a simple symmetry sector cannot be isolated for analysis; not all the boundary conditions on such a sector can be specified a priori.

In general, if a solution is sought to a problem in which the geometry is so irregular as to preclude the accurate representation of the solution by a single series, the region in which the solution is sought may be subdivided into cells. Then a series solution is assumed for each cell with the appropriate boundary conditions specified at adjacent cellular boundaries.

The purpose of the present study is twofold:

- 1 To extend the analytical method of [2] to multi-cell problems.
- 2 To apply the technique to a problem of current interest to the liquid-metal fast breeder reactor (LMFBR) development program.

Specifically, an analytical technique is presented and evaluated for the prediction of the temperature distribution of a fluid flowing parallel to a semi-infinite square array of circular nuclear fuel pins. This geometry simplifies the illustration of the least-squares solution extended to multi-cell cases, by reducing the number of irregular boundaries per cell relative to the tri-

Table 1 Comparison of flow assumptions, infinite triangular pin bundle array

Pitch-to-diameter ratio	Slug flow [8]	Turbulent flow [9]	Laminar flow [10]
Nondimensional maximum rod-wall temperature			
1.1	2.19	1.99 @ Pe = 206 2.14 @ Pe = 1015	1.805
1.2	0.62	0.481 @ Pe = 98.2 0.563 @ Pe = 885	0.809
Nusselt number (based on hydraulic diameter)			
1.1	8.29	6.5 @ Pe = 200 9.2 @ Pe = 1000	2.94
1.2	12.18	10.5 @ Pe = 200 14 @ Pe = 1000	6.90

angular-array pin bundle. The geometry of the system is shown in Fig. 1(A). The assumptions in the analysis are:

- 1 Fully developed heat transfer.
- 2 Constant-velocity (slug) flow parallel to the axis of the rods.
- 3 Uniform heat flux around the perimeter of the fuel pins.
- 4 Zero turbulent energy transport.
- 5 The array of pins is bounded on one side by a thermally insulated wall, as shown in Fig. 1(A).
- 6 All material properties are temperature-independent.

Under the above conditions, the problem solution is independent of the particular fluid in the pin bundle. However, the results presented in Table 1 indicate that assumptions 2 and 4 are relatively good approximations for pin-bundle heat transfer in fully developed, turbulent, low-Peclet-number, liquid-metal flows. These results for maximum rod-wall temperature and Nusselt number in an infinite triangular array of fuel pins were generated by a finite-difference solution for the cases of slug, turbulent, and laminar flows. Neglecting heat transfer in the fuel-pin cladding (assumption 3) results in the overprediction of the magnitude of thermal gradients in the pin bundle.

The minimum symmetry sector for the semi-infinite array considered here is shown in Fig. 1(B) and consists of M cells. In the problem presented here, the wall was positioned such that the flow area of the first cell was 3.67 percent greater than the interior cells. Symmetry considerations suggest that if M is chosen large enough, the boundary condition on the right-hand boundary of cell M will be zero heat flux everywhere. M must be chosen such that the solutions for the remaining $M-1$ cells are unaffected by the choice. The nondimensional fluid temperature distribution in cell M should be identical to the solution for an infinite array of pins with the same pitch-to-diameter ratio (S/R).

A finite-difference solution was obtained to a two-cell problem, i.e., $M = 2$. The purpose of this method of analysis was to com-

Nomenclature

A = cross-sectional area of any cell other than the first, ft²
 A' = cross-sectional area of first cell, ft²
 a_n = cross-sectional area of n th node, ft²
 c = specific heat of fluid, Btu/lb_m-deg F
 K = thermal conductivity of fluid, Btu/hr-ft-deg R
 N = number of unknown coefficients' less one, in the series solution of each cell
 M = total number of cells considered
 \dot{m} = total mass flux of all cells combined, lb_m/sec
 Pe = Peclet number

q = heat flux, Btu/hr-ft²
 Q = dimensionless heat flux
 Nu_i = Nusselt number of i th cell
 R = fuel-rod radius, ft
 r = dimensionless radial coordinate ($r = \rho/R$)
 S = cell boundary length, ft
 T_i = temperature in i th cell, deg R
 t_i = dimensionless temperature in i th cell
 \bar{T}_i = temperature of i th node, deg R
 U = fluid velocity, ft/sec
 V_j = volume of j th node, ft³
 x_n = distance from node j to adjacent node n , ft
 z = axial coordinate, ft
 α = thermal diffusivity of fluid, ft²/sec

Γ_j = rod surface area adjacent to j th node, ft²
 δ = fluid density, lb_m/ft
 θ = angular coordinate, rad
 ρ = radial coordinate, ft
 σ = cell boundary length, ft
 $\bar{\tau}$ = dimensionless overall bulk temperature
 τ_i = dimensionless cellular bulk temperature

Subscripts

s = refers to a boundary surface
 w = fuel-rod wall
 ∞ = refers to an infinite array of fuel rods
 b = bulk

pare the series method of solution with an alternate calculation procedure. The choice of $M = 2$ for the comparison was dictated by three factors related to the finite-difference solution: computer calculation time, nodal limitations of the computer code used for the analysis, and number of memory locations available on the CDC-3600 computer. The finite-difference solution was obtained through the use of the General Electric Transient Heat Transfer Code, Version B (THTB) [7].

Series solutions were obtained for cases involving up to eight cells. Convergence of the solutions is discussed from two aspects: the number of terms in the series expansion necessary for numerical convergence of the series, and the number of cells required for convergence of the solution to the semi-infinite-array problem. The latter was determined by convergence of the Nusselt number and temperature distribution of the M th cell to the infinite-array solution. The number of iterations and the tolerance necessary for numerical convergence of the finite-difference solution are also discussed.

The effects of the bounding-wall location on the fluid temperature distribution and on the fuel-pin Nusselt numbers are calculated for a pitch-to-diameter ratio (S/R) of 1.2. This number is typical of LMFBR fuel-pin subassembly designs.

Series Solution

Based on the aforementioned assumptions, the energy equation for the i th cell is

$$\nabla^2 T_i = \frac{U}{\alpha} \frac{\partial T_i}{\partial z} \quad (1)$$

The condition of a fully developed temperature distribution yields

$$\dot{m}c \frac{\partial T_i}{\partial z} = \pi R q_w M \quad (2)$$

and the continuity equation for all cells is

$$\dot{m} = \delta U [A' + (M - 1)A] \quad (3)$$

Substituting equations (2) and (3) into (1) and nondimensionalizing yields Poisson's equation. In cylindrical coordinates, one obtains

$$\frac{1}{r^2} \frac{\partial^2 t_i}{\partial \theta^2} + \frac{\partial^2 t_i}{\partial r^2} + \frac{1}{r} \frac{\partial t_i}{\partial r} = 1 \quad (4)$$

where

$$t_i = T_i / \left(\frac{q_w R}{KD} \right)$$

The quantity D is a dimensionless geometrical factor

$$D = \frac{1}{2} \left\{ \frac{2S}{M} \left[\frac{\sigma + (2M - 1)S}{\pi R^2} \right] - 1 \right\}$$

The general solution to equation (4) is

$$t_i(r, \theta) = B_0^i + \xi_0^i \ln r + \frac{r^2}{4} + \sum_{n=1}^N [(\xi_n^i r^n + \psi_n^i r^{-n})(Z_n^i \cos n\theta + W_n^i \sin n\theta)]$$

The zero-flux boundary condition

$$\left. \frac{\partial T_i}{\partial \theta} \right|_{\theta=n\pi} = \left. \frac{\partial t_i}{\partial \theta} \right|_{\theta=n\pi} = 0 \quad n = 0, 1$$

yields $W_n^i \equiv 0$. The constant flux condition at the fuel-rod walls

$$-K \left. \frac{\partial T_i}{\partial \rho} \right|_{\rho=R} = q_w$$

in nondimensional form is

$$\left. \frac{\partial t_i}{\partial r} \right|_{r=1} = -D$$

This condition yields

$$\xi_0^i = - \left(D + \frac{1}{2} \right)$$

and

$$\xi_n^i = \psi_n^i$$

Then, for the i th cell, the solution becomes

$$t_i(r, \theta) = B_0^i - \left(D + \frac{1}{2} \right) \ln r + \frac{r^2}{4} + \sum_{n=1}^N B_n^i (r^n + r^{-n}) \cos n\theta \quad (5)$$

The remaining unknown coefficients B_k ($0 \leq k \leq N$) are determined by satisfying the boundary conditions in the least-squares sense on the cell boundaries. At the common boundaries (partitions) between adjacent cells, there are two conditions that must be satisfied; the temperatures and fluxes determined from the solutions in each cell must be equal at the partitions. These conditions present no problem to the point-matching technique; one would simply write two equations, for continuity of temperature and flux at each of several points on the common boundary. However, the method as described in [2] requires integration along the boundary, and only one condition can be met in the equations obtained from a single cell. The rectification of this situation is best described by example.

In the first cell, the condition that $t_1 = t_2$ on the common boundary between cells 1 and 2 was satisfied. In cell number 2, the condition that $q_1 = q_2$ was met on the common boundary between cells 1 and 2. Further, in cell 2, the condition that $t_2 = t_3$ on the boundary between cells 2 and 3 was satisfied. This procedure was continued to the last cell, M , where the condition on the right-hand boundary, Fig. 1(B), was $q_M = 0$ for $0 \leq \theta \leq \pi/4$. The subscripts on t and q refer to cell number. The heat flux, q , may be written as

$$q = -K \nabla T \cdot \bar{N} \quad (6)$$

where \bar{N} is the outward normal at the appropriate surface; Q is defined as

$$Q \equiv \frac{q \rho_s}{K} \frac{DK}{q_w R}$$

where ρ_s is the radial coordinate to the surface mentioned above.

The problem is formulated by equating the boundary conditions on the irregular boundaries to the series solution in the least-squares sense. Application of the boundary conditions in the least-squares sense for the first cell yields

$$\frac{\partial}{\partial B_k^1} \left\{ \int_0^{\pi/4} (t_2 - t_1)^2 d\theta + \int_{\pi/4}^{\pi} Q_1^2 d\theta + \int_{\phi}^{\pi} Q_1^2 d\theta \right\} = 0 \quad (7)$$

$$k = 0, 1, 2, \dots, N$$

where $\phi = \pi - \tan^{-1}(S/\sigma)$. The procedure leading to the formation of equation (7) is discussed in detail in [2]. The flux, Q_1 , on the top boundary of the i th cell is given below. This flux occurs in equation (7) under the integral sign from $\theta = \pi/4$ to $\theta = \phi$ and was obtained directly from relation (6).

$$Q_i = g(\theta) + \sum_{n=1}^N B_n^i F_2(n, \theta) d\theta \quad (8)$$

where

$$g(\theta) = \left(D + \frac{1}{2}\right) \sin \theta - Sr_s/(2R) \quad (9)$$

$$F_2(n, \theta) = r_s^n \sin(n\theta - \theta) + r_s^{-n} \sin(n\theta + \theta) \quad (10)$$

$$r_s = \rho_s/R = S/(R \sin \theta)$$

On a right boundary

$$Q_i = h(S, \theta) + \sum_{n=1}^N nB_n^i E(n, \theta) \quad (11)$$

where

$$E(n, \theta) = -r_s^n \cos(n\theta - \theta) + r_s^{-n} \cos(n\theta + \theta) \quad (12)$$

$$h(y, \theta) = \left(D + \frac{1}{2}\right) \cos \theta - y^2/(2R^2 \cos \theta) \quad (13)$$

$$r_s = S/(R \cos \theta)$$

On a left boundary

$$Q_i = -h(y, \theta) + \sum_{n=1}^N nB_n^i L(n, y, \theta) \quad (14)$$

where

$$L(n, y, \theta) = (-1)^n [r_s^n \cos(n\theta - \theta) - r_s^{-n} \cos(n\theta + \theta)] \quad (15)$$

$$r_s = y/(R \cos \theta)$$

and

$$y = \sigma \text{ for the first cell}$$

$$y = S \text{ for all other cells}$$

The formulation for the j th cell, other than the first or the last, is

$$\frac{\partial}{\partial B_k^j} \left\{ \int_0^{\pi/4} (t_{j+1} - t_j)^2 d\theta + \int_{\pi/4}^{3\pi/4} Q_j^2 d\theta + \int_{\pi/4}^{\pi} (Q_{j-1} + Q_j)^2 d\theta \right\} = 0 \quad (16)$$

$$k = 0, 1, 2, \dots, N$$

The formulation for the last, M th, cell is

$$\frac{\partial}{\partial B_k^M} \left\{ \int_0^{\pi/4} Q_M^2 d\theta + \int_{\pi/4}^{3\pi/4} Q_M^2 d\theta + \int_{3\pi/4}^{\pi} (Q_{M-1} + Q_M)^2 d\theta \right\} = 0 \quad (17)$$

$$k = 1, 2, \dots, N$$

The boundary conditions at all boundaries with the exception of the common partitions are in the form of specified heat flux. Thus, another condition is required in order to obtain an explicit temperature solution. This requirement is apparent in relation (17) where B_σ^M does not appear. The bulk temperature relationship

$$\bar{\tau} = \frac{1}{M\pi D} \left(\sum_i \iint t_i r dr d\theta \right) \quad (18)$$

completes the formulation of the problem. The overall bulk temperature, $\bar{\tau}$, is defined as

$$\bar{\tau} = \frac{T_I}{q_w R} + \frac{\alpha}{UR} \left(\frac{z}{R} \right)$$

and T_I is the temperature at $z = 0$. The bulk temperature of the i th cell, $i > 1$, is also defined.

$$\tau_i = \frac{1}{A} \iint t_i dA$$

For the first cell

$$\tau_1 = \frac{1}{A'} \iint t_1 dA'$$

The following relation is obtained between bulk temperatures:

$$\left(M + \frac{A'}{A} - 1\right) \bar{\tau} = \left(\frac{A'}{A}\right) \tau_1 + \sum_{i=2}^M \tau_i \quad (19)$$

Equations (7), (16), (17), and (18) must now be cast into a convenient form to solve for unknown coefficients B_n^i , $n = 0$ to N and $i = 1$ to M . Performing the differentiation on equation (7) and rearranging, one arrives at the following result:

$$\sum_{n=0}^N [B_n^1 G(k, n)] + \sum_{n=0}^N [B_n^2 X(k, n)] = H^1(k) \quad (20)$$

$$k = 0, 1, 2, \dots, N$$

or in matrix notation

$$\|G\| \|B^1\| + \|X\| \|B^2\| = \|H^1\| \quad (21)$$

The components $G(k, n)$ of the G matrix and $X(k, n)$ of the X matrix correspond to $N + 1$ equations obtained from differentiation with respect to the $N + 1$ coefficients B_n^1 of the series solution in the first cell. In the following list of components, arguments n and k are nonzero unless expressed as zero.

$$G(k, n) = \int_0^{\pi/4} F_1(k, \theta) F_1(n, \theta) d\theta + nk \int_{\pi/4}^{\phi} F_2(k, \theta) F_2(n, \theta) d\theta + nk \int_{\phi}^{\pi} L(k, \sigma, \theta) L(n, \sigma, \theta) d\theta$$

$$G(k, 0) = \int_0^{\pi/4} F_1(k, \theta) d\theta; \quad G(0, n) = \int_0^{\pi/4} F_1(n, \theta) d\theta$$

$$G(0, 0) = \pi/4$$

$$X(k, n) = (-1)^{n+1} \int_0^{\pi/4} F_1(k, \theta) F_1(n, \theta) d\theta$$

$$X(0, n) = (-1)^{n+1} G(0, n); \quad X(k, 0) = -G(k, 0);$$

$$X(0, 0) = -\pi/4$$

The components $H^1(k)$ of the vector H^1 are given by

$$H^1(k) = -k \int_{\pi/4}^{\phi} g(\theta) F_2(k, \theta) d\theta + k \int_{\phi}^{\pi} h(\sigma, \theta) L(k, \sigma, \theta) d\theta$$

$$H^1(0) = 0$$

where

$$F_1(n, \theta) = (r_s^n + r_s^{-n}) \cos n\theta \quad (22)$$

$$r_s = S/(R \cos \theta)$$

Similarly, performing the differentiation of equation (16) yields the following form of results for the i th (intermediate) cell.

$$\|P_1\| \|B^{i-1}\| + \|P_2\| \|B^i\| + \|P_3\| \|B^{i+1}\| = \|H^i\| \quad (23)$$

The result for the last cell has the form

$$\|I\| \|B^{M-1}\| + \|J\| \|B^M\| = \|H^M\| \quad (24)$$

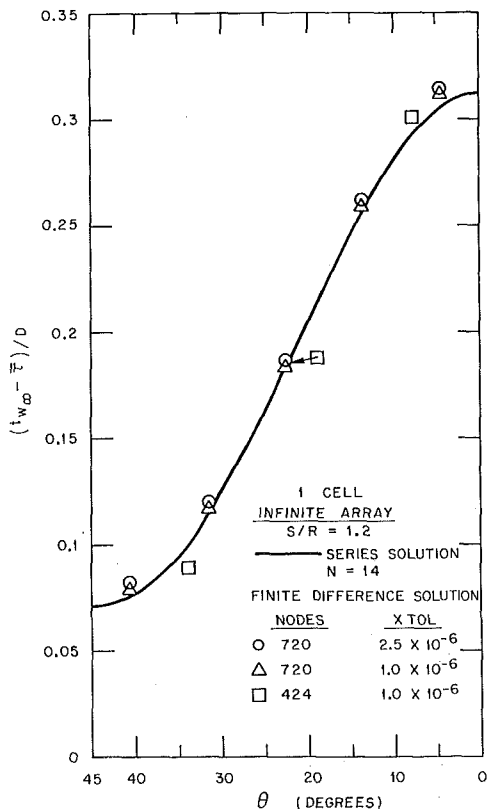


Fig. 3 Comparison of solutions to the infinite-array problem

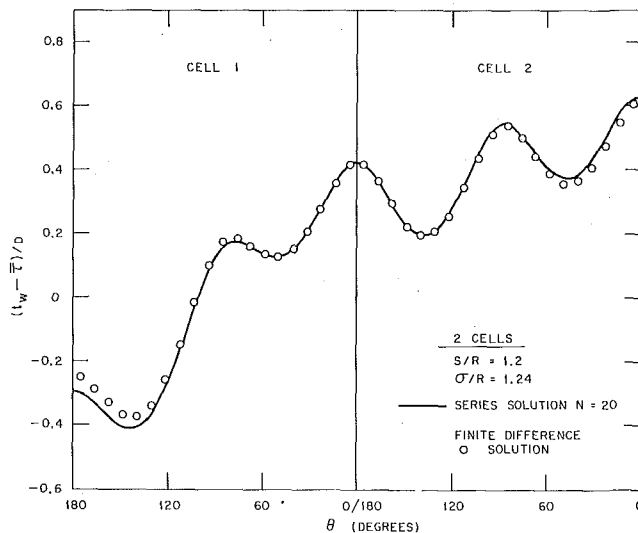


Fig. 4 Comparison of solutions to the two-cell problem

Results

The finite-difference and series solutions to the infinite-array problem ($\sigma = s$) are compared in Fig. 3. Solutions are presented for the rod surface temperature. The series solution was obtained for a single rod in an infinite square array by direct application of the method described in [2]. Fifteen terms ($N = 14$) were found to be sufficient for convergence of the series, where only every fourth term was included, i.e., $n = 0, 4, 8, \dots, 56$. The finite-difference results are presented for computer runs with two total numbers of nodes, and for two values of XTOL. For 720 nodes, and for $XTOL = 1.0 \times 10^{-6}$, the finite-difference solution agrees with the series solution, within 5 percent. It should be noted that the estimated roundoff error in THTB leads

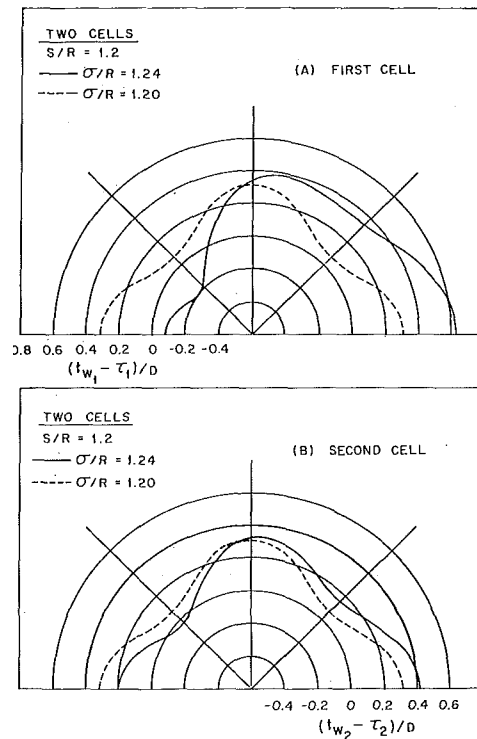


Fig. 5 Two-cell and infinite-array rod-wall temperatures

to an uncertainty of approximately 2-3 percent in the finite-difference solution. From the results discussed below, the numerical evaluation of the series solution is also considered to be accurate to ± 3 percent. Note that the nondimensional temperatures plotted in Fig. 3 are divided by the geometrical factor, D , so that solutions for different values of M are comparable.

The finite-difference and series solutions to the two-cell problem for $\sigma/S = 1.033$ are compared in Fig. 4. The series solution was obtained from equations (26) with $M = 2$; the boundary conditions for multi-cell problems, as specified in the "Series Solution" section of this paper, were applied. Fig. 4 shows that, except for the portion of the rod in cell 1 immediately adjacent to the wall ($120 \text{ deg} < \theta < 180 \text{ deg}$), the agreement between the finite-difference and series solutions to the two-cell problem is excellent. A comparison of computer execution time for the two solution methods is interesting. The finite-difference solution required 2598 iterations, and ran approximately 45 min on the CDC-3600. The series solution, using 20 terms in the series expansion, ran approximately 2 min on the same machine.

Figs. 5(A) and 5(B) show the rod-wall temperature distributions obtained from solution of the two-cell problem ($M = 2$). Two solutions are presented; the infinite-array ($\sigma/R = 1.20$) case, and the extended wall case of $\sigma/R = 1.24$. The two solutions are compared on the basis of the difference between the rod-wall temperature and the bulk temperature of the cell adjacent to the rod. Note that the temperature distribution around the rod in the second cell for $\sigma/R = 1.24$ is close to the infinite-array solution. Similar solutions have been obtained for $M > 2$. The results are entirely analogous, although difficult to represent graphically in a clear manner.

The solution to the eight-cell problem ($M = 8$) is shown in Fig. 6. The dimensionless surface temperatures are presented for each of the eight rods. These results clearly show that the solution for cells far removed from the wall approaches the infinite-array solution.

The number of cells chosen to model the semi-infinite-array problem affects the accuracy of the solution. This effect is shown in Fig. 7. Solutions for the cell adjacent to the wall are

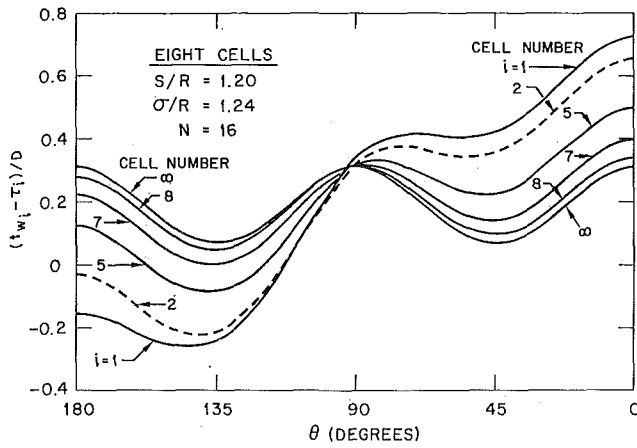


Fig. 6 Rod-wall temperatures for semi-infinite array

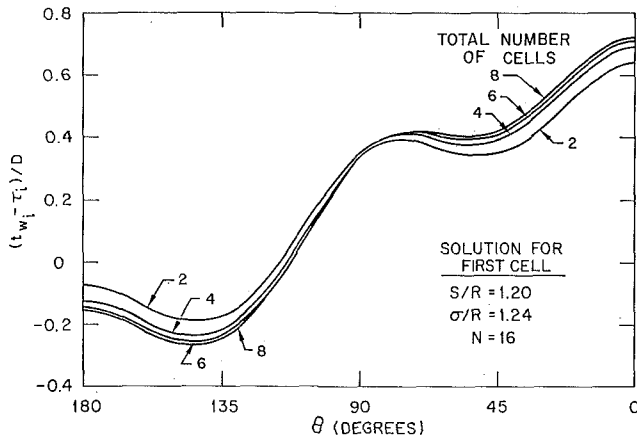


Fig. 7 Comparison of first-cell solution for various values of M

shown for the cases of $M = 2, 4, 6,$ and 8 . Clearly, the accuracy of the solution improves as the number of cells considered in the analysis is increased. The maximum difference between the solutions for $M = 6$ and $M = 8$ is 6 percent.

The Nusselt numbers for the cases $M = 2, 4, 6,$ and 8 are presented in Fig. 8. The Nusselt number of the i th cell, based on the fuel-rod diameter is

$$Nu_i = \frac{2D}{t_{wi}^* - \tau_i} \quad (29)$$

where the average wall temperature, t_{wi}^* is given by

$$t_{wi}^* = \frac{1}{\pi} \int_0^\pi t_{wi}(\theta) d\theta \quad (30)$$

The Nusselt numbers calculated from the cases of $M = 4$ and $M = 8$ agree within ± 0.5 percent. Further, the solution for $M = 8$ shows that the Nusselt numbers of cells 2 through 8 are within 0.5 percent of Nu_∞ . It is interesting to note that the Nusselt numbers are considerably less sensitive to the number of cells used in the computation than the local temperatures. In addition, only the Nusselt number of the rod immediately adjacent to the wall is appreciably affected by the wall. These results indicate that, for the geometry considered here, infinite-array Nusselt numbers may be applied with little error to all rods in the semi-infinite array with the exception of those immediately adjacent to the bounding wall. For these rods, the Nusselt numbers are 5 percent lower than Nu_∞ .

The bulk temperatures as a function of cell number are shown

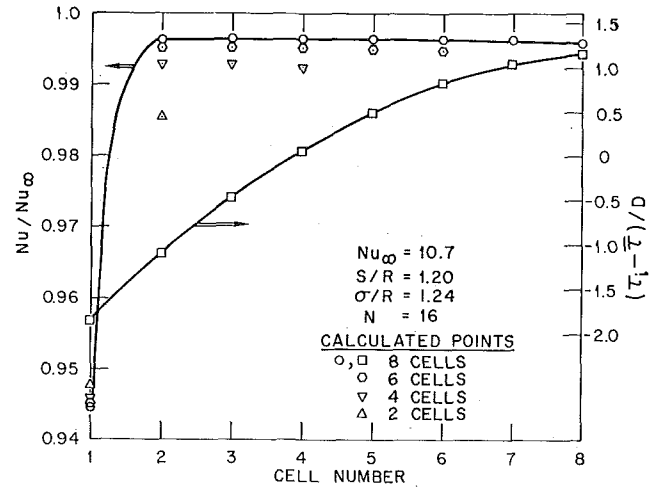


Fig. 8 Cellular Nusselt numbers and bulk temperatures

in Fig. 8 for $M = 8$. These temperatures are related to the overall bulk temperature, $\bar{\tau}$ by equation (19).

Concluding Remarks

The results of the analytical method presented here, and used to compute the fully-developed temperature distribution of a fluid flowing parallel to a square array of circular heat-generating rods, compared favorably to a finite-difference solution. The former is an extension of the series solution technique for satisfying boundary conditions on irregular boundaries to multi-cell problems.

It is of interest to note that if an additional M cells were added to the right-hand side of Fig. 1(B), with the last cell the mirror image of cell 1, the solutions presented here for $M = 2, 4, 6,$ and 8 would be the actual solution for arrays with 4, 8, 12, and 16 rods in a row respectively. The right-hand boundary of cell M would then be the line of symmetry of a square array of rods with a total of $2M$ rods in each row.

References

- 1 Sparrow, E. M., "Temperature Distribution and Heat-Transfer Results for an Internally Cooled, Heat-Generating Solid," *JOURNAL OF HEAT TRANSFER, TRANS. ASME, Series C, Vol. 82, No. 4, Nov. 1960, pp. 389-392.*
- 2 France, D. M., "Analytical Solution to Steady-State Heat-Conduction Problems With Irregularly Shaped Boundaries," ASME Paper No. 71-HT-P; to be published in *JOURNAL OF HEAT TRANSFER.*
- 3 Shih, F. S., "On the Temperature Field of a Square Column Embedding a Heating Cylinder," *AICHE Journal, Vol. 16, 1970, pp. 134-138.*
- 4 Sparrow, E. M., and Haji-Sheikh, A., "Flow and Heat Transfer in Ducts of Arbitrary Shape With Arbitrary Thermal Boundary Conditions," *JOURNAL OF HEAT TRANSFER, TRANS. ASME, Series C, Vol. 88, No. 4, Nov. 1966, pp. 351-358.*
- 5 Nijsing, R., and Eifer, W., "Analysis of Liquid Metal Heat Transfer in Assemblies of Closely Spaced Fuel Rods," *Nuclear Engineering and Design, Vol. 10, 1969, pp. 21-54.*
- 6 Schmid, J., "Longitudinal Flow in an Array of Circular Cylinders," *International Journal of Heat and Mass Transfer, Vol. 9, 1966, pp. 925-937.*
- 7 Stephens, G. L., and Campbell, D. J., "Program THTB for Analysis of General Transient Heat Transfer Systems," General Electric Technical Information Series R60FPD647, 1961.
- 8 Dwyer, O. E., and Berry, H. C., "Slug-Flow Nusselt Numbers for In-Line Flow Through Unbaffled Rod Bundles," *Nuclear Science and Engineering, Vol. 39, 1970, pp. 143-150.*
- 9 Dwyer, O. E., "Analytical Study of Heat Transfer to Liquid-Metals Flowing In-Line Through Closely Packed Rod Bundles," *Nuclear Science and Engineering, Vol. 25, 1966, pp. 343-358.*
- 10 Dwyer, O. E., and Berry, H. C., "Laminar-Flow Heat Transfer for In-Line Flow Through Unbaffled Rod Bundles," *Nuclear Science and Engineering, Vol. 42, 1970, pp. 81-88.*

DISCUSSION

R. Ullrich²

The authors have applied a prior developed extension of the boundary-points least-squares method [2] to the convective heat transfer in adjacent cells of a semi-infinite square-array rod bundle. The characteristic feature of this improved method is that it does not rely anymore on specification of a finite number of points on the irregular boundaries, and thus overcomes some of the inherent deficiencies of the usual boundary-points least-squares method.

However, the discussor would like to present some thoughts on which the authors may wish to comment.

First, I would like to comment on the derivation of equation (6) in reference [2]. If the expression $\left(t - \sum_{n=0}^N A_n X_n\right)$ is considered as an error function, one may follow the procedure given by Collatz³ to obtain equation (6).

Second, I would like to comment on equation (16) of the present paper. The formulation of the j th cell seems to be a bit arbitrary. Changing the procedure for Q and t , it cannot be expected to obtain the same result. For instance, concentrating on the right boundary of cell j , the unknowns B_k^j are affected by the temperature condition and B_k^{j+1} by the heat-flux condition. Now, exchanging Q and t will result in an exchange of the effects. Therefore, in view of accuracy it seems to be more convenient to use the following condition:

$$\frac{\partial}{\partial B_k^j} \left[\int_0^{\pi/4} [a(t_j - t_{j+1})^2 + b(Q_j + Q_{j+1})^2] d\theta + \int_{\pi/4}^{3\pi/4} bQ_j^2 d\theta + \int_{3\pi/4}^{\pi} [a(t_{j-1} - t_j)^2 + b(Q_{j-1} + Q_j)^2] d\theta \right] = 0 \quad (31)$$

² Dipl.-Ing. R. Ullrich, Rechenzentrum der Universität Hamburg, Rothenbaumchaussee 81, D-2000 Hamburg, Germany.

³ Collatz, L., *The Numerical Treatment of Differential Equations*, Springer, Berlin, Göttingen, Heidelberg, 3rd ed., 1960.

In this equation, a and b are positive weighting functions, and $\partial/\partial B_k^j$ designates a differentiation of all coefficients B_k with respect to the cell j . This procedure does not increase the numerical effort, since the number of equations to be used remains unchanged.

Third, I would like to comment on the possible generalization of the authors' procedure. In case of cells with more than two adjacent cells to be considered in the analysis—a situation which occurs in finite hexagonal rod bundles—it seems to be rather difficult to extend their method. In those cases, equations of the form of equation (6) may be both necessary and useful calculational devices.

Further, it seems rather surprising to me that such a high number of nodes as 720 had to be taken in the comparative finite-difference calculations to insure an agreement of about 5 percent with the analytical results.

Authors' Closure

We wish to thank Mr. Ullrich for his interest in this work and for his preparation of a discussion. With regard to the extension of the procedure presented in this paper to hexagonally arranged fuel-element assemblies, there appears to be no difficulty. It is necessary to integrate over four boundaries per cell in a hexagonal array as compared to three per cell in a square array. The manner in which one chooses to satisfy the Q and t boundary conditions in either array is somewhat arbitrary. On a common boundary between two cells, when integrating in the first cell, the t and Q conditions may be satisfied on consecutive segments of that boundary if desired. We have chosen to use a systematic procedure which satisfies a t or Q condition on the entire boundary. Either method is acceptable under the stipulation that integration in the second cell along this same boundary requires one to satisfy the condition t or Q not satisfied in the first cell. Thus the general procedure for satisfying t and Q conditions on inter-cell boundaries is somewhat flexible as long as one observes the stipulation mentioned above.

It would be interesting to see results of an analysis employing equation (31) of the Discussion. The effect on the temperature results due to the redundancy in satisfying t and Q conditions via equation (31) is not apparent, nor is the compensating effect of the weighting functions a and b .

B. ZELDIN

Senior Engineer,
Jet Propulsion Laboratory,
Pasadena, Calif.

F. W. SCHMIDT

Professor of Mechanical Engineering,
The Pennsylvania State University,
University Park, Pa.

Developing Flow with Combined Forced-Free Convection in an Isothermal Vertical Tube¹

The influence of gravity on developing forced, laminar flow in a vertical isothermal tube was investigated by means of a numerical analysis and an associated experiment. Numerically predicted velocity profiles and Nusselt numbers for combined forced-free convection with $Gr/Re = -30$ are compared with their counterparts for pure forced convection, $Gr/Re = 0$, for air with $Re = 500$. The analysis was performed for both the uniform irrotational and the fully developed velocity entrance models. Velocity profiles were measured in a vertical-tube apparatus designed to provide an approximately uniform entrance velocity using air as the test fluid. These are compared with numerical predictions based on test conditions.

Introduction

FLUID MOTION may, under certain circumstances, be strongly influenced by the presence of gravity by virtue of the body force field induced, whose magnitude at a given point is proportional to the local fluid density. The classical example is free convection in which fluid motion occurs in otherwise quiescent fluid as a consequence of distortions in the gravitational body force field caused by density nonuniformities. At the other extreme is the type of flow referred to here as pure forced convection, whose basic character is uninfluenced by gravity. A flow of this nature, however, is usually a limiting case which exists only in concept—for example, the forced flow of a constant-density fluid. More common is the forced flow which, because of density nonuniformities, is influenced to some extent by gravity. When the gravitational effect is significant, this flow is classified as combined forced-free convection.

In the present study, an attempt was made to determine the influence of gravity on the hydrodynamic and thermal characteristics of forced flow in a long vertical tube maintained at a uniform temperature T_w . Two physical models were considered. Fig. 1(a) shows fluid at temperature T_e entering a tube through a well-rounded contraction section designed to provide an approximately uniform entrance velocity. In Fig. 1(b), the tube entrance, defined as $z = 0$, is preceded by a long section of tube maintained at temperature T_e which is intended to provide approximately fully developed entrance velocity and uniform en-

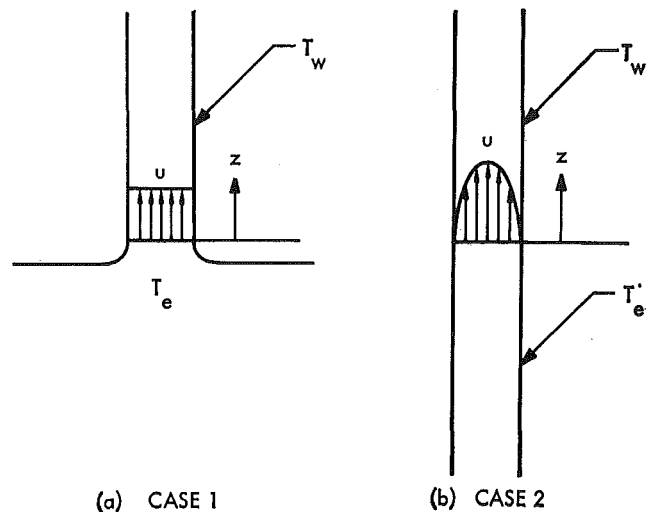


Fig. 1 Entrance configurations

trance temperature. For either entrance configuration, the tube was presumed to be long enough to permit the fluid temperature to approach T_w and the velocity to eventually become fully developed, in which case, $u = 2u_m[1 - (r/r_0)^2]$ and $v = 0$.

The investigation was limited to laminar flows in which the effect of gravity is to accelerate the fluid near the wall of the tube. The implication is that either $T_w > T_e$ if the flow is upward, or $T_w < T_e$ if the flow is downward. The experimental portion of the research was restricted to the case of uniform entrance velocity.

One of the features of the analysis is that the boundary-layer assumptions were not invoked; consequently, the natural elliptic character of the system of conservation equations was preserved.

¹ This work was sponsored by The Pennsylvania State University Department of Mechanical Engineering while the senior author was a National Science Foundation trainee there.

Contributed by the Heat Transfer Division and presented at the ASME-AIChE Heat Transfer Conference, Tulsa, Okla., August 15-18, 1971. Manuscript received by the Heat Transfer Division July 31, 1970. Paper No. 71-HT-6.

The boundary-value problem defined by the conservation equations and the appropriate boundary conditions was solved numerically. A method proposed by Allen [1]² was used to form the difference equations. The numerical analysis was developed for an arbitrary Newtonian fluid; however, the solutions presented were generated specifically for air.

Previous Related Studies

Pure forced convection can be regarded as a limiting case of combined forced-free convection. For this special flow category, the continuity and momentum equations may be solved independently of the energy equation. Early attempts to predict velocity distributions for this class of problems centered about the concept of the boundary layer and made use of the boundary-layer assumptions. These assumptions reduced the equations of motion to a parabolic system which led to initial-value problems. Numerous methods were developed to handle problems of this type. Schiller [2], for example, analyzed the hydrodynamic entrance region of tubes and parallel-plate channels by use of an integral technique. Schlichting [3], on the other hand, used a method in which a perturbation of Blasius' boundary-layer solution, used in the near entrance region, was axially patched to a perturbation of the fully developed velocity profile used farther downstream. Langhaar [4] proposed an approach in which the axial momentum equation is linearized. Finite-difference methods were employed by Hornbeck [5] and Christiansen and Lemmon [6] for analyzing flow in tubes. Of greater significance to the present study was the work of Wang and Longwell [7], who solved the elliptic equations of motion for flow between parallel plates by use of a finite-difference technique based on Allen's method [1]. The elliptic equations of motion were later solved by Vrentas, Duda, and Barger [8] for flow in a tube. Their finite-difference solution utilized the Taylor-series approach. Schmidt and Zeldin [9, 10] also obtained numerical solutions to the elliptic equations of motion for flow in a tube using Allen's method to form the difference equations. Goldberg [11] numerically solved the energy equation for flow in a tube using Langhaar's [4] developing velocity profiles. Axial conduction was neglected. Sellars, Tribus, and Klein [12] and Mercer [13, 14] obtained infinite-series solutions to the energy equation for fully developed hydrodynamic flow in both tubes and parallel-plate channels. Axial conduction was neglected in both instances. Millsaps and Pohlhausen [15] and Singh [16] obtained series

solutions for the same problem for flow in a tube. This time, however, axial conduction was considered. Schmidt and Zeldin [17] employed a numerical solution based on Allen's method to solve the energy equation for both tubes and parallel plates. Again, the velocity was fully developed and axial conduction was included.

Most combined forced-free convection studies for vertical ducts assume a uniform wall heat flux, and fully developed flow is presumed to exist. When the flow is fully developed, the uniform-wall-heat-flux condition is equivalent to the condition of axially linear varying wall temperature. Ostrach [18] studied flow between vertical parallel plates with linear varying wall temperature. Viscous dissipation was included. Mori [19] and Yu [20] considered the effect of a magnetic field parallel to the gravitational body force for flow between parallel plates. In both cases the walls were assumed to be perfect electrical conductors. Srinivasan [21] extended the analysis to include the effect of walls with finite electrical conductivity. Carter and Gill [22], and Gill, Del Casal, and Zeh [23] considered uniform suction and injection under the assumption of similar velocity profiles for flow in both horizontal and vertical channels. Han [24] analyzed the flow of a heat-generating fluid in a vertical rectangular duct with linear varying wall temperature. The same problem was later solved using alternative methods by Tao [25] and Agrawal [26]. Hallman [27] and Hanratty, Rosen, and Kabel [28] studied fully developed flow in vertical tubes.

Lawrence and Chato [29] considered developing flow for combined forced-free convection in a vertical tube with uniform wall heat flux. An experiment using water was performed in addition to obtaining a numerical solution to the boundary-layer-type conservation equations. In their numerical analysis, the entrance velocity and temperature were assumed to be uniform. An integral technique based on boundary-layer theory was used by Murakawa [30] to study developing flow between vertical concentric tubes. The wall temperature of the inner tube was assumed to be an arbitrary function of axial position. Worsøe-Schmidt and Leppert [31] developed a finite-difference solution for flow of an ideal gas in a vertical tube with uniform heat flux. The entrance velocity was assumed to be fully developed and the entrance temperature was uniform. The boundary-layer assumptions were used to simplify the solution.

Description of the Flow Model

The conservation equations, which are capable of describing a very general flow, may be simplified considerably by making

² Numbers in brackets designate References at end of paper.

Nomenclature

c = transformation parameter	P = dimensionless pressure,	z = axial coordinate
c_v = specific heat at constant volume	$(g_c p + \rho g z) / \rho u_m^2$	Z = dimensionless axial coordinate,
e = base of the Napierian logarithm	Pe = modified Peclet number,	z/r_0
g = modulus of the gravitational-acceleration vector	$Re(c_v \mu / K)$	β = volumetric coefficient of expansion, $-(1/\rho)(\partial \rho / \partial T)_p$
g_c = conversion factor, 32.174 lb _m -ft/lb _f -sec ²	r = radial coordinate	ϵ = dimensionless pressure parameter, $\kappa \rho r_0 g / g_c$
Gr = Grashof number,	r_0 = radius of tube	ξ = dimensionless axial coordinate,
$g\beta(T_e - T_w) r_0^3 / \nu^2$	R = dimensionless radial coordinate,	$1 - 1/(1 + cZ)$
h = local heat-transfer coefficient	r/r_0	θ = dimensionless temperature,
h^* = local heat-transfer coefficient based on bulk temperature	Re = Reynolds number, $2r_0 u_m / \nu$	$(T - T_w) / (T_e - T_w)$
\bar{h} = average heat-transfer coefficient	T = temperature	θ_b = dimensionless bulk temperature,
i = axial position index	T_b = bulk temperature	$(T_b - T_w) / (T_e - T_w)$
j = radial position index	T_e = fluid entrance temperature	κ = isothermal compressibility,
K = thermal conductivity	T_w = tube-wall temperature	$(1/\rho)(\partial \rho / \partial p)_T$
Nu = local Nusselt number, $2hr_0/K$	u = axial velocity	μ = dynamic viscosity
Nu^* = local Nusselt number, $2h^*r_0/K$	u_m = mean axial velocity,	ν = kinematic viscosity, μ/ρ
\bar{Nu} = average Nusselt number, $2\bar{h}r_0/K$	$(2/r_0^2) \int_0^{r_0} r u dr$	ρ = mass density
p = pressure	U = dimensionless axial velocity, u/u_m	ψ = dimensionless stream function
	v = radial velocity	Ω = dimensionless vorticity,
	V = dimensionless radial velocity,	$\partial V / \partial Z - \partial U / \partial R$
	v/u_m	

various idealized assumptions with regard to the flow description and the physical properties of the fluid involved. In this study, it was assumed that the flow is laminar, steady, and axially symmetric and that the fluid is Newtonian and possesses constant dynamic viscosity, thermal conductivity, specific heat, and coefficient of expansion. Furthermore, spatial density variations were presumed to be negligible except insofar as they modify the gravitational body force. Viscous dissipation was ignored.

Subject to the listed assumptions and taking into account the vertical orientation of the tube, the dimensionless continuity, momentum, and energy equations become

$$\frac{\partial U}{\partial Z} + \frac{\partial V}{\partial R} + \frac{V}{R} = 0 \quad (1)$$

$$U \frac{\partial U}{\partial Z} + V \frac{\partial U}{\partial R} = -\frac{\partial P}{\partial Z} + \frac{2}{\text{Re}} \left[\frac{\partial^2 U}{\partial Z^2} + \frac{1}{R} \frac{\partial}{\partial R} \left(R \frac{\partial U}{\partial R} \right) \right] - \frac{4}{\text{Re}^2} \left(\frac{gr_0^3}{\nu^2} \right) \left(\frac{\rho' - \rho}{\rho} \right) \quad (2)$$

$$U \frac{\partial V}{\partial Z} + V \frac{\partial V}{\partial R} = -\frac{\partial P}{\partial R} + \frac{2}{\text{Re}} \left[\frac{\partial^2 V}{\partial Z^2} + \frac{1}{R} \frac{\partial}{\partial R} \left(R \frac{\partial V}{\partial R} \right) - \frac{V}{R^2} \right] \quad (3)$$

$$U \frac{\partial \theta}{\partial Z} + V \frac{\partial \theta}{\partial R} = \frac{2}{\text{Pe}} \left[\frac{\partial^2 \theta}{\partial Z^2} + \frac{1}{R} \frac{\partial}{\partial R} \left(R \frac{\partial \theta}{\partial R} \right) \right] \quad (4)$$

A reduced system of equations will now be developed. When equations (2) and (3) are differentiated by R and Z , respectively, and $\partial^2 P / \partial R \partial Z$ is equated to $\partial^2 P / \partial Z \partial R$, the result is

$$\begin{aligned} & \frac{\partial^2}{\partial Z^2} \left(\frac{\partial V}{\partial Z} - \frac{\partial U}{\partial R} \right) + \frac{\partial^2}{\partial R^2} \left(\frac{\partial V}{\partial Z} - \frac{\partial U}{\partial R} \right) \\ & + \frac{1}{R} \frac{\partial}{\partial R} \left(\frac{\partial V}{\partial Z} - \frac{\partial U}{\partial R} \right) - \frac{1}{R^2} \left(\frac{\partial V}{\partial Z} - \frac{\partial U}{\partial R} \right) \\ & = \frac{\text{Re}}{2} \left[U \frac{\partial}{\partial Z} \left(\frac{\partial V}{\partial Z} - \frac{\partial U}{\partial R} \right) + V \frac{\partial}{\partial R} \left(\frac{\partial V}{\partial Z} - \frac{\partial U}{\partial R} \right) \right. \\ & \quad \left. - \frac{V}{R} \left(\frac{\partial V}{\partial Z} - \frac{\partial U}{\partial R} \right) \right] - \frac{2}{\text{Re}} \frac{gr_0^3}{\nu^2} \frac{1}{\rho} \frac{\partial \rho'}{\partial R} \quad (5) \end{aligned}$$

The last term in equation (5), which is proportional to the radial gradient of the gravitational body force, is modified as follows. For an equation of state of the form $\rho' = \rho'(T, p)$,

$$\frac{\partial \rho'}{\partial R} = \frac{\partial \rho'}{\partial T} \frac{dT}{dR} + \frac{\partial \rho'}{\partial p} \frac{\partial p}{\partial R}$$

The volumetric coefficient of expansion and the isothermal compressibility are

$$\beta = -\frac{1}{\rho'} \frac{\partial \rho'}{\partial T} \approx -\frac{1}{\rho} \frac{\partial \rho'}{\partial T}$$

and

$$\kappa = \frac{1}{\rho'} \frac{\partial \rho'}{\partial p} \approx \frac{1}{\rho} \frac{\partial \rho'}{\partial p}$$

respectively. From the definitions of θ and P ,

$$\frac{dT}{d\theta} = T_e - T_w$$

and

$$\frac{\partial p}{\partial P} = \frac{\rho u_m^2}{g_c}$$

With the aid of these expressions, it follows that

$$-\frac{2}{\text{Re}} \frac{gr_0^3}{\nu^2} \frac{1}{\rho} \frac{\partial \rho'}{\partial R} \approx 2 \frac{\text{Gr}}{\text{Re}} \frac{\partial \theta}{\partial R} - \epsilon \frac{\text{Re}}{2} \frac{\partial P}{\partial R}$$

where

$$\text{Gr} = \frac{g\beta}{\nu^2} (T_e - T_w)r_0^3$$

and

$$\epsilon = \kappa \rho \frac{g}{g_c} r_0$$

A separate analysis conducted to evaluate the significance of

$$\epsilon \frac{\text{Re}}{2} \frac{\partial P}{\partial R}$$

on the computed velocity and temperature distributions revealed that this term can be ignored if $0 \leq \epsilon \leq 10^{-3}$. Typical values of ϵ fall well within this range. Consequently, the term was dropped.

By substituting equation (5) for equations (2) and (3) and introducing the dimensionless stream function ψ and the dimensionless vorticity Ω defined by

$$-\frac{1}{R} \frac{\partial \psi}{\partial R} = U, \quad \frac{1}{R} \frac{\partial \psi}{\partial Z} = V$$

and

$$\Omega = \frac{\partial V}{\partial Z} - \frac{\partial U}{\partial R},$$

one obtains the following system:³

$$\frac{\partial^2 \psi}{\partial Z^2} + \frac{\partial^2 \psi}{\partial R^2} - \frac{1}{R} \frac{\partial \psi}{\partial R} = \Omega R \quad (6)$$

$$\begin{aligned} & \frac{\partial^2 \Omega}{\partial Z^2} + \frac{\partial^2 \Omega}{\partial R^2} + \frac{1}{R} \frac{\partial \Omega}{\partial R} - \frac{\Omega}{R^2} \\ & = \frac{\text{Re}}{2} \left(\frac{1}{R} \frac{\partial \psi}{\partial Z} \frac{\partial \Omega}{\partial R} - \frac{1}{R} \frac{\partial \psi}{\partial R} \frac{\partial \Omega}{\partial Z} - \frac{\Omega}{R^2} \frac{\partial \psi}{\partial Z} \right) + 2 \frac{\text{Gr}}{\text{Re}} \frac{\partial \theta}{\partial R} \quad (7) \end{aligned}$$

$$\frac{\partial^2 \theta}{\partial Z^2} + \frac{\partial^2 \theta}{\partial R^2} + \frac{1}{R} \frac{\partial \theta}{\partial R} = \frac{\text{Pe}}{2} \left(\frac{1}{R} \frac{\partial \psi}{\partial Z} \frac{\partial \theta}{\partial R} - \frac{1}{R} \frac{\partial \psi}{\partial R} \frac{\partial \theta}{\partial Z} \right) \quad (8)$$

For the general case of flow in a tube, the boundary conditions on $Z = 0$ are not known explicitly. They are determined not only by the particular geometry of the physical or stream-tube boundaries of the upstream (i.e., $Z < 0$) as well as the downstream regions but depend also on the hydrodynamic and thermal conditions on the boundaries and on $Z = \pm \infty$. The loss of generality inherent in rigidly specifying the upstream region and the considerable increase in computational effort required made this approach impractical. Instead, the boundary conditions on $Z = 0$ were postulated with the underlying assumption that the upstream region is such that these conditions are met, at least approximately.

Two different hydrodynamic entrance conditions were considered. In case 1, the entrance velocity is uniform and irrotational while in case 2, it is fully developed. In both cases the entrance temperature is uniform. For the region $Z \geq 0$, the temperature of the tube is uniform but different from the entrance temperature. Far downstream, the fluid attains the temperature of the tube, and the velocity becomes fully developed.

Since the stream function was defined only in terms of its derivatives, it may be specified arbitrarily at one point. For convenience, we set $\psi = 0$ at $Z = 0, R = 1$. Taking advantage of

³ Equation (6) is merely the definition of Ω expressed in terms of ψ . Equation (1) is not included in the new system since it is automatically satisfied by ψ .

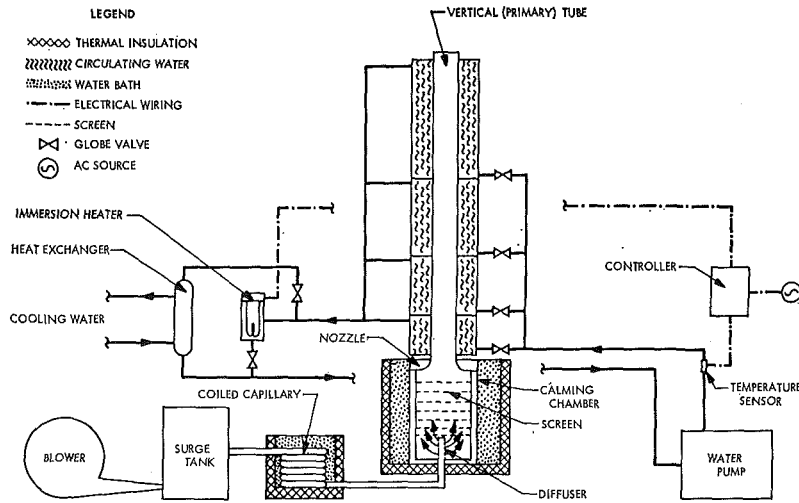


Fig. 2 Cross section of experimental apparatus

symmetry about $R = 0$ results in the following boundary conditions:

$$\left. \begin{aligned} \psi &= \psi_e(R), \quad \Omega = \Omega_e(R), \quad \theta = 1 && \text{for } Z = 0, \quad 0 \leq R < 1 \\ \psi &= \frac{1}{2}(1 - R^2)^2, \quad \Omega = 4R, \quad \theta = 0 && \text{for } Z = \infty, \quad 0 \leq R \leq 1 \\ \psi &= \frac{1}{2}, \quad \Omega = 0, \quad \frac{\partial \theta}{\partial R} = 0 && \text{for } 0 < Z < \infty, \quad R = 0 \\ \psi &= 0, \quad \frac{\partial \psi}{\partial R} = 0, \quad \theta = 0 && \text{for } 0 \leq Z < \infty, \quad R = 1 \end{aligned} \right\}$$

where

$$\psi_e(R) = \frac{1}{2}(1 - R^2), \quad \Omega_e(R) = 0 \quad \text{for case 1}$$

and

$$\psi_e(R) = \frac{1}{2}(1 - R^2)^2, \quad \Omega_e(R) = 4R \quad \text{for case 2.}$$

(9)

Axial Coordinate Transformation

The semi-infinite domain $0 \leq Z < \infty, 0 \leq R \leq 1$ was transformed to the finite domain $0 \leq \xi < 1, 0 \leq R \leq 1$ utilizing the function $\xi = 1 - 1/(1 + cZ)$. The transformed equations are

$$\left(\frac{d\xi}{dZ}\right)^2 \frac{\partial^2 \psi}{\partial \xi^2} + \frac{d^2 \xi}{dZ^2} \frac{\partial \psi}{\partial \xi} + \frac{\partial^2 \psi}{\partial R^2} - \frac{1}{R} \frac{\partial \psi}{\partial R} = \Omega R \quad (10)$$

$$\left(\frac{d\xi}{dZ}\right)^2 \frac{\partial^2 \Omega}{\partial \xi^2} + \frac{d^2 \xi}{dZ^2} \frac{\partial \Omega}{\partial \xi} + \frac{\partial^2 \Omega}{\partial R^2} + \frac{1}{R} \frac{\partial \Omega}{\partial R} - \frac{\Omega}{R^2}$$

$$= \frac{\text{Re}}{2} \left(\frac{1}{R} \frac{d\xi}{dZ} \frac{\partial \psi}{\partial \xi} \frac{\partial \Omega}{\partial R} - \frac{1}{R} \frac{\partial \psi}{\partial R} \frac{d\xi}{dZ} \frac{\partial \Omega}{\partial \xi} - \frac{\Omega}{R^2} \frac{d\xi}{dZ} \frac{\partial \psi}{\partial \xi} \right)$$

$$+ \frac{2\text{Gr}}{\text{Re}} \frac{\partial \theta}{\partial R} \quad (11)$$

$$\left(\frac{d\xi}{dZ}\right)^2 \frac{\partial^2 \theta}{\partial \xi^2} + \frac{d^2 \xi}{dZ^2} \frac{\partial \theta}{\partial \xi} + \frac{\partial^2 \theta}{\partial R^2} + \frac{1}{R} \frac{\partial \theta}{\partial R}$$

$$= \frac{\text{Pe}}{2} \left(\frac{1}{R} \frac{d\xi}{dZ} \frac{\partial \psi}{\partial \xi} \frac{\partial \theta}{\partial R} - \frac{1}{R} \frac{\partial \psi}{\partial R} \frac{d\xi}{dZ} \frac{\partial \theta}{\partial \xi} \right) \quad (12)$$

where

$$\frac{d\xi}{dZ} = c(1 - \xi)^2$$

and

$$\frac{d^2 \xi}{dZ^2} = -2c^2(1 - \xi)^3.$$

The boundary conditions, equations (9), are unchanged except that $Z = 0$ and $Z = \infty$ are replaced by $\xi = 0$ and $\xi = 1$, respectively. It should be pointed out that the transformation fails to be one-to-one at $Z = \infty$. This causes no difficulties, however, since equations (10)–(12) need only be satisfied for $0 < Z < \infty$.

Numerical Approach

The exact solution to the boundary-value problem formulated consists of mathematical expressions ψ , Ω , and θ , which satisfy the differential equations, equations (10)–(12), at every interior point of the solution domain $G = \{(\xi, R): 0 \leq \xi \leq 1, 0 \leq R \leq 1\}$ and the boundary conditions, equations (9), at every limit point of G . On $R = 0$, however, both the energy equation and $\partial \theta / \partial R = 0$ must be satisfied simultaneously since the latter is not a true boundary condition but is rather a condition of symmetry. Because of the complexity of this problem, no attempt was made to obtain an exact solution. Instead, recourse was taken to an approximation technique—namely, the method of the finite differences.

The solution domain was discretized by partitioning the ξ and R directions according to

$$\xi_i = (i - 1)\Delta\xi \quad i = 1, 2, \dots, I$$

where

$$\Delta\xi = \frac{1}{I - 1}$$

and

$$R_j = \ln \left[1 + (e - 1) \left(\frac{j - 1}{J - 1} \right) \right] \quad j = 1, 2, \dots, J^4$$

Subdividing in this manner yielded a more closely spaced mesh in terms of the physical coordinates z near the entrance and r near the wall, where axial and radial gradients, respectively, were ex-

⁴ The variable spacing in R is equivalent to equal spacing in $f(R) = \frac{(e^R - 1)}{(e - 1)}$.

pected to be large. Preliminary numerical solutions were obtained for both $I = J = 11$ and 21 , but the solutions presented were generated for $I = J = 41$. The transformation parameter c was arbitrarily selected so that roughly 99 percent of the total heat transfer to or from the fluid occurs between $\xi_1 = 0$ and $\xi_{40} = 0.975$. This led to the use of the relationship $c = 39/Pe$. The finite-difference approximations of the various differential equations were formed by Allen's method [1]. The resulting system of nonlinear difference equations was solved using a successive over-relaxation technique in which initial estimates of the unknown values of ψ , Ω , and θ were improved by relaxing first the ψ , then the Ω , and finally the θ difference equations. This sequence of operations was repeated until an estimate for the maximum error at any node due to incomplete convergence for both ψ and θ was less than 1×10^{-5} . This degree of convergence was typically obtained only at the expense of nearly 1300 iteration cycles for $I = J = 41$, with relaxation parameters for the ψ , Ω , and θ difference equations ranging from 0.90 to 0.95, 0.80 to 0.85, and 1.35 to 1.40, respectively. Details of the numerical analysis are presented in [32].

Experimental Program

The experimental program was designed to provide measured temperature and axial-velocity profiles at selected axial positions in a vertical, isothermal tube with a nearly uniform entrance velocity and entrance temperature. Air was selected as the test fluid.

A schematic of the experimental apparatus is shown in Fig. 2. Its principal component is a vertically aligned copper tube (referred to as the primary tube) 14 ft long with an inside diameter of 1.612 in. The temperature of the primary tube was controlled by circulating water in the annulus formed by it and a second, larger-diameter tube. The annular region was partitioned into four sections which were sized so that each would supply approximately the same average heat flux to air flowing through the primary tube for a typical Reynolds number of 500. A combination of cooling and intermittent heating was used to control the temperature of the water, which was supplied by a common inlet header to the four sections. Flow from the discharge header was split into two streams, one of which passed through the tubes of a small shell-and-tube heat exchanger and was cooled to approximately 63 deg F by cold tapwater circulated through the shell. The balance of the flow passed through a small chamber housing an immersion heater. Heater voltage was switched on and off by a controller which utilized as the feedback element a mercury-thermometer-type sensor with an adjustable set point. The actual time-wise and spatial temperature variations of the primary tube were held to less than ± 0.08 deg F. This was determined by direct measurement using twenty thermocouples attached to selected points on its outer surface.

The air circulation system consisted of a centrifugal blower, a surge tank to dampen flow pulsations, a coiled capillary flowmeter, a calming chamber equipped with a converging nozzle to produce a uniform entrance velocity, and the primary tube itself. The coiled capillary flowmeter [33] was made of $5/8$ -in.-OD copper refrigeration tubing and had 12 tightly wrapped coils with a mean diameter of 6.8 in. In order to reduce end effects, the pressure drop was measured with a micromanometer across only the inner 10 coils.

Air entered the calming chamber through a diffuser consisting of a $3/4$ -in.-dia cylinder made of fine brass screen, which was capped on one end. The flow into the open end tended to spread out radially and more or less uniformly across the chamber diameter. The air, after passing through a series of seven fine brass screens used to reduce turbulence and flatten the velocity profile, entered a short (0.490 in.) converging nozzle machined out of Plexiglas. The nozzle was designed according to the V. D. I. specifications presented by Streeter [34].

Both the coiled capillary and the calming chamber were com-

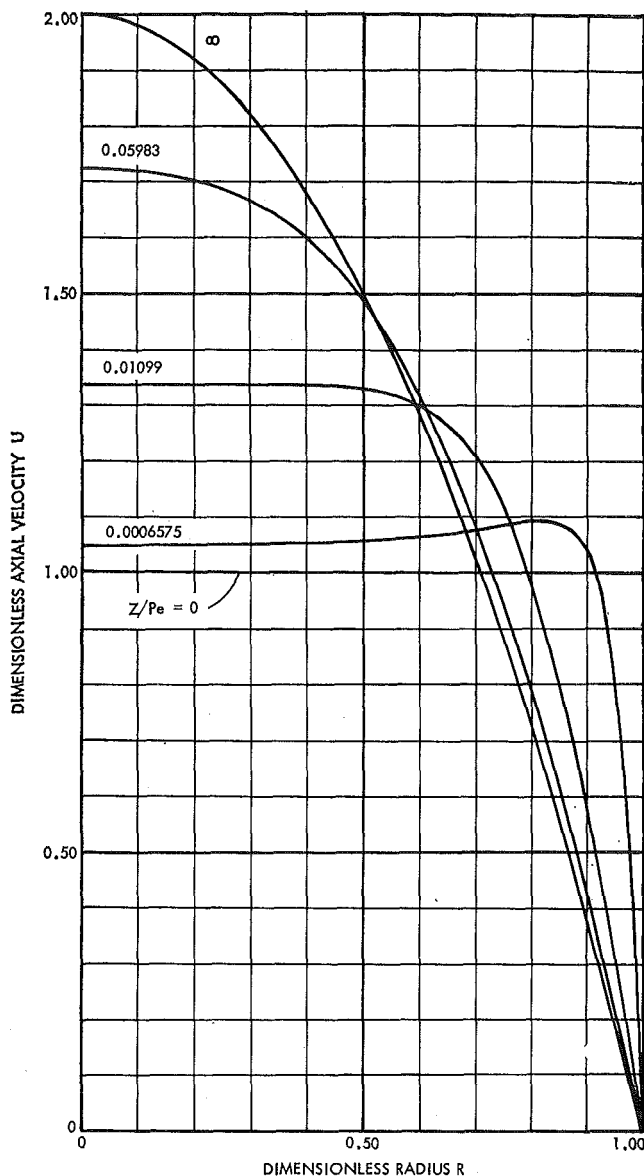


Fig. 3 Dimensionless velocity profiles for uniform entrance velocity and $Gr/Re = 0$

pletely immersed in controlled-temperature water baths in order to establish the temperature of the air entering the primary tube.

Temperature and velocity profiles were measured at $z = 2^{5/16}$, $8^{13/16}$, $23^{13/16}$, $100^{13/16}$, and $164^{13/16}$ in. using a micrometer traversing mechanism. The temperature probe was a No. 30 B. & S. gage, chromel-alumel thermocouple in a 0.059-in.-OD hypodermic tubing sheath.

Velocity measurements were made with a constant-temperature hot-film anemometer system. The sensor portion of the 0.059-in.-dia velocity probe was a platinum hot film 0.001 in. in diameter. Both the velocity and temperature probes were right-angle probes whose 0.25-in.-long tips were pointed toward the oncoming flow.⁵ Because of the rather small velocities involved ($u_m \approx 0.7$ fps), the anemometer bridge voltage varied only slightly over the entire velocity range and, consequently, had to be measured very accurately. A six-place, integrating, digital voltmeter was used to make these measurements.

⁵ The radial velocity component probably had very little effect on velocity measurements. This assertion is supported by consideration of the ratios of computed radial to axial velocity components which indicate that the magnitude of the velocity and its axial component differed by less than 0.01 percent in the region where measurements were actually taken.

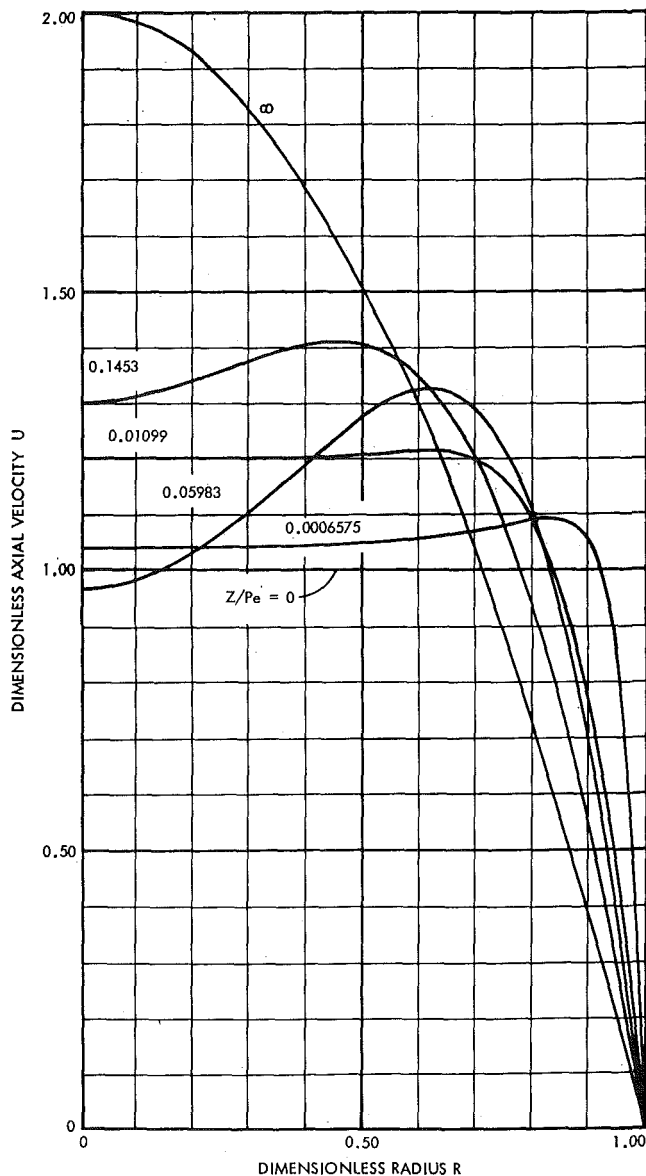


Fig. 4 Dimensionless velocity profiles for uniform entrance velocity and $Gr/Re = -30$

Even though the probe was operated at an overheat ratio of about 1.5, the bridge voltage was found to be extremely sensitive to the temperature of the air flow. To compensate for this effect, a modified King's law, $E_b^2 = (a + bu^c)(d - T)$, was used to correlate the bridge voltage E_b with the velocity u and the temperature T . The free parameters a , b , c , and d were selected using the least-squares criterion for a "best" fit [35].

Results of the Numerical Analysis

The system of difference equations developed was solved with the aid of an IBM Systems 360, Model 67 digital computer. All floating-point computations were performed using double-precision (i.e., 64-bit) arithmetic. Numerical results are presented for $Re = 500$ and $Pe = 252.5$ for both uniform and fully developed entrance velocities. For each of these entrance models, solutions were generated for the case of pure forced convection as well as for combined forced-free convection with $Gr/Re = -30$.

Fig. 3 illustrates the development of the dimensionless axial-velocity profile for the case of uniform irrotational entrance velocity and $Gr/Re = 0$. At $Z/Pe = 0.0006575$, it is evident that the maximum velocity does not occur at the center line.

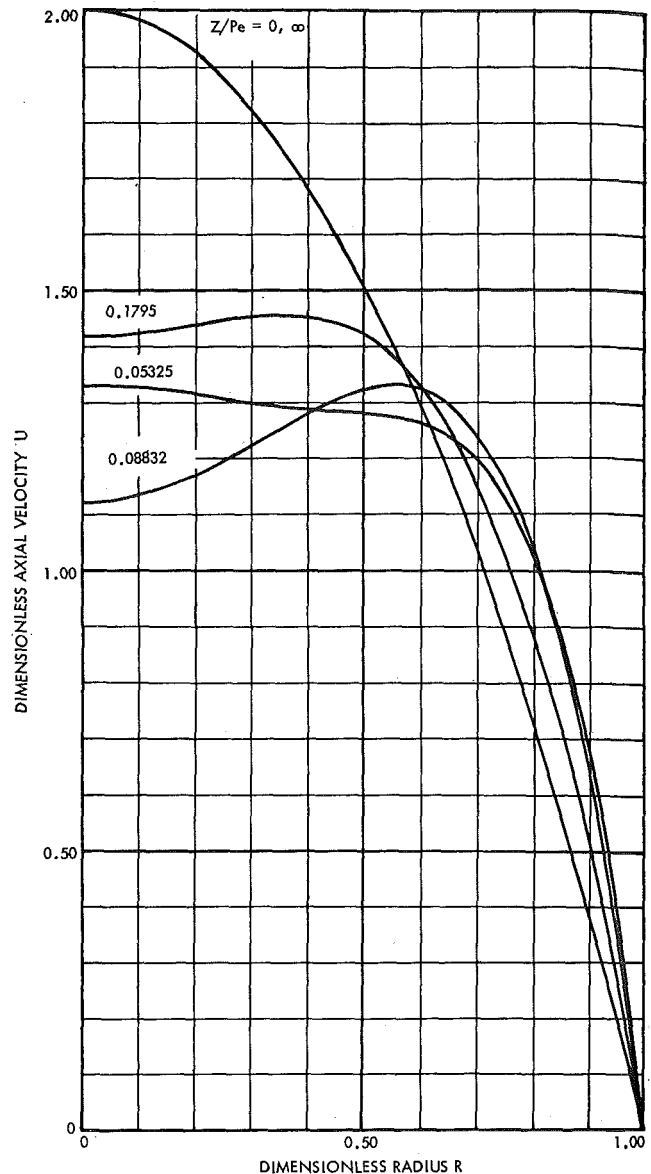


Fig. 5 Dimensionless velocity profiles for fully developed entrance velocity and $Gr/Re = -30$

This central concavity diminishes as Z/Pe increases but does not vanish completely until Z/Pe exceeds 0.0138. Wang and Longwell also reported observing this phenomenon in their numerical solutions. Furthermore, their conjecture that central concavity is a real effect has the support of experimental evidence, as will be discussed later. Vrentas et al. [8] also detected central concavity; however, they concluded that its magnitude increases with Reynolds number. This is in sharp contrast with numerical solutions obtained by Schmidt and Zeldin [10] which clearly indicate that the degree of central concavity decreases as the Reynolds number increases.

The axial-velocity-profile development for $Gr/Re = -30$ is shown in Fig. 4. The profiles for small Z/Pe are essentially similar to those for pure forced convection. However, a bit farther downstream, the center-line velocity decreases dramatically until it reaches a minimum somewhere between $Z/Pe = 0.05983$ and 0.06760 . Beyond this point, the central concavity diminishes. Ultimately, it vanishes altogether and the velocity eventually becomes fully developed. The reason for this behavior can be explained as follows: Consider the fluid in the cross section of the tube at some arbitrary location and let $T_w > T_e$. The temperature of the fluid must increase in the radial di-

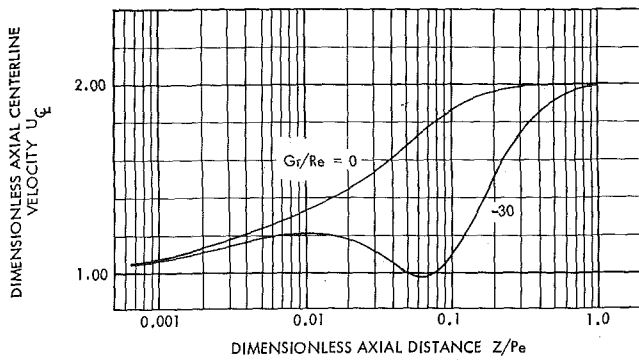


Fig. 6 Development of the dimensionless center-line velocity for uniform entrance velocity

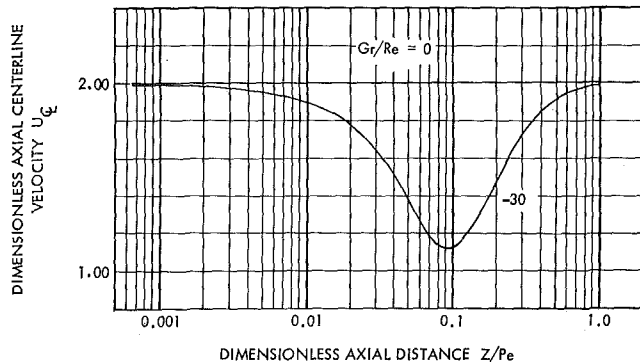


Fig. 7 Development of the dimensionless center-line velocity for fully developed entrance velocity

rection, which for $\beta > 0$ implies that the fluid density decreases with R . Therefore, the decelerative effect of the gravitational body force, which is proportional to the density, decreases in the radial direction. As a result, the fluid near the wall tends to have a higher dimensionless axial velocity than it would have had if Gr/Re were zero, in which case the body force would have been uniformly distributed across the radius. Since $\int_0^1 RUdR$ is invariant, however, the dimensionless axial velocity in the neighborhood of the center line must be correspondingly lower.

As Z/Pe increases, the fluid temperature approaches T_w . Thus, the effect of the gravitational body force ultimately vanishes and the velocity eventually reaches a fully developed state.

Changes in the velocity distribution do not occur in a pure forced convection flow, $Gr/Re = 0$, if the entrance velocity is fully developed. As can be seen in Fig. 5, heat-transfer effects for $Gr/Re = -30$ cause significant changes in the otherwise unchanging velocity profile.

The dependence of the center-line velocity on Gr/Re is clearly illustrated in Figs. 6 and 7. For either entrance condition, the center-line velocity for $Gr/Re = -30$ attains a minimum. Studies using a coarse grid predict that the center-line velocity at the minimum is zero for $Gr/Re \approx -89$ if the entrance velocity is uniform. If it is fully developed, the critical value is about -97 . No numerical solutions could be obtained for Gr/Re less than the critical value for either entrance condition, in the sense that the iteration algorithm could not be forced to converge.

Heat-transfer data are presented in terms of several different Nusselt numbers. The first of these is a local Nusselt number defined as

$$Nu^* = 2r_0 \frac{h^*}{K} \quad (13)$$

where

$$h^* = \frac{K \left. \frac{\partial T}{\partial r} \right|_{r=r_0}}{T_w - T_b} \quad (14)$$

is the local heat-transfer coefficient based on the bulk temperature

$$T_b = \frac{\int_0^{r_0} rTudr}{\int_0^{r_0} rudr} \quad (15)$$

As z increases, Nu^* approaches an asymptote, the value of which is of theoretical interest. Both Nu^* and T_b must be known as a function of axial position, however, if local and average heat fluxes are to be determined. To make these primary quantities more directly attainable, alternative Nusselt numbers are defined which are directly proportional to the local and average wall heat fluxes, respectively. These are

$$Nu = 2r_0 \frac{h}{K} \quad (16)$$

and

$$\bar{Nu} = 2r_0 \frac{\bar{h}}{K} \quad (17)$$

where

$$h = \frac{K \left. \frac{\partial T}{\partial r} \right|_{r=r_0}}{T_w - T_e} \quad (18)$$

and

$$\bar{h} = \frac{1}{z} \int_0^z h dz. \quad (19)$$

Computed Nusselt numbers are presented in Figs. 8-13. Computational techniques as well as Nusselt numbers in tabular form are presented in [32].

An interesting phenomenon was discovered while analyzing a series of numerical data for a coarse grid in which only Gr/Re was varied. For either entrance condition, Nu^* , Nu , and \bar{Nu} were found to be nearly linear functions of Gr/Re for $-50 \leq Gr/Re \leq 0$. In fact, obtaining any one of the Nusselt numbers at $Gr/Re = -10$ or -20 by linear interpolation using the values at $Gr/Re = 0$ and -30 resulted in less than 1 percent error at any axial location. Consequently, Nusselt numbers for any desired value of Gr/Re between -50 and 0 may be approximated by linear interpolation or extrapolation of the given data.

It is appropriate to comment on when gravity can be neglected without causing serious error. Of course, gravity will always produce some effect provided $T_e \neq T_w$ but it was found that changes in the velocity and temperature distributions are barely noticeable if $|Gr/Re| \leq 1$.

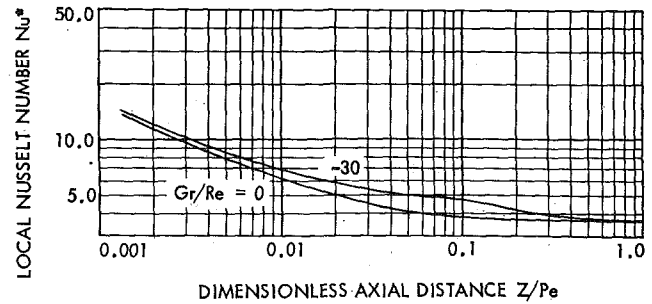


Fig. 8 Effect of Gr/Re on Nu^* for uniform entrance velocity

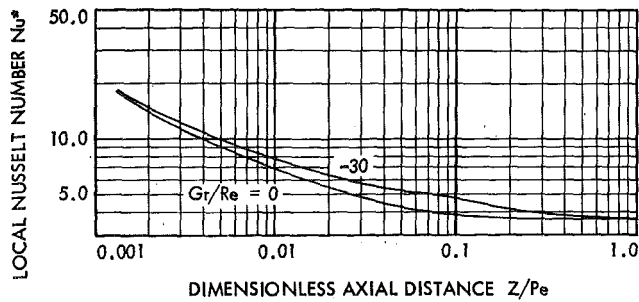


Fig. 9 Effect of Gr/Re on Nu^* for fully developed entrance velocity

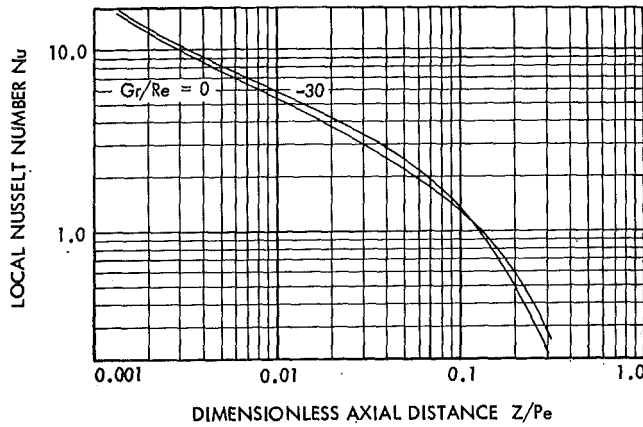


Fig. 10 Effect of Gr/Re on Nu for uniform entrance velocity

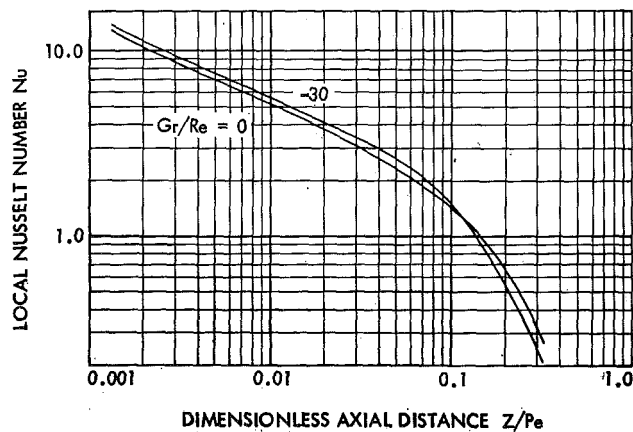


Fig. 11 Effect of Gr/Re on Nu for fully developed entrance velocity

Experimental Results

Of invaluable aid in the design of the experiment was the computer program written earlier for the numerical analysis. By comparing solutions for both pure forced and combined forced-free convection, one could see the effect of gravity on the dimensionless axial-velocity profiles quite clearly. On the other hand, the dimensionless temperature profiles provided no overt clues as to which flow regime they represented. For this reason, the major emphasis was placed on measuring axial-velocity profiles.

Two sets of experimental data were taken. In the first case, the air entered at 75.97 deg F, and the tube wall was maintained at 75.14 ± 0.08 deg F, and the barometric pressure was 737.5 mm Hg. Based on a mean velocity of 0.649 fps (as measured with the coiled capillary flowmeter), the Reynolds number was 509.5 and Gr/Re was 0.735. The second case involved a combined

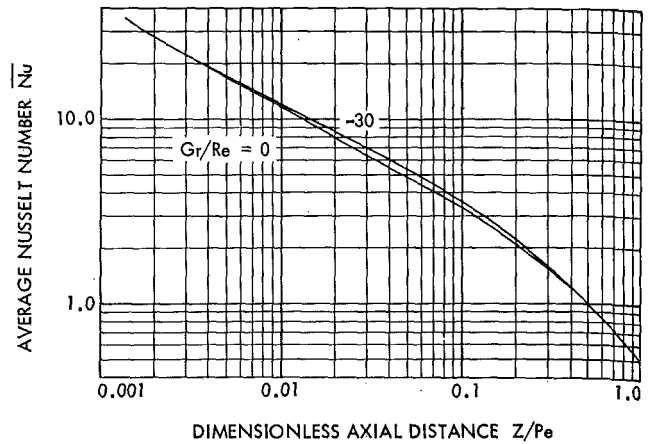


Fig. 12 Effect of Gr/Re on \bar{Nu} for uniform entrance velocity

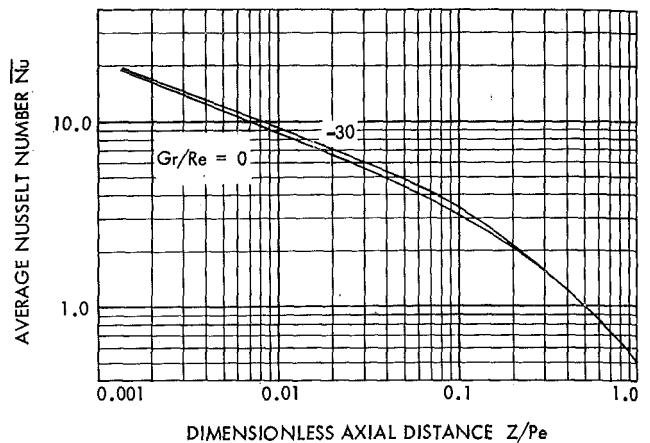


Fig. 13 Effect of Gr/Re on \bar{Nu} for fully developed entrance velocity

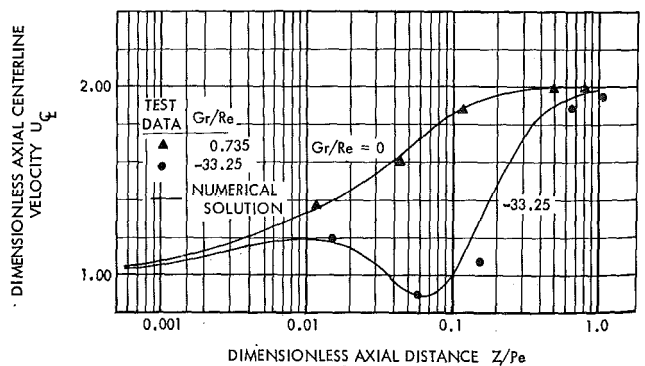


Fig. 14 Comparison of experimental and theoretical dimensionless center-line velocity development

forced-free convection flow. The temperature of the entering air was 72.68 deg F, the tube temperature was 94.91 ± 0.08 deg F, and the barometric pressure was 732.9 mm Hg. This time, the mean velocity was 0.501 fps, which resulted in $Re = 379.8$ and $Gr/Re = -33.25$. All fluid properties were evaluated at the average of the entrance and wall temperatures and, since the pressure drop in the tube was negligible, at the barometric pressure.

In both cases, slight asymmetry was detected in the measured velocity profiles. Without exception, velocities measured from the side of the tube through which the probe entered were slightly

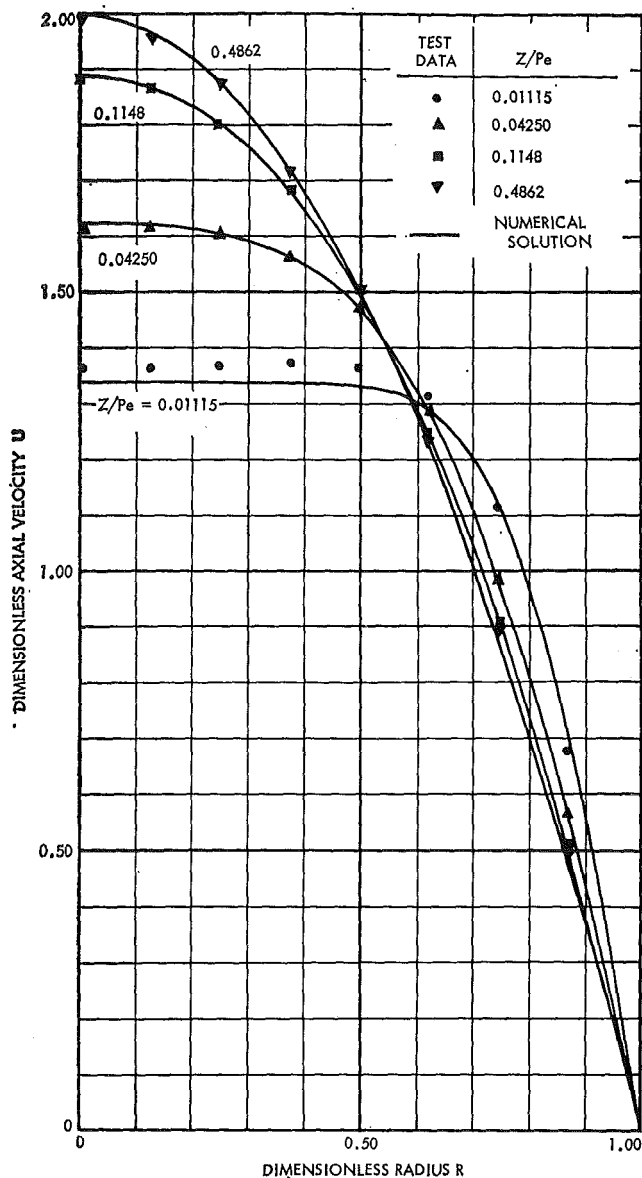


Fig. 15 Comparison of experimental and theoretical dimensionless velocity profiles for forced convection

lower than those measured at the same radial location but on the opposite side of the center line. Sparrow, Hixon, and Shavit [36], who measured velocity profiles for air flowing in rectangular ducts, reported substantially the same type of asymmetry in their 2:1 duct. They also cite Leite [37] and Reshotko [38] as having observed the same phenomenon in tube flow. It may be that in sensing the upstream conditions, the oncoming flow tends to shift away from that portion of the wall which contains the probe. There were indications that the flow adjusted to disturbances at the probe access ports, most noticeably those at the largest values of Z/Pe . Velocity traverses on the side of the tube containing the probe tended to indicate slightly higher velocities when the traversing mechanism-probe assembly was first installed. After waiting, sometimes as long as 15 min, repeatable velocity profiles were obtained.

Once determined, the experimental velocities at a given axial location were numerically integrated to obtain a mean velocity which was used, in turn, to nondimensionalize the velocities at that location.

The numerical solution presented earlier for $Re = 500$ and $Gr/Re = 0$ was judged to be adequate for purposes of comparison with the velocities obtained in the first experiment. On the other

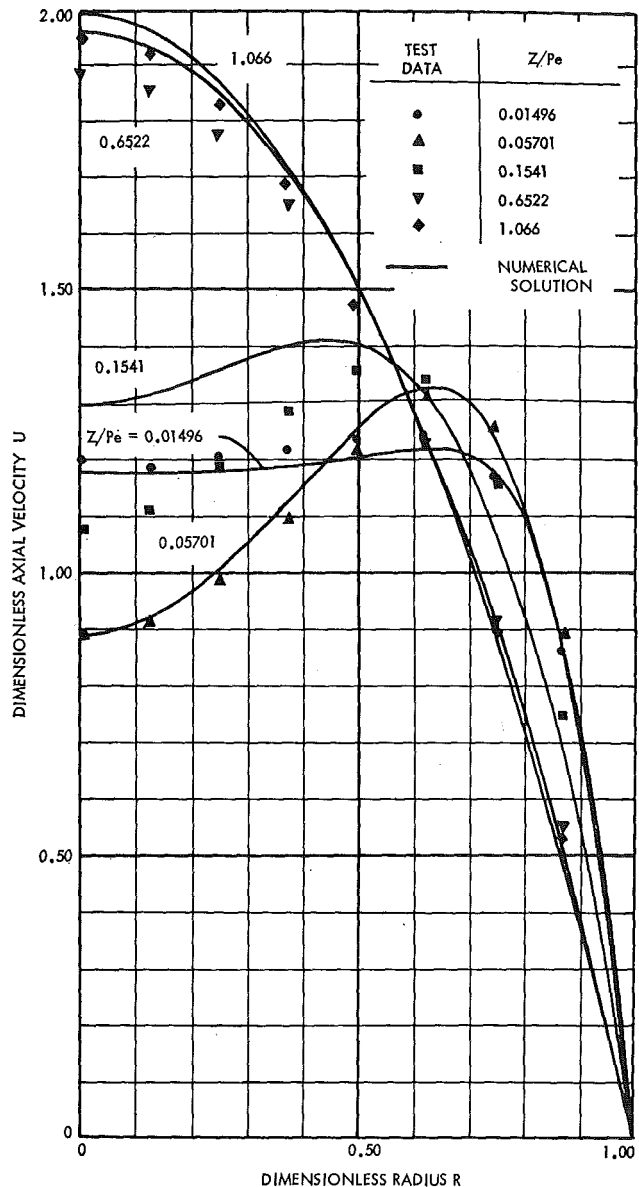


Fig. 16 Comparison of experimental and theoretical dimensionless velocity profiles for combined forced-free convection

hand, a separate numerical solution was generated for $Re = 379.8$ and $Gr/Re = -33.25$ for comparison with the combined forced-free experimental results.

Both nondimensional experimental and theoretical center-line velocities are shown in Fig. 14. There appears to be substantial agreement between theory and experiment for the forced convection flow. For the combined forced-free convection flow, the center-line velocity appears to have been adequately predicted for axial locations upstream of the minimum; however, development beyond this point was slower than expected. Judging from the experimental data, the velocity at the exit plane of the tube was probably not quite fully developed for this case.

Experimental and theoretical dimensionless velocity profiles for forced convection are compared in Fig. 15. Numerical values of U corresponding to the experimental values of Z/Pe were obtained by second-degree interpolation in terms of ξ . Although barely noticeable in the figure, the experimental velocity profile for $Z/Pe = 0.01115$ definitely possesses some central concavity. At $R = 0$, $U = 1.366$, whereas the maximum measured value of U is 1.372 and occurs at $R = 0.372$. This represents a dip of about 0.44 percent. At this axial location, however, the numeri-

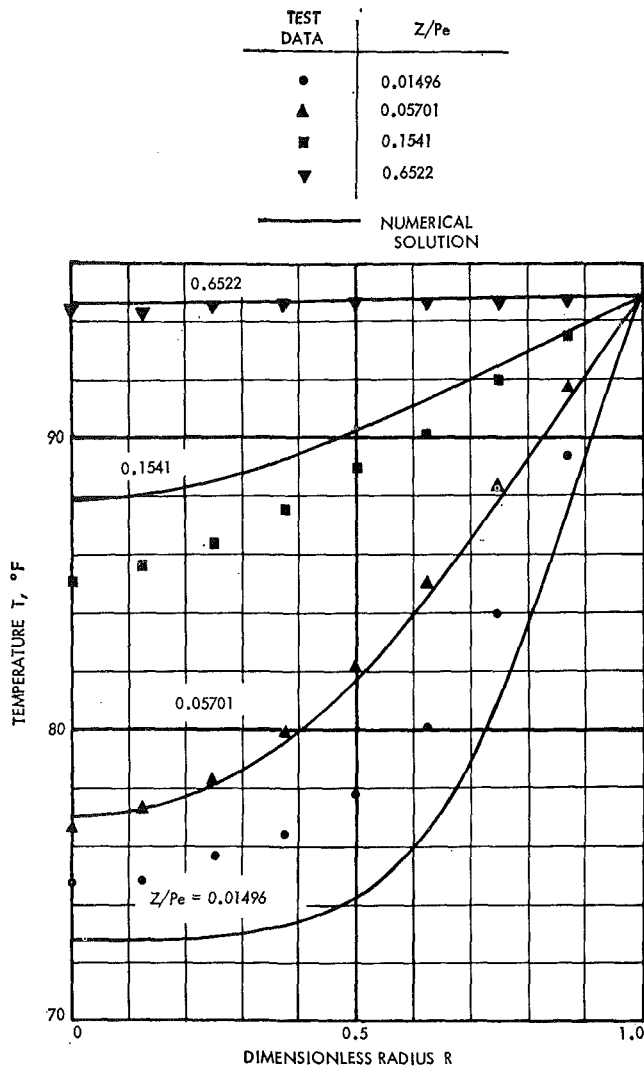


Fig. 17 Comparison of experimental and theoretical temperature profiles for combined forced-free convection

cal solution displays no concavity. Burke and Berman [39] also detected central concavity in the near entrance region in tube flows using a laser Doppler velocimeter. They reported maximum dips of as much as 5.2 percent for Reynolds numbers in the range of 108 to 340.

In Fig. 16, the numerical dimensionless velocities are shown to be in substantial agreement with the experimental values at the first two axial locations. Again, the measured velocity development is slower for larger values of Z/Pe than was predicted by the numerical analysis. Fig. 17 helps to explain the reason for this behavior. The experimental temperature distributions for $Z/Pe \geq 0.1541$ indicate higher radial temperature gradients than were predicted. This could only have resulted in retarding the development of the velocity profile. On the other hand, the discrepancy between the measured and computed temperatures for $Z/Pe = 0.01496$ appears to have had little effect on the velocity profile at that location. This can be partially explained by the fact that the shape of the velocity profile does not characteristically show the full effect of the radial temperature gradient at small values of Z/Pe . It is likely that the plastic nozzle, which was in direct contact with the warm tube, caused the unexpected increase in temperature by preheating the air before it entered the tube. The effect of the assumed preheating is also shown in Fig. 18, which compares the measured and predicted dimensionless bulk temperature distributions.

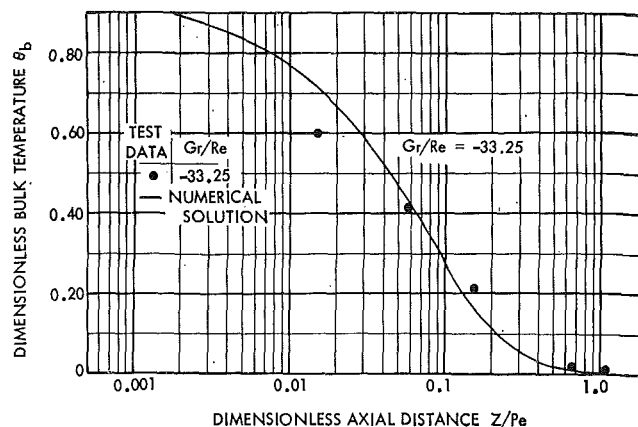


Fig. 18 Comparison of experimental and theoretical dimensionless bulk temperature development for combined forced-free convection

Conclusion

The influence of gravity on forced laminar flow in a vertical tube with uniform wall temperature was investigated by both numerical and experimental means. It was found that as a consequence of the presence of gravity, density gradients induced by heat transfer, though small, may significantly alter the flow characteristics—in particular, the velocity profile.

The predicted velocity profiles for uniform entrance velocity for $Pe = 500$ and $Gr/Re = 0$ exhibited some central concavity near the tube entrance region. The computed velocity profiles for $Re = 500$ and $Gr/Re = -30$ were found to be essentially similar to those for pure forced convection near the tube entrance. A bit farther downstream, however, a high degree of central concavity appeared, induced, this time, by the action of gravity. For $Gr/Re = -30$, the center-line velocity was found to reach a minimum at some axial location dependent upon the entrance-velocity condition. Beyond this position, the center-line velocity increased and the concavity diminished.

It was found that the rate of heat transfer was improved by the action of gravity for $Gr/Re < 0$. Furthermore, it was found that the local and average Nusselt number varied nearly linearly with Gr/Re for $-50 \leq Gr/Re \leq 0$.

References

- Allen, D. N. de G., and Southwell, R. V., "Relaxation Methods Applied to Determine the Motion, in Two Dimensions, of a Viscous Fluid Past a Fixed Cylinder," *Quarterly Journal of Mechanics and Applied Mathematics*, Vol. 8, Part 2, 1955, pp. 129-145.
- Schiller, L., "Die Entwicklung der laminaren Geschwindigkeitsverteilung und ihre Bedeutung für Zähigkeitsmessungen," *Zeitschrift für Angewandte Mathematik und Physik*, Vol. 2, 1922, pp. 96-106.
- Schlichting, H., "Laminare Kanaleinlaufströmung," *Zeitschrift für Angewandte Mathematik und Physik*, Vol. 12, 1934, pp. 368-373.
- Langhaar, H. L., "Steady Flow in the Transition Length of a Straight Tube," *Journal of Applied Mechanics*, Vol. 9, No. 2, TRANS. ASME, Vol. 64, June 1942, pp. A55-A58.
- Hornbeck, R. W., "Laminar Flow in the Entrance Region of a Pipe," *Applied Scientific Research*, Sec. A, Vol. 13, No. 2-3, 1964, pp. 224-232.
- Christiansen, E. B., and Lemmon, H. E., "Entrance Region Flow," *AIChE Journal*, Vol. 11, No. 6, 1965, pp. 995-999.
- Wang, Y. L., and Longwell, P. A., "Laminar Flow in the Inlet Section of Parallel Plates," *AIChE Journal*, Vol. 10, No. 3, 1964, pp. 323-329.
- Vrentas, J. S., Duda, J. L., and Barger, K. G., "Effect of Axial Diffusion of Vorticity on Flow Development in Circular Conduits: Part 1. Numerical Solutions," *AIChE Journal*, Vol. 12, No. 5, 1966, pp. 837-844.
- Schmidt, F. W., and Zeldin, B., "Laminar Flows in Inlet Sections of Tubes and Ducts," *AIChE Journal*, Vol. 15, No. 4, 1969, pp. 612-614.
- Schmidt, F. W., and Zeldin, B., "Laminar Flow in the Inlet

- Section of a Tube," *Proceedings, Fluidics and Internal Flows*, The Pennsylvania State University, Department of Mechanical Engineering, Part II, 1968, pp. 211-251.
- 11 Goldberg, P., "A Digital Computer Solution for Laminar Flow Heat Transfer in Circular Tubes," ME thesis, M.I.T., Cambridge, Mass., 1958.
- 12 Sellars, J. R., Tribus, M., and Klein, J. S., "Heat Transfer to Laminar Flow in a Round Tube or Flat Conduit—the Graetz Problem Extended," *TRANS. ASME*, Vol. 78, Part 1, 1956, pp. 441-448.
- 13 Mercer, A. McD., "The Growth of the Thermal Boundary Layer in Laminar Flow Between Parallel Flat Plates," *Applied Scientific Research*, Sec. A, Vol. 8, No. 5, 1959, pp. 357-365.
- 14 Mercer, A. McD., "The Growth of the Thermal Boundary Layer at the Inlet to a Circular Tube," *Applied Scientific Research*, Sec. A, Vol. 9, No. 6, 1960, pp. 450-456.
- 15 Millsaps, K., and Pohlhausen, K., "Heat Transfer to Hagen-Poiseuille Flows," *Mathematical Reviews*, Vol. 18, 1957, p. 538.
- 16 Singh, S. N., "Heat Transfer by Laminar Flow in a Cylindrical Tube," *Applied Scientific Research*, Sec. A, Vol. 7, No. 5, 1958, pp. 325-340.
- 17 Schmidt, F. W., and Zeldin, B., "Laminar Heat Transfer in the Entrance Region of Ducts," *Applied Scientific Research*, Vol. 23, No. 1/2, 1970, pp. 73-94.
- 18 Ostrach, S., "Combined Natural- and Forced-Convection Laminar Flow and Heat Transfer of Fluids with and without Heat Sources in Channels with Linearly Varying Wall Temperatures," NACA TN3141, 1954.
- 19 Mori, Y., "On Combined Free and Forced Convective Laminar Magnetohydrodynamic Flow and Heat Transfer in Channels with Transverse Magnetic Field," International Heat Transfer Conference, University of Colorado, *International Developments in Heat Transfer*, Part V, 1961, pp. 1031-1037.
- 20 Yu, C. P., "Combined Forced and Free Convection Channel Flows in Magnetohydrodynamics," *AIAA Journal*, Vol. 3, No. 6, 1965, pp. 1184-1186.
- 21 Srinivasan, J., "Combined Natural and Forced Convection Hydromagnetic Flow Between Electrically Conducting Walls," *Applied Scientific Research*, Sec. B, Vol. 11, No. 5, 1965, pp. 361-381.
- 22 Carter, L. F., and Gill, W. N., "Asymptotic Solution for Combined Free and Forced Convection in Vertical and Horizontal Conduits with Uniform Suction and Blowing," *AICHE Journal*, Vol. 10, No. 3, 1964, pp. 330-339.
- 23 Gill, W. N., Del Casal, E., and Zeh, D. W., "Free and Forced Convection in Conduits with Asymmetric Mass Transfer," *AICHE Journal*, Vol. 12, No. 2, 1966, pp. 266-271.
- 24 Hau, L. S., "Laminar Heat Transfer in Rectangular Channels," *JOURNAL OF HEAT TRANSFER*, *TRANS. ASME*, Series C, Vol. 81, No. 2, May 1959, pp. 121-128.
- 25 Tao, L. N., "On Combined Free and Forced Convection in Channels," *JOURNAL OF HEAT TRANSFER*, *TRANS. ASME*, Series C, Vol. 82, No. 3, Aug. 1960, pp. 233-238.
- 26 Agrawal, H. C., "A Variational Method for Combined Free and Forced Convection in Channels," *International Journal of Heat and Mass Transfer*, Vol. 5, 1962, pp. 439-444.
- 27 Hallman, T. M., "Combined Forced and Free-Laminar Heat Transfer in Vertical Tubes With Uniform Internal Heat Generation," *TRANS. ASME*, Vol. 78, 1956, pp. 1831-1841.
- 28 Hanratty, T. J., Rosen, E. M., and Kabel, R. L., "Effect of Heat Transfer on Flow Field at Low Reynolds Numbers in Vertical Tubes," *Industrial and Engineering Chemistry*, Vol. 50, No. 5, 1958, pp. 815-820.
- 29 Lawrence, W. T., and Chato, J. C., "Heat-Transfer Effects on the Developing Laminar Flow Inside Vertical Tubes," *JOURNAL OF HEAT TRANSFER*, *TRANS. ASME*, Series C, Vol. 88, No. 2, May 1966, pp. 214-222.
- 30 Murakawa, K., "Heat Transfer on Double Vertical Pipes in Velocity Entrance Length," *Bulletin of the Japanese Society of Mechanical Engineers*, Vol. 14, No. 4, 1961, pp. 347-351.
- 31 Worsøe-Schmidt, P. M., and Leppert, G., "Heat Transfer and Friction for Laminar Flows of a Gas in a Circular Tube at High Heating Rate," *International Journal of Heat and Mass Transfer*, Vol. 8, 1965, pp. 1281-1301.
- 32 Zeldin, B., "Developing Flow with Combined Forced-Free Convection in an Isothermal Vertical Tube," PhD thesis, The Pennsylvania State University, University Park, Pa., 1969.
- 33 Powell, H. N., and Browne, W. G., "Use of Coiled Capillaries in a Convenient Laboratory Flowmeter," *Review of Scientific Instruments*, Vol. 28, No. 2, 1957, pp. 138-141.
- 34 Streeter, V. L., *Fluid Mechanics*, 2nd ed., McGraw-Hill, New York, 1958, p. 318.
- 35 Zeldin, B., and Schmidt, F. W., "Calibrating a Hot Film Anemometer for Low Velocity Measurement in Non-Isothermal Flow," *Review of Scientific Instruments*, Vol. 41, No. 9, 1970, pp. 1373-1374.
- 36 Sparrow, E. M., Hixon, C. W., and Shavit, G., "Experiments on Laminar Flow Development in Rectangular Ducts," *Journal of Basic Engineering*, *TRANS. ASME*, Series D, Vol. 89, No. 1, Mar. 1967, pp. 116-124.
- 37 Leite, R. J., "An Experimental Investigation of the Stability of Axially Symmetric Poiseuille Flow," Report IP-188, University of Michigan, 1956.
- 38 Reshotko, E., "Experimental Study of the Stability of Pipe Flow," Progress Report No. 20-364, Jet Propulsion Laboratory, California Institute of Technology, Pasadena, Calif., 1958.
- 39 Burke, J. P., and Berman, N. S., "Entrance Flow Development in Circular Tubes at Small Axial Distances," Arizona State University, School of Engineering, 1968.

Section of a Tube," *Proceedings, Fluidics and Internal Flows*, The Pennsylvania State University, Department of Mechanical Engineering, Part II, 1968, pp. 211-251.

11 Goldberg, P., "A Digital Computer Solution for Laminar Flow Heat Transfer in Circular Tubes," ME thesis, M.I.T., Cambridge, Mass., 1958.

12 Sellars, J. R., Tribus, M., and Klein, J. S., "Heat Transfer to Laminar Flow in a Round Tube or Flat Conduit—the Graetz Problem Extended," *TRANS. ASME*, Vol. 78, Part 1, 1956, pp. 441-448.

13 Mercer, A. McD., "The Growth of the Thermal Boundary Layer in Laminar Flow Between Parallel Flat Plates," *Applied Scientific Research*, Sec. A, Vol. 8, No. 5, 1959, pp. 357-365.

14 Mercer, A. McD., "The Growth of the Thermal Boundary Layer at the Inlet to a Circular Tube," *Applied Scientific Research*, Sec. A, Vol. 9, No. 6, 1960, pp. 450-456.

15 Millsaps, K., and Pohlhausen, K., "Heat Transfer to Hagen-Poiseuille Flows," *Mathematical Reviews*, Vol. 18, 1957, p. 538.

16 Singh, S. N., "Heat Transfer by Laminar Flow in a Cylindrical Tube," *Applied Scientific Research*, Sec. A, Vol. 7, No. 5, 1958, pp. 325-340.

17 Schmidt, F. W., and Zeldin, B., "Laminar Heat Transfer in the Entrance Region of Ducts," *Applied Scientific Research*, Vol. 23, No. 1/2, 1970, pp. 73-94.

18 Ostrach, S., "Combined Natural- and Forced-Convection Laminar Flow and Heat Transfer of Fluids with and without Heat Sources in Channels with Linearly Varying Wall Temperatures," NACA TN3141, 1954.

19 Mori, Y., "On Combined Free and Forced Convective Laminar Magnetohydrodynamic Flow and Heat Transfer in Channels with Transverse Magnetic Field," International Heat Transfer Conference, University of Colorado, *International Developments in Heat Transfer*, Part V, 1961, pp. 1031-1037.

20 Yu, C. P., "Combined Forced and Free Convection Channel Flows in Magnetohydrodynamics," *AIAA Journal*, Vol. 3, No. 6, 1965, pp. 1184-1186.

21 Srinivasan, J., "Combined Natural and Forced Convection Hydromagnetic Flow Between Electrically Conducting Walls," *Applied Scientific Research*, Sec. B, Vol. 11, No. 5, 1965, pp. 361-381.

22 Carter, L. F., and Gill, W. N., "Asymptotic Solution for Combined Free and Forced Convection in Vertical and Horizontal Conduits with Uniform Suction and Blowing," *AICHE Journal*, Vol. 10, No. 3, 1964, pp. 330-339.

23 Gill, W. N., Del Casal, E., and Zeh, D. W., "Free and Forced Convection in Conduits with Asymmetric Mass Transfer," *AICHE Journal*, Vol. 12, No. 2, 1966, pp. 266-271.

24 Hau, L. S., "Laminar Heat Transfer in Rectangular Channels," *JOURNAL OF HEAT TRANSFER*, *TRANS. ASME*, Series C, Vol. 81, No. 2, May 1959, pp. 121-128.

25 Tao, L. N., "On Combined Free and Forced Convection in Channels," *JOURNAL OF HEAT TRANSFER*, *TRANS. ASME*, Series C, Vol. 82, No. 3, Aug. 1960, pp. 233-238.

26 Agrawal, H. C., "A Variational Method for Combined Free and Forced Convection in Channels," *International Journal of Heat and Mass Transfer*, Vol. 5, 1962, pp. 439-444.

27 Hallman, T. M., "Combined Forced and Free-Laminar Heat Transfer in Vertical Tubes With Uniform Internal Heat Generation," *TRANS. ASME*, Vol. 78, 1956, pp. 1831-1841.

28 Hanratty, T. J., Rosen, E. M., and Kabel, R. L., "Effect of Heat Transfer on Flow Field at Low Reynolds Numbers in Vertical Tubes," *Industrial and Engineering Chemistry*, Vol. 50, No. 5, 1958, pp. 815-820.

29 Lawrence, W. T., and Chato, J. C., "Heat-Transfer Effects on the Developing Laminar Flow Inside Vertical Tubes," *JOURNAL OF HEAT TRANSFER*, *TRANS. ASME*, Series C, Vol. 88, No. 2, May 1966, pp. 214-222.

30 Murakawa, K., "Heat Transfer on Double Vertical Pipes in Velocity Entrance Length," *Bulletin of the Japanese Society of Mechanical Engineers*, Vol. 14, No. 4, 1961, pp. 347-351.

31 Worsøe-Schmidt, P. M., and Leppert, G., "Heat Transfer and Friction for Laminar Flows of a Gas in a Circular Tube at High Heating Rate," *International Journal of Heat and Mass Transfer*, Vol. 8, 1965, pp. 1281-1301.

32 Zeldin, B., "Developing Flow with Combined Forced-Free Convection in an Isothermal Vertical Tube," PhD thesis, The Pennsylvania State University, University Park, Pa., 1969.

33 Powell, H. N., and Browne, W. G., "Use of Coiled Capillaries in a Convenient Laboratory Flowmeter," *Review of Scientific Instruments*, Vol. 28, No. 2, 1957, pp. 138-141.

34 Streeter, V. L., *Fluid Mechanics*, 2nd ed., McGraw-Hill, New York, 1958, p. 318.

35 Zeldin, B., and Schmidt, F. W., "Calibrating a Hot Film Anemometer for Low Velocity Measurement in Non-Isothermal Flow," *Review of Scientific Instruments*, Vol. 41, No. 9, 1970, pp. 1373-1374.

36 Sparrow, E. M., Hixon, C. W., and Shavit, G., "Experiments on Laminar Flow Development in Rectangular Ducts," *Journal of Basic Engineering*, *TRANS. ASME*, Series D, Vol. 89, No. 1, Mar. 1967, pp. 116-124.

37 Leite, R. J., "An Experimental Investigation of the Stability

of Axially Symmetric Poiseuille Flow," Report IP-188, University of Michigan, 1956.

38 Reshotko, E., "Experimental Study of the Stability of Pipe Flow," Progress Report No. 20-364, Jet Propulsion Laboratory, California Institute of Technology, Pasadena, Calif., 1958.

39 Burke, J. P., and Berman, N. S., "Entrance Flow Development in Circular Tubes at Small Axial Distances," Arizona State University, School of Engineering, 1968.

DISCUSSION

Stuart W. Churchill⁶

The authors are to be commended on a significant contribution, both computationally and experimentally. The good agreement between the experimental data and the computed values confirms the general validity of the mathematical model and the computational procedure but does not constitute a critical test of the convergence of the calculations as the grid size is reduced. The authors imply that the calculations for $I = J = 41$ differ negligibly from the solution which would be obtained as $\Delta\xi$ and $\Delta R \rightarrow 0$. A plot demonstrating the convergence of the solution as I and J were increased and indicating the error due to finite I and J should be provided as a critique of the procedure and as a guide to future investigators.

The statement "When the flow is fully developed, the uniform-wall-heat-flux condition is equivalent to the condition of axially linear varying wall temperature" is not valid for the thermal entrance region. In this region $(T_w - T_c)$ is proportional to $z^{1/3}$ for a uniform wall flux [40].

The paper does not refer to the early work of Elenbaas [41] and of Bodoia and Osterle [42] or to the recent work of Davis and Perona [43] on the same general subject. Comparison of the results with this other work would be of interest.

Comparison of the results for $Gr/Re = 0$ with those of Kays [44] who calculated temperature fields and heat fluxes for the Langhaar and parabolic velocity fields with those of Rosenberg and Hellums [45] who also solved the momentum equations numerically would also be of interest.

The line for $Gr/Re = 0$ in Figs. 6 and 7 should be strengthened to distinguish it from the grid lines.

W. J. Marner⁷

Zeldin and Schmidt are to be congratulated for a rigorous analysis of an interesting problem. Unlike practically all previous investigators who have studied combined free and forced convection in a vertical tube, they have included the effects of both axial conduction and axial momentum change. However, their literature review does not include a number of important related papers, and their treatment of axial conduction for case 2 is open to question.

Kays [46], Tien and Pawelek [47], Ulrichson and Schmitz [48], Hornbeck [49], and Manohar [50] have all considered the problem of simultaneously developing velocity and temperature profiles in an isothermal tube under conditions of forced convection with constant fluid properties. In each case, however, axial diffusion of heat and momentum was neglected.

In 1942 Martinelli and Boelter [51] made the initial attack on combined free and forced laminar convection in a vertical isothermal tube for the case when the velocity profile is initially parabolic (case 2). They derived the following expression for the arithmetic-mean Nusselt number:

$$\bar{Nu}_{lam} = 1.75F_1[Gz + 0.0722F_2(Gr Pr D/z)^{0.75}]^{1/3} \quad (20)$$

where $D = 2r_0$ is the tube diameter, $Pr = c_p\mu/K$ is the Prandtl

⁶ The Carl V. S. Patterson Professor of Chemical Engineering, University of Pennsylvania, Philadelphia, Pa.

⁷ Assistant Professor of Mechanical Engineering, South Dakota School of Mines and Technology, Rapid City, S. D. Assoc. Mem. ASME.

number, $Gz = \rho u_m \pi r_0^2 c_p / Kz$ is the Graetz number, and F_1 and F_2 are coefficients which are functions of \overline{Nu}_{am} . Martinelli et al. [52] found the Nusselt numbers predicted by equation (20) to be low; however, by changing the exponent 0.75 to 0.84 they were able to correlate five sets of experimental data, obtained using water and oil, to within ± 20 percent. However, the presence of some turbulence undoubtedly contributed to the high experimental values of \overline{Nu}_{am} . Pigford [53] and Rosen and Hanratty [54] followed with approximate analyses for case 2 which also included a temperature-dependent viscosity. Marner and McMillan [55], in a recent numerical study, found that for sufficiently large (magnitude) values of Gr/Re , the local Nusselt number Nu^* shows the unusual behavior of increasing with increasing axial distance near the point of maximum velocity-profile distortion. Jackson, Harrison, and Boteler [56] considered combined free and forced laminar convection in a vertical tube with constant wall temperature for the situation when both the velocity and temperature profiles are initially uniform (case 1). They derived the following approximate expression for the logarithmic-mean Nusselt number:

$$\overline{Nu}_{lm} = 1.128[Re Pr D/z + (3.02\{Gr Pr D/L\}Pr)^{0.4}]^{1/2} \quad (21)$$

where L is the length of the heated section. This equation successfully fit the experimental data obtained for air flowing in a 5-ft-long, 3/4-in-ID tube with Graetz numbers ranging from 15.0 to 57.1. In a numerical investigation Bradley and Entwistle [57], as a portion of their study, considered fully developed cooling of air in upflow in an isothermal vertical tube under conditions of combined free and forced convection. They found the axial momentum change to be important for large temperature differences, an effect which was essentially independent of the Reynolds number. Axial conduction was found to become increasingly important as the Reynolds number was reduced below 200.

Hennecke [58] has carried out a numerical investigation of forced convection in a circular tube which takes axial conduction into account. Both constant wall temperature and constant wall heat flux were considered. He has included a rather thorough literature review of papers which consider the effects of axial conduction. More recently, Jones [59] has presented an analytical solution for forced convection in an isothermal tube taking axial conduction into account. The work of both Hennecke and Jones shows that when axial conduction is important the proper thermal boundary condition for the fluid is $T(r, -\infty) = T_w$, rather than $T(r, 0) = T_w$. In other words, heat is conducted upstream beyond the point where heating begins, such that the temperature profile at $z = 0$ is not uniform.

Of particular interest for the problem under consideration is the relative importance of axial conduction and axial diffusion of momentum. The following discussion will attempt to shed some light on this aspect of the problem for case 2.

Tabulated in Table 1 are values of the local Nusselt number Nu^* for the Graetz solution which neglects axial conduction—obtained using the eigenvalues of Sellars, Tribus, and Klein [12]—along with the corresponding values of Zeldin and Schmidt—obtained from reference [32]—which include axial conduction. Since $Gr/Re = 0$ the velocity profile remains parabolic, and there is no axial diffusion of momentum in this case. Thus, this comparison gives some indication of the importance of axial conduction as predicted by Zeldin and Schmidt, at least for pure forced convection. As can be seen from Table 1, Zeldin and Schmidt predict increases in Nu^* of up to 39.7 percent for $Pe = 252.5$; however, an increase of this magnitude is not in agreement with the results of Hennecke [58]. For example, at $Z/Pe = 0.001$ Hennecke predicts an increase in Nu^* due to axial conduction of less than 40 percent for $Pe = 50$. Unfortunately, Hennecke does not give results for Peclet numbers larger than 50; however, since the importance of axial conduction decreases sharply with increasing Pe , it is safe to say that the influence of axial conduction for $Pe = 252.5$ will be considerably less than for

Table 1 Comparison of local Nusselt numbers for pure forced convection with $Pe = 252.5$

Z/Pe	Sellars, Tribus, and Klein	Zeldin and Schmidt	Percentage change
0.0006575	14.78	20.65	+39.7
0.00135	11.56	13.30	+15.1
0.002849	8.986	9.557	+6.35
0.004525	7.713	8.010	+3.85
0.006410	6.893	7.076	+2.65
0.01099	5.831	5.919	+1.51
0.02564	4.610	4.641	+0.67
0.04762	4.037	4.059	+0.54
0.1026	3.704	3.722	+0.49
0.2308	3.656	3.659	+0.08

Table 2 Comparison of local Nusselt numbers for $Gr/Re = -30$ and $Pe = 252.5$

Z/Pe	Marner and McMillan	Zeldin and Schmidt	Percentage change
0.0006575	15.42	21.62	+40.2
0.00135	12.20	14.11	+15.7
0.002849	9.630	10.29	+6.85
0.004525	8.347	8.724	+4.52
0.006410	7.525	7.789	+3.51
0.01099	6.479	6.648	+2.61
0.02564	5.345	5.451	+1.98
0.04762	4.910	4.989	+1.61
0.1026	4.688	4.634	-1.15
0.2308	4.069	4.039	-0.74

$Pe = 50$. Jones [59], for the same problem, predicts a Nusselt number of 7.508 at $Z/Pe = 0.005$ for $Pe = 200$ compared with the Graetz solution value of 7.466, i.e., an increase of 0.56 percent. For this range of Z/Pe Zeldin and Schmidt predict an increase of approximately 3 percent due to axial conduction. Apparently these differences are due to the different thermal boundary conditions used by Hennecke and Jones, $T(r, -\infty) = T_w$, in contrast to that used by Zeldin and Schmidt, $T(r, 0) = T_w$. As discussed previously, a uniform temperature profile at $z = 0$ is not realistic when axial conduction is important. Thus, it appears that the local Nusselt number predictions of Zeldin and Schmidt for pure forced convection are high due to the assumed uniform temperature profile at $z = 0$.

In Table 2 comparisons are made with solutions for combined free and forced convection obtained using the numerical procedure developed by Marner and McMillan [55], who neglected both axial diffusion of heat and momentum, along with the tabulated results of Zeldin and Schmidt [32] for $Gr/Re = -30$ and $Pe = 252.5$. Since the velocity profile in this case is being distorted, both axial conduction and axial momentum change are important to some extent. In the entrance region ($Z/Pe < 0.003$), however, the velocity profile has had little chance to become distorted due to free convection effects. Thus, in this region the increase in Nu^* predicted by Zeldin and Schmidt is due primarily to axial conduction. It will be noted in Table 2 that the percentage increase over that of Marner and McMillan is essentially the same as in the case of pure forced convection for small Z/Pe . Based on the preceding argument, the Nusselt numbers of Zeldin and Schmidt for combined free and forced convection are probably high for small values of Z/Pe . Fortunately, solutions for $Z/Pe = 0.003$ when $Pe = 252.5$ correspond to a physical axial distance of $z = 0.76r_0$ which is of little practical interest. It is noted that Zeldin and Schmidt predict a difference in Nu^* of over 1 percent at $Z/Pe = 0.1026$, a larger difference than for pure forced convection at the same axial location. Since axial conduction is probably negligible in this region, this difference may be attributed to axial momentum change. This is not surprising in view of the fact that at $Z/Pe = 0.1026$ the centerline velocity is approximately 1.08 as compared to the fully developed value of 2.0.

Turning to case 1, a uniform temperature profile at $Z/Pe = 0$

is realistic, even when axial conduction is important, so the results of Zeldin and Schmidt should be quite accurate for all values of Z/Pe . It would, however, be of interest to determine the relative importance of the axial conduction and axial momentum change contributions in this case.

Finally, Zeldin and Schmidt have presented mean Nusselt numbers with the convective heat transfer coefficient based on $T_w - T_c$. Perhaps a more useful mean Nusselt number, which is based on $T_w - T_b$, is that presented, for example, by Kays [60]

$$\overline{Nu}_m = \frac{1}{2Z/Pe} \ln [1/\theta_b] \quad (22)$$

for constant-wall-temperature tubes. In addition to being computationally straightforward, this expression also has the advantage that it asymptotically approaches the value of the fully developed local Nusselt number, 3.656.

Authors' Closure

The authors wish to thank Professors Churchill and Marner for presenting written discussions on the subject paper.

Professor Churchill has reminded the authors to describe the method used to verify the accuracy of the numerical solution. As stated previously, solutions were obtained for $I = J = 11, 21$, and 41. A comparison of the results at common grid points for all three mesh sizes indicated that the increase in accuracy to be expected by using $I = J = 81$ instead of 41 (i.e., halving $\Delta\xi$ and ΔR) would not be sufficient to warrant the increased computational effort and expense.

As pointed out, it is true that the uniform-wall-heat-flux condition is not equivalent to the condition of an axially linear-varying wall temperature for the thermal entrance region. However, the fully developed flow alluded to (in our discussion of the papers, paragraph 2 of the "Previous Related Studies") is both *hydrodynamically* and *thermally* fully developed.

The authors do not wish to become involved in a point-by-point rebuttal of Professor Marner's rather lengthy discussion. With the exception of [55], which was published after the submission of our manuscript, his additional references and the major portion of his discussion add little to the information already presented by Schmidt and Zeldin [17] and more recently by Schmidt and Wimmer [61]. In these studies, the effect of Pe on Nu^* was presented for a thermally developing, pure-forced convective flow. In [61], the region preceding the tube entrance was accounted for.

Professor Marner contends that the authors' tabular values of Nu^* for case 2 [32] are too high for small positive values of Z/Pe . Too high compared to what? Too high compared to the values of Nu^* for pure forced convection computed on the basis of a different thermal entrance condition such as used by Jones, or the boundary-layer-type equations used by Sellars, Tribus, and Klein? Too high compared to the values of Nu^* for combined forced-free convection computed on the basis of the less refined mathematical model utilized by Marner and McMillan? The authors have presented, among other things, Nusselt numbers corresponding to a specific set of differential equations and boundary conditions and believe them to be reasonably accurate for the model presented.

Marner's suggestion that equation (22) is a more useful expression for computing the mean Nusselt number than equation (17) is surprising—especially since the very derivation of equation (22) hinges on the assumption that the axial conduction term in the

energy equation can be neglected. This is most certainly not the case in the present study.

Additional References

40 Bird, R. B., "Zur Theorie des Wärmetübergangs an nicht-Newtonische Flüssigkeiten bei laminarer Rohrströmung," *Chemie-Ing. Techn.*, Vol. 31, 1959, pp. 569-572.

41 Elenbaas, W., "The Dissipation of Heat by Free Convection. The Inner Surface of Vertical Tubes of Different Shapes of Cross-Section," *Physica*, Vol. 9, 1942, pp. 865-874.

42 Bodoia, J. R., and Osterle, J. F., "The Development of Free Convection Between Heated Vertical Plates," *JOURNAL OF HEAT TRANSFER, TRANS. ASME, Series C, Vol. 84, No. 1, Feb. 1962*, pp. 40-44.

43 Davis, L. P., and Perona, J. J., "Development of Free Convection Flow of a Gas in a Heated Vertical Open Tube," *International Journal of Heat and Mass Transfer*, Vol. 14, 1971, pp. 889-903.

44 Kays, W. M., "Numerical Solutions for Laminar-Flow Heat Transfer in Circular Tubes," *TRANS. ASME, Vol. 77, 1955*, pp. 1265-1274.

45 Rosenberg, D. E., and Hellums, J. D., "Flow Development and Heat Transfer in Variable Viscosity Fluids," *Ind. Eng. Chem. Funda.*, Vol. 4, 1965, pp. 417-422.

46 Kays, W. M., "Numerical Solutions for Laminar-Flow Heat Transfer in Circular Tubes," *TRANS. ASME, Vol. 58, 1955*, pp. 1265-1274.

47 Tien, C., and Pawelek, R. A., "Laminar Flow Heat Transfer in the Entrance Region of Circular Tubes," *Applied Scientific Research*, Vol. 13, Sec. A, 1964, pp. 317-331.

48 Ulrichson, D. L., and Schmitz, R. A., "Laminar-Flow Heat Transfer in the Entrance Region of Circular Tubes," *International Journal of Heat and Mass Transfer*, Vol. 8, 1965, pp. 253-258.

49 Hornbeck, R. W., "An All-Numerical Method for Heat Transfer in the Inlet of a Tube," *ASME Paper No. 65-WA/FE-4*.

50 Manohar, R., "Analysis of Laminar-Flow Heat Transfer in the Entrance Region of Circular Tubes," *International Journal of Heat and Mass Transfer*, Vol. 12, 1968, pp. 15-22.

51 Martinelli, R. C., and Boelter, L. M. K., "The Analytical Prediction of Superposed Free and Forced Viscous Convection in a Vertical Pipe," *University of California Publications in Engineering*, Vol. 5, 1942, pp. 23-58.

52 Martinelli, R. C., Southwell, C. J., Alves, G., Craig, H. L., Weinberg, E. B., Lansing, N. F., and Boelter, L. M. K., "Heat Transfer and Pressure Drop for a Fluid Flowing in the Viscous Region through a Vertical Pipe," *Trans. AIChE*, Vol. 38, 1942, pp. 493-530.

53 Pigford, R. L., "Nonisothermal Flow and Heat Transfer Inside Vertical Tubes," *Chemical Engineering Progress Symposium Series*, Vol. 51, No. 17, 1955, pp. 79-92.

54 Rosen, E. M., and Hanratty, T. J., "Use of Boundary-Layer Theory to Predict the Effect of Heat Transfer on the Laminar-Flow Field in a Vertical Tube with Constant-Temperature Wall," *AIChE Journal*, Vol. 7, 1961, pp. 112-123.

55 Marner, W. J., and McMillan, H. K., "Combined Free and Forced Laminar Convection in a Vertical Tube With Constant Wall Temperature," *JOURNAL OF HEAT TRANSFER, TRANS. ASME, Series C, Vol. 92, No. 3, Aug. 1970*, pp. 559-562.

56 Jackson, T. W., Harrison, W. B., and Boteler, W. C., "Combined Free and Forced Convection in a Constant-Temperature Vertical Tube," *TRANS. ASME, Vol. 80, 1958*, pp. 739-745.

57 Bradley, D., and Entwistle, A. G., "Developed Laminar Flow Heat Transfer from Air for Variable Physical Properties," *International Journal of Heat and Mass Transfer*, Vol. 8, 1965, pp. 621-638.

58 Hennecke, D. K., "Heat Transfer by Hagen-Poiseuille Flow in the Thermal Development Region with Axial Conduction," *Wärme- und Stoffübertragung*, Bd. 1, 1968, pp. 177-184.

59 Jones, A. S., "Extensions to the Solution of the Graetz Problem," *International Journal of Heat and Mass Transfer*, Vol. 14, 1971, pp. 619-623.

60 Kays, W. M., *Convective Heat and Mass Transfer*, McGraw-Hill, New York, N. Y., 1966, pp. 123-124.

61 Schmidt, F. W., and Wimmer, K., "Laminar Heat Transfer in Tubes with Step Change in Cross Section," *Heat Transfer in Low Reynolds Number Flow*, ASME Publication HTD, Vol. 5, 1971.

N. D. ERYOU¹

N. V. Philips,
Gloeilampenfabrieken,
Eindhoven, Netherlands

L. R. GLICKSMAN

Associate Professor,
Massachusetts Institute of
Technology,
Cambridge, Mass.
Mem. ASME

An Experimental and Analytical Study of Radiative and Conductive Heat Transfer in Molten Glass

One-dimensional temperature profiles and heat fluxes within a slab of molten glass were measured experimentally. The glass slab was contained between two parallel platinum-lined ceramic plates. The plate temperatures were kept above 2000 deg F so that radiation heat flux was always equal to or larger than conduction. An optical method of temperature measurement was developed in which a helium-neon laser beam was directed along an isothermal path through the glass. The attenuation of the beam was a strong function of temperature and was used to evaluate the local temperatures within the glass slab. In order to perform a theoretical analysis the spectral absorption coefficient of the glass was measured from 2000 to 2300 deg F. Two analyses were performed: one for a diffuse platinum-glass boundary and the other for a specular boundary. The calculated temperatures agree with the measured values within 5 deg F throughout the slab, and the measured and predicted heat fluxes agree within 10 percent.

Introduction

THE ACCURATE prediction of temperature profiles and heat flux in a non-gray medium with simultaneous radiation and conduction is important to designers of rocket engines, ablation heat shields, and glass melting furnaces. Numerous theoretical treatments of simultaneous conduction and radiative transfer have been published in recent years, see, for example, references [1-9].² In these works, a great diversity of analytical models has been studied, e.g., gray diffuse walls, gray media, simple non-gray walls, etc.

There is a dearth of experimental results available due to the difficulties inherent in performing controlled experiments. A number of spectral measurements of the emission from isothermal and nonisothermal gases have been made [10-12]. The experiments were conducted to verify proposed band models for the gas; temperature gradients were imposed by conduction from nonisothermal walls, and the influence of radiative transfer on the temperature distribution of the gas was negligible. Spectral measurements of rocket exhaust plumes have been made in an effort to predict the temperature distribution within the plumes

[13]. For this case, turbulent convection occurs along with conduction and radiation and the process defies precise analysis.

Gille and Goody [14] in the course of an important investigation of radiation and convection measured the temperature distribution and heat flux for radiation and conduction in ammonia contained between isothermal parallel plates. However, the results are for the optically thin region, the departure of the temperature from a linear profile is at most 3 percent, and the bounding walls were assumed gray with the value of emissivity adjusted to fit the heat-flux data.

Nishimura et al. [15] measured the temperature distribution in a slab of molten glass using thermocouples embedded in the glass. When the glass was optically thin, agreement between the measurements and the theoretical results was poor. This was probably due to the distortion of the temperature distribution in the glass caused by the presence of the thermocouple.

Finch et al. [16] measured the heat flux through glass plates at temperatures up to 1000 deg F. The surfaces of the plates were adjacent to transparent media. The work was performed to evaluate a computer program to predict the heat flux; the agreement between the experimental and the numerical results was poor.

In this paper experimental results are presented for a non-gray medium in which radiation absorbed and emitted by the medium is of the same order of magnitude as conduction within the medium. For simplicity, the heat transfer is steady and one-dimensional. The temperature distribution measured within the glass and the net heat flux are compared with analytical predictions.

¹ Formerly Research Assistant, Massachusetts Institute of Technology, Cambridge, Mass.

² Numbers in brackets designate References at end of paper.

Based on a paper contributed by the Heat Transfer Division and presented at the Winter Annual Meeting, New York, N. Y., November 29-December 3, 1970, of THE AMERICAN SOCIETY OF MECHANICAL ENGINEERS as Paper No. 70-WA/HT-10. Manuscript received by the Heat Transfer Division August 10, 1970; revised manuscript received February 16, 1971.

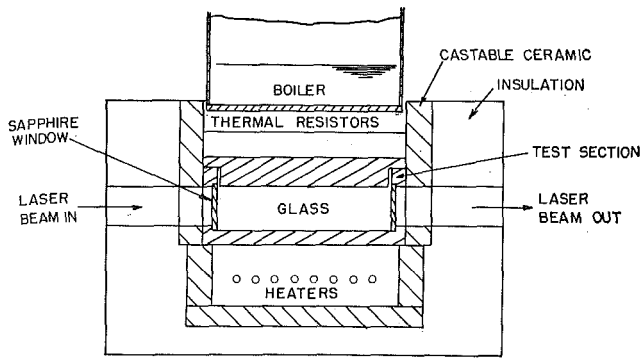


Fig. 1 Experimental apparatus

This work was also undertaken to develop techniques which could be applied to experiments of simultaneous radiation, conduction, and convection.

Experimental Measurements

Glass was chosen as the experimental medium because the variation of absorption coefficient with wavelength does not exhibit complex line-absorption behavior characteristic of a gas. In addition, the high viscosity of glass permits experiments at relatively high temperatures without natural convection. High temperatures are necessary to achieve radiative interactions which are the same order of magnitude as conduction. Radiative interaction refers to the radiation absorbed and emitted by the medium. For a completely transparent medium, the radiative heat flux through the medium might be significant but radiative interactions would not be present and the temperature distribution would be solely determined by conduction. High temperatures also cause the glass to soften, eliminating contact resistance at the boundaries. Water white³ glass, an iron-free glass, was used in the experiments because its spectral-absorption coefficient changes gradually with temperature and almost stepwise with wavelength.

The glass was contained between two parallel horizontal plates or slabs shown in Fig. 1. The plates were 8.25 in. square and the plate separation distance was 1½ in. The sides were insulated to minimize heat losses. Platinum-platinum/10 percent rhodium thermocouples were used to measure the plate temperature; five thermocouples were placed on each surface. For all of the tests, the maximum temperature difference along the surface of a plate was less than 1 percent. The heat flux was found by measuring the temperature difference across the bottom slab. The temperatures of the plates were varied from a maximum of 2635 deg R to a minimum of 2240 deg R. Lower temperatures could not be used since the glass crystallized when kept at temperatures near 2200 deg R.

³ Trademark of Pittsburgh Plate Glass Co.

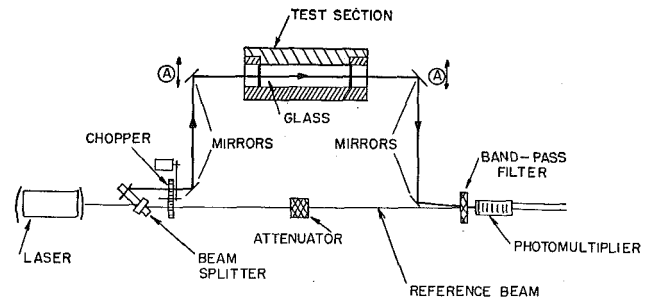


Fig. 2 Optical system for temperature measurement

The slabs were made from a fusion-cast high-purity alumina ceramic monofrax A,⁴ which does not react chemically with the glass. The slabs were carefully selected to minimize voids within the material. The surfaces of the slabs were grooved for the thermocouple leads. The slabs were lined with platinum foil in order to have boundaries with known optical constants. At high temperatures, glass seeped through slits in the foil to eliminate any contact resistance between the foil and the ceramic surface.

Thermocouples were not used to measure the local temperatures within the glass because the thermocouple supports would distort the temperature field. An optical method of temperature measurement was developed for use in the experiments wherein the variation of the monochromatic absorptivity of the glass with temperature was used to measure the local temperature within the glass.

Fig. 2 shows a diagram of the optical system used to measure the one-dimensional temperature profiles within the glass. A brief description of the temperature-measuring technique follows and more detailed information can be found in reference [17]. The output of a continuous helium-neon laser beam was split into a sample beam and a reference beam, which were chopped out of phase. Narrow synthetic sapphire windows were placed in the side walls of the test section to transmit the sample beam into and out of the test section. The intensity of the reference beam was set equal to the intensity of the sample beam by adjusting the variable attenuator. The attenuator settings were calibrated over a range of temperatures by using an isothermal test section of known temperature. In Fig. 3 the results of the calibrations are presented as absorption coefficient versus temperature. Losses at the air-window and glass-window interfaces have been accounted for. The results shown are for two isothermal test sections, a cylindrical test cell [18], and the parallel-plate system shown in Fig. 1.

By traversing the mirrors labeled A in Fig. 2, the temperature profile across the test section was measured. During the experiments the edges of the sapphire windows in the test section were obstructed by leaking glass and therefore temperature near the upper and lower boundaries could not be measured.

⁴ Trademark of Carborundum Co.,

Nomenclature

B = wall radiosity (Btu/hr-ft²)
 e_b = black-body emissive power (Btu/hr-ft²)
 I = intensity of radiation (Btu/hr-ft²-steradian)
 k_T = thermal conductivity (Btu/hr-ft-deg F)
 k = absorption coefficient (cm⁻¹)
 L = plate separation (ft)
 n = index of refraction
 N = dimensionless conduction-radiation parameter, $k_T k / 4\sigma T_1^4$
 q = heat flux (Btu/hr-ft²)

s = path length (ft)
 T = temperature (deg R)
 t = dummy variable of integration, see equation (4)
 y = distance from boundary (ft)
 ϵ = emissivity
 θ = angle from surface normal
 λ = wavelength (μ m)
 μ = $\cos \theta$
 σ = Stefan-Boltzmann constant (Btu/hr-ft²-deg R⁴)
 ρ = reflectivity
 τ = optical thickness, ky

τ_0 = optical thickness, kL
 ω = solid angle

Subscripts

h = hot wall
 i = denotes isothermal layer
 j = denotes a wavelength interval
 L = denotes $y = L$
 p = perpendicularly polarized component
 r = radiative
 1 = lower wall
 2 = upper wall
 λ = monochromatic

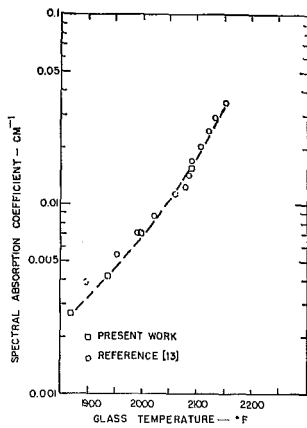


Fig. 3 Spectral-absorption coefficient of glass at 0.6328 μm

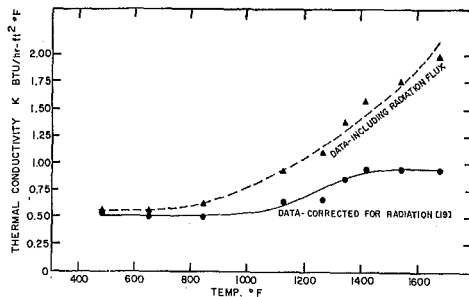


Fig. 4 Thermal conductivity of glass

Analysis

For the case at hand, one-dimensional steady conduction and radiation in a stationary medium, the energy equation is

$$\frac{d}{dy} \left(-k_T \frac{dT}{dy} \right) = \frac{dq_r}{dy} \quad (1)$$

The radiative flux is defined in terms of the monochromatic intensity by

$$q_r = \int_0^\infty \int_{4\pi} I_\lambda \cos \theta \, d\omega \, d\lambda \quad (2)$$

where θ is measured from the y direction, the direction normal to the isothermal planes. The monochromatic intensity can be found from the equation of transfer assuming local thermal equilibrium exists and no scattering occurs:

$$\frac{dI_\lambda(s)}{ds} = -k_\lambda \left[I_\lambda(s) - \frac{e_b \lambda}{\pi} \right] \quad (3)$$

The first term on the right-hand side represents the decrease in intensity due to absorption within the medium; the second term represents the increase in intensity due to emission from the medium. Equations (2) and (3) can be combined with equation (1) to yield a nonlinear integro-differential equation for the temperature distribution in the medium. With the temperature distribution known, the heat flux can be calculated.

In order to solve the equations the properties of the medium and the boundary conditions must be specified. The analyses in this work differ from those of previous investigators in that both the wavelength-dependent properties of the glass medium and the boundaries will be accounted for.

Properties of the Medium and Boundaries

The medium between the boundaries did not significantly scatter radiant energy. All of the entrained air bubbles in the

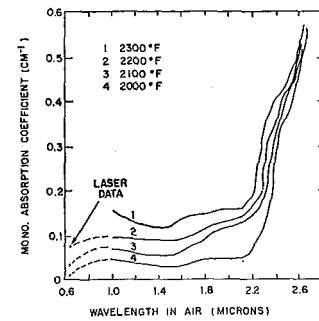


Fig. 5 Spectral-absorption coefficient of glass

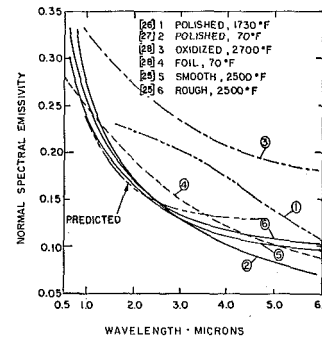


Fig. 6 Normal spectral emissivity of platinum-air interface

glass were removed by continuous heating above 2000 deg F, and scattering effects were not observed when a collimated beam of light was passed through the glass.

At the temperature level of the experiments, the thermal conductivity of the medium was not a function of temperature. The data shown in Fig. 4 taken from reference [19] indicate that the thermal conductivity increases with temperature up to 1800 deg F, and then remains constant at higher temperatures.

Above 4.5 μ (measured in air) glass is a strong absorber and a negligible amount of radiative energy is transmitted. Below 4.5 μ , the glass does not absorb strongly; therefore, the index of refraction can be considered a real quantity. Based on the limited data available [20, 21], it was assumed that the index of refraction does not vary with wavelength or temperature. A value of $1\frac{1}{2}$ was used for the index of refraction.

At the outset of this program, the absorption coefficient of the glass was measured at elevated temperatures between 0.6328 μ and 2.7 μ , in air. The data, shown in Fig. 5, indicate that the absorption coefficient increases monotonically with temperature and almost stepwise with wavelength.

For wavelengths between 2.7 μ and 4.5 μ in air, data taken from the literature for glass of similar composition [22-24] indicate that the absorption coefficient is approximately 4 cm^{-1} . Precise values of the absorption coefficient are not necessary for wavelengths greater than 2.7 μ because the majority of the radiant exchange occurs at lower wavelengths; above 2.7 μ the optical thickness is greater than 10. For the analysis, the wavelength-dependence of the absorption coefficient was modeled as a series of discontinuous steps; for all calculations, three steps were used, with discontinuities at 2.7 and 4.5 μ . The variation of absorption coefficient with temperature was not included in the calculation of a specific case.

Measurements of the emissivity of a platinum-air interface have been reported [25-28], but measurements have not been made for a platinum-glass interface. The emissivity of a platinum-air interface was calculated using the results of classical electromagnetic theory for a smooth interface and using tabulated optical constants for platinum [29]. Results are presented in Figs. 6 and 7. The excellent agreement with experimental data

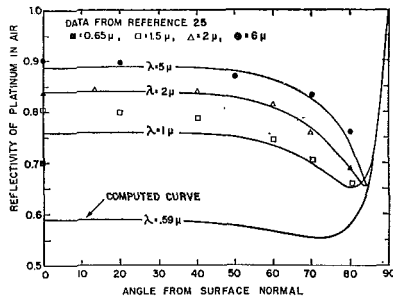


Fig. 7 Directional hemispherical reflectivity of platinum in air

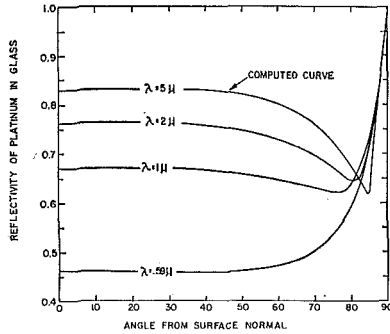


Fig. 8 Directional hemispherical reflectivity of platinum in glass

is somewhat unexpected since the optical constants are room-temperature values while the reflectivity data were taken at 2500 deg F. The same optical constants were used to predict the emissivity of the platinum-glass interface at elevated temperatures, assuming the index of refraction for glass is $1\frac{1}{2}$ and is real. Representative results are shown in Fig. 8.

Photomicrographs of the platinum-foil boundary at the conclusion of the experiments revealed that the surface roughness had increased. However, it could not be determined if the changes occurred during the tests or as a result of uneven thermal contraction during cooling. To account for the uncertainty in the surface condition during the experiments, two models of the interface were used in the analysis. In the first model, the interface was assumed to reflect specularly and the results presented in Fig. 8 were used to predict the angular variation of the monochromatic emissivity. In the second model, the surface was assumed to reflect and to emit diffusely. The same value of hemispherical emissivity was used for both models and the optical constants of platinum were taken as a step function of wavelength.

Solution for Diffuse Boundaries

When the details of the radiative transfer are included, the energy equation becomes a nonlinear integro-differential equation in which the temperature appears in both the first and fourth powers. For diffuse boundaries equation (1) becomes

$$k_T \frac{d^2 T'}{dy^2} = - \int_0^\infty k_\lambda \left[2B_{1\lambda} E_2(\tau_\lambda) + 2B_{2\lambda} E_2(\tau_{0\lambda} - \tau_\lambda) + 2 \int_0^{\tau_{0\lambda}} e_{b\lambda}(t) E_1(|\tau_\lambda - t|) dt - 4e_{b\lambda}(\tau_\lambda) \right] d\lambda \quad (4)$$

The term on the left-hand side represents conduction, the first two terms on the right-hand side represent radiation absorbed at point y due to energy emitted or reflected from the boundaries, the third term represents emission from all other points in the medium absorbed at point y , and the final term represents emission from the medium at y .

The exponential integral is defined as

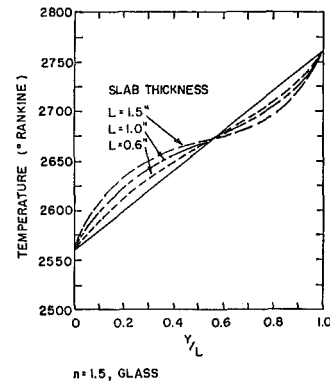


Fig. 9 Temperature distribution for varying thicknesses of glass contained between parallel diffuse plates

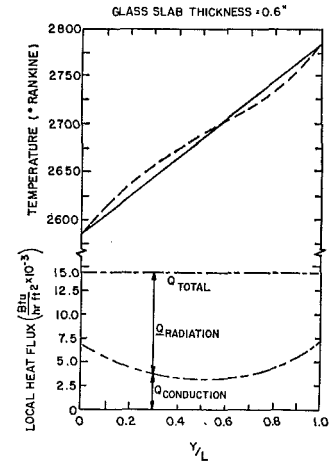


Fig. 10 Local radiative and conductive fluxes in a glass slab, diffuse boundaries

$$E_n(x) = \int_0^1 \mu^{n-2} \exp(-\tau/\mu) d\mu$$

The wall radiosities are given by the following pair of simultaneous equations:

$$B_{1\lambda} = \epsilon_{1\lambda} e_{b1\lambda} + 2(1 - \epsilon_{1\lambda}) \left[B_{2\lambda} E_3(\tau_{0\lambda}) + \int_0^{\tau_{0\lambda}} e_{b\lambda}(t) E_2(t) dt \right] \quad (5)$$

$$B_{2\lambda} = \epsilon_{2\lambda} e_{b2\lambda} + 2(1 - \epsilon_{2\lambda}) \left[B_{1\lambda} E_3(\tau_{0\lambda}) + \int_0^{\tau_{0\lambda}} e_{b\lambda}(t) E_2(\tau_0 - t) dt \right] \quad (6)$$

The boundary conditions are

$$\begin{aligned} \text{at } y = 0 & \quad T = T_1 \\ \text{at } y = L & \quad T = T_2 \end{aligned} \quad (7)$$

The energy equation was solved numerically by the method of successive approximations. The monochromatic radiative properties were assumed to vary stepwise so the integral over wavelength could be replaced by a summation. The method of solution was similar to the work of Viskanta and Grosh [1] for a gray medium.

Figs. 9 and 10 show temperature profiles and boundaries. Fig. 9 shows the effect of varying thickness with fixed boundary temperatures. The departure from a linear temperature profile increases for larger slab thickness. Fig. 10 shows the variation in local conductive and radiative fluxes within a slab of glass

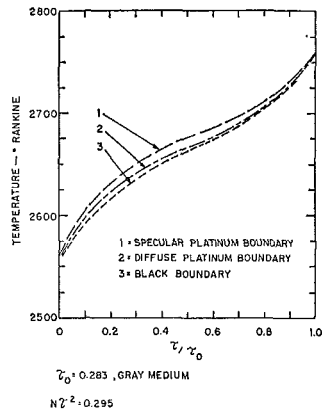


Fig. 11 Temperature distributions for radiation and conduction with specular, diffuse, and black boundaries

0.6 in. thick. Although the sum of the local conductive and radiative fluxes is constant, there is considerable redistribution of flux from conduction to radiation throughout the medium, indicating a significant amount of radiative interaction within the medium.

Solution for Specular Boundaries

The solution for specularly reflecting boundaries is more difficult than for diffuse boundaries, since the intensity of radiation leaving a boundary varies with the angle from the surface normal and the "history" of the radiation must be kept as it is reflected from boundary to boundary. An implicit solution for the temperature profile was derived by dividing the medium up into a number of isothermal layers of equal thickness. A heat balance is complicated because radiative energy can arrive at a given layer by direct exchange or by energy which has been reflected from the specular boundaries a number of times.

The energy balance for a given layer becomes

$$\begin{aligned}
 & [\Sigma \text{ absorbed radiation, emitted from} \\
 & \quad \text{boundaries and other layers}]_{\text{direct}} \\
 & \quad \quad \quad \text{exchange} \\
 & + [\Sigma \text{ absorbed radiation, emitted from} \\
 & \quad \text{boundaries and other layers}]_{\text{reflected}} \\
 & \quad \quad \quad \text{by one or} \\
 & \quad \quad \quad \text{more walls} \\
 & + \text{net conduction to layer} \\
 & - \text{energy emitted by layer} \\
 & + \text{energy emitted by layer which is reabsorbed} = 0 \quad (8)
 \end{aligned}$$

The terms representing direct exchange are straightforward and are identical to the terms in equation (4) except that for radiation from the boundaries the monochromatic intensity was integrated over angle and summed over wavelength to account for the nonisotropic non-gray conditions. The integration over angle was approximated by Gaussian quadrature.

The terms representing reflections from the boundaries at a given angle comprised an infinite series, which converged to a closed-form expression. For example, let $I_{\lambda\theta p}(L)$ represent the component of radiation incident on the upper surface at angle θ and polarized perpendicular to the plane of incidence. Then the amount of $I_{\lambda\theta p}(L)$ which arrives at y traveling in the direction of increasing y , due to one or more reflections, is

$$\left[I_{\lambda\theta p}(L)\rho_p e^{-\frac{k_\lambda y}{\cos\theta}} \right] \left[\rho_p e^{-\frac{k_\lambda L}{\cos\theta}} + \rho_p^3 e^{-\frac{3k_\lambda L}{\cos\theta}} + \dots \right] \quad (9)$$

This can be written using the binomial series as

$$I_{\lambda\theta p}(L)\rho_p^2 e^{-\frac{k_\lambda(L+y)}{\cos\theta}} \left[\frac{1}{1 - \rho_p^2 e^{-\frac{2k_\lambda L}{\cos\theta}}} \right] \quad (10)$$

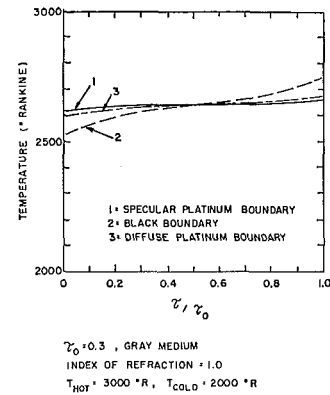


Fig. 12 Temperature distributions for radiative equilibrium with specular, diffuse, and black boundaries

Similarly, the amount of $I_{\lambda\theta p}(L)$ which arrives at y traveling in the direction of decreasing y , due to one or more reflections, is

$$I_{\lambda\theta p}(L)\rho_p^2 e^{-\frac{k_\lambda(L-y)}{\cos\theta}} \left[\frac{1}{1 - \rho_p^2 e^{-\frac{2k_\lambda L}{\cos\theta}}} \right] \quad (11)$$

The derivation of equations (10) and (11) assumes that the monochromatic directional reflectivities of the upper and lower surfaces are identical. Reference [17] gives the derivations of all the terms in equation (8).

A system of nonlinear algebraic equations was formulated by writing the energy balance for layers of finite thickness. It is convenient to express the equations in matrix notation as follows:

$$[A_{ij}][T_j] + [B_{ij}][T_j^4] + [C_{ij}] = 0 \quad (12)$$

where A_{ij} , B_{ij} , and C_{ij} represent, respectively, coefficients in the heat balance due to conduction, radiative exchange between layers (by direct exchange and reflected by the walls), and radiation emitted by the walls. C_{ij} is a constant since the boundary temperatures are known.

The Newton-Raphson iterative method was used to solve the resulting set of nonlinear algebraic equations. The matrix equation was solved in terms of the emissive power. A trial temperature vector was substituted into the heat-balance equation and a non-zero residual vector resulted if the trial vector was not the correct solution. Convergence required 10 iterations for an accuracy of 1 deg F in the temperature.

Results

Figs. 11 and 12 show a comparison of diffuse and specular wall results for gray media. Fig. 11 compares the temperature profiles for radiation plus conduction. Specular boundaries cause a more uniform profile in the center of the medium than diffuse or black boundaries. Fig. 12 shows the temperature profiles for radiative equilibrium (the conductivity is absolutely zero) which bears out the tendency of specular walls to flatten out the profile. Conduction tends to mask some of the effects of specularly reflecting walls by requiring temperature continuity at the boundaries.

Figs. 13-16 show the predicted temperature profiles and the experimental results. The test conditions for each figure are tabulated in Table 1. Notice that for all cases the radiative interaction is strong, causing a marked distortion of the temperatures away from a linear profile. For specular walls, the temperature gradient in the center of the medium is smaller than the gradient for diffuse walls, just as in the case of gray media. To explain this, consider a ray of energy incident on the boundary at an angle near the normal to the surface. If the boundary reflects diffusely, the incident ray is reflected over a hemisphere

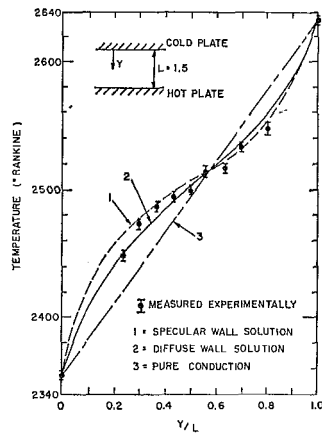


Fig. 13 Experimental versus predicted temperature distributions in glass

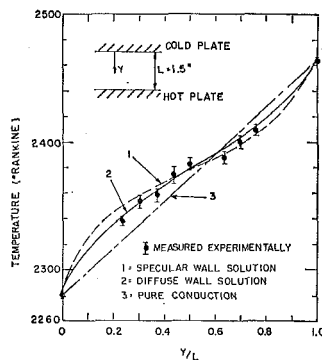


Fig. 14 Experimental versus predicted temperature distributions in glass

and only a small fraction of the energy reflected at angles far from the surface normal reaches the other boundary. For the experimental conditions of this study, the average path length for energy emitted diffusely from one boundary, reflected at the opposite boundary, and returned to the original boundary is 30 percent less for specularly reflecting boundaries than for diffusely reflecting boundaries.

Since the average path length between specular surfaces is lower than the path length between diffuse surfaces, the net heat flux should be higher. Also radiation emitted by elements near one wall should have more influence on elements near the opposite wall when the surfaces are specular, leading to a more uniform temperature distribution throughout the medium.

The measured temperature profiles are shown in Figs. 13–16 along with estimated limits of uncertainty. For all cases, the data fall between the predictions for specular and diffuse walls. Fig. 13 contains the data for the greatest temperature difference between the upper and lower boundaries; the ratio of the emissive power of the hot wall to the cold wall is 1.575. This represents a test condition where the nonlinear behavior of the energy equation is emphasized.

Table 1 shows the calculated and measured heat fluxes. The measured heat fluxes tend to agree with the diffuse-model predictions. The value of the thermal conductivity of the ceramic used to evaluate the measured heat fluxes was extrapolated from measured values at 1600 and 2000 deg F. Due to the similarity

Table 1 Net heat flux (Btu/hr-ft²)

Fig.	Calculated		Experimental Measured	Plate temperatures (°R)	
	Specular	Diffuse		T_1	T_2
13	13,326	12,804	12,400	2633	2347
14	7,000	6,612	6,700	2465	2280
15	4,270	3,656	3,800	2440	2335
16	5,987	5,672	5,100	2400	2230

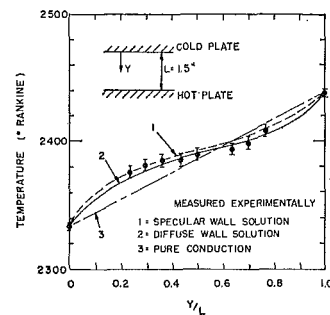


Fig. 15 Experimental versus predicted temperature distributions in glass

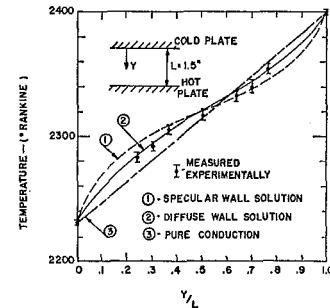


Fig. 16 Experimental versus predicted temperature distributions in glass

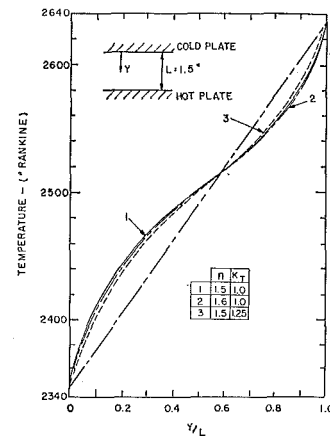


Fig. 17 Influence of index of refraction and thermal conductivity on temperature distributions in glass

of the diffuse and specular predictions and the experimental uncertainties, no conclusions can be drawn regarding the exact nature of the glass-platinum interface.

The errors in the glass and wall temperatures were estimated to be ± 3 deg F. The effect of a temperature drop at the end of the isotherms, caused by heat losses from the sapphire windows, was investigated. The magnitude of the temperature drop was evaluated for two extreme cases, an optically thin medium and an optically thick medium. The results indicate that temperature perturbations caused by the windows would decay within 0.75 in. of the window. The heat flux measured through the side wall gives an estimate of the temperature gradient in the inside of the wall. The data indicate that the temperature gradient at the wall is less than 10 deg F per inch assuming that the heat transfer in the glass takes place by conduction alone.

Due to uncertainties in the values of the thermophysical properties, the diffuse model was tested to evaluate its sensitivity to changes in the thermal conductivity, the index of refraction, and the absorption coefficient, Fig. 17. For the experimental conditions shown in Fig. 13, a 25 percent change in the thermal conductivity produces a maximum change of 5 deg F in the tem-

perature and an 8 percent change in the total heat flux. A 14 percent change in the refractive index causes a maximum change of 4 deg F in the temperature and a 25 percent change in the heat flux; a 20 percent change in the absorption coefficient below 2.7μ produces a 4 deg F change in temperature and an 11 percent change in the heat flux.

Due to the high viscosity of the glass and the small plate spacing, natural convection is absent. For the experiment with the highest wall temperatures, the Rayleigh number is approximately 500 when the glass viscosity is evaluated at the hot-wall temperature. When the viscosity is evaluated at the cold-wall temperature, the Rayleigh number is 50. For transparent media, the critical Rayleigh number for the inception of convection is taken to be 1700. It has been demonstrated that the presence of radiative interactions increases the critical Rayleigh number [14].

Conclusions

The optical method of temperature measurement yields accurate results when the laser is directed along the isothermal path, the medium does not scatter radiation, and the dependence of the spectral absorption with temperature is known.

Glass is a useful medium for controlled experiments of radiative transfer in absorbing and emitting media. Experiments in which the radiation interaction is the same order of magnitude as conduction can be performed with glass. The temperature level can vary substantially without convection occurring. The spectral-absorption coefficient of glass can be accurately modeled as a series of step functions.

Specularly reflecting boundaries with a directional-emissivity characteristic of a metal-dielectric interface cause a higher heat flux and a flatter temperature profile away from the walls than diffuse boundaries. For the conditions of this study, the differences between the predicted results for specular boundaries and for diffuse boundaries are slight. The experimental results fall between the specular and the diffuse predictions. Due to experimental uncertainties, it is impossible to conclude which model of the boundary condition is most nearly correct.

Acknowledgment

This program was supported by the National Aeronautics and Space Administration sustaining university grant number NSA-496. The computations were performed at the M.I.T. Information Processing Center.

References

- 1 Viskanta, R., and Grosh, R. J., "Heat Transfer by Simultaneous Conduction and Radiation in an Absorbing Medium," *JOURNAL OF HEAT TRANSFER*, TRANS. ASME, Series C, Vol. 84, No. 1, Feb. 1962, pp. 63-72.
- 2 Viskanta, R., and Grosh, R. J., "Effect of Surface Emissivity on Heat Transfer by Simultaneous Conduction and Radiation," *International Journal of Heat and Mass Transfer*, Vol. 5, pp. 729-734.
- 3 Einstein, T. H., "Radiant Heat Transfer to Absorbing Gases Enclosed Between Parallel Flat Plates with Flow and Conduction," NASA Tech. Report R-154.
- 4 Chui, G. K., and Gardon, R., "Interaction of Radiation and Conduction in Glass," *Journal of the American Ceramic Society*, Vol. 52, No. 10, 1969, pp. 548-553.
- 5 Lick, W., "Energy Transfer by Radiation and Conduction," *Proceedings of the 1963 Heat Transfer and Fluid Mechanics Institute*, Stanford University Press, Palo Alto, Calif., 1963, pp. 14-26.
- 6 Greif, R., "Energy Transfer by Radiation and Conduction with Variable Gas Properties," *International Journal of Heat and Mass Transfer*, 1964, p. 891.
- 7 Kadanoff, L. P., "Radiative Transport Within an Ablating Body," *JOURNAL OF HEAT TRANSFER*, TRANS. ASME, Series C, Vol. 83, No. 2, May 1961, pp. 215-225.
- 8 Kellett, B. S., "The Steady Flow of Heat Through Hot Glass," *Journal of the Optical Society of America*, Vol. 42, No. 5, May 1952, pp. 339-343.
- 9 Gardon, R., "Calculation of Temperature Distributions in Glass Plates Undergoing Heat-Treatment," *Journal of the American Ceramic Society*, Vol. 11, No. 6, June 1958, pp. 200-209.
- 10 Edwards, D. K., "Radiation Interchange in a Nongray Enclosure Containing an Isothermal Carbon-Dioxide-Nitrogen Gas Mixture," *JOURNAL OF HEAT TRANSFER*, TRANS. ASME, Series C, Vol. 84, No. 1, Feb. 1962, pp. 1-11.
- 11 Simmons, F., "Band Models for Non-isothermal Radiating Gases," *Applied Optics*, Vol. 5, 1966, p. 1801; Vol. 6, 1967, p. 1423.
- 12 Krakow, B., and Babrov, H., "Review of Experimental Verification of the Curtis-Godson Approximation for Infrared Spectral Radiation from High Temperature Gases," *Specialist Conference on Molecular Radiation*, R. Goulard, ed., NASA TMX-53711.
- 13 Herget, W., "Temperature and Concentration Measurements in Model Exhaust Plumes Using Inversion Techniques," *Specialist Conference on Molecular Radiation*, R. Goulard, ed., NASA TMX-53711.
- 14 Gille, J., and Goody, R., "Convection in a Radiating Gas," *Journal of Fluid Mechanics*, Vol. 20, Part 1, 1964, pp. 47-49.
- 15 Nishimura, M., Hasatani, M., and Sugiyama, S., "Simultaneous Heat Transfer by Radiation and Conduction. High Temperature One-Dimensional Heat Transfer in Molten Glass," *Int. Chem. Eng.*, Vol. 8, 1968, p. 739.
- 16 Finch, H., Noland, M., and Moeller, C., "Experimental Verification of the Analyses and Computer Programs Concerning Heat Transfer Through Semi-Transparent Materials," Technical Report AFFDL-TR-65-136, Air Force Flight Dynamics Laboratory, Wright-Patterson Air Force Base, Ohio, July 1965.
- 17 Eryou, N. D., "An Experimental and Theoretical Study of Radiative and Conductive Heat Transfer in Nongray Semi-Transparent Media," Ph.D. thesis, Department of Mechanical Engineering, M.I.T., Cambridge, Mass., Oct. 1969.
- 18 Jeryan, R. A., "An Optical Temperature Measuring Technique for Semi-Transparent Media," S.M. thesis, M.I.T., Cambridge, Mass., June 1969.
- 19 Chen, K. H., "Measurement of Thermal Conductivity of Glass at High Temperature," S.M. thesis, Department of Mechanical Engineering, M.I.T., Cambridge, Mass., June 1969.
- 20 Phillips, C. J., *Glass—Its Industrial Applications*, Reinhold, New York, N. Y., 1960.
- 21 Neuroth, N., "Der Temperatureinfluss auf die Optischen Konstanten von Glas im Gebiet Starker Absorption," (The Temperature Effects on Optical Constants of Glass in the Range of Strong Absorption), *Glastech. Ber.*, Vol. 28, No. 11, 1955, pp. 411-422.
- 22 Grove, F. J., and Jellyman, P. E., "Infrared Transmission of Glass in the Range Room Temperature to 1400°," *Journal of the Society of Glass Technology*, Vol. 39, No. 186, 1955, pp. 3-15T.
- 23 Neuroth, N., "Der Einfluss der Temperatur auf die Spektrale Absorption von Glasern im Ultraroten, I," (Effect of Temperature on Spectral Absorption of Glasses in the Infrared, I), *Glastech. Ber.*, Vol. 25, No. 8, 1952, pp. 242-249.
- 24 Neuroth, N., "Der Einfluss der Temperatur auf die Spektrale Absorption von Glasern im Ultraroten, II," *Glastech. Ber.*, Vol. 26, No. 3, 1953, pp. 66-69.
- 25 Rolling, R., "Effect of Surface Roughness on the Spectral and Total Emittance of Platinum," *Progress in Aeronautics and Astronautics*, Vol. 20, 1967, pp. 91-114.
- 26 Seban, R. A., "Thermal Radiation Properties of Materials, Part III," WADD TR-60-370, Pt. III, University of California, Berkeley, Calif., Aug. 1963.
- 27 Gubareff, G., Janssen, J., and Torborg, R., "Thermal Radiation Properties Survey," Honeywell Research Center, Minneapolis, Minn.
- 28 Touloukian, Y. S., ed., *Thermophysical Properties of High Temperature Solid Materials*, Vol. 1, Macmillan, New York, N. Y., 1967.
- 29 Weast, R. C., ed., *Handbook of Chemistry and Physics*, 44th ed., Chemical Rubber Co., 1962.

This section consists of contributions of 1500 words or less (about 5 double-spaced typewritten pages, including figures). Technical briefs will be reviewed and approved by the specific division's reviewing committee prior to publication. After approval such contributions will be published as soon as possible, normally in the next issue of the journal.

Impingement Heat-Transfer Rates from Torch Flames

E. H. SCHULTE¹

The heat-transfer profiles of small natural gas-oxygen and acetylene-air flames to flat cooled surfaces were experimentally determined. Results show that the heat-transfer profiles can be relatively flat over a given area and that the best operating condition must be determined experimentally.

ALTHOUGH it is possible to calculate the heat-transfer characteristics of a gas flame, the task is difficult and the calculation must be verified experimentally [1].² This is particularly true of studies made of areas near the tip of the reaction zone [2]. Two theoretical approaches have been used: one using the net reaction rates and absolute molar enthalpies, the other using the molar heat capacity and thermal conductivity [2, 3].

A literature search was conducted during an investigation of the properties of germanium-surface thermocouples [4] exposed to convective heat fluxes on the order of 25 Btu/ft²-sec. Though numerous references on gas flames [2] are available, it was found that very few data on flat cold-wall heat-transfer-rate profiles in small gas flames have been published. This absence of information may be due to the difficulties involved in accurately measuring the heat-transfer rates on small cooled surfaces. Anderson and Stresino [1] have performed an analysis and presented heat-transfer data on oxyhydrogen, oxypropane, oxyacetylene, and air-methane flames but have stated that their experimental data may be subject to large errors. A limited amount of heat-transfer data in an oxyacetylene flame are also presented by Morgan and Andrews [5].

In this study the principal investigations centered about a Prest-O-Lite torch [6] with a No. 1 tip having a 0.079-in-dia opening. It burned a mixture of acetylene and air. The acetylene flow was adjustable and the air was self-regulating. Two additional torches which burned a mixture of natural gas and oxygen were tested and in each the gases were individually controllable. One was a Meco type N Midget torch [7] with an N-O tip having a 0.021-in-dia opening. The other was a National type 3A blowpipe torch [8] with an OX-3 tip having a 0.065-in-dia opening. The three torches burned premixed reactants (oxygen, natural gas, and air-acetylene) and had approximately laminar flames. While the actual gas flows to the torches were not measured, it was assumed that near-stoichiometric mixtures were burning. Under these conditions the reaction

zone of the flames was a well-defined flat-sided cone with a rounded tip, the length of the primary cone being indicative of the gas flow rate.

The heat-transfer profiles on the impingement plane in the flames were determined with a recently developed water-cooled heat-flux transducer [9]. This sensor has a flat, cool, approximately isothermal sensing surface and a small sensing area. The transducer used in this test was calibrated to an accuracy of 3 percent and the transducer output versus input heat flux is linear for a uniform input heat flux and has a sensitivity of 27.5 (Btu/ft²-sec)/mv. (Similar transducers are now available commercially [10].)

In the test setup the heat-flux transducer was surrounded by a water-cooled guard plate, thus providing a cool-plate impingement plane for the torch flame. The gas torch was attached to a two-axis slide vernier, thereby permitting the torch to be moved both parallel and perpendicular to the transducer face. The transducer output was monitored on a millivolt recorder.

The test procedure consisted of establishing a water flow rate for the transducer and guard shield, setting up a given length of primary cone on the torch, adjusting the torch valves for maximum indicated heat transfer, and moving the torch horizontally in increments of 0.05 in. across the face of the sensor. Since the transducer has a finite radial sensitivity beyond ± 0.025 in. of its center, and since the test data are at 0.050-in. increments, each datum point is a weighted integration, i.e., on an axial point the true axial value will be somewhat different. Each reading is an average value taken over a time interval sufficiently long to smooth the observed torch fluctuations. For all the test conditions except those greater than approximately 200 Btu/ft²-sec, the transducer sensing surface and guard shield were completely covered by a film of water condensed from the gas flames, insuring a cold-wall temperature considerably less than 200 deg F.

The data obtained using the Prest-O-Lite torch are presented in Fig. 1. Variations in data make it appear that either the torch movement perpendicular to the heat-flux transducer was slightly off-axis or that air currents within the room caused some slight movement of the flame. This latter possibility became apparent only when flames with primary cones longer than 0.4 in. were utilized. In these tests the primary concern was with the heat-transfer variations within a 0.2-in-dia area. Fig. 2 shows the variation in heat-transfer rate within this area. Similar curves for other diameters can readily be extracted from the data shown in Fig. 1. For this particular torch and tip, the flattest heat-transfer profile was obtained with a primary cone length of about 0.3 in. as shown in Fig. 2. However, under these conditions the heat transfer is not adjustable over a wide range by merely changing the torch-tip-to-sensor-plane distance as noted in Fig. 3.

The data obtained with the Meco torch are shown in Fig. 4. They are of the form normally expected of a torch having a small orifice, i.e., a narrow well-defined heat-transfer profile. At the tip of the primary cone is a heat-transfer maximum which decreases with increasing distance from the primary cone.

¹ Test Engineer, Materials Laboratories, McDonnell Aircraft Co., St. Louis, Mo.

² Numbers in brackets designate References at end of technical brief.

Contributed by the Heat Transfer Division of THE AMERICAN SOCIETY OF MECHANICAL ENGINEERS. Manuscript received by the Heat Transfer Division March 8, 1971; revised manuscript received September 13, 1971.

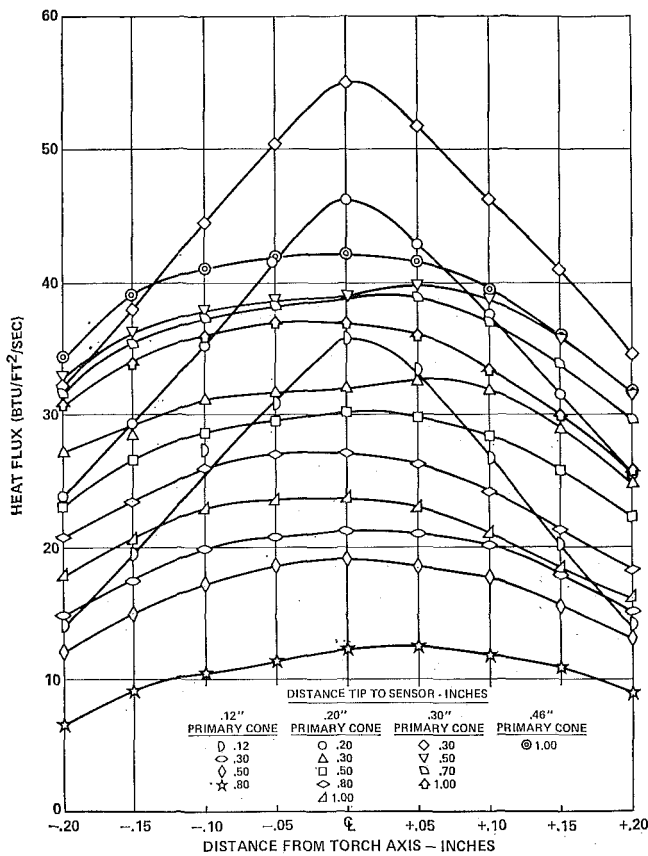


Fig. 1 Heat transfer in acetylene-air flame (Prest-O-Lite torch with No. 1 tip)

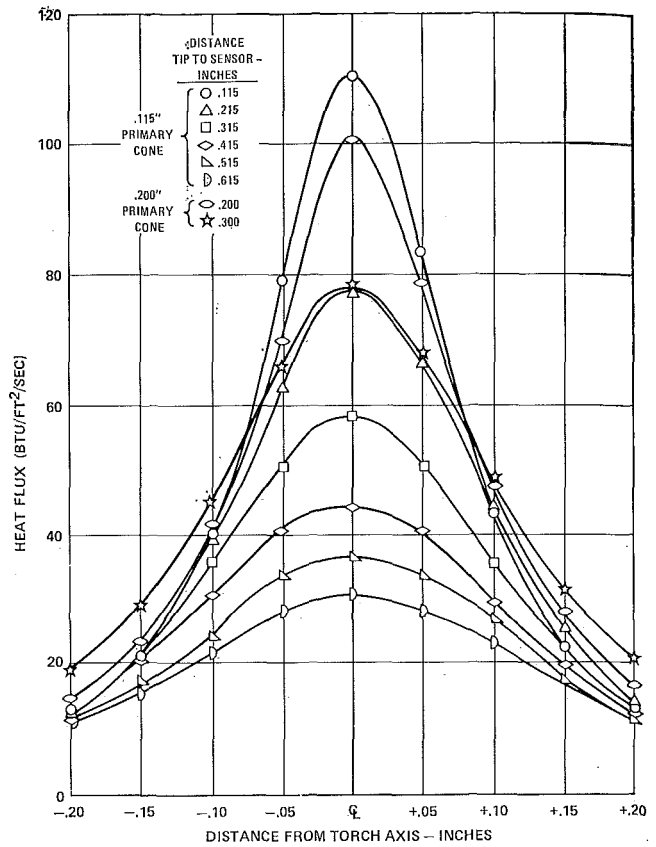


Fig. 4 Heat transfer in natural gas-oxygen flame (Meco torch with N-O tip)

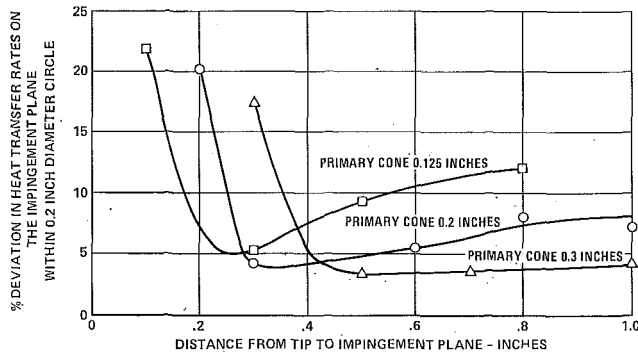


Fig. 2 Variation of heat-transfer rates around the stagnation point (Prest-O-Lite torch with No. 1 tip)

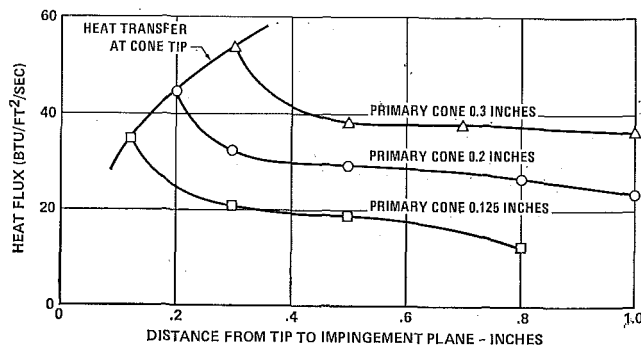


Fig. 3 Heat-transfer rates at the stagnation point (Prest-O-Lite torch with No. 1 tip)

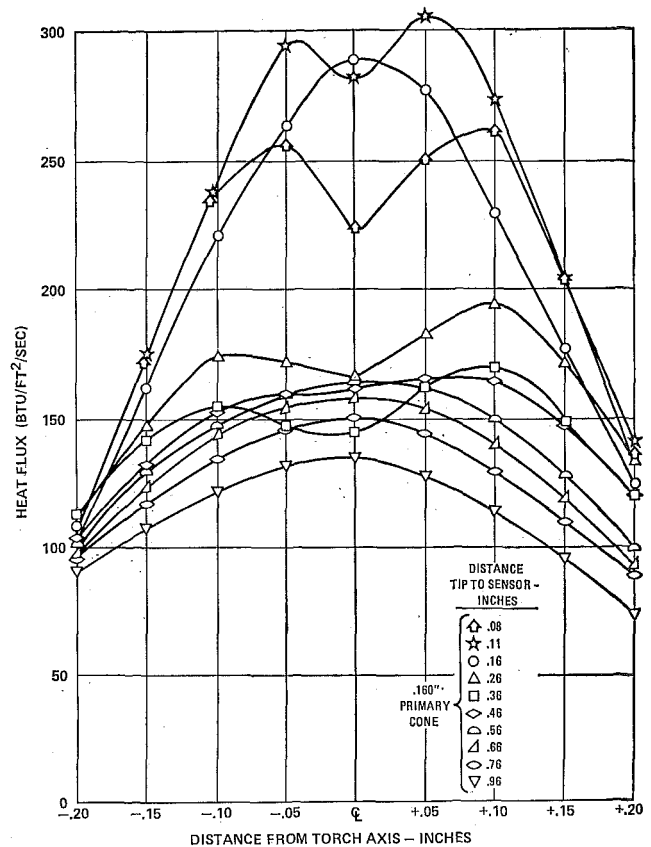


Fig. 5 Heat transfer in natural gas-oxygen flame (National type 3A blowpipe with OX-3 tip)

Fig. 5 shows the data obtained using the National torch. Here some apparent anomalies are found; a dip in the heat-transfer rate occurs beyond the tip of the primary cone. This dip is similar to the decrease observed in passing through the primary cone. Other investigators [11] have noted similar dips in temperature profiles of other gas flames, but no explanation has been presented. The severity of the dip is apparently indicative of the mixture ratio [11], possibly implying a non-stoichiometric gas mixture.

The results of this study show that the heat transfer resulting from the Prest-O-Lite torch with a No. 1 tip is relatively uniform within a central 0.2-in-dia circle. Further, results show that although the heat-transfer rates can be varied by adjusting the length of the primary cone, the distance from the torch to the test article also must be changed in order to maintain a relatively flat heat-transfer profile.

References

- 1 Anderson, J. E., and Stresino, E. F., "Heat Transfer From Flames Impinging on Flat and Cylindrical Surfaces," *JOURNAL OF HEAT TRANSFER*, TRANS. ASME, Series C, Vol. 85, No. 1, Feb. 1963, pp. 49-54.
- 2 Fristrom, R. M., and Westenberg, A. A., *Flame Structure*, McGraw-Hill, New York, N. Y., 1965.
- 3 Fristrom, R. M., and Westenberg, A. A., "Experimental Chemical Kinetics From Methane-Oxygen Laminar Flame Structure," *Eighth Symposium on Combustion Proceedings*, Williams and Wilkins, Baltimore, Md., 1962, pp. 438-448.
- 4 Kendall, D. N., Dixon, W. P., and Schulte, E. H., "Semiconductor Surface Thermocouples for Determining Heat Transfer Rates," *IEEE Transactions on Aerospace and Electrical Systems*, Vol. AES-3, No. 4, July 1967, pp. 596-603.
- 5 Morgan, C. C., and Andrews, J. C., "Morgandyne Heat Transfer Transducer and a Flame-Torch Calibration Technique for Hypervelocity Wind Tunnels," *Arnold Engineering Development Center Report TR-60-1*, Feb. 1960.
- 6 Prest-O-Lite, Union Carbide Corp., Linde Div., Indianapolis, Ind.
- 7 Modern Engineering Co., 3555 Scott Ave., St. Louis, Mo.
- 8 National Welding Equipment Div., Veriflo Corp., Richmond, Calif.
- 9 Schulte, E. H., and Kohl, R. F., "A Transducer for Measuring High Heat Transfer Rates," *Rev. Sci. Instr.*, Vol. 41, Dec. 1970, p. 732.
- 10 Hy-Cal Engineering, 12105 Los Nietos Road, Sante Fe Springs, Calif.
- 11 Lewis, B., and Von Elbe, G., "Combustion, Flames and Explosions in Gases," Academic Press, New York, N. Y., 1951.

Thermal and Combined Entry Problems for Laminar Flow between Parallel Porous Plates

JOHN R. DOUGHTY¹ and HENRY C. PERKINS, JR.²

Introduction

LAMINAR-FLOW porous-wall entrance problems are being analytically investigated by the authors for constant- and variable-property flows. Solutions to the hydrodynamic entry

¹ Major, USAF, Air Force Weapons Laboratory, Kirtland AFB, New Mexico. Mem. ASME.

² Professor, Energy, Mass, and Momentum Transfer Laboratory, Aerospace and Mechanical Engineering Department, University of Arizona, Tucson, Ariz. Mem. ASME.

Contributed by the Heat Transfer Division of THE AMERICAN SOCIETY OF MECHANICAL ENGINEERS. Manuscript received by the Heat Transfer Division January 11, 1971; revised manuscript received August 16, 1971.

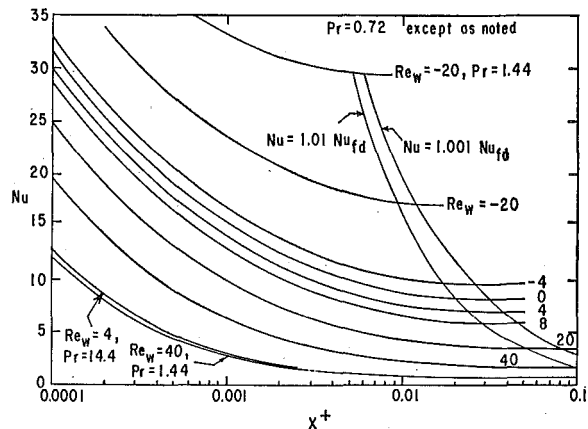


Fig. 1 Constant-property Nusselt numbers for parallel porous plates, constant heat flux

problem have been presented in [1].³ The thermal entry problem for constant-property flow with the boundary condition of constant- and equal-temperature walls is given in an earlier note [2]. This brief presents constant-property solutions for: (1) the thermal entry problem for uniform injection and suction through the channel walls and (2) the combined thermal and hydrodynamic entry problem for uniform injection and suction. Both solutions are for the common boundary condition of constant and equal heat flux into the fluid.

The velocity profiles employed for the constant-heat-flux thermal entry problem are completely fully developed including the effects of injection or extraction, i.e., the dimensionless velocity profile u/U_b has become invariant with regard to axial position. The temperature profile at the entrance to the heated section is uniform. Raithby [3], using the approach of Siegel, Sparrow, and Hallman [4], has given solutions to this problem. We have employed a different method, that of Patankar and Spalding [5] as modified by Bankston and McEligot [6], to obtain solutions to the constant-heat-flux thermal entry problem and the combined entry problem. The method consists of a sequential solution of the continuity, axial-momentum, and energy equations at each axial station and is a marching-integration routine which depends upon the values obtained at the previous station.

Results

Thermal Entry, Constant Wall Heat Flux. The behavior of the Nusselt number in the thermal entrance region is given in Fig. 1. The Nusselt number is defined on the hydraulic diameter which is twice the plate spacing. The behavior is similar to the constant-temperature-wall case given in [2] and is also analogous to that of the friction factor in the hydrodynamic entry region [1] in that the effect of injection is to reduce friction and heat transfer. The Nusselt number for porous plates is higher for the constant-heat-flux cases than for the constant-temperature-wall cases for the same wall Peclet number. This is similar to the usual results for these two boundary conditions for $Re_w = 0$.

The criterion for thermal development is taken to be when the local Nusselt number is within a certain percentage of the fully developed Nusselt number. The thermal entry lengths for cases where the Nusselt number is within 1 and 0.1 percent of the fully developed value are shown in Fig. 1. The effect of injection is to increase the thermal entry length continuously and monotonically, an effect similar to the constant-temperature-wall case [2]. All thermal-entry Nusselt-number curves shown in Fig. 1 have generally the same shape. The amount of injection or extraction determines whether the curves are below or above the impermeable-wall case.

³ Numbers in brackets designate References at end of technical brief.

Fig. 5 shows the data obtained using the National torch. Here some apparent anomalies are found; a dip in the heat-transfer rate occurs beyond the tip of the primary cone. This dip is similar to the decrease observed in passing through the primary cone. Other investigators [11] have noted similar dips in temperature profiles of other gas flames, but no explanation has been presented. The severity of the dip is apparently indicative of the mixture ratio [11], possibly implying a non-stoichiometric gas mixture.

The results of this study show that the heat transfer resulting from the Prest-O-Lite torch with a No. 1 tip is relatively uniform within a central 0.2-in-dia circle. Further, results show that although the heat-transfer rates can be varied by adjusting the length of the primary cone, the distance from the torch to the test article also must be changed in order to maintain a relatively flat heat-transfer profile.

References

- 1 Anderson, J. E., and Stresino, E. F., "Heat Transfer From Flames Impinging on Flat and Cylindrical Surfaces," *JOURNAL OF HEAT TRANSFER*, TRANS. ASME, Series C, Vol. 85, No. 1, Feb. 1963, pp. 49-54.
- 2 Fristrom, R. M., and Westenberg, A. A., *Flame Structure*, McGraw-Hill, New York, N. Y., 1965.
- 3 Fristrom, R. M., and Westenberg, A. A., "Experimental Chemical Kinetics From Methane-Oxygen Laminar Flame Structure," *Eighth Symposium on Combustion Proceedings*, Williams and Wilkins, Baltimore, Md., 1962, pp. 438-448.
- 4 Kendall, D. N., Dixon, W. P., and Schulte, E. H., "Semiconductor Surface Thermocouples for Determining Heat Transfer Rates," *IEEE Transactions on Aerospace and Electrical Systems*, Vol. AES-3, No. 4, July 1967, pp. 596-603.
- 5 Morgan, C. C., and Andrews, J. C., "Morgandyne Heat Transfer Transducer and a Flame-Torch Calibration Technique for Hypervelocity Wind Tunnels," *Arnold Engineering Development Center Report TR-60-1*, Feb. 1960.
- 6 Prest-O-Lite, Union Carbide Corp., Linde Div., Indianapolis, Ind.
- 7 Modern Engineering Co., 3555 Scott Ave., St. Louis, Mo.
- 8 National Welding Equipment Div., Veriflo Corp., Richmond, Calif.
- 9 Schulte, E. H., and Kohl, R. F., "A Transducer for Measuring High Heat Transfer Rates," *Rev. Sci. Instr.*, Vol. 41, Dec. 1970, p. 732.
- 10 Hy-Cal Engineering, 12105 Los Nietos Road, Sante Fe Springs, Calif.
- 11 Lewis, B., and Von Elbe, G., "Combustion, Flames and Explosions in Gases," Academic Press, New York, N. Y., 1951.

Thermal and Combined Entry Problems for Laminar Flow between Parallel Porous Plates

JOHN R. DOUGHTY¹ and HENRY C. PERKINS, JR.²

Introduction

LAMINAR-FLOW porous-wall entrance problems are being analytically investigated by the authors for constant- and variable-property flows. Solutions to the hydrodynamic entry

¹ Major, USAF, Air Force Weapons Laboratory, Kirtland AFB, New Mexico. Mem. ASME.

² Professor, Energy, Mass, and Momentum Transfer Laboratory, Aerospace and Mechanical Engineering Department, University of Arizona, Tucson, Ariz. Mem. ASME.

Contributed by the Heat Transfer Division of THE AMERICAN SOCIETY OF MECHANICAL ENGINEERS. Manuscript received by the Heat Transfer Division January 11, 1971; revised manuscript received August 16, 1971.

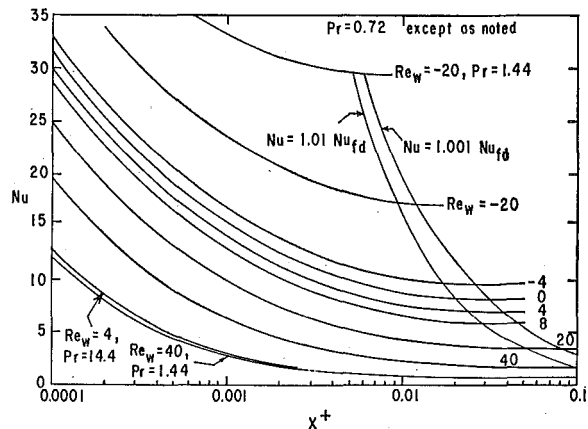


Fig. 1 Constant-property Nusselt numbers for parallel porous plates, constant heat flux

problem have been presented in [1].³ The thermal entry problem for constant-property flow with the boundary condition of constant- and equal-temperature walls is given in an earlier note [2]. This brief presents constant-property solutions for: (1) the thermal entry problem for uniform injection and suction through the channel walls and (2) the combined thermal and hydrodynamic entry problem for uniform injection and suction. Both solutions are for the common boundary condition of constant and equal heat flux into the fluid.

The velocity profiles employed for the constant-heat-flux thermal entry problem are completely fully developed including the effects of injection or extraction, i.e., the dimensionless velocity profile u/U_b has become invariant with regard to axial position. The temperature profile at the entrance to the heated section is uniform. Raithby [3], using the approach of Siegel, Sparrow, and Hallman [4], has given solutions to this problem. We have employed a different method, that of Patankar and Spalding [5] as modified by Bankston and McEligot [6], to obtain solutions to the constant-heat-flux thermal entry problem and the combined entry problem. The method consists of a sequential solution of the continuity, axial-momentum, and energy equations at each axial station and is a marching-integration routine which depends upon the values obtained at the previous station.

Results

Thermal Entry, Constant Wall Heat Flux. The behavior of the Nusselt number in the thermal entrance region is given in Fig. 1. The Nusselt number is defined on the hydraulic diameter which is twice the plate spacing. The behavior is similar to the constant-temperature-wall case given in [2] and is also analogous to that of the friction factor in the hydrodynamic entry region [1] in that the effect of injection is to reduce friction and heat transfer. The Nusselt number for porous plates is higher for the constant-heat-flux cases than for the constant-temperature-wall cases for the same wall Peclet number. This is similar to the usual results for these two boundary conditions for $Re_w = 0$.

The criterion for thermal development is taken to be when the local Nusselt number is within a certain percentage of the fully developed Nusselt number. The thermal entry lengths for cases where the Nusselt number is within 1 and 0.1 percent of the fully developed value are shown in Fig. 1. The effect of injection is to increase the thermal entry length continuously and monotonically, an effect similar to the constant-temperature-wall case [2]. All thermal-entry Nusselt-number curves shown in Fig. 1 have generally the same shape. The amount of injection or extraction determines whether the curves are below or above the impermeable-wall case.

³ Numbers in brackets designate References at end of technical brief.

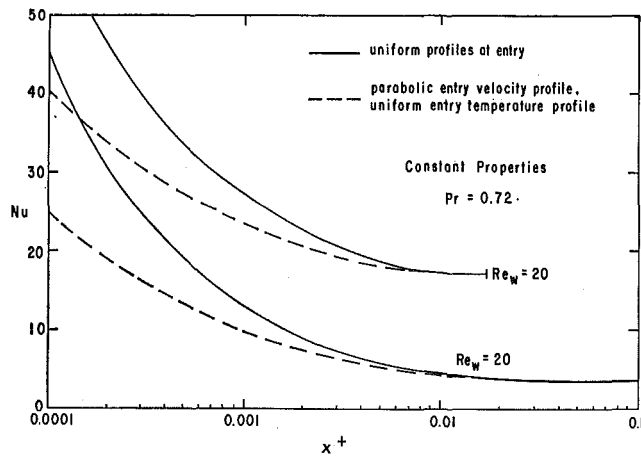


Fig. 2 Comparison of entry velocity profile conditions on the entrance region Nusselt number, constant wall heat flux

With the behavior of entry-region solutions established, it is interesting to determine what effect variation of parameters such as the injection rate and Prandtl number might have upon the Nusselt number.

Injection causes an increase in the axial gradient of both the wall and bulk temperatures over the case for $Re_w = 0$. This is physically proper as the effect of injecting fluid at the local wall temperature would be to cause a more rapid increase in the wall and bulk temperatures due to the energy input by convection assisting the conduction. Opposite effects were found for the suction cases. The convected thermal energy removed due to suction opposes the conduction such that the wall and bulk temperatures increase very slowly as compared to the impermeable-wall case. For example, at $X^+ = 0.01$, the difference $T_w^+ - T_b^+$ is 0.0585, 0.114, and 0.229 for $Re_w = -20, 0, 20$, respectively. Fully developed dimensionless temperature profiles for various injection and suction rates are given in [7] and are similar in form to those of the constant-temperature-wall case given in [2].

For a fixed injection rate the effect of increasing the Prandtl number and consequently the wall Peclet number is to decrease the Nusselt number. Physically, increasing the Prandtl number affects the transport of thermal energy by convection. The wall Peclet modulus, made up of the product of the wall Reynolds number and the Prandtl number, can be transformed into a ratio of transverse convection to transverse conduction $(\rho c_p V_w \Delta T) / (k \Delta T / D)$. Thus if one desires to decrease the heat transfer to a porous-walled channel, one could, for instance, double either the Prandtl number by an appropriate change in the working fluid or the injection rate without changing the fluid medium and achieve essentially the same resultant Nusselt number.

If the wall Peclet number and wall heat flux are held constant, there is practically no variation in the dimensionless temperature profile or Nusselt number at a fixed X^+ even though there may be a wide variation in the wall Reynolds number and Prandtl number individually. The small variation in Nusselt number is seen in the lower curve of Fig. 1 ($Pe_w = 57.6$) where the curve with the highest injection rate ($Re_w = 40$) gives the lower Nusselt number. Opposite behavior is noted for the suction case where for the same wall Peclet number, the higher Nusselt numbers are obtained with the higher suction rate.

Combined Entry Problem. The local Nusselt numbers for the constant-wall-heat-flux condition obtained by Hwang and Fan [8] for the impermeable-wall case compare quite well with those of the present work. There is excellent overall agreement, especially between the numerically obtained value for fully developed flow, 8.232, and the exact value, 8.235. Previous works in which the local Nusselt number for constant-temperature-wall cases is presented could not be found. The same general heat-transfer behavior as is found for the impermeable-wall case

was noted for both injection and suction, i.e., the effect of the uniform velocity at the entrance is to yield a local Nusselt number that is always higher than if the velocity were parabolic at the entrance. Representative results for the constant-temperature-wall case in [7] indicate the changing velocity profile causes a modest increase in the Nusselt number in the extreme first portion of the entrance region. Similar behavior is noted for the constant-wall-heat-flux case as shown here in Fig. 2. Once hydrodynamically fully developed flow is attained, usually by the point $X^+ = 0.01$, the Nusselt-number curves for the two different entry conditions have merged together.

Acknowledgments

This work was supported by the Air Force Institute of Technology, Wright-Patterson AFB, Ohio, and the Air Force Weapons Laboratory, Kirtland AFB, New Mexico. The authors wish to acknowledge the computer time furnished by the latter organization and the University of Arizona Computer Center. Partial financial support was also provided by NASA grant NGR-03-002-213. This note represents a portion of the work done by Major Doughty to partially fulfill the requirements for the doctor of philosophy degree at the University of Arizona.

References

- 1 Doughty, J. R., and Perkins, H. C., Jr., "Hydrodynamic Entry Length for Laminar Flow Between Parallel Porous Plates," *Journal of Applied Mechanics*, Vol. 37, TRANS. ASME, Series E, Vol. 92, No. 2, June 1970, pp. 548-550.
- 2 Doughty, J. R., and Perkins, H. C., Jr., "The Thermal Entry Problem for Laminar Flow Between Parallel Porous Plates," *JOURNAL OF HEAT TRANSFER*, TRANS. ASME, Series C, Vol. 93, No. 4, Nov. 1971, pp. 476-478.
- 3 Raithby, G., "Laminar Heat Transfer in the Thermal Entrance Region of Circular Tubes and Two-Dimensional Rectangular Ducts with Wall Suction and Injection," *International Journal of Heat and Mass Transfer*, Vol. 14, 1971, pp. 223-243.
- 4 Siegel, R., Sparrow, E. M., and Hallman, T. M., "Steady Laminar Heat Transfer in a Circular Tube with Prescribed Wall Heat Flux," *Applied Scientific Research*, Vol. 7A, 1958, pp. 386-392.
- 5 Patankar, S. V., and Spalding, D. B., "A Finite-Difference Procedure for Solving the Equations of the Two-Dimensional Boundary Layer," *International Journal of Heat and Mass Transfer*, Vol. 10, 1967, pp. 1389-1411.
- 6 Bankston, C. A., and McEligot, D. M., "Numerical Solutions for Turbulent and Laminar Thermal Entries with Gas Property Variations," *International Journal of Heat and Mass Transfer*, Vol. 13, 1970, pp. 319-343.
- 7 Doughty, J. R., "Heat and Momentum Transfer Between Parallel Porous Plates," PhD dissertation, University of Arizona, Tucson, Ariz., 1971.
- 8 Hwang, C., and Fan, L., "Finite-Difference Analysis of Forced-Convection Heat Transfer in Entrance Region of a Flat Rectangular Duct," *Applied Scientific Research*, Vol. 13A, 1964, pp. 401-422.

Some Remarks on Thermoconvective Instability in Completely Confined Regions

P. A. JENNINGS¹ and R. L. SANI¹

Nomenclature

- D = three-dimensional domain
 dv = infinitesimal volume element
 ∂D = boundary of domain D

¹ Department of Chemical Engineering, School of Chemical Sciences, University of Illinois, Urbana, Ill.

Contributed by the Heat Transfer Division of THE AMERICAN SOCIETY OF MECHANICAL ENGINEERS. Manuscript received by the Heat Transfer Division June 4, 1971.

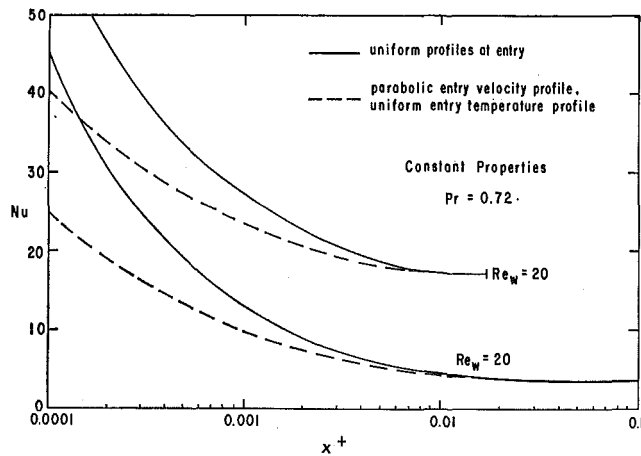


Fig. 2 Comparison of entry velocity profile conditions on the entrance region Nusselt number, constant wall heat flux

With the behavior of entry-region solutions established, it is interesting to determine what effect variation of parameters such as the injection rate and Prandtl number might have upon the Nusselt number.

Injection causes an increase in the axial gradient of both the wall and bulk temperatures over the case for $Re_w = 0$. This is physically proper as the effect of injecting fluid at the local wall temperature would be to cause a more rapid increase in the wall and bulk temperatures due to the energy input by convection assisting the conduction. Opposite effects were found for the suction cases. The convected thermal energy removed due to suction opposes the conduction such that the wall and bulk temperatures increase very slowly as compared to the impermeable-wall case. For example, at $X^+ = 0.01$, the difference $T_w^+ - T_b^+$ is 0.0585, 0.114, and 0.229 for $Re_w = -20, 0, 20$, respectively. Fully developed dimensionless temperature profiles for various injection and suction rates are given in [7] and are similar in form to those of the constant-temperature-wall case given in [2].

For a fixed injection rate the effect of increasing the Prandtl number and consequently the wall Peclet number is to decrease the Nusselt number. Physically, increasing the Prandtl number affects the transport of thermal energy by convection. The wall Peclet modulus, made up of the product of the wall Reynolds number and the Prandtl number, can be transformed into a ratio of transverse convection to transverse conduction $(\rho c_p V_w \Delta T) / (k \Delta T / D)$. Thus if one desires to decrease the heat transfer to a porous-walled channel, one could, for instance, double either the Prandtl number by an appropriate change in the working fluid or the injection rate without changing the fluid medium and achieve essentially the same resultant Nusselt number.

If the wall Peclet number and wall heat flux are held constant, there is practically no variation in the dimensionless temperature profile or Nusselt number at a fixed X^+ even though there may be a wide variation in the wall Reynolds number and Prandtl number individually. The small variation in Nusselt number is seen in the lower curve of Fig. 1 ($Pe_w = 57.6$) where the curve with the highest injection rate ($Re_w = 40$) gives the lower Nusselt number. Opposite behavior is noted for the suction case where for the same wall Peclet number, the higher Nusselt numbers are obtained with the higher suction rate.

Combined Entry Problem. The local Nusselt numbers for the constant-wall-heat-flux condition obtained by Hwang and Fan [8] for the impermeable-wall case compare quite well with those of the present work. There is excellent overall agreement, especially between the numerically obtained value for fully developed flow, 8.232, and the exact value, 8.235. Previous works in which the local Nusselt number for constant-temperature-wall cases is presented could not be found. The same general heat-transfer behavior as is found for the impermeable-wall case

was noted for both injection and suction, i.e., the effect of the uniform velocity at the entrance is to yield a local Nusselt number that is always higher than if the velocity were parabolic at the entrance. Representative results for the constant-temperature-wall case in [7] indicate the changing velocity profile causes a modest increase in the Nusselt number in the extreme first portion of the entrance region. Similar behavior is noted for the constant-wall-heat-flux case as shown here in Fig. 2. Once hydrodynamically fully developed flow is attained, usually by the point $X^+ = 0.01$, the Nusselt-number curves for the two different entry conditions have merged together.

Acknowledgments

This work was supported by the Air Force Institute of Technology, Wright-Patterson AFB, Ohio, and the Air Force Weapons Laboratory, Kirtland AFB, New Mexico. The authors wish to acknowledge the computer time furnished by the latter organization and the University of Arizona Computer Center. Partial financial support was also provided by NASA grant NGR-03-002-213. This note represents a portion of the work done by Major Doughty to partially fulfill the requirements for the doctor of philosophy degree at the University of Arizona.

References

- 1 Doughty, J. R., and Perkins, H. C., Jr., "Hydrodynamic Entry Length for Laminar Flow Between Parallel Porous Plates," *Journal of Applied Mechanics*, Vol. 37, TRANS. ASME, Series E, Vol. 92, No. 2, June 1970, pp. 548-550.
- 2 Doughty, J. R., and Perkins, H. C., Jr., "The Thermal Entry Problem for Laminar Flow Between Parallel Porous Plates," *JOURNAL OF HEAT TRANSFER*, TRANS. ASME, Series C, Vol. 93, No. 4, Nov. 1971, pp. 476-478.
- 3 Raithby, G., "Laminar Heat Transfer in the Thermal Entrance Region of Circular Tubes and Two-Dimensional Rectangular Ducts with Wall Suction and Injection," *International Journal of Heat and Mass Transfer*, Vol. 14, 1971, pp. 223-243.
- 4 Siegel, R., Sparrow, E. M., and Hallman, T. M., "Steady Laminar Heat Transfer in a Circular Tube with Prescribed Wall Heat Flux," *Applied Scientific Research*, Vol. 7A, 1958, pp. 386-392.
- 5 Patankar, S. V., and Spalding, D. B., "A Finite-Difference Procedure for Solving the Equations of the Two-Dimensional Boundary Layer," *International Journal of Heat and Mass Transfer*, Vol. 10, 1967, pp. 1389-1411.
- 6 Bankston, C. A., and McEligot, D. M., "Numerical Solutions for Turbulent and Laminar Thermal Entries with Gas Property Variations," *International Journal of Heat and Mass Transfer*, Vol. 13, 1970, pp. 319-343.
- 7 Doughty, J. R., "Heat and Momentum Transfer Between Parallel Porous Plates," PhD dissertation, University of Arizona, Tucson, Ariz., 1971.
- 8 Hwang, C., and Fan, L., "Finite-Difference Analysis of Forced-Convection Heat Transfer in Entrance Region of a Flat Rectangular Duct," *Applied Scientific Research*, Vol. 13A, 1964, pp. 401-422.

Some Remarks on Thermoconvective Instability in Completely Confined Regions

P. A. JENNINGS¹ and R. L. SANI¹

Nomenclature

- D = three-dimensional domain
 dv = infinitesimal volume element
 ∂D = boundary of domain D

¹ Department of Chemical Engineering, School of Chemical Sciences, University of Illinois, Urbana, Ill.

Contributed by the Heat Transfer Division of THE AMERICAN SOCIETY OF MECHANICAL ENGINEERS. Manuscript received by the Heat Transfer Division June 4, 1971.

e_1, e_2, e_3 = unit vectors of orthogonal curvilinear coordinate system

p = pressure field

Ra = Rayleigh number

T = dimensionless temperature field

u, w = dimensionless velocity field

(x_1, x_2, x_3) = curvilinear coordinate system

γ = aspect ratio, length of side to depth of layer

ϕ = dimensionless temperature field

Subscript

cr = critical value

Superscript

T = transpose

Introduction

ALTHOUGH the linear theory of thermoconvective instability of a horizontal fluid layer heated from beneath has been investigated extensively, only recently [1-4]² has attention been focused on the stability of fluids completely confined in vertical cylindrical domains with solid impervious boundaries. It is the purpose herein to prove two important properties satisfied by the solution to the linear stability problem appropriate to such domains, to point out some inconsistencies in results previously reported in the literature, and to report some new results for a domain with rectangular cross section.

Formulation

The mathematical characterization of the linear stability problem can be cast in the following dimensionless form:

$$\nabla^2 u + \sqrt{Ra} e_3 T = \nabla p \quad (1)$$

$$\nabla \cdot u = 0 \quad (2)$$

$$\nabla^2 T + \sqrt{Ra} e_3 \cdot u = 0 \quad (3)$$

in the domain D and

$$u = 0, \quad T = 0 \quad (4)$$

on ∂D , the boundary of D . Here e_3 is a unit vector directed along the x_3 axis, antiparallel to the gravitational field, and constant in direction; the region D is assumed to be the interior of a finite vertical cylinder whose cross-sectional shape is sufficiently regular that the variational formulation (5) is well posed. The stability problem addresses itself to the determination of the smallest possible value of the Rayleigh number, Ra_{cr} , for which nontrivial solutions exist.

In a completely confined region the mathematical system (1)-(4) is nonseparable and in each instance [2-4] an alternative variational formulation was solved approximately by the Rayleigh-Ritz technique. Namely,

$$\frac{1}{\sqrt{Ra_{cr}}} = \underset{(w, \phi) \in V}{\text{maximum}} \frac{\int_D 2(\phi e_3 \cdot w) dv}{\int_D \{ \nabla w : (\nabla w)^T + \nabla \phi \cdot \nabla \phi \} dv} \quad (5)$$

where V is a linear vector space of sufficiently smooth couples (w, ϕ) with $\nabla \cdot w = 0$ in D and $w = 0, \phi = 0$ on ∂D .

Properties of Solution

It is well known that the Rayleigh-Ritz technique is a powerful tool for computing values of Ra_{cr} since a first-order error in the approximate dynamic state leads to a second-order error in Ra ; on the other hand, the quality of the pointwise Rayleigh-Ritz approximation to the dynamic state must be carefully

assessed. The following two properties can aid in the assessment in certain cases.

Property 1. The velocity field u appropriate to a bounded vertical cylinder of rectangular cross section is three-dimensional.

Property 2. The critical Rayleigh number Ra_{cr} is a nonincreasing function of the size of the domain D .

The proof of Property 1 was recently given by Davies-Jones [5], and Property 2 is proven by adopting a scheme utilized by Garabedian [6].

Comparison with Previous Authors

A perusal of the previously reported results of Davis [4] and Catton [2] establishes that Properties 1 and 2 are violated in both cases. Apparently the violation results from numerical error in solving the algebraic eigenvalue problem associated with the variational formulation—a possibility already recognized by Davis [4] who pointed out his conclusions were correct modulo a certain numerical error. On the other hand the results of Charlson and Sani [3] are consistent with both properties; in fact, Property 2 was used to check the internal consistency of the results.

New Results

In order to investigate the three-dimensionality of the critical dynamic state as well as the error in critical Rayleigh number introduced by the finite-roll restriction, the case of a vertical cylinder of rectangular cross section was reexamined. The Rayleigh-Ritz method was implemented by using the same trial functions as Catton [2], and numerical accuracy as well as internal consistency of the results were critically scrutinized. Some characteristic results are summarized in Table 1. (The aspect ratio γ_i is defined as the ratio of the length of side i to the depth of the layer.) The results were judged to be valid to at least three significant figures by varying the number of trial functions, and the internal consistency of the data was checked by comparison with bounds derived from the results of Charlson and Sani [3] in conjunction with Property 2. (That is, the critical Rayleigh number is bounded from below by the critical Rayleigh number of a circular cylinder which just encloses it and from above by the critical Rayleigh number of a circular cylinder which just fits within the domain.) The values of the critical Rayleigh number for fully three-dimensional flow are as much as 16 percent lower than the corresponding finite-roll configuration. Note that in the cases $\gamma_1 = \gamma_2 > 2$ the percent difference in critical values decreases with increasing aspect ratio. This trend is consistent with the well-known result that two-dimensional roll-cell dynamic state is an exact solution when the fluid layer is infinite in lateral extent. The trend reverses for aspect ratios below approximately two; this phenomenon was also observed by Davies-Jones [5] who attributed it to an in-

Table 1 Values of Ra_{cr} for finite rolls and fully three-dimensional flow

Aspect ratios		Number* of rolls	Critical Rayleigh numbers		
width/ depth	length/ depth		finite rolls	fully 3-D	percent difference
0.25	1.00	2	76014	75669	0.454
0.50	0.50	1	49692	49510	0.366
0.50	2.00	2	10877	10596	2.58
1.00	1.00	1	7093	6830	3.71
1.00	2.00	2	4037	3779	6.39
1.00	3.00	3	3541	3319	6.27
2.00	2.00	2	2772	2322	16.2
3.00	3.00	3	2356	2105	10.7
2.00	4.00	4	2215	2010	9.25
3.00	3.00	3	2155	1971	8.54
4.00	4.00	4	1953	1861	4.71
5.00	5.00	5	1860	1806	2.90
10.00	10.00	10	1739	1734	0.288

* Since the transverse component of velocity is small, the fully three-dimensional flow pattern closely resembles that for finite rolls. Thus the term "rolls" may be applied to both cases.

² Numbers in brackets designate References at end of technical brief.

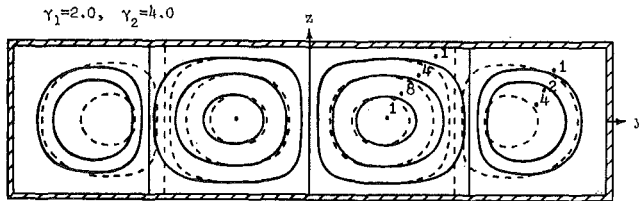
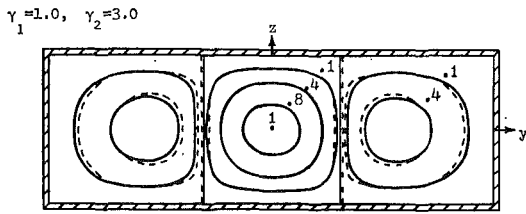


Fig. 1 Stream function and pseudo stream function at $x = 0$; — three-dimensional flow, - - - finite rolls

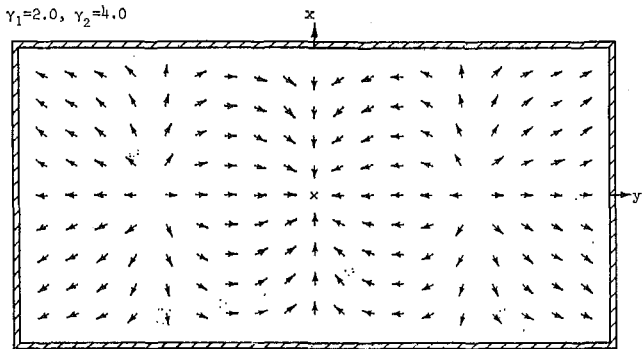
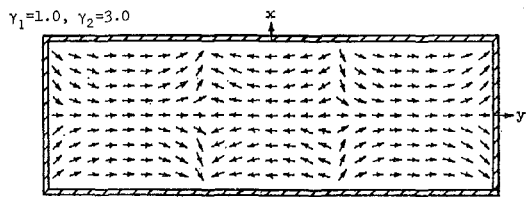


Fig. 2 Projection of velocity field on a horizontal plane ($z = 0.25$)

creased inhibition of the transverse flow by boundary-layer effects.

The influence of the transverse component of velocity on the velocity field is illustrated in Fig. 1 for two specific cases. The broken curves represent "pseudo streamlines" calculated for the fully three-dimensional flow pattern by using the projection of the velocity field onto an $x_1 = \text{const.}$ plane. The solid curves are streamlines calculated for the corresponding finite-roll solution.

The major difference is a slight shift in position. This behavior is further illustrated in Fig. 2 which displays a projection of the fully three-dimensional velocity field onto a horizontal plane. The effect of the transverse component of velocity is evident only near cell boundaries where the magnitude of the velocity field is small. In general, the finite-roll approximation is quite good except in a certain range of aspect ratios, $1 < \gamma_1$, $\gamma_2 < 4$, for which it appears from the limited number of cases investigated that the transverse component of velocity can be important. Since lateral-heat-loss effects make it difficult to experimentally simulate the system for small aspect ratios, the

results tabulated in Table 1 may, as pointed out by a reviewer, be of only academic interest. However, there are results in the literature [7, 8] which suggest that such heat losses can be minimized to such an extent that Table 1 can be used in predicting the point of manifest convection.

Finally, it is noteworthy that while the linear stability analysis predicts the point of onset of convection it is only capable of suggesting the detailed structure of the convection at supercritical states. The latter is in the realm of a nonlinear stability analysis.

References

- 1 Catton, I., and Edwards, D. K., "Initiation of Thermal Convection in Finite Right Circular Cylinders," *AIChE Journal*, Vol. 16, 1970, pp. 594-601.
- 2 Catton, I., "Convection in a Closed Rectangular Region: The Onset of Motion," *JOURNAL OF HEAT TRANSFER, TRANS. ASME, Series C*, Vol. 92, No. 1, Feb. 1970, pp. 186-188.
- 3 Charlson, G. S., and Sani, R. L., "Thermoconvective Instability in a Bounded Cylindrical Fluid Layer," *International Journal of Heat and Mass Transfer*, Vol. 13, 1970, pp. 1479-1496.
- 4 Davis, S. H., "Convection in a Box: Linear Theory," *Journal of Fluid Mechanics*, Vol. 30, 1967, pp. 465-478.
- 5 Davies-Jones, R. P., "Thermal Convection in an Infinite Channel With No-Slip Sidewalls," *Journal of Fluid Mechanics*, Vol. 44, 1970, pp. 695-704.
- 6 Garabedian, P., *Partial Differential Equations*, Interscience, New York, N. Y., 1964, pp. 400-401.
- 7 Mitchell, W. T., and Quinn, J. A., "Thermal Convection in a Completely Confined Fluid Layer," *AIChE Journal*, Vol. 12, 1966, pp. 1116-1124.
- 8 Heitz, W. I., and Westwater, J. W., "Critical Rayleigh Numbers for Natural Convection of Water Confined in Square Cells with L/D From 0.5 to 8," *JOURNAL OF HEAT TRANSFER, TRANS. ASME, Series C*, Vol. 93, No. 2, May 1971, pp. 188-196.

Explosive Vapor Formation

P. GROENVELD¹

Nomenclature

$$a = \text{capillary constant, } a = \left(\frac{2\sigma}{\Delta\rho g}\right)^{1/2}$$

$$g = \text{gravitational constant, cm/sec}^2$$

$$t = \text{time, sec}$$

$$v = \text{velocity, cm/sec}$$

$$\text{We} = \text{dimensionless Weber number, } \text{We} = \frac{\rho v^2 r}{\sigma}$$

$$\rho = \text{density, gram/cc}$$

$$\Delta\rho = \text{density difference, gram/cc}$$

$$\sigma = \text{surface tension, dyne/cm}$$

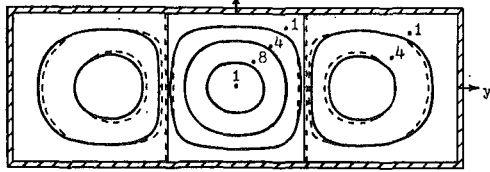
Introduction

AN EXPLOSIVE vapor formation may occur when molten material contacts a cool liquid. This happens when the molten fluid is somehow well dispersed in the quench liquid. The heat transfer is considerably increased by the high interfacial area and the vapor formation consequently proceeds in an explosive manner. Vapor explosions occur in the paper industry when

¹ Heat Transfer Section, Department of Engineering Physics, Delft University of Technology, The Netherlands.

Contributed by the Heat Transfer Division of THE AMERICAN SOCIETY OF MECHANICAL ENGINEERS. Manuscript received by the Heat Transfer Division November 6, 1970; revised manuscript received June 11, 1971.

$$\gamma_1 = 1.0, \gamma_2 = 3.0$$



$$\gamma_1 = 2.0, \gamma_2 = 4.0$$

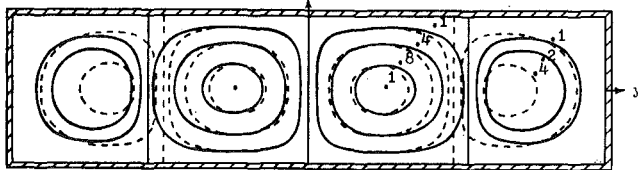
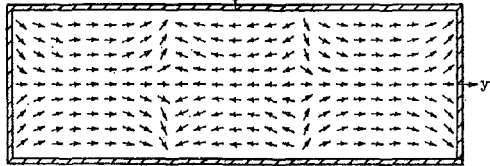


Fig. 1 Stream function and pseudo stream function at $x = 0$; — three-dimensional flow, - - - finite rolls

$$\gamma_1 = 1.0, \gamma_2 = 3.0$$



$$\gamma_1 = 2.0, \gamma_2 = 4.0$$

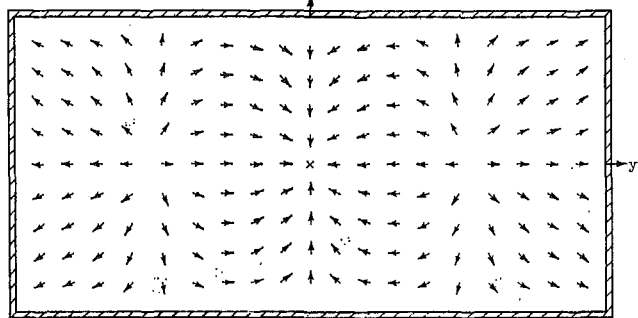


Fig. 2 Projection of velocity field on a horizontal plane ($z = 0.25$)

creased inhibition of the transverse flow by boundary-layer effects.

The influence of the transverse component of velocity on the velocity field is illustrated in Fig. 1 for two specific cases. The broken curves represent "pseudo streamlines" calculated for the fully three-dimensional flow pattern by using the projection of the velocity field onto an $x_1 = \text{const.}$ plane. The solid curves are streamlines calculated for the corresponding finite-roll solution.

The major difference is a slight shift in position. This behavior is further illustrated in Fig. 2 which displays a projection of the fully three-dimensional velocity field onto a horizontal plane. The effect of the transverse component of velocity is evident only near cell boundaries where the magnitude of the velocity field is small. In general, the finite-roll approximation is quite good except in a certain range of aspect ratios, $1 < \gamma_1$, $\gamma_2 < 4$, for which it appears from the limited number of cases investigated that the transverse component of velocity can be important. Since lateral-heat-loss effects make it difficult to experimentally simulate the system for small aspect ratios, the

results tabulated in Table 1 may, as pointed out by a reviewer, be of only academic interest. However, there are results in the literature [7, 8] which suggest that such heat losses can be minimized to such an extent that Table 1 can be used in predicting the point of manifest convection.

Finally, it is noteworthy that while the linear stability analysis predicts the point of onset of convection it is only capable of suggesting the detailed structure of the convection at supercritical states. The latter is in the realm of a nonlinear stability analysis.

References

- 1 Catton, I., and Edwards, D. K., "Initiation of Thermal Convection in Finite Right Circular Cylinders," *AIChE Journal*, Vol. 16, 1970, pp. 594-601.
- 2 Catton, I., "Convection in a Closed Rectangular Region: The Onset of Motion," *JOURNAL OF HEAT TRANSFER, TRANS. ASME, Series C*, Vol. 92, No. 1, Feb. 1970, pp. 186-188.
- 3 Charlson, G. S., and Sani, R. L., "Thermoconvective Instability in a Bounded Cylindrical Fluid Layer," *International Journal of Heat and Mass Transfer*, Vol. 13, 1970, pp. 1479-1496.
- 4 Davis, S. H., "Convection in a Box: Linear Theory," *Journal of Fluid Mechanics*, Vol. 30, 1967, pp. 465-478.
- 5 Davies-Jones, R. P., "Thermal Convection in an Infinite Channel With No-Slip Sidewalls," *Journal of Fluid Mechanics*, Vol. 44, 1970, pp. 695-704.
- 6 Garabedian, P., *Partial Differential Equations*, Interscience, New York, N. Y., 1964, pp. 400-401.
- 7 Mitchell, W. T., and Quinn, J. A., "Thermal Convection in a Completely Confined Fluid Layer," *AIChE Journal*, Vol. 12, 1966, pp. 1116-1124.
- 8 Heitz, W. I., and Westwater, J. W., "Critical Rayleigh Numbers for Natural Convection of Water Confined in Square Cells with L/D From 0.5 to 8," *JOURNAL OF HEAT TRANSFER, TRANS. ASME, Series C*, Vol. 93, No. 2, May 1971, pp. 188-196.

Explosive Vapor Formation

P. GROENVELD¹

Nomenclature

$$a = \text{capillary constant, } a = \left(\frac{2\sigma}{\Delta\rho g}\right)^{1/2}$$

$$g = \text{gravitational constant, cm/sec}^2$$

$$t = \text{time, sec}$$

$$v = \text{velocity, cm/sec}$$

$$\text{We} = \text{dimensionless Weber number, } \text{We} = \frac{\rho v^2 r}{\sigma}$$

$$\rho = \text{density, gram/cc}$$

$$\Delta\rho = \text{density difference, gram/cc}$$

$$\sigma = \text{surface tension, dyne/cm}$$

Introduction

AN EXPLOSIVE vapor formation may occur when molten material contacts a cool liquid. This happens when the molten fluid is somehow well dispersed in the quench liquid. The heat transfer is considerably increased by the high interfacial area and the vapor formation consequently proceeds in an explosive manner. Vapor explosions occur in the paper industry when

¹ Heat Transfer Section, Department of Engineering Physics, Delft University of Technology, The Netherlands.

Contributed by the Heat Transfer Division of THE AMERICAN SOCIETY OF MECHANICAL ENGINEERS. Manuscript received by the Heat Transfer Division November 6, 1970; revised manuscript received June 11, 1971.

soda smelt is dissolved [1-4],² in the metal industry when molten steel, aluminum, or lead are dropped in water [5, 6], and in the nuclear industry when during accidental power excursions of reactors hot molten core material is dispersed in the coolant [7-9].

Witte, Cox, and Bouvier [6] recently have given a survey of the various proposed fragmentation theories:

Entrapment Theory. Liquid is trapped between the molten metal and the surface of the container. The liquid vaporizes and expands rapidly, blowing the melt apart. Long [5] could in this way explain his experiments with molten aluminum being poured in a water tank.

Violent-Boiling Theory. The forces generated by the transition from film to nucleate boiling of the liquid may overcome the surface tension of the molten mass and tear it apart [7, 8].

Weber-Number Theory. The inertial forces exerted on the molten mass by the cooling medium overcome the surface tension of the globule if the globule exceeds either the critical size or the critical velocity while in motion through the liquid. The globule is then split into several parts. The critical dimensionless number is the Weber number:

$$We = \frac{\rho v^2 r}{\sigma} > 10 \quad (1)$$

with ρ the density of the surrounding fluid, v the velocity, r the radius, and σ the interfacial tension. Hinze [10, 11] determined that drops will fragment at We numbers above about 10. Generally, however, the drops are not broken up to sufficiently small size by this mechanism to explain the explosive heat transfer actually observed.

Shell Theory. Liquid trapped inside the falling globule is suddenly vaporized and the rapidly expanding vapor blows the globule apart. Brauer, Green, and Mesler [9] observed the disintegration of molten aluminum and lead. They did not observe any violent boiling, but the drops seemed to be blown apart by some internally generated pressure. They hypothesized that quench liquid is forced through a porous solid-metal shell due to voids formed by an increase in the interior-metal density. This increase in density could be caused by a cooling of the interior molten metal after the outer shell had formed.

In the following we will describe a new encapsulating mechanism based on the collision of the globule with the surrounding fluid.

Experimental

Metals are not transparent, and therefore it is impossible to directly see any encapsulated drops. Water drops in combination with organic fluids were therefore used in the experiments instead of molten metal. Globules can suddenly be exposed to a moving fluid, either when drops enter the liquid from the air or when a high-speed jet disintegrates in the liquid. Hinze calculated that a drop suddenly exposed to a moving surrounding fluid will disintegrate when the flattening caused by the stagnation pressure of the surrounding fluid exceeds a specific value. Our measurements with water drops falling into a bath of hexane, toluene, or ether are in agreement with the critical value of Hinze, Fig. 1. Deviations occur with large globules, in which case surface-tension forces are negligible. The criterion, when the capillary forces are larger than the gravitational forces, is

$$\frac{\Delta \rho g v^3}{\sigma r} = r^2 \frac{\Delta \rho g}{2\sigma} = \left(\frac{v}{a}\right)^2 \ll 1$$

Disintegration, however, was not the only phenomenon observed by this author. The globules encapsulated a small drop of the surrounding liquid during the collision with, and the deceleration in, the surrounding fluid at We numbers above about the same critical value. The encapsulated drops could be ob-

² Numbers in brackets designate References at end of technical brief.

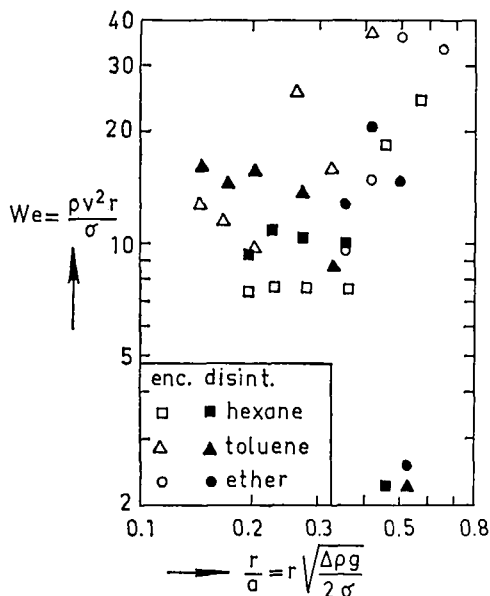


Fig. 1 The minimum We number above which bath fluid is encapsulated (We_{enc}) and above which a drop disintegrates (We_{disint}) during a collision with an interface; the We numbers are shown to vary with the dimensionless drop radius

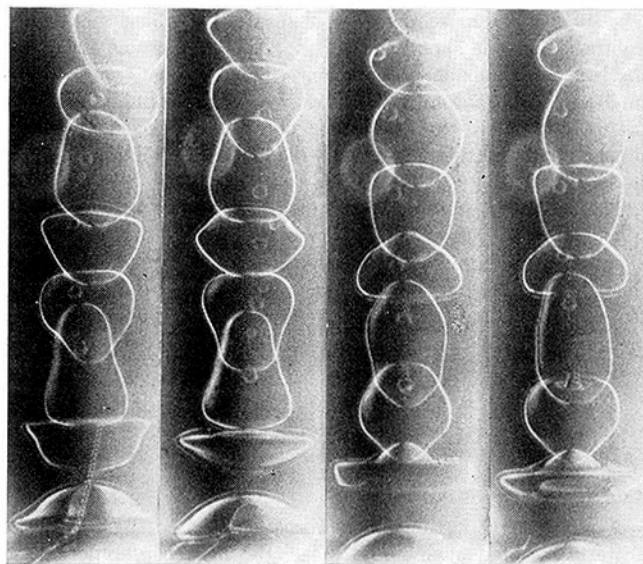


Fig. 2 Water globules encapsulating a drop of hexane ($r = 1.92 \times 10^{-3}$ m, $We = 10$, stroboflash 5000 rpm)

served in stroboscopic light. Fig. 2 shows the observed encapsulating process. Encapsulated drops were also observed inside the globules resulting from a disintegrated water jet. The minimum We numbers for disintegration and encapsulating by collision with an interface were determined for different drop diameters by measuring the critical height above the bath. The drop diameter could be varied with the diameter of the capillary. The critical We number for encapsulating is generally slightly lower than for disintegration.

Encapsulating Mechanism

The mechanism as derived from the photographs is that the acceleration of the virtual mass of surrounding fluid [13, 14] and the stagnation pressure of the surrounding fluid at the front of the drop decelerate the globule. This decelerated fluid in the globule moves out sideways [15]. The high forward velocity of the drop is lost when it has replaced a mass of surrounding

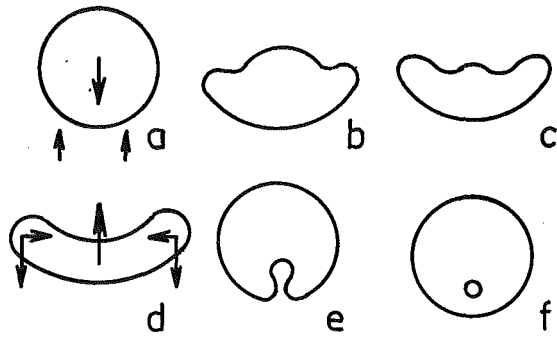


Fig. 3 The schematic encapsulating process of a drop colliding with an interface

fluid about equal to its own mass. The shape is that shown in Fig. 3(d). This "stationary" cup-shaped globule subsequently relaxes under influence of the interfacial tension. The sides will move inward because of the flat shape, and the rim will move forward and the center backward because of the cup shape. The combination of these two motions enables the globule to encapsulate some of the surrounding liquid at the front of the drop. This liquid can be separated from the bulk through coalescence of the interface connecting the encapsulated fluid and the bath fluid. Soap (teepol) prevents coalescence, and therefore also prevents the entrainment of a small drop. This was verified experimentally. It also points to a possible way to prevent this type of vapor explosion. A surfactant which makes the interface inelastic should be added. The encapsulated drop can shatter the globule on evaporation. The fragments will be very small and will have high velocities when the globule freezes on the outside before the encapsulated liquid is vaporized. The resulting sharp increase in surface area can explain explosive heat transfer.

The proposed process for the disintegration of a large quantity of melt discharged in a quenching liquid is the subsequent disintegration through Rayleigh instabilities, first to jets and then to globules, followed by the encapsulating by the globules of some quench liquid. The time required for this encapsulating process is the deceleration time of the globules in the liquid added to the subsequent capillary relaxing time [13].

$$t_{enc} = \frac{\rho_{glob}}{\rho_{quench}} \frac{2r}{v} + \left[\frac{(3\rho_{glob} + 2\rho_{quench})r^3}{24\sigma} \right]^{1/2} \quad (2)$$

Conclusion

A new fragmentation mechanism is proposed, based on the entrapment of quench liquid inside the molten globule caused by the collision of the globule with the surrounding liquid. This encapsulating mechanism explains the entrapped liquid better than the shell theory of Brauer, Green, and Mesler. The collision mechanism is supported by the observation of Brauer et al. that quench liquid was encapsulated in nonfragmenting experiments, and that the fragmentation of lead and aluminum occurred due to an internal vapor pressure, without any sign of violent boiling. The encapsulating mechanism also explains the success in preventing explosions of air or steam jets used to break up the melt stream before entering the quench liquid [4]. One would expect an increase in boiling violence caused by the increased surface area. The explanation can be that the We number of the resulting small drops is below the value 10 required for the encapsulating process. Encapsulated drops were directly observed when water was dropped or jetted into organic liquids at higher We numbers.

References

- 1 Sallack, J. A., *Pulp and Paper Magazine of Canada*, Vol. 56, No. 10, 1955, p. 114.
- 2 Nelson, W., and Kennedy, E. H., *Paper Trade Journal*, Vol. 140, No. 29, 1956, p. 50.

- 3 Trobecks, K. G., Swedish patent 167,780, July 14, 1959.
- 4 Gettle, J. T., U. S. patent 3,122,421, Feb. 25, 1964.
- 5 Long, G., *Metal Progress*, Vol. 71, May 1957, p. 107.
- 6 Witte, L. C., Cox, J. E., and Bouvier, J. E., *Journal of Metals*, Feb. 1970, p. 39.
- 7 Argonne National Laboratory, Chem. Eng. Div., ANL-7425, July-Dec. 1967.
- 8 Argonne National Laboratory, Chem. Eng. Div., ANL-7399, Nov. 1967.
- 9 Brauer, F. E., Green, N. W., and Mesler, R. B., *Nuclear Science and Engineering*, Vol. 31, 1968, p. 551.
- 10 Hinze, J. O., *Applied Scientific Research*, Vol. A1, 1948, p. 263.
- 11 Hinze, J. O., *Applied Scientific Research*, Vol. A1, 1948, p. 273.
- 12 Soo, S. L., *Fluid Dynamics of Multiphase Systems*, Blaisdell, 1967.
- 13 Lamb, H., *Hydrodynamics*, Cambridge, England, 1935.
- 14 Richardson, E. G., *Dynamics of Real Fluids*, Edward Arnold, London, England, 1950.
- 15 Wachters, L. H. J., *Chem. Eng. Sci.*, Vol. 21, No. 10, 1966, p. 923.

Evaporation from a Semi-infinite Region with a Nonvolatile Solute

K. R. CHUN¹

Nomenclature

- D = diffusion coefficient
 t = time
 U = constant velocity
 w = concentration of the nonvolatile solute
 y = coordinate normal to the phase boundary
 δ_c = concentration boundary-layer thickness

Subscripts

- 0 = at the phase boundary
 ∞ = at infinity

Introduction

THE PROBLEM under consideration is a semi-infinite region of uniform concentration with a nonvolatile solute. At time $t > 0$, the solution begins to evaporate at a constant rate at the boundary. An equivalent problem would be condensation at the phase boundary of the vapor-gas mixture with a noncondensable gas.

The exact solution is obtained for the transient concentration profile and compared with an approximate solution by the Goodman-type integral method. The results show that the approximate method, while satisfactory at short times, overestimates the surface concentration by 50 percent at long times.

Analysis

Taking the origin at the liquid-vapor interface (see Fig. 1) the liquid solution is viewed as moving to the left at a constant velocity U . The partial differential equation for the concentration profile is

$$\frac{\partial w}{\partial t} + U \frac{\partial w}{\partial y} = D \frac{\partial^2 w}{\partial y^2} \quad (1)$$

with the initial condition

¹ Member, Senior Technical Staff, Northrop Corporate Laboratories, Hawthorne, Calif. Assoc. Mem. ASME.

Contributed by the Heat Transfer Division of THE AMERICAN SOCIETY OF MECHANICAL ENGINEERS. Manuscript received by the Heat Transfer Division June 7, 1971.

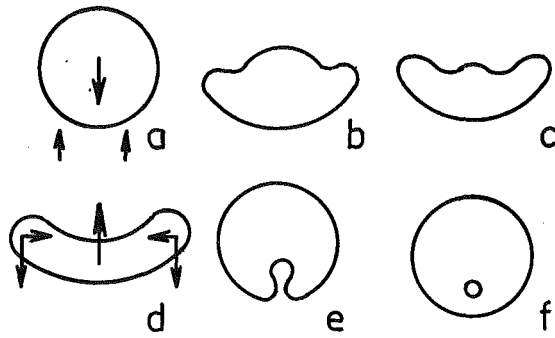


Fig. 3 The schematic encapsulating process of a drop colliding with an interface

fluid about equal to its own mass. The shape is that shown in Fig. 3(d). This "stationary" cup-shaped globule subsequently relaxes under influence of the interfacial tension. The sides will move inward because of the flat shape, and the rim will move forward and the center backward because of the cup shape. The combination of these two motions enables the globule to encapsulate some of the surrounding liquid at the front of the drop. This liquid can be separated from the bulk through coalescence of the interface connecting the encapsulated fluid and the bath fluid. Soap (teepol) prevents coalescence, and therefore also prevents the entrainment of a small drop. This was verified experimentally. It also points to a possible way to prevent this type of vapor explosion. A surfactant which makes the interface inelastic should be added. The encapsulated drop can shatter the globule on evaporation. The fragments will be very small and will have high velocities when the globule freezes on the outside before the encapsulated liquid is vaporized. The resulting sharp increase in surface area can explain explosive heat transfer.

The proposed process for the disintegration of a large quantity of melt discharged in a quenching liquid is the subsequent disintegration through Rayleigh instabilities, first to jets and then to globules, followed by the encapsulating by the globules of some quench liquid. The time required for this encapsulating process is the deceleration time of the globules in the liquid added to the subsequent capillary relaxing time [13].

$$t_{enc} = \frac{\rho_{glob}}{\rho_{quench}} \frac{2r}{v} + \left[\frac{(3\rho_{glob} + 2\rho_{quench})r^3}{24\sigma} \right]^{1/2} \quad (2)$$

Conclusion

A new fragmentation mechanism is proposed, based on the entrapment of quench liquid inside the molten globule caused by the collision of the globule with the surrounding liquid. This encapsulating mechanism explains the entrapped liquid better than the shell theory of Brauer, Green, and Mesler. The collision mechanism is supported by the observation of Brauer et al. that quench liquid was encapsulated in nonfragmenting experiments, and that the fragmentation of lead and aluminum occurred due to an internal vapor pressure, without any sign of violent boiling. The encapsulating mechanism also explains the success in preventing explosions of air or steam jets used to break up the melt stream before entering the quench liquid [4]. One would expect an increase in boiling violence caused by the increased surface area. The explanation can be that the We number of the resulting small drops is below the value 10 required for the encapsulating process. Encapsulated drops were directly observed when water was dropped or jetted into organic liquids at higher We numbers.

References

- 1 Sallack, J. A., *Pulp and Paper Magazine of Canada*, Vol. 56, No. 10, 1955, p. 114.
- 2 Nelson, W., and Kennedy, E. H., *Paper Trade Journal*, Vol. 140, No. 29, 1956, p. 50.

- 3 Trobecks, K. G., Swedish patent 167,780, July 14, 1959.
- 4 Gettle, J. T., U. S. patent 3,122,421, Feb. 25, 1964.
- 5 Long, G., *Metal Progress*, Vol. 71, May 1957, p. 107.
- 6 Witte, L. C., Cox, J. E., and Bouvier, J. E., *Journal of Metals*, Feb. 1970, p. 39.
- 7 Argonne National Laboratory, Chem. Eng. Div., ANL-7425, July-Dec. 1967.
- 8 Argonne National Laboratory, Chem. Eng. Div., ANL-7399, Nov. 1967.
- 9 Brauer, F. E., Green, N. W., and Mesler, R. B., *Nuclear Science and Engineering*, Vol. 31, 1968, p. 551.
- 10 Hinze, J. O., *Applied Scientific Research*, Vol. A1, 1948, p. 263.
- 11 Hinze, J. O., *Applied Scientific Research*, Vol. A1, 1948, p. 273.
- 12 Soo, S. L., *Fluid Dynamics of Multiphase Systems*, Blaisdell, 1967.
- 13 Lamb, H., *Hydrodynamics*, Cambridge, England, 1935.
- 14 Richardson, E. G., *Dynamics of Real Fluids*, Edward Arnold, London, England, 1950.
- 15 Wachters, L. H. J., *Chem. Eng. Sci.*, Vol. 21, No. 10, 1966, p. 923.

Evaporation from a Semi-infinite Region with a Nonvolatile Solute

K. R. CHUN¹

Nomenclature

- D = diffusion coefficient
 t = time
 U = constant velocity
 w = concentration of the nonvolatile solute
 y = coordinate normal to the phase boundary
 δ_c = concentration boundary-layer thickness

Subscripts

- 0 = at the phase boundary
 ∞ = at infinity

Introduction

THE PROBLEM under consideration is a semi-infinite region of uniform concentration with a nonvolatile solute. At time $t > 0$, the solution begins to evaporate at a constant rate at the boundary. An equivalent problem would be condensation at the phase boundary of the vapor-gas mixture with a noncondensable gas.

The exact solution is obtained for the transient concentration profile and compared with an approximate solution by the Goodman-type integral method. The results show that the approximate method, while satisfactory at short times, overestimates the surface concentration by 50 percent at long times.

Analysis

Taking the origin at the liquid-vapor interface (see Fig. 1) the liquid solution is viewed as moving to the left at a constant velocity U . The partial differential equation for the concentration profile is

$$\frac{\partial w}{\partial t} + U \frac{\partial w}{\partial y} = D \frac{\partial^2 w}{\partial y^2} \quad (1)$$

with the initial condition

¹ Member, Senior Technical Staff, Northrop Corporate Laboratories, Hawthorne, Calif. Assoc. Mem. ASME.

Contributed by the Heat Transfer Division of THE AMERICAN SOCIETY OF MECHANICAL ENGINEERS. Manuscript received by the Heat Transfer Division June 7, 1971.

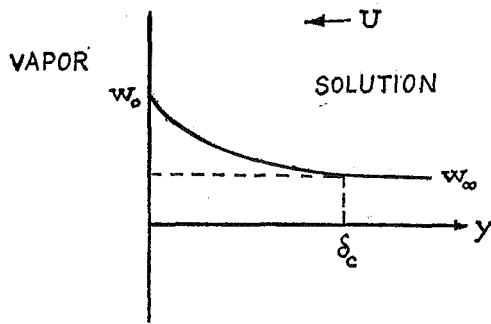


Fig. 1 Coordinate system

$$w = w_\infty \quad \text{at } t = 0 \quad \text{for all } y \quad (2)$$

and the boundary condition

$$Uw_0 - D \frac{\partial w}{\partial y} = 0 \quad \text{at } y = 0 \quad (3)$$

Using the Laplace transform, the transformed equation (1) is

$$\frac{d^2 \bar{w}}{dy^2} - \frac{U}{D} \frac{d\bar{w}}{dy} - \frac{p}{D} \bar{w} = -\frac{w_\infty}{D} \quad (\text{with } p \text{ real}) \quad (4)$$

The general solution is of the form

$$\bar{w} = C_1 e^{r_1 y} + C_2 e^{r_2 y} + \frac{w_\infty}{p} \quad (5)$$

The roots are

$$r_{1,2} = \frac{1}{2} \left[\frac{U}{D} \pm \sqrt{\left(\frac{U}{D}\right)^2 + 4 \frac{p}{D}} \right]$$

In order for the solution to be finite at $y = \infty$, $C_1 = 0$ and C_2 is found by the transformed surface condition

$$\left. \frac{d\bar{w}}{dy} \right|_0 = \frac{U}{D} \bar{w}_0$$

Equation (5) after some rearranging then becomes

$$\bar{w} = \frac{w_\infty}{p} - \frac{w_\infty U}{D} e^{\frac{1}{2} \frac{U}{D} y} \left[\frac{\exp\left(-\frac{y}{\sqrt{D}} \sqrt{\frac{U^2}{4D} + p}\right)}{p \left(\frac{1}{2} \frac{U}{D} + \frac{1}{\sqrt{D}} \sqrt{\frac{U^2}{4D} + p}\right)} \right] \quad (6)$$

Defining a new set of variables

$$\alpha = \frac{U^2}{4D}, \quad Y = \frac{y}{\sqrt{D}}, \quad s = \alpha + p \quad (7)$$

the term inside the square bracket of equation (6) after some manipulation becomes

$$-\frac{U}{2} \left[\frac{e^{-Y\sqrt{s}}}{(s-\alpha)^2} - \frac{1}{\sqrt{\alpha}} \frac{\sqrt{s} e^{-Y\sqrt{s}}}{(s-\alpha)^2} \right] \quad (8)$$

Calling the first term inside the bracket of (8) $\mathcal{L}(f)$, the second term can be written as

$$\frac{1}{\sqrt{\alpha}} \frac{d\mathcal{L}(f)}{dY}$$

But $\frac{d}{dY} \mathcal{L}(f) = \mathcal{L}\left(\frac{df}{dY}\right)$ for physically reasonable f since \mathcal{L} operates only with respect to t . The inverse transform of $\mathcal{L}(f)$, i.e., f , is given in formula 29 of Appendix V of Carslaw and Jaeger.² The inverse transform of $\mathcal{L}(df/dY)$, i.e., (df/dY) , is

² Carslaw, H. S., and Jaeger, J. C., *Conduction of Heat in Solids*, 2nd ed., Oxford Press, 1959, p. 496.

readily obtained by differentiation of f with respect to Y . The final expression for the concentration profile is

$$\frac{w}{w_\infty} = 1 + \frac{1}{2} \left\{ -\operatorname{erfc}\left(\frac{y}{2\sqrt{Dt}} - \frac{U}{2} \sqrt{\frac{t}{D}}\right) + \left(1 + \frac{U^2}{D} t + \frac{U}{D} y\right) e^{\frac{U}{D} y} \operatorname{erfc}\left(\frac{y}{2\sqrt{Dt}} + \frac{U}{2} \sqrt{\frac{t}{D}}\right) - \frac{2}{\sqrt{\pi}} U \sqrt{\frac{t}{D}} \exp\left[-\left(\frac{y^2}{4Dt} - \frac{U}{2D} y + \frac{U^2 t}{4D}\right)\right] \right\} \quad (9)$$

Defining a new set of variables

$$\eta = \frac{1}{4} \frac{|U|}{D} y, \quad \tau = \frac{1}{2} |U| \sqrt{\frac{t}{D}}, \quad \frac{\eta}{\tau} = \frac{y}{2\sqrt{Dt}}$$

and noting that $U < 0$, equation (9) is rewritten as

$$\frac{w}{w_\infty} = 1 + \frac{1}{2} \left\{ -1 + \operatorname{erf}\left(\frac{\eta}{\tau} + \tau\right) + (1 + 4\tau^2 - 4\eta)e^{-4\eta} \left[1 - \operatorname{erf}\left(\frac{\eta}{\tau} - \tau\right) \right] + \frac{4}{\sqrt{\pi}} \tau \exp\left[-\left(\frac{\eta}{\tau} + \tau\right)^2\right] \right\} \quad (10)$$

The surface concentration at $\eta = 0$ becomes

$$\frac{w_0}{w_\infty} = 1 + \frac{1}{2} \left\{ (4\tau^2 + 2) \operatorname{erf} \tau + 4\tau^2 + \frac{4}{\sqrt{\pi}} \tau e^{-\tau^2} \right\} \quad (11)$$

At $\tau \ll 1$, the above expression simplifies to

$$\frac{w_0}{w_\infty} \cong 1 + \frac{1}{2} \left\{ \left(\frac{4}{\sqrt{\pi}} \tau\right) + \frac{4}{\sqrt{\pi}} \tau \right\} \cong 1 + 2.26\tau \quad (12)$$

At $\tau \gg 1$,

$$\frac{w_0}{w_\infty} \cong 1 + \frac{1}{2} \{4\tau^2 + 2 + 4\tau^2\} \cong 4\tau^2 \quad (13)$$

This concludes the exact solution. Next, the same problem will be solved by the integral method and compared with the exact solution.

Assume a profile of the form

$$w = a + by + cy^2 \quad (14)$$

The conditions

$$\left. \frac{\partial w}{\partial y} \right|_0 = \frac{U}{D} w_0 \quad \text{at } y = 0$$

$$w = w_\infty \quad \text{and} \quad \frac{\partial w}{\partial y} = 0 \quad \text{at } y = \delta_c$$

determine the profile

$$\frac{w}{w_\infty} = \frac{\left(1 + \frac{U}{D} y - \frac{U}{2D\delta_c} y^2\right)}{\left(1 + \frac{U}{2D} \delta_c\right)} \quad (15)$$

and the conservation of solute

$$\int_0^{\delta_c} w dy = w_\infty \int_0^t \left(\frac{d\delta_c}{dt} - U\right) dt = w_\infty(\delta_c - Ut)$$

determines δ_c

$$\delta_c = \frac{3Ut + \sqrt{9U^2 t^2 + 24Dt}}{2} \quad (16)$$

The surface concentration is

$$\frac{w_0}{w_\infty} = \frac{1}{1 + 3\tau^2 - 3\tau\sqrt{\tau^2 + \frac{2}{3}}} \quad (17)$$

where

$$\tau = \frac{|U|}{2} \sqrt{\frac{l}{D}}$$

as before. For small values of τ ,

$$\frac{w_0}{w_\infty} \cong \frac{1}{1 - \sqrt{6}\tau} \cong 1 + \sqrt{6}\tau = 1 + 2.45\tau \quad (18)$$

This result is seen to slightly overestimate the surface concentration compared with the exact solution, equation (12), where 2.26τ rather than 2.45τ resulted. For $\tau \gg 1$, equation (17) yields $w_0/w_\infty \cong 6\tau^2$ in comparison with $4\tau^2$ of equation (13). This then indicates that the use of the integral method is acceptable for $\tau \ll 1$, while 50 percent error results for $\tau \gg 1$.

When the solute becomes saturated at the surface and subsequent precipitation of solid phase sets in, the solution presented here is no longer valid and the concentration in the liquid phase will not rise beyond the saturation value. The imposed condition of constant evaporation rate becomes physically impossible as soon as a complete sheet of solid phase forms on the surface.

Forced Heat Transfer over Thin Needles

JAI PRAKASH NARAIN¹ and MAHINDER S. UBEROI²

Nomenclature

- a = size of needle
- c = constant
- C_f = coefficient of friction at wall
- E_1 = exponential integral function of order 1
- K = thermal diffusivity
- Pr = Prandtl number, ν/K
- R = $a/4$, curvature parameter [1, 6]³
- r = radial coordinate
- Re_x = local Reynolds number, $u_\infty x/\nu$
- St = Stanton number
- T, T_∞ = local and free-stream temperatures of fluid
- T_w = wall temperature of needle
- u, u_∞ = local and free-stream axial-velocity components
- v = radial-velocity component
- x = axial coordinate
- z = transformed independent variable
- δ^* = displacement thickness [2]
- θ = transformed temperature function
- ν = kinematic viscosity
- ρ = density of fluid
- ψ = stream function
- ϕ = transformed stream function

¹ Research Assistant, Department of Aerospace Engineering Sciences, University of Colorado, Boulder, Colo.

² Professor and Chairman, Department of Aerospace and Engineering Sciences, University of Colorado, Boulder, Colo.

Contributed by the Heat Transfer Division of THE AMERICAN SOCIETY OF MECHANICAL ENGINEERS. Manuscript received by the Heat Transfer Division June 20, 1971.

Superscript

' = ordinary differentiation with respect to z

Subscripts

- ∞ = free-stream value
- a = w , wall conditions
- x = local value

Introduction

THE boundary-layer flow of viscous incompressible fluid flowing axially over a thin paraboloid-of-revolution-shaped needle has been considered by Mark [1],³ Lee [2], and Miller [3]. Jafe and Okamura [4] considered the effect of transverse curvature on the incompressible laminar boundary layer for longitudinal flow over a cylinder. Cebeci, Na, and Mosinskis [5] have extended Mark's [1] results to compressible, forced heat-transfer flows. This analysis was primarily intended to present a set of numerical solutions of simplified Lee's [2] similarity equations and was further extended to cover the problem of forced heat transfer over such needles. Recently Tam [6] has proved the existence of such solutions by considering the asymptotic nature of the similarity equations.

Basic Equations

A needle is assumed "thin" when its thickness is smaller than or comparable to that of the boundary layer over it [2]. Neglecting pressure variations along the needle and retaining the effect of transverse curvature [2, 4], the steady, viscous, incompressible boundary-layer equations are

$$\frac{\partial(rv)}{\partial x} + \frac{\partial(rv)}{\partial r} = 0, \quad u \frac{\partial u}{\partial x} + v \frac{\partial u}{\partial r} = \nu \left(\frac{\partial^2 u}{\partial r^2} + \frac{1}{r} \frac{\partial u}{\partial r} \right) \quad (1)$$

$$u \frac{\partial T}{\partial x} + v \frac{\partial T}{\partial r} = K \left(\frac{\partial^2 T}{\partial r^2} + \frac{1}{r} \frac{\partial T}{\partial r} \right)$$

Introducing an axisymmetric stream function ψ , we use the following transformations:

$$\begin{aligned} \psi &= \nu x \phi(z), & T - T_\infty &= (T_w - T_\infty) \theta(z) \\ z &= \frac{u_\infty}{\nu} \frac{r^2}{x} \end{aligned} \quad (2)$$

The equations (1) have similarity form

$$(z\phi'')' + 1/2 z \phi \phi'' = 0 \quad (3)$$

and

$$(z\theta')' + 1/2 Pr \phi \theta' = 0 \quad (4)$$

The surface of a paraboloid of revolution corresponding to $z = a$ refers to the wall of the needle. Equation (3) is a modified version of Lee's [2] equation, which incidentally could be obtained from the similarity equation in [3-6] with the proper transformations. The no-slip conditions at the wall and isothermal wall conditions give the following boundary conditions on the surface $z = a$:

$$\phi(a) = \phi'(a) = 0 \quad \text{and} \quad \theta(a) = 1 \quad (5)$$

The free-stream conditions are the following:

$$\phi'(\infty) = 1/2 \quad \text{and} \quad \theta(\infty) = 0 \quad \text{as} \quad z \rightarrow \infty \quad (6)$$

We define the skin-friction coefficient and Stanton number by the following expressions:

³ Numbers in brackets designate References at end of technical brief.

$$\frac{w_0}{w_\infty} = \frac{1}{1 + 3\tau^2 - 3\tau\sqrt{\tau^2 + \frac{2}{3}}} \quad (17)$$

where

$$\tau = \frac{|U|}{2} \sqrt{\frac{l}{D}}$$

as before. For small values of τ ,

$$\frac{w_0}{w_\infty} \cong \frac{1}{1 - \sqrt{6}\tau} \cong 1 + \sqrt{6}\tau = 1 + 2.45\tau \quad (18)$$

This result is seen to slightly overestimate the surface concentration compared with the exact solution, equation (12), where 2.26τ rather than 2.45τ resulted. For $\tau \gg 1$, equation (17) yields $w_0/w_\infty \cong 6\tau^2$ in comparison with $4\tau^2$ of equation (13). This then indicates that the use of the integral method is acceptable for $\tau \ll 1$, while 50 percent error results for $\tau \gg 1$.

When the solute becomes saturated at the surface and subsequent precipitation of solid phase sets in, the solution presented here is no longer valid and the concentration in the liquid phase will not rise beyond the saturation value. The imposed condition of constant evaporation rate becomes physically impossible as soon as a complete sheet of solid phase forms on the surface.

Forced Heat Transfer over Thin Needles

JAI PRAKASH NARAIN¹ and MAHINDER S. UBEROI²

Nomenclature

- a = size of needle
- c = constant
- C_f = coefficient of friction at wall
- E_1 = exponential integral function of order 1
- K = thermal diffusivity
- Pr = Prandtl number, ν/K
- R = $a/4$, curvature parameter [1, 6]³
- r = radial coordinate
- Re_x = local Reynolds number, $u_\infty x/\nu$
- St = Stanton number
- T, T_∞ = local and free-stream temperatures of fluid
- T_w = wall temperature of needle
- u, u_∞ = local and free-stream axial-velocity components
- v = radial-velocity component
- x = axial coordinate
- z = transformed independent variable
- δ^* = displacement thickness [2]
- θ = transformed temperature function
- ν = kinematic viscosity
- ρ = density of fluid
- ψ = stream function
- ϕ = transformed stream function

¹ Research Assistant, Department of Aerospace Engineering Sciences, University of Colorado, Boulder, Colo.

² Professor and Chairman, Department of Aerospace and Engineering Sciences, University of Colorado, Boulder, Colo.

Contributed by the Heat Transfer Division of THE AMERICAN SOCIETY OF MECHANICAL ENGINEERS. Manuscript received by the Heat Transfer Division June 20, 1971.

Superscript

' = ordinary differentiation with respect to z

Subscripts

- ∞ = free-stream value
- a = w , wall conditions
- x = local value

Introduction

THE boundary-layer flow of viscous incompressible fluid flowing axially over a thin paraboloid-of-revolution-shaped needle has been considered by Mark [1],³ Lee [2], and Miller [3]. Jafe and Okamura [4] considered the effect of transverse curvature on the incompressible laminar boundary layer for longitudinal flow over a cylinder. Cebeci, Na, and Mosinskis [5] have extended Mark's [1] results to compressible, forced heat-transfer flows. This analysis was primarily intended to present a set of numerical solutions of simplified Lee's [2] similarity equations and was further extended to cover the problem of forced heat transfer over such needles. Recently Tam [6] has proved the existence of such solutions by considering the asymptotic nature of the similarity equations.

Basic Equations

A needle is assumed "thin" when its thickness is smaller than or comparable to that of the boundary layer over it [2]. Neglecting pressure variations along the needle and retaining the effect of transverse curvature [2, 4], the steady, viscous, incompressible boundary-layer equations are

$$\frac{\partial(rv)}{\partial x} + \frac{\partial(rv)}{\partial r} = 0, \quad u \frac{\partial u}{\partial x} + v \frac{\partial u}{\partial r} = \nu \left(\frac{\partial^2 u}{\partial r^2} + \frac{1}{r} \frac{\partial u}{\partial r} \right) \quad (1)$$

$$u \frac{\partial T}{\partial x} + v \frac{\partial T}{\partial r} = K \left(\frac{\partial^2 T}{\partial r^2} + \frac{1}{r} \frac{\partial T}{\partial r} \right)$$

Introducing an axisymmetric stream function ψ , we use the following transformations:

$$\psi = \nu x \phi(z), \quad T - T_\infty = (T_w - T_\infty) \theta(z) \quad (2)$$

$$z = \frac{u_\infty}{\nu} \frac{r^2}{x}$$

The equations (1) have similarity form

$$(z\phi'')' + 1/2 z \phi \phi'' = 0 \quad (3)$$

and

$$(z\theta')' + 1/2 Pr \phi \theta' = 0 \quad (4)$$

The surface of a paraboloid of revolution corresponding to $z = a$ refers to the wall of the needle. Equation (3) is a modified version of Lee's [2] equation, which incidentally could be obtained from the similarity equation in [3-6] with the proper transformations. The no-slip conditions at the wall and isothermal wall conditions give the following boundary conditions on the surface $z = a$:

$$\phi(a) = \phi'(a) = 0 \quad \text{and} \quad \theta(a) = 1 \quad (5)$$

The free-stream conditions are the following:

$$\phi'(\infty) = 1/2 \quad \text{and} \quad \theta(\infty) = 0 \quad \text{as} \quad z \rightarrow \infty \quad (6)$$

We define the skin-friction coefficient and Stanton number by the following expressions:

³ Numbers in brackets designate References at end of technical brief.

$$C_f = \frac{\rho\nu \left(\frac{\partial u}{\partial r} \right)_{z=a}}{1/2 \rho u_\infty^2} = 8\sqrt{a} \phi''(a) \text{Re}_x^{-1/2} \quad (7)$$

and

$$\text{St} = -\frac{x \left(\frac{\partial T}{\partial r} \right)_{z=a}}{(T_w - T_\infty) \text{Re}_x \text{Pr}} = -2\sqrt{a} \theta'(a) \text{Re}_x^{-1/2} \text{Pr}^{-1} \quad (8)$$

Results and Discussion

The similarity equations (3) and (4) with boundary conditions (5) were integrated using "shooting" methods until free-stream conditions (6) were identically satisfied. The upper part of Fig. 1 showing axial-velocity profiles $\phi'(z) = u/2u_\infty$ for various values of needle size agrees with Lee's [2] observation that the boundary-layer thickness increases very slowly with progressively increasing needle size. We found that skin-friction coefficients in two computations agree quite well. Table 1 further compares the values of $C_f(\text{Re}_x)^{1/2}$ obtained in the present computation and those obtained by using Mark's [1] formula

$$C_f(\text{Re}_x)^{1/2} = \frac{2}{(R)^{1/2}} \left[\frac{1}{\ln [1/Rc]} - \frac{2.210}{\{\ln (1/Rc)\}^3} \right] \quad (9)$$

where $\ln c = 0.5772$ and $R = a/4$. As observed previously [1-3, 5], the skin-friction coefficient increases with decreasing size of the needles and is independent of Prandtl number. The values of $\phi''(a)$ shown in Table 1 are well within the bounds given by Tam [6] as

$$0 < \phi''(a) < e(1 + 1/R) \quad (10a)$$

The bound for $\theta'(a)$ given by Tam [6] is in error due to mistakes in his energy-equation transformations. The correct limits could be obtained as

$$-\frac{e^{-\text{Pr} R}}{R E_1(\text{Pr} R)} < \theta'(a) < 0 \quad (10b)$$

and

$$-\text{Pr} < \theta'(a) < 0 \quad \text{as } \text{Pr} R \rightarrow \infty$$

Our numerical results are well within the above asymptotic bounds. The maximum size of the needle is determined by the condition that $\delta^*/a \geq 1$. For a needle of size $a = 10^{-1}$, this ratio is around 6; hence we limit the thickness of needles below $a = 10^{-1}$.

For a given size of the needle, the heat-transfer behavior is similar to that in the case of flat plates [7]. The middle part of Fig. 1 confirms this observation, where the variation of excess

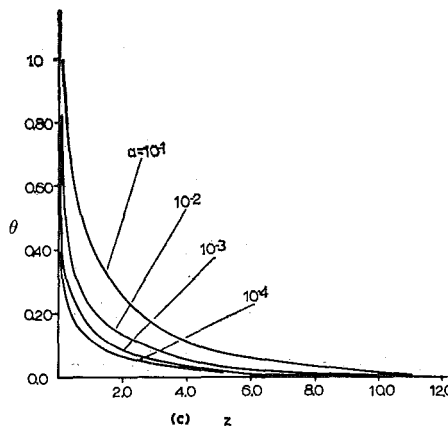
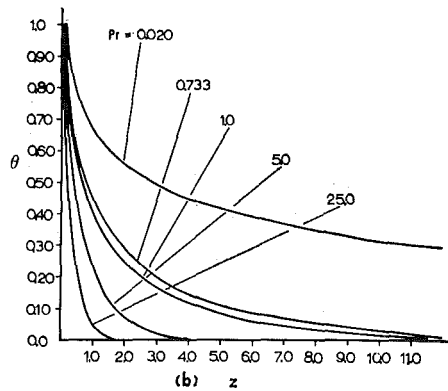
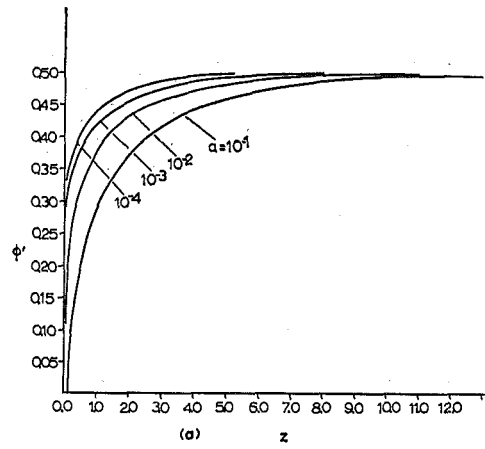


Fig. 1(a) The axial velocity function $\phi' = u/2u_\infty$ for various needle sizes; (b) the transformed temperature variable θ for $a = 10^{-1}$ and various Prandtl numbers; (c) the transformed temperature θ for $\text{Pr} = 1$ and various needle sizes

Table 1 Local skin-friction coefficient over thin needle

a	$\phi''(a)$	$C_f(\text{Re}_x)^{1/2}$	
		Present computation	Mark's equation
10^{-1}	1.28883	3.20	3.120
10^{-2}	8.49244	6.80	6.848
10^{-3}	62.16372	15.60	15.70
10^{-4}	487.10152	38.9681	39.116

Table 2 Effect of needle size and Prandtl number on heat transfer

Needle size	$a = 10^{-1}$		$a = 10^{-2}$		$a = 10^{-3}$		$a = 10^{-4}$	
	Pr	$\text{St}(\text{Re}_x)^{1/2}$	$\frac{2 \text{St}}{C_f}$	$\text{St}(\text{Re}_x)^{1/2}$	$\frac{2 \text{St}}{C_f}$	$\text{St}(\text{Re}_x)^{1/2}$	$\frac{2 \text{St}}{C_f}$	$\text{St}(\text{Re}_x)^{1/2}$
0.020	47.0	28.90	112.92	33.25	291.0	37.05	776.64	39.80
0.733	2.10	1.290	4.44	1.310	10.40	1.30	25.90	1.33
1.0	1.60	1.00	3.40	1.00	7.80	1.0	19.48	1.0
5.0	0.444	0.272	0.860	0.254	1.89	0.240	4.52	0.2324
25.0	0.126	0.0776	0.226	0.0620	0.469	0.0596	1.055	0.0542
125.0	0.039	0.0224	0.0625	0.0184	0.120	0.01530	0.260	0.01340

temperature θ across the boundary layer for various values of Prandtl numbers and for $a = 10^{-1}$ has been shown. The lower part of Fig. 1 shows the effect of needle size on temperature variation for a constant $Pr = 1$. The rate of heat transfer increases with decreasing needle size; however, the thermal boundary layer decreases very slowly with it. The values of $St(Re_x)^{1/2}$ shown in Table 2 increase (i) with decreasing needle size at a given Prandtl number [5], and (ii) with decreasing values of Prandtl number at a given size of the needle. Furthermore, the values of $2 St/C_f$ shown in Table 2 are related to the Prandtl number, within 35 percent error in the range of needle size being considered, by

$$2 St/C_f = Pr^{-0.860} \quad (11)$$

References

- 1 Mark, R. M., "Laminar Boundary Layer on Slender Bodies of Revolution in Axial Flow," Rept. 21, Guggenheim Aeronautical Laboratory, California Institute of Technology, Pasadena, Calif., July 1954.
- 2 Lee, L. L., "Boundary Layer over a Thin Needle," *Physics of Fluids*, Vol. 10, No. 4, 1967, pp. 820-822.
- 3 Miller, D. R., "The Boundary Layer on a Paraboloid of Revolution," *Proc. Camb. Philos. Soc.*, Vol. 65, 1969, pp. 285-299.
- 4 Jafe, N. A., and Okamura, T. T., "The Transverse Curvature Effects on the Incompressible Laminar Boundary Layer for Longitudinal Flow over a Cylinder," *ZAMP*, Vol. 19, 1968, pp. 564-574.
- 5 Cebeci, T., Na, T. Y., and Mosinskis, G., "Laminar Boundary Layer on Slender Paraboloids," *AIAA Journal*, Vol. 7, 1969, pp. 1372-1374.
- 6 Tam, K. K., "On the Asymptotic Solution of Viscous Incompressible Flow Past a Heated Paraboloid of Revolution," *SIAM J. App. Mech.*, Vol. 20, No. 4, 1971, pp. 714-721.
- 7 Schlichting, H., *Boundary Layer Theory*, McGraw-Hill, New York, N. Y., 1960, pp. 311-317.

Turbulent-Boundary-Layer Measurements along a Supersonic Nozzle with and without Wall Cooling¹

LLOYD H. BACK² and ROBERT F. CUFFEL³

Introduction

THE PURPOSE of this note is to present boundary-layer measurements along a slightly heated axisymmetric nozzle (wall-to-stagnation-temperature ratio, $T_w/T_{10} \sim 1.1$) and to compare the results to semi-empirical analyses and to those results previously obtained [1]⁴ with wall cooling ($T_w/T_{10} \sim 0.5$). The heated-wall conditions were obtained by using ambient-temperature air at a stagnation pressure of 150 psia and circulating heated water through the coolant passages of a conical nozzle which

¹ This work presents the results of one phase of research carried out in the Propulsion Research and Advanced Concepts Section of the Jet Propulsion Laboratory, California Institute of Technology, under Contract No. NAS7-100 sponsored by the National Aeronautics and Space Administration.

² Member, Technical Staff, Jet Propulsion Laboratory, California Institute of Technology, Pasadena, Calif. Mem. ASME.

³ Member, Technical Staff, Jet Propulsion Laboratory, California Institute of Technology, Pasadena, Calif. Assoc. Mem. ASME.

⁴ Numbers in brackets designate References at end of technical brief.

Contributed by the Heat Transfer Division of THE AMERICAN SOCIETY OF MECHANICAL ENGINEERS. Manuscript received by the Heat Transfer Division November 5, 1971.

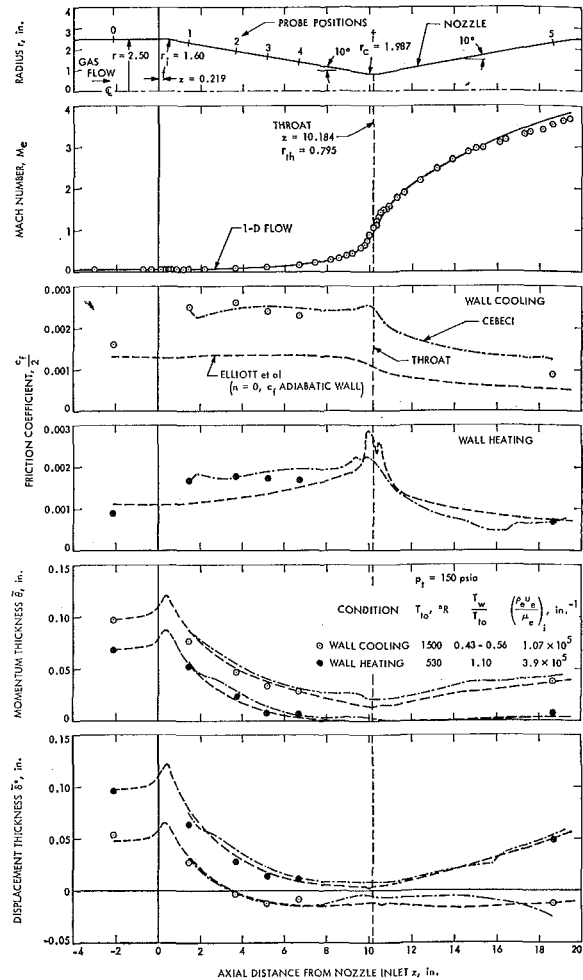


Fig. 1 Mach number, friction coefficient, and momentum and displacement thickness distributions along the nozzle with a small amount of wall heating and wall cooling

had 10 deg half-angles of convergence and divergence (Fig. 1). Data are also shown at intermediate values of T_w/T_{10} and at lower stagnation pressures to indicate the trends better (Fig. 2). A description of the apparatus, measurements, analyses, nomenclature, and cooled-wall results appears in [1].

Results

The free-stream-Mach-number distribution (Fig. 1), determined primarily by the nozzle shape, was essentially the same for either thermal boundary condition and was nearly that for a one-dimensional flow because of the gradual contour of the nozzle, except in the inlet section where the measured pressure rise was probably sufficient to separate the inner portion of the boundary layer with reattachment occurring before the beginning of the conical section ($z = 0.5$ in.), and at $z = 15$ in. where weak compressive waves which originated downstream of the throat in the vicinity of the circular-arc-conical-section tangency ($z = 10.53$ in.) produced a small change in the free-stream Mach number.

The momentum defect (Fig. 1) was less with a small amount of wall heating than it was with wall cooling, partly because of the lower stagnation temperature and thus higher unit Reynolds number that governed the turbulent-boundary-layer growth along the heated circular tube preceding the nozzle, but also because of the combined effects of wall heating and acceleration as determined by the momentum balance

$$\frac{d}{dx} (r \rho_e u_e^2 \delta^*) = r \frac{dp}{dx} \delta^* + r \tau_w$$

temperature θ across the boundary layer for various values of Prandtl numbers and for $a = 10^{-1}$ has been shown. The lower part of Fig. 1 shows the effect of needle size on temperature variation for a constant $Pr = 1$. The rate of heat transfer increases with decreasing needle size; however, the thermal boundary layer decreases very slowly with it. The values of $St(Re_x)^{1/2}$ shown in Table 2 increase (i) with decreasing needle size at a given Prandtl number [5], and (ii) with decreasing values of Prandtl number at a given size of the needle. Furthermore, the values of $2 St/C_f$ shown in Table 2 are related to the Prandtl number, within 35 percent error in the range of needle size being considered, by

$$2 St/C_f = Pr^{-0.860} \quad (11)$$

References

- 1 Mark, R. M., "Laminar Boundary Layer on Slender Bodies of Revolution in Axial Flow," Rept. 21, Guggenheim Aeronautical Laboratory, California Institute of Technology, Pasadena, Calif., July 1954.
- 2 Lee, L. L., "Boundary Layer over a Thin Needle," *Physics of Fluids*, Vol. 10, No. 4, 1967, pp. 820-822.
- 3 Miller, D. R., "The Boundary Layer on a Paraboloid of Revolution," *Proc. Camb. Philos. Soc.*, Vol. 65, 1969, pp. 285-299.
- 4 Jafe, N. A., and Okamura, T. T., "The Transverse Curvature Effects on the Incompressible Laminar Boundary Layer for Longitudinal Flow over a Cylinder," *ZAMP*, Vol. 19, 1968, pp. 564-574.
- 5 Cebeci, T., Na, T. Y., and Mosinskis, G., "Laminar Boundary Layer on Slender Paraboloids," *AIAA Journal*, Vol. 7, 1969, pp. 1372-1374.
- 6 Tam, K. K., "On the Asymptotic Solution of Viscous Incompressible Flow Past a Heated Paraboloid of Revolution," *SIAM J. App. Mech.*, Vol. 20, No. 4, 1971, pp. 714-721.
- 7 Schlichting, H., *Boundary Layer Theory*, McGraw-Hill, New York, N. Y., 1960, pp. 311-317.

Turbulent-Boundary-Layer Measurements along a Supersonic Nozzle with and without Wall Cooling¹

LLOYD H. BACK² and ROBERT F. CUFFEL³

Introduction

THE PURPOSE of this note is to present boundary-layer measurements along a slightly heated axisymmetric nozzle (wall-to-stagnation-temperature ratio, $T_w/T_{10} \sim 1.1$) and to compare the results to semi-empirical analyses and to those results previously obtained [1]⁴ with wall cooling ($T_w/T_{10} \sim 0.5$). The heated-wall conditions were obtained by using ambient-temperature air at a stagnation pressure of 150 psia and circulating heated water through the coolant passages of a conical nozzle which

¹ This work presents the results of one phase of research carried out in the Propulsion Research and Advanced Concepts Section of the Jet Propulsion Laboratory, California Institute of Technology, under Contract No. NAS7-100 sponsored by the National Aeronautics and Space Administration.

² Member, Technical Staff, Jet Propulsion Laboratory, California Institute of Technology, Pasadena, Calif. Mem. ASME.

³ Member, Technical Staff, Jet Propulsion Laboratory, California Institute of Technology, Pasadena, Calif. Assoc. Mem. ASME.

⁴ Numbers in brackets designate References at end of technical brief.

Contributed by the Heat Transfer Division of THE AMERICAN SOCIETY OF MECHANICAL ENGINEERS. Manuscript received by the Heat Transfer Division November 5, 1971.

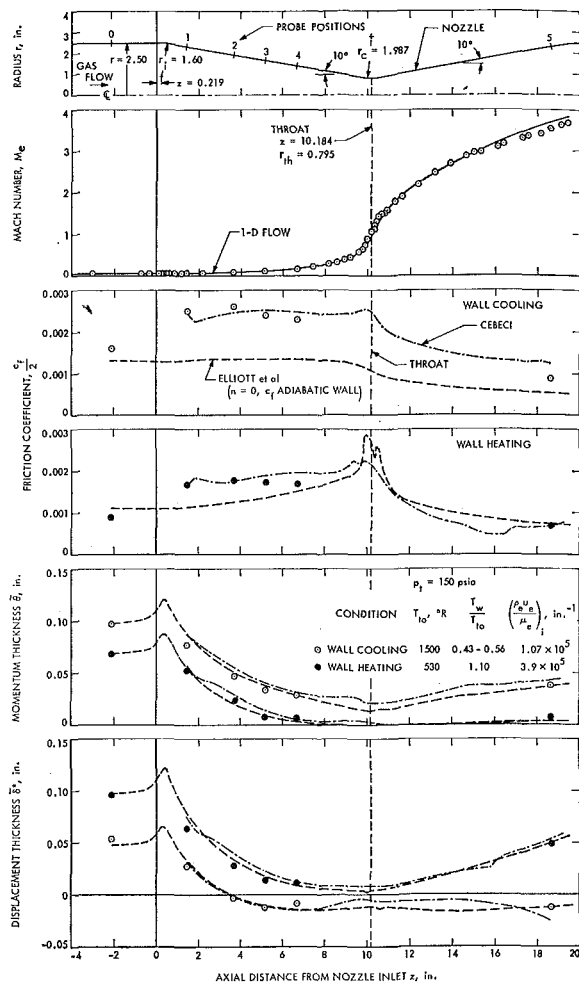


Fig. 1 Mach number, friction coefficient, and momentum and displacement thickness distributions along the nozzle with a small amount of wall heating and wall cooling

had 10 deg half-angles of convergence and divergence (Fig. 1). Data are also shown at intermediate values of T_w/T_{10} and at lower stagnation pressures to indicate the trends better (Fig. 2). A description of the apparatus, measurements, analyses, nomenclature, and cooled-wall results appears in [1].

Results

The free-stream-Mach-number distribution (Fig. 1), determined primarily by the nozzle shape, was essentially the same for either thermal boundary condition and was nearly that for a one-dimensional flow because of the gradual contour of the nozzle, except in the inlet section where the measured pressure rise was probably sufficient to separate the inner portion of the boundary layer with reattachment occurring before the beginning of the conical section ($z = 0.5$ in.), and at $z = 15$ in. where weak compressive waves which originated downstream of the throat in the vicinity of the circular-arc-conical-section tangency ($z = 10.53$ in.) produced a small change in the free-stream Mach number.

The momentum defect (Fig. 1) was less with a small amount of wall heating than it was with wall cooling, partly because of the lower stagnation temperature and thus higher unit Reynolds number that governed the turbulent-boundary-layer growth along the heated circular tube preceding the nozzle, but also because of the combined effects of wall heating and acceleration as determined by the momentum balance

$$\frac{d}{dx} (r \rho_e u_e^2 \delta^*) = r \frac{dp}{dx} \delta^* + r \tau_w$$

B. L. POSITION	z in.	TEST	M _e	P ₁ psia	T ₁₀ ' °R	T _w /T ₁₀	β	α	P _e u _w β / μ _e	c _f / 2
0	-2.14	P260	0.058	15.2	527	1.13	0.064	0.139	2,970	1.36 × 10 ⁻³
		P259	0.065	20.1	528	1.14	0.078	0.126	4,020	1.29
		P258	0.065	20.2	525	1.14	0.074	0.116	5,740	1.26
		P257	0.064	45.1	523	1.14	0.066	0.104	7,700	1.16
		P256	0.065	74.9	523	1.12	0.068	0.102	13,300	1.04
		P255	0.066	100.1	522	1.13	0.065	0.097	17,300	0.96
		P254	0.065	150.4	526	1.11	0.068	0.096	26,600	0.88
1.	1.42	P250	0.074	149.8	532	1.03	0.053	0.064	22,700	1.68
		P248	0.103	150.0	536	1.03	0.024	0.028	14,200	1.77
2	3.67	S25	0.096	100.4	995	0.63	0.037	0.002	6,940	2.4
		P253	0.138	150.7	523	1.08	0.0077	0.014	6,400	1.72
3	5.17	P257	0.197	45.1	523	1.14	0.0036	0.013	1,260	2.20
		P256	0.197	74.9	523	1.12	0.0050	0.012	2,900	1.96
		P255	0.197	100.1	522	1.12	0.0052	0.013	4,060	1.85
		P254	0.197	150.4	526	1.09	0.0068	0.012	8,000	1.70
		P233	0.193	45.2	524	1.0	0.0062	0.0073	2,140	2.3
		P224	0.193	75.3	522	1.0	0.0080	0.0090	4,350	2.1
		P212	0.193	100.4	525	1.0	0.0098	0.0108	7,470	1.9
		P216	0.193	125.2	532	1.0	0.0091	0.0101	8,510	1.8
		P241	0.193	149.6	555	1.0	0.0096	0.012	10,500	1.8
		S24	0.191	100.4	1005	0.63	0.022	-0.005	7,520	2.3
5	18.65	P304	3.61	100.4	526	1.10	0.0069	0.051	5,900	0.76
		P303	3.61	150.2	533	1.10	0.0065	0.049	8,300	0.68

BL POSITION	TEST	c _f / 2	β	α	K	R = K / (c _f / 2) ^{3/2}	
○	0	S12	1.6 × 10 ⁻³	-0.038	0	0	0
●	0	P254	0.88	0.004	0	0	0
○	4	S12	2.3	-0.025	0	0.84 × 10 ⁻⁶	0.0076
●	4	P254	1.70	0.003	0	0	0.0033
○	5	S54	0.88	-0.030	0.0023	0.059	0.0023
●	5	P303	0.68	0.008	0.0018	0.014	0.0008

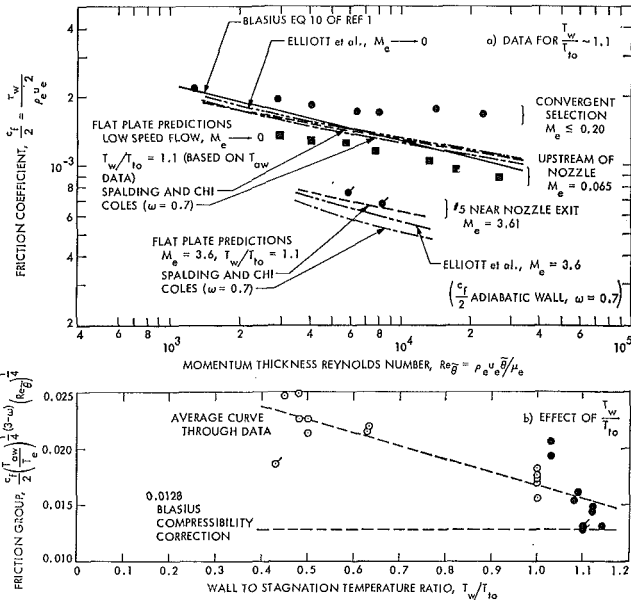


Fig. 2 Friction coefficients

The displacement thickness (Fig. 1) remained positive with wall heating rather than becoming negative as it did with the combined effects of wall cooling and acceleration.

The friction coefficient (Fig. 2) was found to exceed values for nonaccelerating flow, to decrease with wall heating, and to decrease because of compressibility. Existing formulations based on nonaccelerating flows [2, 3] underestimated the friction coefficient along the nozzle (Fig. 2).

Predicted momentum and displacement thickness from an integral analysis formulated previously [4] and from a solution of the differential form of the boundary-layer equations [5] were generally found to be in relatively good agreement with the data (Fig. 1). This occurred for the integral analysis in spite of the much lower predicted friction coefficients with wall cooling, although the agreement in the friction coefficient was somewhat better with a small amount of wall heating (Fig. 1). Predicted friction coefficients by Cebeci [5] agreed fairly well with the data with a small amount of wall heating. However, with wall cooling the predicted friction coefficient [5] became too large along the divergent section where the combined effects of wall cooling and compressibility became important [1].

With a small amount of wall heating the friction coefficient could be inferred from the constant-property von Karman pro-

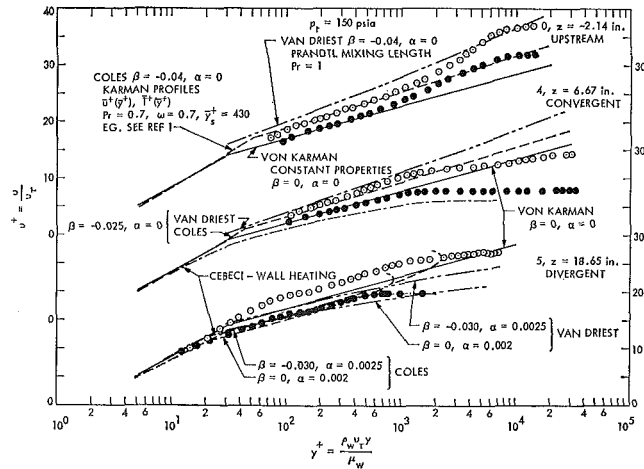


Fig. 3 Velocity profiles

file (Fig. 3) in the low-speed region upstream and along the convergent section of the nozzle. Near the end of the nozzle the boundary-layer measurements extended into the sublayer so that the friction coefficient could be estimated directly for either thermal boundary condition.

The velocity profiles on a u^+, y^+ basis (Fig. 3) indicate the influence of the thermal boundary condition. To establish a reference basis, predicted profiles from mixing-length theory [6] and Coles' transformation theory [3] are shown. These profiles depend upon a cooling or heating parameter β and a frictional heating parameter α [1]. The influence of wall cooling is to shift the velocity profiles upward in the same direction as indicated by the reference profiles, both upstream and along the nozzle. Agreement in magnitude is found with this shift in the convergent section, but not near the nozzle exit where the predicted profiles are reduced because of frictional heating. There is fairly good agreement between the measured and predicted velocity profiles of Cebeci with a small amount of wall heating, and this is consistent with the agreement in the friction coefficient (Fig. 1).

References

- 1 Back, L. H., and Cuffel, R. F., "Turbulent Boundary Layer and Heat Transfer Measurements Along a Convergent-Divergent Nozzle," *JOURNAL OF HEAT TRANSFER, TRANS. ASME, Series C*, Vol. 93, No. 4, Nov. 1971, pp. 397-407.
- 2 Spalding, D. B., and Chi, S. W., "The Drag of a Compressible Turbulent Boundary Layer on a Smooth Flat Plate with and without Heat Transfer," *Journal of Fluid Mechanics*, Vol. 18, 1964, pp. 117-143.
- 3 Coles, D., "The Turbulent Boundary Layer in a Compressible Fluid," *Phys. Fluids*, Vol. 7, No. 9, Sept. 1964, pp. 1403-1423.
- 4 Elliott, D. G., Bartz, D. R., and Silver, S., "Calculation of Turbulent Boundary-Layer Growth and Heat Transfer in Axisymmetric Nozzles," TR 32-387, Jet Propulsion Laboratory, Pasadena, Calif., Feb. 1963.
- 5 Cebeci, T., "Calculation of Compressible Turbulent Boundary Layers with Heat and Mass Transfer," *ATAA Journal*, Vol. 9, No. 6, June 1971, pp. 1091-1097.
- 6 Van Driest, E. R., "Turbulent Boundary in Compressible Fluids," *J. Aeronaut. Sci.*, Vol. 18, No. 3, Mar. 1951, pp. 145-160.

Response of Finite-Thickness Gardon Heat-Flux Sensors

ROBERT H. KIRCHHOFF¹

The temperature-time response of a Gardon heat-flux sensor of finite thickness has been calculated by the integral-transform technique. Through the introduction of the aspect ratio, results are presented which characterize the response of a finite-thickness probe compared to a probe of zero thickness.

Introduction

IN PREVIOUS work [1, 2]² on the Gardon heat-flux sensor, the effect of the finite thickness of the foil on the temperature-time response has been neglected. Gardon's original laboratory probes ranged from 0.00025 to 0.0025 cm thick. In order to design a thicker probe for a more robust environment, it is necessary to know the effect of the finite probe thickness L on the temperature-time response of the probe. It is the purpose of this note to present such an analysis. Fig. 1 is a cross-sectional sketch of the sensor under study. Heat flux q incident on the front face of the foil creates a temperature difference between the foil center and the constant-temperature heat sink at the foil edge. This temperature difference can be related to the incident heat flux q by measuring the emf between the copper wire and copper heat sink.

Theoretical Analysis

Assuming constant foil conductivity k and diffusivity α , neglecting any effect of the central wire and neglecting any losses, the analysis of the temperature-time response of the foil in Fig. 1 can be reduced to the following two-dimensional unsteady heat-conduction problem. The equation for the temperature T is

$$\frac{\partial^2 T}{\partial r^2} + \frac{1}{r} \frac{\partial T}{\partial r} + \frac{\partial^2 T}{\partial z^2} = \frac{1}{\alpha} \frac{\partial T}{\partial t} \quad (1)$$

where α is the thermal diffusivity of the constantan foil. The boundary conditions are

$$\left. \begin{aligned} \frac{\partial T}{\partial z} \Big|_{z=L} &= q/k; & \frac{\partial T}{\partial z} \Big|_{z=0} &= 0 \\ \text{and} & & & \\ T(z, b, t) &= 0 \quad \text{for all } t > 0 \end{aligned} \right\} \quad (2)$$

The insulated back face condition is the most reasonable one for the design of a probe. The initial condition is

$$T(z, r, 0) = 0 \quad (3)$$

Applying the Fourier transform and the Hankel transform to equation (1) and using the kernels and eigenvalues appropriate to the boundary conditions, equation (2), as set forth in [3], the solution may be written as

$$T^* = 2 \sum_{m=1}^{\infty} \frac{1}{\beta_m^3} \frac{J_0(\beta_m R)}{J_1(\beta_m)} (1 - e^{-F_0 \beta_m^2}) + 4 \sum_{n=1}^{\infty} \sum_{m=1}^{\infty} (-1)^n \frac{\cos(n\pi Z)}{\beta_m} \frac{J_0(\beta_m R)}{J_1(\beta_m)}$$

¹ Assistant Professor, Mechanical and Aerospace Engineering Department, University of Massachusetts, Amherst, Mass.

² Numbers in brackets designate References at end of technical brief.

Contributed by the Heat Transfer Division of THE AMERICAN SOCIETY OF MECHANICAL ENGINEERS. Manuscript received by the Heat Transfer Division August 9, 1971.

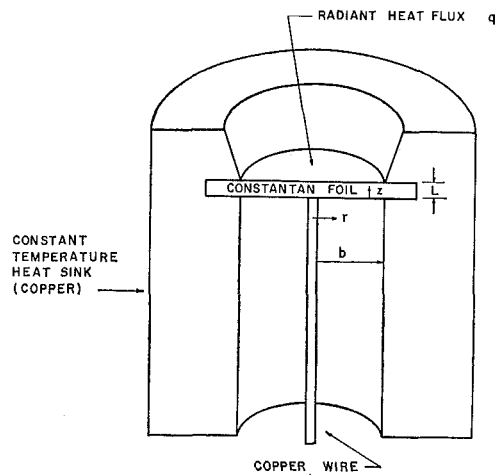


Fig. 1 Gardon heat-flux probe

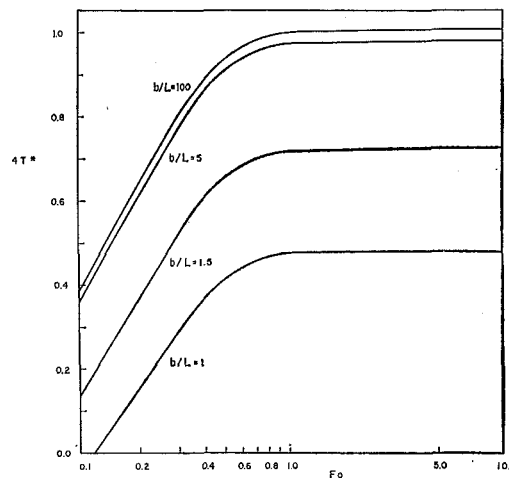


Fig. 2 Probe response characteristic $4T^*(0, 0, t)$ versus F_0 and b/L

$$\times \left[\frac{1 - e^{-F_0 (\beta_m^2 + n^2 \pi^2 \frac{b^2}{L^2})}}{(\beta_m^2 + n^2 \pi^2 \frac{b^2}{L^2})} \right] \quad (4)$$

where the following nomenclature has been used:

$$T^* = kTL/qb^2, \quad F_0 = \alpha t/b^2, \quad R = r/b, \quad Z = z/L$$

J_0 and J_1 are Bessel functions of order 0 and 1 respectively, β_m denotes the zeros of J_0 , and m and n are integers.

Equation (4) is one of the interesting cases which sometimes arise when problems are solved by the integral-transform technique. The boundary condition at $Z = L$ cannot be checked by termwise differentiation of equation (4). The difficulty is that the function represented by the Fourier series of equation (4) does not meet the conditions for the differentiability of its Fourier series [4]. In general, this function is not known a priori; if it were, the problem would already be solved. Equation (4) has been found to agree with the previously known solutions for a thin probe $b/L \rightarrow \infty$ for all time t and for a probe of finite b/L in the steady state. This agreement is taken as sufficient evidence to accept equation (4) as the solution.

Of interest in the design of a Gardon probe is the relationship between the measured temperature difference, the incident heat flux, and the probe geometry. These quantities are related in a dimensionless form and are plotted as $4T^*(0, 0, t)$ versus F_0 and b/L in Fig. 2. For all values of $b/L \geq 100$ the solution was indistinguishable with the solution of Ash [2] for $b/L \rightarrow \infty$. The

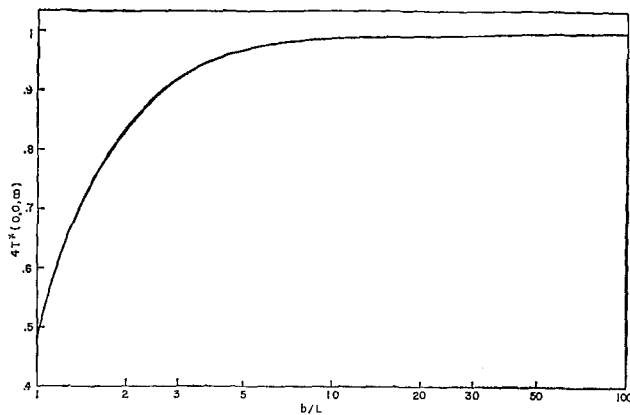


Fig. 3 Probe response characteristic $4T^*(0, 0, \infty)$ versus b/L

response time τ to steady state, $F_0 \geq 1$, can be seen in Fig. 2 to be independent of b/L and have the value $\tau = b^2/\alpha$. Thus probes of appreciable thickness can be used without any loss in response time.

The heat flux q is calculated from the dimensionless quantity $4T^*(0, 0, \infty)$ plotted in Fig. 3 as a function of b/L . For all probes with $b/L \geq 100$ the quantity $4T^*(0, 0, \infty)$ can be taken as unity. For probes thicker than $b/L = 100$ the incident heat flux q should be calculated using Fig. 3.

Conclusion

The results of this study provide more flexibility in the design of a Gardon heat-flux sensor than was heretofore available. Instead of making the probe as thin as possible and assuming that the infinitely thin solution was valid, this study has introduced the aspect ratio b/L and provided the probe response characteristics as functions of this parameter.

References

- 1 Gardon, R., "An Instrument for the Direct Measurement of Thermal Radiation," *Review of Scientific Instruments*, Vol. 24, May 1953, pp. 366-370.
- 2 Ash, R., "Response Characteristics of Thin Foil Heat Flux Sensors," *AIAA Journal*, Vol. 7, No. 12, Sept. 1969, pp. 2332-2335.
- 3 Ozisik, N., *Boundary Value Problems of Heat Conduction*, International Textbook Co., Scranton, Pa., 1968.
- 4 Rektorys, R., *Survey of Applicable Mathematics*, M.I.T. Press, Cambridge, Mass., 1969, p. 711.

Radiation and Convection Heat Transfer from an Internally Heated Slab, Cylinder, or Sphere

F. C. WESSLING, JR.¹

Nomenclature

- $b = \alpha T_0$
 $B = hL/k, hR/k$, Biot number
 $C =$ Table 1 and equation (13)
 $E = \epsilon \sigma L T_0^3/k, \epsilon \sigma R T_0^3/k$

¹ Assistant Professor, Department of Mechanical Engineering, University of New Mexico, Albuquerque, N. M. Assoc. Mem. ASME.

Contributed by the Heat Transfer Division of THE AMERICAN SOCIETY OF MECHANICAL ENGINEERS. Manuscript received by the Heat Transfer Division November 23, 1971.

- $F =$ Table 1 and equation (14)
 $H =$ internal energy generation per unit volume and time
 $h =$ surface convective heat-transfer coefficient
 $k =$ thermal conductivity of slab
 $L =$ width of the slab
 $N =$ 1 for slab, 2 for cylinder, 3 for sphere
 $Q = HL^2/kT_0, HR^2/kT_0$
 $r =$ radial coordinate
 $R =$ radius of cylinder or sphere
 $T =$ absolute temperature
 $x =$ spatial coordinate
 $z =$ defined in equation (9)
 $\alpha =$ temperature coefficient of internal energy generation
 $\epsilon =$ emissivity of the surface $\eta = 1$
 $\eta = x/L$ or r/R
 $T = T/T_0$
 $\sigma =$ Stephan-Boltzmann constant

Subscripts

- $s =$ at location of radiating or convecting surface $\eta = 1$
 $0 =$ ambient condition

TRANSIENT solutions for slabs, cylinders, and spheres with internal energy generation and convective boundary conditions are well known [1].² An approximate transient solution for the combined boundary condition of heat transfer by both convection and radiation into black isothermal surroundings has been discussed by Zyszkowski [2] using Biot's variational method. In this brief, the exact steady-state solution for the combined boundary condition is presented. Internal energy generation is assumed to be a linear function of temperature. Uniform energy generation is included as a special case.

The convective heat-transfer coefficient h and the emissivity ϵ are uniform on the surface located at $\eta = 1$. The surface $\eta = 0$ has a zero temperature derivative. The nondimensionalized steady-state equations for the problem with the radiation and convection boundary conditions and constant thermal conductivity are

$$\eta \frac{d^2 T}{d\eta^2} + (N-1) \frac{dT}{d\eta} + \eta Q[1 + bT] = 0 \quad 0 \leq \eta \leq 1 \quad (1)$$

$$\frac{dT}{d\eta} = 0 \quad \text{at } \eta = 0 \quad (2)$$

$$- \frac{dT}{d\eta} = E(T^4 - 1) + B(T - 1) \quad \text{at } \eta = 1 \quad (3)$$

Here N equals one for the slab, two for the infinitely long cylinder, and three for the sphere. The solutions of these equations are,

for the slab, $N = 1$

$$T = \frac{(1 + bT_s) \cos(\eta\sqrt{Qb})}{b \cos\sqrt{Qb}} - \frac{1}{b} \quad (4)$$

for the infinitely long cylinder, $N = 2$

$$T = \frac{(1 + bT_s) J_0(\eta\sqrt{Qb})}{b J_0(\sqrt{Qb})} - \frac{1}{b} \quad (5)$$

for the sphere, $N = 3$

$$T = \frac{(1 + bT_s) \sin(\eta\sqrt{Qb})}{b\eta \sin\sqrt{Qb}} - \frac{1}{b} \quad (6)$$

where in equations (4), (5), and (6) T_s is the solution of

² Numbers in brackets designate References at end of technical brief.

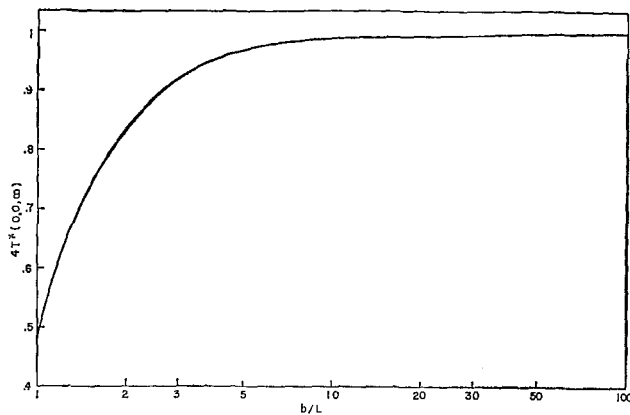


Fig. 3 Probe response characteristic $4T^*(0, 0, \infty)$ versus b/L

response time τ to steady state, $F_0 \geq 1$, can be seen in Fig. 2 to be independent of b/L and have the value $\tau = b^2/\alpha$. Thus probes of appreciable thickness can be used without any loss in response time.

The heat flux q is calculated from the dimensionless quantity $4T^*(0, 0, \infty)$ plotted in Fig. 3 as a function of b/L . For all probes with $b/L \geq 100$ the quantity $4T^*(0, 0, \infty)$ can be taken as unity. For probes thicker than $b/L = 100$ the incident heat flux q should be calculated using Fig. 3.

Conclusion

The results of this study provide more flexibility in the design of a Gardon heat-flux sensor than was heretofore available. Instead of making the probe as thin as possible and assuming that the infinitely thin solution was valid, this study has introduced the aspect ratio b/L and provided the probe response characteristics as functions of this parameter.

References

- 1 Gardon, R., "An Instrument for the Direct Measurement of Thermal Radiation," *Review of Scientific Instruments*, Vol. 24, May 1953, pp. 366-370.
- 2 Ash, R., "Response Characteristics of Thin Foil Heat Flux Sensors," *AIAA Journal*, Vol. 7, No. 12, Sept. 1969, pp. 2332-2335.
- 3 Ozisik, N., *Boundary Value Problems of Heat Conduction*, International Textbook Co., Scranton, Pa., 1968.
- 4 Rektorys, R., *Survey of Applicable Mathematics*, M.I.T. Press, Cambridge, Mass., 1969, p. 711.

Radiation and Convection Heat Transfer from an Internally Heated Slab, Cylinder, or Sphere

F. C. WESSLING, JR.¹

Nomenclature

- $b = \alpha T_0$
 $B = hL/k, hR/k$, Biot number
 $C =$ Table 1 and equation (13)
 $E = \epsilon \sigma L T_0^3/k, \epsilon \sigma R T_0^3/k$

¹ Assistant Professor, Department of Mechanical Engineering, University of New Mexico, Albuquerque, N. M. Assoc. Mem. ASME.

Contributed by the Heat Transfer Division of THE AMERICAN SOCIETY OF MECHANICAL ENGINEERS. Manuscript received by the Heat Transfer Division November 23, 1971.

- $F =$ Table 1 and equation (14)
 $H =$ internal energy generation per unit volume and time
 $h =$ surface convective heat-transfer coefficient
 $k =$ thermal conductivity of slab
 $L =$ width of the slab
 $N =$ 1 for slab, 2 for cylinder, 3 for sphere
 $Q = HL^2/kT_0, HR^2/kT_0$
 $r =$ radial coordinate
 $R =$ radius of cylinder or sphere
 $T =$ absolute temperature
 $x =$ spatial coordinate
 $z =$ defined in equation (9)
 $\alpha =$ temperature coefficient of internal energy generation
 $\epsilon =$ emissivity of the surface $\eta = 1$
 $\eta = x/L$ or r/R
 $T = T/T_0$
 $\sigma =$ Stephan-Boltzmann constant

Subscripts

- $s =$ at location of radiating or convecting surface $\eta = 1$
 $0 =$ ambient condition

TRANSIENT solutions for slabs, cylinders, and spheres with internal energy generation and convective boundary conditions are well known [1].² An approximate transient solution for the combined boundary condition of heat transfer by both convection and radiation into black isothermal surroundings has been discussed by Zyszkowski [2] using Biot's variational method. In this brief, the exact steady-state solution for the combined boundary condition is presented. Internal energy generation is assumed to be a linear function of temperature. Uniform energy generation is included as a special case.

The convective heat-transfer coefficient h and the emissivity ϵ are uniform on the surface located at $\eta = 1$. The surface $\eta = 0$ has a zero temperature derivative. The nondimensionalized steady-state equations for the problem with the radiation and convection boundary conditions and constant thermal conductivity are

$$\eta \frac{d^2 T}{d\eta^2} + (N-1) \frac{dT}{d\eta} + \eta Q[1 + bT] = 0 \quad 0 \leq \eta \leq 1 \quad (1)$$

$$\frac{dT}{d\eta} = 0 \quad \text{at } \eta = 0 \quad (2)$$

$$- \frac{dT}{d\eta} = E(T^4 - 1) + B(T - 1) \quad \text{at } \eta = 1 \quad (3)$$

Here N equals one for the slab, two for the infinitely long cylinder, and three for the sphere. The solutions of these equations are,

for the slab, $N = 1$

$$T = \frac{(1 + bT_s) \cos(\eta\sqrt{Qb})}{b \cos\sqrt{Qb}} - \frac{1}{b} \quad (4)$$

for the infinitely long cylinder, $N = 2$

$$T = \frac{(1 + bT_s) J_0(\eta\sqrt{Qb})}{b J_0(\sqrt{Qb})} - \frac{1}{b} \quad (5)$$

for the sphere, $N = 3$

$$T = \frac{(1 + bT_s) \sin(\eta\sqrt{Qb})}{b\eta \sin\sqrt{Qb}} - \frac{1}{b} \quad (6)$$

where in equations (4), (5), and (6) T_s is the solution of

² Numbers in brackets designate References at end of technical brief.

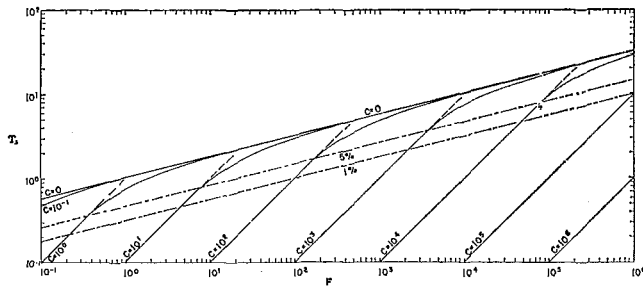


Fig. 1

Table 1 Expressions for C and F of equation (7)

N	C	F
1	$\frac{B}{E} - \frac{\sqrt{Qb} \tan \sqrt{Qb}}{E}$	$1 + \frac{B}{E} + \frac{\sqrt{Qb}}{bE} \tan(\sqrt{Qb})$
2	$\frac{B}{E} - \frac{\sqrt{Qb} J_1(\sqrt{Qb})}{E J_0(\sqrt{Qb})}$	$1 + \frac{B}{E} + \frac{\sqrt{Qb} J_1(\sqrt{Qb})}{bE J_0(\sqrt{Qb})}$
3	$\frac{B}{E} + \frac{\sqrt{Qb} \cot(\sqrt{Qb}) - 1}{E}$	$1 + \frac{B}{E} - \frac{(\sqrt{Qb} \cot(\sqrt{Qb}) - 1)}{bE}$

$$\Upsilon_s^4 + C\Upsilon_s = F \quad (7)$$

The quantities C and F are given in Table 1 for each of the three geometries. The solutions for Υ_s as a function of C and F are given in Fig. 1 and can be calculated from Cardano's formulae [3], which are as follows:

$$\Upsilon_s = -(z/2)^{1/2} + [(F + z^2)^{1/2} - z/2]^{1/2} \quad (8)$$

where z is given by

$$z = \left[\frac{C^2}{16} - \left[\left(\frac{C^2}{16} \right)^2 + \frac{F^3}{27} \right]^{1/2} \right]^{1/3} + \left[\frac{C^2}{16} + \left[\left(\frac{C^2}{16} \right)^2 + \frac{F^3}{27} \right]^{1/2} \right]^{1/3} \quad (9)$$

The line $C = 0$ is the limiting value for pure radiation with no convection and is given by

$$\Upsilon_s = (F)^{1/4} \quad (10)$$

The dashed extensions of the family of C curves are the solutions for pure convection with no radiation and are given by

$$\Upsilon_s = F/C \quad (11)$$

The broken lines labeled 1% and 5% delimit the region below which the error in Υ_s is less than 1% and 5%, respectively, when Υ_s is calculated by equation (11) rather than by equations (8) and (9).

For the case of $b = 0$, that is, for uniform internal heat generation, the solution simplifies for all three values of N to

$$\Upsilon = \Upsilon_s + \frac{Q}{2N} [1 - \eta^2] \quad (12)$$

$$C = \frac{B}{E} \quad (13)$$

$$F = 1 + \frac{B}{E} + \frac{Q/N}{E} \quad (14)$$

The solutions presented in equations (12), (13), and (14) agree with the asymptotic solutions for time approaching infinity as given by Zyszkowski.

References

- 1 Carslaw, H. S., and Jaeger, J. C., *Conductions of Heat in Solids*, 2nd ed., Oxford at the Clarendon Press, 1959, pp. 130, 205, 246.
- 2 Zyszkowski, W., "The Transient Temperature Distribution in One-Dimensional Heat-Conduction Problems With Nonlinear Boundary Conditions," *JOURNAL OF HEAT TRANSFER*, TRANS. ASME, Series C, Vol. 91, No. 1, Feb. 1969, pp. 77-82.
- 3 Richardson, M., *College Algebra*, Prentice-Hall, Englewood Cliffs, N. J., 1947, p. 261.

Interfacial Shear Stress in Annular-Mist Condensing Flow

M. R. BERRY, JR.¹ and W. P. GOSS²

ONE COMMON flow pattern in two-phase systems is the confined concurrent flow of a vapor and a liquid in a circular duct where a portion of the liquid flows in a low-velocity annular film in contact with the duct wall while the remainder of the liquid flows as entrained particles in a relatively high-velocity gaseous core. For single-component fluids which wet the duct wall, cooling at the duct wall will cause the vapor to condense, and the thickness of the wavy annular liquid film will increase. In systems of this type, the predictions of pressure drop and heat-transfer coefficients are of primary concern and depend on both the wall and interfacial shear stresses. Analytical predictions of these shear stresses are complicated, since the interaction of the slow-moving liquid film and the high-speed vapor core results in interfacial wave characteristics which are not well understood. Qualitatively what occurs is the development of a turbulent liquid layer which has random waves traveling along the vapor-liquid interface. At sufficiently high vapor velocities, the vapor core will be turbulent also. The interaction between the vapor core and liquid layer, in addition to creating the interfacial waves, will shear off the top of the waves, thus causing some of the liquid to flow in the core as entrained liquid particles. A recent paper by Pogson et al. [1]³ describes this entrainment situation in some detail.

The prediction of the interfacial shear stress is therefore quite dependent on the entrainment momentum transfer. It is also quite dependent upon the particular model used to define the liquid-vapor interface. Inasmuch as these problems are still not well modeled, empirical means must be resorted to. An empirical correlation for the interfacial shear stress in the two-phase annular-mist flow of condensing steam is presented in this note. The correlation is intended for use with flow models which assume a time-averaged annular liquid film with a smooth liquid-vapor interface.

¹ Food Process Evaluation Branch, Food and Drug Administration, Cincinnati, Ohio; formerly, Mechanical Engineering Department, Virginia Polytechnic Institute and State University, Blacksburg, Va. Assoc. Mem. ASME.

² Assistant Professor, Mechanical and Aerospace Engineering Department, University of Massachusetts, Amherst, Mass.; formerly, Mechanical Engineering Department, Virginia Polytechnic Institute and State University, Blacksburg, Va. Mem. ASME.

³ Numbers in brackets designate References at end of technical brief. Contributed by the Heat Transfer Division of THE AMERICAN SOCIETY OF MECHANICAL ENGINEERS. Manuscript received by the Heat Transfer Division May 21, 1971.

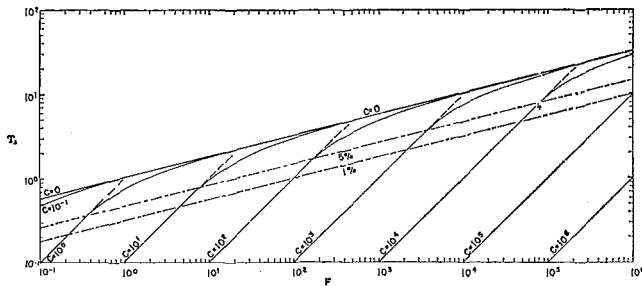


Fig. 1

Table 1 Expressions for C and F of equation (7)

N	C	F
1	$\frac{B}{E} - \frac{\sqrt{Qb} \tan \sqrt{Qb}}{E}$	$1 + \frac{B}{E} + \frac{\sqrt{Qb}}{bE} \tan(\sqrt{Qb})$
2	$\frac{B}{E} - \frac{\sqrt{Qb} J_1(\sqrt{Qb})}{E J_0(\sqrt{Qb})}$	$1 + \frac{B}{E} + \frac{\sqrt{Qb} J_1(\sqrt{Qb})}{bE J_0(\sqrt{Qb})}$
3	$\frac{B}{E} + \frac{\sqrt{Qb} \cot(\sqrt{Qb}) - 1}{E}$	$1 + \frac{B}{E} - \frac{(\sqrt{Qb} \cot(\sqrt{Qb}) - 1)}{bE}$

$$\Upsilon_s^4 + C\Upsilon_s = F \quad (7)$$

The quantities C and F are given in Table 1 for each of the three geometries. The solutions for Υ_s as a function of C and F are given in Fig. 1 and can be calculated from Cardano's formulae [3], which are as follows:

$$\Upsilon_s = -(z/2)^{1/2} + [(F + z^2)^{1/2} - z/2]^{1/2} \quad (8)$$

where z is given by

$$z = \left[\frac{C^2}{16} - \left[\left(\frac{C^2}{16} \right)^2 + \frac{F^3}{27} \right]^{1/2} \right]^{1/3} + \left[\frac{C^2}{16} + \left[\left(\frac{C^2}{16} \right)^2 + \frac{F^3}{27} \right]^{1/2} \right]^{1/3} \quad (9)$$

The line $C = 0$ is the limiting value for pure radiation with no convection and is given by

$$\Upsilon_s = (F)^{1/4} \quad (10)$$

The dashed extensions of the family of C curves are the solutions for pure convection with no radiation and are given by

$$\Upsilon_s = F/C \quad (11)$$

The broken lines labeled 1% and 5% delimit the region below which the error in Υ_s is less than 1% and 5%, respectively, when Υ_s is calculated by equation (11) rather than by equations (8) and (9).

For the case of $b = 0$, that is, for uniform internal heat generation, the solution simplifies for all three values of N to

$$\Upsilon = \Upsilon_s + \frac{Q}{2N} [1 - \eta^2] \quad (12)$$

$$C = \frac{B}{E} \quad (13)$$

$$F = 1 + \frac{B}{E} + \frac{Q/N}{E} \quad (14)$$

The solutions presented in equations (12), (13), and (14) agree with the asymptotic solutions for time approaching infinity as given by Zyszkowski.

References

- 1 Carslaw, H. S., and Jaeger, J. C., *Conductions of Heat in Solids*, 2nd ed., Oxford at the Clarendon Press, 1959, pp. 130, 205, 246.
- 2 Zyszkowski, W., "The Transient Temperature Distribution in One-Dimensional Heat-Conduction Problems With Nonlinear Boundary Conditions," *JOURNAL OF HEAT TRANSFER*, TRANS. ASME, Series C, Vol. 91, No. 1, Feb. 1969, pp. 77-82.
- 3 Richardson, M., *College Algebra*, Prentice-Hall, Englewood Cliffs, N. J., 1947, p. 261.

Interfacial Shear Stress in Annular-Mist Condensing Flow

M. R. BERRY, JR.¹ and W. P. GOSS²

ONE COMMON flow pattern in two-phase systems is the confined concurrent flow of a vapor and a liquid in a circular duct where a portion of the liquid flows in a low-velocity annular film in contact with the duct wall while the remainder of the liquid flows as entrained particles in a relatively high-velocity gaseous core. For single-component fluids which wet the duct wall, cooling at the duct wall will cause the vapor to condense, and the thickness of the wavy annular liquid film will increase. In systems of this type, the predictions of pressure drop and heat-transfer coefficients are of primary concern and depend on both the wall and interfacial shear stresses. Analytical predictions of these shear stresses are complicated, since the interaction of the slow-moving liquid film and the high-speed vapor core results in interfacial wave characteristics which are not well understood. Qualitatively what occurs is the development of a turbulent liquid layer which has random waves traveling along the vapor-liquid interface. At sufficiently high vapor velocities, the vapor core will be turbulent also. The interaction between the vapor core and liquid layer, in addition to creating the interfacial waves, will shear off the top of the waves, thus causing some of the liquid to flow in the core as entrained liquid particles. A recent paper by Pogson et al. [1]³ describes this entrainment situation in some detail.

The prediction of the interfacial shear stress is therefore quite dependent on the entrainment momentum transfer. It is also quite dependent upon the particular model used to define the liquid-vapor interface. Inasmuch as these problems are still not well modeled, empirical means must be resorted to. An empirical correlation for the interfacial shear stress in the two-phase annular-mist flow of condensing steam is presented in this note. The correlation is intended for use with flow models which assume a time-averaged annular liquid film with a smooth liquid-vapor interface.

¹ Food Process Evaluation Branch, Food and Drug Administration, Cincinnati, Ohio; formerly, Mechanical Engineering Department, Virginia Polytechnic Institute and State University, Blacksburg, Va. Assoc. Mem. ASME.

² Assistant Professor, Mechanical and Aerospace Engineering Department, University of Massachusetts, Amherst, Mass.; formerly, Mechanical Engineering Department, Virginia Polytechnic Institute and State University, Blacksburg, Va. Mem. ASME.

³ Numbers in brackets designate References at end of technical brief. Contributed by the Heat Transfer Division of THE AMERICAN SOCIETY OF MECHANICAL ENGINEERS. Manuscript received by the Heat Transfer Division May 21, 1971.

There is very little information, either experimental or analytical, available on the shear stress at the liquid-vapor interface of a turbulent two-phase system. A number of investigators have assumed that the slow-moving, wavy-annular liquid layer may be treated, insofar as the vapor is concerned, as a rough cylindrical solid boundary. The interfacial shear stress is then correlated with the vapor kinetic energy and a roughness parameter associated with the wave dimensions. This method has the obvious drawback that the literature is also lacking in the area of interfacial wave characteristics in two-phase annular systems. Also, an analysis for shear stress which may be valid for turbulent flow in the vicinity of a solid boundary should not be expected to hold for turbulent flow in the vicinity of a vapor-liquid interface. This is because the liquid, although essentially incompressible, is a fluid which can transmit shear through turbulent fluctuations, while a solid cannot, due to the no-slip condition at the gas-solid interface.

Levy [2] has developed a widely accepted correlation for interfacial shear stress based on experimental data taken for the adiabatic flow of water or alcohol and argon or nitrogen flowing annularly. Goss [3] compared the experimental data for condensing-steam flows taken by Hilding [4] to Levy's correlation. Levy's correlation predicted higher interfacial shear stresses in general; however, the same trend was present. In their note, Linehan et al. [5] discuss the models for evaluating the interfacial shear stress during annular-film condensation. They demonstrate the necessity for including the effect of mass transfer on the interfacial shear and conclude that a model including this effect must be used to accurately predict pressure drop, and therefore heat-transfer coefficients.

The correlation presented in this note is based on values of interfacial shear stress reported by Hilding [4] which were derived from experimental data for high-velocity condensing steam (entrance velocities in excess of 600 fps) flowing in a horizontal coaxial-tube condenser. To the authors' knowledge, these are the only values of interfacial shear stress presented in the literature for single-component, two-phase annular-mist condensing flow. It was found that when the quantity $(1 + \tau_I \theta / \tau_w)$ was plotted versus the dynamic quality (θ) , the ratio of vapor flow rate to total flow rate) as shown in Fig. 1, a useful correlation resulted.

The following expressions correlate the data very well for dynamic qualities between 10 and 95 percent:

for $1.0 > \theta > 0.745$

$$1 + \tau_I \theta / \tau_w = 2.0 \theta^{0.589} \quad (1)$$

for $0.745 \geq \theta > 0.1$

$$1 + \tau_I \theta / \tau_w = 1.735 \theta^{0.111}$$

The above expressions are solved for the interfacial shear stress τ_I as a function of the wall shear stress τ_w and dynamic quality as:

for $1.0 > \theta > 0.745$

$$\tau_I = \frac{\tau_w}{\theta} (2.0 \theta^{0.589} - 1) \quad (2)$$

for $0.745 \geq \theta > 0.1$

$$\tau_I = \frac{\tau_w}{\theta} (1.735 \theta^{0.111} - 1)$$

It is seen from the above expressions that for low dynamic qualities (thick annular films) the interfacial shear stress may be several times larger than the corresponding wall shear stress. Also, it is noted that as the dynamic quality approaches 100 percent (no liquid present), the interfacial shear stress assumes the correct value equal to the wall shear stress. It should not be surprising that the dynamic quality is useful in correlating the interfacial shear stress. Goodykoontz and Brown [6] found that local heat-transfer coefficients for high-vapor-velocity condensing steam and Freon-113 correlated reasonably well with the vapor flow rate. The interfacial shear, which is related to interfacial

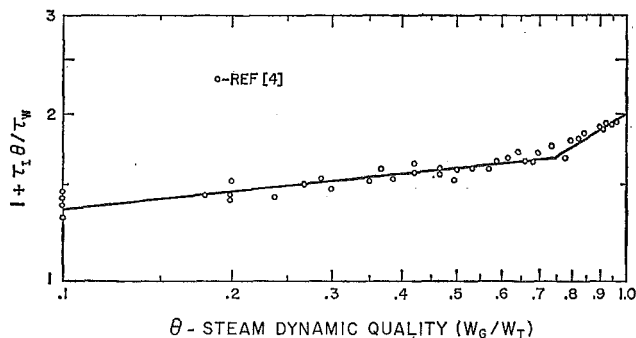


Fig. 1 Interfacial-shear-stress correlation

momentum transfer, and the liquid-film heat-transfer coefficient, which is related to the interfacial energy transfer, should exhibit similar characteristics.

The local interfacial shear stress (i.e., at any quality) predicted by the correlation presented in this note is a function of local wall shear stress. Before a numerical value of the interfacial shear stress can be obtained, the wall shear stress must be determined. Wall shear stresses for use in predicting two-phase annular-mist flows have been determined in several ways by various investigators. These range from semiempirical correlations to superficial friction factors similar to the well-known Blasius friction factor for single-phase flow. Unfortunately, very few correlations exist which were developed for high-speed condensing flows. The wall-shear-stress correlation of Kammula [7] was found to work well with the interfacial-shear-stress correlation presented here. In Kammula's correlation the equations normally used to predict the velocity distributions and eddy viscosities in single-phase flow are adapted to fit condensing annular-mist flows with high interfacial drag by including a term which accounts for the interfacial shear stress and mass transfer. An input to this correlation is the ratio of interfacial to wall shear stress (τ_I / τ_w) which is obtained from equation (1). Once the wall shear stress is obtained iteratively from Kammula's correlation, the interfacial shear stress is determined from equation (2). Berry [8] used the above technique in an integral analysis of two-phase annular-mist condensing flows to compare with several sets [4, 9, 10] of experimental data. The pressure drop predicted by the analytical model is quite sensitive to the value of the interfacial shear. However, use of the interfacial-shear correlation presented in this note resulted in the accurate prediction of the condenser length necessary for complete condensation and, with a reasonable degree of accuracy, the dynamic quality, heat-transfer characteristics, and axial static-pressure distribution.

In conclusion, an empirical interfacial-shear-stress correlation for high-vapor-velocity, two-phase annular-mist condensing flows is presented. The correlation has been used successfully in analyzing high-performance tube condensers. Further refinement is necessary to extend the range of applicability to fluids other than water by including surface-tension and viscosity-variation effects.

References

- 1 Pogson, J. T., Roberts, J. H., and Waibler, P. J., "An Investigation of the Liquid Distribution in Annular-Mist Flow," *JOURNAL OF HEAT TRANSFER*, TRANS. ASME, Series C, Vol. 92, No. 4, Nov. 1970, pp. 651-658.
- 2 Levy, S., "Prediction of Two-Phase Annular Flow with Liquid Entrainment," *International Journal of Heat and Mass Transfer*, Vol. 9, 1966, pp. 171-188.
- 3 Goss, W. P., "Two-Phase, Annular-Mist Flow," PhD thesis, University of Connecticut, Storrs, Conn., 1967.
- 4 Hilding, W. E., and staff, "An Analytical and Experimental Investigation of the Two-Phase Flow of a High Velocity Vapor Condensing in a Tube—Part II," Report to NASA from the University of Connecticut, Storrs, Conn., Aug. 1967.
- 5 Linehan, J. H., Petrick, M., and El-Wakil, M. M., "On the Interface Shear Stress in Annular Flow Condensation," *JOURNAL OF*

6 Goodykoontz, J. H., and Brown, W. F., "Local Heat-Transfer and Pressure Distributions for Freon-113 Condensing in Downward Flow in a Vertical Tube," NASA TN D-3952, 1967.

7 Kammula, K., "An Integral Technique for Predicting Wall and Interfacial Shear Stresses in Turbulent, Condensing, Annular-Mist Flow," MS thesis, Virginia Polytechnic Institute, Blacksburg, Va., 1970.

8 Berry, M. R., Jr., "An Integral Analysis of Two-Phase Annular-Mist Condensing Flows," PhD thesis, Virginia Polytechnic Institute, Blacksburg, Va., 1970.

9 Taliaferro, B., "A Study of Interfacial Waves and Heat Transfer for Turbulent Condensation in a Vertical Tube," MS thesis, Virginia Polytechnic Institute, Blacksburg, Va., 1970.

10 Goodykoontz, J. H., and Dorsch, R. G., "Local Heat-Transfer Coefficients and Static Pressures for Condensation of High-Velocity Steam Within a Tube," NASA TN D-3953, 1967.

The Vapor Shear Boundary Condition for Laminar Film Condensation¹

V. SOUTH III² and V. E. DENNY³

Nomenclature

- C_{f_x} = local shear-stress coefficient = $\tau_w/0.5\rho u_e^2$
 Re_x = Reynolds number = $u_e x/\nu$
 u, v = x, y velocity components, respectively
 x, y = streamwise and normal coordinates, respectively
 ν = kinematic viscosity
 ρ = density
 τ = shear stress

Subscripts

- \dot{a} = asymptotic value
 d = dry-wall value
 e = at outer edge of vapor boundary layer
 i = at liquid-vapor interface

ONE OF the more difficult problems in the analysis of film condensation is the specification of the appropriate boundary condition at the liquid-vapor interface. Here, the vapor flow is characterized by a relatively high velocity toward the interface and a velocity gradient due to vapor drag on the liquid film. The magnitude of the velocity gradient depends upon the degree of forced vapor flow and the interfacial velocity of the liquid film in both the normal direction and in the direction of flow. In the liquid-film analysis, where the Nusselt assumptions are commonly invoked, it is only necessary to obtain the interfacial shear (velocity gradient) from the vapor-side problem to obtain a solution to the liquid-side problem and hence the condensation and heat-transfer rates [1].⁴ The purpose of this note, then, is to present a simple

¹ This work was supported by the Department of the Interior, OSW grant No. 14-30-2673. Computer time for the numerical calculations was provided in part by the Campus Computing Network of the University of California, Los Angeles, Calif.

² Postgraduate Research Engineer, School of Engineering and Applied Science, University of California, Los Angeles, Calif.

³ Assistant Professor, School of Engineering and Applied Science, University of California, Los Angeles, Calif.

⁴ Numbers in brackets designate References at end of technical brief.

Contributed by the Heat Transfer Division of THE AMERICAN SOCIETY OF MECHANICAL ENGINEERS. Manuscript received by the Heat Transfer Division September 3, 1971.

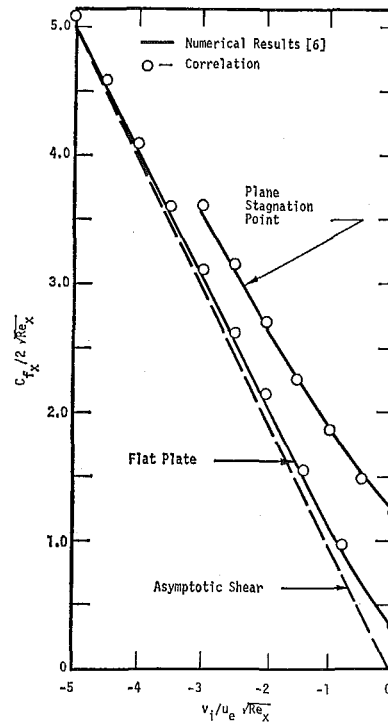


Fig. 1 Comparison of dimensionless shear correlation with numerical results of Hartnett and Eckert [6]

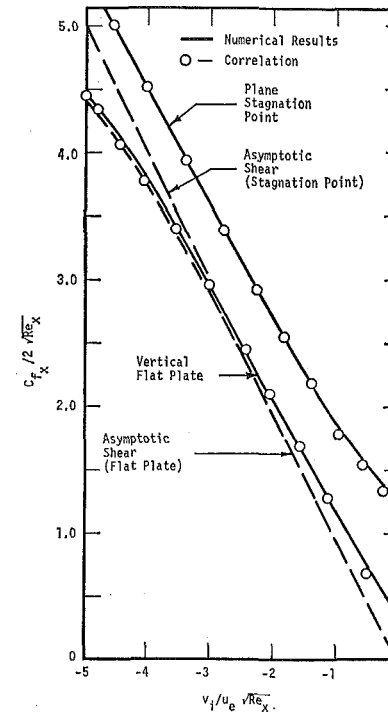


Fig. 2 Comparison of dimensionless shear correlation with numerical results for laminar film condensation down a vertical flat plate and a horizontal cylinder

expression for predicting the interfacial shear.

The expression for asymptotic shear, which applies in the limit of strong suction (regardless of pressure gradient), has been used with some success in predicting condensation heat transfer [1, 2]. This is the well-known relationship

$$\tau_a = \rho v_i(u_e - u_i)$$

For a flat plate, it has been determined [3] that this expression is

6 Goodykoontz, J. H., and Brown, W. F., "Local Heat-Transfer and Pressure Distributions for Freon-113 Condensing in Downward Flow in a Vertical Tube," NASA TN D-3952, 1967.

7 Kammula, K., "An Integral Technique for Predicting Wall and Interfacial Shear Stresses in Turbulent, Condensing, Annular-Mist Flow," MS thesis, Virginia Polytechnic Institute, Blacksburg, Va., 1970.

8 Berry, M. R., Jr., "An Integral Analysis of Two-Phase Annular-Mist Condensing Flows," PhD thesis, Virginia Polytechnic Institute, Blacksburg, Va., 1970.

9 Taliaferro, B., "A Study of Interfacial Waves and Heat Transfer for Turbulent Condensation in a Vertical Tube," MS thesis, Virginia Polytechnic Institute, Blacksburg, Va., 1970.

10 Goodykoontz, J. H., and Dorsch, R. G., "Local Heat-Transfer Coefficients and Static Pressures for Condensation of High-Velocity Steam Within a Tube," NASA TN D-3953, 1967.

The Vapor Shear Boundary Condition for Laminar Film Condensation¹

V. SOUTH III² and V. E. DENNY³

Nomenclature

- C_{f_x} = local shear-stress coefficient = $\tau_w/0.5\rho u_e^2$
 Re_x = Reynolds number = $u_e x/\nu$
 u, v = x, y velocity components, respectively
 x, y = streamwise and normal coordinates, respectively
 ν = kinematic viscosity
 ρ = density
 τ = shear stress

Subscripts

- \dot{a} = asymptotic value
 d = dry-wall value
 e = at outer edge of vapor boundary layer
 i = at liquid-vapor interface

ONE OF the more difficult problems in the analysis of film condensation is the specification of the appropriate boundary condition at the liquid-vapor interface. Here, the vapor flow is characterized by a relatively high velocity toward the interface and a velocity gradient due to vapor drag on the liquid film. The magnitude of the velocity gradient depends upon the degree of forced vapor flow and the interfacial velocity of the liquid film in both the normal direction and in the direction of flow. In the liquid-film analysis, where the Nusselt assumptions are commonly invoked, it is only necessary to obtain the interfacial shear (velocity gradient) from the vapor-side problem to obtain a solution to the liquid-side problem and hence the condensation and heat-transfer rates [1].⁴ The purpose of this note, then, is to present a simple

¹ This work was supported by the Department of the Interior, OSW grant No. 14-30-2673. Computer time for the numerical calculations was provided in part by the Campus Computing Network of the University of California, Los Angeles, Calif.

² Postgraduate Research Engineer, School of Engineering and Applied Science, University of California, Los Angeles, Calif.

³ Assistant Professor, School of Engineering and Applied Science, University of California, Los Angeles, Calif.

⁴ Numbers in brackets designate References at end of technical brief.

Contributed by the Heat Transfer Division of THE AMERICAN SOCIETY OF MECHANICAL ENGINEERS. Manuscript received by the Heat Transfer Division September 3, 1971.

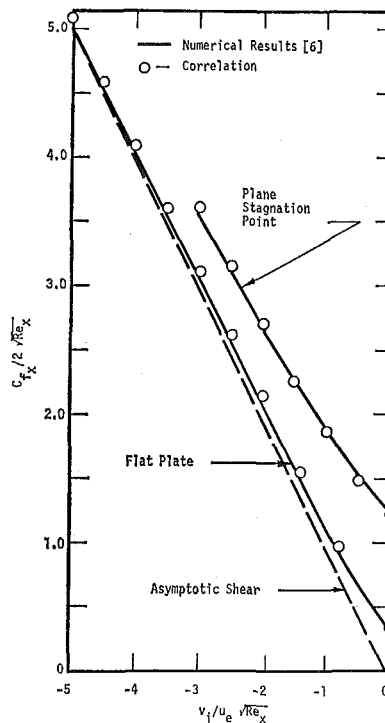


Fig. 1 Comparison of dimensionless shear correlation with numerical results of Hartnett and Eckert [6]

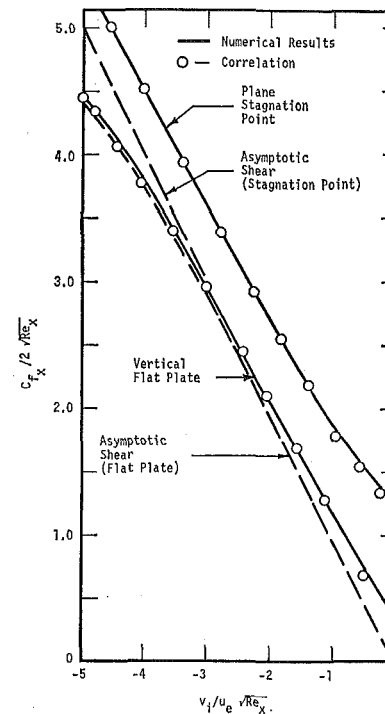


Fig. 2 Comparison of dimensionless shear correlation with numerical results for laminar film condensation down a vertical flat plate and a horizontal cylinder

expression for predicting the interfacial shear.

The expression for asymptotic shear, which applies in the limit of strong suction (regardless of pressure gradient), has been used with some success in predicting condensation heat transfer [1, 2]. This is the well-known relationship

$$\tau_a = \rho v_i(u_e - u_i)$$

For a flat plate, it has been determined [3] that this expression is

accurate for values of the suction parameter, $(v_i/u_e)(Re_x^{1/2})$, less than -2.0 . This is verified in both Figs. 1 and 2. However, for plane stagnation-point flow, Figs. 1 and 2 show a considerable discrepancy between actual and asymptotic shear for values of the suction parameter well below -2.0 . And, of course, as the suction parameter approaches zero (small condensation rates), the asymptotic expression gives way to the dry-wall value of the shear for the particular geometry involved. This suggests that a simple interpolation formula between the two extremes could be used for the entire range. A formula of the form [4]

$$\tau = [\tau_a^n + \tau_d^n]^{1/n}$$

was selected, following Acrivos, who suggested a similar relationship for correlating mass-transfer conductances. A value of $n = 1.375$ was found to give good agreement with the numerical results for both the flat-plate and stagnation-point flow over the entire range of suction parameter.

The numerical results of Fig. 2 were obtained by solving the full conservation equations in boundary-layer form for laminar film condensation: the flat-plate results were for pure steam condensing on a vertical flat plate using a full finite-difference analogue in the vapor phase (as in, e.g., [7]) and the stagnation-point results for both steam-air and steam-methanol mixtures flowing vertically down upon a horizontal cylinder where the vapor-phase solution was determined using a similarity transfor-

mation [5]. In view of the good agreement, it is suggested that equation (1) be used for all surface geometries.

References

- 1 Denny, V. E., and Mills, A. F., "Nonsimilar Solutions for Laminar Film Condensation on a Vertical Surface," *International Journal of Heat and Mass Transfer*, Vol. 12, 1969, pp. 965-979.
- 2 Denny, V. E., and Mills, A. F., "Laminar Film Condensation of a Flowing Vapor on a Horizontal Cylinder at Normal Gravity," *JOURNAL OF HEAT TRANSFER*, TRANS. ASME, Series C, Vol. 91, No. 4, Nov. 1969, pp. 495-501.
- 3 Iglisch, R., "Exact Calculation of Laminar Boundary Layer in Longitudinal Flow over a Flat Plate with Homogeneous Suction," NACA TN 1205, Apr. 1949.
- 4 Acrivos, A., "Mass Transfer in Laminar-Boundary-Layer Flows with Finite Interfacial Velocities," *AIChE Journal*, Vol. 6, 1960, pp. 410-414.
- 5 Denny, V. E., and South, V., "Effects of Forced Flow, Noncondensables, and Variable Properties on Film Condensation of Pure and Binary Vapors near the Forward Stagnation Point of a Horizontal Cylinder," accepted for publication in the *International Journal of Heat and Mass Transfer*.
- 6 Hartnett, J. P., and Eckert, E. R. G., "Mass-Transfer Cooling in a Laminar Boundary Layer With Constant Fluid Properties," *TRANS. ASME*, Vol. 79, 1957, pp. 247-254.
- 7 Denny, V. E., Mills, A. F., and Jusonis, V. J., "Laminar Film Condensation From a Steam-Air Mixture Undergoing Forced Flow Down a Vertical Surface," *JOURNAL OF HEAT TRANSFER*, TRANS. ASME, Series C, Vol. 93, No. 3, Aug. 1971, pp. 297-304.

Thermal Conductivity of Two-Phase Systems

PRADEEP B. DESHPANDE¹ and JAMES R. COUPER²

Nomenclature

- f = volume fraction of solid phase, dimensionless
 K_c = thermal conductivity of liquid phase, Btu/hr-ft-deg F
 K_d = thermal conductivity of solid phase, Btu/hr-ft-deg F
 K_e = effective thermal conductivity of two-phase system, Btu/hr-ft-deg F
 P_1 = one-dimensional porosity, dimensionless
 P_2 = two-dimensional porosity, dimensionless
 r, t = parameters of beta distribution
 \bar{r}, \bar{t} = maximum likelihood estimates of r and t
 x = random variable defined as the one-dimensional porosity, P_1
 Pr = probability

Introduction

A REVIEW of the past work on conductance of heterogeneous systems reveals that there exist a relatively large number of approximate relationships for prediction of the effective thermal conductivity of two-phase systems. Most of these relationships utilize two parameters, e.g., thermal conductivity of the pure phases and the volume fraction of each phase, in describing the thermal conductivity of two-phase systems. Recently some investigators [1, 2]³ have attempted to relate the thermal conductivity of two-phase systems to additional parameters which describe the spatial distribution of the two phases. The object of this brief is to present a model, which accounts for the spatial distribution of solid particles, for prediction of the effective thermal conductivity of solid-liquid two-phase systems.

¹ Assistant Professor of Chemical Engineering, Howard University, Washington, D. C.

² Professor and Head, Chemical Engineering Department, University of Arkansas, Fayetteville, Ark.

³ Numbers in brackets designate References at end of technical brief.

Contributed by the Heat Transfer Division of THE AMERICAN SOCIETY OF MECHANICAL ENGINEERS. Manuscript received by the Heat Transfer Division April 5, 1971.

Theoretical Development

In a theoretical paper Tsao [1] presented a model for prediction of the two-phase thermal conductivity. He considered a cubical liquid-solid system of unit dimensions and proposed the following equation for prediction of the effective thermal conductivity:

$$K_e = \frac{1}{\int_0^1 \frac{dP_1}{K_c + (K_d - K_c)P_2}} \quad (1)$$

where P_1 is one-dimensional porosity defined as the fraction of the linear space occupied by solids and P_2 is two-dimensional porosity defined as the fraction of the area occupied by solids.

To solve equation (1), a relation between P_1 and P_2 is required. Based on a stochastic model, Tsao proposed the following equation for relating P_1 and P_2 :

$$P_2 = \frac{1}{\sqrt{2\pi}\sigma} \int_{P_1}^1 \exp\left\{-\frac{1}{2} \left[\frac{(P_1 - \mu)}{\sigma}\right]^2\right\} dP_1 \quad (2)$$

where μ and σ are the mean and the standard deviations of P_1 respectively.

Tsao suggested the normal distribution, equation (2), as an approximation to the point binomial distribution. Since this expression involves a density function which does not integrate to 1 over its sample space ($0 \leq P_1 \leq 1$), Baxley [3] suggested the beta distribution, which is the limiting case of the point binomial distribution, for relating P_1 and P_2 .

$$P_2 = \frac{\Gamma(r+t)}{\Gamma(r)\Gamma(t)} \int_{P_1}^1 x^{r-1}(1-x)^{t-1} dx \quad (3)$$

where r and t are the parameters of the beta distribution.

Before the beta distribution can be used for prediction of the effective thermal conductivity, the parameters r and t must be estimated. Leek et al. [4] conducted a study to determine the spatial distribution of particles in a solid-liquid two-phase system. The solid phase consisted of uranium-impregnated Pyrex glass cylinders. A mixture composed of 85 percent glycerol and 15 percent benzyl alcohol was used as the liquid phase. A special spectrophotometer was used for measuring P_1 . One-dimensional porosity data on two different-sized glass

accurate for values of the suction parameter, $(v_i/u_e)(Re_x^{1/2})$, less than -2.0 . This is verified in both Figs. 1 and 2. However, for plane stagnation-point flow, Figs. 1 and 2 show a considerable discrepancy between actual and asymptotic shear for values of the suction parameter well below -2.0 . And, of course, as the suction parameter approaches zero (small condensation rates), the asymptotic expression gives way to the dry-wall value of the shear for the particular geometry involved. This suggests that a simple interpolation formula between the two extremes could be used for the entire range. A formula of the form [4]

$$\tau = [\tau_a^n + \tau_d^n]^{1/n}$$

was selected, following Acrivos, who suggested a similar relationship for correlating mass-transfer conductances. A value of $n = 1.375$ was found to give good agreement with the numerical results for both the flat-plate and stagnation-point flow over the entire range of suction parameter.

The numerical results of Fig. 2 were obtained by solving the full conservation equations in boundary-layer form for laminar film condensation: the flat-plate results were for pure steam condensing on a vertical flat plate using a full finite-difference analogue in the vapor phase (as in, e.g., [7]) and the stagnation-point results for both steam-air and steam-methanol mixtures flowing vertically down upon a horizontal cylinder where the vapor-phase solution was determined using a similarity transfor-

mation [5]. In view of the good agreement, it is suggested that equation (1) be used for all surface geometries.

References

- 1 Denny, V. E., and Mills, A. F., "Nonsimilar Solutions for Laminar Film Condensation on a Vertical Surface," *International Journal of Heat and Mass Transfer*, Vol. 12, 1969, pp. 965-979.
- 2 Denny, V. E., and Mills, A. F., "Laminar Film Condensation of a Flowing Vapor on a Horizontal Cylinder at Normal Gravity," *JOURNAL OF HEAT TRANSFER*, TRANS. ASME, Series C, Vol. 91, No. 4, Nov. 1969, pp. 495-501.
- 3 Iglisch, R., "Exact Calculation of Laminar Boundary Layer in Longitudinal Flow over a Flat Plate with Homogeneous Suction," NACA TN 1205, Apr. 1949.
- 4 Acrivos, A., "Mass Transfer in Laminar-Boundary-Layer Flows with Finite Interfacial Velocities," *AIChE Journal*, Vol. 6, 1960, pp. 410-414.
- 5 Denny, V. E., and South, V., "Effects of Forced Flow, Noncondensables, and Variable Properties on Film Condensation of Pure and Binary Vapors near the Forward Stagnation Point of a Horizontal Cylinder," accepted for publication in the *International Journal of Heat and Mass Transfer*.
- 6 Hartnett, J. P., and Eckert, E. R. G., "Mass-Transfer Cooling in a Laminar Boundary Layer With Constant Fluid Properties," *TRANS. ASME*, Vol. 79, 1957, pp. 247-254.
- 7 Denny, V. E., Mills, A. F., and Jusonis, V. J., "Laminar Film Condensation From a Steam-Air Mixture Undergoing Forced Flow Down a Vertical Surface," *JOURNAL OF HEAT TRANSFER*, TRANS. ASME, Series C, Vol. 93, No. 3, Aug. 1971, pp. 297-304.

Thermal Conductivity of Two-Phase Systems

PRADEEP B. DESHPANDE¹ and JAMES R. COUPER²

Nomenclature

- f = volume fraction of solid phase, dimensionless
 K_c = thermal conductivity of liquid phase, Btu/hr-ft-deg F
 K_d = thermal conductivity of solid phase, Btu/hr-ft-deg F
 K_e = effective thermal conductivity of two-phase system, Btu/hr-ft-deg F
 P_1 = one-dimensional porosity, dimensionless
 P_2 = two-dimensional porosity, dimensionless
 r, t = parameters of beta distribution
 \bar{r}, \bar{t} = maximum likelihood estimates of r and t
 x = random variable defined as the one-dimensional porosity, P_1
 Pr = probability

Introduction

A REVIEW of the past work on conductance of heterogeneous systems reveals that there exist a relatively large number of approximate relationships for prediction of the effective thermal conductivity of two-phase systems. Most of these relationships utilize two parameters, e.g., thermal conductivity of the pure phases and the volume fraction of each phase, in describing the thermal conductivity of two-phase systems. Recently some investigators [1, 2]³ have attempted to relate the thermal conductivity of two-phase systems to additional parameters which describe the spatial distribution of the two phases. The object of this brief is to present a model, which accounts for the spatial distribution of solid particles, for prediction of the effective thermal conductivity of solid-liquid two-phase systems.

¹ Assistant Professor of Chemical Engineering, Howard University, Washington, D. C.

² Professor and Head, Chemical Engineering Department, University of Arkansas, Fayetteville, Ark.

³ Numbers in brackets designate References at end of technical brief.

Contributed by the Heat Transfer Division of THE AMERICAN SOCIETY OF MECHANICAL ENGINEERS. Manuscript received by the Heat Transfer Division April 5, 1971.

Theoretical Development

In a theoretical paper Tsao [1] presented a model for prediction of the two-phase thermal conductivity. He considered a cubical liquid-solid system of unit dimensions and proposed the following equation for prediction of the effective thermal conductivity:

$$K_e = \frac{1}{\int_0^1 \frac{dP_1}{K_c + (K_d - K_c)P_2}} \quad (1)$$

where P_1 is one-dimensional porosity defined as the fraction of the linear space occupied by solids and P_2 is two-dimensional porosity defined as the fraction of the area occupied by solids.

To solve equation (1), a relation between P_1 and P_2 is required. Based on a stochastic model, Tsao proposed the following equation for relating P_1 and P_2 :

$$P_2 = \frac{1}{\sqrt{2\pi}\sigma} \int_{P_1}^1 \exp\left\{-\frac{1}{2} \left[\frac{(P_1 - \mu)}{\sigma}\right]^2\right\} dP_1 \quad (2)$$

where μ and σ are the mean and the standard deviations of P_1 respectively.

Tsao suggested the normal distribution, equation (2), as an approximation to the point binomial distribution. Since this expression involves a density function which does not integrate to 1 over its sample space ($0 \leq P_1 \leq 1$), Baxley [3] suggested the beta distribution, which is the limiting case of the point binomial distribution, for relating P_1 and P_2 .

$$P_2 = \frac{\Gamma(r+t)}{\Gamma(r)\Gamma(t)} \int_{P_1}^1 x^{r-1}(1-x)^{t-1} dx \quad (3)$$

where r and t are the parameters of the beta distribution.

Before the beta distribution can be used for prediction of the effective thermal conductivity, the parameters r and t must be estimated. Leek et al. [4] conducted a study to determine the spatial distribution of particles in a solid-liquid two-phase system. The solid phase consisted of uranium-impregnated Pyrex glass cylinders. A mixture composed of 85 percent glycerol and 15 percent benzyl alcohol was used as the liquid phase. A special spectrophotometer was used for measuring P_1 . One-dimensional porosity data on two different-sized glass

Table 1 Thermal conductivity of various two-phase systems

System	K_d/K_e	f	K_e experi- mental Btu/hr- ft-°F	K_e Desh- pande Btu/hr- ft-°F
Zinc sulfate-lard	$\frac{0.354}{0.114} = 3.1$	0.1924	0.1425 [12]	0.1387
		0.2273	0.1475	0.1443
		0.2834	0.1550	0.1543
		0.4245	0.1790	0.1679
		0.4560	0.1850	0.1756
Marble-Vaseline	$\frac{1.72}{0.107} = 16.1$	0.1924	0.1375 [12]	0.1640
		0.2273	0.1450	0.1804
		0.2834	0.1640	0.2134
		0.4245	0.250	0.2168
		0.4560	0.270	0.2441
Selenium-polypropylene glycol	$\frac{3.0}{0.081} = 37$	0.1924	0.1250 [2]	0.1376
		0.2273	0.1380	0.1555
		0.2834	0.1630	0.1936
		0.4245	0.240	0.1816
		0.4560	0.260	0.2117
Aluminum oxide-polypropylene glycol	$\frac{22.5}{0.081} = 278$	0.1924	0.220 [2]	0.1728
		0.2273	0.280	0.2077
		0.2834	0.375	0.2915
		0.4245	0.760	0.2167
		0.4560	0.88	0.2711
		0.4787	0.970	0.2423

cylinders (5 mm diameter by 6 mm long and 3 mm diameter by 4 mm long) were obtained. From the data the estimates \bar{r} and \bar{l} were determined using the maximum-likelihood method [5].

To solve equation (1) for the effective thermal conductivity, the two-dimensional porosity P_2 must be known. There are three methods available for determination of P_2 from equation (3).

Determination of P_2 by Integration of Density Function. By expressing the term $(1-x)^{l-1}$ in binomial series, equation (3) can be readily evaluated to yield

$$P_2 = 1 - \frac{P_1^{\bar{r}} \Gamma(\bar{r} + \bar{l})}{\Gamma(1 - \bar{l})\Gamma(\bar{r})\Gamma(\bar{l})} \sum_{i=0}^{\infty} \frac{\Gamma(1 - \bar{l} + i)}{(\bar{i} + \bar{r})i!} P_1^i \quad (4)$$

In equation (4) the maximum-likelihood estimates \bar{r} and \bar{l} have been substituted for r and l .

Determination of P_2 by Paulson Method. Paulson [6] has shown that if a random variable u is distributed according to the F distribution, the probability that its value is less than or equal to F is given by

$$\Pr(u \leq F) \simeq \frac{1}{2} [1 + \operatorname{erf}(v/\sqrt{2})] \quad (5)$$

where

$$v = \frac{(1 - 1/9\bar{l})F^{1/3} - (1 - 1/9\bar{r})}{[(1/9\bar{l})F^{2/3} + 1/9\bar{r}]^{1/2}} \quad (6)$$

If a random variable s , on the other hand, has the beta distribution, then the probability that its value is less than or equal to P_1 can be expressed as

$$\Pr(S \leq P_1) = \Pr\left[\frac{\bar{l}}{\bar{r}} \left(\frac{s}{1-s}\right) \leq \frac{\bar{l}}{\bar{r}} \left(\frac{P_1}{1-P_1}\right)\right] \quad (7)$$

$$= \Pr(u \leq F)$$

where

$$F = \frac{\bar{l}}{\bar{r}} \left(\frac{P_1}{1-P_1}\right)$$

Equation (7) is valid since the relation between s and u is $s/(1-s) = \bar{r}u/\bar{l}$ (Dunn [7]).

Table 2 Statistical analysis of the results

	Average % error	Error variance	Average bias
Deshpande	17.96	0.495	-5.56
Tsao [1]	17.79	0.423	6.88
Baxley [2]	26.16	0.80	27.17
Jefferson [9]	22.42	0.88	18.34
Maxwell [10]	26.26	0.93	20.04
Rayleigh [11]	26.23	0.93	20.08

The two-dimensional porosity can then be calculated as

$$P_2 = 1 - \Pr(s \leq P_1)$$

$$= 1 - \frac{1}{2} [1 + \operatorname{erf}(v/\sqrt{2})] \quad (8)$$

The approximation is valid for $\bar{l} \geq 3/2$ and $P_1 > \bar{r}/\bar{r} + \bar{l}$.

Determination of P_2 from Pearson's Tables. Pearson [8] developed extensive tables for the determination of the beta probabilities. These tables can be used to obtain P_2 from P_1 .

Determination of the Effective Thermal Conductivity. After evaluating P_2 , equation (1) can be solved numerically for K_e , the effective thermal conductivity of two-phase systems.

Presentation of Results

All calculations were made on the IBM 7040 computer. The two-dimensional porosity P_2 was evaluated for the beta-distribution model by the three methods discussed in this paper.

Thermal conductivity of 10 two-phase systems was determined by equation (1) using data from the large-cylinder model as well as the small-cylinder model. As an illustration, the results for four of these systems, obtained from the large-cylinder model, are presented in Table 1.

A statistical analysis of the results from the large-cylinder model was made. The performance of the beta-distribution model was compared with that of the models of Tsao [1], Baxley [2], Jefferson [9], Maxwell [10], and Rayleigh [11]. These results are presented in Table 2.

Discussion of Results

The maximum-likelihood estimates \bar{r} and \bar{l} were calculated for the six large-cylinder samples and four small-cylinder samples using the experimental P_1 data of Leek et al. [4].

For some samples computational difficulties were encountered in the determination of P_2 by the direct-integration method and the Dunn-Paulson method. Therefore it was decided to resort to the tables of the incomplete beta function [8] for evaluating P_2 .

For all the 10 two-phase systems, the authors' large-cylinder model gave good results when the solid volume fraction f was less than 0.3. For higher-volume-fraction solids, the model was unsatisfactory (see Table 1).

One possible reason for this behavior may be the effect of particle interaction on the thermal conductivity of two-phase systems. These effects may be small in a two-phase system with low-volume-fraction solids so that the spatial-distribution model is adequate for predicting the effective thermal conductivity. The particle interaction effects may become significant, however, as the solid volume fraction is increased, so that the two-phase system can no longer be described by the spatial distribution of the solid particles alone. Consequently, the statistical model fails for high-volume-fraction solids. It may also be noted that the deviation of the model-predicted thermal conductivity from the experimental value becomes more pronounced as the ratio K_d/K_e is increased.

With small cylinders the authors' model fails completely, indicating a strong dependence of particle size on the thermal conductivity of two-phase systems.

From Table 2 it can be seen that the authors' model along

with Tsao's model gives, for $f \leq 0.30$, better results than any other model tested.

Conclusions

From the results of this study it was concluded that:

1 With large cylinders, the beta-distribution model predicted the two-phase thermal conductivity very well for low-volume-fraction solids ($f \leq 0.30$). The model failed completely for $f > 0.30$.

2 The thermal conductivity of suspensions was dependent on the size of the suspended particles.

3 Although theoretically unsound, the predictability of Tsao's model (large cylinders, $f \leq 0.30$) was as good as that of the authors' model. His model was also inadequate for high-volume-fraction solids.

Acknowledgment

The project was sponsored by the National Science Foundation through grant GK-1151. Other financial assistance was given by the Diamond Shamrock Corp. through their summer fellowship award.

References

1 Tsao, G. T., "Thermal Conductivity of Two-Phase Materials," *Industrial and Engineering Chemistry*, Vol. 53, 1961, pp. 395-397.

2 Baxley, A. L., and Couper, J. R., "Thermal Conductivity of Two-Phase Systems. Part IV: Thermal Conductivity of Suspensions," University of Arkansas Engineering Experiment Station Research Report Series, No. 8, Nov. 1966.

3 Baxley, A. L., Department of Chemical Engineering, University of Arkansas, Fayetteville, Ark., private communication, 1967.

4 Leek, L. M., Deshpande, P. B., and Couper, J. R., "Spatial Distribution of Particles in a Suspension," *Industrial and Engineering Chemistry Fundamentals*, Vol. 8, 1969, pp. 540-547.

5 Mood, A. M., and Graybill, F. A., *Introduction to Theory of Statistics*, 2nd ed., McGraw-Hill, New York, N. Y., 1963, pp. 178-186.

6 Paulson, E., "An Approximate Normalization of the Analysis of Variance Distribution," *Annals of Mathematical Statistics*, Vol. 13, 1942, pp. 233-235.

7 Dunn, J. E., Department of Mathematics, University of Arkansas, Fayetteville, Ark., private communication, 1968.

8 Pearson, K., ed., *Tables of the Incomplete Beta Function*, Cambridge University Press, Cambridge, England, 1934.

9 Jefferson, T. B., Witzell, O. W., and Sibbitt, W. L., "Thermal Conductivity of Graphite-Silicone Oil and Graphite-Water Suspensions," *Industrial and Engineering Chemistry*, Vol. 50, 1958, pp. 1589-1592.

10 Maxwell, J. C., *A Treatise on Electricity and Magnetism*, 3rd ed., Oxford University Press, London, England, 1904, pp. 435-449.

11 Rayleigh, R. J. S., "On the Influence of Obstacles Arranged in Rectangular Order Upon the Properties of a Medium," *Philosophical Magazine*, Vol. 5, No. 34, 1892, pp. 481-502.

12 Lees, C. H., "On the Thermal Conductivities of Single and Mixed Solids and Liquids and Their Variation with Temperature," *Proceedings of the Royal Society*, London, Series A, Vol. 191, 1898, pp. 339-400.

On the Freezing of Tissue

T. E. COOPER¹ and G. J. TREZEK²

Nomenclature

- c_b = blood specific heat
 k, k_f = thermal conductivity of unfrozen and frozen phases, respectively
 K_0, K_1 = modified Bessel functions
 m_b = blood mass flow rate
 r, x = position in field
 r_0, x_0 = probe radius or half-thickness
 R, L = location of frozen-unfrozen interface
 S_b, S_m = heat generation due to blood flow and metabolism, respectively
 T, T_f = temperatures in unfrozen and frozen phases, respectively
 T_b = systemic arterial blood temperature
 T_0 = tissue temperature far from probe
 T_{pc} = phase-change temperature
 T_s = probe surface temperature
 θ = nondimensional unfrozen-tissue temperature, $[(T - T_0)/(T_s - T_0)]$
 θ_f = nondimensional frozen-tissue temperature, $[(T_f - T_0)/(T_s - T_0)]$
 θ_{pc} = nondimensional phase-change temperature, $[(T_{pc} - T_0)/(T_s - T_0)]$
 Φ = nondimensional probe surface temperature, $(-k_f/k) \times [(T_{pc} - T_s)/(T_{pc} - T_0)]$
 β = blood flow parameter, $m_b c_b r_0^2/k$ or $m_b c_b x_0^2/k$
 R, X = nondimensional position, r/r_0 or x/x_0
 r^*, x^* = nondimensional ice-front location, R/r_0 or L/x_0

CRYOSURGERY, the technique of surgically destroying tissue by use of extreme cold, is a relatively new procedure which accomplishes tissue destruction by dropping the temperature of the target region below the freezing point. The frozen region, the lesion, is created by use of a cryogenic cannula (cryoprobe) which may be of various geometrical configurations. This technique has been used in a host of surgical applications [1]³ which generally require the creation of one of two basic types of lesions, namely, those formed by an external application of the probe or those formed by inserting the probe deep into the tissue. The latter type of lesion formation has been used extensively in brain surgery as a means of destroying cancerous tumors and also as a treatment for Parkinson's disease.

For the most part, cryosurgery, as presently practiced, is highly empirical [2]. Our objective is to show how the analytical methods of heat transfer can be used to predict the steady-state, or maximum, lesion size which may be formed using standard cylindrical or spherical cryoprobes. A third probe configuration, the planar case, is included mainly as a reference datum to depict geometrical effects.

Bio-Heat Transfer Equation

The steady-state energy equation governing the developed temperature field in *in-vivo* tissue takes the form

$$k\nabla^2 T + S_m + S_b = 0 \quad (1)$$

where S_m represents the effect of metabolic heat generation, S_b accounts for the addition or removal of heat by the local blood flow, and k represents the thermal conductivity of the unfrozen tissue. When equation (1) is applied to the frozen tissue the terms S_m and S_b vanish and there results $\nabla^2 T_f = 0$.

The quantity S_m is a function of the oxygen consumption rate of the tissue and, in a simplistic manner, the quantity S_b can be related to the perfusion rate, blood heat capacity, and the difference between the local tissue temperature and the blood temperature as follows:

$$S_b = m_b c_b (T_b - T) \quad (2)$$

³ Numbers in brackets designate References at end of technical brief.

¹ Assistant Professor, Department of Mechanical Engineering, Naval Postgraduate School, Monterey, Calif. Assoc. Mem. ASME.

² Associate Professor, Department of Mechanical Engineering, Thermal Systems Division, University of California, Berkeley, Calif. Mem. ASME.

Contributed by the Heat Transfer Division of THE AMERICAN SOCIETY OF MECHANICAL ENGINEERS. Manuscript received by the Heat Transfer Division April 22, 1971; revised manuscript received July 6, 1971.

with Tsao's model gives, for $f \leq 0.30$, better results than any other model tested.

Conclusions

From the results of this study it was concluded that:

1 With large cylinders, the beta-distribution model predicted the two-phase thermal conductivity very well for low-volume-fraction solids ($f \leq 0.30$). The model failed completely for $f > 0.30$.

2 The thermal conductivity of suspensions was dependent on the size of the suspended particles.

3 Although theoretically unsound, the predictability of Tsao's model (large cylinders, $f \leq 0.30$) was as good as that of the authors' model. His model was also inadequate for high-volume-fraction solids.

Acknowledgment

The project was sponsored by the National Science Foundation through grant GK-1151. Other financial assistance was given by the Diamond Shamrock Corp. through their summer fellowship award.

References

1 Tsao, G. T., "Thermal Conductivity of Two-Phase Materials," *Industrial and Engineering Chemistry*, Vol. 53, 1961, pp. 395-397.

2 Baxley, A. L., and Couper, J. R., "Thermal Conductivity of Two-Phase Systems. Part IV: Thermal Conductivity of Suspensions," University of Arkansas Engineering Experiment Station Research Report Series, No. 8, Nov. 1966.

3 Baxley, A. L., Department of Chemical Engineering, University of Arkansas, Fayetteville, Ark., private communication, 1967.

4 Leek, L. M., Deshpande, P. B., and Couper, J. R., "Spatial Distribution of Particles in a Suspension," *Industrial and Engineering Chemistry Fundamentals*, Vol. 8, 1969, pp. 540-547.

5 Mood, A. M., and Graybill, F. A., *Introduction to Theory of Statistics*, 2nd ed., McGraw-Hill, New York, N. Y., 1963, pp. 178-186.

6 Paulson, E., "An Approximate Normalization of the Analysis of Variance Distribution," *Annals of Mathematical Statistics*, Vol. 13, 1942, pp. 233-235.

7 Dunn, J. E., Department of Mathematics, University of Arkansas, Fayetteville, Ark., private communication, 1968.

8 Pearson, K., ed., *Tables of the Incomplete Beta Function*, Cambridge University Press, Cambridge, England, 1934.

9 Jefferson, T. B., Witzell, O. W., and Sibbitt, W. L., "Thermal Conductivity of Graphite-Silicone Oil and Graphite-Water Suspensions," *Industrial and Engineering Chemistry*, Vol. 50, 1958, pp. 1589-1592.

10 Maxwell, J. C., *A Treatise on Electricity and Magnetism*, 3rd ed., Oxford University Press, London, England, 1904, pp. 435-449.

11 Rayleigh, R. J. S., "On the Influence of Obstacles Arranged in Rectangular Order Upon the Properties of a Medium," *Philosophical Magazine*, Vol. 5, No. 34, 1892, pp. 481-502.

12 Lees, C. H., "On the Thermal Conductivities of Single and Mixed Solids and Liquids and Their Variation with Temperature," *Proceedings of the Royal Society*, London, Series A, Vol. 191, 1898, pp. 339-400.

On the Freezing of Tissue

T. E. COOPER¹ and G. J. TREZEK²

Nomenclature

- c_b = blood specific heat
 k, k_f = thermal conductivity of unfrozen and frozen phases, respectively
 K_0, K_1 = modified Bessel functions
 m_b = blood mass flow rate
 r, x = position in field
 r_0, x_0 = probe radius or half-thickness
 R, L = location of frozen-unfrozen interface
 S_b, S_m = heat generation due to blood flow and metabolism, respectively
 T, T_f = temperatures in unfrozen and frozen phases, respectively
 T_b = systemic arterial blood temperature
 T_0 = tissue temperature far from probe
 T_{pc} = phase-change temperature
 T_s = probe surface temperature
 θ = nondimensional unfrozen-tissue temperature, $[(T - T_0)/(T_s - T_0)]$
 θ_f = nondimensional frozen-tissue temperature, $[(T_f - T_0)/(T_s - T_0)]$
 θ_{pc} = nondimensional phase-change temperature, $[(T_{pc} - T_0)/(T_s - T_0)]$
 Φ = nondimensional probe surface temperature, $(-k_f/k) \times [(T_{pc} - T_s)/(T_{pc} - T_0)]$
 β = blood flow parameter, $m_b c_b r_0^2/k$ or $m_b c_b x_0^2/k$
 R, X = nondimensional position, r/r_0 or x/x_0
 r^*, x^* = nondimensional ice-front location, R/r_0 or L/x_0

CRYOSURGERY, the technique of surgically destroying tissue by use of extreme cold, is a relatively new procedure which accomplishes tissue destruction by dropping the temperature of the target region below the freezing point. The frozen region, the lesion, is created by use of a cryogenic cannula (cryoprobe) which may be of various geometrical configurations. This technique has been used in a host of surgical applications [1]³ which generally require the creation of one of two basic types of lesions, namely, those formed by an external application of the probe or those formed by inserting the probe deep into the tissue. The latter type of lesion formation has been used extensively in brain surgery as a means of destroying cancerous tumors and also as a treatment for Parkinson's disease.

For the most part, cryosurgery, as presently practiced, is highly empirical [2]. Our objective is to show how the analytical methods of heat transfer can be used to predict the steady-state, or maximum, lesion size which may be formed using standard cylindrical or spherical cryoprobes. A third probe configuration, the planar case, is included mainly as a reference datum to depict geometrical effects.

Bio-Heat Transfer Equation

The steady-state energy equation governing the developed temperature field in *in-vivo* tissue takes the form

$$k\nabla^2 T + S_m + S_b = 0 \quad (1)$$

where S_m represents the effect of metabolic heat generation, S_b accounts for the addition or removal of heat by the local blood flow, and k represents the thermal conductivity of the unfrozen tissue. When equation (1) is applied to the frozen tissue the terms S_m and S_b vanish and there results $\nabla^2 T_f = 0$.

The quantity S_m is a function of the oxygen consumption rate of the tissue and, in a simplistic manner, the quantity S_b can be related to the perfusion rate, blood heat capacity, and the difference between the local tissue temperature and the blood temperature as follows:

$$S_b = m_b c_b (T_b - T) \quad (2)$$

³ Numbers in brackets designate References at end of technical brief.

¹ Assistant Professor, Department of Mechanical Engineering, Naval Postgraduate School, Monterey, Calif. Assoc. Mem. ASME.

² Associate Professor, Department of Mechanical Engineering, Thermal Systems Division, University of California, Berkeley, Calif. Mem. ASME.

Contributed by the Heat Transfer Division of THE AMERICAN SOCIETY OF MECHANICAL ENGINEERS. Manuscript received by the Heat Transfer Division April 22, 1971; revised manuscript received July 6, 1971.

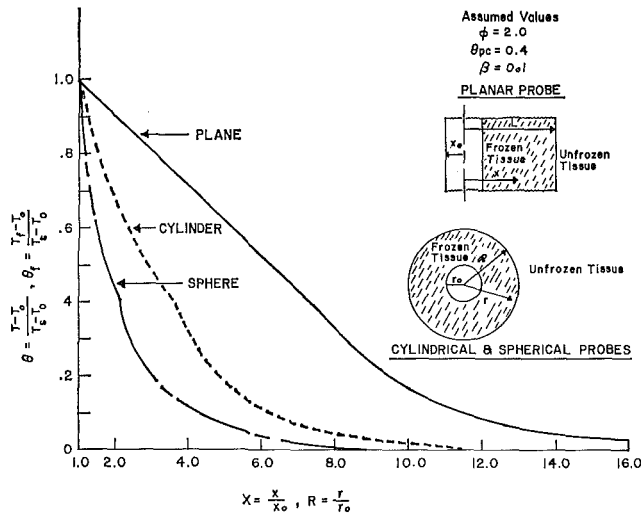


Fig. 1 Frozen phase and tissue temperature profiles for planar, cylindrical, and spherical cryoprobes for a nondimensional probe surface temperature Φ of 2, nondimensional phase-change temperature θ_{pc} of 0.4, and blood flow parameter β of 0.1

Basically, this relation is akin to that of a perfect heat exchanger in that it assumes that the blood acquires the tissue temperature as it exits a unit volume of tissue. Relations similar to equations (1) and (2) are consistent with a previous model proposed by Pennes [3] and by Perl [4]. If S_m and m_b are treated as constants, equation (1) can be rewritten as

$$k\nabla^2 T + m_b c_b (T_0 - T) = 0 \quad (3)$$

where

$$T_0 = T_b + S_m / m_b c_b$$

As an example, in the human brain, T_0 is approximately 0.5 deg C higher than the systemic arterial blood temperature T_b . Blood flow thus acts as a coolant to the brain.

Steady-State Solutions

The nature of the freezing problem requires that the system must be treated as a composite body, that is, equation (3) must be solved for both the frozen and unfrozen phases subject to the appropriate boundary conditions. The resulting solutions yield the temperature profiles in the frozen and unfrozen tissue along with the location of the ice front.

The equations governing the simple case of steady-state one-dimensional heat flow are, in nondimensional form:

$$\text{frozen phase} \quad \frac{d(R^n d\theta_f / dR)}{dR} = 0 \quad (4)$$

$$\text{unfrozen phase} \quad \frac{1}{R^n} \frac{d(R^n d\theta / dR)}{dR} - \beta\theta = 0 \quad (5)$$

where the exponent n has a value of 0, 1, or 2 for planar, cylindrical, or spherical coordinates, respectively. Thus, for a planar probe (cartesian coordinates) equation (4) is simply $d^2\theta/dX^2 = 0$, that is, R is replaced by X . The appropriate nondimensional groups are listed in the Nomenclature. The boundary conditions are: (a) At the probe surface $R = 1$, $\theta_f = 1$, (b) at the frozen-unfrozen-tissue interface $R = r^*$, $\theta_f = \theta_{pc} = \theta$, and $k_f d\theta_f / dR = k_d d\theta / dR$, (c) at large distances from the probe, $R \rightarrow \infty$, $\theta \rightarrow 0$. In the cartesian system r , R , L , and r^* are replaced by x , X , L , and x^* , respectively.

When the above boundary conditions are applied to the general solutions of equations (4) and (5) the following sets of solutions are obtained for the three coordinate systems:

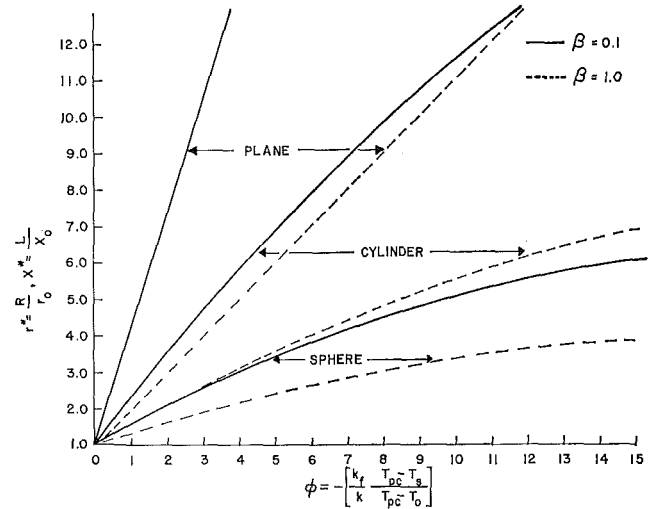


Fig. 2 Lesion size nomograms for planar, cylindrical, and spherical cryoprobes for blood flow parameter β of 0.1 and 1.0

Planar Probe

$$\theta_f = \left[\frac{\theta_{pc} - 1}{x^* - 1} \right] X + \left[\frac{x^* - \theta_{pc}}{x^* - 1} \right] \quad (6)$$

$$\theta = \theta_{pc} e^{-\sqrt{\beta}(X - x^*)} \quad (7)$$

$$x^* = 1 - \frac{\Phi}{\sqrt{\beta}} \quad (8)$$

Cylindrical Probe

$$\theta_f = [\theta_{pc} - 1] \ln R / \ln r^* + 1 \quad (9)$$

$$\theta = \theta_{pc} K_0(\sqrt{\beta} R) / K_0(\sqrt{\beta} r^*) \quad (10)$$

The solution of the following transcendental equation yields the ice-front location:

$$\Phi = \sqrt{\beta} r^* [K_1(\sqrt{\beta} r^*) / K_0(\sqrt{\beta} r^*)] \ln r^* \quad (11)$$

Spherical Probe

$$\theta_f = 1 + (\theta_{pc} - 1) \left(\frac{r^*}{1 - r^*} \right) \left(\frac{1 - R}{R} \right) \quad (12)$$

$$\theta = \frac{\theta_{pc} r^*}{R} e^{-\sqrt{\beta}(R - r^*)} \quad (13)$$

$$r^* = \frac{(\sqrt{\beta} - 1)}{2\sqrt{\beta}} + \left[\frac{(1 - \sqrt{\beta})^2}{4\beta} + \frac{(1 + \Phi)}{\sqrt{\beta}} \right]^{1/2} \quad (14)$$

Discussion

A comparison of the nondimensional temperature profiles for the planar, cylindrical, and spherical systems is shown in Fig. 1 for a value of β equal to 0.1. The quantity $\beta = m_b c_b r_0^2 / k$, which shall be referred to as the blood flow parameter, results from nondimensionalizing the governing bio-heat transfer equation. In this sense it is unique to heat transfer in an *in-vivo* system. However, it is important to note that β is geometry-dependent and hence cannot be construed as a property of the system. Rather, it is a relative comparison of convective effects due to blood flow and tissue conductive effects. It is analogous to the classical Biot number and may be viewed as a "bio-Biot number." The β value used in Fig. 1 is germane to typical cryosurgical applications.

The location of the ice-tissue interface for each of the three coordinate systems is shown in Fig. 2. This type of representation can be used as a convenient surgical nomogram. For ex-

ample, assuming typical values of $T_0 = 38$ deg C, $T_{pc} = 0$ deg C, $T_s = -75$ deg C, $k_f/k = 3$, and $\beta \simeq 0.1$ for a probe radius or half-thickness of 2 mm, the following ice-front locations are found: (a) For the planar probe $L = 39.6$ mm, (b) for the cylindrical probe $R = 15.2$ mm, and (c) for the spherical probe $R = 7.4$ mm. The assumed thermal-conductivity ratio of 3 for frozen and unfrozen tissue is consistent with existing biological thermal-conductivity data [5-7].

Thermal conductivity k , blood flow m_b , and metabolic heat generation S_m are temperature-dependent and for brain tissue the latter two quantities vary with a Q_{10} of between two and three [8]. A Q_{10} of 3 (the notation is ostensibly that of the physiologist) implies that for each 10 deg C decrease in temperature, m_b or S_m drops by a factor of 3. The implications of treating k , m_b , and S_m equal to constants have been previously considered [9].

The medium into which the ice front propagates is actually two components, blood and tissue, and hence the question of whether this model actually describes the freezing process can be raised. Since the thermal properties of the two components are essentially identical and the blood velocity in the capillaries is small, it appears that the proposed model serves as a good first approximation. General agreement between the predicted ice-front location and the very limited available experimental data for a hemispherical cannula [10] has been achieved. Other physiological considerations along with an adaptation of the freezing results to the development of a cryosurgical atlas have been reported [11, 12].

It is hoped that this attempt to provide a fundamental analytical basis to a heretofore totally empirical science will aid cryosurgeons in selecting appropriate probe geometries, sizes, and temperature ranges for the creation of controlled surgical lesions.

References

- 1 Galton, L., "Sub-Zero Surgery," *Family Circle Magazine*, March 1968.
- 2 Cooper, I. S., "Cryogenic Surgery," *Engineering in the Practice of Medicine*, B. L. Segal and D. G. Kilpatrick, eds., The Williams and Wilkins Co., Baltimore, Md., 1967, pp. 122-141.
- 3 Pennes, H. H., "Analysis of Tissue and Arterial Blood Temperatures in the Resting Human Forearm," *J. Appl. Physiol.*, Vol. 1, 1948, pp. 93-122.
- 4 Perl, W., "Heat and Matter Distribution in Body Tissues and the Determination of Tissue Blood Flow by Local Clearance Methods," *J. Theoret. Biol.*, Vol. 2, 1962, pp. 201-235.
- 5 Cooper, T. E., and Trezek, G. J., "A Probe Technique for Determining the Thermal Conductivity of Tissue," *JOURNAL OF HEAT TRANSFER*, TRANS. ASME, Series C, Vol. 94, No. 2, May 1972, pp. 133-140.
- 6 Cooper, T. E., and Trezek, G. J., "Correlation of Thermal Properties of Some Human Tissue with Water Content," *Aerospace Medicine*, Vol. 42, No. 1, Jan. 1971, pp. 24-27.
- 7 Poppendiek, H. F., et al., "Thermal Conductivity Measurements and Predictions for Biological Fluids and Tissue," *Cryobiology*, Vol. 3, 1966, pp. 318-327.
- 8 Rosomoff, H. L., and Holaday, D. A., "Cerebral Blood Flow and Cerebral Oxygen Consumption during Hypothermia," *Am. J. Physiol.*, Vol. 179, 1954, pp. 85-88.
- 9 Trezek, G. J., and Jewett, D. L., "Nodal Network Simulation of Transient Temperature Fields from Cooling Sources in Anesthetized Brain," *IEEE Trans. on Bio-Medical Engineering*, Vol. BME-17, No. 4, Oct. 1970, pp. 281-286.
- 10 Rutkin, R. B., and Barish, E. Z., "Localized Thermal Distributions in Brain," *Proc. 17th Annual Conf. on Engineering in Medicine and Biology*, 1964.
- 11 Cooper, T. E., and Trezek, G. J., "Analytical Prediction of the Temperature Field Emanating from a Cryosurgical Cannula," *Cryobiology*, Vol. 7, No. 2-3, 1970, pp. 79-93.
- 12 Cooper, T. E., and Trezek, G. J., "Rate of Lesion Growth around Spherical and Cylindrical Cryoprobes," *Cryobiology*, Vol. 7, No. 4-6, 1971, pp. 183-190.

Critical Rayleigh Numbers for Natural Convection of Water Confined in Square Cells With L/D From 0.5 to 8¹

Chi Tien² and Yin-Chao Yen.³ In a recent article, Heitz and Westwater presented experimental results on the thermal instability of water confined in a rectangular cavity subject to adverse temperature gradient. The study was focused on the effect of L/D (L = vertical dimension of liquid layer and D the horizontal dimension of the cavity) on the onset of convection. Another aspect of the study was to determine the effect due to the anomalous temperature-density behavior of water, which exhibits a maximum density at approximately 4 deg C. It is to this density-inversion effect that the present discussion is directed.

To account for this maximum-density effect, Heitz and Westwater utilized a modified Rayleigh number originally proposed by Boger and Westwater [14].⁴ The definition was proposed on an empirical basis and became identical with the conventional definition, if the lower surface temperature coincides with the maximum density. They concluded that their experimental results disagree with the theoretical value obtained by Tien [17].

A number of investigations concerning the maximum-density effect on thermal instability have, in fact, been carried out in addition to the work of Tien [17]. Because of the incomplete references made by Heitz and Westwater, it may be in order to recite these investigations briefly. Both Debler [18] and Vernois [19] as well as Tien [17] studied this problem by assuming the following temperature-density relationship:

$$\rho - \rho_{\max} = -\rho_{\max}\gamma(T - T_{\max})^2 \quad (1)$$

The onset of convection begins when the Rayleigh number defined as

$$N_{Ra} = \frac{(2\gamma_1 A \Delta T)g(\Delta T)d^3}{\nu\kappa} \quad (2)$$

exceeds its critical value which is a function of the parameter A given as

$$A = \frac{T_l - T_{\max}}{T_l - T_u} \quad (3)$$

For $A < 0.25$, the asymptotic expression of $(N_{Ra})_{cr}$ is found to be

$$(N_{Ra})_{cr} \sim 1186.4 \left(\frac{1}{A}\right)^4 \quad (4)$$

A more recent study by Sun, Tien, and Yen [20] extended the earlier studies by considering a density-temperature relationship of the following type:

$$\frac{\rho - \rho_{\max}}{\rho_{\max}} = -\gamma_1(T - T_{\max})^2 - \gamma_2(T - T_{\max})^3 \quad (5)$$

The corresponding Rayleigh number becomes

$$N_{Ra} = \frac{(2\gamma_1 A \Delta T)g(\Delta T)d^3 \left(1 + \frac{3}{2} \frac{\gamma_2}{\gamma_1} A \Delta T\right)}{\nu\kappa} \quad (6)$$

and the critical value is found to be a function of two parameters, λ_1 and λ_2 , defined as

$$\lambda_1 = \left(-\frac{1}{A}\right) \left[\frac{1 + 3 \frac{\gamma_2}{\gamma_1} A \Delta T}{1 + \frac{3}{2} \frac{\gamma_2}{\gamma_1} A \Delta T} \right] \quad (7)$$

$$\lambda_2 = \frac{1}{A^2} \frac{\frac{3}{2} \frac{\gamma_2}{\gamma_1} A \Delta T}{1 + \frac{3}{2} \frac{\gamma_2}{\gamma_1} A \Delta T} \quad (8)$$

The theoretically calculated critical Rayleigh numbers were found to agree, on the average, within 8 percent of the experimental value as shown in [20]. It is perhaps worthwhile to mention that all these analyses [17-20] were based on the principle of linear stability analysis, and the procedures used for calculating the critical Rayleigh numbers were essentially the same used for the classical thermal instability problem. The application of linear stability analysis in predicting thermal instability, in general, has been rather successful as indicated by the good agreement between theoretical analysis and experimental observation in most of the previous works.

This argument, obviously, is at variance with the contention of Heitz and Westwater that their results disagree with the theoretical results based on linear analysis. The discussers are of the opinion that these comparisons were largely meaningless because of the significant difference between the experimental conditions of the measurement and the basic assumptions used in the analysis. One of the basic assumptions used in the analyses of [17-20] is that the liquid layer is of infinite extent, i.e., $L/D \rightarrow 0$, while the experiments were conducted with L/D ranging from 0.5 to 8. In this connection, it is difficult to comprehend the true significance of Fig. 15 of the discussed paper. In this figure, which was labeled as "Comparison of new data with results of Tien," the Rayleigh number is plotted against L/D , while in Tien's work [17], L/D was not considered as a variable at all because of the assumption of the fluid layer being confined in

¹ By W. L. Heitz and J. W. Westwater, published in May, 1971, issue of the JOURNAL OF HEAT TRANSFER, TRANS. ASME, Series C, Vol. 93, No. 2, pp. 188-196.

² Professor and Chairman, Department of Chemical Engineering and Materials Science, Syracuse University, Syracuse, N. Y.

³ Chief, Physical Sciences Branch, U. S. Army Cold Regions Research and Engineering Laboratory; also Visiting Professor of Chemical Engineering, University of New Hampshire, Durham, N. H.

⁴ Numbers in brackets designate References in the article under discussion as well as Additional References at end of discussion.

extent. There also remains the question of the difference in the definition of the Rayleigh number between that based on the result of linear stability analysis and the empirical one of Boger and Westwater, and it was not clear which definition was used in comparison.

Another statement also deserves comment: "Tien and Yen state that the critical Rayleigh number of the onset of convection varies with the temperature of heated boundary. This possibility was examined also in the present study. The results, Fig. 12, show no effect, nor does the temperature of the cold boundary affect the critical Rayleigh number." The critical Rayleigh number based on linear stability analysis is found to be a function of parameter A defined by equation (3), and is not just a function of heated boundary temperature. The most one can conclude from Fig. 12 appears to be that the empirically defined Rayleigh number used by the authors is independent of the heated boundary temperature. Even this conclusion is perhaps somewhat questionable, since only very few data points among those indicated in the lower curve of this figure were obtained when maximum-density effect was involved. In any event, it is difficult to conceive how this conclusion can be used to either invalidate or, for that matter, substantiate the results based on linear stability analysis.

A more interesting point of Heitz and Westwater's work is the revelation of its disagreement with the experimental data reported by Yen [16]. This is difficult to explain since both investigations were carried out with considerable care, and in view of the agreement of both sets of measurements to other investigators in the limiting case when the maximum-density effect is absent. Heitz and Westwater reported the agreement of their data with that of Schmidt and Silveston [9]. Yen's result, however, was also found to agree with earlier work in the limiting case of no density inversion. The fact that Heitz and Westwater's results agree with those of Catton and Edwards [10] does not add credence to the accuracy of their data insofar as the effect of maximum density is concerned, since the substance employed by Catton and Edwards in their experiment exhibits no density-inversion effect. It therefore appears that only through further experimentation can this controversy be clearly resolved. In this connection, it may be worthwhile to point out that in both Yen's work and that of Heitz and Westwater, a phase change occurred continuously during the course of measurements. The experimental conditions, therefore, can be described, at best, as pseudo-steady-state. In the future, it may be advisable to conduct measurements without this complication so that a true steady state can be realized.

Additional References

- 18 Debler, W. R., "On the Analogy between Thermal and Rotational Hydrodynamic Stability," *Journal of Fluid Mechanics*, Vol. 24, Part 1, 1966, pp. 165-176.
- 19 Vernois, G., "Penetrative Convection," *Astrophysical Journal*, Vol. 137, 1963, pp. 641-663.
- 20 Sun, Z. S., Tien, Chi, and Yen, Yin-Chao, "Thermal Instability of a Horizontal Layer of Liquid with Maximum Density," *AIChE Journal*, Vol. 15, No. 6, 1969, pp. 910-915.

Authors' Closure

We appreciate the interest shown by Tien and Yen in our work and their discussion of our recent article.

In our introduction we presented a brief and representative summary of previous contributions to the study of natural convection in confined liquids. We acknowledge and are aware of many valuable contributions in addition to those mentioned.

The models of Davis [8] and Charlson and Sani [15] still appear to be among the most rigorous thus far presented. The "theory" of Tien, Yen, and co-workers is not, in fact, theory, but rather is mathematical modeling. The results of such modeling should not be referred to as "theoretical." For example, the assumption that the density of water depends on temperature as a parabolic

function, symmetric about 4 deg C, is not a physical fact, although it is very convenient mathematically.

The article by Heitz and Westwater is the presentation of an experimental study in which multiple, independent means were used to detect critical Rayleigh numbers. The results, as indicated in the title of the article, were determined for L/D from 0.5 to 8 and at no point were they extrapolated to an L/D of 0. We are confident of our results and have compared them with the results of other investigators (Fig. 13) to illustrate areas of agreement and areas of disagreement.

It is quite true that Tien did not include the parameter L/D in his work [17]; a basic assumption is that $L/D \cong 0$. It was Tien, however, who chose to substantiate his work by comparing his results with experimental data, obtained by Boger and Westwater [14], for which L/D ranged up to 3. Our Fig. 15, "Comparison of new data with results of Tien," was included to illustrate that Tien's model does not appear to be valid for $L/D > 0$. The critical Rayleigh numbers, labeled "Tien model," were calculated using Tien's model and the data presented by Tien in [17, Table 1]. As mentioned in our paper, incorrect values of liquid depth d were used by Tien. Correct values were used in our Fig. 15.

We are aware that Tien, Yen, and co-workers expressed the critical Rayleigh number in terms of the parameter A which is a function of the upper and lower boundary temperatures and the maximum-density temperature. Yen [16] also presented the empirical relationship

$$Ra_{cl} = 1.42 \times 10^4 \exp(-6.64 \times 10^{-2} T_s)$$

where T_s is the temperature of the heated boundary. We do not feel that the critical Rayleigh number is correctly represented by the lower boundary temperature alone, or even by the parameter A alone. Our Fig. 14, "Effect of L/D on Ra_{cl} ; data of Yen," was plotted using the data of Yen [16, Table 1], and clearly shows that the critical Rayleigh number is a function of L/D as well as boundary temperatures, even as $L/D \rightarrow 0$. Our Fig. 12 further shows that the critical Rayleigh numbers are not a sole function of the heated boundary, but rather a function of temperature differences and L/D .

Reasons for the disagreement between Yen's experimental data and the data of other investigators, Fig. 13, are not known at this time. We believe that all investigations were carried out with considerable care and agree with Tien and Yen that a possible explanation lies in the fact that data were obtained at pseudo steady state. In the region of interest, our critical Rayleigh numbers were obtained under conditions such that, in terms of interfacial motion, phase change could not be detected. During the final 30 min of approach to transition, Ra was also constant to within measuring accuracy.

On the Rohsenow Pool-Boiling Correlation¹

W. M. Rohsenow.² Frost and Li present new data for pool-boiling of water at sub-atmospheric pressures (0.92-14.45 psia) and plot it on the correlating coordinates suggested in their reference [1] in 1951. At that time available Prandtl number data was wrong and led to an exponent on the Prandtl number

¹ By C. W. Frost and K. W. Li, published in the May, 1971, issue of the *JOURNAL OF HEAT TRANSFER*, TRANS. ASME, Series C, Vol. 93, No. 2, pp. 232-234.

² Professor, Department of Mechanical Engineering, Massachusetts Institute of Technology, Cambridge, Mass.

extent. There also remains the question of the difference in the definition of the Rayleigh number between that based on the result of linear stability analysis and the empirical one of Boger and Westwater, and it was not clear which definition was used in comparison.

Another statement also deserves comment: "Tien and Yen state that the critical Rayleigh number of the onset of convection varies with the temperature of heated boundary. This possibility was examined also in the present study. The results, Fig. 12, show no effect, nor does the temperature of the cold boundary affect the critical Rayleigh number." The critical Rayleigh number based on linear stability analysis is found to be a function of parameter A defined by equation (3), and is not just a function of heated boundary temperature. The most one can conclude from Fig. 12 appears to be that the empirically defined Rayleigh number used by the authors is independent of the heated boundary temperature. Even this conclusion is perhaps somewhat questionable, since only very few data points among those indicated in the lower curve of this figure were obtained when maximum-density effect was involved. In any event, it is difficult to conceive how this conclusion can be used to either invalidate or, for that matter, substantiate the results based on linear stability analysis.

A more interesting point of Heitz and Westwater's work is the revelation of its disagreement with the experimental data reported by Yen [16]. This is difficult to explain since both investigations were carried out with considerable care, and in view of the agreement of both sets of measurements to other investigators in the limiting case when the maximum-density effect is absent. Heitz and Westwater reported the agreement of their data with that of Schmidt and Silveston [9]. Yen's result, however, was also found to agree with earlier work in the limiting case of no density inversion. The fact that Heitz and Westwater's results agree with those of Catton and Edwards [10] does not add credence to the accuracy of their data insofar as the effect of maximum density is concerned, since the substance employed by Catton and Edwards in their experiment exhibits no density-inversion effect. It therefore appears that only through further experimentation can this controversy be clearly resolved. In this connection, it may be worthwhile to point out that in both Yen's work and that of Heitz and Westwater, a phase change occurred continuously during the course of measurements. The experimental conditions, therefore, can be described, at best, as pseudo-steady-state. In the future, it may be advisable to conduct measurements without this complication so that a true steady state can be realized.

Additional References

- 18 Debler, W. R., "On the Analogy between Thermal and Rotational Hydrodynamic Stability," *Journal of Fluid Mechanics*, Vol. 24, Part 1, 1966, pp. 165-176.
- 19 Vernois, G., "Penetrative Convection," *Astrophysical Journal*, Vol. 137, 1963, pp. 641-663.
- 20 Sun, Z. S., Tien, Chi, and Yen, Yin-Chao, "Thermal Instability of a Horizontal Layer of Liquid with Maximum Density," *AIChE Journal*, Vol. 15, No. 6, 1969, pp. 910-915.

Authors' Closure

We appreciate the interest shown by Tien and Yen in our work and their discussion of our recent article.

In our introduction we presented a brief and representative summary of previous contributions to the study of natural convection in confined liquids. We acknowledge and are aware of many valuable contributions in addition to those mentioned.

The models of Davis [8] and Charlson and Sani [15] still appear to be among the most rigorous thus far presented. The "theory" of Tien, Yen, and co-workers is not, in fact, theory, but rather is mathematical modeling. The results of such modeling should not be referred to as "theoretical." For example, the assumption that the density of water depends on temperature as a parabolic

function, symmetric about 4 deg C, is not a physical fact, although it is very convenient mathematically.

The article by Heitz and Westwater is the presentation of an experimental study in which multiple, independent means were used to detect critical Rayleigh numbers. The results, as indicated in the title of the article, were determined for L/D from 0.5 to 8 and at no point were they extrapolated to an L/D of 0. We are confident of our results and have compared them with the results of other investigators (Fig. 13) to illustrate areas of agreement and areas of disagreement.

It is quite true that Tien did not include the parameter L/D in his work [17]; a basic assumption is that $L/D \cong 0$. It was Tien, however, who chose to substantiate his work by comparing his results with experimental data, obtained by Boger and Westwater [14], for which L/D ranged up to 3. Our Fig. 15, "Comparison of new data with results of Tien," was included to illustrate that Tien's model does not appear to be valid for $L/D > 0$. The critical Rayleigh numbers, labeled "Tien model," were calculated using Tien's model and the data presented by Tien in [17, Table 1]. As mentioned in our paper, incorrect values of liquid depth d were used by Tien. Correct values were used in our Fig. 15.

We are aware that Tien, Yen, and co-workers expressed the critical Rayleigh number in terms of the parameter A which is a function of the upper and lower boundary temperatures and the maximum-density temperature. Yen [16] also presented the empirical relationship

$$Ra_{cl} = 1.42 \times 10^4 \exp(-6.64 \times 10^{-2} T_s)$$

where T_s is the temperature of the heated boundary. We do not feel that the critical Rayleigh number is correctly represented by the lower boundary temperature alone, or even by the parameter A alone. Our Fig. 14, "Effect of L/D on Ra_{cl} ; data of Yen," was plotted using the data of Yen [16, Table 1], and clearly shows that the critical Rayleigh number is a function of L/D as well as boundary temperatures, even as $L/D \rightarrow 0$. Our Fig. 12 further shows that the critical Rayleigh numbers are not a sole function of the heated boundary, but rather a function of temperature differences and L/D .

Reasons for the disagreement between Yen's experimental data and the data of other investigators, Fig. 13, are not known at this time. We believe that all investigations were carried out with considerable care and agree with Tien and Yen that a possible explanation lies in the fact that data were obtained at pseudo steady state. In the region of interest, our critical Rayleigh numbers were obtained under conditions such that, in terms of interfacial motion, phase change could not be detected. During the final 30 min of approach to transition, Ra was also constant to within measuring accuracy.

On the Rohsenow Pool-Boiling Correlation¹

W. M. Rohsenow.² Frost and Li present new data for pool-boiling of water at sub-atmospheric pressures (0.92-14.45 psia) and plot it on the correlating coordinates suggested in their reference [1] in 1951. At that time available Prandtl number data was wrong and led to an exponent on the Prandtl number

¹ By C. W. Frost and K. W. Li, published in the May, 1971, issue of the *JOURNAL OF HEAT TRANSFER*, TRANS. ASME, Series C, Vol. 93, No. 2, pp. 232-234.

² Professor, Department of Mechanical Engineering, Massachusetts Institute of Technology, Cambridge, Mass.

Heat Transfer Due to Combined Free and Forced Convection in a Horizontal and Isothermal Tube¹

D. R. Oliver,² It is good to see the results of natural convection heat transfer work carried out in a tube of low L/D (28.4). I feel that the authors are correct in asserting that the L/D term is of little importance. In one of our papers [15] subsequent to that quoted by the authors [2], the L/D term does not appear and the result is an equation rather similar to that quoted by Jackson, Spurlock, and Purdy [8]. I should like to have seen this equation tested by the type of plot shown in Fig. 3 (which greatly enlarges the "scatter" due to the use of Nu^3 rather than Nu as in Figs. 4, 5, and 6).

The authors have utilised a wide range of experimental data in arriving at their final equation, which may be written as

$$Nu \left(\frac{\mu_w}{\mu_b} \right)^{0.14} = 1.75(Gz + 0.12Gz^{0.88}Gr^{0.29}Pr^{0.32})^{0.33}$$

However, I am not too happy with the apparent importance of the Graetz number (power 0.88) in the natural convection term. All our work in tubes of high L/D showed natural convection effects dying away at high flow rates. I can understand the argument of Brown and Thomas that high mass flow rates should permit the natural convection driving forces to remain high, but would expect the power on Gz to be much lower than 1.33 or 0.88. The inclusion of a function of Gz in the natural convection term also implies that no convective heat transfer will occur in the absence of forced flow. In fact this heat transfer will be quite large whilst significant temperature gradients remain within the liquid.

There is general agreement over the omission of the L/D term, but a new problem has arisen regarding the relative importance of Gz on the one hand, and $(Gr Pr)$ on the other, in the natural convection term. Recent reviews [16] have not focussed attention on this problem, but workers active in the field should regard it as worthy of further attention. The authors are to be complimented on an interesting and stimulating paper.

Additional References

- 15 Oliver, D. R., and Jenson, V. G., *Chem. Eng. Sci.*, Vol. 19, 1964, p. 115.
- 16 Porter, J. E., *Trans. Inst. Chem. Engrs. (London)*, Vol. 49, No. 1, 1971.

¹ By C. A. Depew and S. E. August, published in the November, 1971, issue of the *JOURNAL OF HEAT TRANSFER, TRANS. ASME, Series C*, Vol. 93, No. 4, pp. 380-390.

² Senior Lecturer in Chemical Engineering, The University of Birmingham, Birmingham, England.

³ Numbers in brackets designate References in the article under discussion as well as Additional References at end of discussion.

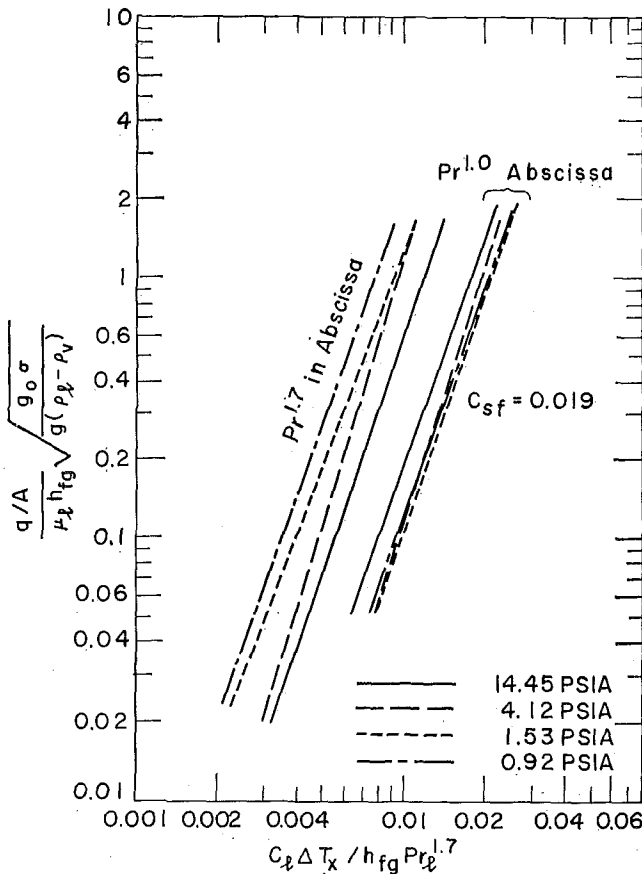


Fig. 1 Comparison of the Rohsenow correlations

of 1.7. This remains correct for all other fluids but for water it should be 1.0.

The attached Fig. 1 is the authors' Fig. 6 with their data curves plotted on the same coordinates except the $Pr^{1.7}$ is changed to $Pr^{1.0}$ in the abscissa. Agreement with the correlation is then excellent. The data is correlated by

$$\frac{C_1 \Delta T_x}{h_{f0}} = 0.019 \left(\frac{q/A}{\mu_b h_{f0}} \sqrt{\frac{g_0 \sigma}{g(\rho_l - \rho_v)}} \right)^{0.33} Pr_l^{1.0}$$

The coefficient 0.019 is valid for the surface used in these tests and has been found to depend on the cavity-size distribution in the solid surface.

Authors' Closure

The authors wish to thank Professor Rohsenow for his interest and suggestions for this paper. The authors also agree that with the exponent of Prandtl number equal to 1.0 the Rohsenow pool-boiling equation would better correlate the data presented in this work.

Heat Transfer Due to Combined Free and Forced Convection in a Horizontal and Isothermal Tube¹

D. R. Oliver,² It is good to see the results of natural convection heat transfer work carried out in a tube of low L/D (28.4). I feel that the authors are correct in asserting that the L/D term is of little importance. In one of our papers [15] subsequent to that quoted by the authors [2], the L/D term does not appear and the result is an equation rather similar to that quoted by Jackson, Spurlock, and Purdy [8]. I should like to have seen this equation tested by the type of plot shown in Fig. 3 (which greatly enlarges the "scatter" due to the use of Nu^3 rather than Nu as in Figs. 4, 5, and 6).

The authors have utilised a wide range of experimental data in arriving at their final equation, which may be written as

$$Nu \left(\frac{\mu_w}{\mu_b} \right)^{0.14} = 1.75(Gz + 0.12Gz^{0.88}Gr^{0.29}Pr^{0.32})^{0.33}$$

However, I am not too happy with the apparent importance of the Graetz number (power 0.88) in the natural convection term. All our work in tubes of high L/D showed natural convection effects dying away at high flow rates. I can understand the argument of Brown and Thomas that high mass flow rates should permit the natural convection driving forces to remain high, but would expect the power on Gz to be much lower than 1.33 or 0.88. The inclusion of a function of Gz in the natural convection term also implies that no convective heat transfer will occur in the absence of forced flow. In fact this heat transfer will be quite large whilst significant temperature gradients remain within the liquid.

There is general agreement over the omission of the L/D term, but a new problem has arisen regarding the relative importance of Gz on the one hand, and $(Gr Pr)$ on the other, in the natural convection term. Recent reviews [16] have not focussed attention on this problem, but workers active in the field should regard it as worthy of further attention. The authors are to be complimented on an interesting and stimulating paper.

Additional References

- 15 Oliver, D. R., and Jenson, V. G., *Chem. Eng. Sci.*, Vol. 19, 1964, p. 115.
- 16 Porter, J. E., *Trans. Inst. Chem. Engrs. (London)*, Vol. 49, No. 1, 1971.

¹ By C. A. Depew and S. E. August, published in the November, 1971, issue of the *JOURNAL OF HEAT TRANSFER, TRANS. ASME, Series C*, Vol. 93, No. 4, pp. 380-390.

² Senior Lecturer in Chemical Engineering, The University of Birmingham, Birmingham, England.

³ Numbers in brackets designate References in the article under discussion as well as Additional References at end of discussion.

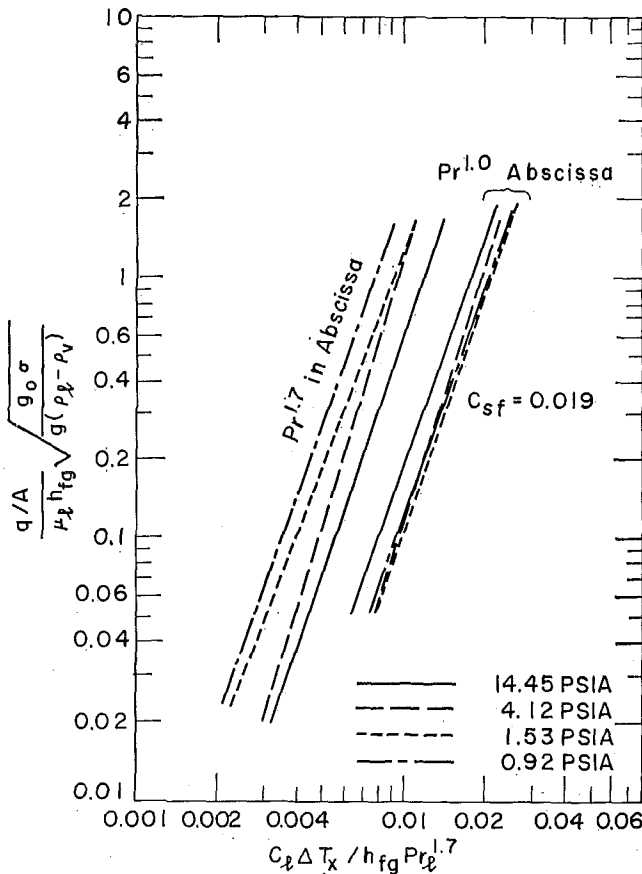


Fig. 1 Comparison of the Rohsenow correlations

of 1.7. This remains correct for all other fluids but for water it should be 1.0.

The attached Fig. 1 is the authors' Fig. 6 with their data curves plotted on the same coordinates except the $Pr^{1.7}$ is changed to $Pr^{1.0}$ in the abscissa. Agreement with the correlation is then excellent. The data is correlated by

$$\frac{C_1 \Delta T_x}{h_{f0}} = 0.019 \left(\frac{q/A}{\mu_b h_{f0}} \sqrt{\frac{g_0 \sigma}{g(\rho_l - \rho_v)}} \right)^{0.33} Pr_l^{1.0}$$

The coefficient 0.019 is valid for the surface used in these tests and has been found to depend on the cavity-size distribution in the solid surface.

Authors' Closure

The authors wish to thank Professor Rohsenow for his interest and suggestions for this paper. The authors also agree that with the exponent of Prandtl number equal to 1.0 the Rohsenow pool-boiling equation would better correlate the data presented in this work.